

Yongdong Xu
Xiu-Tian Yan

Engineering Materials
and Processes

Chemical Vapour Deposition

An Integrated Engineering Design
for Advanced Materials

 Springer

Engineering Materials and Processes

Series Editor

Professor Brian Derby, Professor of Materials Science
Manchester Materials Science Centre, Grosvenor Street, Manchester, M1 7HS, UK

Other titles published in this series

Fusion Bonding of Polymer Composites
C. Ageorges and L. Ye

Composite Materials
D.D.L. Chung

Titanium
G. Lütjering and J.C. Williams

Corrosion of Metals
H. Kaesche

Corrosion and Protection
E. Bardal

Intelligent Macromolecules for Smart Devices
L. Dai

Microstructure of Steels and Cast Irons
M. Durand-Charre

*Phase Diagrams and Heterogeneous
Equilibria*
B. Predel, M. Hoch and M. Pool

*Computational Mechanics of Composite
Materials*
M. Kamiński

*Gallium Nitride Processing for Electronics,
Sensors and Spintronics*
S.J. Pearton, C.R. Abernathy and F. Ren

Materials for Information Technology
E. Zschech, C. Whelan and T. Mikolajick

Fuel Cell Technology
N. Sammes

Casting: An Analytical Approach
A. Reikher and M.R. Barkhudarov

*Computational Quantum Mechanics for
Materials Engineers*
L. Vitos

Modelling of Powder Die Compaction
P.R. Brewin, O. Coube, P. Doremus
and J.H. Tweed

Silver Metallization
D. Adams, T.L. Alford and J.W. Mayer

Microbiologically Influenced Corrosion
R. Javaherdashti

*Modeling of Metal Forming and Machining
Processes*
P.M. Dixit and U.S. Dixit

*Electromechanical Properties in Composites
Based on Ferroelectrics*
V.Yu. Topolov and C.R. Bowen

Charged Semiconductor Defects
E.G. Seebauer and M.C. Kratzer

*Modelling Stochastic Fibrous Materials
with Mathematica®*
W.W. Sampson

*Ferroelectrics in Microwave Devices, Circuits
and Systems*
S. Gevorgian

Porous Semiconductors
F. Kochergin and H. Föll

Yongdong Xu · Xiu-Tian Yan

Chemical Vapour Deposition

An Integrated Engineering Design for
Advanced Materials

 Springer

Prof. Yongdong Xu†
late of Northwestern Polytechnical
University
School of Materials Science & Engineering
710072 Xian
China

Dr. Xiu-Tian Yan
University of Strathclyde
Department of Design, Manufacture
and Engineering Management
75 Montrose St.
Glasgow G1 1XJ
UK

x.yan@strath.ac.uk

ISSN 1619-0181

ISBN 978-1-84882-893-3

e-ISBN 978-1-84882-894-0

DOI 10.1007/978-1-84882-894-0

Springer London Dordrecht Heidelberg New York

British Library Cataloguing in Publication Data

A catalogue record for this book is available from the British Library

Library of Congress Control Number: 2009940607

© Springer-Verlag London Limited 2010

Apart from any fair dealing for the purposes of research or private study, or criticism or review, as permitted under the Copyright, Designs and Patents Act 1988, this publication may only be reproduced, stored or transmitted, in any form or by any means, with the prior permission in writing of the publishers, or in the case of reprographic reproduction in accordance with the terms of licenses issued by the Copyright Licensing Agency. Enquiries concerning reproduction outside those terms should be sent to the publishers.

The use of registered names, trademarks, etc., in this publication does not imply, even in the absence of a specific statement, that such names are exempt from the relevant laws and regulations and therefore free for general use.

The publisher makes no representation, express or implied, with regard to the accuracy of the information contained in this book and cannot accept any legal responsibility or liability for any errors or omissions that may be made.

Cover design: eStudioCalamar, Figueres/Berlin

Printed on acid-free paper

Springer is part of Springer Science+Business Media (www.springer.com)

Foreword

Coatings and thin films impinge upon every aspect of modern life.

As I look around my office the first thing I see is the rather low-tech coating on the wall in front of me. Paint protects the wall against dirt and moisture and also gives it a decorative finish. Then I notice some photos which have coatings of inks and dyes that transform a piece of plain paper into an image that generates memories and brings immense pleasure. The lightbulb which brightens the room has an internal coating that produces light at a low temperature. My eyeglass lenses have an anti-reflection coating that enhances my vision and protects the plastic lenses against scratching. And although I cannot see them, I am aware of other coatings that form an integral part of my everyday life. My computer is made up of many thousands of semiconductor devices all of which have a range of coating layers, as does the screen on which I can see what I am typing. The external hard drive that I am saving this file on has composite thin films that allow megabits of information to be stored. And the broadband connection that lets me send the file to a colleague will have coated optical fibres to provide fast and efficient communication.

Yes, indeed, society today couldn't exist without coatings and thin films, particularly high-tech ones. In fact, the annual worldwide market for thin film technology is worth several hundred billion dollars and is growing in excess of 10% per annum. Of that market about 50% is for data storage, 30% is in the semiconductor industry, 6% is with telecommunications, and 3% is for optical coatings. This 89% constitutes the high-tech 'glamour' sector of the market. The remaining 11% may not be quite as glamorous or as high profile, but it nevertheless plays a vitally important role in our society. And what is that 11%? It is the domain of engineering coatings.

Engineering coatings also impinge upon our everyday lives. Sometimes we might be aware of them when, for example, we use a hard-coated bit to drill into a concrete wall, or even when we shave with a razor blade that has a diamond-like coating to prolong its life. On other occasions we are probably unaware of the importance of high performance surfaces in, for example, the protection of piston heads in our car engine, or the advanced composites with high wear resistance that are used for aircraft braking materials.

This book is about the production of such high-tech engineering coatings by a technique known as chemical vapour deposition (CVD). CVD is a process whereby a thin solid film is produced from the gaseous phase by a chemical reaction. A very primitive example of CVD is the way in which, when I was a boy, we used to produce a layer of soot on a glass sheet by playing a smoky candle flame onto the glass to allow us to view an eclipse. In that example the molten wax hydrocarbon is burnt in insufficient oxygen to produce carbon, which condenses out on the glass. That, of course, is a low-tech illustration, although

little did we know at the time that we were also producing a high-tech material, too – fullerene, or C_{60} .

CVD is to be distinguished from physical vapour deposition (PVD), which also produces a thin film on a surface from the gaseous phase but without any chemical reaction. A simple illustration of PVD is the conversion of water into ice flakes and its deposition on a cold surface as snow. It starts off as H_2O and finishes as H_2O , albeit in a different form.

It is the richness of the chemistry of a CVD process that makes the technique so versatile and capable of producing a vast range of layers with different compositions, structures and properties. However, with diversity and variability comes complexity. And in this book the authors provide a sound theoretical basis that both the tyro and seasoned CVD practitioner should find instructive and helpful. The authors also give some useful practical insights into CVD technology, of how microstructures evolve, and how CVD processes can be controlled to produce thin films tailored to practical needs.

There are a number of modern texts on CVD, but this one fills a niche in that it focuses on engineering coatings, particularly for the manufacture of fibre-reinforced ceramic composite materials. As such it makes a valuable contribution to CVD technology. It is tragic that the senior author Professor Yongdong Xu, who had published extensively internationally on composites and who won many awards in his native China, died just months before the publication of this book. The book is a fitting memorial to his career, and I hope it will inspire young chemists, physicists and engineers to make that invaluable melding of science and technology that is essential for the continued growth of thin-film markets.

Professor Michael Hitchman
Glasgow, 2009

Preface

Materials and associated technology developments have influenced humanity's cultural evolution and have made a significant impact on improvements of life quality. The names given to historical epochs, e.g. Stone Age, Bronze Age and Iron Age, make evident the importance and significance of the materials and associated technologies. Since its inception in the 1940s as an effective method to purify refractory metals, chemical vapour deposition (CVD) has evolved into the key technology to manufacture very large-scale integrated circuit chips. This has created revolutionary computer technology for modern society and led to the arrival of the information technology era. Over the last two to three decades, CVD technology has been further developed as an advanced technology to manufacture high-performance materials. One of the most representative and commercially valuable developments is the manufacture of fibre-reinforced ceramic composite materials (including carbon/carbon composites).

With the rapid development of CVD technology and applications in the aforementioned areas, it became imperative to produce a general-purpose reference book about this technology with a particular focus on advanced materials. Whilst there are a number of books introducing CVD in micro-electronic applications, there are no books about CVD applications in high-performance materials; this book aims to fill this gap.

In recent years, the interdisciplinary approach has had a profound influence on materials science and engineering, which are being transformed from a passive trial-error approach-based engineering into fields with a more proactive methodology than they previously had. Materials science and associated engineering technologies have become an advanced interdisciplinary field, which is closely related to physics, chemistry, engineering and so forth. In the 1990s, a well-known statement was made to indicate interdisciplinary nature of the aforementioned fields and to define the discipline: an outstanding material scientist should be a chemist in front of a physicist and a physicist in front of a chemist. At the same time, he should be a scientist in front of an engineer and an excellent engineer in front of a scientist. This identifies the knowledge and skill set for a good material scientist, who should possess broad and in-depth knowledge in physics, chemistry and engineering. Only equipped with the above knowledge can a material scientist innovate and develop new materials and products. At the same time, it also implies that an engineer must have a good understanding of these disciplines in order to develop innovative products. Above all, an innovator needs to have all the above essential knowledge and pursue and investigate interdisciplinary research and development areas in order to discover new materials, develop novel products and design new manufacturing systems for new and advanced products to meet ever increasing market demands.

Physics, chemistry and physical chemistry are the foundations of materials science and engineering. Materials researchers are also required to possess the sensitive vision and active thinking necessary for developing new materials based on innovative ideas. It is important for them to possess engineering ability to establish new prototype equipment for any research investigation. Many past experiences, both successful and unsuccessful, demonstrate the importance and necessity of the above qualities.

An understanding of the above characteristics and requirements for materials science and engineering forms the basis of the structure of this book, as it summarises precisely the essential knowledge requirements for CVD technology. Whilst the authors tackle a wide range of theoretical topics, the focus of the book is on the fibre-reinforced ceramic matrix composites used by the CVD or chemical vapour infiltration (CVI) processes. Based on the requirement of a systematic understanding of CVD processes, the related materials by some special CVD techniques and their potential applications, the book is structured as follows.

Starting with an introduction to the CVD process, Chapter 1 introduces basic features, historical developments, perspectives and literature of the CVD processes. A compendium has been compiled consisting of all key publications in the fields broken down into journals published in the field, books and handbooks produced, as well as proceedings of some of the most key conferences. Chapter 2 is concerned with the physical fundamentals involved in CVD processes. These include the theory of gas kinetics, vacuum technology, gas transport characteristics and so forth. As a key chapter for CVD processes, Chapter 3 explains the working principles, functional behaviours and design procedures of a CVD system. Furthermore, this chapter introduces a concurrent design and process modelling approach and associated design and analysis of the equipment used. In addition, some special techniques, such as continuous CVD and fluidised bed CVD, are introduced in this chapter. Chapter 4 explains the thermodynamics of chemical reactions of a CVD process and the methods of calculating CVD phase diagrams. It goes further by analysing some typical CVD phase diagrams. CVD kinetics is also discussed for homogeneous reaction, heterogeneous reaction and surface kinetics. Focusing on fibre-reinforced ceramic matrix composites, Chapter 5 introduces some typical CVI processes, their developments and applications. Physical and mathematical models are also established in the chapter to analyse the densification behaviour of the composites. Using the carbon fibre-reinforced silicon carbide composite as an example, the mechanical properties of these composites manufactured by CVI processes are also discussed in detail. Chapter 6 describes the theory of the microstructure evolution of the deposits, the control methods of a CVD process and the relationship between microstructures and the processing parameters. Computational fluid dynamics is introduced as an effective scientific method to simulate the velocity field of the gas flow within the CVD chamber and to optimise the processing parameters.

A substantial collection of CVD reaction systems and CVD phase diagrams has been compiled and included in Appendixes 3 and 4. This book is meant to be used as a reference and to serve as a rich information source for those who are interested in exploring and investigating further other CVD processes.

With the above information, it is also important to emphasise that the development of advanced materials requires innovative thinking and a visionary philosophy. As an example, when ceramics attracted much research interest and wide spread attention as a potential structural material in the 1970s, researchers explored different ways of overcoming its intrinsic weakness – brittleness. Among many methods tried, it was difficult to imagine that the brittleness of ceramic materials could be overcome by compositing several brittle constituent materials together. These radical approaches and results were pioneered by Professor Naslain in Bordeaux University, France, and Professor Fitzer of Karlsruhe University, Germany. It has been proven that carbon fibre-reinforced silicon carbide composites and silicon carbide fibre-reinforced silicon carbide composites exhibit excellent toughness. Of course, the interphase (also a brittle material) between the fibre and matrix plays an important role in this feature. This combination of brittle materials resulting in a new, strong and tough composite could be considered analogous to the mathematical principle of “a negative number multiplied by a negative number gives a positive number”. With the inspirational and innovative development of high-performance materials detailed in this book, it is the hope of the authors that new materials will be further developed based on CVD technology to benefit humanity in the future.

The authors of the book would like to express their thanks to the European Commission for its financial support in preparing the book under the Asia Link Programme for a project entitled FASTAHEAD (A Framework Approach to Strengthening Asian Higher Education in Advanced Design and Manufacture). The authors would also like to thank Dr Zhengwei Pan of the University of Georgia, Dr Remi Zante and Dr Daniel Rhodes of the University of Strathclyde for their constructive suggestions and comments, and Dr Yan’s researchers for their help in preparing some simulations and references. Finally, the authors would like to thank their families for their support, without which it would not have been possible to complete this book.

Yongdong Xu
Northwestern Polytechnical University, Xi’an, P R China
and

Xiu-Tian Yan
University of Strathclyde, Glasgow, UK
December 2008

Shortly after the authors jointly finished the most of the contents of this book and wrote the above text for this preface, Yongdong passed away suddenly at the young age of 43. He still had so much to work for and so much potential to contribute to the field. He was even hoping and planning to revise this text for

further editions. Sadly this will not be possible with his inputs. The second author would like to dedicate this book to Yongdong for his contribution, dedication and hard work in writing the relevant chapters of this book and his scholarly work in the field for the last 20 years.

Xiu-Tian Yan
University of Strathclyde, Glasgow, UK
March 2009

Contents

Chapter 1	Introduction to Chemical Vapour Deposition	1
1.1	Definition of CVD.....	1
1.2	Characteristics of Chemical Vapour Deposition	2
1.3	Overview of CVD Development	6
1.3.1	Stage 1: Early Development Era.....	7
1.3.2	Stage 2: Refining or Purification of Metals Era.....	7
1.3.3	Stage 3: Microelectronics Manufacture Era	9
1.3.4	Stage 4: Wider Applications Era	10
1.4	High-performance Ceramic Matrix Composites and Chemical Vapour Infiltration.....	13
1.5	Literature Sources.....	16
1.5.1	Books.....	16
1.5.2	Handbooks.....	17
1.5.3	Journals.....	17
1.5.4	Conference Proceedings	17
1.5.5	Representative Papers.....	20
References	21
Chapter 2	Physical Fundamentals of Chemical Vapour Deposition	29
2.1	Gas Laws and Kinetic Theory	29
2.1.1	Gas Laws	29
2.1.2	Gas Kinetic Theory.....	31
2.2	Vacuum Technology	37
2.2.1	Definition and Classification of Vacuum	37
2.2.2	Quantitative Description of the Pumping Process	39
2.2.3	Vacuum Pumps.....	41
2.2.4	Vacuum Measurement and Leak Detection.....	51
2.3	Fundamentals of Gas Transport.....	54
2.3.1	Transport Coefficients	55
2.3.2	Boundary Layer Theory.....	61
2.3.3	Some Dimensionless Parameters.....	63
2.4	Vapour Pressures of Chemical Vapour Deposition Precursors	68
References	70
Chapter 3	Chemical Vapour Deposition Systems Design	73
3.1	Proactive Design Approach for Chemical Vapour Deposition Systems	73
3.2	General Description of a Chemical Vapour Deposition System	75

3.2.1	Classification of the Chemical Vapour Deposition Methods.....	75
3.2.2	Configuration of a Chemical Vapour Deposition Apparatus.....	77
3.3	Precursor Delivery System.....	80
3.3.1	Selection Criteria for Chemical Vapour Deposition Precursors.....	80
3.3.2	Chemical Vapour Deposition Precursors and Their Classification.....	80
3.3.3	Delivery Methods.....	82
3.3.4	Devices and Components for the Delivery System.....	86
3.4	Reaction Chambers.....	89
3.4.1	Retorts.....	91
3.4.2	Gas Inlet Injectors.....	92
3.4.3	Gas Distributors.....	92
3.4.4	Exits.....	95
3.5	Heating Systems.....	98
3.6	Pumping Systems.....	100
3.7	Exhaust Gas Handling Systems.....	103
3.7.1	Cold Traps.....	103
3.7.2	Chemical Traps.....	105
3.7.3	Particle Traps.....	106
3.7.4	Exhaust Gas Scrubbers.....	106
3.7.5	Venting.....	107
3.8	Some Special CVD Processes.....	107
3.8.1	Laser-induced CVD Process.....	108
3.8.2	Continuous Chemical Vapour Deposition Process.....	111
3.8.3	Fluidised-bed Chemical Vapour Deposition Process.....	114
3.8.4	Catalyst-assisted Chemical Vapour Deposition Process.....	118
3.8.5	Combustion Chemical Vapour Deposition.....	120
3.8.6	High-temperature Chemical Vapour Deposition Process.....	122
	References.....	125

Chapter 4 Thermodynamics and Kinetics of Chemical Vapour Deposition 129

4.1	Introduction.....	129
4.2	Thermodynamics of Chemical Vapour Deposition.....	129
4.2.1	Chemical Reaction Feasibility.....	129
4.2.2	Chemical Vapour Deposition Phase Diagrams.....	134
4.3	Kinetics of Chemical Vapour Deposition Process.....	146
4.3.1	Chemical Vapour Deposition Phenomena.....	147
4.3.2	Homogeneous Chemical Reactions.....	147
4.3.3	Heterogeneous Chemical Reactions.....	153
4.3.4	Surface Kinetics of Chemical Reactions.....	154
4.3.5	General Description of Chemical Vapour Deposition Growth Kinetics.....	158
	References.....	162

Chapter 5 Chemical Vapour Infiltration 165

5.1	Introduction.....	165
5.2	Isothermal and Isobaric Chemical Vapour Infiltration.....	168

5.2.1	General Description.....	168
5.2.2	Isothermal and Isobaric Chemical Vapour Infiltration Process Model.....	168
5.2.3	Characteristics of Fibre-reinforced Ceramic-matrix Composites .	174
5.2.4	Isothermal and Isobaric Chemical Vapour Infiltration Applications	178
5.3	Thermal Gradient and Forced Flow Chemical Vapour Infiltration ...	179
5.3.1	General Description.....	179
5.3.2	Forced-Flow-Chemical Vapour Infiltration Model.....	183
5.3.3	Characteristics of Forced-Flow-Chemical Vapour Infiltration Composites	186
5.4	Thermal Gradient Chemical Vapour Infiltration	188
5.4.1	General Description.....	188
5.4.2	Some Typical Thermal Gradient/Isobaric Chemical Vapour Infiltration Techniques	189
5.4.3	Temperature Profile Within the Preform.....	196
5.5	Liquid-immersion Chemical Vapour Infiltration.....	198
5.5.1	General Description.....	198
5.5.2	Model of Liquid-immersion Chemical Vapour Infiltration	200
5.6	Pulsed Chemical Vapour Infiltration.....	204
5.6.1	General Description.....	204
5.6.2	Model.....	204
5.6.3	Applications.....	207
5.7	Chemical Vapour Composite	209
	References	210

Chapter 6 Microstructure Evolution and Process Control215

6.1	Introduction	215
6.2	Microstructure Evolution of Chemical Vapour Deposition Deposits	216
6.2.1	Film Formation and Structure Zone Model.....	216
6.2.2	Microstructure Characteristics of Chemical Vapour Deposition Deposits	220
6.3	Quantitative Control of Chemical Vapour Deposition Process Parameters	229
6.3.1	Quantitative Control Method Based on Chemical Reaction Mechanism	229
6.3.2	Experimental Basis for Quantitative Control Parameters.....	238
6.3.3	Quantitative Control Parameters on the Basis of Fluid Mechanics Consideration	243
6.4	Numerical Design and Analysis Techniques for Flow Field.....	247
6.4.1	Governing Conservation Partial Equations Used in Computational Fluid Dynamic Approach.....	248
6.4.2	Computational Fluid Dynamics in Chemical Vapour Deposition.....	251
6.4.3	Geometry Discretisation and Mesh Generation.....	252
6.4.4	Boundary and Initial Conditions.....	257
6.4.5	Iterative Problem Solving Strategy.....	259

6.4.6	Postprocessing and Visualisation	261
6.4.7	Some Computational fluid dynamics Application Examples	261
References	267
Appendix A.	Conversion Factors for Pressure Units	271
Appendix B.	Vapour Pressure of Precursors.....	273
Appendix C.	Chemical Vapour Deposition Materials and Their Corresponding Precursors	279
Appendix D.	Chemical Vapour Deposition Phase Diagram Collection	293
D.1	Chemical Vapour Deposition Phase Digrams for Borides.....	293
D.2	Chemical Vapour Deposition Phase Diagrams for Carbides	295
D.3	Chemical Vapour Deposition Phase Diagrams for Nitrides.....	308
D.4	Chemical Vapour Deposition Phase Diagrams for Oxides	312
D.5	Chemical Vapour Deposition Phase Diagrams for Silicides.....	313
Appendix E.	Acknowledgment of Figures and Tables Adopted from Other Sources	321
Index	335

Chapter 1 Introduction to Chemical Vapour Deposition

Being an effective way of constructing a wide range of components and products with potentially different material composition, chemical vapour deposition (CVD) has been developed since its inception as a novel manufacturing process in several industrial sectors. Notably, these include the semiconductor industry, ceramic industry and so forth. A trend of expanding its applications from initial mass semiconductor and microelectronics production to a wider range of applications has gained momentum in recent years as a result of intensive research and development work being undertaken by academic researchers and industrial end-users.

1.1 Definition of CVD

There are several definitions of CVD in the published literature. A practical and common definition of CVD is that it is a complex process of depositing solid materials at a high temperature as a result of a chemical reaction. This deposition forms a special type of material commonly known as ordered crystal grown from vapour.

Whilst the above definition introduces the basic high level understanding and observations of the process, a more concise and scientific definition for CVD is a process whereby a thin solid film is deposited onto a substrate through chemical reactions of the gaseous species. For structural component applications, the deposition typically takes place at a temperature of around 1000°C. It is the reactive processes that distinguish CVD process from physical vapour deposition (PVD) processes, such as physical evaporation process, sputtering and sublimation processes [1].

Figure 1.1a gives a typical example of a CVD system, where reactant gases, normally called precursor gases of CH_3SiCl_3 and H_2 , are delivered into a reaction chamber at a suitably determined temperature. As they pass through the reactor these gases come into contact with a heated substrate; they then react and form a solid SiC layer deposited onto the surface of a substrate. Usually, an inert gas, such as Ar, is used as a diluent gas. The depositing temperature and pressure are the critical parameters in this process. After the reactions, the exhaust gases containing HCl species are trapped by NaOH and then condensed by liquid N_2 trap before being released into the atmosphere.

CVD is therefore a generic name for a group of processes that involve forming a thin layer via chemical reaction and depositing a solid material layer onto substrates. Figure 1.1b shows a model consisting of the sequential physical and chemical steps that occur during a CVD process, developed by Spear in 1982 [2]. They are summarised as follows:

1. Mass transport of reactant gaseous species to vicinity of substrate;

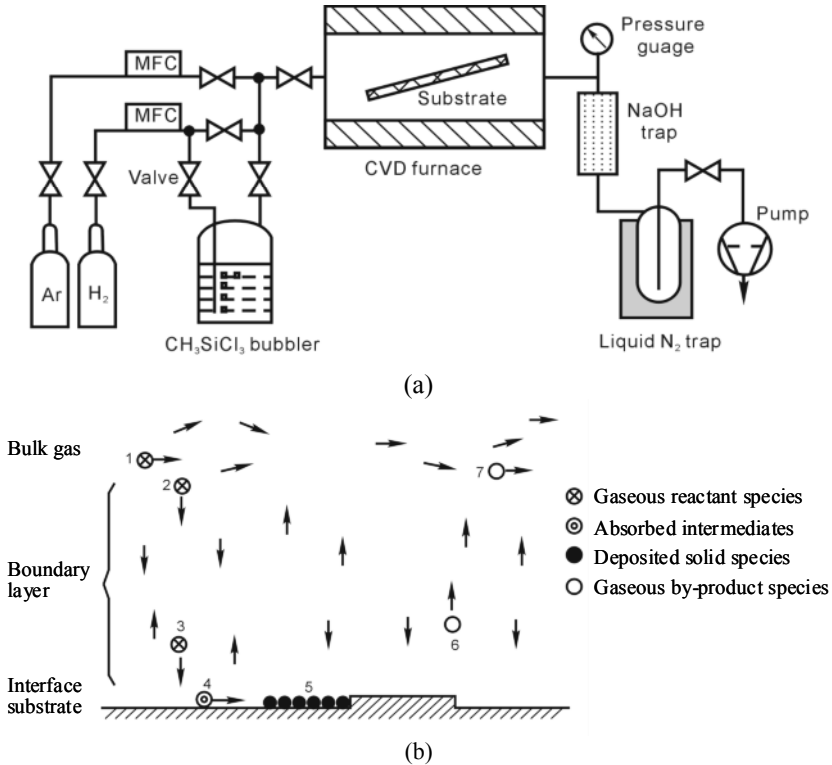


Figure 1.1. Schematics of a CVD process: (a) arrangement of a CVD system and (b) a CVD model

2. Diffusion of reactant species through the boundary layer to the substrate surface or homogeneous chemical reactions to form intermediates;
3. Adsorption of reactant species or intermediates on substrate surface;
4. Surface migration, heterogeneous reaction, inclusion of coating atoms into the growing surface, and formation of by-product species;
5. Desorption of by-product species on the surface reaction;
6. Diffusion of by-product species to the bulk gas; and
7. Transport of by-product gaseous species away from substrate (exhaust).

1.2 Characteristics of Chemical Vapour Deposition

Mechanical manufacturing techniques have been developed based on different working principles and component manufacturing techniques. These can be classified into two main categories, namely additive methods and subtractive methods (see Figure 1.2), using the method of component formation as a criterion. Traditional manufacturing techniques, such as milling, turning, drilling, grinding and cutting, rely on processes in which a component is gradually formed by

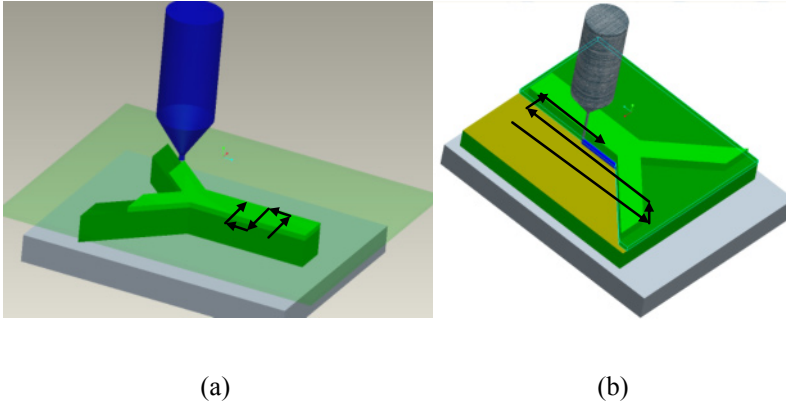


Figure 1.2. Components made by (a) additive method and (b) subtractive method

removing or subtracting materials from a simple shaped and larger block of uniform material by casting, forging, rolling or extruding, usually called a work piece. These techniques are hence called subtractive methods as materials are gradually subtracted or removed from the work piece.

Recent new techniques have been developed to gradually build up a component by adding more material in solid powder form followed by sintering or soldering, in fluid form followed by solidification, or in gaseous form followed by chemical reactions or physical deposition. These techniques mostly work on the so-called layer manufacturing principle. A close control of the layer-based addition process is therefore required to achieve the final dimensions, accuracy and surface finishes.

CVD processes work on the principle of adding a new layer of material onto a substrate surface and hence belong to the additive manufacturing technique family. They employ a suitable substrate as the base component and gradually deposit new material onto the base to form a component. In contrast to other additive manufacturing techniques, CVD processes do not require any external driver or causes for their solidification processes, such as laser-based solidification found in stereolithography technique, or spread binders in powder-based 3-D printing. They rely on chemical reactions to form a strong bond for deposits. These reactions occur at the atomic level; hence the deposition formed on a substrate can be very fine and be comprised of thin layers of coating. CVD processes can therefore be considered an accurate manufacturing technique at the micro or even nano level.

CVD has a number of advantages as a method for depositing layers of thin-film materials onto a substrate.

1. Quite different from some physical vapour deposition methods (PVD), CVD is a non-line-of-sight process which leads to the good conformality in term of uniform thickness of the coating. Figure 1.3 (a) shows an example of conformal coverage of a step shaped substrate coated by a CVD process. CVD also has high throwing power which is exceeded only by plasma spraying. As a result, the coatings can be uniformly deposited over substrate contours and complex surfaces. This means that the coatings can

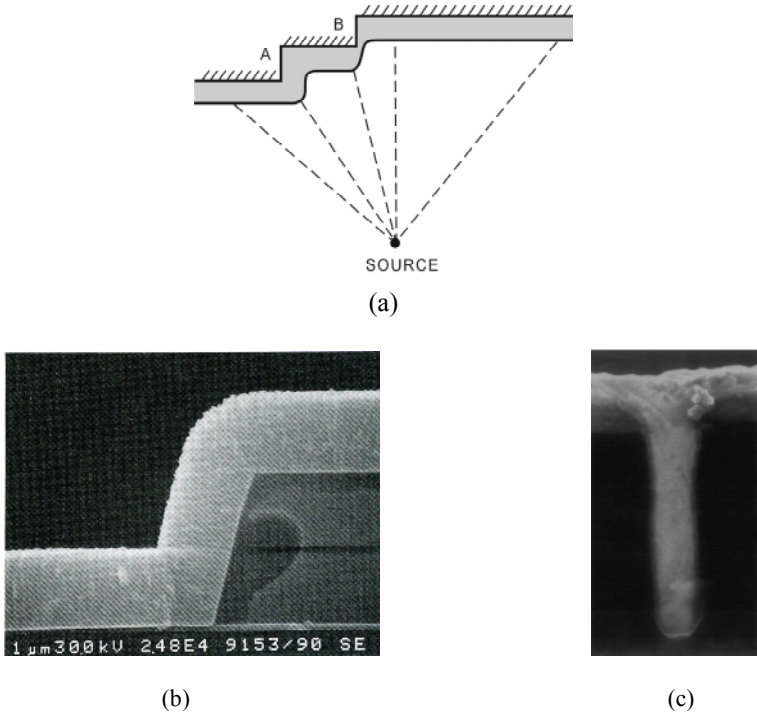
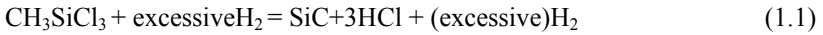


Figure 1.3. Comparison between PVD and CVD processes: (a) PVD coating on a step substrate, (b) CVD TiN on a step Si substrate [3] and (c) CVD Cu into a micro-trench [4]

be applied to elaborately shaped work pieces, including those with the interior and underside features, and those with high aspect ratio holes and other similar features which can be completely filled. Deep recesses, holes, and other difficult three-dimensional features can usually be coated with relative ease by the CVD process. For instance, a micro-trench with an aspect ratio of 10:1 can be completely filled with copper using CVD technique, as shown in Figure 1.3 (b). In contrast, PVD techniques, such as sputtering or evaporation, generally require a line-of-sight between the surface to be coated and the source, e.g. the coating source should have a straight line path to the surface on the substrate, as shown in Figure 1.3 (c).

2. CVD processes have a greater flexibility of using a wide range of chemical precursors such as halides, hydrides, organo-metallic compounds and so forth which enable the deposition of a large spectrum of materials, including metals, non-metallic elements, carbides, nitrides, oxides, sulphides, as well as polymers. Up to now, around 70% of elements in the periodic table have been deposited by the CVD technique, some of which are in the form of the pure element, however, more often the compound materials.

- The CVD technique requires relatively low deposition temperatures. This effectively enables the desired materials to be deposited in-situ at low energies through vapour phase reactions. This enables the deposition of refractory materials at a temperature much lower than their melting temperatures. For example, refractory materials such as SiC (sublimation point: 2700 °C) can be deposited at about 1000 °C using the following chemical reaction:



Furthermore, the deposition temperature could be significantly decreased to around 300 °C with the enhancement techniques such as by using plasma, photo, or laser tools.

- CVD also has the ability to control the crystal structure, stoichiometry, surface morphology and orientation of the CVD manufactured products by tailor-making through controlling the deposition parameters. Figure 1.4 shows two structures produced using the CVD technique, which illustrate a high quality formation of multilayered coatings composed of HfC/SiC for the image on the left and PyC/SiC on the right.
- The deposition rate can be adjusted readily. Low deposition rate is favoured for the growth of epitaxial thin film for microelectronic applications. However, for the deposition of thick protective coatings, a high deposition rate is preferred and it can be greater than tens of micrometers per hour. The deposition rate using CVD technique is high and thick coatings can be readily obtained (in some cases centimetres in thickness). The process is generally competitive compared with other techniques and, in some cases, CVD is more economical than PVD processes.
- Compared with the facilities used in PVD, the CVD equipment does not normally require ultra-high vacuum working environments and the equipment generally can be adapted to many process variations. This great flexibility is advantageous such that it allows many changes in composition

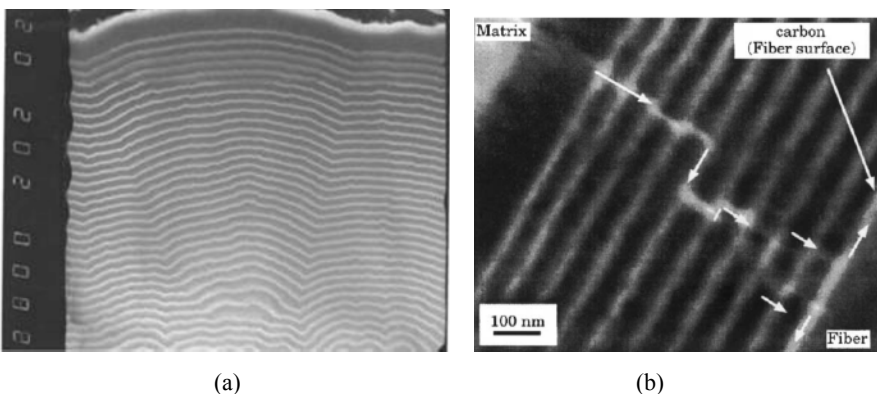


Figure 1.4. Multilayered coatings by CVD processes: (a) HfC/SiC [5] and (b) PyC/SiC [6]

during the deposition, and the co-deposition of elements or compounds into multiple layers or mixed layers can be readily achieved using the CVD technique.

However, CVD processes also have several disadvantages as follows:

1. A major disadvantage is that CVD requires chemical precursors as the essential reactants, which can often present safety and health hazards as they can be at times extremely toxic, corrosive, flammable and explosive. CVD precursors can be highly toxic even at low concentration (e.g. $\text{Ni}(\text{CO}_4)$), explosive such as B_2H_6 , or corrosive (e.g. SiCl_4). Some precursors, especially the metal-organic precursors, can be quite expensive to use. The exhaust gases consist of chemical reaction by-products, intermediates and others, such as CO , H_2 or HCl , which can also be hazardous, toxic, corrosive and flammable. These gases must be properly treated before they are released into the environment. The treatment processes include neutralisation, condensation and filtering etc, which may be very costly and environmentally controversial.
2. Compared with other vapour-phase deposition methods, CVD method is perhaps the most complex. Unlike growth by physical deposition such as evaporation or Molecular Beam Epitaxy (MBE), this method requires numerous test runs to determine and reach suitable growth parameters, especially for single-crystal growth. The complexity of this method results from the following facts:
 - the chemical reactions generally involve multiple gaseous species and produce a number of intermediates;
 - during the above complex reactions, it is extremely difficult to identify the reaction processes and detect the resultant intermediates in most cases;
 - for a CVD, there are a sequence of chemical reaction steps for deposition compared with much simpler physical methods, and
 - CVD process is also difficult to control and requires a lot of experience and tests before a reliable control algorithm can be fully developed to control the gas which has greater freedom to flow in a typical deposition chamber.

Compared with other material forming methods such as ceramic sintering and liquid metal casting, CVD shows much more challenges and difficulties in devising effective and flexible control methods due to the above reasons.

1.3 Overview of CVD Development

As an important step-change and disruptive technology, the CVD has been developed since 1960s into a relatively mature and reliable manufacturing technique. The development of CVD could be divided into four key eras, based on the maturity and the application nature of the technology:

1.3.1 Stage 1: Early Development Era

The formation of soot in a furnace due to incomplete oxidation of firewood during prehistoric times is probably the first observation, by human being, of deposition using a CVD process. The development of the above observation is in common with many technology developments and has been closely linked to the practical needs of societies. Later, this method was used to produce carbon black pigment from the soot and prepare pre-historic art on the walls.

A more recent application and the industrial exploitation of CVD could be traced back to a patent filed by de Lodyguine in 1893[7, 8]. His invention was to deposit Tungsten (W) onto carbon lamp filaments through the reduction of WCl_6 by H_2 . This advancement transferred the CVD from a trivial technique used to make colour pigment into a major industrialisation technique which benefited human beings significantly by producing reliable, more accessible and cheaper light bulbs.

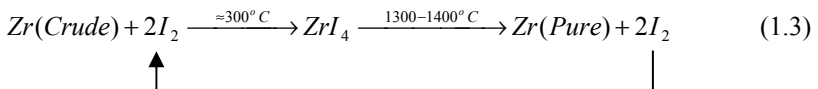
1.3.2 Stage 2: Refining or Purification of Metals Era

Following the initial deposition applications of metals, CVD method was further developed and widely used mainly for refining or purification of some metals (especially metals such as Ni, Zr, Ti etc) until the 1940s.

One of the earliest industrial CVD applications developed during this stage is a carbonyl process for refining nickel (Ni), developed by Mond in 1890 [9, 10]. The famous Mond extraction process uses the following chemical reaction process:



Later, a new extraction process was developed by Anton Eduard van Arkel and Jan Hendrik de Boer in 1925, known as van Arkel and De Boer process [11, 12], and the process uses the following chemical reaction:



The van Arkel-de Boer process has been used to extract Zr, Ta, etc. The extraction principle is explained through the schematic diagram of Zr extraction process and associated equipment, as shown in Figure 1.5. This process uses a U-shaped hot filament connected to the tungsten electrodes, and the temperature of the heating element surface can reach to around 1300 – 1400 °C. In zirconium (Zr) purification process, Zr heating filament is the best choice although W or Mo can be used. At this temperature, zirconium from zirconium crude metal attaches to the chamber interior wall whose temperature is around 300 °C, reacts with iodine (I_2) from its container to form ZrI_4 in gas state, which is then transported to the hot filament due to its concentration gradient. ZrI_4 is then decomposed into Zr and I_2 at 1300 – 1400 °C, resulting in zirconium depositing onto the surface of the hot filament. Using this way, pure zirconium is produced, whereas iodine returns back to the crude Zr

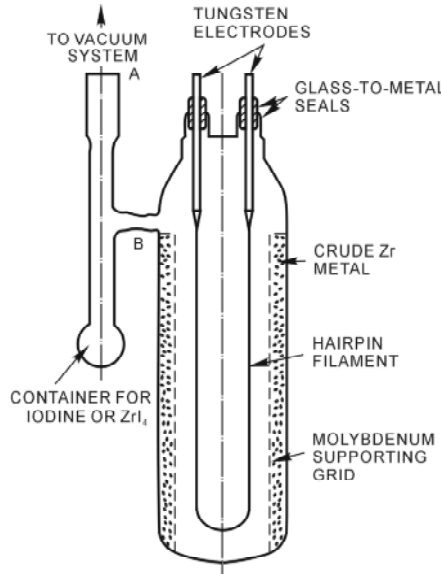
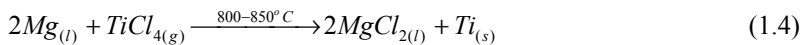


Figure 1.5. Schematic for van Arkel and De Boer process [13]

area to react in the next cycle with the crude zirconium metal. This cyclic and repetitive reaction between iodine and crude zirconium metal continues to produce more ZrI_4 , which in turn is decomposed at the hot filament and pure zirconium is deposited further onto the hot filament surface. The above process continues till all crude zirconium metal is converted into pure zirconium. During the above process, many other impurities including oxides and nitrides do not react with iodine, whereas metal impurities (e.g. Fe, Cr, Ni and Cu etc) react with iodine, but their resultant products are vaporised very slowly under the above process conditions. The above processes help to produce high-grade pure zirconium.

Another typical process called Kroll process was developed by Kroll in 1940s [14, 15]. This process is still being widely employed to manufacture titanium (Ti) by magnesium reduction of the titanium tetrachloride through the following reaction:



It was also during this period that silicon was first deposited using a method of hydrogen reduction of silicon tetrachloride by Pring and Fielding in 1909 [16]. The development and availability of this particular technique made it possible to develop and manufacture microelectronic devices in a large scale.

1.3.3 Stage 3: Microelectronics Manufacture Era

The evolution of the CVD technique had not reached a critical and significant stage until the rapid development of demands and corresponding technologies became a main industrial driving force to start electronic revolution in 1960s [17, 18]. It is only in the past 40 years that a considerable in-depth understanding of the process has been made and the increased applications of CVD explored. During this period, CVD technology evolved as a key technology to produce micro scale electronic components, driven by the demands of miniaturisation of computer components. The ultra-fine scale deposition characteristics of a CVD process possesses a desirable capability to produce super fine films required for semiconductors and other applications. In early 1970s CVD became a successful technique to manufacture electronic semiconductors and protective coatings for electronic circuits. This significantly reduces the size of electronic components by replacing large electric vacuum tubes with silicon circuits which integrate many individual electric components onto a single silicon wafer. Figure 1.6 shows a typical schematic diagram of a MOS field effect transistor, in which the poly-silicon, dielectric SiO_2 and Si_3N_4 are produced by the CVD processes [19].

In manufacturing microelectronic devices, CVD processes are used to fabricate several kinds of films made of the following materials [18]:

1. Active semiconductor materials, including
 - group IV doped elements and compounds such as Si, Ge, SiGe and SiC;
 - group III-V compounds such as AlN, AlAs, AlP; GaN, GaP, GaAs; InP, InAs; AlGeAs, GaAsP, GaAsSb, GaInP, GaInAs, InAsP, as well as GaInAsP;
 - group II-VI compounds such as ZnS, ZnSe, ZnTe, CdS, CdSe and CdTe;
 - miscellaneous semiconductors: ScN, YN, SnO_2 , In_2O_3 , PbSnTe, etc.
2. Conductive interconnect materials:
 - some element metals and alloys: Ag, Al, Al_3Ta , Au, Be, Cu, Ir, Mo, Nb, Pt, Re, Rh, V, Ta, Ta-W, W, W-Mo-Re, etc.
3. Insulating dielectric materials:
 - aluminosilicate glass (AISG) deposited from $\text{SiH}_4\text{-Al}(\text{CH}_3)_3\text{-O}_2\text{-N}_2$; $\text{Si}_3\text{N}_4\text{-Al}$ etc. $\text{Si}_x\text{O}_y\text{N}_z$, etc.
 - arsenosilicate glass (AsSG) deposited from $\text{Si}(\text{OC}_2\text{H}_5)_4\text{-AsCl}_3\text{-O}_2\text{-N}_2$;
 - borosilicate glass (BSG) deposited from $\text{SiH}_4\text{-B}_2\text{H}_6$ system;
 - phosphorsilicate glass (PSG) deposited from $\text{SiCl}_4\text{-PClCl}_3\text{-H}_2\text{O}$, $\text{PH}_3\text{-SiH}_4\text{-O}_2$;
 - oxides SiO_2 , Al_2O_3 , TiO_2 , ZrO_2 , HfO_2 , Ta_2O_5 and Nb_2O_5 ;

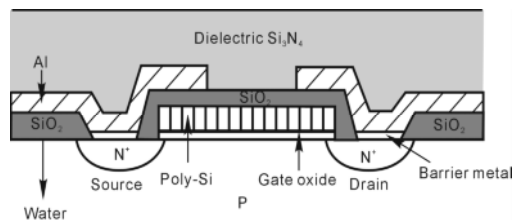


Figure 1.6. Schematic of an n-type metal-oxide-semiconductor (MOS) field transistor cross-section [19]

The research and development of CVD in recent years have focused on solid state microelectronic devices. This rapidly moving technology demands continuously improved materials and processes for the fabrication of even more advanced semiconductor devices. It is well recognized that computer chips would not be manufactured in their current capacity and structure if CVD techniques were not transferred and developed from the material extraction method into the deposition technology.

1.3.4 Stage 4: Wider Applications Era

In recent years, a great deal of success has been achieved and CVD techniques have been widely applied and further developed because of the following enablers and reasons [18].

The market needs for more advanced materials provide the driving force of the CVD processes. For example, the development of high performance aero-engines requires the strong and tough fibre reinforced ceramic matrix composites with low density which can potentially be used in ultra-high temperatures.

With more advanced instruments available, it is possible to identify the reactant gaseous species of the chemical reactions. This in turn helps to improve the understanding of the underlying chemical reactions and the processes;

The sophisticated and more efficient CVD systems can be designed and constructed with the aid of computational fluid dynamics (CFD) and high performance computers. At the same time, control technology has advanced such that it becomes much easy to accurately control the CVD processing parameters, such as temperature, pressures and flow rate, etc;

Tremendous fundamental research especially in the CVD technologies and precursor synthesis extends the applicability to some new area. These technologies include metal-organic CVD (MOCVD), plasma-enhanced CVD, photo CVD and laser induced CVD etc. The advancement of the synthesis technology provides new precursors to deposit a variety of materials with high purity.

Based on the above advancement, CVD processes have been widely used to manufacture various semiconductor devices, MEMS, nanomaterials, and advanced structural materials for ultra-high temperature applications. Some of these applications are briefly introduced and summarized as follows.

1. Communication industry [20]
 - Complex epitaxial hetero-structures of SiGe or compound semiconductor (e.g. AlGaAs) for high frequency (1 - 100 GHz) applications;
 - High purity SiO₂ optical fibre for the desired refractive index profile;
2. Optoelectronic [21, 22]
 - High brightness blue and green LEDs based on group-III nitride alloys (e.g. InGaN).
 - The light emitting diodes (LEDs) have been widely used in recent years as a general source of white light. They exhibit many desirable features as a light source, namely, high luminescence efficiency, fast response time, and reliable long service life. Red LEDs have been made widely available, but the high intensity blue and green LEDs were unavailable before 1990s. As

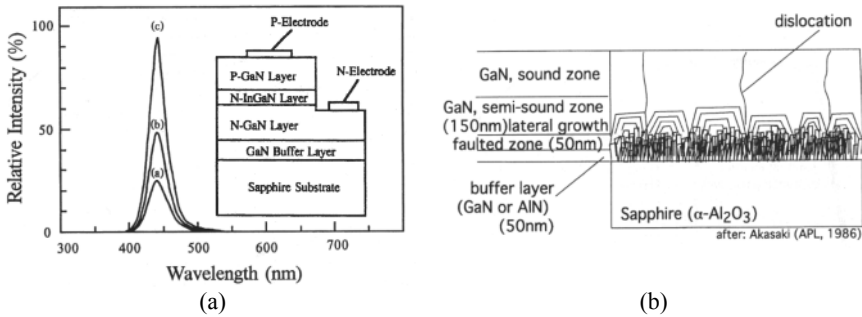


Figure 1.7. GaN blue LEDs by MOCVD: (a) Electroluminescence spectra and (b) Structure of a buffer layer [22]

blue is one of the three primary colours, the development such a LED is required to produce full colour spectrum and pure white light. In his well recognised attempt in 1993, Nakamura and his group used metal-organic CVD technique to developed GaN and related semiconductors which are the key components for the blue LEDs. Figure 1.7 shows the electroluminescence wavelength and its structural configuration of a blue LED. It is believed that GaN-based LEDs may well soon replace incandescent light bulbs and fluorescent tubes in a similar way as silicon circuits replaced vacuum tubes in the past.

3. Microelectromechanical structures (MEMs) [23, 25]

- Complex and smart micro-components with the size as small as 50 – 200 μm

4. Nanotechnology

- Some nano-materials and nano-devices fabricated primarily for functional applications, such as nanopowder [26], nanowire [27], nanobelt [28], nanotube [29] as well as nanocoil [30].

5. Coatings

- Diamond-like carbon (DLC) coatings [31, 32]
- SiC for oxidation protection for carbon-based composites [33]
- Refractory metal coatings [34], such as Re/Ir coating for the oxidation resistance and gas tightness of composite chamber at ultra-high temperatures
- hard coating (TiN, B₄C, TiC and Ti–Si–C–N) for the anti-wear of cutting tools [35], [36]
- Corrosion protection coating for gas turbines [37, 38]
- Reflection mirror, such as SiC [39]

6. High temperature (T_c) superconductors [40]

YBa₂Cu₃O_{7-x} and Bi–Sr–Ca–Cu–O oxides

7. High-purity bulk materials [41, 42] ZnS, ZnSe, CdS, CdTe, SiC, Si₃N₄, B₄C, GaAs, Rh and W etc. Some of the components are as shown in Figure 1.8.

8. Refractory composites

- high-performance ceramic fibres: SCS–SiC and B monofilaments [43, 44];

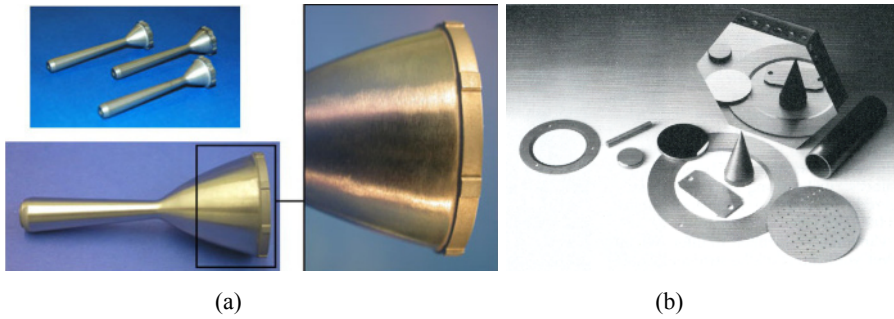


Figure 1.8. CVD fabricated monolithic components: (a) thin-wall Rh thruster chamber [5] and (b) SiC components [42]

- carbon/carbon composite for friction and ultra-high-temperature applications in aircraft braking systems[45];
- carbon/silicon carbide composites for thermal protection systems of space shuttles [46], as shown in Figure 1.9;
- silicon carbon/silicon carbide composite components for long service-time in aero-engines with high thrust/weight ratio [47] as well as the first wall used in a nuclear fission reactor [48];
- carbon/(carbon-carbide) multi-matrix composites for ablation resistance [49].

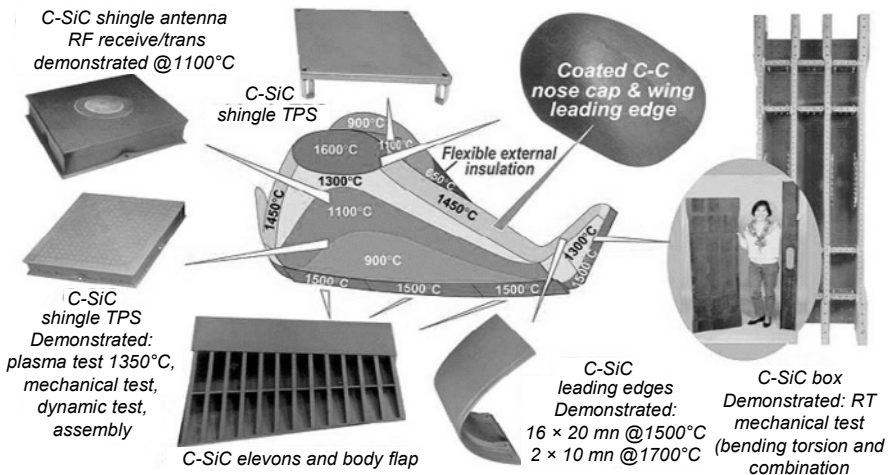


Figure 1.9. C/SiC component for HERMES thermal protection system [46]

1.4 High-performance Ceramic Matrix Composites and Chemical Vapour Infiltration

CVD has also been developed into an advanced version named Chemical Vapour Infiltration and has found an important application of making higher performance ceramic materials. Compared with super-alloys, advanced ceramics exhibit superior performances which include very low density, high strength and excellent erosion resistance to the harsh service environments at elevated temperatures. However, the brittleness causing low reliability is the key problem, limiting their wide range of applications. Research on how to obtain tough advanced ceramics has received considerable interests. As illustrated in Figure 1.10, the development of tough ceramics can be divided into three stages [50]:

In the middle of 1960s, the fracture mechanics was developed to a stage where it was possible to apply it to the new applications. The development of the indentation fracture helps to focus the design attention on flaw elimination in ceramics, which aim to achieve the highest degree of homogeneity and density in monolithic ceramics. As a result, dense ceramics were produced and they possess higher mechanical strength, but they are still brittle.

The great success of tough ZrO_2 ceramics inspired material scientists to develop new materials by design. This should establish a closer relationship among processing, characterizing, testing, modelling and so forth. Especially, the mechanical properties of ceramics can be significantly improved by designing its microstructure through the incorporation of whisker, elongated crystal, platelet, and fibre.

Fibre-reinforced ceramic matrix composites with high workload for fractures were firstly demonstrated in the early of 1970s. Vigorous activities were pursued after high performance Nicalon/glass-ceramic matrix composites were reported by Prewo and Brennan [51, 52], and carbon/silica glass as well as carbon/silicon nitride by Guo [53, 54] in the early 1980s.

Various methods have been developed to fabricate the tough ceramics, which

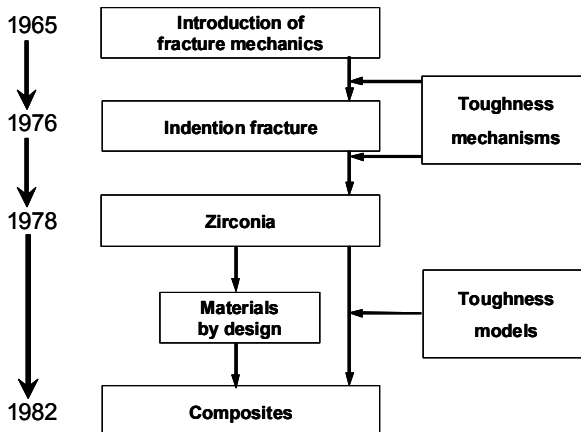


Figure 1.10. Overall chronological developments of high-toughness ceramics [50]

Table 1.1. Comparison among various toughening methods for ceramics [50]

Mechanism	Highest toughness (MPa·m ^{1/2})	Materials
Transformation	~20	ZrO ₂ /Al ₂ O ₃ , Ce-TZP, Y-TZP
Microcracking	~10	Al ₂ O ₃ /ZrO ₂ , Si ₃ N ₄ /SiC, SiC/TiB ₂
Metal dispersion	~25	Al ₂ O ₃ /Al, ZrB ₂ /Zr, Al ₂ O ₃ /Ni, WC/Co
Whiskers/platelets	~15	Si ₃ N ₄ /SiC, Si ₃ N ₄ /Si ₃ N ₄ , Al ₂ O ₃ /SiC
Self toughing	12	In-situ Si ₃ N ₄ [55], LaB ₆ -ZrB ₂ [56], Al ₂ O ₃ /Y ₃ Al ₅ O ₁₂ , Al ₂ O ₃ /GdAlO ₃ [57]
Fibres	≥30	SiC/LAS, SiC/CAS, SiC/MAS, C/BAS, SiC/SiC, C/SiC [58]

*LAS: Li₂O–Al₂O₃–SiO₂, CAS: CaO–Al₂O₃–SiO₂
 MAS: MgO–Al₂O₃–SiO₂, BAS: Li₂O–Al₂O₃–SiO₂
 Y-TZP: tetragonal zirconia polycrystal stabilised by Y₂O₃

are listed in Table 1.1. Among them, fibre reinforcement is considered as the most promising method. In 1986, the outstanding mechanical properties of the CVI SiC/SiC composites were systematically reported by Lamicq *et al.* As shown in Figure 1.11, the CVI SiC/SiC composites exhibited excellent fracture behaviours. The fracture toughness can be as high as 25 MPa·m^{1/2} from room temperature up to 1400 °C and a very high level of fracture work of more than 10 kJ·m⁻² is required.

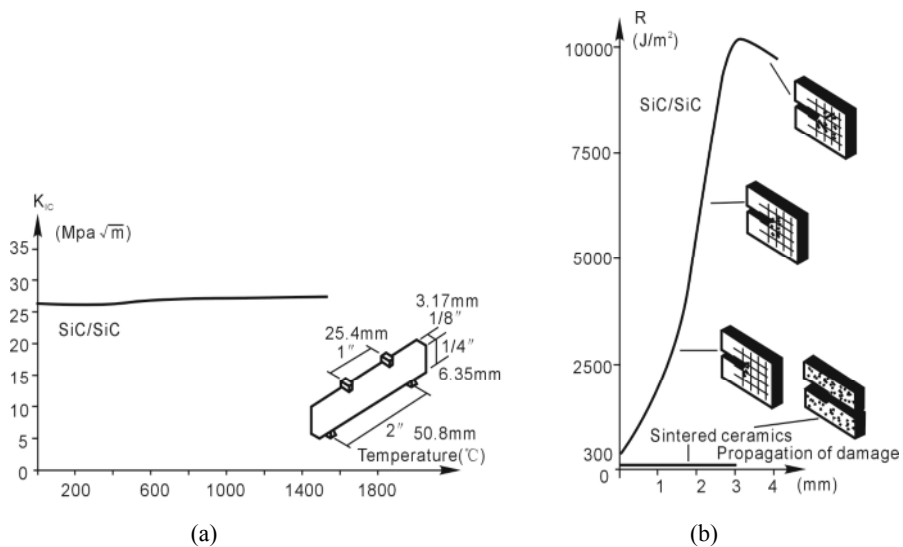


Figure 1.11. Mechanical properties of 2-D SiC/SiC composites [59]: (a) fracture toughness and (b) fracture resistance curve

In this method, a thin layer between fibre and matrix with proper interfacial bonding plays critical role for the crack deflection and fibre pull-out as shown in Figure 1.12. The CVI technique possesses outstanding advantages to deposit thin coatings on the surface of individual fibres within the preform then followed by the subsequent infiltration of the matrix phase.

Chemical vapour infiltration (CVI) is an extension of CVD processes only when a CVD process occurs on an internal surface of a porous substrate (especially for the fibre preform). As compared with CVD, the CVI process for ceramics is much more effective and important because it is the optimal technique to fabricate fibre reinforced ceramics and particularly carbon fibre reinforced carbon and advanced ceramic matrix composites. Both CVI and CVD techniques share some common features in overall chemistry, however, the CVI is much more complex than the CVD process in mass transport and chemical reactions.

For a CVD process, the mass transport and chemical reactions occur only on the surface of a dense substrate, producing a thin layer of coating. For a CVI process, the reactant gases must be transported into the porous fibre preform, in which the size of the pores varies with a large distribution, e.g. from the large pores ($\sim 10^2 \mu\text{m}$) among the fibre bundles to the small pores ($10^0 \sim 10^{-1} \mu\text{m}$) among the fibres within a bundle. The homogeneous chemical reactions are therefore competing with the heterogeneous chemical reactions within the pores, resulting in a complex deposition process. The mass of the deposit in a component made from a CVI process is two to ten times greater than that of the fibre preform because the deposit becomes the main constituent of the composites. In order to obtain the required density and improve the density uniformity of the composites, some special CVI techniques have been developed, including isothermal/isobaric CVI, forced CVI, thermal gradient CVI, liquid immersion CVI, pulsed CVI, and so forth. Up to now, CVI techniques have become the commercial method to manufacture the fibre reinforced ceramic matrix composites and carbon/carbon composites.

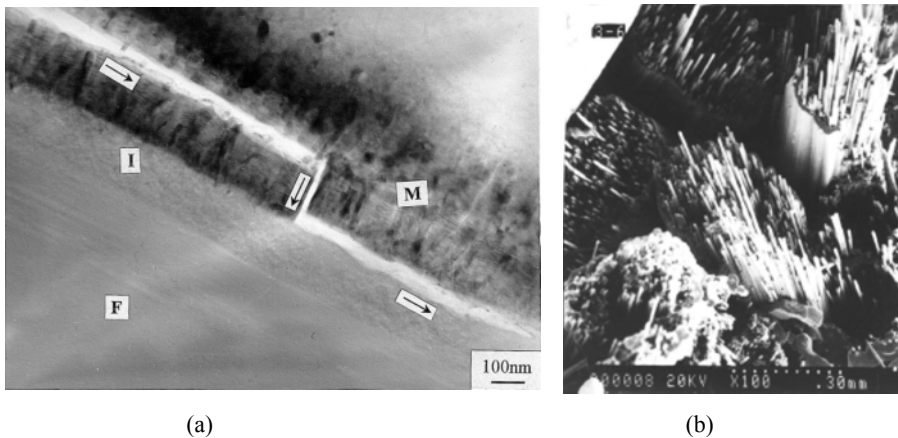


Figure 1.12 Crack deflection and fibre pull-out in 3-D C/SiC composites: (a) crack deflection along the interface [60] and (b) fibre pull-out [58]

1.5 Literature Sources

Whilst this chapter and indeed the book aim to provide a clear and insightful introduction to the complex CVD subject area, it is necessary to cover both theoretical and application based topics. This is because that CVD itself has evolved for many years into different applications and it is also built on evolving related theoretical developments. As the emphasis of the book is to provide an in-depth explanation of the subject from engineering application points of view, the book hence will have a light touch on the development of related theories as well as non-main stream applications. In order to compensate this slight lack of introduction to theories due to the above approach, a list of comprehensive literature references has been compiled to further the understanding of the theory, particular applications and more specialised topics. The literatures on the subject of CVD have been structured into the categories of books, handbooks, journals, conference proceedings and general representative papers.

From these references, it is not difficult to see that chemical vapour deposition has been advanced based on a very extensive literature of books, journals and conference proceedings with various aspects of the subject. The list in this section aims to provide a comprehensive source of readings of the most recent and relevant references for readers to pursue the subject further.

1.5.1 Books

- *Vapour Deposition*, Powell, Oxley and Blocher Jr, 1966 [61]
- *Thin Film Processes*, Vossen and Kern, 1978 [62]
- *Chemical Vapour Deposition*, Hawkins, 1981 [63]
- *Chemical Vapour Deposition for Microelectronics*, Sherman, 1987 [64]
- *Thin Films by Chemical Vapour Deposition*, Morosanu, 1990 [65]
- *Thin Film Processes II*, Vossen and Kern, 1991 [66]
- *The Materials Science of Thin Films*, Ohring, 1992 [67]
- *Chemical Vapour Deposition: Principles and Applications*, Hitchman and Jensenin, 1993 [1]
- *The Chemistry of Metal CVD*, Kudas and Hampden-Smith, 1994 [68]
- *CVD of Nonmetals*, Rees, 1996 [69]
- *CVD of Compound Semiconductors*, Jones and O'Brien, 1997 [70]
- *Chemical Vapour Deposition: Thermal and Plasma Deposition Electronic Materials*, Sivaram, 1995 [71]
- *Chemical Vapour Deposition*, Park and Sudarshan, 2001 [72]

1.5.2 Handbooks

- *Handbook of Thin Film Deposition Processes and Techniques*, Schuergraf, 1988 [73]

- *Handbook of Deposition Technologies for Films and Coatings* (2nd ed), Bunshahin, 1994 [74]
- *Handbook of Thin Film Process Technology*, Glocker and Shah, 1995 [75]
- *Handbook of Chemical Vapour Deposition (CVD)*, Pierson, 1999 [76]
- *Handbook of Composite Materials Vol. 5: Ceramic Matrix Composites*, USA Department of Defense, 2002 [77]
- *Handbook of Ceramic Composites*, Bansal, 2005 [78]

1.5.3 Journals

The journals covering CVD techniques and the applications are:

- *American Ceramic Society Bulletin*
- Carbon
- Ceramic Science and Engineering Proceedings
- Chemical Vapour Deposition
- Journal of the American Ceramic Society
- Journal of Crystal Growth
- Journal of Materials Science
- Journal of the Electrochemical Society
- Journal of the European Ceramic Society
- Journal of Vacuum Science and Technology
- Materials Science and Engineering
- Solid Thin Films
- *Surface and Coatings Technology*

1.5.4 Conference Proceedings

The international conferences on chemical vapour deposition are held in every two or three year intervals since 1967, sponsored primarily by the American Electrochemical Society as well as the American Nuclear Society. In parallel, since 1977, the European conferences on Chemical Vapour Deposition have been held 16 times sometimes co-sponsored by the American Electrochemical Society as well as the American Nuclear Society. The Asian conferences on chemical vapour deposition have been held 3 times. These proceedings were published with following details.

1.5.4.1 International Conferences on CVD

- *Conference on Chemical Vapour Deposition of Refractory Metals, Alloys and Compounds*, Gatlinburg, TN, USA, 1967 [79]
- *2nd International Conference on Chemical Vapour Deposition*, Los Angeles, CA, USA, 1970 [80]

- *3rd International Conference on Chemical Vapour Deposition*, Salt Lake City, UT, USA, 1972 [81]
- *4th International Conference on Chemical Vapour Deposition*, Boston, MA, USA, 1973 [82]
- *5th International Conference on Chemical Vapour Deposition*, Fulmer, England, 1975 [83]
- *6th International Conference on Chemical Vapour Deposition*, Atlanta, GA, USA, 1977 [84]
- *7th International Conference on Chemical Vapour Deposition*, Los Angeles, CA, USA, 1979 [85]
- *8th International Conference on Chemical Vapour Deposition*, Paris, France, 1981 [86]
- *9th International Conference on Chemical Vapour Deposition*, Cincinnati, OH, USA, 1984 [87]
- *10th International Conference on Chemical Vapour Deposition*, Honolulu, HI, USA, 1987 [88]
- *11th International Conference on Chemical Vapour Deposition*, Seattle, WA, USA, 1990 [89]
- *12th International Conference on Chemical Vapour Deposition*, Honolulu, HI, USA, 1993 [90]
- *13th International Conference on Chemical Vapour Deposition*, Paris, France, 1996 [91]
- *14th International Conference on Chemical Vapour Deposition*/Jointly held with the Euro CVD-11, Paris, France, 1997 [92]
- *15th International Symposium on Chemical Vapour Deposition*, Toronto, Canada, 2000 [93]
- *16th International Symposium on Chemical Vapour Deposition*/Jointly held with the Euro CVD-14, Paris, France, 2003 [94]

1.5.4.2 European CVD Conferences

- *1st European Conference on Chemical Vapour Deposition* (Euro CVD-1), Paris, France, 1977
- *2nd European Conference on Chemical Vapour Deposition* (Euro CVD-2), Heidelberg, Germany, 1979
- *3rd European Conference on Chemical Vapour Deposition* (Euro CVD-3), Neuchatel, Switzerland, 1980 [95]
- *4th European Conference on Chemical Vapour Deposition* (Euro CVD-4), Eindhoven, The Netherlands, 1983 [96]
- *5th European Conference on Chemical Vapour Deposition* (Euro CVD-5), Uppsala, Sweden, 1985 [97]
- *6th European Conference on Chemical Vapour Deposition* (Euro CVD-6), Jerusalem, Israel, 1987 [98]
- *7th European Conference on Chemical Vapour Deposition* (Euro CVD-7), Perpignan, France, 1989 [99]

- *8th European Conference on Chemical Vapour Deposition* (Euro CVD-8), Glasgow, UK, 1991 [100]
- *9th European Conference on Chemical Vapour Deposition* (Euro CVD-9), Tampere, Finland, 1993 [101]
- *10th European Conference on Chemical Vapour Deposition* (Euro CVD-10), Venice, Italy, 1995 [102]
- *14th International Conference on Chemical Vapour Deposition*/Jointly held with the Euro CVD-11, Paris, France, 1997 [92]
- *12th European Conference on Chemical Vapour Deposition* (Euro CVD-12), Sitges, Spain, 1999 [103]
- *13th European Conference on Chemical Vapour Deposition* (Euro CVD-13), Athens, Greece, 2001 [104]
- *16th International Symposium on Chemical Vapour Deposition*/Jointly held with the Euro CVD-14, Paris, France, 2003 [94]
- *15th European Conference on Chemical Vapour Deposition* (Euro CVD-15), Bochum, Germany, 2005 [105]
- *16th European Conference on Chemical Vapour Deposition* (Euro CVD-16), The Hague, The Netherlands, 2007 [106]

1.5.4.3 Asian CVD Conferences

- *1st Asian Conference on Chemical Vapour Deposition* (Asian CVD-1), Shanghai, China, 1999 [107]
- *2nd Asian Conference on Chemical Vapour Deposition* (Asian CVD-2), Gyeongju, Korea, 2001
- *3rd Asian Conference on Chemical Vapour Deposition* (Asian CVD-3), Taipei, Taiwan, 2004 [108]

1.5.4.4 Conferences on Refractory Metals and Ceramics

- *Chemical Vapour Deposition of Refractory Metals and Ceramics*, Boston, MA, USA, 1989 [109]
- *Chemical Vapour Deposition of Refractory Metals and Ceramics II*, Boston, MA, USA, 1991 [110]
- *Chemical Vapour Deposition of Refractory Metals and Ceramics III*, Boston, MA, USA, 1994 [111]

1.5.4.5 Conferences on High Temperature Ceramic Matrix Composites

- *High Temperature Ceramic Matrix Composites*, Bordeaux, France, 1993 [112]
- *2nd International Conference on High-Temperature Ceramic-Matrix Composites*, Santa Barbara, CA, USA, 1995 [113]

- 3rd International High Temperature Ceramic Matrix Composites, Osaka, Japan, 1998 [114]
- 4th International High Temperature Ceramic Matrix Composites, Munich, Germany, 2001 [115]
- 5th International Conference on High Temperature Ceramic Matrix Composites, Seattle, WA, USA, 2005 [116]
- 6th International Conference on High Temperature Ceramic Matrix Composites, New Delhi, India, 2007 [117]

1.5.5 Representative Papers

Some representative papers on chemical vapour deposition, ceramic and ceramic matrix composites and related area are listed here:

- *Processing of carbon/carbon composites—an overview*, Stoller and Frye, 1972 [118]
- Chemical vapour deposition of electronic materials, Tietjen, 1973 [119]
- *Deposition of pyrolytic carbon in porous solid*, Kotlensky, 1973 [120]
- Structure/property/process relationships in chemical vapour deposition CVD, Blocher, 1974 [121]
- *CVD/PAN felt carbon/carbon composites*, Lieberman *et al*, 1975 [122]
- *Chemical vapour-deposited silicon nitride*, Niihara and Hirai, 1976 [123]
- *The fundamentals deposition of chemical vapour deposition*, Bryant, 1977 [124]
- A thermodynamic and experimental approach of silicon carbide CVD, application to the CVD-infiltration of porous carbon composites, Christin, Naslain and Bernard, 1979 [125]
- Chemical vapor deposition of silicon carbide and silicon nitride and its application for preparation of improved silicon ceramics, Fitzer, Hegen and Strohmeier, 1979 [126]
- *Principles and applications of chemical vapour deposition*, Spear, 1982 [2]
- Fabrication of fibre-reinforced ceramic composites by chemical vapor infiltration, Caputo and Lackey, 1984 [127]
- *Ceramic matrix composites, a literature review*, Schioler and Stigligh, 1986 [128]
- *Progressing of metal and ceramic matrix composites*, Cornie, Chiang and Uhlmann *et al*, 1986 [129]
- *Fibre-reinforced silicon carbide*, Fitzer and Gadow, 1986 [130]
- *SiC/SiC composite ceramics*, Laicq, Bernhart and Dauchier *et al*. 1986 [131]
- Review deposition processes for films and coatings, Biswas, 1986 [132]
- *The future of carbon-carbon composites*, Fitzer, 1987 [133]
- *Advanced ceramics by chemical vapour deposition techniques*, Stinton *et al*. 1988 [134]
- *Carbon-carbon, an overview*, Buckley, 1988 [135]

- *Ceramic coatings for carbon-carbon composites*, Strife and Sheehan, 1988 [136]
- *Monolithic material fabrication by chemical vapour deposition*, Goela and Taylor, 1988 [137]
- Review, status, and future of the chemical vapour infiltration process for fabrication of fibre-reinforced ceramic composites, Lackey, 1989 [138]
- Preform fibre architecture for ceramic-matrix composites, Ko, 1989 [139]
- Fabrication of fibre-reinforced ceramic composites by chemical vapour infiltration, Lackey and Starr, 1990 [140]
- Chemical vapour deposition – a review of 25 years experience, Fitzer, 1991 [141]
- Vapour-phase fabrication and properties of continuous-filament ceramic composites, Besmann, 1991 [142]
- *CVI composites*, Naslain, 1992 [143]
- *CVD scaled up for commercial production of bulk SiC*, Haigis and Pickering, 1993 [42]
- *Advanced SiC composites for fusion applications*, Snead and Schwarz, 1995 [144]
- Rapid vapour-phase densification of refractory composites, Golecki, 1997 [145]
- *Radiation resistant ceramic matrix composites*, Jones, 1997 [146]
- Chemical vapour deposition and infiltration processes of carbon materials, Delhaes, 2002 [147]
- Design, fabrication, and application of thermostructural composites (TSC) like C/C, C/SiC, and SiC/SiC composites, Christin, 2002 [148]
- *SiC-matrix composite materials for advanced jet engines*, Naslain and Christ, 2003 [47]
- *Chemical vapour deposition of coatings*, Choy, 2003 [149]
- *Fundamentals of chemical vapour deposition in hot wall reactors*, Huttinger, 2003 [150]
- Design, preparation and properties of non-oxide CMCs for application in engines and nuclear reactors: an overview, Naslain, 2004 [151]
- *Principles and applications of CVD powder technology*, Vahlas *et al.* 2006 [152]

References

- [1] Hitchman ML, Jensen KF (1993) *Chemical vapour deposition: principles and applications*. Academic, New York
- [2] Spear KE (1982) Principles and applications of chemical vapour deposition. *Pure Appl Chem* 54:1297–1311
- [3] Buiting MJ, Reader AH (1990) Influence of impurities and microstructure on the resistivity of LPCVD titanium nitride films. In: Besmann T M, Gallois B M (eds)

- Chemical vapour deposition of refractory metals and ceramics. Materials Research Society, Pittsburgh, PA, pp199–204
- [4] Komiyama H, Shimogaki Y, Egashira Y (1999) Chemical reaction engineering in the design of CVD reactors. *Chem Eng Sci* 54:1941–1957
- [5] www.ultramet.com
- [6] Naslain R, Pailler R, Bourrat X, Bertrand S, Heurtevent F, Dupel P, Lamouroux F (2001) Synthesis of highly tailored ceramic matrix composites by pressure-pulsed CVI. *Solid State Ion* 141-142: 541–548
- [7] Lodyguine A D (1897) Illuminant for incandescent lamps. US Patent 575,002
- [8] Lodyguine A D (1897) Illuminant for incandescent lamps. US Patent 575,668
- [9] Mond L, Langer C, Quincke F (1890) Action of carbon monoxide on nickel. *J Chem Trans* 57:749
- [10] Mond L (1891) Process of depositing nickel. US Patent 455,230
- [11] van Arkel A E, de Boer J H (1925) *Z anorg u allgem Chem* 148: 345–350
- [12] van Arkel A E, de Boer J H (1928) US Patent 1,671,213
- [13] Shapiro Z M (1955) Iodide-deposition process for production of zirconium. In: Lustman B, Kerze F (eds) *The metallurgy of zirconium*. McGraw-Hill, New York, pp135–215
- [14] Kroll W J (1940) Production of ductile titanium. *Trans Electrochem Soc* 78:35–47
- [15] Kroll W J (1940) Method for manufacture of titanium and alloys thereof, US Patent 2,205,854
- [16] Pring J N, Fielding W (1909) *J Chem Soc* 95:1497–1506
- [17] Vossen J L, Kern W (eds) (1978) *Thin film processes*. Academic, New York
- [18] Vossen J L, Kern W (eds) (1991) *Thin film processes II*. Academic, New York
- [19] Ohring M (1992) *The materials science of thin films*. Academic, San Diego
- [20] Kiehl R A, Sollner T C L G (eds) (1994) *High speed heterostructure devices*. Academic, Boston
- [21] Yeh P (1990) *Handbook of fibre optics*. Academic, San Diego
- [22] Nakamura S, Fasol G (1997) *The blue laser diode*. Springer, Berlin
- [23] Sniegowski JJ, de Boer MP (2000) IC-compatible polysilicon surface micromachining. *Annu Rev Mater Sci* 30:299–333
- [24] Lehmann O, Stuke M (1995) Laser-CVD 3D rapid prototyping of laser driven moveable micro-objects. *J Phys IV5:C5-601–606*
- [25] Duty CE, Jean DL, Lackey WJ (1999) Design of a laser CVD rapid prototyping system. *Ceram Eng Sci Proc* 20:347–354
- [26] Pan ZW, Li HL, Zhang LT (1998) Laser synthesis and crystallization of nanocomposite Si/C/N powder. *J Mater Res* 13:1996–2002
- [27] Wang N, Cai Y, Zhang R Q (2008) Growth of nanowires. *Mater Sci Eng R60*:1–51
- [28] Calestani D, Zha M, Zappettini A, Lazzarini L, Salvati G (2005) Structural and optical study of SnO₂ nanobelts and nanowires. *Mater Sci Eng C25*:625–630
- [29] Pan ZW, Xie SS, Chang BH, Wang CY, Lu L, Liu W, Zhou WY, Li WZ (1998) Very long carbon nanotube. *Nature* 394:631–632
- [30] Motojima S, Kagiya S, Iwanaga H (1996) Preparation of micro-coiled SiC and TiC fibres by vapour phase metallizing of micro-coiled carbon fibres. *J Mater Sci* 31:4641–4645
- [31] Clausing RE, Horton LL, Angus JC, Koidl P (eds) (1991) *Diamond and diamond-like films and coatings*. Plenum, New York
- [32] Yarbrough WA, Messier R (1990) Current issues and problems in the chemical vapor deposition of diamond. *Science* 247:688–696
- [33] Strife JS, Sheehan JS (1988) Ceramic coatings for carbon-carbon composites. *Am Ceram Soc Bull* 67:369–374

- [34] Wakefield GF (1966) Refractory metal coatings by chemical vapour deposition. Accession no. AD0805048
- [35] Buiting MJ, Reader AH (1990) Influence of impurities and microstructure on the resistivity of LPCVD titanium nitride films. In: Besmann TM, Gallois BM (eds) Chemical vapour deposition of refractory metals and ceramics. Materials Research Society, Pittsburgh, PA, pp199–204
- [36] Gao Y, Ma SL, Xue KW (2007) Effect of carbon content and annealing temperature on the microstructure and hardness of super hard Ti–Si–C–N nanocomposite coatings. *Surf Coat Technol* 201:5240–5243
- [37] Watchtell RL, Seelig RP (1962) Diffusion coating of non-ferrous metals. US Patent 3,037,883
- [38] Bunshah RF (1994) Handbook of deposition technologies for films and coatings, 2nd ed. Noyes, Park Ridge, NJ
- [39] www.cvdmaterials.com, accessed January 2009
- [40] Leskela M, Truman JK, Mueller CH, Holloway PH (1989) Preparation of superconducting Y-Ba-Cu-O thin films. *J Vac Sci Technol A* 7(6):3147–3171
- [41] Goela JS, Taylor RL (1988) Monolithic material fabrication by chemical vapour deposition. *J Mater Sci* 23:4331–4339
- [42] Haigis B, Pickering M (1993) CVD scaled up for commercial production of bulk SiC. *Am Ceram Soc Bull* 72:74–78
- [43] Moore AW (1992) Facility for continuous CVD coating of ceramic fibres. In: Besmann T M, Gallois B M, Warren W (eds) Chemical vapour deposition of refractory metals and ceramics II. Materials Research Society, Pittsburgh, PA, pp269–274
- [44] www.specmaterials.com, accessed January 2009
- [45] Morgen P (2005) Carbon fibres and their composites. Taylor & Francis, London
- [46] Christin F (2002) Design, fabrication, and application of thermostructural composites (TSC) like C/C, C/SiC, and SiC/SiC composites. *Adv Eng Mater* 4:903–912
- [47] Naslain R, Christin F (2003) SiC-matrix composite materials for advanced jet engines. *MRS Bull*, 28:9:654–658
- [48] Snead LL, Schwarz OJ (1995) Advanced SiC composites for fusion applications. *J Nucl Mater* 219:3–14
- [49] Liu WC, Wei YZ, Deng JY (1995) Carbon-fibre-reinforced C–SiC binary matrix composites. *Carbon* 33:441–447
- [50] Evans AG (1990) Perspective on the development of high-toughness ceramics. *J Am Ceram Soc* 73:187–206
- [51] Prewo KM, Brennan JJ (1980) High-strength silicon carbide fibre-reinforced glass-matrix composites. *J Mater Sci* 15:463–468
- [52] Prewo KM, Brennan JJ, Layden GK (1986) Fibre reinforced glass and glass-ceramics for high performance applications. *Am Ceram Soc Bull* 65:305–313
- [53] Guo JK, Mao ZQ, Bao CD, Huang R, Yan DS (1982) Carbon fibre-reinforced silicon composite nitride. *J Mater Sci* 17:3611–3616
- [54] Guo JK (1987) Brittleness and toughening of ceramics. *J Ch Ceram Soc* 15:385–393
- [55] Xu YD, Cheng LF, Zhang LT, Luo XT, Zhou WC (1999) Preparation and mechanical properties of self-reinforced in situ Si₃N₄ composite with La₂O₃ and Y₂O₃ additives. *Composites A* 30:945–950
- [56] Chen CM, Zhang LT, Zhou WC, Hao ZZ, Jiang YJ, Yang SL (2001) Microstructure, mechanical performance and oxidation mechanism of boride in situ composites. *Comp Sci Technol* 61:971–975
- [57] Waku Y, Nakagawa N, Wakamoto T, Ohtsubo H, Shimizu K, Kohtoku Y (1997) A ductile ceramic eutectic composite with high strength at 1873 K. *Nature* 389:49–52

- [58] Xu YD, Cheng LF, Zhang LT, Yin HF, Yin XW (2001) Mechanical properties of 3D fibre reinforced C/SiC composites. *Mater Sci Eng A300*:196–202
- [59] Laicq PJ, Bernhart GA, Dauchier MM, Mace JG (1986) SiC/SiC composite ceramics. *Am Ceram Soc Bull* 65:336–338
- [60] Li JZ, ZhangLT, Cheng LF, Xu YD, Li DX (2005) Investigation on interfacial zone in continuous fibre-reinforced ceramic composites. *Rare Metal Mater Eng* 34:170–175
- [61] Powell CF, Oxley JH, Blocher JM Jr (eds) (1966) *Vapour deposition*. Wiley, New York
- [62] Vossen JL, Kern W (eds) (1978) *Thin film processes*. Academic, New York
- [63] Hawkins DT (1981) *Chemical vapour deposition*. Plenum, New York,
- [64] Sherman A (1987) *Chemical vapour deposition for microelectronics: principles, technology and applications*. Noyes, Park Ridge, NJ
- [65] Morosanu CE (1990) *Thin films by chemical vapour deposition*. Elsevier, Amsterdam
- [66] Vossen JL, Kern W (eds) (1991) *Thin film processes II*. Academic, New York
- [67] Ohring M (1992) *The materials science of thin films*. Academic, San Diego
- [68] Kodas T, Hampden-Smith M (eds) (1994) *The chemistry of metal CVD*. VCH, New York
- [69] Rees WS Jr (1996) *CVD of nonmetals*. Wiley
- [70] Jones AC, O'Brien P (1997) *CVD of compound semiconductors*. VCH, New York
- [71] Sivaram S (1995) *Chemical vapour deposition: thermal and plasma deposition electronic materials*. Van Nostrand Reinhold, New York
- [72] Park JH, Sudarshan TS (eds) (2001) *Chemical vapour deposition*. ASM International, Materials Park, OH
- [73] Schuergraf KK (1988) *Handbook of thin film deposition processes and techniques*. Noyes, Park Ridge, NJ
- [74] Bunshah RF (1994) *Handbook of deposition technologies for films and coatings*, 2nd ed. Noyes, Park Ridge, NJ
- [75] Glocker DA, Shah SI (eds) (1995) *Handbook of thin film process technology*. Institute of Physics, Bristol, UK
- [76] Pierson HO (1999) *Handbook of chemical vapour deposition (CVD), principles, technology, and applications*, 2nd ed. Noyes, Park Ridge, NJ
- [77] Department of defense, handbook composite materials Vol 5: ceramic matrix composites (2002) MIL-HDBK-17-5
- [78] Bansal NP (ed) (2005) *Handbook of ceramic composites*. Kluwer, Boston
- [79] Schaffhauser AC (ed) (1967) *Proceedings of the conference on chemical vapour deposition of refractory metals, alloys and compounds*, Gatlinburg, TN, American Nuclear Society, La Grange Park, IL
- [80] Blocher JM, Withers JC (eds) (1970) *Proceedings of the 2nd international conference on chemical vapour deposition*. Los Angeles. Electrochemical Society, Pennington, NJ
- [81] Glaski FA (ed) (1972) *Proceedings of the 3rd international conference on chemical vapour deposition*. Salt Lake City, American Nuclear Society, Hinsdale, UT,IL
- [82] Wakefield GF, Blocher JM (eds) (1973) *Proceedings of the 4th international conference on chemical vapour deposition*, Boston. Electrochemical Society, Pennington, NJ
- [83] Blocher JM, Hintermann HE (eds) (1975) *Proceedings of the 5th international conference on chemical vapour deposition*, Fulmer, England. Electrochemical Society, Pennington, NJ

- [84] Donaghey LF, Raichondhurg P (eds) (1977) Proceedings of the 6th international conference on chemical vapour deposition, Atlanta, GA. Electrochemical Society, Pennington, NJ
- [85] Sedgwick TO, Lydtin H (eds) (1979) Proceedings of the 7th international conference on chemical vapour deposition, Los Angeles. Electrochemical Society, Pennington, NJ
- [86] Blocher JM, Vuillard GE, Wahl G (eds) (1981) Proceedings of the 8th international conference on chemical vapour deposition, Paris, France. Electrochemical Society, Pennington, NJ
- [87] Robinson Mc D, Brekel C H J, Cullen G W, Blocher J M (eds) (1984) Proceedings of the 9th international conference on chemical vapour deposition, Cincinnati, OH. Electrochemical Society, Pennington, NJ
- [88] Cullen GW (ed) (1987) Proceedings of the 10th international conference on chemical vapour deposition, Honolulu, HI. Electrochemical Society, Pennington, NJ
- [89] Spear KE, Cullen GW (eds) (1990) Proceedings of the 11th international conference on chemical vapour deposition, Seattle, WA. Electrochemical Society, Pennington, NJ
- [90] Jensen KN, Cullen GW (eds) (1993) Proceedings of the 12th international conference on chemical vapour deposition, Honolulu, HI. Electrochemical Society, Pennington, NJ
- [91] Besmann TM, Allendorf MD, Robinson M, Ulrich RK (eds) (1996) Proceedings of the 13th international conference on chemical vapour deposition, Paris, France. Electrochemical Society, Pennington, NJ
- [92] Allendorf MD, Bernard C (eds) (1997) Proceedings of the 14th international conference on chemical vapour deposition/Jointly held with the Euro CVD-11, Paris, France. Electrochemical Society, Pennington, NJ
- [93] Allendorf MD, Hitchman ML (eds) (2000) Proceedings of the 15th international symposium on chemical vapour deposition, Toronto, Canada. Electrochemical Society, Pennington, NJ
- [94] Allendorf MD, Maury F, Teyssandier F (eds) (2003) Proceedings of 16th international symposium on chemical vapour deposition/Jointly held with the Euro CVD-14, Paris, France. Electrochemical Society, Pennington, NJ, USA
- [95] Hintermann HE (ed) (1980) Proceedings of the 3rd European conference on chemical vapour deposition (Euro CVD-3), Neuchatel, Switzerland
- [96] Verspui JG, Wolff LR (eds) (1983) Proceedings of the 4th European conference on chemical vapour deposition (Euro CVD-4), Eindhoven, The Netherlands
- [97] Carlsson JO, Lindstrom J (eds) (1987) Proceedings of the 5th European conference on chemical vapour deposition (Euro CVD-5), Uppsala, Sweden
- [98] Porat R (ed) (1985) Proceedings of the 6th European conference on chemical vapour deposition (Euro CVD-6), Jerusalem, Israel
- [99] Ducarrier M, Bernard C, Vandenbulcke L (eds) (1989) Proceedings of the 7th conference on chemical vapour deposition (Euro CVD-7), Perpignan, France. *J Phys*, C5
- [100] Hitchman ML, Archer NJ (eds) (1991) Proceedings of the 8th European conference on chemical vapour deposition (Euro CVD-8), Glasgow, UK. *J Phys* IV, C2
- [101] Mantyla T (ed) (1993) Proceedings of the 9th European conference on chemical vapour deposition (Euro CVD-9), Tampere, Finland. *J Phys* 3, C3
- [102] Battiston GA, Gerbasi R, Porchia M (eds) (1995) Proceedings of the 10th European conference on chemical vapour deposition (Euro CVD-10), Venice, Italy. *J Phys* 5, C5
- [103] Figueras A (ed) (1999) Proceedings of the 12th European conference on chemical vapour deposition (Euro CVD-12), Sitges, Spain. *J Phys* IV, 9, Pr8

- [104] Davazoglou D, Vahlas C (eds) (2001) Proceedings of 13th European conference on chemical vapour deposition (Euro CVD-13), Athens, Greece. *J Phys IV*, 11, Pr3
- [105] Devi A, Parala H, Hitchman M L (eds) (2005) Proceedings of 15th European conference on chemical vapour deposition (Euro CVD-15), Bochum, Germany. Electrochemical Society, Pennington, NJ
- [106] Kleijn C R (ed) (2007) Proceedings of the 16th European conference on chemical vapour deposition (Euro CVD-16), The Hague, The Netherlands. In: *Surf Coat & Technol* 201:8797–9442
- [107] Zhang DW, Wang JT, Liang JW (eds) (1999) Proceedings of the 1st Asian conference on chemical vapour deposition (Asian CVD-1). *Thin Solid Film* 368(2)
- [108] Feng ZC, Chen CF, Kuo CT, Williams K, Shan W (eds) (2006) Proceedings of the 3rd Asian conference on chemical vapour deposition (Asian CVD-3), 2004. In: *Surface Coat Technol* 200:3103–3398
- [109] Besmann TM, Gallois BM (eds) (1990) Chemical vapour deposition of refractory metals and ceramics. Materials Research Society, Pittsburgh, PA
- [110] Besmann TM, Gallois BM, Warren JW (eds) (1992) Chemical vapour deposition of refractory metals and ceramics II. Materials Research Society, Pittsburgh, PA
- [111] Gallois BM, Lee WY, Pickering MA (eds) (1995) Chemical vapour deposition of refractory metals and ceramics III. Materials Research Society, Pittsburgh, PA
- [112] Naslain R, Lamon J, Doumeings D (eds) (1993) High temperature ceramic matrix composites (HT-CMC1), Bordeaux, France. Woodhead, Cambridge, UK
- [113] Evans AG, Naslain R (eds) (1995) Proceedings of the 2nd international conference on high-temperature ceramic-matrix composites, Santa Barbara, CA, 21–24 August 1995, American Ceramic Society, Westerville, OH
- [114] Niihara K, Kyokai NS (eds) (1999) High-temperature ceramic matrix composites III. Proceedings of the 3rd international high-temperature ceramic-matrix composites. Trans Tech, Stafa–Zurich, Switzerland
- [115] Krenkel W, Naslain R, Weinheim HS (eds) (2001) High temperature ceramic matrix composites, Wiley-VCH, New York
- [116] Singh M, Keranskerans RJ, Lara–Curzio E, Naslain R (2005) Proceedings of the 5th international conference on high temperature ceramic matrix composites. American Ceramic Society, Westerville, OH
- [117] Singh M (2008) 6th international conference on high temperature ceramic matrix composites. New Delhi, India, 4–7 September 2007, American Ceramic Society, Westerville, OH
- [118] Stoller HM, Frye ER (1972) Processing of carbon/carbon composites—an overview. *SAMPE Q* 3:10–22
- [119] Tietjen JJ (1973) Chemical vapour deposition of electronic materials. *Annu Rev Mater Sci* 3:317–326
- [120] Kotlensky WV (1973) Deposition of pyrolytic carbon in porous solid. In: Walker PL Jr, Thrower PA (eds) *Chemistry and physics of carbon*. Dekker, New York 9, pp173–262
- [121] Blocher JM Jr (1974) Structure/property/process relationships in chemical vapour deposition CVD. *J Vac Sci Technol* 11:680–686
- [122] Lieberman ML, Curlee RM, Braaten FH, Noles GT (1975) CVD/PAN felt carbon/carbon composites. *J Comp Mater* 9:337–346
- [123] Niihara K, Hirai T (1976) Chemical vapour-deposited silicon nitride Part 1 Preparation and some properties. *J Mater Sci* 11:593–603
- [124] Bryant WA (1977) Review: the fundamentals deposition of chemical vapour deposition. *J Mater Sci* 12:1285–1306
- [125] Christin F, Naslain R, Bernard C (1979) A thermodynamic and experimental approach of silicon carbide CVD. Application to the CVD-infiltration of porous

- carbon composites. In: Sedgwick T O, Lydtin H (eds) Proceedings of the 7th international conference on chemical vapour deposition, Los Angeles. Electrochemical Society, Pennington, NJ, pp499–514
- [126] Fitzer E, Hegen D, Strohmeier H (1979) Chemical vapor deposition of silicon carbide and silicon nitride and its application for preparation of improved silicon ceramics. In: Sedgwick TO, Lydtin H (eds) Proceedings of the 7th international conference on chemical vapour deposition, Los Angeles. Electrochemical Society, Pennington, NJ, pp525–535
- [127] Caputo AJ, Lackey WJ (1984) Fabrication of fibre-reinforced ceramic composites by chemical vapor infiltration. *Ceram Eng Sci Proc* 5:654–667
- [128] Schioler LJ, Stiglich JJ, Jr (1986) Ceramic matrix composites, a literature review. *Am Ceram Soc Bull* 65:289–292
- [129] Cornie JA, Chiang YM, Uhlmann DR, Mortensen A, Collins JM (1986) Progressing of metal and ceramic matrix composites. *Am Ceram Soc Bull* 65(2):293–304
- [130] Fitzer E, Gadow R (1986) Fibre-reinforced silicon carbide. *Am Ceram Soc Bull* 65:326–335
- [131] Laicq PJ, Bernhart GA, Dauchier MM, Mace JG (1986) SiC/SiC composite ceramics. *Am Ceram Soc Bull* 65:336–338
- [132] Biswas D (1986) Review Deposition processes for films and coatings. *J Mater Sci* 21:2217–2223
- [133] Fitzer E (1987) The future of carbon-carbon composites. *Carbon* 25:163–190
- [134] Stinton DP, Besmann TM, Lowden RA (1988) Advanced ceramics by chemical vapour deposition techniques. *Am Ceram Soc Bull* 67:350–355
- [135] Buckley JD (1988) Carbon-carbon, an overview. *Am Ceram Soc Bull* 67:364–368
- [136] Strife JS, Sheehan JS (1988) Ceramic coatings for carbon-carbon composites. *Am Ceram Soc Bull* 67:369–374
- [137] Goela J S, Taylor R L (1988) Monolithic material fabrication by chemical vapour deposition. *J Mater Sci* 23:4331–4339
- [138] Lackey WJ (1989) Review, status, and future of the chemical vapour infiltration process for fabrication of fibre-reinforced ceramic composites. *Ceram Eng Sci Proc* 10:577–584
- [139] Ko FK (1989) Preform fibre architecture for ceramic-matrix composites. *Am Ceram Soc Bull* 68:401–413
- [140] Lackey WJ, Starr TL (1990) Fabrication of fibre-reinforced ceramic composites by chemical vapour infiltration: processing, structure and properties. In: Mazdiyasi K S (ed) *Fibre reinforced ceramics*. Noyes, Park Ridge, NJ, pp397–450
- [141] Fitzer E (1991) Chemical vapour deposition-a review of 25 years experience. *J Phys IV* 2:C2-509–537
- [142] Besmann TM, Sheldon BW, Lowden RA, Stinton DP (1991) Vapour-phase fabrication and properties of continuous-filament ceramic composites. *Science* 253:1104–1109
- [143] Naslain R (1992) CVI composites. In: Warren R (ed) *Ceramic-matrix composites*. Chapman Hall, New York, pp199–244
- [144] Snead LL, Schwarz OJ (1995) Advanced SiC composites for fusion applications. *J Nuclear Mater* 219:3–14
- [145] Golecki I (1997) Rapid vapour-phase densification of refractory composites. *Mater Sci Eng R20*:37–124
- [146] Jones RH, Steiner D, Heinisch HL, Newsome GA, Kerch HM (1997) Review: radiation resistant ceramic matrix composites. *J Nucl Mater* 245:87–107
- [147] Delhaes P (2002) Review: chemical vapour deposition and infiltration processes of carbon materials. *Carbon* 40:641–657

- [148] Christin F (2002) Design, fabrication, and application of thermostructural composites (TSC) like C/C, C/SiC, and SiC/SiC composites. *Adv Eng Mater* 4:903–912
- [149] Choy KL (2003) Chemical vapour deposition of coatings. *Prog Mater Sci* 48:57–170
- [150] Huttinger KJ (2003) Fundamentals of chemical vapour deposition in hot wall reactors. In: Dlhães P (ed) *Fibres and composites*. Taylor & Francis, London, pp75–86
- [151] Naslain R (2004) Design, preparation and properties of non-oxide CMCs for application in engines and nuclear reactors: an overview. *Comp Sci Technol* 64:155–170
- [152] Vahlas C, Caussat BG, Serp P, Angelopoulos GN (2006) Principles and applications of CVD powder technology. *Mater Sci Eng R*53:1–72

Chapter 2 Physical Fundamentals of Chemical Vapour Deposition

The CVD techniques rely on the gases which are transported into a reaction chamber for deposition. In this chapter, the fundamental physics relating to these techniques are introduced to enable a thorough theoretical understanding of the phenomena occurring in a CVD process and the process control parameters. The topics introduced in this chapter include basic gas laws and kinetic theory, vacuum technology, gas transport phenomena and vapour pressures of some commonly used CVD reactant gases.

2.1 Gas Laws and Kinetic Theory

To study gas movement, some basic assumptions are commonly made to facilitate the understanding of the flow behaviour of the gases for a CVD process. Based on these assumptions the investigation can then focus on theory and practice of what is termed an ideal or perfect gas. This is a theoretical concept which corresponds to and is based upon the following assumptions:

1. the molecules themselves are very small spheres and a gas consists of a huge number of particles;
2. the volume of all molecular spheres is much smaller than that actually occupied by the gas;
3. the molecules are independent such that they do not exert any force on each other;
4. they move randomly along rectilinear paths;
5. the molecules are considered to be rigid solids and they make perfect elastic collisions.

Some real gases, such as elements in the periodical table of elements (e.g. H₂, N₂, O₂ and Ar) and gases used in a CVD process (e.g. CH₄ and CH₃SiCl₃ etc.), exhibit the approximate behaviour of ideal gases at atmospheric pressures. At lower pressures (vacuum) many more gases can be treated as the ideal gases. Based on the above assumptions and the model of kinetic theory of gases, the following specific laws of the gases have been generalized and established [1, 2].

2.1.1 Gas Laws

2.1.1.1 Boyle's Law

Ideal or perfect gases obey Boyle's law at all temperatures. This fact was established by Boyle and Mariotte in 1662. According to this law, the product of P and V is constant for a given mass of gas at a constant temperature, where P is the pressure of the gas and V is its volume.

$$PV = \text{const} \quad (2.1)$$

2.1.1.2 State Equation of an Ideal Gas

The volume of a gas is directly proportional to the absolute temperature and inversely proportional to the pressure. This is expressed as

$$PV = nRT \quad (2.2)$$

where n is the number of gas molecules in a mole and R is the universal gas constant ($8.31\text{J}\cdot\text{K}^{-1}\cdot\text{mol}^{-1}$)

2.1.1.3 Dalton's Law of Partial Pressures

The total pressure exerted by a mixture of gases is equal to the sum of the partial pressures exerted by the individual components. This empirical law was observed by John Dalton in 1801 and is expressed by

$$P_{\text{tot}} = p_1 + p_2 + p_3 + \dots + \text{etc.} \quad (2.3)$$

where P_{tot} is the total pressure and p_1, p_2, p_3 and so on are the pressures of an individual gas in a gas mixture.

2.1.1.4 Partial Pressures

The partial pressure exerted by any one component of a mixture of gases is the pressure exerted by the component gas as if it occupied that whole volume alone.

2.1.1.5 Avogadro's Law

Equal volumes of all ideal gases measured at the same temperature and pressure contain the same number of molecules. This law was hypothesised by Amedeo Avogadro in 1811.

2.1.1.6 Avogadro's Number

The number of molecules in one mole of a gas or any gas substance is a universal constant value of 6.02×10^{23} .

2.1.1.7 Mole Volume

The volume occupied by a mole molecule of a gas is a universal constant found experimentally to be 22.4 litres under standard conditions, i.e. a pressure of 101.3 kPa and a temperature of 273 K.

In accordance with the perfect gas laws, the densities of some gases used in CVD processes are listed in Table 2.1. It is clear that there exist considerable density differences for various gases. For the $\text{CH}_3\text{SiCl}_3\text{-H}_2$ reaction system, the density of the CH_3SiCl_3 gas is 75 times greater than that of H_2 under standard conditions. To obtain a homogeneous mixture of the gases, it is necessary to mix the individual gases homogeneously before they are introduced into the reaction chamber. In addition, N_2 or Ar is usually employed as a purge gas before and after

Table 2.1. Density of some gases for CVD applications (at 25°C, 1 atm)

Species	M (g·mol ⁻¹)	ρ (g·l ⁻¹)	Species	M (g·mol ⁻¹)	ρ (g·l ⁻¹)	Species	M (g·mol ⁻¹)	ρ (g·l ⁻¹)
Ar	40	1.79	CH ₄	16	0.71	SiCl ₄	170	7.59
H ₂	2	0.09	C ₃ H ₆	42	1.875	TiCl ₄	190	8.48
N ₂	28	1.25	NH ₃	17	0.76	ZrCl ₄	233	10.40
O ₂	32	1.43	SiH ₄	32	1.43	WF ₆	298	13.30
Air	29	1.29	AlCl ₃	133.5	5.96	CH ₃ SiCl ₃	149.5	6.67
CO ₂	44	1.96	BCl ₃	117.5	5.25	Mo(CO) ₆	264	11.79
H ₂ O	18	0.80	ReCl ₅	363.5	16.23	Ir(acac) ₃	489	21.83

Note: Ir(acac)₃ stands for Ir(C₅H₇O₂)₃

the CVD process. The reason is that the density of N₂ gas is almost the same as that of air, and the density of Ar gas is slightly greater than that of air. Therefore, such a purge gas is very helpful in avoiding the contamination of the water vapour from the air in the chamber.

2.1.2 Gas Kinetic Theory

Gas kinetic theory, for the purposes of this book, consists of the relationships defining the simple pressure, gas velocity distribution, mean free path and impinging flux of gases to the surface of a substrate, and other relevant theoretical relationships. These collective descriptions of the gases form a set of comprehensive theoretical understanding and representation for CVD processes. The following subsections briefly describe this constituent theory.

2.1.2.1 Pressure

Pressure is defined as the force per unit area which a gas exerts on the surface and is given by

$$P = \frac{1}{3} N m u_{av}^2 \quad (2.4)$$

where P is the pressure, N is the molecular number per unit volume, m is the mass of molecule and u_{av} is the mean velocity of the gas molecules. There are many kinds of units for the pressure of a gas; the conversion factors are listed in Appendix A.

2.1.2.2 Maxwell–Boltzmann Distribution

Molecules travel at different velocities. The Maxwell–Boltzmann distribution of velocity is used to define the velocity profile of molecules and is written as

$$f(u) = 4\pi\left(\frac{m}{2\pi kT}\right)^{3/2} u^2 \exp\left(-\frac{mu^2}{2kT}\right) \quad (2.5)$$

where $f(u)$ is the probability of a molecule having a certain velocity, m is the mass of one molecule, k is the Boltzmann constant ($1.38 \times 10^{-23} \text{ J}\cdot\text{K}^{-1}$), u is the magnitude of the velocity of a molecule and T is the temperature in Kelvin.

The most probable velocity, u_p , is the velocity most likely to be possessed by any molecule in the system and corresponds to the maximum value or mode of $f(u)$:

$$u_p = \sqrt{\frac{2kT}{m}} = \sqrt{\frac{2RT}{M}} \quad (2.6)$$

where M is the mole mass of the gas.

The mean velocity is the mathematical average of the velocity (u_{av}) distribution:

$$u_{av} = \int_0^{\infty} u f(u) du = \sqrt{\frac{8kT}{\pi m}} = \sqrt{\frac{8RT}{\pi M}} \quad (2.7)$$

For nitrogen at 298 K, substituting $k = 1.38 \times 10^{-23} \text{ J}\cdot\text{K}^{-1}$, and $M = 28 \text{ g}\cdot\text{mol}^{-1}$. Then, the average velocity is $475 \text{ m}\cdot\text{s}^{-1}$, which is much faster than that of the speed of sound. This implies that the thermal movement of gaseous molecules is very intense.

The root mean square velocity, u_{rms} , is the square root of the average squared velocity.

$$u_{rms} = \sqrt{\int_0^{\infty} u^2 f(u) du} = \sqrt{\frac{3kT}{m}} = \sqrt{\frac{3RT}{M}} \quad (2.8)$$

Figure 2.1 shows the velocity distribution of hydrogen gas at different temperatures ranging from 298 K to 1273 K. The most probable velocity, the mean velocity and the root mean velocity increase with increases in temperature. Moreover, there are more molecules with a higher velocity at higher temperatures because the curve becomes flatter.

The above three velocities have been defined to measure the velocity of molecules from different viewpoints. Three kinds of velocities are used for different applications: the root mean square velocity (u_{rms}) is used for the calculation of the average dynamic energy, the mean velocity u_{av} for the mean distance between molecules, and the most probable velocity (u_p) for the distribution of velocity.

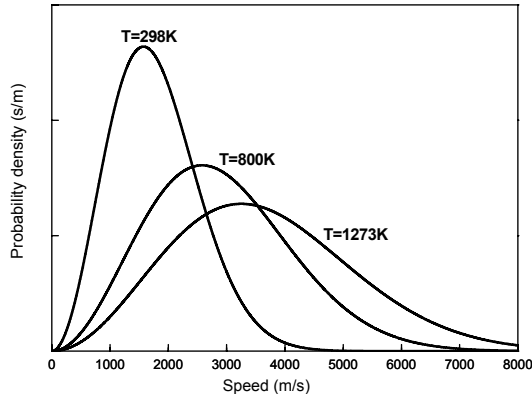


Figure 2.1. Velocity distribution of H_2 gas at different temperatures

These velocities are inherently used to express the same molecular behaviour, and therefore there is a close relationship among them, which is defined as follows:

$$u_{av} = 1.128u_p, u_{rms} = 1.225u_p \quad (2.9)$$

2.1.2.3 Mean Free Path

Though molecules travel at a very high speed, over 400 m per second at ambient temperature, they do not travel in straight lines. They frequently collide with other molecules as they travel. Hence they bounce around and form a zigzag pattern as shown in Figure 2.2.

The molecules in a gas are in constant random motion, periodically colliding with one another and moving off in new directions. The average distance that a molecule moves before colliding with another molecule is called the mean free path and is given by

$$\lambda = \frac{kT}{\sqrt{2}\pi Pd^2} \quad (2.10)$$

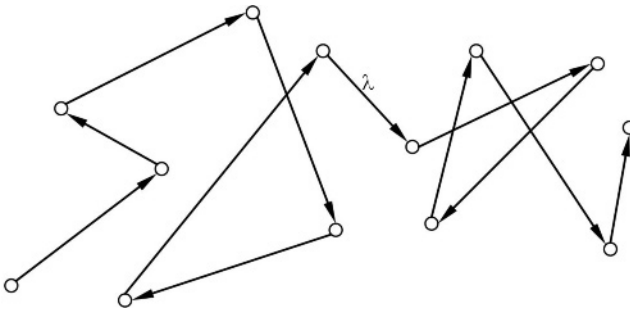


Figure 2.2. Schematic of gas molecule movement and mean free path

where d is the molecular diameter, T is the temperature in *Kelvin*, k is the Boltzmann constant and P is the pressure.

At room temperature, a simple expression is used for the calculation of the mean free path of air [3]:

$$\lambda = \frac{5 \times 10^{-3}}{P} \text{ (cm)} \quad (2.11)$$

where P is the pressure in torr.

According to Equation 2.10, λ differs for various gases and is inversely proportional to the pressure. Table 2.2 lists the diameters, mean free path and three commonly used velocities of some typical gases.

Table 2.2. Molecular diameters, mean free path and velocities of some gases

Gas	M (g/mol)	$d(\times 10^{-10} \text{ m})$	$\lambda(\times 10^{-8} \text{ m})$	$u_p \text{ (m/s)}$	$u_{av} \text{ (m/s)}$	$u_{rm} \text{ (m/s)}$
Air	29	3.76	6.48	413	466	506
Ar	40	3.69	6.73	352	397	431
B ₂ H ₆	28	4.70	4.15	421	475	515
Ba(thd) ₂	503	9.38	1.04	99	112	122
CH ₄	16	4.18	5.25	557	628	681
C ₂ H ₂	26	4.96	3.73	436	492	534
CH ₃ SiCl ₃	149.5	5.11	3.51	182	205	223
Cl ₂	71	5.51	3.02	264	298	324
CO ₂	44	4.66	4.22	335	379	411
Cu(thd) ₂	429.5	9.34	1.05	107	121	132
H ₂	2	2.83	11.44	1574	1776	1927
He	4	2.20	14.09	1113	1256	1363
N ₂	28	3.78	6.41	421	475	515
NH ₃	17	4.57	4.39	540	609	661
O ₂	32	3.61	7.03	393	444	483
SiH ₄	32	4.08	5.51	393	444	483
Si(OC ₂ H ₅) ₄	208	6.90	1.92	154	174	189
WF ₅	279	5.21	3.38	133	150	163
WF ₆	298	5.21	3.38	129	145	158
Y(thd) ₃	638	10.7	0.8	88	99	108

Note: 1. Gases are at the conditions of 25°C, 1 atm,

2. thd: 2,2,6,6-tetramethyl-3,5-heptandionate, C₁₁H₁₉O₂

It should be noted that the mean free path is different from the average distance between molecules. Considering the example of N_2 gas at 25°C and 1 atm, the mean free path and mean distance are $6.42 \times 10^{-8}\text{m}$ and $3.34 \times 10^{-9}\text{m}$, respectively. It is clear that the mean free path is one order greater than the mean distance. Due to molecules with small size but high velocity of thermal movement, gaseous molecules are unlikely to collide with each other quickly, hence resulting in a larger mean free path.

2.1.2.4 Knudsen Law (Cosine Law) [4]

In an equilibrium state, the number of the gaseous molecules impinging onto a specific area obeys the Cosine law, or Knudsen law. The details are explained as follows.

It is assumed that the gaseous molecules are equally distributed in all directions at all the places and they move randomly. For a specific area (dA) on the inner surface of a chamber, the probability of the molecules moving from the solid angle ($d\omega$) is equal to $d\omega/4\pi$. It is noted that there is an inclusion angle (θ) formed between the normal line of this area and the solid angle, as shown in Figure 2.3. For the molecules within the velocity range from u to $u+du$, the number of the molecules (dN) impinging onto the dA area in the unit time from the solid angle is given by

$$dN = \frac{d\omega}{4\pi} n \cdot f(u) \cdot u \cdot \cos\theta \cdot dA \quad (2.12)$$

where n is the number of molecules within the unit volume and $f(u)$ is the Maxwell–Boltzmann distribution function in Equation 2.5.

By integrating the velocity from 0 to infinity, the total number of molecules impinging on the area of dA is given by

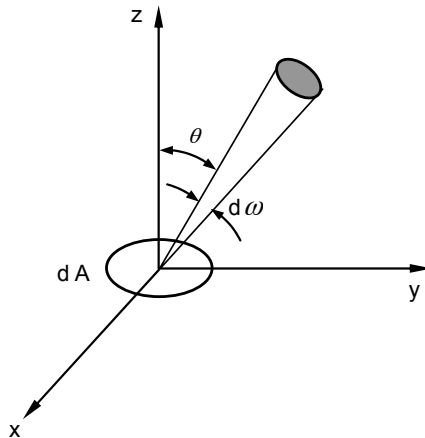


Figure 2.3. Schematic of Knudsen's law

$$N = \frac{d\omega}{4\pi} n \cos \theta dA \int_0^{\infty} u f(u) du = \frac{d\omega}{4\pi} n u_{av} \cos \theta dA \quad (2.13)$$

The cosine law of Equation 2.10 means that the number of molecules impinging on an area is proportional to the cosine function of the angle (θ).

To explain the significance of this law, Knudsen assumed that a molecule is wholly adsorbed by the surface of a solid and remains on the surface for a period of time; it is subsequently “rebounded” from the surface in a direction which does not depend on the incidence angle or its history before the adsorption takes place. This explanation has been confirmed and validated by considerable experimental observations.

The residence time (τ) of a molecule on the surface is of interest in understanding a CVD mechanism, and the following expression has been established [5]:

$$\tau = \tau_0 \exp\left(-\frac{Q}{RT}\right) \quad (2.14)$$

where τ_0 is equal to the period of the gas molecule vibration, which should be of the order of 10^{-13} s, and Q is the adsorption heat. For example, for CO on the crystal plane (111) of Pd, the residence time over the temperature range of 580 to 700 K is in the range of 0.1 to 10 ms.

According to the cosine law, the number of gas molecule collisions on a wall in per unit area and per unit time is given by

$$n_0 = \frac{1}{4} n u_{av} \quad (2.15)$$

where n is the number of gas molecules in unit volume.

2.1.2.5 Hertz–Knudsen Law

During the CVD process, the molecules to be incorporated into the lattice of substrate must be delivered to the surface from the bulk gas. The flux of incident molecules onto the substrate surface is defined by the Hertz–Knudsen equation [3, 6]:

$$F = \frac{P}{\sqrt{2\pi MRT}} \text{ [mole}\cdot\text{cm}^{-2}\cdot\text{s}^{-1}] \quad (2.16)$$

where P is the gas pressure in torr, M is the mole mass of the gas in $\text{g}\cdot\text{mol}^{-1}$ and T is the absolute temperature in Kelvin.

Another useful expression is given by [3, 6]

$$F = 3.35 \times 10^{22} \frac{P}{\sqrt{MT}} \text{ [molecules}\cdot\text{cm}^{-2}\cdot\text{s}^{-1}] \quad (2.17)$$

2.2 Vacuum Technology

A vacuum vessel or chamber is normally required to create a suitable environment for a CVD process to take place. The quality and the controllability of such a vacuum environment are critical to a CVD process. The technologies associated with vacuum generation and maintenance is therefore important and is described in this section.

2.2.1 Definition and Classification of Vacuum

The constituents of the normal atmosphere are mainly nitrogen and oxygen in the ratio of 80% to 20%, together with a small amount of rare gases, such as carbon dioxide, argon, neon and helium and a variable quantity of water vapour depending on ambient temperature and humidity conditions. The abundance of each gas can be conveniently expressed as either mass percentage, volume percentage or the pressure that each constituent gas contributes to the total. The detailed values of these measurements for each gas are listed in Table 2.3.

Table 2.3. Composition of dry atmospheric air at sea level [7]

Component	Mass(%)	Volume(%)	Partial pressure(kPa)
N ₂	75.51	78.1	79.2
O ₂	23.01	20.93	21.2
Ar	1.29	0.93	0.947
CO ₂	0.04	0.83	3.1×10 ⁻²
Ne	1.2×10 ⁻³	1.8×10 ⁻³	1.9×10 ⁻³
He	7×10 ⁻⁵	7×10 ⁻⁵	5.3×10 ⁻⁴
CH ₄	2×10 ⁻⁴	2×10 ⁻³	2×10 ⁻⁴
Kr	3×10 ⁻⁴	1.1×10 ⁻⁴	1.1×10 ⁻⁴
N ₂ O	6×10 ⁻⁵	5×10 ⁻⁵	5×10 ⁻⁵
H ₂	5×10 ⁻⁶	5×10 ⁻⁵	5×10 ⁻⁵
Xe	4×10 ⁻⁵	8.7×10 ⁻⁶	9×10 ⁻⁶
O ₃	9×10 ⁻⁶	7×10 ⁻⁶	7×10 ⁻⁶
	Σ100%	Σ100%	Σ101.3
50%RH at 20°C	1.6	1.15	11.7

Note: water vapour pressure is 7 Torr and varies largely according to the humidity

According to the definition of the American Vacuum Society originally defined in 1958, the vacuum is defined as the fact that a given space filled with gas at pressure below the atmospheric pressure, i.e. having a density of less than about

2.5×10^{19} molecules·cm⁻³. The general term of vacuum includes nowadays about 19 orders of magnitude of pressures (or densities) below that corresponding to the standard atmosphere. Considering the atmospheric pressure to be 10^5 Pa, the vacuum definition using the above standard is at a pressure of 10^{-14} Pa [3].

A perfect or absolute vacuum implies the unrealisable state of space entirely devoid of matter, which is extremely difficult to achieve. For practical purposes, four levels of vacuum are defined for CVD processes. To be more specific, these four pressure ranges and some features are listed in Table 2.4.

A CVD process is generally performed in a vacuum condition. The two main factors that require a vacuum condition are (1) to remove or minimise the active atmospheric constituents that could cause undesirable physical or chemical reactions (especially oxygen and water vapour) and (2) to improve the coating uniformity by increasing the mean free path of precursor gases. As the pressure is decreased from its atmospheric value of almost 760 Torr to 0.5 to 1 Torr, the free mean path increases by a factor of 1000, as shown by Equation (2.10).

Most CVD systems operate in the low or medium vacuum regimes. To ensure a clean chamber, however, CVD systems are often pumped into the high vacuum regime before introducing the reactant precursor gases.

In order to express the state of a vacuum system, various sources of undesirable gases existing in the system must be considered to reflect the dynamic equilibrium during the pumping process. The sources of gases in a vacuum system are as follows:

1. the gas molecules of the initial atmosphere enclosed in the vacuum system;
2. the gas which penetrates into the system as a result of leakage, especially from the areas where there are moving parts and sealing elements, causing

Table 2.4. Classification of vacuum

	Low vacuum	Medium vacuum	High vacuum	Ultra high vacuum
Pressure (Torr)	760–1	$1-1 \times 10^{-3}$	$10^{-3}-10^{-8}$	$<10^{-8}$
Pressure (Pa)	1.01×10^5 -1×10^2	10^2-10^{-1}	$10^{-1}-10^{-6}$	$<10^{-7}$
Number of molecules in cm ³	2.69×10^{19} -3.54×10^{16}	3.54×10^{16} -3.54×10^{13}	3.54×10^{13} -3.54×10^8	$<3.54 \times 10^8$
Mean free path (cm)	6.7×10^{-6} -5.1×10^{-3}	5.1×10^{-3} -5.1	5.1 -5.1×10^{-5}	$<5.1 \times 10^{-5}$
Molecule incidence rate (molec·cm ⁻² ·s ⁻¹)	2.87×10^{23} -3.78×10^{20}	3.78×10^{20} -3.78×10^{17}	3.78×10^{17} -3.78×10^{12}	3.78×10^{12}
Flow characteristics	Continuum flow	Transition region	Free molecular flow	Molecule motion

- wear and further leakage;
3. the gas desorbed from the thermal insulator materials with the porous structure and the cold surface of the chamber;
 4. the gas entering the system by permeation through walls and windows; and
 5. the gas delivered into the reaction chamber for the CVD process.

Taking into consideration the above factors, it is possible to understand the influence of various gas sources on the vacuum system and how to design such a vacuum system. It is helpful to use this understanding to judge if the vacuum system is in good condition, as well as to analyse and eliminate any problems with the vacuum that might arise.

2.2.2 Quantitative Description of the Pumping Process

The conductance C of a duct (or a pipe) for a flow of gas is the rate of flow under pressure gradient. As shown in Figure 2.4, it is used to measure the ease of gas flow and defined by [7, 8]

$$C = \frac{Q}{P_1 - P_2} \quad (2.18)$$

where P_1 and P_2 are the pressure at the inlet and at the outlet of a duct, respectively, Q is the flow throughput.

If the duct is assumed smooth, round, straight and sufficiently long ($L \gg d$), the conductance for the viscous flows can be expressed as

$$C_v = \frac{\pi d^4 P}{128 \mu L} \quad (2.19)$$

For molecular gas flows, the conductance is given by

$$C_m = \frac{1}{6} \sqrt{\frac{2\pi RT}{M}} \cdot \frac{d^3}{L} \quad (2.20)$$

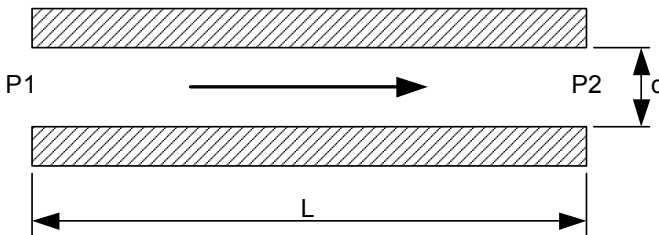


Figure 2.4. Conductance of gas flow in a pipe

For intermediate flows, the expression is given as

$$C_t = C_v + \frac{1 + c_1 P}{1 + c_2 P} C_m \quad (2.21)$$

where c_1 and c_2 are two constants related to the gas species and pipe diameter, M is the molar mass of the gas, P is the average pressure along the pipe, R is the gas constant and T is temperature.

For the air at a temperature of 20°C, its viscosity is 18.2×10^{-6} Pa-s, and the above conductance expressions can be rewritten as follows:

$$C_v = 1.366 \frac{d^4 P}{L} \quad (2.22)$$

$$C_m = 12.1 \frac{d^3}{L} \quad (2.23)$$

$$C_t = \frac{d^3}{L} [136.5dP + 12.1(\frac{1 + 192dP}{1 + 237dP})] \quad (2.24)$$

It is important to note that in the molecular flow regime the conductance depends on the cube of the diameter of the tube and the $-1/2$ power of the mole mass of the gas being pumped, but the conductance is independent of the pressure.

For the parallel connection of the ducts, the total conductance (C) is the sum of all individual conductances and is given by [9]

$$C = C_1 + C_2 + \dots + C_n \quad (2.25)$$

where C_1 , C_2 and C_n are the different individual conductances respectively.

For the series connection of the ducts, the total conductance (C) is expressed by [9]

$$\frac{1}{C} = \frac{1}{C_1} + \frac{1}{C_2} + \dots + \frac{1}{C_n} \quad (2.26)$$

Because of the resistance to gas flow in the connection between a vacuum chamber and the pump, the effective pump volume speed (S) at the chamber is usually less than the volume flow rate of the pump (S_p) at its inlets. The relationship between S and S_p is given by [3]

$$\frac{1}{S} = \frac{1}{C} + \frac{1}{S_p} \quad (2.27)$$

where C is the effective conductance of the system from the pump to the vacuum chamber and S_p is the pumping speed.

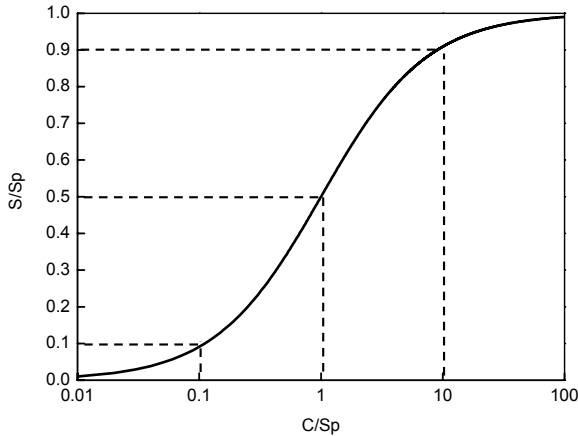


Figure 2.5. Relationship between S/S_p and C/S_p

In Figure 2.5, it can be seen that S/S_p only reaches 50% if the value of the conductance equals that of the pumping speed, i.e. the ratio of C/S_p equals 1. $S/S_p = 90\%$ can be achieved when the conductance is 10 times S_p . If the conductance is much less than S_p , then S is determined entirely by the conductance of the duct but not by the speed of the pump. For this reason, it is not useful to increase the pump performance or speed if the conductance of the pipe is the limiting factor. To ensure sufficient conductance, it is necessary to minimise the duct length between the vacuum chamber and the vacuum pump, as well as to use the duct with a large enough diameter.

2.2.3 Vacuum Pumps

2.2.3.1 Vacuum Pump Parameters and Classification

The pump parameters are used to define the behaviour of a pump system and are very important in selecting a suitable pump and in designing a vacuum system. These parameters mainly include the lowest pressure, pressure range, pumping velocity and exhaust pressure. The selectivity of the pump and the compositions of the residual gases are the additional parameters if the ultra-high vacuum is required in some applications. The following sections give more detailed definitions and descriptions of these parameters [3].

Lowest Pressure

The lowest pressure is the extreme low pressure which can be achieved by a vacuum pump at its inlet. This pressure is mainly dependent on the working principle of a vacuum system and the type of pumps used in such a system. For a given vacuum pump, the lowest pressure is determined either by the leakage pressure in the pump itself, at which point the pump becomes ineffective in maintaining the desirable pressure, or by the vapour pressure of the fluid used.

Pressure Range

The pressure range is the pressure difference of the maximum pressure and the minimum pressure in which a vacuum pump can work efficiently. It is necessary to combine the different types of pumps together to generate high vacuum pressure.

Pumping Speed

Pumping speed is defined as the volume of gas evacuated by a pump within the unit time. It is expressed by

$$S_p = \frac{dV_{P,T}}{dt} \quad (2.28)$$

where S_p is pumping speed, t is time, $V_{P,T}$ is the gas volume evacuated under a pressure P and at a temperature T . It is an important parameter for selecting the capacity of a pump according to the size of the vacuum chamber for a given CVD process.

Exhaust Pressure

The exhaust pressure is the pressure at the outlet of a pump. If the maximum pressure of a pump is lower than the atmospheric pressure (e.g. roots pump and oil diffusion pump), it must be backed with a mechanical rotary pump. In addition, some types of pumps have no outlet, such as ionisation and sorption pumps.

Vacuum pumps are generally divided into 13 categories according to the working principle, as listed in Table 2.5. They include water jet pump, water ring pump, steam ejector, oil-sealed rotary pump, Roots pump, vacuum diffusion pump, oil vapour booster pump, sputtering-ion pump, radial field pump, titanium sublimation pump, sorption pump, molecular pump and cryopump [9].

Table 2.5. Vacuum pump classification and related parameters

Vacuum pump	Maximum capacities (l·s⁻¹)	Operating pressure range (Torr)
Water jet pump	500	760 to 15~25
Water ring pump	1 to 2500	760 to 100 (1 stage), 760 to 25 (2 stage)
Steam ejector	100,000	760 to 75 (1 stage), 125 to 20 (2 stage) 30 to 2.5 (3 stage), 5 to 0.03 (4 stage)
Oil-sealed rotary pump	0.25 to 500	760 to 2×10 ⁻² (1 stage), 760 to 5×10 ⁻³ (2 stage)
Roots pump	50 to 35,000	10 to 10 ⁻³
Vacuum diffusion pump	95,000	From 10 ⁻² to 10 ⁻⁹
Oil vapour booster pump	23,000	1 to 10 ⁻⁴

Table 2.5. (continued)

Sputtering-ion pump	7,000	10^{-2} to below 10^{-11}
Radial field pump	400 to 800	10^{-4} to below 10^{-11}
Titanium sublimation pump	Thousands	10^{-3} to below 10^{-11}
Sorption pump	1,000	760 to 10^{-2} (1 stage), 760 to 10^{-5} (multistage)
Molecular pump	10,000	10^{-1} to 10^{-10}
Cryopump	Million	10^{-3} to below 10^{-10}

Because of the large gas output involved in some CVD processes, a combination of a rotary pumping system with a Roots pump is commonly used to give the desired output flow rate. Since the rotary pump works in an oil environment, the current trend is to replace the rotary pumps with dry pumps, which operate without oil, to reduce oil contamination. For very low pressure operation, a turbomolecular pump is used to provide an extra-high vacuum. For the halides, the Roots pump is still used since turbomolecular pumps do not withstand long operation in acid conditions. An additional turbomolecular or cryogenic pump-based system is commonly used to ensure reactor cleanliness before actual runs of the gases in the reaction chamber, with the typical pressure in the 10^{-9} Torr range.

The following section describes the working principles of the mechanical rotatory pump and the Roots pump, as well as related topics.

2.2.3.2 Mechanical Pumps

Principle and Characteristics

Mechanical pumps are used directly to produce a low and medium vacuum, as well as extensively to back Roots vacuum, turbomolecular and diffusion pumps. These pumps are also called oil-sealed rotary vane pumps as they rely on the use of vanes or blades to compress gases.

A rotary vacuum pump is essentially a gas compressor. The mechanism of the pump is designed such that it has an eccentric blade or vane rotating to cause four distinctive actions, namely gas introduction, isolation, compression and gas exhaust. The working principle of the mechanism is therefore divided into four steps during the rotation of the vanes, as illustrated in Figure 2.6:

1. Gas is introduced into the pump from a working chamber to be vacuumed.
2. Then the gas is isolated into the pump cavity between the rotor and the stator by the vanes when they rotate passing the seal-off point.
3. The trapped gas is continuously compressed by the rotation of the rotary vane. As the rotor is eccentric to the inner surface of the stator, the further rotation of the vanes compresses the gas into a smaller space. During this operation, the vanes loaded by the spring and helped by the centrifugal force can seal the contact area even though they are rotating eccentrically.

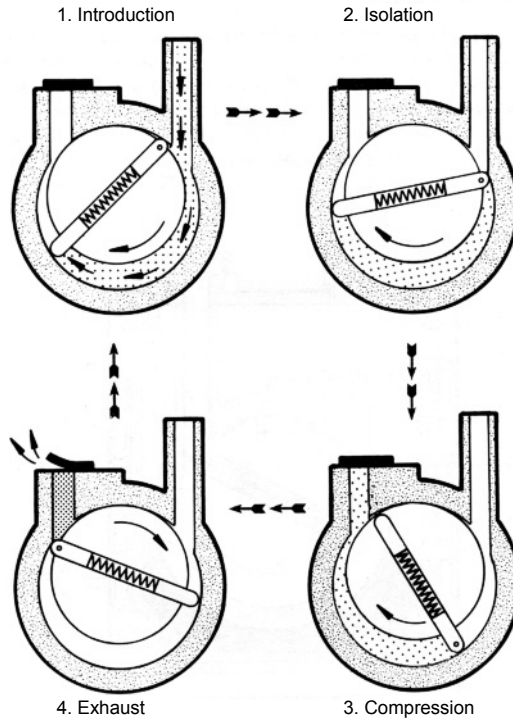


Figure 2.6. Working principle of a rotary vane pump [10]

4. The compressed gas is either flushed out to the atmosphere via the controlled exhaust valves or conveyed to the next stage for further compression.

These pumps are immersed in the oil during operation. Oils are used on the one hand to lubricate the moving parts, e.g. rotor, vanes and contact between rotor and stator, and on the other hand, to seal the rubbing interface between the stator and the vanes. Gas leakage between the rotor and stator interfaces is prevented by a close contact between the vanes and the stator. The centrifugal force also helps the vanes to keep in close contact with the stator. The seal between the stator and vane blades is created by a thin layer of oil film formed by the small quantity of oil between the stator and rotor surface. A vane rotor pump with a good oil sealing can achieve a compression ratio (the ratio of pressure at the outlet to that at the inlet) of as high as 10^5 or 10^6 .

In theory, the lowest pressure achieved by oil-sealed rotary vane pumps is determined by the outlet pressure which can be discharged either to the atmosphere or the inlet of the next stage of the vane pumps. When the exhaust gas pressure becomes lower than the atmospheric pressure, the gas trapped inside the pump cannot be discharged. If the inlet pressure of 10^{-2} Torr is produced for the

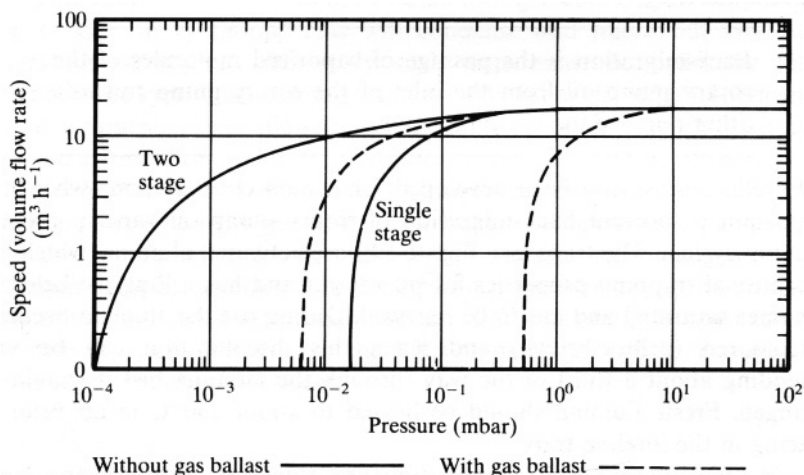


Figure 2.7. Pumping velocity versus pressure curves of mechanical pump [10]

atmospheric exhaust pressure, then the compression ratio of the pump should reach the order of 10^5 . If an even lower inlet pressure is desired, it is necessary to introduce the next stage of pumping action.

In cases of such requirements, the lowest pressure can be further reduced by using two stages of a pump configured in series. The first stage, usually called the high vacuum stage, is connected to the second stage, called the low vacuum stage, through an internal duct. This series arrangement enables the exhaust pressure of the high vacuum stage to discharge the gas at a pressure much lower than atmospheric pressure, due to a second compression at the low vacuum stage. The lowest pressure of a single-stage rotary pump is usually 5×10^{-2} Torr, and the two-stage pumps can achieve a 1×10^{-4} Torr inlet pressure, thereby giving two-stage pumps a higher compression ratio close to 10^7 .

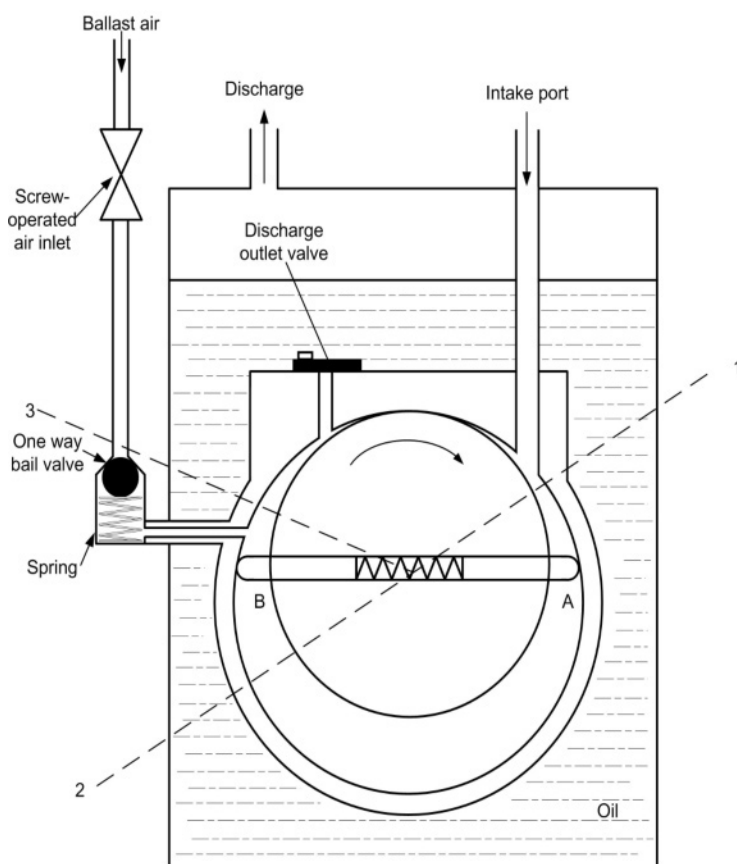
The speed curve of a mechanical rotary pump is shown in Figure 2.7. The pumping speed is nearly a constant in the pressure range of 760 to 10 Torr. Then, it is significantly decreased when the pressure is below 10 Torr. Furthermore, the speed decrease of a single-stage pump is much more rapid than that of a two-stage pump. The pumping speed becomes zero when the pressure reaches the lowest value.

The performance of the mechanical pump is mainly dependent on the finish of the parts, the sealing between the tips of the vanes of the rotator and the bore of the stator and between the sides of the vanes and the rotator. The suitable spacing between the vanes and the slot of the rotator is typically in the range of 0.04 to 0.1 mm. If the gap is too small, the vanes may be “stuck” within the slot, thereby decreasing the rotation speed and the pumping efficiency. If the gap is too large, leakage occurs, resulting in lower vacuum generated.

Gas Ballast

For mechanical pumps, the potential condensation of vapours from the work chamber can cause problems for the pumps, especially for a CVD process. The compression of the vapour leads to condensation, which forms liquid droplets, if the partial pressure of a gaseous vapour reaches its saturated vapour pressure of a liquid. These condensed liquid droplets may contain water, HCl and some chlorosilanes. They mix with the pump oil and result in corrosion of pump parts. For example, the vapour pressure of methyltrichlorosilane (a kind of precursor for SiC deposition) at 28°C is about 200 Torr. If this gas is compressed by a factor of 10^7 by a two-stage pump, methyltrichlorosilane will be condensed if its partial pressure in the reaction chamber is more than 2×10^{-5} Torr.

In order to solve this problem, a gas ballast valve was first designed by Gaede in 1935 [3], as shown in Figure 2.8, which periodically injects a small amount of air, or an inert gas such as N_2 [11], into the pump in a controlled manner at the



1, 2 and 3 denote successive positions of A during a revolution

Figure 2.8. Working principle of the gas-ballast pump [12]

compression stage. The leading vane, A, rotates from position 2 to position 3, and the valve is open, resulting in the introduction of air into the pump. During this period, the isolated gas is not compressed. Instead, the injected air mixes with the isolated gas. When the mixture of the gases reaches the ejection pressure at the outlet port, the partial pressure of the vapour remains below its saturated pressure such that it can prevent the condensation of the vapour, as shown by the dashed line in Figure 2.7. In such a case, the lowest pressure of the pump is dropped by two orders of magnitude.

Pump Oil

Pump oil plays an important role in oil-sealed mechanical pumps. Its primary functions in such a system include [7, 12]

- lubrication of mechanical moving parts such as the bearings of the rotor, the spring-loading sliding vanes onto the rotor, and rubbing surfaces between the tips of the vanes and the inner surfaces of the stator;
- provision of a thin film of oil to seal off the gap between the moving vanes and the inner surfaces of the stator; and
- dissipation of the heat from the pump oil through the pump stator to the atmosphere which is generated from the surface frictions among moving parts and the gas compression [13].

Hence, the pump oils for oil-sealed rotary vacuum pumps must meet the following essential function requirements: a suitably low vapour pressure, a good thermal stability up to 100°C, a good spreadability to seal the moving surfaces in the pump, a good lubrication capability for the moving parts, a good chemical resistance to react with the pumped gases and oxygen, and so forth.

Commonly, three types of pump oils, namely mineral oil, white oil and synthetic oil, are used in rotary pumps.

Mineral oils are the by-products of the distillation of petroleum and are also called hydrocarbon oils and are obtained directly from petroleum refineries. The composition of these kinds of oil is predominately alkanes with trace amounts of aromatics and heterocyclics. They exhibit good lubricating properties and allow the attainment of low ultimate pressures. However, their chemical resistance is relatively poor, particularly to vigorous oxidants. As a result, mineral oils are very suitable for general-purpose use in vacuum pumps.

The technical white oil series of hydrocarbon fluids are further distilled from petroleum stocks that are processed to remove aromatics, heterocyclics and olefinic materials. As a result of removing these substances, they exhibit a good chemical reaction resistance and can be used for pumping corrosive gases and vapours such as halogens, hydrogen halides, Lewis acids (AlCl_3 , FeCl_3 , BCl_3 etc.) and halocarbon. Their service lives are increased by two to three times compared with the normal mineral oils or doubly distilled oils. However, this kind of hydrocarbon oil is subject to reaction with oxygen.

Synthetic pump oils are also called inert oils. So far, there are mainly two types of synthetic pump oils available: perfluoropolyethers (PFPE) and polychlorotrifluoroethylenes (CTFE). PFPE oils are not flammable and inert to most gases and by-products of CVD processes. They are stable and most useful in highly

Table 2.6. Comparison of three different kinds of pump oils [7, 12]

	Mineral oil	Technical white oil	Perfluoropolyether
Resistance to halogens and halogen compounds	Low	Medium	High
Temperature resistance	Medium	Low	High
Resistance to oxidation	Medium	Low	High
Wetting properties	High	High	Low
Solvent power for abraded parts	High	Medium	Low
Minimal dwell period of reactive gases in sealant	Low	Medium	High
Resistance to Lewis acids	Low	Low	Medium
Solvent power for SiO ₂	Low	Low	Low
Solvent power for NH ₄ Cl	Low	Low	Low
Solvent power for silicon-nitrogen compounds	High	Low	Low

corrosive environments and in the presence of large quantities of oxygen. Although PFPE oils do not react with most processing gases, many gases are highly soluble in the oils. Therefore, filtering and neutralisation techniques must be used to remove the soluble gases to prevent the acids attacking the pump parts. The main limitations of PFPE oils are their high cost and ease of decomposition by ammonia and aluminium chloride. Another problem of PFPE oils is their relatively high vapour pressure. CTFE oils share many of the properties of PFPEs, but they are much less expensive. They are stable in the presence of oxygen, halogens, hydrogen and halides; however, they are also easily decomposed by ammonia and aluminium chloride.

To summarise the performance of the three aforementioned oils, Table 2.6 has been compiled to compare and contrast these oils for CVD purposes.

As oils may react with exhaust gases and trapped soluble substances, they can produce corrosive substances and particles inside the pump will eventually cause damage to the pump. It is therefore necessary to change the oils regularly to achieve their maximum designed life. Otherwise, they may increase the mechanical wear of moving parts, leading to higher expenditures on repair and maintenance and lower efficiency in vacuum generation. When frequent oil changes are required to maintain oil quality and vacuum generation efficiency, it is necessary to consider the introduction of partial-flow or full-flow type filters (Figure 2.9). A partial-flow filter, also called a bypass filter, returns filtered oil directly to the reservoir of the pump system. The oil used to lubricate the pump is directly

pumped from the reservoir, which may contain untreated oil. This can potentially cause wear and corrosion if the untreated oil contains particles or chemically reactive substances. With a full-flow system, the filter treats the oils from the reservoir pumped by an oil pump within the vacuum pump. Purified oil is then introduced into the pump to perform its three functions. The oil filters work on either physical or chemical principles. The former uses porous filters to remove very small particles, whereas chemical filters use activated alumina to adsorb high molecular weight compounds. Activated alumina filters also act as a mechanical filter to remove particles with size down to 3 μm .

2.2.3.3 Roots Pump

In some applications a flow throughput is required to rapidly extract the gas from a chamber. In order to achieve this two methods can be employed: to increase the volume pumped on each stroke by making a bigger pump or to increase the pump rotation velocity. The former will lead to higher cost. The latter is subject to the limitations of heat dissipation within the pump and the rotation speed of the vane pumps, which is normally less than 2000 r mp. Alternatively, one can construct a pump without sliding seals. This allows very high rotational velocities because the mechanical contact friction between the vanes and the walls of the stator does not exist. Compression is achieved by using a narrow clearness between the rotating parts and the walls. In the simplest case this can be used as precompressor for a conventional rotary pump. This kind of vacuum pump is named after its inventor – the brothers Philander and Francis Roots, who patented their design in 1860.

The working principle of the Roots pump is shown in Figure 2.10. It consists of two impellers constructed in a shape of Arabic numeral eight (figure 8). These impellers are rotated in opposite directions within the pump housing. The shaft of the driving impeller is directly connected to a motor or via a belt, whereas the shaft of the driving impeller is normally connected to gears and rotates in the opposite direction. When one of the impellers is at its vertical position as shown in Figure 2.10a, its bottom surface is tangential to the middle section surface of the other impeller, which is in a horizontal orientation. This arrangement of the impellers ensures the isolation of the inlet from the exhaust outlet. When the top impeller rotates further to the horizontal orientation with the bottom impeller in a vertical

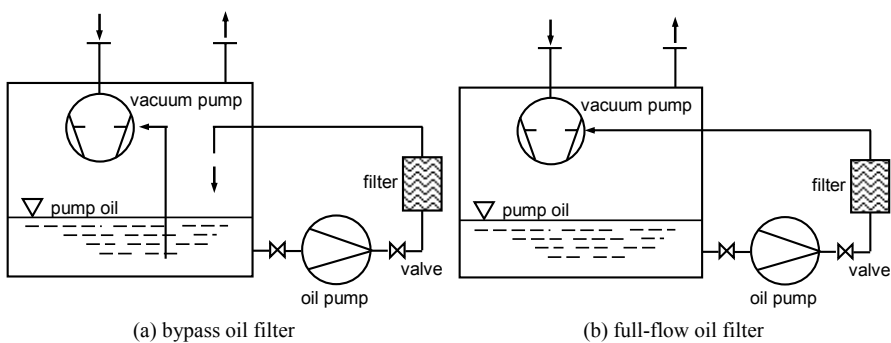


Figure 2.9. Schematic of oil filtration system for oil-sealed rotary pumps [7]

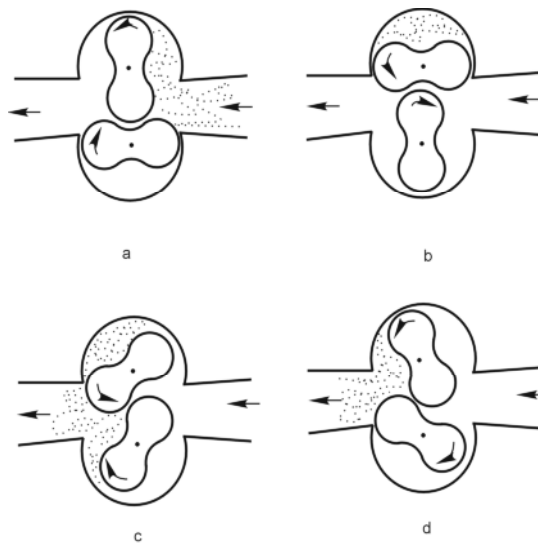


Figure 2.10. Working principle of Roots pump [3]

position as shown in Figure 2.10b, the gas withdrawn into the top chamber is separated from the inlet channel and forced into the exhaust outlet. A further rotation by the top impeller forces the gas into the exhaust outlet as the bottom impeller seals off the bottom half of the impeller housing, shown in Figure 2.10c. For every rotation by the top impeller, there are two cycles of gas pumping actions, in other words, twice as much as the gas shown in the shaded area in Figure 2.10b is pumped or forced through the Roots pump system.

The Roots pump is always connected to a mechanical pump, which provides a second-stage pumping between it and the atmosphere. The pressure difference

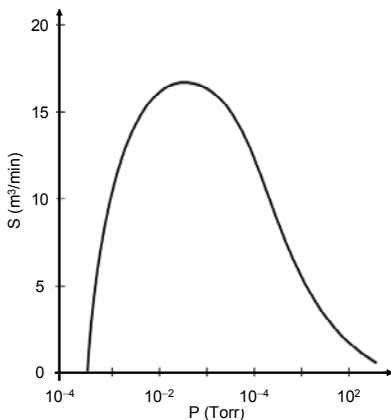


Figure 2.11. Typical pumping velocity curve of a Roots pump [3]

across a typical Roots pump is much less than 760 Torr. Because the oil usually creates undesirable vapour pressure, it is not necessary for sealing the clearance ($\sim 10^{-1}$ mm) between two impellers and impeller/housing. Oil is only used to lubricate the gears, which ensures the very accurate synchronisation of the rotors. The results shown in Figure 2.11 indicate that a Roots pump is suitable for high velocity pumping in the pressure range of 10^{-2} to 10 Torr. Maximum efficiency occurs when the pump is operated at a compression ratio of about 10 at a pressure on the order of 5×10^{-2} Torr; thus the pump must be connected to and backed by a suitable mechanical pump.

As there is no oil sealing for Roots pumps, the impellers have to be designed and manufactured with a close fitness between them and the pump housing. The profiles of the two impellers are designed not to touch each other, nor do they touch the internal surface of the housing when the impellers are rotating. To ensure minimum gas leakage or back flow from the compressing region to other areas, the clearance caused by the geometry definition and the tolerances of the impeller profile has to be very small, usually about 0.1 to 0.5 mm between these surfaces. This design thus ensures that the inlet port is almost isolated from the outlet port. The small clearance between parts causes a small back flow of gas from the exhaust port to the inlet port. Accordingly, the efficiency of compression is much lower than that of oil-sealed pumps. However, the essential design requirements here are the high throughputs generated by high pumping speed. The avoidance of rubbing and sliding contacts between the propellers and the housing allows much higher velocities of rotation in the range of 1400 to 4000 rpm as against the highest speed of 2000 rpm for mechanical pumps, and consequently much higher pumping speed.

2.2.4 Vacuum Measurement and Leak Detection

With the above introduction to the vacuum generation technologies, it is also important to accurately measure and to detect the level of the vacuum within a chamber. This section introduces the basic working principles of these devices covering the most common CVD systems.

2.2.4.1 Vacuum Measurement

As mentioned before, the vacuum pressure covered in current vacuum technologies is about 19 orders of magnitude from 10^4 Pa (rough vacuum) to 10^{-15} Pa (outer space vacuum). It is impossible to measure the pressure with a single pressure gauge over the whole vacuum range. Consequently, a series of vacuum gauges have been designed and developed, and they fall into two groups: direct measurement (e.g. mechanical phenomena gauges) and indirect measurement (i.e. transport phenomena gauges and ionisation gauges).

The mechanical phenomena gauges measure the actual force exerted by the gas. They include a U-tube, a capsule dial, a strain, a capacitance manometer, a McLeod gauge, etc. Vacuum is measured according to the displacement of an elastic material or by measuring the force required to compensate its displacement. The measurement ranges from atmospheric pressure to 10^2 Pa in rough vacuum conditions.

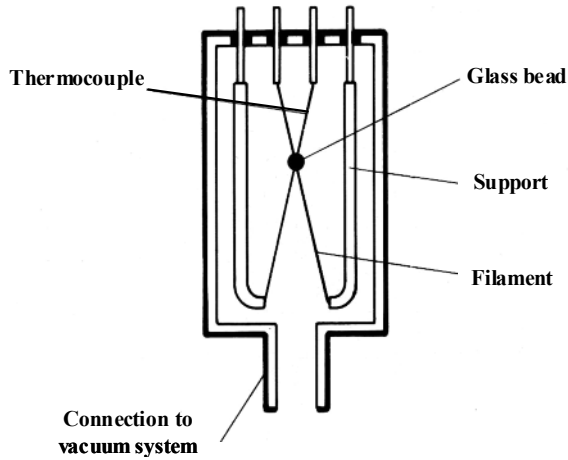


Figure 2.12. Measure principle of thermocouple gauge [10]

The thermocouple gauge is a typical indirect measurement device in a CVD system, and its working principle is as shown in Figure 2.12. The filament is heated by electric current with a constant power. The thermocouples are connected with the filament by a small glass bead, which ensures thermal contact rather than electric contact. In such a case, the temperature of the heated filament is measured by the thermocouple. According to the state equation of perfect gases, the amount of molecules is proportional to the pressure within a chamber. If the pressure is high, the collision frequency between the molecules and the heated filament is also high. Therefore, a high flux of the heat is transferred away from the heated filament. If the pressure is decreased, there are fewer molecules to take away the heat from the filament. The pressure within the vacuum chamber can be indirectly measured by the temperature. At relatively low pressure, the heat transfer from the hot to the cold surface (Q) is proportional to the pressure and is given by [3]

$$Q = \frac{\alpha}{2} \cdot \frac{Pu_{av}(T_s - T_i)}{T_i} \quad (2.29)$$

where α is the accommodation coefficient, P is the pressure, u_{av} is the average velocity of the gas at the temperature T_i , and T_s is the temperature of the hot surface.

2.2.4.2 Leak Detection

Creating a required vacuum in a reaction chamber is the first step in any CVD process. Maintaining the required level of vacuum is the next important task. An important aspect of maintaining the required vacuum is avoiding or minimising any leakage of external gases. It is inevitable to have some level of leakage as it is impossible to manufacture a 100% sealed system, due to various manufacturing constraints and tolerances, mechanical wear and the requirements of dynamic gas circulation within a system. As long as the leakage is within acceptable levels, a

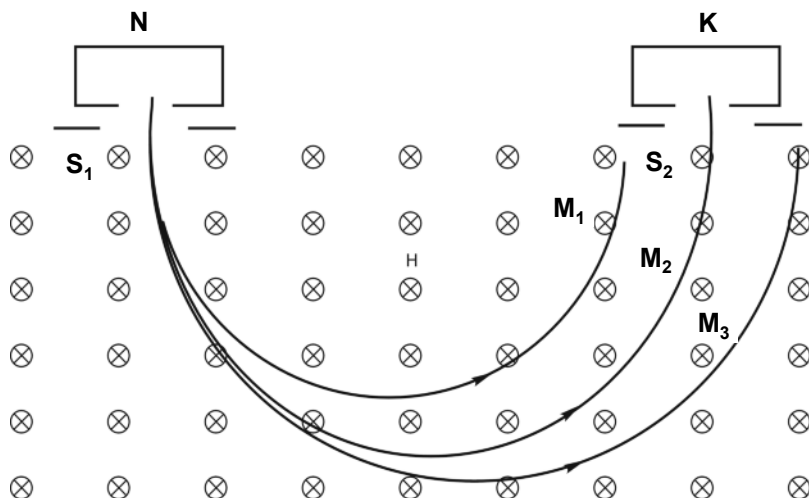


Figure 2.13. Schematic of helium-specific mass spectrometer leak detector
 H: uniform magnetic field; N: ionisation chamber; K: ion collector, S_1 : entrance of ions, S_2 : exit of ions

CVD operation can still produce satisfactory products. It is therefore important and essential for the system to be able to detect the leakage occurring before and during a CVD operation. Once an acceptable level of leakage is maintained, a CVD process may commence. If there is an unacceptable level of leakage, it can cause a severe problem for the CVD process and the quality of the deposit.

There are normally two types of leakage detection systems, namely halide leak detector and helium-specific mass spectrometer leak detector, based on the types of gases to be detected. As CVD systems usually use large quantities of halides as reactant precursors, there are normally some residual halides within the reaction chamber. This consequently influences the accuracy of the halide leak detector. In this case, helium-specific mass spectrometer leak detectors are normally used to avoid this problem.

The working principle of a helium-specific mass spectrometer leak detector is as follows [7]. The mass spectrometer mainly consists of three parts: an ion source, a deflection system and an ion collector. When the atoms pass the ionisation chamber of the detector, they are ionised to become positive ions. When these ions are then accelerated in the ionisation chamber, they obtain sufficient energy and enter into the magnetic field of the detector. These positive ions travel in a specific orbit in the magnetic field. As different ions have specific orbit radii; only ions with the same orbit radius as that of the spectrometer can pass a narrow gap, as indicated by K in Figure 2.13, and reach the ion collector K to form an ion stream.

Under the influence of a homogeneous magnetic field, perpendicular to the path of the ions, they are deflected into circular orbits of a radius given by

$$r = \frac{1}{B} \sqrt{\frac{2mV}{ze}} \quad (2.30)$$

where m is the mass of ion in kilograms, V is the ion-accelerating voltage in volts, e is the electric charge in “A·s”, z is the number of charges carried by the ion and B is magnetic flux density in “kg·s⁻²·A⁻¹”.

When helium is used as an indicative gas, it is possible to adjust the voltage and the intensity of the magnetic field described above such that only helium ions can reach the ion collector K in Figure 2.13 with a suitable orbiting radius. During gas leakage detection, if helium ions appear on the helium-specific mass spectrometer, it is clear that there is a leakage in the system. In the above detection process helium has been used as the detection gas for the leakage; its advantages and the reasons for such a selection are as follows:

1. there exist very small quantities of helium in the air and the residual gas in the work chamber. Therefore, it is easy to detect its presence.
2. Helium is very light and its molecule is very small, making it easy for it to pass the narrow leakage gap to reach the ion collector of a mass spectrometer, and travelling at a higher speed in the work chamber than other gases guarantees a good sensitivity of the leakage detection.
3. Helium is also an inert gas; it does not react chemically with other gases and mechanical parts, resulting in an ideal search gas which maintains its molecular quantity in the system for easy and reliable detection.

2.3 Fundamentals of Gas Transport

In CVD processes, the access of the reactant gases to the substrate surface is governed by the transport phenomena; it requires careful and timely control in order to achieve good quality and efficiency. The driving forces for the transport are the concentration gradient, pressure gradient and temperature gradients of the gases. As the gases flow, their momentum, energy and mass all vary, and therefore gas transport greatly influences not only the deposition rate but also the quality and deposition mechanism. This section discusses these key issues and aims to establish the impact of gas transport on CVD processes and the necessity of designing accurately controlled equipment for gas transport.

Momentum, thermal and mass transports are three basic physical phenomena of any fluid flow. In a CVD process, when the precursor gases enter a high temperature reaction chamber from room temperature, the aforementioned three transports occur under certain velocity, temperature and concentration gradients. The common underlying physical laws for these three transports are all based on a molecule's thermal motion. Three specific underlying laws which describe the three transports are Newton's viscous law, Fourier law and Fick's law respectively. For a simple one-dimensional system, these laws can be expressed by [14]

$$\text{Momentum flux } \tau = -\mu \frac{du}{dy} \quad (2.31)$$

$$\text{Thermal flux } q = -\alpha \frac{dT}{dy} \quad (2.32)$$

$$\text{Mass flux } J = -D \frac{d\rho}{dy} \quad (2.33)$$

where $\frac{du}{dy}$, $\frac{dT}{dy}$ and $\frac{d\rho}{dy}$ are velocity gradient, temperature gradient and concentration gradient respectively; μ , α and D are dynamic viscosity, thermal conductivity and diffusivity (diffusion coefficient) respectively.

2.3.1 Transport Coefficients

Transport coefficients are a group of coefficients used to predict the diffusivity, thermal conductivity and viscosity of gases. These in turn define the impact of the momentum, energy and mass of the gas flow. Two theories have been developed to estimate these coefficients.

2.3.1.1 Prediction from Elementary Kinetic Theory [15, 17]

Molecules move randomly in the gas state and collide with each other. They transfer momentum, energy and mass if there are gradients in their velocity, temperature and concentration. In the dilute gas region and at low pressure near atmospheric pressure, the transport coefficients can be predicted by using a kinetic theory of gases. The elementary kinetic theory (EKT) assumes all molecules to be non-interacting rigid spheres with a specific diameter, d (with mass m), moving randomly at a mean velocity, u_{av} . Using the EKT, the transport coefficients of diffusivity (D_{AB}), thermal conductivity (α) and viscosity (μ) are defined as

$$D_{AB} = \frac{1}{3} u_{av} \lambda = \frac{2}{3 p d_{AB}^2} \sqrt{\frac{k^3 T^3}{\pi^3 m_{AB}}} \quad (2.34)$$

$$\alpha = 2kZ\lambda = \frac{1}{d^2} \sqrt{\frac{k^3 T}{\pi^3 m}} \quad (2.35)$$

$$\mu = \frac{1}{3} \rho u_{av} \lambda = \frac{2}{3 d^2} \sqrt{\frac{mkT}{\pi^3}} \quad (2.36)$$

where ρ is the density of gas; Z is the number of molecules per unit area per unit time crossing a plane from one side; u_{av} , λ , m and d are the average velocity, mean free path, mass of one molecule and molecular diameter of gas respectively.

These equations are approximately correct because they successfully establish the relationship between the coefficients of transport with pressure and temperature. For example, the molecular diffusivity is proportional to the 3/2

power of temperature but inversely proportional to the pressure. However, both the thermal conductivity and viscosity are dependent on temperature only.

2.3.1.2 Prediction from Chapman–Enskog Theory [15, 17]

The forces of attraction and repulsion between molecules must be considered for a more accurate and rigorous representation of the gas flow. Chapman and Enskog proposed a well-known theory in which they use a distribution function, the Boltzmann equation, instead of the mean free path. Using this approach, for a pair of non-polar molecules, an intermolecular potential, $V(r)$, is given in the potential function proposed by the Lennard–Jones potential:

$$V(r) = 4\varepsilon\left[\left(\frac{\sigma}{r}\right)^{12} - \left(\frac{\sigma}{r}\right)^6\right] \quad (2.37)$$

where r is the radial distance between the two molecules, σ is the collision diameter determined from quantum mechanics and ε is the characteristic energy.

Based on these, more accurate expressions to calculate the coefficients are obtained. The detailed deviations of these coefficients can be found in the references [18, 19]; the results are given as follows.

The diffusivity D_{AB} is given by

$$D_{AB} = \frac{0.00188}{P\sigma_{AB}^2\Omega_{D,AB}} \sqrt{\left(\frac{1}{M_A} + \frac{1}{M_B}\right)T^3} \quad (\text{cm}^2\cdot\text{s}^{-1}) \quad (2.38)$$

where P is the pressure in atmospheric pressure, T is the temperature in Kelvin, σ_{AB} is the characteristic length in angstrom, $\Omega_{D,AB}$ is the diffusion collision integral, dimensionless, and M_A and M_B are the mole masses of gases A and B in $\text{g}\cdot\text{mol}^{-1}$ respectively.

The viscosity μ is expressed by

$$\mu = \frac{26.69}{\sigma^2\Omega_\mu} \sqrt{MT} \quad (\mu\text{Pa}\cdot\text{s}) \quad (2.39)$$

where M is the mole mass in grams per mole, T is the temperature in Kelvin, σ is the collision diameter in angstrom, and Ω_μ is the viscosity collision integral, dimensionless.

The thermal conductivity α is presented as

$$\alpha = \frac{2.63 \times 10^{-23}}{\sigma^2\Omega_\alpha} \sqrt{\frac{T}{M}} \quad (\text{W}\cdot\text{m}^{-1}\cdot\text{K}^{-1}) \quad (2.40)$$

where M is the mole mass in kilograms per mole, T is the temperature in Kelvin, σ is the collision diameter in meters, and Ω_α is the thermal conductivity collision integral, dimensionless.

Unlike the elementary kinetic theory, the three collision integrals ($\Omega_{D,AB}$, Ω_μ and Ω_α) are introduced in the Chapman–Enskog theory. Moreover, the collision diameter (σ) is used instead of the molecular diameter (d).

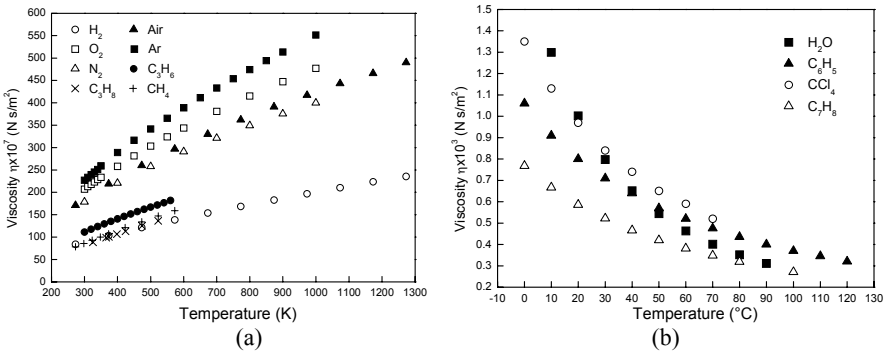


Figure 2.14. Relationship between viscosity of various fluids and temperature, data from [21]: (a) for gases and (b) for liquids

It is interesting to note that the viscosity of gas is independent of pressure and increases with temperature, whereas in the case of liquids the viscosity is known to decrease as the temperature increases [20]. The temperature dependence of viscosities for the gases and the liquids are shown in Figure 2.14a and b respectively. This difference in the effect of temperature on the viscosity of liquids and gases can be explained by structural differences between liquids and gases. In liquids, molecules exert strong cohesive forces between molecules as they are closely arranged spatially. The intermolecular forces determine the relative motions between adjacent layers of a fluid. As the temperature increases, molecules become more active and the intermolecular cohesive forces are reduced, implying a reduction in interlayer resistance to motion. As the viscosity is a measure of internal friction or resistance within fluids, the viscosity is therefore reduced by an increase in temperature as a result of the reduction of the intermolecular cohesive forces. However, the gas molecules are spaced so widely that their intermolecular forces become negligible. When the gas temperature increases, their resistance increases due to the fact that more molecules are colliding with each other, resulting in higher resistance for the molecules to move in an intended direction. In contrast to the liquids, the viscosity of gases increases as the temperature rises, caused by the random molecular collision and momentum exchange.

Example:

Calculation of the diffusivity for CH₄ in N₂ at 20°C and 1 atm.

In order to use Equation (2.39), it is necessary to compute the values of the collision diameter, σ_{AB} , and the collision integral, Ω_D . The collision integral, in turn, depends on the parameter KT/ϵ . The individual values for gas A—CH₄ and gas B—N₂ can be found in the tables in [14–17]:

$$M_A=16.04, \sigma_A=3.822 \text{ \AA}, \epsilon_A/K=137 \text{ K} \tag{2.41}$$

$$M_B=28.02, \sigma_B=3.681 \text{ \AA}, \varepsilon_B/K=91.5 \text{ K} \quad (2.42)$$

The parameters σ_{AB} and ε_{AB} for the collision of CH_4 with N_2 may be estimated by means of the following equations:

$$\sigma_{AB} = \frac{\sigma_A + \sigma_B}{2} = \frac{3.822 + 3.681}{2} = 3.752 \text{ \AA} \quad (2.43)$$

$$\varepsilon_{AB} / K = \sqrt{\varepsilon_A \varepsilon_B} = \sqrt{137 \times 91.5} = 111.96 \quad (2.44)$$

$$KT / \varepsilon_{AB} = 293 / 111.96 = 2.617 \quad (2.45)$$

Interpolating the values of collision integrals found in the tables in [14–17]: we obtain a value for the collision integral of CH_4 and N_2 , $\Omega_D = 0.9860$, and then the substitution of the foregoing values into Equation (2.38) gives

$$D_{AB} = \frac{0.00188}{1.0 \times (3.752)^2 \times 0.9860} \sqrt{\left(\frac{1}{16.04} + \frac{1}{28.02}\right) \times 293^3} = 0.21 \text{ cm}^2\text{s}^{-1} \quad (2.46)$$

2.3.1.3 Transport Coefficients in Multicomponent Gas Mixtures

This rigorous theory developed by Chapman and Enskog can also be used to calculate the transport coefficients of multicomponent gas mixture. For a diluent gas mixture, the diffusivity of the diluent component (i) into a homogeneous gas mixture (D_{im}) is given by [15]

$$D_{im} = \left(\sum_{\substack{j=1 \\ j \neq i}}^n \frac{x_j}{D_{ij}} \right)^{-1} \quad (2.47)$$

where D_{ij} is the binary diffusivity of the ij gas system and x_j is the mole fraction of the j th gas in the gas mixture.

Under conditions of low pressure, the viscosity expression of the multicomponent mixture is much more complex. It is usual to use two simple methods which were developed by Wilke as well as Hering and Zipperer.

In Wilke's approach, the second-order effects are neglected and the final expression of the viscosity is given by [15, 22]

$$\mu_m = \sum_{i=1}^n \frac{y_i \mu_i}{\sum_{j=1}^n y_j \Phi_{ij}} \quad (2.48)$$

where μ_m is the viscosity of the multicomponent gas mixture, μ_i is the viscosity of the pure i th gas, y_i is the mole fraction of the i th gas in the mixture and Φ_{ij} is the interacting parameter for gas mixture viscosity and given by [15]

$$\Phi_{ij} = \frac{[1 + (\mu_i / \mu_j)^{1/2} (M_j / M_i)^{1/4}]^2}{[8(1 + M_i / M_j)]^{1/2}} \tag{2.49}$$

$$\Phi_{ji} = \frac{\mu_j}{\mu_i} \frac{M_i}{M_j} \Phi_{ij} \tag{2.50}$$

where μ_i and μ_j are the viscosities of the pure i th and j th gases respectively; M_i and M_j are the mole masses of the i th and j th gases respectively.

In Herring and Zipperen’s approach, the relationship between Φ_{ij} and Φ_{ji} is much simpler than that of the method proposed by Wilke. The expression is written as [15, 23]

$$\Phi_{ij} = \left(\frac{M_j}{M_i}\right)^{1/2} = \Phi_{ji}^{-1} \tag{2.51}$$

At relatively low pressure, the thermal conductivity of a gas mixture, α_m , is presented as follows [15, 24]:

$$\alpha_m = \frac{\sum_{i=1}^n y_i \alpha_i}{\sum_{j=1}^n y_j A_{ij}} \tag{2.52}$$

where α_i is the thermal conductivity of the pure i th gas. A_{ij} is a function for the gas mixture thermal conductivity and is equal to Φ_{ij} in Equation (2.51).

2.3.1.4 Diffusion of Gases in Porous Media [25, 26]

Gas diffusion in a porous structure is of particular interest to this book as many porous fibre preforms are densified by CVI. The diffusion of gases in porous media can be classified into three regimes according to the ratio of the free mean path to the pore diameter within the structure. As shown in Figure 2.15, they are Fick gas diffusion, transition gas diffusion and Knudsen gas diffusion.

Fick diffusion takes place when the pore diameter is much greater than the mean free path of the molecule. In this case, the collisions between the molecules dominate and the collision between the molecule and the walls of the pore is negligible in Figure 2.15a. The driving force of the Fick diffusion is the concentration gradient of the gaseous species and the diffusivity discussed above.

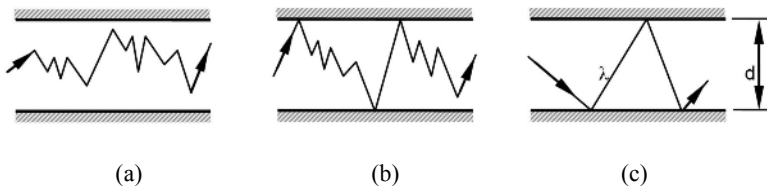


Figure 2.15. Gas diffusion types within a pore: (a) fick diffusion, (b) transition diffusion and (c) Knudsen diffusion

If the pore diameter is comparable to the mean free path of the molecules, the collision between the molecules and the walls of the pore becomes dominant in Figure 2.15c. The mass transport is determined by the Knudsen diffusion. In such a case, the Knudsen diffusion occurs in the small channels among the fibres within the fibre bundle of the preform. When the mean free path λ is intermediate in length between the above two limits, the transition diffusion happens as shown in Figure 2.15b.

The Knudsen diffusivity is calculated from the following expression:

$$D_K = \frac{2}{3} r u_{av} \quad (2.53)$$

where D_K is diffusivity in square metres per second, r and u_{av} is the average pore radius in meter and molecular velocity for the gaseous component A in metres per second. By using the kinetic theory of gases, D_K is rewritten as

$$D_K = 97.0 r \left(\frac{T}{M_A} \right)^{1/2} \quad (2.54)$$

where M_A is the molecular mass of A and T is temperature in Kelvin.

The Knudsen diffusivity is proportional to the radius of the pore and the temperature but inversely proportional to the mole mass of the gas. This implies that small gaseous species exhibit high diffusivity. Unlike the Fick diffusivity, the Knudsen diffusivity is independent of pressure.

For the transition-type diffusion, the efficient diffusivity (D_e) is given by

$$\frac{1}{D_e} = \frac{1}{D_F} + \frac{1}{D_K} \quad (2.55)$$

2.3.1.5 Permeability

Permeability is a parameter defined to measure the physical influence of a porous structure on fluid flow, and for a CVI process it is an important physical parameter for fibre preforms. Another important parameter for porous structure is the porosity, which is the most important geometrical property. According to Darcy's law, the volumetric flow rate Q of a fluid through a porous medium is proportional to the hydrostatic pressure difference (ΔP) across the structure (see Figure 2.16), the permeability and the cross-section area, and is also inversely proportional to the length of the structure and the viscosity of the fluid, as given by [26]

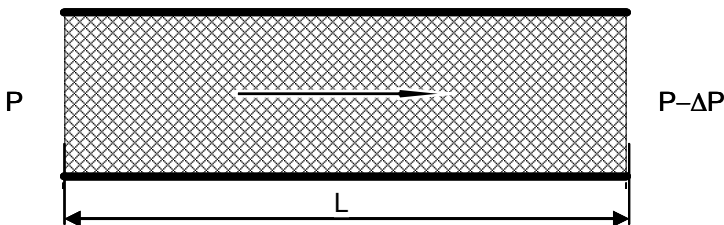


Figure 2.16. Fluid flow through a porous medium

$$Q = \frac{\kappa A \Delta P}{\mu L} \quad (2.56)$$

where A and L are the normal cross area and the length of the porous structure, κ is the permeability of the porous structure and μ is the dynamic viscosity of the fluid.

To understand this permeability, many investigations have been undertaken and empirical relationships have been established. Following Tai and Chou [27], the empirical expression for the local permeability distribution is adopted for the fibre preform. Permeability is thus obtained as

$$\kappa = \frac{\pi d^2 \ln[0.64/(1-\phi)^2]}{24.4} \frac{\phi}{1-\phi} \quad (2.57)$$

where d is the diameter of the fibre and ϕ is the porosity of the preform. Within a unit cell of fibre preform, the local porosity of a unit cell can be expressed as

$$\phi = 1 - \frac{(9.928L - 23.659r)\pi r^2}{L^3} \quad (2.58)$$

where L is the length of the unit cell and r is the radius of the fibre.

2.3.2 Boundary Layer Theory

The boundary layer theory is very important for understanding the transport phenomena and the growth kinetics of a CVD coating. It was proposed to address the questions that neither theoretical hydrodynamics nor experimental hydraulics could explain well in the past. At the end of the 19th century fluid mechanics studies were dominated by two distinctively different schools of thought which had nothing in common [28]. The science of theoretical hydrodynamics, evolved from Euler's theory for ideal frictionless and non-viscous liquids, was developed to a high degree of completeness. However, the hydrodynamic theory could not explain some experimental results such as the pressure losses in pipes and drag force. Based on its frictionless assumption, one famous deduced paradoxical example, the so-called Alembert Paradox, states that a body moving through a uniform fluid which extends to infinity experiences no drag or force acting in the opposite direction of its motion. This obviously is not the case and hence this school of thought became useless for addressing practical engineering problems, as many important practical flow problems could not be solved.

For this reason, practical engineers developed their own highly empirical understanding of hydraulics which appeared to be more pragmatic and effective in solving important practical engineering problems. The hydraulics was developed on the basis of a large number of experimental tests; however, the methods differed greatly from each other, making the results difficult to generalise into theory-based knowledge.

The boundary layer theory was first developed by Ludwig Prandtl in 1904. The theory points out that the fluid flow along the surface of a body is divided into two regions: the boundary layer and the flow outside the boundary layer.

The boundary layer is a thin fluid film that forms on the surface of a solid body moving through a viscous fluid. The majority of the drag force experienced by the moving body which is immersed in a fluid is due to viscous shear and inertial forces within the boundary layer;

The flow outside the boundary layer is determined by inertial forces only. Shear forces and the viscosity of the fluid within the boundary layer can be neglected without significant effects on the solution.

The boundary layer theory reconciles the important contradictions between experimental hydraulics and theoretical hydrodynamics. It effectively combines both approaches into an integrated theory.

The thickness of the velocity boundary layer is normally defined as the distance from the solid body to the fluid layer at which the flow velocity reaches 99% of the free stream velocity, as illustrated in Figure 2.17. For a flat-plate body emerging in an incompressible and laminar fluid, the boundary layer thickness is given by

$$\delta = \frac{5.0}{\sqrt{Re}} x \quad (2.59)$$

where x is the distance from the leading edge of the plate and Re is the Reynolds number of the flow.

The velocity boundary layer concept can be extended to define the temperature and concentration of a fluid. The temperature boundary layer thickness is the distance from the body to a layer at which the temperature is 99% of the temperature from an inviscid solution. The boundary layer thickness for the fluid concentration has the same definition. Their relationships are expressed by [29]

$$(T_s - T)/(T_s - T_\infty) = 0.99 \quad (2.60)$$

$$(C_s - C)/(C_s - C_\infty) = 0.99 \quad (2.61)$$

The boundary layer theory has been widely accepted and used to describe the transport phenomena in CVD processes. High-performance CVD systems require designers to focus on the geometrical parameters of the reaction chamber, the orientation and arrangement of the preforms in the chamber, as well as some other important components, such as pipes, distributor, exit and so forth. Due to drag effects around the boundary layer of preforms, it is very important to design the preforms and the reaction chamber and aim to avoid the boundary layer separation such that they experience a minimum drag force. The details of these effects are discussed in Chapter 6.

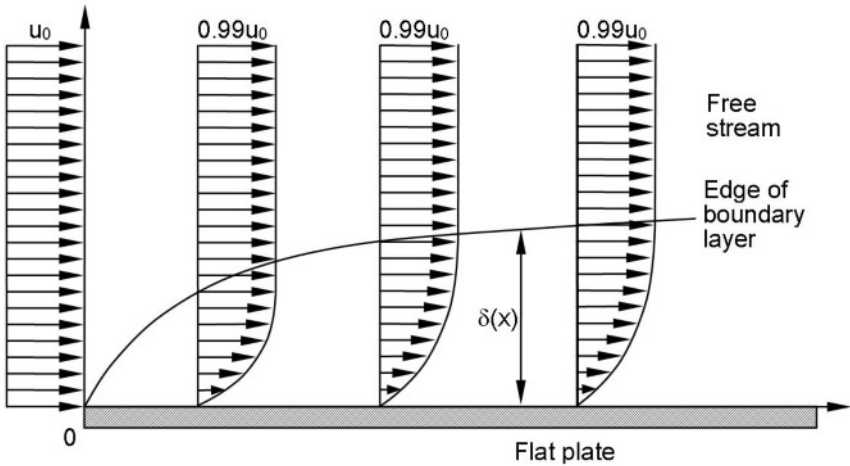


Figure 2.17. Profile of a boundary layer along a flat plate

2.3.3 Some Dimensionless Parameters

Having introduced some theoretical and empirical developments, it is also important to introduce several dimensionless parameters. These parameters could basically characterise the transport processes of gases.

2.3.3.1 Knudsen Number [25, 30]

A fluid is usually considered as a continuous substance under normal conditions. In fact, it is composed of myriads of continuously moving molecules. For gases at 1 atm, 25°C, the spacing between molecules is on the order of 10^{-3} μm , and for the liquids it is on the order of 10^{-4} μm . The number of molecules per cubic micrometer is 2.69×10^7 for air and 3.21×10^{10} for water. Hence, it is reasonable to assume and treat the fluid as a continuum.

The Knudsen number (Kn) is used to determine the different regimes of the gas flow. These regimes can be divided into continuous flow, transitional flow and free molecular flow. This division is based on the understanding that the flow behaviour differs within each of the flow regimes. The Knudsen number is defined as

$$Kn = \frac{\lambda}{L} = \frac{kT}{\sqrt{2}\pi d^2 PL} \quad (2.62)$$

where λ is the mean free path, L is the characteristic length, k is Boltzmann's constant, T is the temperature, d is the molecular diameter and P is the total pressure.

When $\lambda \ll L$ or $Kn \ll 0.01$, many collisions between molecules occur, hence the gas can be regarded as a continuum. Under this condition or regime, the flow of

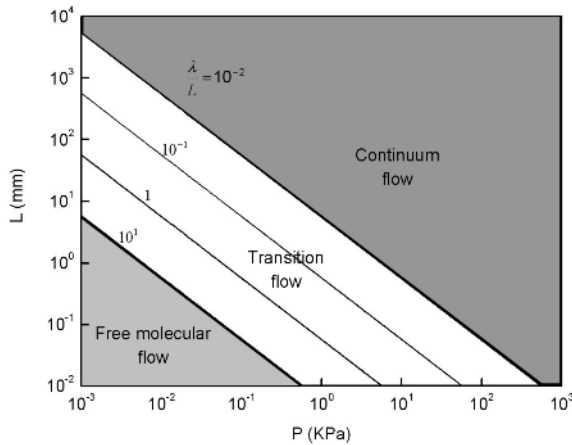


Figure 2.18. Map of different flow regimes of H₂

the gases can be described by the Navier–Stokes equation. Such conditions are fulfilled in the rough vacuum range of some CVD processes. The next regime is called transition regime, where $0.01 < Kn < 10$. Within this regime, it is very difficult to establish a theoretical model at the present time. In high and ultra-high vacuum conditions, λ is significantly greater than L , that is $Kn > 10$. This regime corresponds to the free molecular flow in which the wall collisions dominate and the molecules undergo few collisions with each other.

The detailed flow regime flow map for hydrogen gas is shown in Figure 2.18. For the CVI techniques discussed in Chapter 5, the process is usually performed at a pressure of 10 to 30 kPa. The gas flow can be treated as continuum flow if the characteristic length is more than 1 mm.

2.3.3.2 Reynolds Number [14, 20]

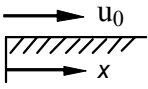
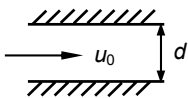
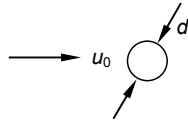
The Reynolds number is undoubtedly the most famous dimensionless parameter in fluid mechanics. It is named in honour of Osborne Reynolds, a British engineer who first demonstrated in 1883 that a dimensionless variable can be used as a criterion to distinguish the flow patterns of a fluid either being laminar or turbulent. Typically, a Reynolds number is given as follows:

$$Re = \frac{\rho u L}{\mu} = \frac{u L}{\nu} \tag{2.63}$$

where u is the mean fluid velocity, L is the characteristic length, ρ is the density of a fluid, and μ and ν are the dynamic viscosity and kinematic viscosity of a fluid respectively. Their relationship is given by

$$\nu = \frac{\mu}{\rho} \tag{2.64}$$

Table 2.7. Characteristic velocity and length for three flow cases

Flow type	Flow over a flat plate	Flow in a pipe	Flow around a cylinder
			
Characteristic velocity	Stream velocity (u_0)	Mean velocity within the pipe (u_0)	Remote velocity of flow (u_0)
Characteristic length	Distance measured from leading edge of plate (x)	Diameter of pipe (d)	Diameter of cylinder or sphere (d)
Critical Re	5×10^5	2100	3×10^5

In fluid mechanics, the physical implication of a Reynolds number is the ratio of inertial forces ($u\rho$) to viscous forces (μ/L). It is, therefore, used to illustrate the relative importance and dominance of these two types of forces for a given flow. Depending on the magnitude of the Reynolds number, the flow regimes can be classified as either laminar or turbulent flow. If a flow has a low Reynolds number, a laminar flow occurs, where viscous forces are dominant. The flow is therefore smooth. When the Reynolds number for a flow is greater than a critical value, the flow becomes turbulent flow and is dominated by inertial forces, resulting in random eddies, vortices and other flow fluctuations. Some of the examples are illustrated in Table 2.7.

Most CVD reactors operate in the laminar regime ($Re < 100$) due to the low precursor flow rate [31, 32].

2.3.3.3 Grashof Number [14]

The Grashof number plays the same role in free convection as the Reynolds number plays in forced convection. The Reynolds number provides a measure of the ratio of the inertial to viscous forces acting on a fluid. By contrast, the Grashof number is a ratio of the buoyancy force to the viscous force acting on a fluid. It is named after the German engineer Franz Grashof and the expression is given by

$$Gr = \frac{g\beta\Delta TL^3}{\nu^2} \tag{2.65}$$

where g is the gravitational acceleration, L is the characteristic length, ΔT is the temperature difference, β is the volume thermal expansion coefficient of a fluid and ν is kinematic viscosity.

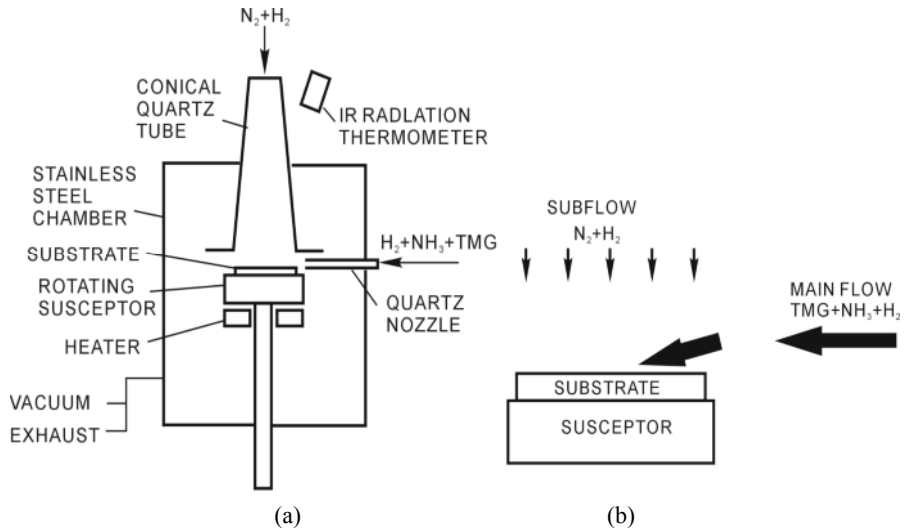


Figure 2.19. Design of gas flow for MOCVD GaN [36]: (a) schematic of MOCVD chamber and (b) flow directions of the gases

The Grashof number is a dimensionless parameter used to analyse the flow patterns of a fluid. When the Gr number is much greater than 1, the viscous force is negligible compared to the buoyancy forces. When buoyant forces overcome viscous forces, the flow starts a transition to the turbulent regime [28, 34]. For a flat plate in vertical orientation, this transition occurs at a Gr number of around 10^9 .

It is clear that the free convection flow becomes significant with an increase in the temperature difference and characteristic length. A large CVD reactor possesses a large characteristic length. For a CVD process, free convection flow is always undesirable because it is uncontrollable [35, 36]. A good example is the MOCVD reactor design for GaN thin-film deposition proposed by Nakamura as shown in Figure 2.19. If the precursor gases of H_2 - NH_3 -TMG are only delivered parallel to the sapphire substrate, it is impossible to obtain the continuous GaN film. When another subflow of N_2 - H_2 gas flow is introduced perpendicular to the reactant precursor gas flow, the inert subflow of H_2 - N_2 forces the reactant gases to flow towards and closer to the substrate, rather than flow away from the substrate surface due to free convection. This allows high-quality GaN film to be successfully deposited.

2.3.3.4 Prandtl Number [14, 25]

The Prandtl number is a dimensionless number named after Ludwig Prandtl. It is defined as the ratio of momentum diffusivity (kinematic viscosity) to the thermal diffusivity, as well as the ratio of viscous diffusion rate to thermal diffusion rate:

$$\text{Pr} = \frac{\nu}{\alpha} = \frac{C_p \mu}{k} \quad (2.66)$$

where C_p is the specific heat, α is the thermal conductivity, k is the thermal diffusivity, ν is the kinematic viscosity and μ is the dynamic viscosity.

The ratio of the velocity boundary layer (δ) to temperature boundary layer (δ_T), as discussed in Section 2.3.2, is governed by the Prandtl number. If the Prandtl number is 1, the two boundary layers have the same thickness. If the Prandtl number is greater than 1, the thermal boundary layer is thinner than the velocity boundary layer. If the Prandtl number is less than 1, which is the case for CVD reactant gases under standard conditions, the thermal boundary layer is thicker than the velocity boundary layer. The relationship between the velocity boundary layer (δ) to temperature boundary layer (δ_T) is given by

$$\frac{\delta}{\delta_T} = \text{Pr}^{1/3} \quad (2.67)$$

The Prandtl numbers of gases (such as H_2 and Ar) commonly used in the CVD processes are around 0.7. Accordingly, the velocity boundary layer is just slightly thinner than that of the thermal boundary layer. For liquid metals (e.g. mercury) with small Prandtl numbers and low viscosities, the thickness of the velocity boundary layer is much thinner than that of the thermal boundary layer. For oils with large Prandtl numbers and high viscosities, the thickness of the thermal boundary layer is one order less than that of the velocity boundary layer, as shown in Figure 2.20.

The Prandtl values for some fluids are listed in Table 2.8. For mercury, heat conduction is more effective compared to convection when thermal diffusivity is dominant. For engine oil, convection is very effective in transferring energy from an area, compared to pure conduction, where the momentum diffusivity is dominant. In heat transfer problems, the Prandtl number controls the relative

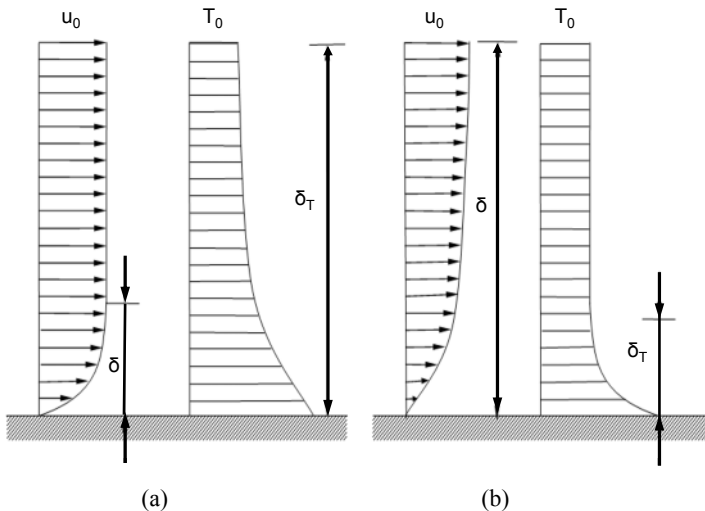


Figure 2.20. Comparison of boundary layers between the different fluids: (a) $\text{Pr} \rightarrow 0$ (for liquid metal) and (b) $\text{Pr} \rightarrow \infty$ (for viscous oil)

Table 2.8. Pr values for different fluids

Fluid	Air	H ₂	He	N ₂	Water	Engine oil	Mercury
Pr	0.7	0.71	0.7	0.71	7	100–40,000	0.015

thickness of the momentum and thermal boundary layers. Typical Prandtl values are as listed in Table 2.8.

2.3.3.5 Schmidt Number [14, 25]

The Schmidt number is defined as the ratio of molecular momentum to mass diffusivity. It is used to characterise fluid flows in which there are simultaneous momentum and mass diffusion convection processes. It is named after Ernst Schmidt and expressed as

$$Sc = \frac{\nu}{D} \quad (2.68)$$

where ν is the kinematic viscosity and D is the mass diffusivity.

The Schmidt number for the mass transfer is analogous to the Prandtl number for heat transfer. Its physical implication means the relative thickness of the hydrodynamic layer and mass-transfer boundary layer. The ratio of the velocity boundary layer (δ) to concentration boundary layer (δ_c) is governed by the Schmidt number. The relationship is given by

$$\frac{\delta}{\delta_c} = Sc^{1/3} \quad (2.69)$$

If the Schmidt number is 1, the two boundary layers have the same thickness. If the Schmidt number is greater than 1, the thermal boundary layer is thinner than the velocity boundary layer. If the Schmidt number is less than 1, which is the case for a CVD process operated in normal conditions, the concentration boundary layer is thicker than the velocity boundary layer.

2.4 Vapour Pressures of Chemical Vapour Deposition Precursors

For CVD processes, both liquid and solid substances are usually used as precursors. In some cases, they must be heated to the required temperature to produce sufficient supply. As shown in Figure 2.21, the vapour pressures of three liquid substances (i.e. C₂H₅OH, CCl₄ and C₆H₆Cl) are increased as the temperature increases. However, the temperature dependence of vapour pressure is not linear.

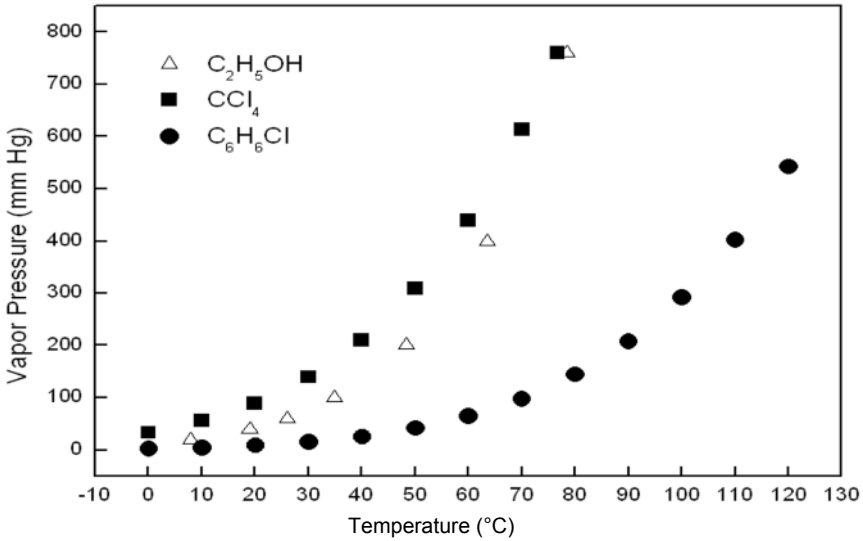


Figure 2.21. Relation of vapour pressure and temperature of liquids

The saturated vapour pressure (P) of a liquid precursor is governed by the Clausius–Clapeyron equation as follows [37, 38]:

$$\frac{dP}{dT} = \frac{\Delta H_{vap}}{T\Delta V_m} \quad (2.70)$$

where ΔH_{vap} is the enthalpy of vaporisation, ΔV_m is the change in molar volume of two phases and T is the absolute temperature in Kelvin.

It is well known that the volume of a vapour, $V_{(g)}$, is much larger than that of the equivalent amount of a liquid. As a result, it is reasonable that the $V_{(g)}$ of vapour volume represents the volume change of ΔV_m . Further, the vapour can be considered a perfect gas. Based on the state equation of perfect gases for a mole gas, the Clausius–Clapeyron equation can be rewritten as

$$\frac{d(\ln P)}{dT} = \frac{\Delta H_{vap}}{RT^2} \quad (2.71)$$

where R is the gas constant.

It is recognised that ΔH_{vap} depends only weakly on T . This equation can be integrated to give the following approximate equation:

$$\ln P = A - \frac{\Delta H_{vap}}{RT} = A - \frac{B}{T} \quad (2.72)$$

where A and B are two constants.

The Clausius–Clapeyron equation can also be applied to estimate the vapour pressure of a solid precursor. In this case, the enthalpy of sublimation (ΔH_{sub}) should replace the enthalpy of vaporisation.

Vapour pressure data of some CVD precursors are listed in Appendix B.

References

- [1] Resnick R, Halliday D, Krane KS (2002) Physics vol 1, 5th edn. Wiley, New York
- [2] Sears F W, Zemansky M W, Young H D (1987) University physics, 17th edn. Addison–Wesley, London
- [3] Roth A (1990) Vacuum technology, 3rd edn. North–Holland, New York
- [4] Knudsen M (1952) The kinetic theory of gases. Methuen, London, pp26–28
- [5] Thomas J M, Thomas W J (1997) Principles and practice of heterogeneous catalysis. VCH, Weinheim, pp85–87
- [6] Ohring M (1992) The materials science of thin films. Academic, New Jersey
- [7] Hucknall D (1991) Vacuum technology and application. Butterworth Heinemann, Oxford, UK, pp40–307
- [8] Chambers A, Fitch RK, Halliday BS (1998) Basic vacuum technology, 2nd edn. Institute of Physics, Bristol, UK
- [9] Yarwood J ed (1975) High vacuum technique, 4th revised edn. Chapman & Hall, New York, pp16–103
- [10] Harris NS (1989) Modern vacuum practice. McGraw–Hill, London, pp72–85
- [11] Levesque A, Bouteville A (2001) Evaluation of corrosion behaviour of tantalum coating obtained by low pressure chemical vapour deposition using electrochemical polarization. J Phys IV11:Pr3-915–920
- [12] Dennis NTM, Heppell TA (1968) Vacuum system design. Chapman & Hall, London
- [13] Kuhn M, Bachmann P (1987) Selection and analytical monitoring of backing pump fluids in semiconductor processes. J Vac Sci Technol A5:2534–253
- [14] Bird R B, Stewart W E, Lightfoot E N (1960) Transport phenomena. Wiley, New York
- [15] Reid RC, Prausnitz JM, Poling BE (1987) The properties of gases and liquids, 4th edn. McGraw–Hill, New York
- [16] Beek WJ, Muttzall KMK, van Heuven JW (1999) Transport phenomena, 2nd edn. Wiley, New York
- [17] Thomson WJ (2000) Introduction to transport phenomena. Prentice Hall, Upper Saddle River, NJ
- [18] Chapman S, Cowling TG (1974) The mathematical theory of nonuniform gases, 3rd edn. Cambridge University Press, Cambridge
- [19] Hirschfelder JO, Curtiss CF, Bird RB (1954) Molecular theory of gases and liquids. Wiley, New York
- [20] Munson BR, Young DF, Okiishi TH (2006) Fundamentals of fluid mechanics, 5th edn. Wiley, New York
- [21] Vargaftik NB (1983) Handbook of physical properties of liquids and gases, pure substances and mixtures, 2nd edn. Hemisphere, Washington, DC
- [22] Wilke CR (1950) J Chem Phys 18:517
- [23] Herning F, Zipperer L (1936) Gas wasserfach 79:49
- [24] Wassiljew A (1904) Physik Z 5:737
- [25] Ceankoplis CJ (1993) Transport processes and unit operations, 3rd edn. Prentice Hall, Engelwood Cliffs, NJ

- [26] Dullien FAL (1979) Porous media: fluid transport and pore structure. Academic, New York
- [27] Tai NH, Chou TW (1990) Modelling of an improved chemical vapor infiltration process for ceramic composites fabrication. *J Am Ceram Soc* 73:1489–1498
- [28] Schlichting H (1979) Boundary-layer theory, 7th edn. translated by J Kestin. McGraw–Hill, New York
- [29] Incropera FP, Dewitt DP, Bergman TL, Lavine AS (2007) Fundamentals of heat and mass transfer, 6th edn. Wiley, New York, pp348–351
- [30] Jensen KF (1993) Fundamentals of chemical vapour deposition. In: Hitchman ML, Jensen KF (eds) Chemical vapour deposition: principles and applications. Academic, New York
- [31] Choy KL (2003) Chemical vapor deposition of coatings. *Prog Mater Sci* 48:57–170
- [32] Jensen KF (1993) Fundamentals of chemical vapour deposition. In: Hitchman ML, Jensen KF (eds) Chemical vapour deposition: principles and applications. Academic, New York, pp31–90
- [33] Glocker DA, Shah SI (eds) (1995) Handbook of thin film process technology. Institute of Physics, Bristol, UK
- [34] Visser EP, Kleijn CR, Govers CAM., Hoogendoorn CJ, Giling LJ (1989) Return flows in horizontal MOCVD reactors studied with the use of TiO₂ particle injection and numerical calculations. *J Crystal Growth* 94:929–946
- [35] Ellison A, Zhang J, Peterson J, Henry A, Wahab Q, Bergman, JP, Makarov YN, Vorob'ev A, Vehanen A, Janzen E (1999) High temperature CVD growth of SiC. *Mater Sci Eng B* 61-62:113–120
- [36] Nakamura S, Fasol G (1997) The blue laser diode. Springer, Berlin Heidelberg New York
- [37] Adam NK (1958) Physical chemistry. Oxford University Press, London
- [38] McQuarrie DA, Simon JD (1997) Physical chemistry. University Science Books, Sausalito, CA

Chapter 3 Chemical Vapour Deposition Systems Design

This chapter introduces new equipment design and a CVD process methodology. The chapter then gives details of the most commonly used subsystems followed by some special applications of CVD processes.

3.1 Proactive Design Approach for Chemical Vapour Deposition Systems

Engineering design has been traditionally considered a sequential process in which a design solution to a problem is generated following a series of prescribed steps. Based on traditional design process models and approaches, as illustrated in many classic books such as those by French [1] and Pahl and Beitz [2] and current industry practice, a new product is normally developed following through a number of stages, namely market research, conceptual design, detailed design, design analysis, prototyping and testing, production process planning, manufacturing, assembly, inspection and sale.

In contrast to traditional engineering design approaches, a new concurrent product and manufacturing/assembly design process model has been proposed by the authors as shown in Figure 3.1. This model is based on the life-cycle design model [3, 4] and a mechatronic system design model [5]. It depicts the process of using an ideal computer design environment in product development. The development of a product using such an ideal computer support system goes through the following stages: *design initialisation and task clarification* stage through the analysis of need, *concepts and qualitative modelling* through concept generation, computer-based modelling and evaluation, *embodiment and quantitative modelling* taking place at the traditional embodiment/detailed design stage, but characterised here by interactive simulation of product performance through finite element analysis (FEA) and dynamic analysis models, and evaluation of multiperspective models covering geometry, costs and so on. Product definition models are gradually evolving and expanding from the initial design stage to the final embodiment/detail design stage. During this process, more and more design decisions are made to concretise and quantify design solutions. Evaluation of design alternatives is carried out to facilitate designers to make informed design decisions. A set of dictionaries containing the established design functions and associated means and libraries storing the past, well-proven design modules can be reused to assist designers to generate a working solution. A modular approach is adopted in this process and basic component/product building blocks can be generalised to construct these libraries. During this design solution generation process, design solutions evolve from being abstract, qualitative and vague to being detailed, quantitative and concrete. Design solution information expands to a richer level through this process as indicated by a gradually darkening shade for the product information model. This is a reflection of more decisions

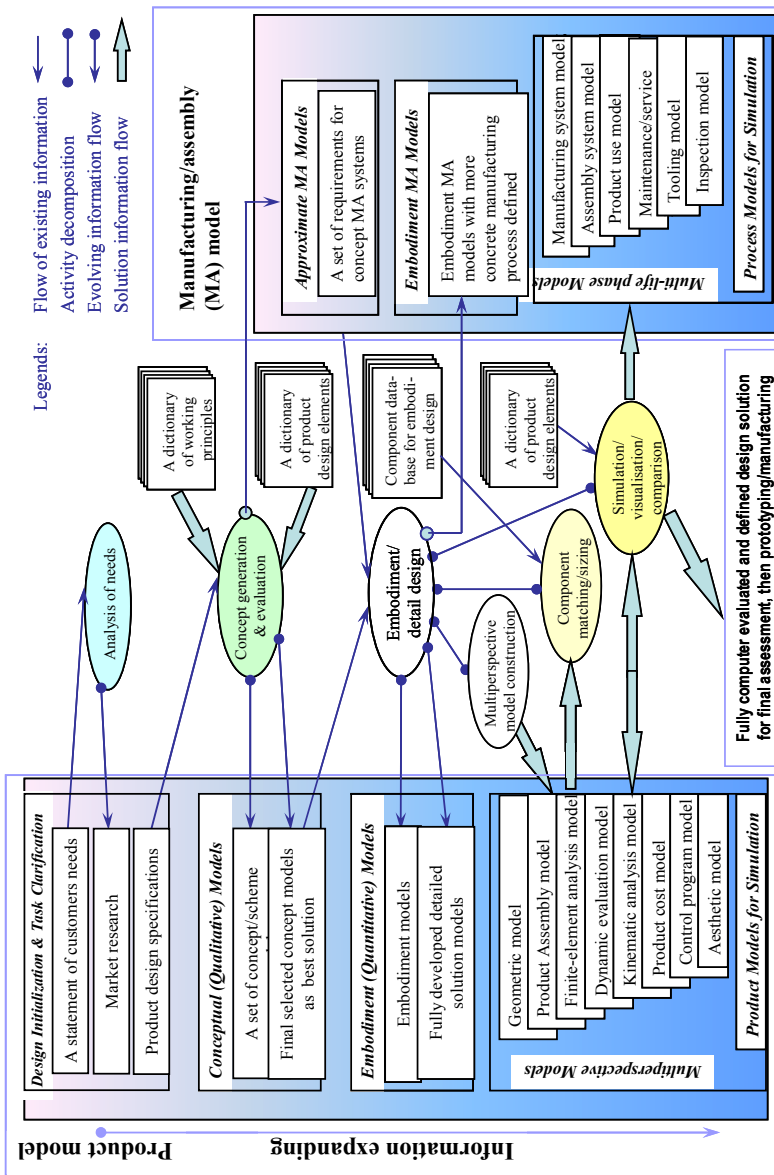


Figure 3.1. Concurrent product and manufacturing/assembly design process model

being made and recorded in the process. A set of dictionaries and libraries is used to support the generation of product models.

The final outcome using an ideal computer support system is a set of multiperspective design models, namely a model to describe the geometric information of a product, an assembly model, an FEA model, a dynamic valuation

model, a kinematic model, a product cost model, a control program model for a mechatronic product, an aesthetic model, a product disposal model and so on. Each of these models describes a perspective view of that product with a certain level of accuracy and details, but collectively these models fully define the properties of the product in terms of its physical definition, its intended purpose and life time use and disposal. The behaviour of a product in its various anticipated life-cycle environments can also be predicted even if the product only exists as a virtual product in its virtual computer models.

Equally important in Figure 3.1 is the modelling of life-cycle systems. This is specifically represented as manufacturing/assembly modelling. On the right-hand side of the concurrent design process model, an evolving manufacturing/assembly tool element (MATE) model is represented to show that concurrent product and MATE modelling can be established from the interaction of component/product model with available MATE knowledge by extracting relevant product information. For example, knowing that a sheet metal component requires a holefeature as part of its design decision, a punch-die tooling design can be derived to form a tooling model. This deduction leads to the concurrent development of tooling for the product. It can also be seen that MATE models are also expanding and evolving as more MATE model details can be added with more product design decisions made.

Applying the above design process concept and methodology in CVD system and product design, it is possible to improve the design performance significantly. With a good understanding of this approach, equipment designers and process engineers are encouraged to consider the design of a product at the same time as the manufacturing process is determined. The following sections introduce the details of each of the commonly used subsystems for a CVD process. It is aimed at giving readers a good understanding of these subsystems before fully starting to utilise the above design and manufacturing process concept.

3.2 General Description of a Chemical Vapour Deposition System

3.2.1 Classification of the Chemical Vapour Deposition Methods

According to the characteristics of the CVD processing parameters, CVD methods are generally classified and categorised into seven main types of fabrication, as shown in Figure 3.2. The parameters used to characterise a CVD process include temperature, pressure, wall/substrate temperature, precursor nature, depositing time, gas flow state and activation manner [6–8].

For structural oriented product manufacturing applications, high-temperature CVD (usually in a range above 1000°C) is predominantly used. Low-temperature CVD (around 300°C) is mainly used for fabrication where the substrate cannot sustain high temperature. For semiconductor device processing CVD processes are conducted at a low temperature because the substrate is aluminium or plastic which cannot stand a high-temperature environment. Ultra-high-temperature CVD techniques were developed for the single-crystal epitaxial growth of semiconductor

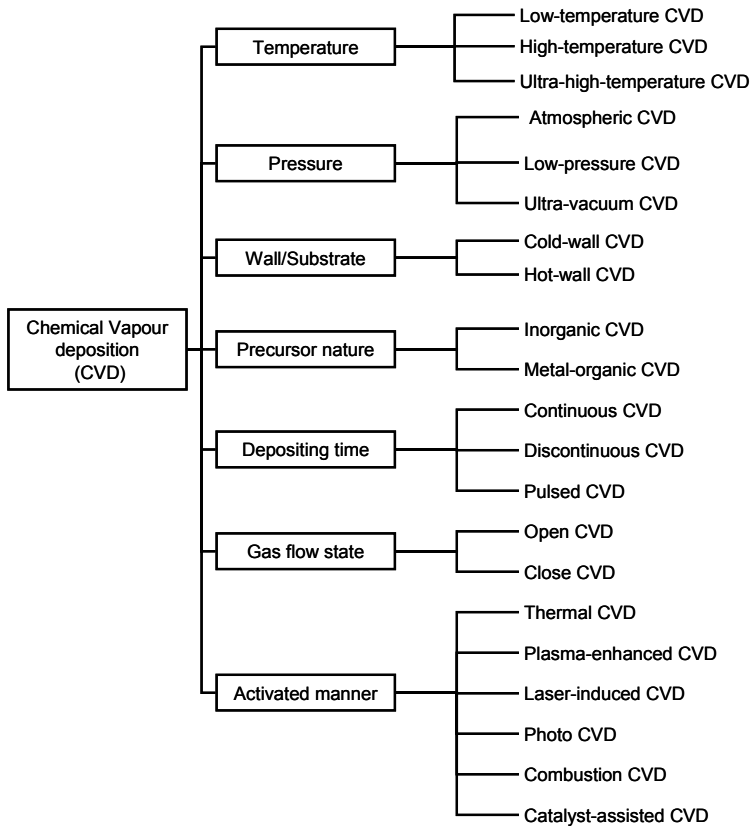


Figure 3.2. Classification of CVD methods

materials. For example, the CVD SiC process from SiH_4 and hydrocarbon gas is operated at temperatures of 1750 to 1900°C [9].

When pressure is used to control the deposition process, CVD can be classified into three categories, namely atmospheric-pressure CVD, low-pressure CVD (i.e. <1 Torr) or ultra-high vacuum CVD (i.e. 10^{-3} Torr) [10]. Pressure has a considerable effect on the deposition rate and quality of the finished products, in terms of coating thickness uniformity. Detailed impacts of the pressure control are discussed in Chapter 4.

In a cold-wall CVD only the substrates are heated either inductively or resistively and the wall of the reactor is colder than that of the substrate. Therefore, the deposition mainly occurs on the heated substrate, and negligible deposition on the walls of the reactor. Cold-wall reactors are mainly used for continuous deposition of fibres and depositions where a thermal gradient is required to facilitate CVI. Hot-wall CVD reactors represent one of the major categories of CVD reactors. In such systems, the chamber containing the parts is heated by a furnace from outside. In general, hot-wall reactors have the advantages of being

able to process a large number of substrates and having good process parameter control. As a result, it is easy for these hot-wall reactors to be scaled up for industrial application.

In terms of the process time control, CVD can be divided into three categories, namely continuous, discontinuous and pulsed CVD (P-CVD). Discontinuous CVD is used in most CVD processes, whereas continuous CVD is extensively used for fibre coating and high-volume production of semiconductor devices. In order to improve the coating thickness uniformity and its microstructure, P-CVD is commonly used.

CVD can be performed in a so-called “closed” or “open” system. In “closed” CVD, both reactants and products are recycled for reuse within an enclosure [11]. The “closed reactor” CVD method is primarily used for metal purification and protection coating for aero-engine blades (e.g. pack cementation for aluminising, chromising, etc.). In most cases, CVD happens in an open state which is described in Chapter 1 and Figure 1.1.

CVD can also be classified using its activation methods. Thermal activated CVD processes are initiated only with the thermal energy of resistance heating, RF heating or by infrared radiation. They are widely used to manufacture the materials for high-temperature and hard-to-wear applications. In some cases enhanced CVD methods are employed, which includes plasma-enhanced CVD (PECVD), laser-induced CVD (LCVD), photo CVD (PCVD), catalysis-assisted CVD and so on. In a plasma-enhanced CVD process the plasma is used to activate the precursor gas, which significantly decreases the deposition temperature.

3.2.2 Configuration of a Chemical Vapour Deposition Apparatus

Regardless of the number of CVD types discussed above, a CVD system must meet the following four basic requirements [12–14]:

1. to deliver and control all of the precursor gas, carrier gas and the diluent gas into the reaction chamber;
2. to provide an energy source to initiate and drive the chemical reaction;
3. to remove the by-product exhaust gases from the reaction chamber and to dispose them safely;
4. to precisely control the process parameters (temperature, pressure, gas flow rate) automatically so that the quality of deposited products and the reproducibility can be maintained from run to run.

These basic requirements must commonly be met for research applications in laboratory. For large-scale applications, some other additional requirements should be taken into account. These include the throughput, economy, safety and routine maintenance.

Based on these industrial requirements, a CVD system usually consists of several basic subsystems.

- Gas delivery system

This subsystem is used to supply the precursor in a controlled manner. After the reactant gases are mixed with carrier gas and diluent gas homogeneously, the mixture gas is delivered into the reaction chamber

- Reaction chamber or reactor

The reaction chamber is the heart of a CVD system where chemical vapour deposition takes place. It consists of retort, gas inlet injector, distributor and outlet exit. The quality of the deposit is mainly dependent on the design of the reaction chamber, which determines the uniformity of temperature, concentration and pressure.

- Loading/unloading system

This is normally a mechanical system to transport substrates, preforms, mandrels, etc. from the outside to the inside of the reaction chamber or *vice versa*. This subsystem should be designed to reduce the labour intensity and save cost.

- Energy system

An energy system must provide the energy required for the precursors to react at elevated temperatures, and control and maintain the temperatures within the reaction chamber. When the CVD process is enhanced by some other methods (e.g. plasma), additional energy supplies are required.

- Vacuum system

This consists of vacuum pumps, pipes, valves and connections, etc. This subsystem is used to evacuate the gases and control the pressure within the reaction chamber.

- Process automatic control system

A computer controlled system is designed and installed to automatically measure and control the deposition parameters such as pressure, flow rate, depositing temperature and time. In some cases, a gas analyser is used to monitor the CVD process [15, 16]. This subsystem is usually incorporated within the relevant aforementioned subsystems to ensure the quality of the deposition.

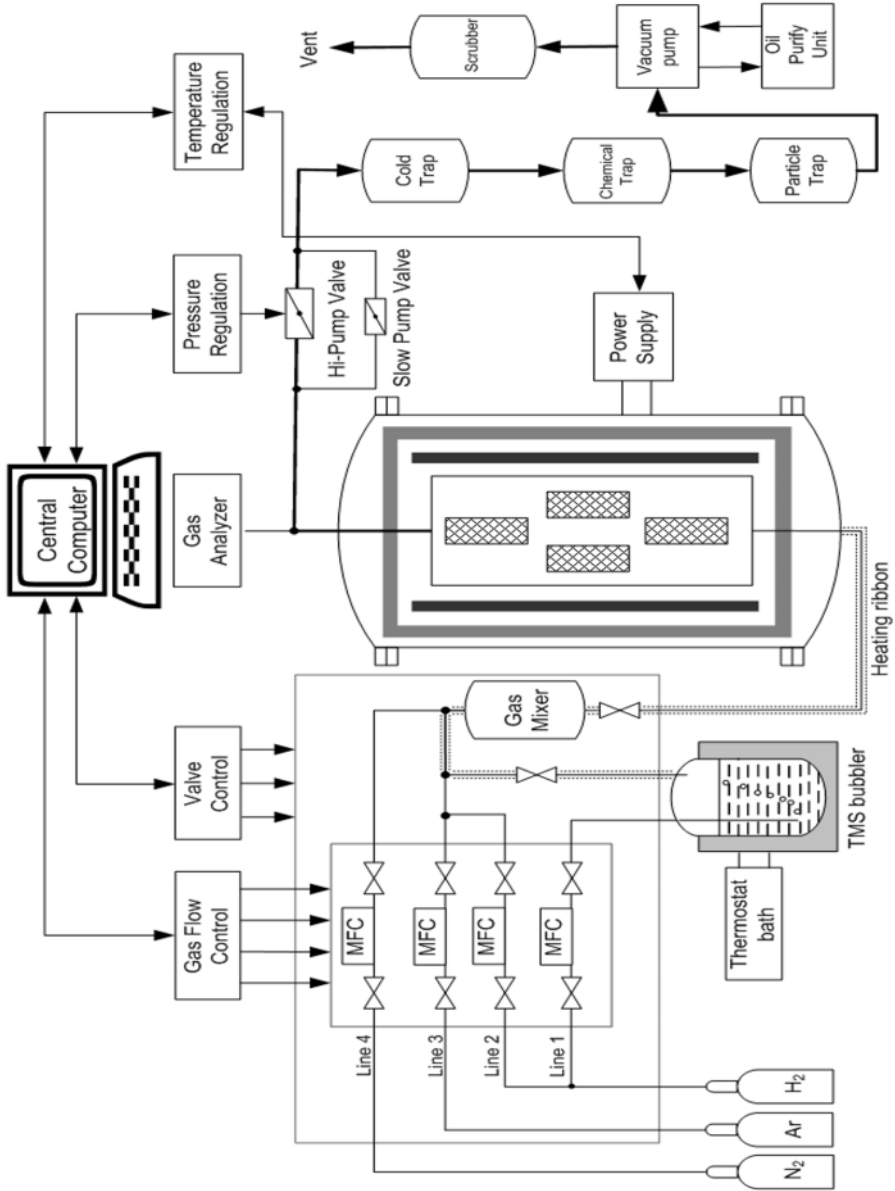
- Exhaust gas treatment system

This consists of a cold trap, a chemical trap, a particle trap, a wet scrubber, etc. Exhaust gases for CVD are usually hazardous and toxic. Hence, they should be treated to a safe and harmless level and converted into safe compounds before being released into the atmosphere.

A general description of a typical CVD system is presented in Figure 3.3.

CVD systems should be designed and operated under optimum processing conditions to ensure the quality of coating in terms of uniform thickness, microstructure and chemical composition. In the past most CVD systems were designed empirically. Recently, theories and methods of fluid dynamics and heat transfer such as computational fluid dynamics (CFD) have been advanced and become widely used to help the design and evaluation of such systems [17]. Commercial production equipment is more sophisticated and complex in design, as compared to laboratory CVD equipment, in order to accommodate large batch sizes or large-scale deposition. For example, reactant depletion is commonly a severe problem in large CVD reactors, which can result in non-uniform coatings. Such problems can be overcome using multiple gas injection ports through which

more uniform chemical reactions are stimulated and enabled, hence ensuring the quality of the deposition.



Legend: MFC – mass flow controller

Figure 3.3. Description of subsystems in a CVD apparatus

3.3 Precursor Delivery System

3.3.1 Selection Criteria for Chemical Vapour Deposition Precursors

For the deposition of a given material, there are generally a number of precursors available. The selection criteria of a suitable chemical precursor for coating applications are as follows [7, 8, 18]:

3.3.1.1 Low Vaporisation Temperature and Sufficient Volatility

The vapour pressure of the precursors must be high enough for the reasonable growth rates of the deposit. In order to prevent the vaporised gas from condensing in the delivery pipelines, the vaporising temperature should be set to a relatively low temperature, particularly lower than the deposition temperature.

3.3.1.2 High Stability at Relatively Low Temperatures

Whilst the precursors are required to be reactive at high temperatures, they should be stable enough to be carried into the reactor chamber, and no chemical reactions should take place below the deposition temperature.

3.3.1.3 High Safety

Some chemicals present high levels of hazards such as high toxicity i.e. $\text{Ni}(\text{CO})_4$ or AsH_3 , pyrophoricity (i.e. CH_4 , SiH_4), explosiveness (i.e. B_2H_6), corrosiveness [i.e. CH_3SiCl_3], and combinations of the above. Hence, it is especially desirable for large-scale industrial applications to use safe precursors to avoid any potential risk. Metal-organic precursors are generally less hazardous than hydrides and have been widely used in the semiconductor industry.

3.3.1.4 Low Cost

Precursor cost determines not only the cost of a precursor gas itself, but also the deposition efficiency and its environmental related costs. The above overall costs should be considered in the context of the precursor cost. Compared with the hydrides and halides, the metal-organic precursors are much more expensive.

3.3.2 Chemical Vapour Deposition Precursors and Their Classification

The precursors used in the CVD process can be divided into three categories as follows [7, 8]:

3.3.2.1 Halides

These precursors are very simple and generally consist of small molecules where the central species is bonded to other species such as a halide (F, Cl, less commonly Br or I). Some of the halides are solid at room temperature (e.g. AlCl_3 , WCl_5 and ZrCl_4 etc.) and their sublimation is difficult to control. In such cases *in situ* halogenation is usually used to form the halide precursor, which is then conveyed to the reaction chamber by the carrier gas.

Halides are often used for the deposition of high-temperature materials (such as refractory metals and advanced ceramics) with a high growth rate. They are also

used to deposit thin films at relatively low temperatures and with low growth rates for microelectronic applications. The common halides include AlCl_3 , BCl_3 , CH_3SiCl_3 , SiCl_4 , TaCl_5 , TiCl_4 , WF_6 and ZrCl_4 .

3.3.2.2 Hydrides

Hydrides are negative ions of hydrogen, H^- , and they are widely used to describe the compounds of hydrogen with elements of IA to VIA in the periodic table of elements. These precursors are employed for deposition at low temperatures but with high growth rates. The common hydrides include B_2H_6 , CH_4 , GeH_4 and SiH_4 .

3.3.2.3 Metal-organic Compounds

These compounds are used as the precursors for MOCVD processes. Compared with halides and hydrides, the metal-organic compounds have much more complex structures because they contain large functional groups (e.g. allyl, butyl, methyl etc) and ligands (such as carbonyl, acetylacetonate, hexafluoroacetyl acetone and so forth). Some representative examples are listed below [19, 22]:

- Metal alkyls: $\text{Al}(\text{CH}_3)_3$, $\text{Be}(\text{C}_4\text{H}_9)_2$, $\text{Ir}(\text{C}_3\text{H}_5)_3$, etc.
- Metal alkyamides: $\text{Ti}(\text{NMe}_2)_4$, $\text{Ti}[\text{N}(\text{EtMe})_2]_4$, etc.
- Metal alkoxides: $\text{Al}(\text{OC}_3\text{H}_7)_3$, $\text{Si}(\text{OC}_2\text{H}_5)_5$, $\text{Ti}(\text{OC}_3\text{H}_7)_4$, etc.
- Metal carboxylates : $\text{Cu}(\text{CH}_3\text{COO})_2$, $\text{Zn}(\text{CH}_3\text{COO})_2$, etc.

Table 3.1. Typical β -diketonate precursors

Abbreviation	Name and molecular formula	R_1	R_2
aa/acac	Pentane-2,4-dionate, acetylacetonate, $\text{C}_5\text{H}_7\text{O}_2$	CH_3	CH_3
dhd	1,1-dimethylhexane-3,5-dionate, $\text{C}_8\text{H}_{13}\text{O}_2$	CH_3	$\text{C}(\text{CH}_3)_3$
dbm	1,3-diphenylpropane-1,3-dionate, dibenzoylmethane, $\text{C}_{15}\text{H}_{11}\text{O}_2$	C_6H_5	C_6H_5
dmhd	Dimethyl-heptandionate, $\text{C}_7\text{H}_{11}\text{O}_2$	C_2H_5	C_2H_5
dpm	Dipivaloylmethanate, $\text{C}_{11}\text{H}_{19}\text{O}_2$	$\text{C}(\text{CH}_3)_3$	$\text{C}(\text{CH}_3)_3$
etob	Ethylacetoacetate, $\text{C}_8\text{H}_{13}\text{O}_2$	CH_3	$\text{C}_2\text{H}_5\text{O}$
fod	6,6,7,7,8,8-heptafluoro-2,2-dimethyl-3,5-octandion, $\text{C}_{10}\text{F}_7\text{H}_{10}\text{O}_2$	C_3F_7	C_4H_9
hfa/hfac	1,1,1,5,5,5-hexafluoropentane-2,4-dionate, hexafluoroacetylacetonate, $\text{C}_5\text{F}_6\text{HO}_2$	CF_3	CF_3
mhd	6-methylheptane-2,4-dionate, $\text{C}_8\text{H}_{13}\text{O}_2$	CH_3	C_4H_9
pta	Pivaloyltrifluoroacetate, $\text{C}_8\text{F}_3\text{H}_{10}\text{O}_2$	CF_3	$\text{C}(\text{CH}_3)_3$
pva	Pivaloylacetonate, $\text{C}_8\text{H}_{13}\text{O}_2$	CH_3	$\text{C}(\text{CH}_3)_3$
tdf	1,1,1,2,2,3,3,7,7,8,8,9,9,9-tetradecafluorononane-4,6-dionate, $\text{C}_9\text{F}_{14}\text{HO}_2$	$\text{CF}_2\text{CF}_2\text{CF}_3$	$\text{CF}_2\text{CF}_2\text{CF}_3$
tfa/tfac	1,1,1-trifluoropentane-2,4-dionate, trifluoroacetylacetonate, $\text{C}_5\text{F}_3\text{H}_4\text{O}_2$	CF_3	CH_3
thd/dmp/tmhd	2,2,6,6-tetramethyl-3,5-heptandionate, $\text{C}_{11}\text{H}_{19}\text{O}_2$	C_4H_9	C_4H_9

Note: ML_n , $n = 2, 3, 4$; $\text{L} = \text{R}_1\text{COCHCOR}_2$

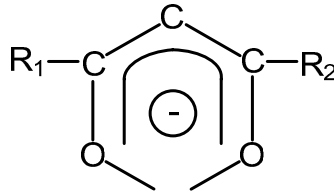


Figure 3.4. Molecular structure formula of β -diketonate ligand

- Metal carbonyls: $\text{Al}_2[\text{N}(\text{CH}_3)_2]_6$, $\text{Hf}[\text{N}(\text{C}_2\text{H}_5)_2]_4$, $\text{N}_6[\text{N}(\text{CH}_3)_2]_5$, $\text{Ti}[\text{N}(\text{CH}_3)_2]_4$, etc.
- Metal cyclopentadienyls : $\text{Ba}(\text{Me}_5\text{Cp})_2$, $\text{Mg}(\text{Cp})_2$, $\text{Mn}(\text{Cp})_2$, ZrCp_2Cl_2 , etc.
- Metal diketonates: $\text{Cu}(\text{acac})_2$, $\text{Ir}(\text{acac})_3$, $\text{Ni}(\text{thd})_2$, $\text{Y}(\text{thd})_3$, etc.

Many kinds of β -diketonate precursors can be synthesised with different R_1 and R_2 groups; some of them are listed in Table 3.1. The molecular structure formula is shown in Figure 3.4.

Occasionally some pure elements can also be used as precursors. For example, both Zn and Cd are vaporised as precursors for ZnS and CdS [23] respectively.

The materials for CVD processes and related precursors are collected in Appendix C for reference.

3.3.3 Delivery Methods

The role of this system is to generate precursor vapour, and then deliver it to the CVD reactor. Gaseous precursors are preferred because they can be readily metered to control the gas flow parameters. Liquid and solid reactants can usually be vaporised at suitable temperatures and transported by a carrier gas to the reaction chamber. A typical gas delivery system with four delivery lines is shown in Figure 3.3. In lines 1, 2 and 3 gas flows and their associated parameters (e.g. flow rate, pressure) are regulated by three mass flow controllers and the relevant valves. H_2 , MTS- H_2 and Ar gases are conveyed to the gas mixer, then to the CVD chamber. Line 4 is employed to purge the reactor before and after the CVD process. For a delivery system, three types of precursors should be considered.

3.3.3.1 Gaseous Precursors

Gaseous precursors refer to the source gases which are in the gas state at ambient temperature. It is very convenient to deliver the gaseous precursors by using pressure controllers, gauges and flow meters. However, some gaseous precursors are pyrophobic, expensive and dangerous. It is necessary to dilute them with other inert gases to avoid safety problems. In addition, it is also important to ensure that there are no chemical reactions between the gaseous precursors and all components of flow meters, valves, gauges and pipes to minimise corrosion. Leakage must also be avoided in the gas delivery system.

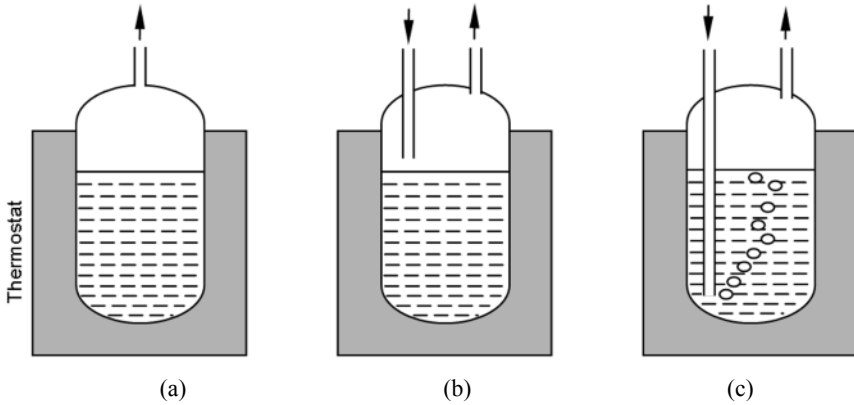


Figure 3.5. Schematics for delivery of liquid precursor [24]: (a) direct vaporisation, (b) carrier gas sweeping and (c) bubbling method

3.3.3.2 Liquid Precursors

Many CVD precursors are in liquid state at room temperature. The precursors must be heated to a proper temperature for vaporisation and transported the reaction chamber by a carrier gas. There are three kinds of methods to deliver the liquid precursor, namely direct vaporisation by itself without carrier gas, as shown in Figure 3.5a, transport by a carrier gas sweeping over the liquid surface (Figure 3.5b) and bubbling through the liquid, as shown in Figure 3.5c. The bubbling method is preferred and is generally used because it is an easier and reliable method to obtain a uniform mixture of gases immediately. The downstream pipes for the vaporised precursors must be sufficiently heated to prevent their recondensation.

In order to improve the reproducibility of the precursor gas flow, it is necessary to control the temperature and the height of the liquid precursor level accurately because the pick-up rate of the carrier gas changes with these parameters. The precursor container is usually placed into an oil bath which is kept at a constant temperature by stirring the oil. The carried vapour flow rate (n) is given by the following equation [25];

$$F_{vap} = \frac{p_{vap} P_{cyl}}{P_{cyl} - p_{vap}} \cdot \frac{F}{RT_{std}} \quad (3.1)$$

where F_{vap} is the mole flow rate in moles per minute, p_{vap} is the saturated vapour pressure of the liquid precursor at bath temperature T_b , P_{cyl} is the total pressure in the precursor cylinder, F is the volume flow rate through the bubbler in litres per minute, R is the gas constant, and $T_{std} = 273$ K.

Flash evaporation is another liquid vaporisation method as shown in Figure 3.6. By using a micropump (e.g. syringe pump, peristaltic pump), the amount of liquid can be accurately metered. When the liquid precursor is injected into the heat exchanger, it is immediately vaporised into gas, which in turn is introduced into the

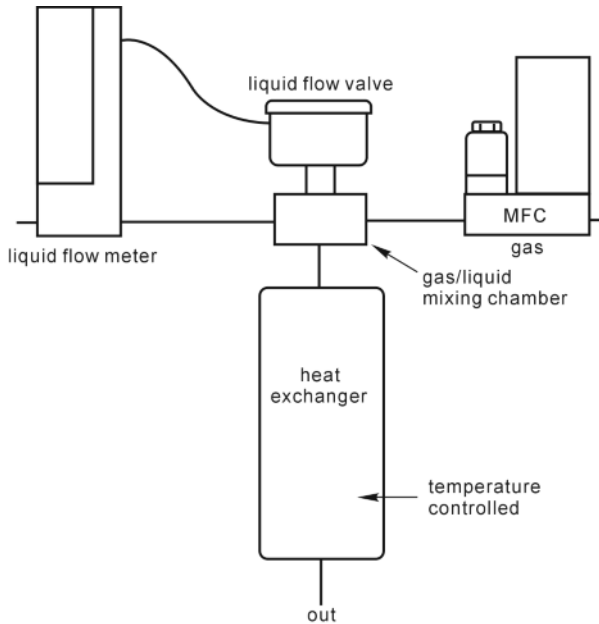


Figure 3.6. Controlled evaporation and mixing system [24]

reaction chamber by a carrier gas. The flash method can be used to deliver solid precursors if they can be dissolved in a suitable liquid. Up to now this method has been widely used in MOCVD processes.

The usual carrier gas used for the CVD processes is H_2 because of its low density and viscosity for better flow behaviour. Moreover, the recirculation in the reactor chamber can obviously be reduced because of its high thermal conductivity. Under conditions of the same gas flow velocity and substrate temperature the temperature gradients in Ar and N_2 are steeper than that in H_2 within the boundary layer. In some cases H_2 also plays the role of reaction agent. Sometimes Ar, N_2 or O_2 is used as carrier gas according to the processing requirements. The physical properties of some gases are listed in Table 3.2, including the density (ρ), viscosity (μ), thermal conductivity (α) and specific heat (C_p).

3.3.3.3 Solid Precursors

Solid precursors exhibit some problems because they must be heated to their vapourisation temperature, which may be relatively high in some cases. *In situ* synthesis is often used to produce precursors. Figure 3.7 shows an example of the deposition of spinel ($MgAl_2O_4$) from $MgCl_2$ - $AlCl_3$ - CO_2 system. It is convenient to generate the reactant gas *in situ*. The aluminium, in the form of chips, pellets, or powder, is placed in a chlorinator to form $AlCl_3$ by Al-HCl reaction at $650^\circ C$. $MgCl_2$ is vaporised at $930^\circ C$, which is very close to the required deposition temperature of $950^\circ C$. The top part of Figure 3.7 shows the schematic diagram of a

Table 3.2. Typical physical properties of some gases at 300 K, 1 atm [26]

Gas	ρ ($\text{g}\cdot\text{l}^{-1}$)	C_p ($\text{kJ}\cdot\text{kg}^{-1}\cdot\text{K}^{-1}$)	μ ($\times 10^{-6} \text{ N}\cdot\text{s}\cdot\text{m}^{-2}$)	α ($\times 10^{-3} \text{ W}\cdot\text{m}^{-1}\cdot\text{K}^{-1}$)
Ar	1.79	0.522	22.71	17.7
CH ₄	0.71	2.24	11.14	33.2
C ₃ H ₈	1.96	1.68	81.6	18.1
H ₂	0.09	14.7	1.45	183
N ₂	1.25	1.041	17.88	25.9
O ₂	1.43	0.92	20.72	26.8

solid precursor generation system and process and the bottom graph shows the temperature increases by each heater within the system.

For safety reasons the chlorinator has to be designed carefully to prevent explosion caused by mixing chlorine and hydrogen. The explosion would take place if the content of hydrogen reached 3.5% in the chlorine gas. Figure 3.8 shows the *in situ* synthesis of the ReCl₅ precursor from the reaction between Re and Cl₂. For this case only chlorine can be directly introduced into the chlorinator while hydrogen is introduced to the outside of the chlorinator within the reaction chamber.

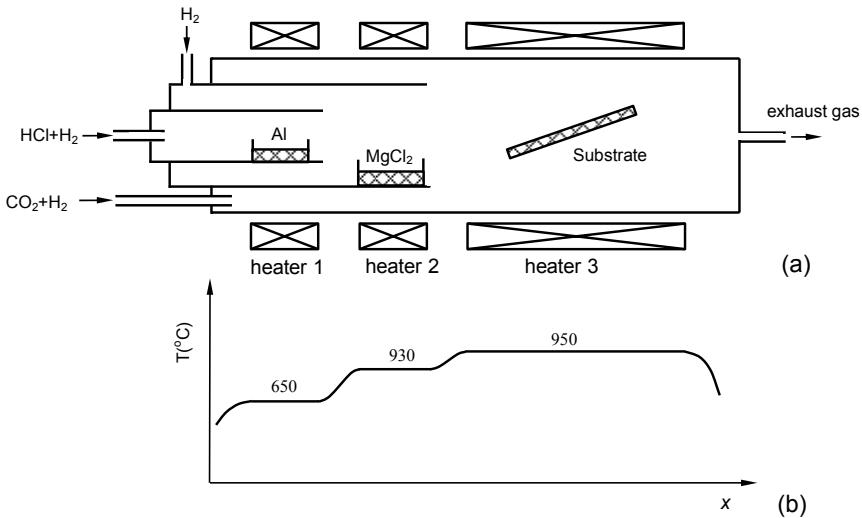


Figure 3.7. Generation of solid precursors [27]: (a) an example of CVD system using in situ reactant gas generator and (b) the temperature changes within the system

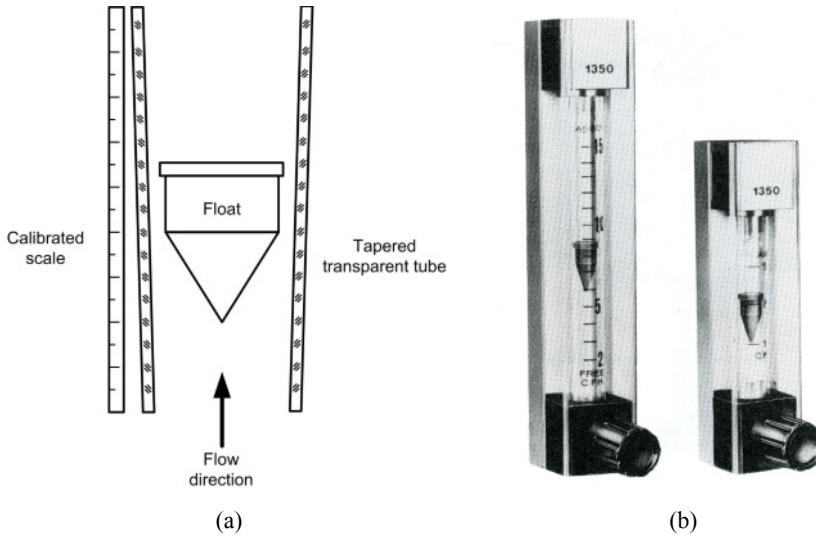


Figure 3.8. *In situ* synthesis of ReCl_5 for the foam Re deposition [28]

3.3.4 Devices and Components for the Delivery System

3.3.4.1 Gas Flow Meters

Rotator flow meter and mass flow controller are usually used to measure and control the gas flow rate.

The rotator flow meter is installed in a vertical position on the pipeline. The gas flows through the tube from the bottom to the top of the meter. The rotator flow meter works on the principle that the flowing fluid exerts a drag force on the float within a transparent tube. As a result it gives the volume flow rate of the gas according to the height of the float within the calibrated pipe as shown in Figure 3.9. This kind of flow meter is a simpler and cheaper option. The accuracy could be affected by the ambient temperatures and the pressure difference between the bottom inlet and the top outlet, and it is typically within $\pm 5\%$ of the full scale in the given conditions.

The mass flow meter, also called mass flow controller (MFC), operates by measuring variations in the temperature of flowing gas subjected to heat flux. The temperature variation is related to the amount and the heat capacity of the gas. The transferred heat (Q) is calculated by [30]

$$Q = WC_p(T_2 - T_1) \quad (3.2)$$

where C_p is the specific heat capacity of the flow gas, T_1 and T_2 are the temperatures of the fluid before and after the heat is transferred, respectively and W is the mass flow rate of the gas.

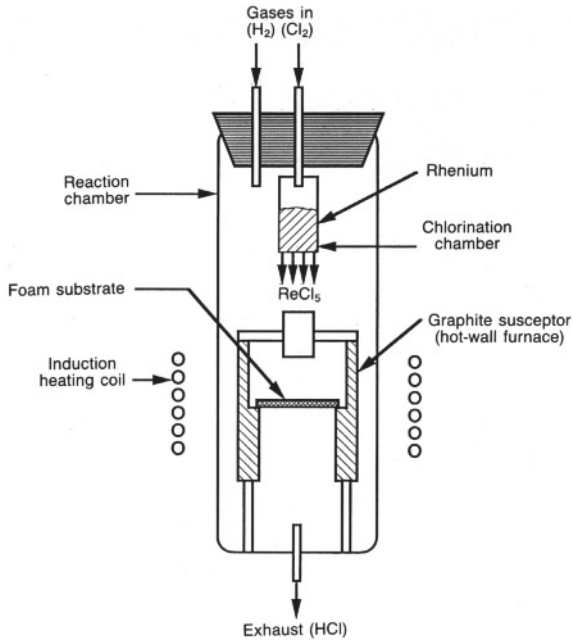


Figure 3.9. Schematic of a rotator flow meter [29]

Figure 3.10 shows the working principle of the mass flow meter. The gas is forced to flow through a tube with a small diameter and the thermal components are placed on the outside of the tube. The temperature profile is symmetric if there is no gas flowing through the tube. The peak of the temperature profile will shift downward if the gas flows inside the tube. The difference between the temperature profile peaks is proportional to the mass flow rate and the flow rate and hence can be detected indirectly by readings from the temperature sensors.

Compared with rotator meters, mass flow meters are more accurate, typically giving an accuracy of $\pm 2\%$ of the full scale. Another distinct advantage is the ease of automation and programming for the CVD processes according to the requirements.

Needle valves are used to accurately control the gas flow in the gas lines, while butterfly valves are employed to regulate the gas flow and the pressure in the CVD reaction chamber.

3.3.4.2 Valves

As illustrated in Figure 3.11a, a needle valve has a small orifice with a long, tapered and conical seat. A needle-shaped plunger can exactly fit the seat driven by a screw at the other end. Turning the screw leads to the forward or backward movement of the plunger. Hence the gas flow can be accurately regulated by controlling the size of the orifice, if the correlation between the gas properties, e.g. viscosity and temperature, and orifice sizes can be established. Figure 3.11b shows the structure of a butterfly valve. A flat circular plate is positioned at the centre of

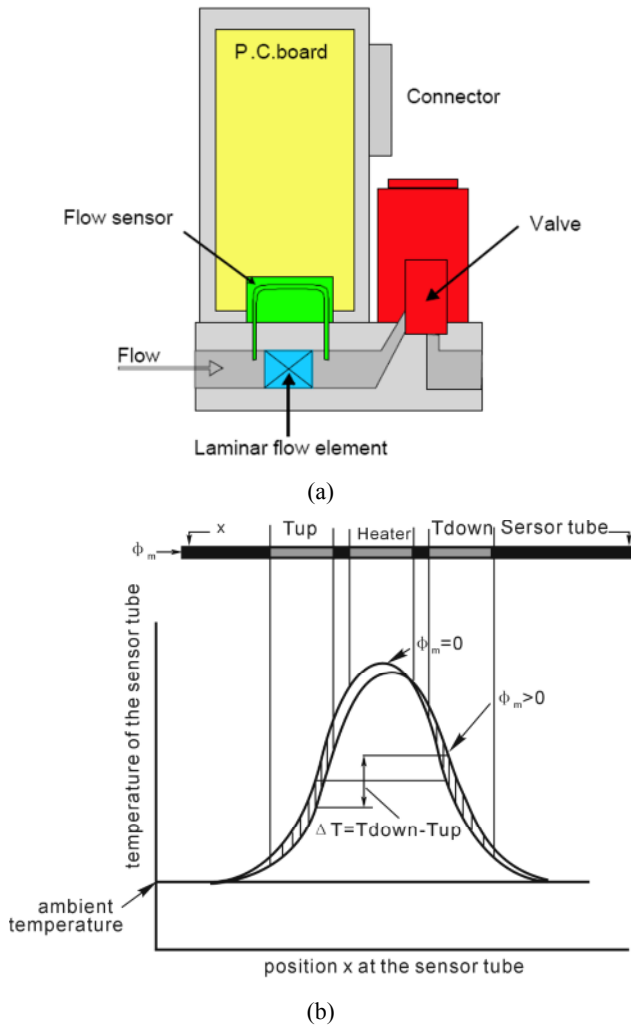


Figure 3.10. Thermal mass flow controller [31]: (a) schematic cross view and (b) working principle

the valve. A metal rod on the plate is connected with an actuator on the outside of the valve. The plate is forced to turn by the actuator, and the gas flow is controlled by the angle between the plate and flow direction. If the plate is turned parallel to the flow direction, the valve is fully open. If the plate is turned perpendicular to the flow direction, the passage way is completely blocked off.

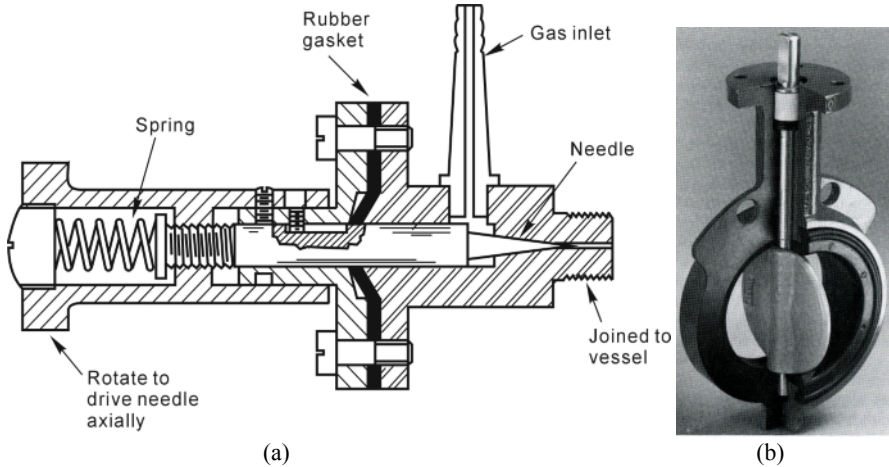


Figure 3.11. Schematics of two kinds of valves: (a) needle valve [32] and (b) butterfly valve [33]

3.3.4.3 Mixers

For the deposition of a coating with complex chemical compositions, the gases should be mixed homogeneously on line before they are delivered to the reactor [34, 35]. In order to ensure uniform gas mixing it is necessary to provide a sufficient space and time for the gases to be fully mixed. Regardless of the structures and types of mixing equipment used, the mixture among the different gaseous species mainly depends on the manner of mass transport such as diffusion or convection, where the mixing time is a critical factor.

It is important to generate rapid and turbulent gas movements such as turbulent flow or spiral gas flow. This helps to speed up the mass transport, hence shortening the mixing time and improving mixing efficiency.

Stirring by blades is a very useful and widely used mixing method which meets the above two conditions. For a CVD precursor gas delivery system, however, this method is not suitable and reliable because of the strong corrosiveness of precursors and rigid gas tightness required. To solve these problems, it is very useful to place suitably designed blades inside the mixing chamber [29]. This can generate strong turbulent gas flow, thereby accelerating homogenisation of the gases.

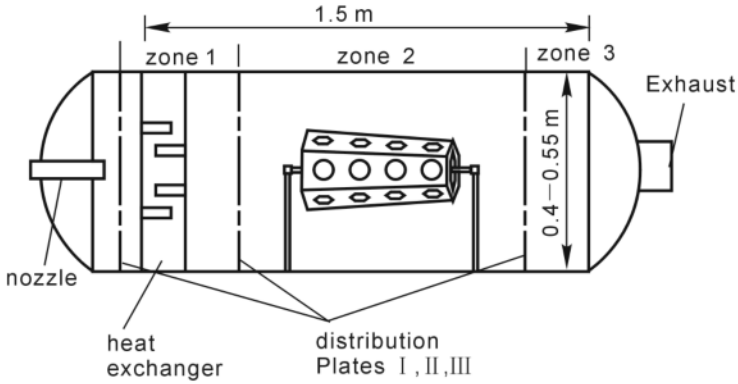
3.4 Reaction Chambers

A reaction chamber, also called a reactor, is the key subsystem of a CVD system, in which a chemical vapour deposition process takes place. In general a reaction chamber consists of the following parts as shown in Figure 3.12:

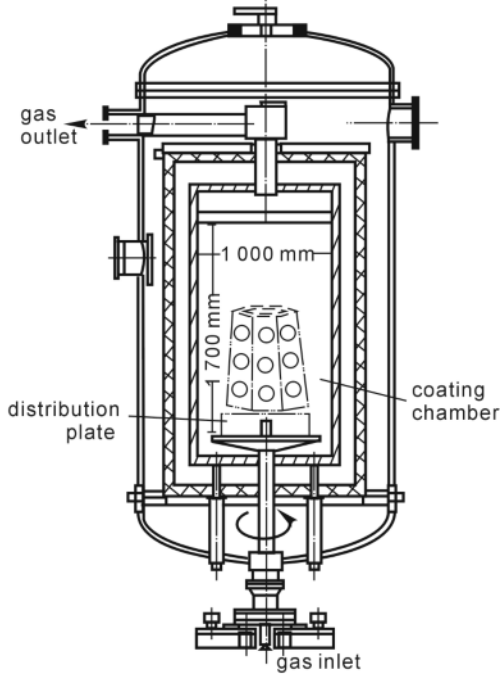
- A water-cooled jacket made of stainless steel;

- A retort with an inlet injector, a gas distributor, an exit and a substrate holder;
- A heating system comprised of the heating element, insulator, temperature sensor and automatic temperature controller.

For a CVD SiC process from a $\text{CH}_3\text{SiCl}_3\text{-H}_2$ reaction system, two kinds of reactors were reported by Brennfleck and Reich in 1993 [36], as shown in Figure 3.12. The retort of the horizontal reactor has a diameter of 550 mm and a length of 1500 mm, while the vertical reactor is comparatively larger, the diameter and the



(a)



(b)

Figure 3.12. Two types of CVD SiC reactors: (a) horizontal type and (b) vertical type [36]

height are 1000 mm and 2000 mm respectively. Recently, much larger reactors with a diameter of 2500 mm were produced for SiC deposition by the Snecma Company [37, 38].

3.4.1 Retorts

According to its functions, a retort is typically divided into three different zones as shown in Figure 3.12.

Zone I: the reactant gases are introduced into this zone, preheated and distributed through the distribution plate or distributor;

Zone II: the CVD process takes place on the surface of the substrate within this region; and

Zone III: the downstream region is designed and optimised to conduct the exhaust gases efficiently.

For a large vertical reactor there are two possible methods to introduce the gases into the retort: the top-down direction and the bottom-up direction.

When gases are introduced into the retort, they are heated immediately and consequently experience the volumetric expansion correspondingly. The density variations of the gases result in a natural convection of gases within the retort, which is very common in our daily lives, such as the rising smoke from a cigarette or from a chimney. Natural convection (or free convection) is very undesirable in a CVD reactor because it is a kind of uncontrolled gas flow.

Natural convection always takes place in the upward direction because of the effect of the the force of gravity. If the reactant gases are introduced at the top of the retort ,the opposite direction between forced reactant gas flow and natural convection will result in a complicated flow pattern and recirculation as shown in Figure 3.13a.

If the precursor gases are introduced into the chamber in a bottom-to-top direction, the buoyancy and inlet flow have the same direction, which results in a stable density gradient, thereby reducing or eliminating the natural convection [39]. This is confirmed by the simulated results as shown in Figure 3.13b, where the left-hand side shows the temperature profile and the right-hand side is the velocity profile. It is clear that the recirculation is completely eliminated in front of the substrate when the gases are introduced at the bottom of the reactor and extracted at the top through the nozzle.

According to the ratio of $Gr/(Re)^2$ the gas flow pattern is divided into three kinds [41, 42]: (a) both free convection and forced convection must be considered when $0.3 < Gr/(Re)^2 < 16$; (b) the forced convection flow is dominant if $0 < Gr/(Re)^2 < 0.3$ and; (c) the forced convection flow could be ignored if $Gr/(Re)^2 > 16$. For the CVD processes the pressure within the reaction chamber has considerable effect on the flow pattern. The main reason for this is that the viscosity of the gas is independent of the pressure; however, the density is proportional to the pressure and velocity is proportional to the reciprocal pressure according to the state equation of the perfect gas. Thus, recirculations driven by natural convection will disappear with decreasing pressure.

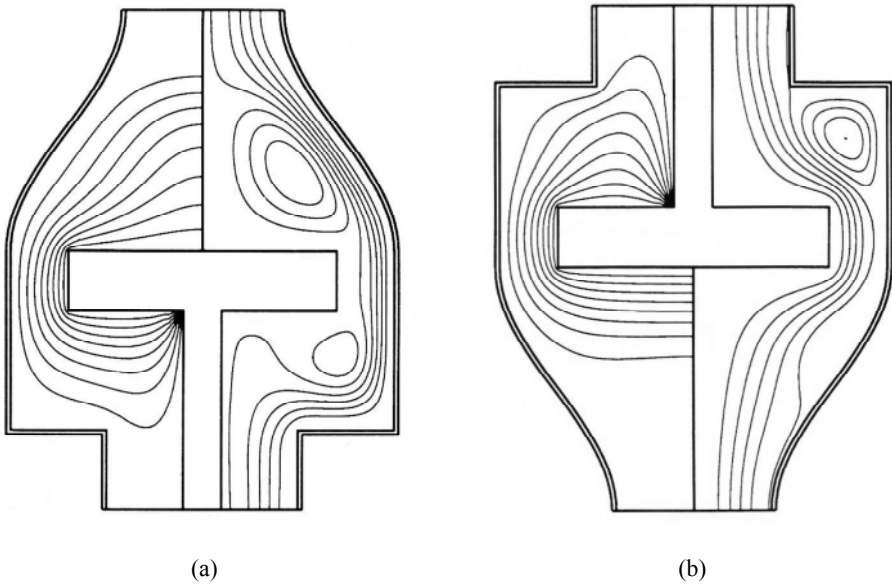


Figure 3.13. Comparison between two kinds of gas introduction directions [40]: (a) top-down direction and (b) bottom-up direction

3.4.2 Gas Inlet Injectors

In many cases the reactant gases can be injected into the retort with one single injector. However, the gas inlet injector should be specially designed for some strong active precursor systems such as $\text{SiCl}_4\text{-NH}_3$, $\text{Ti}(\text{OC}_3\text{H}_7)_4\text{-H}_2\text{O}$ system, $\text{SiH}_4\text{-O}_2$ system, etc. For example, SiCl_4 is easy to react with NH_3 to form undesirable solid diimide at room temperature. As shown in Figure 3.14a, NH_3 and $\text{SiCl}_4\text{-H}_2$ have to be separately introduced into the reaction chamber. When SiO_2 is prepared with an atmospheric CVD process, in order to overcome the heterogeneous deposition from the $\text{SiH}_4\text{-O}_2$ reaction system, a segmented showerhead is designed to keep the reactant gases separated until they reach the substrates to be coated. Figure 3.14b illustrates the details of such a design solution. The inert gas is used as a curtain between the SiH_4 gas and O_2 gas.

3.4.3 Gas Distributors

For large CVD reaction chambers the diameter of the injector is much smaller than that of the retort. For example, the diameter of the injector is 20 mm; however, the diameter of the retort can range from 500 to 2500 mm. Figure 3.15 indicates through the flow vectors that a sudden enlargement results in the eddy current or recirculation around two corners at the enlarging interface, which causes local uneven flow patterns and the energy loss of gas flow. This kind of energy loss is

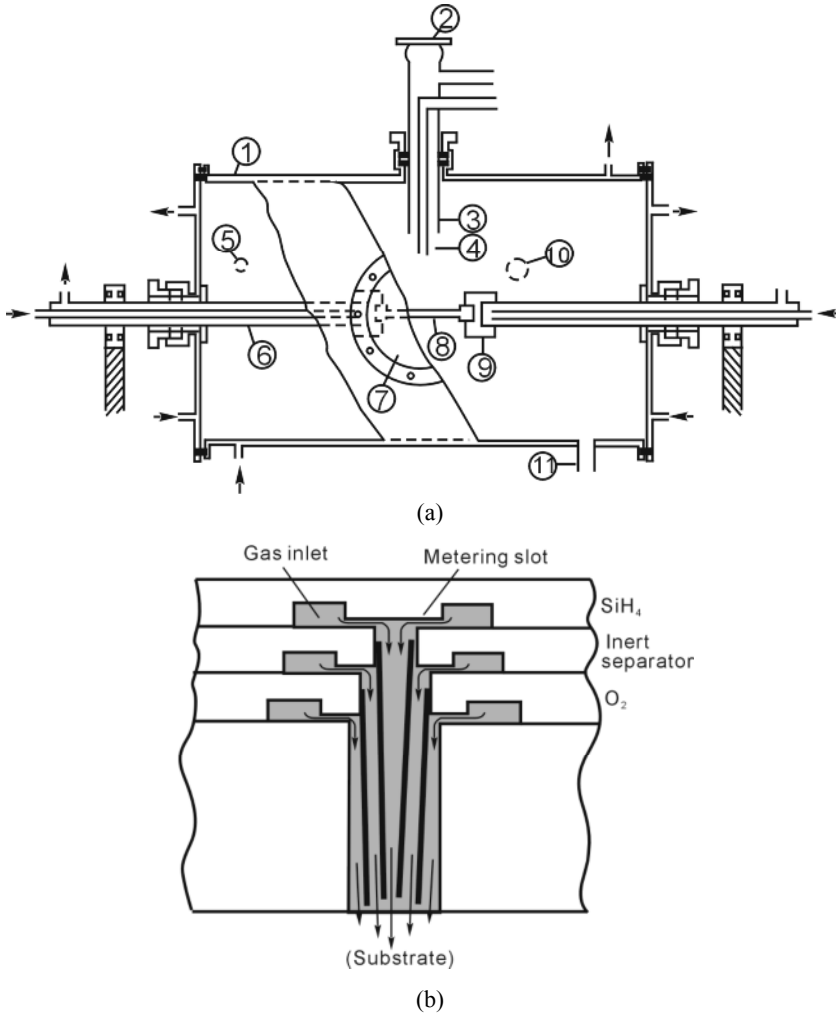


Figure 3.14. Gas injector design: (a) $\text{SiCl}_4\text{-NH}_3$ for Si_3N_4 deposition [43] and (b) $\text{SiH}_4\text{-O}_2$ for SiO_2 deposition [44]

quantitatively expressed in terms of a loss coefficient, which is discussed in the details of the fluid mechanics [45, 46].

The above gas flow pattern is not desirable for a CVD process, and the sudden expansion design shown in Figure 3.15 is the gas flow simulation result of a typical early reactor chamber design. It is clear from the simulation that there is a sudden expansion of gas flow and this causes turbulent flow, which in turn results in uneven deposition.

To avoid such types of undesirable gas flows, it is necessary to adjust and control the pressure distribution within the reactor chamber or, more precisely, before the gas flows reach the substrates located in the chamber.

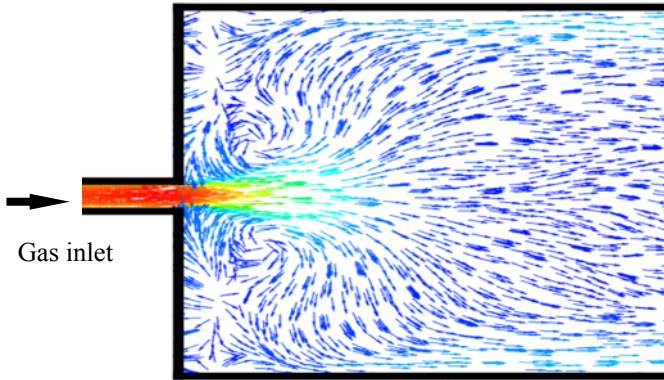


Figure 3.15. Sudden enlargement of pipe

There are two methods and devices which are commonly used in engineering to generate a uniform flow pattern. A diffuser is actually a conical tube with a suitable conical angle to allow gradual expansion of gases and gradual velocity change. A diffuser should have a conical angle of about 8° as shown in Figure 3.16a. This small conical angle implies that the diffuser should have a long structure. Obviously, this is not acceptable from an engineering point of view since it will result in a long CVD reaction chamber and inefficient use of space.

A gas distributor, shown in Figure 3.16b, on the other hand, is a plate placed at a suitable distance from the inlet port and has many small holes through which the gases are evenly distributed in the deposition zone for the CVD process. When the precursor gases flow into the distribution zone initially at a suitable pressure, the gases flow radially due to a lower pressure at the circumference of the distribution zone and the resistance from the distribution plate. This gradually develops the distribution zone. If the sizes and the number of the holes on the distributor are suitable, then an ideal gas distribution can be achieved, as shown in Figure 3.17a. The design of these holes, their numbers and the arrangement of hole patterns therefore become an important and tricky task in CVD system design. It is desirable to design the distributor in such a way that it can evenly distribute the

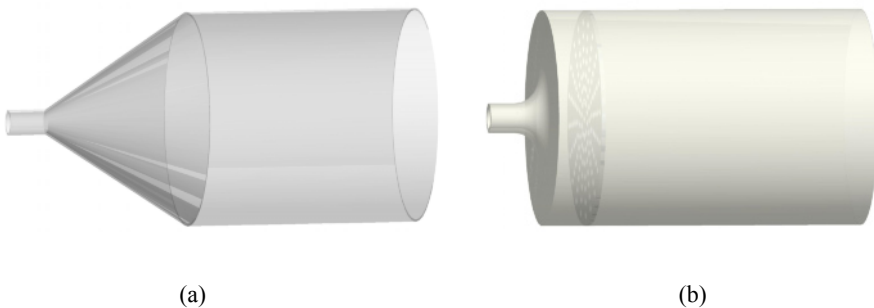


Figure 3.16. Design of gas entrance region for gas distribution: (a) conical diffuser and (b) streamline injector and a distributor

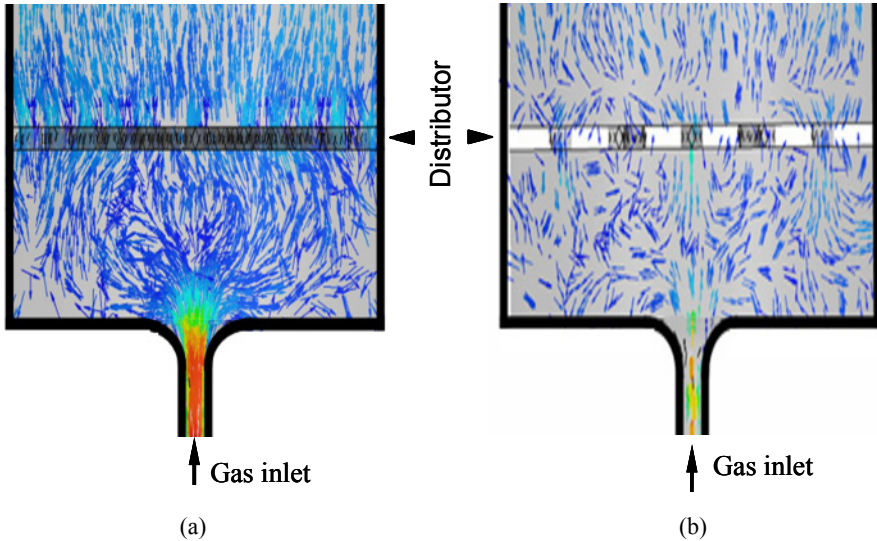


Figure 3.17. Schematic of gas distributor on gas flow pattern: (a) distributor with suitable resistance and (b) distributor with too large resistance

gases whilst at the same time exhibiting minimal resistance to allow gases to pass through. Nevertheless, if the resistance becomes too small, then gases will pass through the holes without flow radially to a sufficient level; hence the gas distribution around the outer circumference area is normally poor. As the resistance increases and becomes too large, the gases pass through the holes of the distributor at a much high velocity. This causes an uneven velocity distribution, as shown in Figure 3.17b.

On the other hand, the distance between the distributor and the gas inlet port is also an important factor in CVD system design. If the distance is too small, it does not have sufficient space for the radial flow of the gases. Hence, the resulting gases pass through some central holes at a higher pressure than that of gases passing through the outer holes of the distributor plate. If the distance is too large, the efficiency will obviously decrease.

3.4.4 Exits

The situation of a gas passing through a sudden contraction is quite different from that of a sudden enlargement. The streamlines entering the contraction continue to converge until reaching a minimum cross-sectional area. This phenomenon is called a *vena contracta* effect, which is attributed to the inability of the fluid to turn the sharp 90° corner illustrated in Figure 3.18.

Based on fluid mechanics, the different types of exits have different loss coefficients and streamline plots as shown in Figure 3.19. The re-entrant exit exhibits the greatest loss coefficient close to 1, while the well-rounded exit

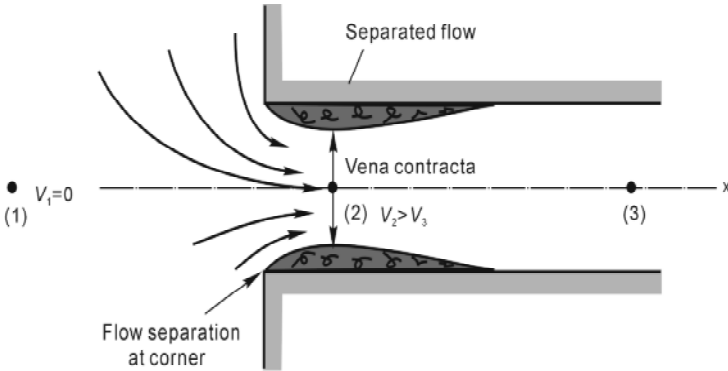


Figure 3.18. vena contracta effect of fluid flow through a sharp-edge exit [46]

presents a minimal loss coefficient of 0.04. Both the orifice and sharp-edge exits have the same loss coefficient of 0.61.

The head loss coefficient (K_{exit}) for the exit is expressed by [45]

$$K_{exit} = \frac{1}{C_v^2} - 1 \tag{3.3}$$

where C_v is the velocity coefficient.

For the rounded exit, further investigations reveal that the loss coefficient has a close relationship with the radius of the exit. The loss coefficient is significantly decreased to less than 0.2 when the exit edge is only slightly rounded, corresponding to a ratio of $r/D = 0.05$, as shown in Figure 3.20.

To determine the discharge of the flow, the discharge coefficient (C_d) is defined as the ratio of the actual volume discharged from the orifice in a given time to the theoretical discharge. Similarly, the coefficient of contraction (C_c) is the ratio of the actual area of the jet at the *vena contracta* to the area of orifice. The relationship between the coefficients is as follows:

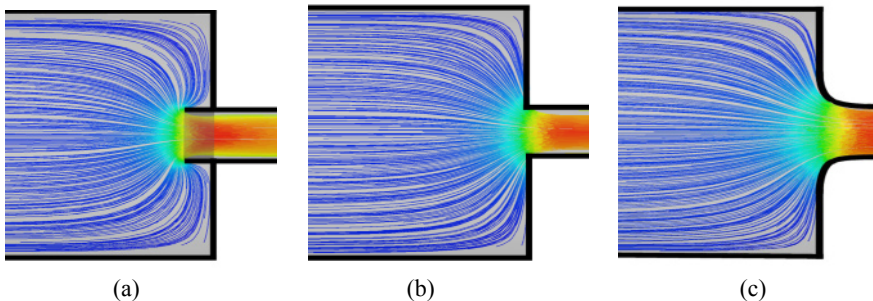


Figure 3.19. Flow patterns for different exits: (a) re-entrant exit, (b) sharp edge exit and (c) rounded exit

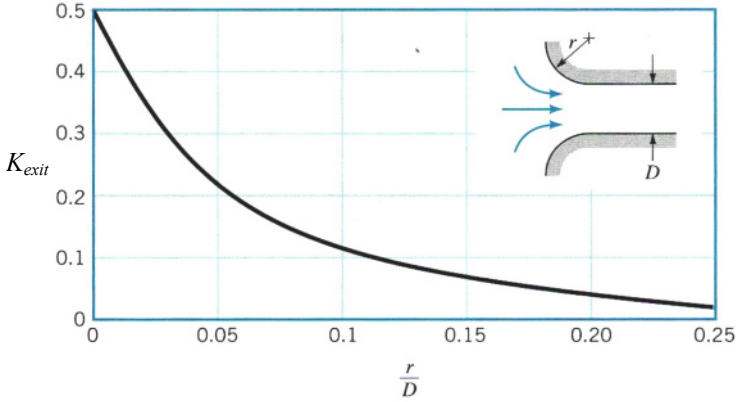


Figure 3.20. Relation between loss coefficient and rounding of edge [46]

$$C_d = C_C \times C_v \tag{3.4}$$

where C_v is the coefficient of velocity.

Table 3.3 lists the values of the coefficient of loss, coefficient of contraction, coefficient of velocity and coefficient of discharge for various exits. It can be seen that a well-rounded exit is characterised by the smallest coefficient of loss as a result of minimal resistance and the highest velocity and mass flow rates. This puts it as the most qualified exit design for CVD systems. Contracted exits have small cross-section area, small resistance and high velocity coefficient. Therefore, they are most suitable for applications where there is no need to produce very high velocity of a fluid. They can be found in many jet car washing systems. Expanded exits have a high degree of vacuum and high volume flow rate and they are more

Table 3.3. Values of the different kinds of coefficients and exits [47]

Exit type	Orifice	Sharped edged	Re-entrant	Contracted ($\theta=13-14^\circ$)	Expanded ($\theta=5-7^\circ$)	Well rounded
Exit shape						
Coefficient of loss	0.06	0.5	1	0.09	4	0.04
Coefficient of Contraction	0.64	1	1	0.98	1	1
Coefficient of velocity	0.97	0.82	0.71	0.96	0.45	0.98
Coefficient of discharge	0.62	0.82	0.71	0.95	0.45	0.98

suitable for applications with a high flow rate and slower flow velocity. They can be found in water pumps for power stations. Though the velocity coefficient is only 0.45 for the expanded exits, the exit cross-section is about two to three times bigger than that at the initial exit, hence a high flow rate.

3.5 Heating Systems

There are several suitable energy sources to heat CVD reaction chambers which mainly include:

- resistance heating with large electricity current but low voltage;
- radiant heating with high-intensity radiation lamps, such as halide lamp;
- electric induction heating; and
- laser heating.

Electrical resistance heating is widely used in various reaction chambers from small size to large. Graphite is most frequently used as a heating material because of its low cost, good machining ability and excellent corrosive resistance to CVD processing gases at high temperatures. Compared with electrical resistance heating, induction heating exhibits higher equipment investment cost but relatively lower maintenance and running costs. Usually, the induction frequencies range from 10 to 450 kHz. Graphite is also commonly used as the induction susceptor for heating elements. In special cases the surface of the graphite should be coated with a layer of SiC to prevent undesirable carbon species resulting from graphite sublimation at elevated temperatures. Table 3.4 lists the properties of the typical heating element materials.

The temperature is measured using either a pyrometer or thermocouples. A pyrometer is usually used to measure the processing temperature for cold-wall reactors where the hot areas are visible through a transparent window (e.g. fused silica glass and Al₂O₃ ceramic). Thermocouples are used in hot-wall reactors and are placed between the retort and heating element at various places along the retort. The temperature sensors are connected to the regulator, which maintains the CVD

Table 3.4. Properties of some heating element materials [48, 49]

Material	Density (g·cm ⁻³)	Resistivity at 20°C (Ω·mm ² ·m ⁻¹)	Coefficient of thermal resistivity (°C)	Melting temperature (°C)	Max service temperature (°C)	Service Environment
Cr15Ni60	8.15	1.10	14×10 ⁻⁵	1390	1000	Oxidising
Cr20Ni80	8.4	1.11	8.5×10 ⁻⁵	1400	1100	Oxidising
Cr25Al5	7.19	1.42	5×10 ⁻⁵		1300	Oxidising
Pt	21.46	0.10	4×10 ⁻³	1770	1400	Oxidising
Mo	10.3	0.045	5.5×10 ⁻³	2630	1650	Reducing
Ta	16.62	0.15	4.1×10 ⁻³	2996	2500	Reducing
W	19.34	0.045	5.5×10 ⁻³	3410	2500	Reducing
SiC	3.1	1000~2000		2227	1450	Oxidising
MoSi ₂	5.3	0.25~0.32	4.8×10 ⁻³	2030	1680	Oxidising

processing temperature as prescribed.

Temperature uniformity within the reactor is one of the key parameters to be precisely controlled for CVD processes. For thin film deposition on the surface of silicon wafers, multizone (up to five zones) resistively heated furnaces are designed to enable a uniform temperature field for the deposition of the thin film, as shown in Figure 3.21. Several kinds of thermocouples (Types B, K, R and S) are available for CVD systems to measure temperatures. The features of these thermocouples are listed in Table 3.5. Because the CVD processing atmosphere

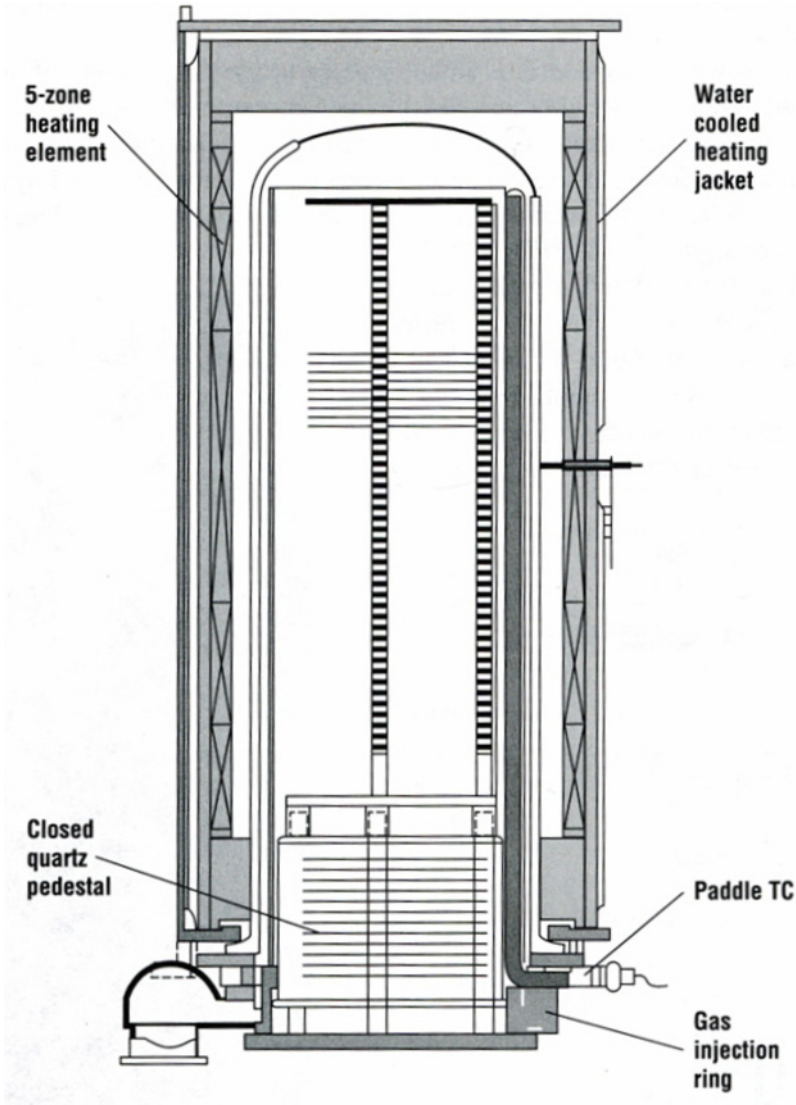


Figure 3.21. Schematic of a CVD reactor with 5-zone heating element [44]

Table 3.5. Characteristics of several types of thermocouples [50]

ISA Type	Positive Wire	Negative Wire	Service atmosphere	Temperature range (°C)	Tolerance
B	Pt70-Rh30	Pt94-Rh6	Inert or Slow oxidizing	200–1700	600–1700°C, ±0.0025T
K	Chromel Ni90Cr10	Alumel Ni95Mn2Al2Si	oxidizing	0–1100	0–333°C, ±2.5°C 333–1100°C, ±0.0075T
R	Pt87-Rh13	Platinum	oxidizing	0–1400	0–600°C, ±1.5°C 600–1400°C, ±0.0025T
S	Pt90-Rh10	Platinum	oxidizing	0–1400	0–600°C, ±1.5°C 600–1400°C, ±0.0025T

(e.g. H₂) is reductive, the thermocouples must be protected with a special sheath of refractory materials (such as the alumina ceramics, molybdenum, etc.).

3.6 Pumping Systems

A vacuum system is the assembly of the components which are used to generate, measure and maintain a level of vacuum required for CVD processes. This vacuum system typically includes chamber, pumps, valves, gauges and pipes connected together.

For pumping system design it is important to minimise the loss coefficient of the gas flow caused by the bends and valves, thereby decreasing the residence time of the reactant gases within the reaction chamber and eliminating the undesirable deposition [51]. Because of the large gas output involved in a CVD process, a combination of a rotary pump with a Roots pump is normally used to meet the gas flow requirement. For ultra-high CVD operation, turbomolecular pumps are used. As discussed in Chapter 2, the compression ratio of rotary pumps is very high (10^7), which results in high exhaust pressure at the early pumping stage. The pump oil may be pumped out of the oil reservoir and may be formed into liquid droplets or even sprayed into the smoke which will severely pollute the environment. An effective solution to address this problem is to design parallel pipelines. The slow pumping line is installed with a small butterfly valve and the high pumping line is controlled by a large butterfly valve, as illustrated in Figure 3.3. The slow pumping line has small conductance and is normally used to work at the first pumping stage. The hi-pumping line works at the next pumping stage and for the whole CVD process.

Bends in the pipes may produce significantly greater head loss than the straight pipes. This type of loss results from the boundary separation and the swirling secondary flow. The boundary separation happens near the inside of the bend. The swirling secondary flow occurs due to the imbalance of centripetal forces as a result of the curvature of the pipe centreline, and this results in energy losses. The loss coefficient (K_L) is mainly dependent on the ratio of R/D as shown in Figure

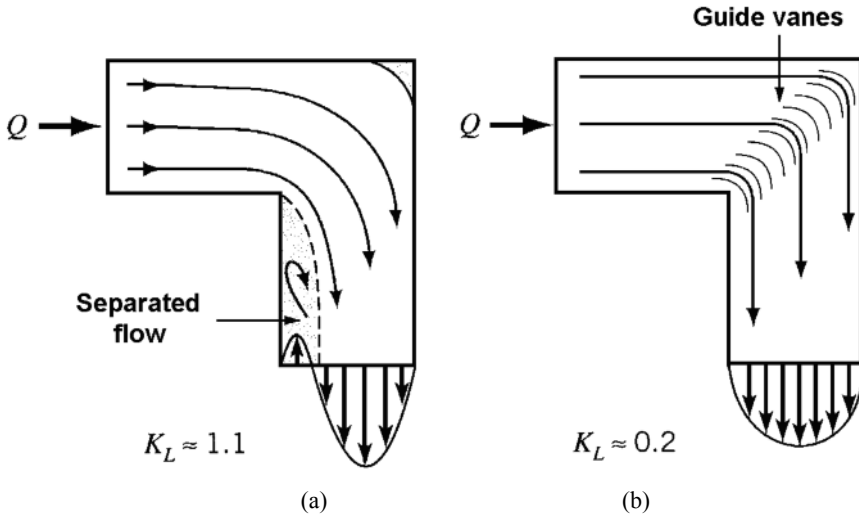


Figure 3.22. The bend design [46]: (a) without guide vanes and (b) with guide vanes

3.22. Increasing the radius of the pipe centreline is very helpful for decreasing the loss coefficient.

Some applications may disallow this increase as the space is constrained. In this circumstance a flow direction change is often accomplished by use of sharp bends rather than well-rounded bends, as shown in Figure 3.23a. The losses in such

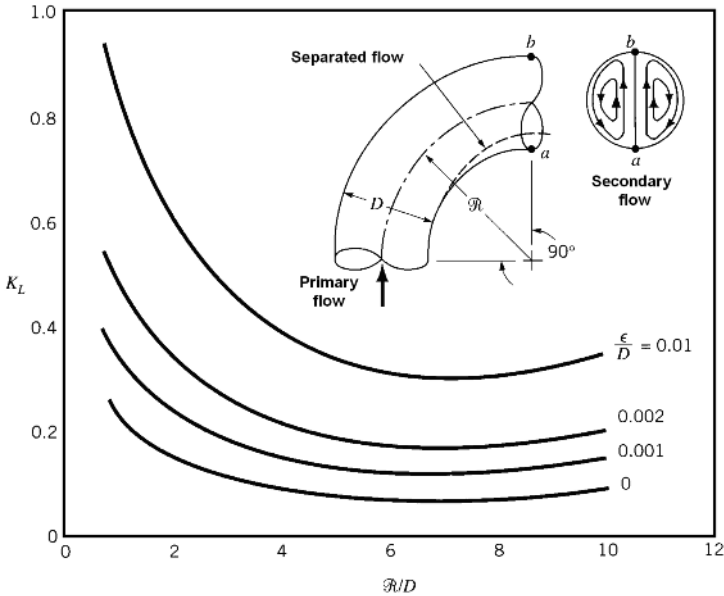


Figure 3.23. Loss coefficient of flow in a 90° bend [46]

bends however can be decreased from 1.1 to 0.2 by using suitably designed guide vanes installed within the bend, as shown in Figure 3.23b, which help to direct the flow with less unwanted swirl and disturbances.

Similar to the energy loss of flow gas in case of sudden changes as discussed in Section 3.4.4, various types of valves and fittings in the CVD vacuum pipelines also produce a head loss, a so-called minor loss. As listed in Table 3.6, the head loss (h_f) associated with these parts and fittings can be expressed in terms of the head loss coefficient (K)

$$h_f = K \frac{u^2}{2g} \tag{3.5}$$

where K is the head loss coefficient, u is flow velocity and g is gravity acceleration. For various components, the associated head loss coefficients are listed in Table 3.6.

Table 3.6. Head loss coefficients for pipe components [46]

Component	K	
a. Elbows		
Regular 90°, flanged	0.3	
Regular 90°, threaded	1.5	
Long radius 90°, flanged	0.2	
Long radius 90°, threaded	0.7	
Long radius 45°, flanged	0.2	
Regular 45°, threaded	0.4	
b. 180° return bends		
180° return bend, flanged	0.2	
180° return bend, threaded	1.5	
c. Tees		
Line flow, flanged	0.2	
Line flow, threaded	0.9	
Branch flow, flanged	1.0	
Branch flow, threaded	2.0	
d. Union, threaded	0.08	
e. Valves		
Globe, full open	10	
Angle, fully open	2	
Gate, fully open	0.15	
Gate, 1/4 closed	0.26	
Gate, 1/2 closed	2.1	
Gate, 3/4 closed	17	
Swing check, forward flow	2	
Swing check, backward flow	∞	
Ball valve, fully closed	0.05	
Ball valve, 1/3 closed	5.5	
Ball valve, 2/3 closed	210	

3.7 Exhaust Gas Handling Systems

For a typical CVD process, the conversion efficiency of the precursor is usually less than 10 per cent. Therefore, unreacted chemical substances, by-products and intermediates flow into the exhaust lines. All these effluents have to be safely treated before they can be released into the atmosphere [52]. Careful design and construction of exhaust systems is essential. The exhaust handling subsystem is arranged in a sequence as shown in Figure 3.2, which includes [7, 53]:

- a cold trap to condense the unreacted precursors and reaction intermediates,
- a chemical trap to neutralise the chemicals containing acid such as HCl gas,
- a particle trap to collect solid particles originating in the reactor,
- a wet scrubber to collect the untrapped gaseous products to prevent them from entering the atmosphere and
- a vent to provide fresh air and prevent the toxic and explosive gases from accumulating.

In addition, alarms and safety devices (such as extinguisher) must also be provided in this category.

3.7.1 Cold Traps

Cold traps are cryogenic devices which are used primarily to condense and collect volatile gases. Meanwhile, they can significantly cool the hot exhaust gases from the reaction chamber prior to being released into the vacuum pump. The hot exhaust can increase the pump oil temperature and decrease the viscosity of the oil, thereby reducing the pumping efficiency.

The design of cold traps should meet the following requirements:

1. The trap should generate sufficiently low temperature to condense vapour species from the reaction chamber.
2. There should be no warm surface path connected to the cold area. The trap should maintain a low coolant consumption rate and adequate reservoir capacity.
3. The trap should have minimum impedance to gas flow.
4. The trap should not be sensitive to coolant height level.
5. Operators should have easy access to the trap interior for cleaning.

As shown in Figure 3.24, three kinds of gas trapping mechanisms are recognised as cryocondensation, cryosorption and cryotrapping. For cryocondensation, the gas molecules are bound with the same species which are pre-covered on the cold surface. The condensation energy is equal to the evaporation energy. Cryosorption is a process whereby gas molecules are physically adsorbed and bond at the activated sites of a clear and clean substrate. The binding energy equals the adsorption heat. If the gas is not easily condensable, cryotrapping takes place and the reactant gas molecules are trapped in the

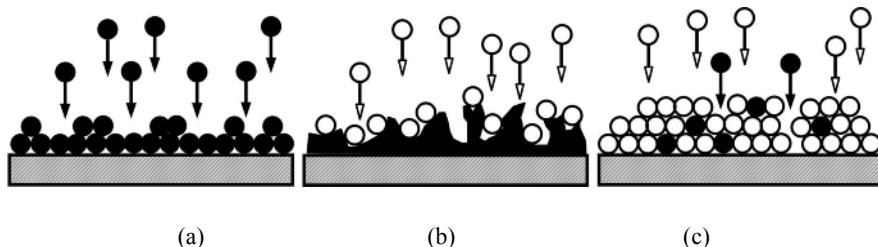


Figure 3.24. Schematic of three kinds of gas trapping mechanisms [54]: (a) cryocondensation, (b) cryosorption and (c) cryotrapping

continuously growing condensate formed by easily condensable gaseous molecules.

A typical cold trap with two chambers is illustrated in Figure 3.25. The coolant (such as liquid nitrogen) is loaded in the interior chamber. The exhaust gases are forced to flow through the exterior chamber. In order to improve the trapping efficiency, a group of metal guidance plates are designed and welded on the outer surface of the interior chamber in a spiral form to increase the gas contact area and gas flow path. The deflector is arranged in spiral shape to reduce the impedance of the gas flow. Furthermore, a metal with high thermal conductivity, such as copper, is used as guide plate materials.

The common coolants are listed in Table 3.7. Solid carbon dioxide (dry ice) is

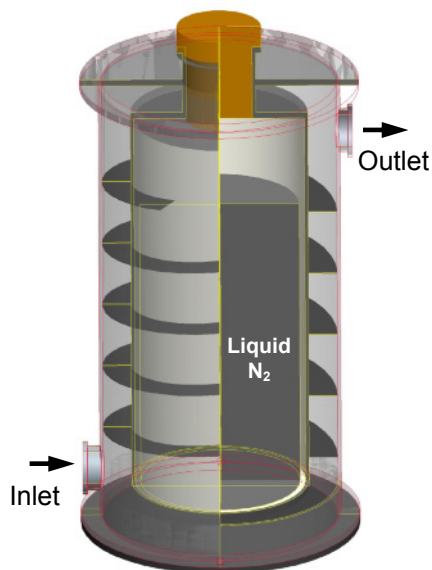


Figure 3.25. Schematic of liquid N₂ trap

Table 3.7. Minimum temperature S of some coolants

Compositions	Temperature (°C)
KCl (19.75%): Ice (80.25%)	-11
Ethylene glycol (50%): De-ionized H ₂ O (50%)	-12
NaCl (23.4%): Ice (77.6%)	-21
NaCl (23.0%):Na ₂ SO ₄ ·10H ₂ O (0.2%): Ice (76.8%)	-21
NaCl (21.8%):NaNO ₃ (20.5%): Ice (57.7%)	-26
Glycerine (70%): Water (30%)	-39
CaCl ₂ ·6H ₂ O (58.8%): Ice (41.2%)	-55
ZnCl ₂ (51.0%): Ice (49.0%)	-62
Chloroform: Dry ice	-64
Liquid SO ₂	-76
Aceton: Dry ice	-77
Methanol: Dry ice	-78
Methyl bromide: Dry ice	-78
Solid carbon dioxide (dry ice)	-78
Liquid air	-183
Liquid nitrogen	-196

cheap and usually crushed into small pieces or made into sludge with some other substances (acetone and methanol etc.). This kind of coolant can reach a minimum temperature of -78°C and often is used for small glass traps in the laboratory. Liquid air and liquid nitrogen are both excellent for cold traps. If liquid air is used, however, necessary measures must be taken to avoid violent explosion because liquid oxygen inside can vaporise and explode. Liquid nitrogen is a perfect coolant and is widely used in both laboratory and industry. It should be noted that some coolants are hazardous. For example, liquid SO₂ and methyl bromide-dry ice are extremely toxic to the lungs and skin. Special precautions should be taken to protect the operator's eyes and skin when handling these coolants.

3.7.2 Chemical Traps

A chemical trap provides protection against various corrosive gases which attack the pump and pump oil as well as pollute the environment. These traps operate on the principle of chemical reactions between the exhaust gases and the chemical trapping reagents. The usual trapping materials are a mixture of activated charcoal and chemicals. Hydrogen chlorides in product gas can be neutralised by sodium or

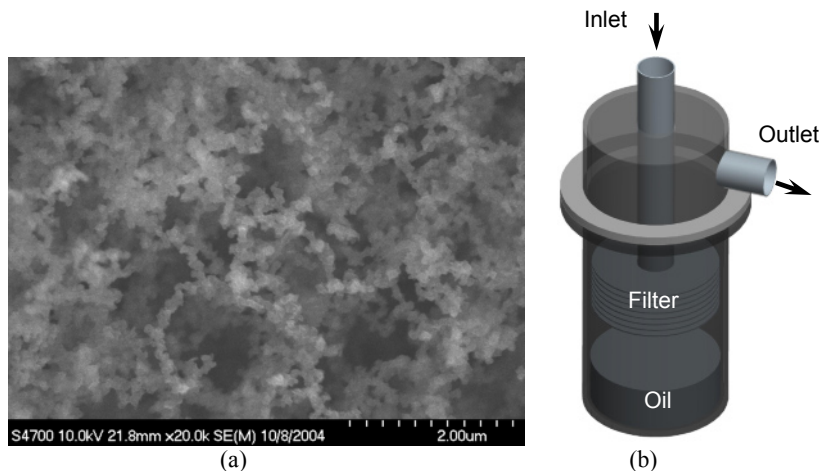


Figure 3.26. Particle trap with oil and metal filter: (a) pyrocarbon soot from $\text{CH}_4\text{-N}_2$ deposition system and (b) a particle trap

calcium hydroxide. Hydrogen fluorides are usually trapped by passing through granules of sodium carbonate [14].

3.7.3 Particle Traps

Particle traps are required because the particles generated from CVD processes might be introduced into the vacuum pump to cause pump wear. Figure 3.26a shows the carbon soot formed from the pyrolysis of CH_4 gas during a CVD process. A schematic of a particle trap is shown in Figure 3.26 b. Because the oil is located at the bottom of the chamber and the exhaust gas has to flow over the surface of the oil, most of the particles can be trapped and absorbed by the oil. If some of the particles still manage to escape from this trapping mechanism, the porous filters as the second tier filtering mechanism stop them going further. It should be noted that the impedance of the filter reduces the pumping speed by approximately 10% at a pressure of 1 mbar and 25% at a pressure of 10^{-2} mbar [55].

3.7.4 Exhaust Gas Scrubbers

A schematic diagram of a wet scrubber is shown in Figure 3.27. The exhaust gases are collected and then forced to flow through the NaOH solution with the aid from an air pump. During the bubbling process through the liquid most of the acid gaseous species in the exhaust are immediately dissolved in water and neutralised by NaOH. The escaped exhaust gases flow upwards within the tank and then react with the liquid droplets sprayed from the nozzles. In order to further improve the removal efficiency of acid gaseous species, a second array of spraying nozzles are designed at the upper position. The filter is used to increase the residence time of exhaust gases in the scrubber and to ensure the complete neutralisation reactions within the tank. Finally, the cleaned gases (mainly containing carrier gas and

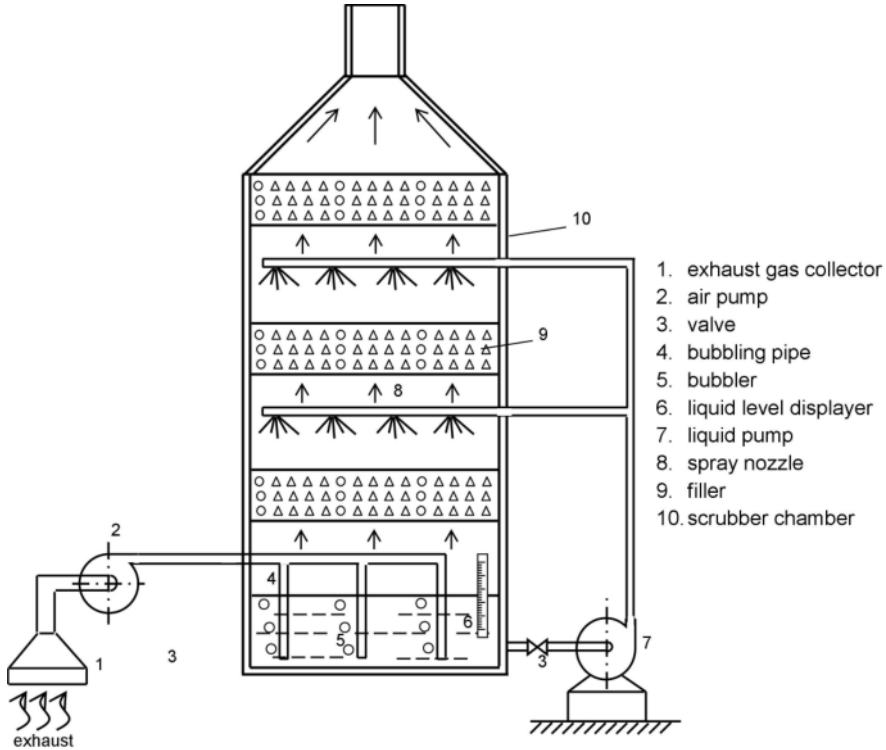


Figure 3.27. Schematic of a wet scrubber

diluent gas) are released into the atmosphere before the water vapour is separated with the water. In this kind of system the removal efficiency can reach 95% if the concentration of NaOH is 2 to 6% in the water.

3.7.5 Venting

More or less leakage of gases is inevitable during a CVD process. A good venting system is necessary to avoid the accumulation of these gases under any circumstances. For example, hydrogen leads to the flame propagating downwards when its concentration reaches 2 to 3% in the air. If the concentration of hydrogen is up to 4%, then the flame would propagate both upwards and downwards. Some of the inherent properties of the common precursors are listed in Table 3.8.

3.8 Some Special CVD Processes

In previous sections we introduced the basic elements for a conventional CVD system; this section introduces some special CVD processes and their equipments.

Table 3.8. Flash point, self-ignition point, ignitability limit and explosion limits in air of some precursors [56]

	Flash point (°C)	Self-ignition point (°C)	Ignitability volume limit (%)		Ignitability temperature limit (°C)		Explosion limit in air (%)	
			lower	upper	lower	upper	lower	upper
HSiCl ₃	<-50.0	175.0	1.2	90.5	-56.0	28.0	6.9	>70.0
CH ₃ SiHCl ₂	<-70.0	175.0	0.2	91.0	<-70.0	37.0	4.5	>70.0
(CH ₃) ₃ SiCl	-28.0	395.0	-	-	-28.0	30.0	3.6	6.4
CH ₃ SiCl ₃	6.0	408.0	8.0	99.0	3.0	64.0	7.2	11.9
(CH ₃) ₂ SiCl ₂	-28.0	380.0	0.8	39.3	-41.0	42.0	5.5	10.4
C ₂ H ₅ SiHCl ₂	<-70.0	220.0	0.2	58.0	<-70.0	57.0	-	-
C ₂ H ₅ SiCl ₃	14.0	-	-	-	-	-	-	-
(C ₂ H ₅) ₂ SiCl ₂	-6.0	295.0	0.2	77.5	-18.0	122.0	-	-
C ₆ H ₅ SiHCl ₂	4.0	390.0	-	-	1.0	169.0	-	-
C ₆ H ₅ SiCl ₃	49.0	508.0	0.3	77.5	49.0	170.0	-	-
(C ₆ H ₅) ₂ SiCl ₂	-	400.0	-	-	-	-	-	-
CH ₃ C ₆ H ₅ SiCl ₂	38.0	490.0	0.2	5.7	20.0	111.0	-	-
CH ₃ (C ₆ H ₅) ₂ SiCl	72.0	480.0	-	-	72.0	200.0	-	-
CH ₃ (CH ₂ CH)SiCl ₂	-12.0	300.0	0.7	87.0	-35.0	87.0	-	-

By illustrating these special approaches it is aimed to deepen the understanding of CVD processes and their potential applications in other areas.

3.8.1 Laser-induced CVD Process

Nanopowders have been of particular interest in recent years as they can be used to make high-performance products due to their superior properties. Manufacturing of these powders is therefore important. Such a system using a laser-induced cold-wall CVD reactor is shown in Figure 3.28. It mainly consists of five parts: a reactor with two reaction zones, an oven for vaporising hexamethyl disilylamine (HMDS-

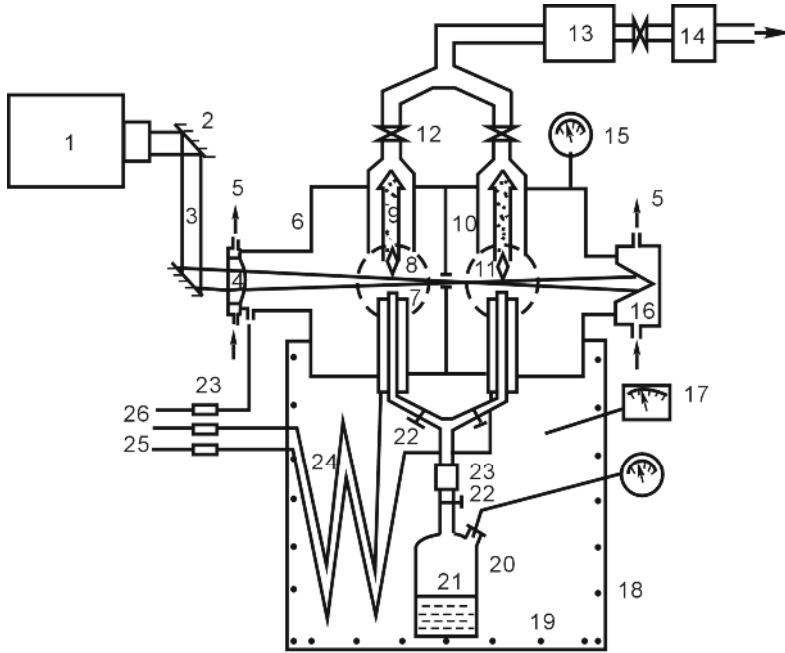


Figure 3.28. Schematic of laser-induced cold-wall CVD reactor [57] (1: CO₂ laser, 2: reflector, 3: laser beam, 4: GaAs lens, 5: cooling water, 6: reactor, 7: nozzle, 8: reaction flame, 9: particle plume, 10: board, 11: window, 12: throttling valve, 13: powder collector, 14: pump, 15: pressure gauge, 16: water-cooled Cu block, 17: temperature controller, 18: oven, 19: heater, 20: precursor vessel, 21: liquid HMDS, 22: needle valve, 23: flow meter, 24: preheating tube, 25: co-axial protection gas, 26: lens protective gas)

Si₂NH(CH₃)₆ precursor, a filter holder for powder collection, a rotary vacuum pump and a continuous-wave CO₂ laser.

The reactor has two reaction zones and is made of a stainless steel vessel with five access ports: two vertical access ports which are used for the introduction of reactant gases and the collection of powders, one horizontal access port which is composed of GaAs lens and water-cooled copper block, items 4 and 16 of Figure 3.28, allowing passage of the laser beam, and the remaining two accesses with quartz glass windows to monitor the reaction zones. A stainless steel plate with a suitable hole is placed between two reaction zones to minimise their interaction.

The GaAs lens is used to focus the CO₂ laser beam. Argon gas is used to protect the GaAs lens by sweeping or flowing over it. For the present design system, the laser powder in the left reaction zone is slightly greater than that in the right one. This is attributed to the fact that some of the laser energy is adsorbed by the reactant gaseous precursors in the left zone. During the CVD process the pressure within the reactor is 6.1×10^4 Pa.

For this system the oven is installed below the reactor. Liquid hexamethyl disilyamine (HMDS, Si₂NHMe₂), with a boiling point of 125°C, is contained in a

stainless steel vessel which is placed inside the oven. To ensure sufficient vaporisation of HMDS, the temperature is controlled in the range of 125 to 130°C. The vapour gases can be divided into two branches and introduced into two reactors. The outlets of the nozzles are arranged such that vapour exits a few millimetres below the laser beam. Once the reactant gases are contacted with the laser beam, the CVD process is immediately induced. The reactant gas stream is surrounded by a co-axial argon stream outside, which is used as curtain to minimise the reactant gases spreading out; hence the powders formed in the CVD process are constrained within a specific region. The argon gas must be sufficiently heated to prevent the condensation of HMDS. It is important to control the velocity of the reactant stream and that of the coaxial argon stream to be approximately same so that there is a smooth and non-turbulent interface between them.

The reactant gaseous streams are irradiated by a continuous-wave CO₂ laser beam. The laser power is usually between 600 and 1500 W, and the laser beam in the left reaction zone is typically 10 to 11 mm in diameter, while the right one is 9 to 10 mm in diameter. The chemical reaction of the HMDS precursor results in a bright yellow flame. The powders are conducted into a filter holder for collection driven by the vacuum pump.

The powders produced from the above method are very fine. TEM observation in Figure 3.29 shows that the typical powder is composed of equiaxed particles and has a size in the range of 50 to 80 nm. Experimental results reveal that the chemical composition of the powders depends weakly on processing conditions. The main chemical compositions of the powders are 50% wt of Si, 28% wt of C, 16% wt of N, while there is a small amount of O and H, 4% wt and 2% wt respectively. Selected area electron diffraction (SAED) also reveals the existence of a partial crystalline phase in the amorphous structure, this being a unique material feature which cannot normally be obtained using other manufacturing techniques. This feature makes it possible for the powders to be used as good functional materials, such as radar wave absorption materials.

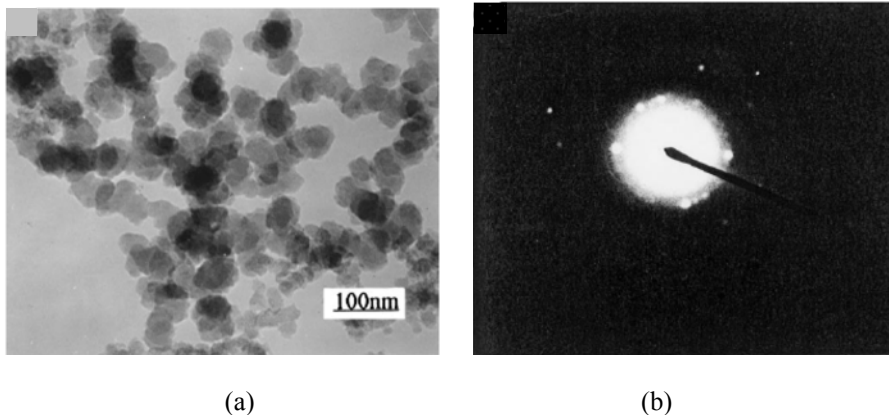


Figure 3.29. Microstructure of Si–C–N nanopowder [57]: (a) TEM photomicrograph (b) SAED pattern

3.8.2 Continuous Chemical Vapour Deposition Process

3.8.2.1 Cold-wall Continuous Chemical Vapour Deposition Process

Silicon carbide fibres produced using a CVD process, trade named SCS fibres, were developed by ACVO Specialty Products Division, now Specialty Materials Inc, USA. This kind of fibre has received considerable attention because of its superior properties, including a low density of $3.0 \text{ g}\cdot\text{cm}^{-3}$, high tensile strength of 3950 MPa, high tensile modulus of 400 GPa and high thermal stability. Among the SCS series fibres the SCS-6 fibre has been widely used in making metal-matrix and ceramic-matrix composites, especially the SCS-6 fibre reinforced titanium-alloy composites, which have been successfully used in high-performance aero-engines. The following paragraphs introduce the details of this process.

As shown in Figure 3.30, a cold-wall reactor is used for CVD process. A carbon filament with large diameter ($33 \mu\text{m}$) is used as a substrate and heated by passing an electric current through it. The CVD process takes place within a quartz glass tube. To keep good contact during the continuous movement of the filament, the electricity is supplied through the liquid metal (i.e. mercury) which is also used as a gas-tight seal of the glass tube reactor. The fabrication is divided into three stages. First, a thin pyrocarbon layer is deposited on the surface of the carbon filament with propane as precursor gas. Second, the coated filament is deposited by SiC with Si-containing precursor gas. Finally, the filament is coated with a carbon-rich layer to improve its strength and ensure the interfacial compatibility for the composites by changing the Si/C ratio in the reactant gases. In addition, this method is also used to manufacture boron filaments.

Figure 3.31 shows the SEM micrograph and the schematic drawing of this

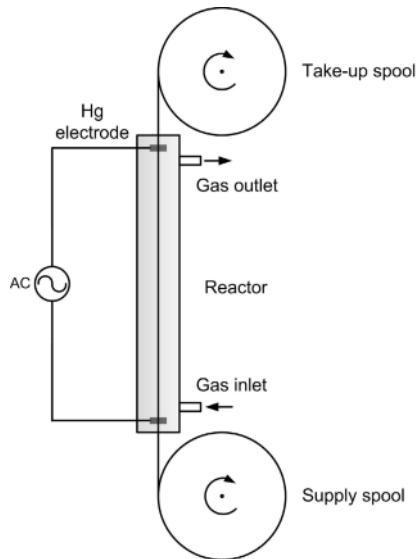


Figure 3.30. Schematic diagram of a process for SCS fibre by cold-wall CVD [58]

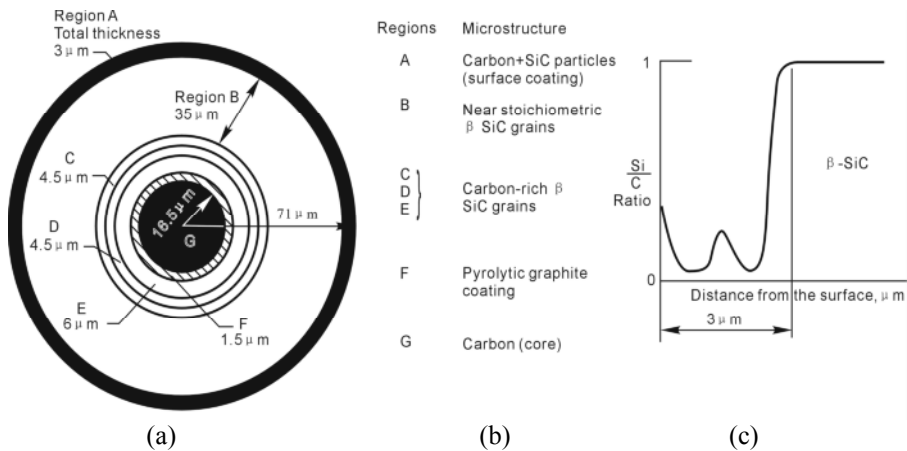


Figure 3.31. Cross-sectional SEM micrograph of SCS-6 fibre: (a) SEM micrograph of the cross-section [58], (b) schematic of the cross-section and (c) composition variation within outer layer [60]

filament microstructure. The inner pyrocarbon layer is 1.5 μm thick. Its function is to smooth the surface and ensure sufficient electrical conductivity of the carbon filament.

The thickness of the SiC layer is around 50 μm ; however, this layer can be further divided into four sublayers resulting from the variation of the depositing parameters [59]. These four sublayers are indicated as B, C, D and E in Figure 3.31a. Sublayer B is composed of near stoichiometric β -SiC grains; however, the other three regions (C, D and E) comprise carbon-rich β -SiC grains, as shown in Figure 3.31b. The SEM micrograph of the cross-section of the fibre is shown in Figure 3.31a. The outer layer is 3 μm thick, but its chemical composition distribution is very complex, as shown in Figure 3.31c.

Figure 3.32 illustrates another application example of fabricating carbon fibre yarns (1K, 1000 monofilaments) 6 to 7 μm in diameter using a similar continuous CVD process. To meet the requirement of enhancing the performance of aluminium-alloy composites (C/A1), carbon fibre with functionally gradient coatings is used as reinforcement. The functionally gradient coating consists of three well-integrated layers: the inner layer, the intermediate layer and the outer layer. The chemical composition of the inner layer is pyrocarbon and the outer layer is silicon. The intermediate layer is formed by a complex gradient composition from carbon to pure silicon, consisting of three sublayers: C-SiC, SiC and SiC-Si. Within the first C-SiC sublayer, the chemical composition changes gradually from 100% pyrolysis carbon to silicon carbide. This is followed by a sublayer of SiC coating. The final SiC-Si sublayer is deposited with materials from silicon carbide to pure silicon. SiCl_4 , C_4H_{10} , H_2 and Ar are used as precursor gases. The carbon fibre yarn is directly heated by passing electricity through it.

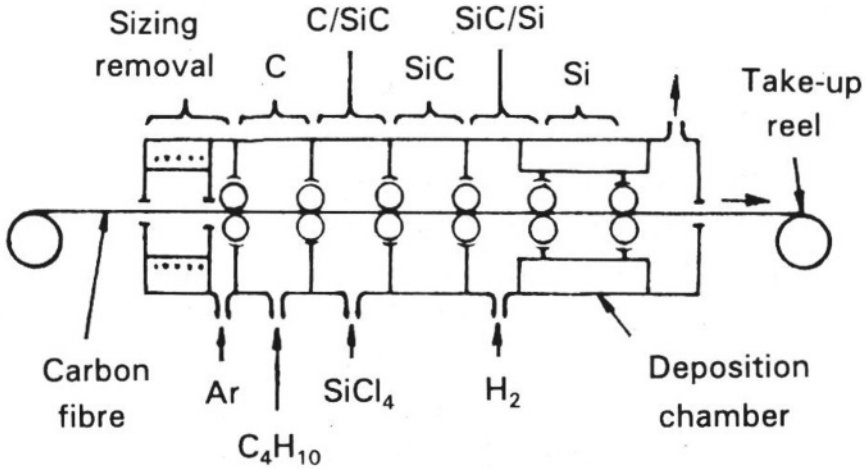


Figure 3.32. Schematic of a multiple coating CVD apparatus [61]

In order to obtain a uniform coating on the individual fibre within the yarn a preheating zone is designed to remove the sizing on each fibre monofilament. For different purposes the reactor is divided into five depositing zones used for the deposition of C, C+SiC, SiC, SiC+Si and Si, respectively. Within each zone the processing parameters can be independently controlled. The processing parameters include the deposition temperature, the types and the flow rate of the precursor gases.

Figure 3.33a shows the stepped fracture surface of the carbon fibres with functionally gradient coatings. Figure 3.33b exhibits a clear change in the chemical compositions of the coating, resulting in three physical sublayers. These sublayers include the pyrolysis carbon, the gradient sublayer with different Si/C ratio and pure silicon sublayer, corresponding to a thickness of 200 nm, 100 nm and 70 nm respectively.

By use of this functionally gradient coating the carbon-fibre-reinforced aluminium composites (C/Al) exhibit excellent mechanical properties. The ultimate tensile strength reaches 1250 MPa when the fibre volume fraction is 35%.

3.8.2.2 Hot-wall Continuous CVD Process

A typical hot-wall continuous CVD reactor is as shown in Figure 3.34. The hot zone has a large size with a diameter of 150 mm and a length of 300 mm; it can be used as-pilot-plant coating application. This hot zone is heated by induction with a frequency of 10 kHz and a power supply of 30 kW. Graphite is used as susceptor for heating. The reactant precursor gases (e.g. BCl_3 , NH_3) are introduced into the reaction chamber by a water-cooled stainless steel gas injector. A gas deflector is designed to distribute the reactant gases, hence leading to uniform deposition within the reactor. The processing temperature is measured and controlled with an optical pyrometry.

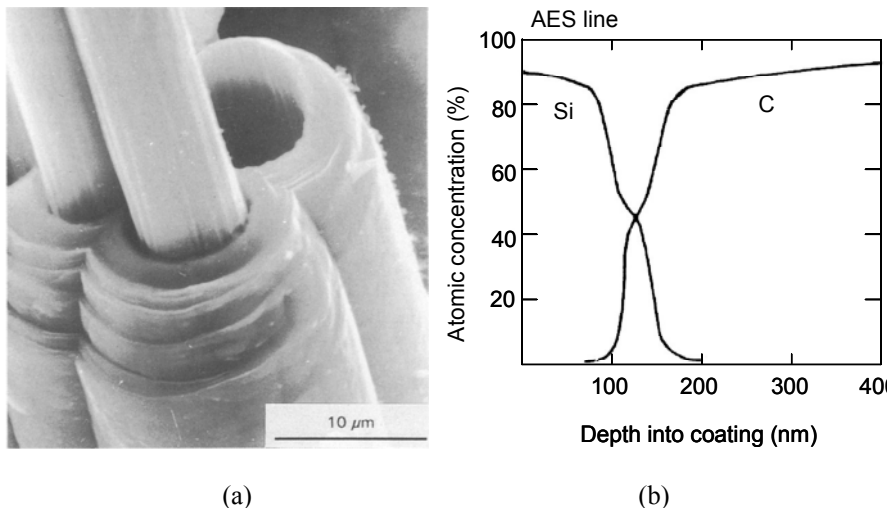


Figure 3.33. Functionally gradient coating on the carbon fibre [61]: (a) microstructure and (b) chemical composition distribution

The fibre yarn is fed and collected by two spools which should have a large diameter to prevent damage to the coated fibres. After a fibre yarn is drawn from the feeding spool it is uniformly spread by Teflon pulleys with the help of tension indicators. The movement of the fibre yarn is driven by a motor connected with the collecting spool at the upper position. In order to minimize and eliminate oxygen contamination from the air the reactor and two spools are placed within an enclosure which can be evacuated. In the system the heating temperature can reach a maximum temperature of 2000°C and the pressure is evacuated to 0.05 to 0.1 Torr during the CVD process by vacuum pumps.

The hot-wall CVD process has a number of advantages over the cold-wall CVD process. These advantages are as follows: (1) the thickness uniformity of the coating is better since the deposition temperature and temperature uniformity can be easily controlled in a relatively small chemical reaction chamber and (2) there is no requirement for the fibre and coating to be electrically conductive, hence this technique can be used to coat a large number of materials.

The above CVD techniques have been widely applied and used to fabricate superconductor wires and interphase layers for fibre-reinforced metal- and ceramic- matrix composite materials.

3.8.3 Fluidised-bed Chemical Vapour Deposition Process

Fluidised-bed CVD is a special technique to coat nuclear-fuel particles for high-temperature gas-cooled nuclear reactors which was developed in the late 1950s. This technique has also been used in other applications, such as the production of biomedical components (e.g. heart valves deposited by pyrolysis carbon) and some special functional coatings on ceramic particles.

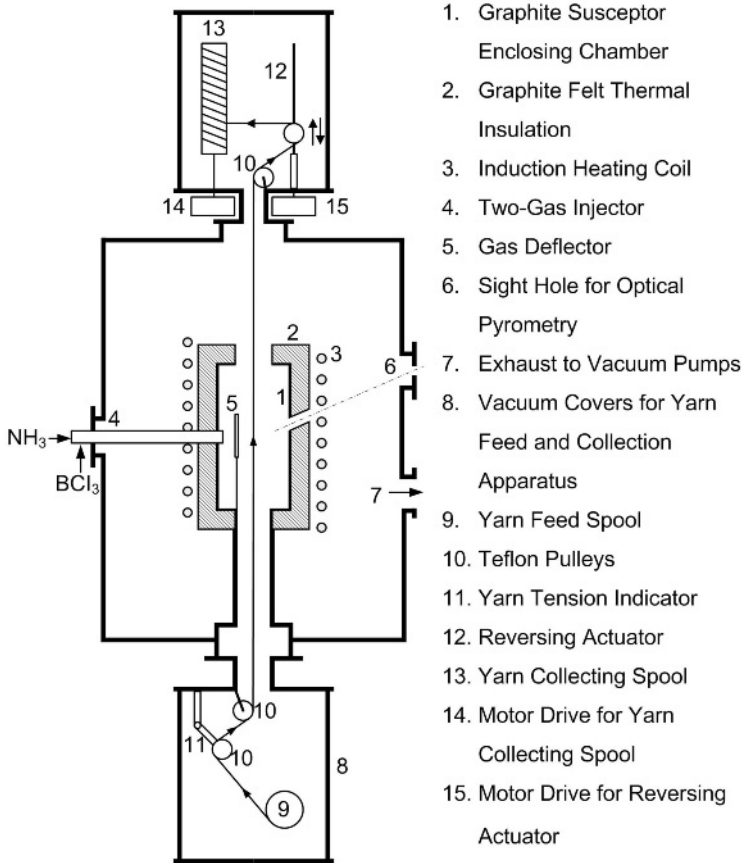


Figure 3.34. Hot-wall continuous CVD reactor [62]

The key technical issue in this method is the formation of a so-called fluidised bed. In this case the particles are used as the substrate and are suspended by the reactant gases within a retort as shown in Figure 3.35.

When the gas stream flows upwards through a packed bed of particles, there is a pressure drop due to the flow resistance from these particles. This pressure drop increases with the gas velocity based on the theory of fluid mechanics [64]. A fluidised bed of particles is formed if the pressure drop across the bed is equal to the weight of the bed particles per unit area, i.e. the pressure (or the force in a unit area) for pushing the particle upwards to form the fluidised bed equals the weight of the particles of the unit area, as shown in Figure 3.36.

In practice the minimum gas flow velocity is used, which corresponds to the critical pressure drop required for fluidisation. If the particle size is larger than 100 μm , then the minimum gas velocity (u_{mf}) is calculated by the following equation [65]:

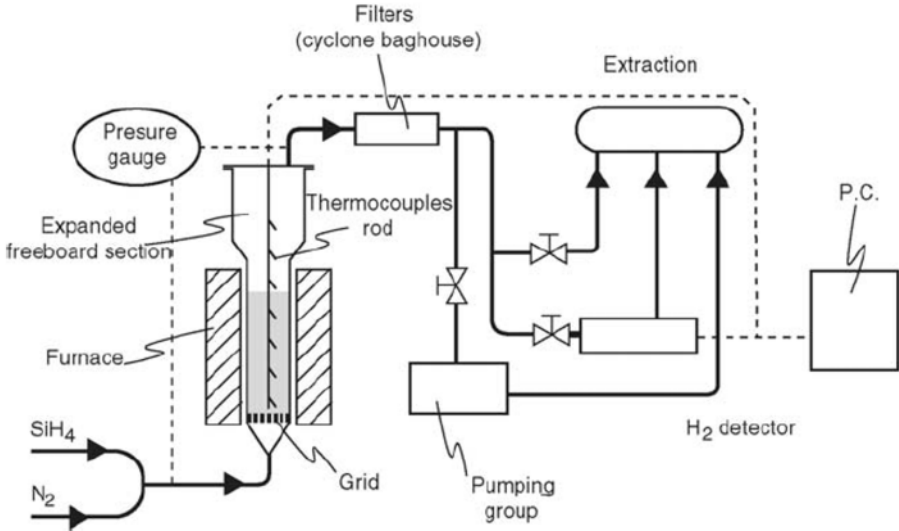


Figure 3.35. A typical fluidised-bed CVD reactor [63]

$$u_{mf} = \frac{\mu}{d_p \rho_g} \left\{ \left[33.7^2 + 0.0408 \frac{d_p^3 \rho_g (\rho_p - \rho_g) g}{\mu^2} \right]^{1/2} - 33.7 \right\} \quad (3.6)$$

where d is the diameter of the particle, μ is the viscosity of the reactant gas, and ρ_g and ρ_p are the densities of the reactant gas and the particle respectively.

If the size of particles is smaller than $100 \mu\text{m}$, then the minimum gas velocity is expressed by [65]

$$u_{mf} = \frac{(\rho_p - \rho_g)^{0.934} g^{0.934} d_p^{18}}{1111 \mu^{0.87} \rho_g^{0.066}} \quad (3.7)$$

Once the above control parameters can be determined it is possible to fabricate the coated particles using the above fluidised-bed CVD process. Figure 3.37 shows the microstructure of multiple coatings on a UO_2 kernel by a fluidised-bed CVD process. These multiple coatings are divided into four sublayers from the inner region to the outer region of the coating [66].

3.8.3.1 Buffer Layer (Buffer)

The buffer layer is a low-density pyrocarbon layer. The density is less than $1.05 \text{ g}\cdot\text{cm}^{-3}$ and the thickness is $95 \pm 20 \mu\text{m}$. This layer is deposited with C_2H_2 as the reactant gas. Due to the relatively low density, the buffer layer can provide the void volume for the gaseous fission products and fuel swelling as well as the accommodation for the kernel dimensional change.

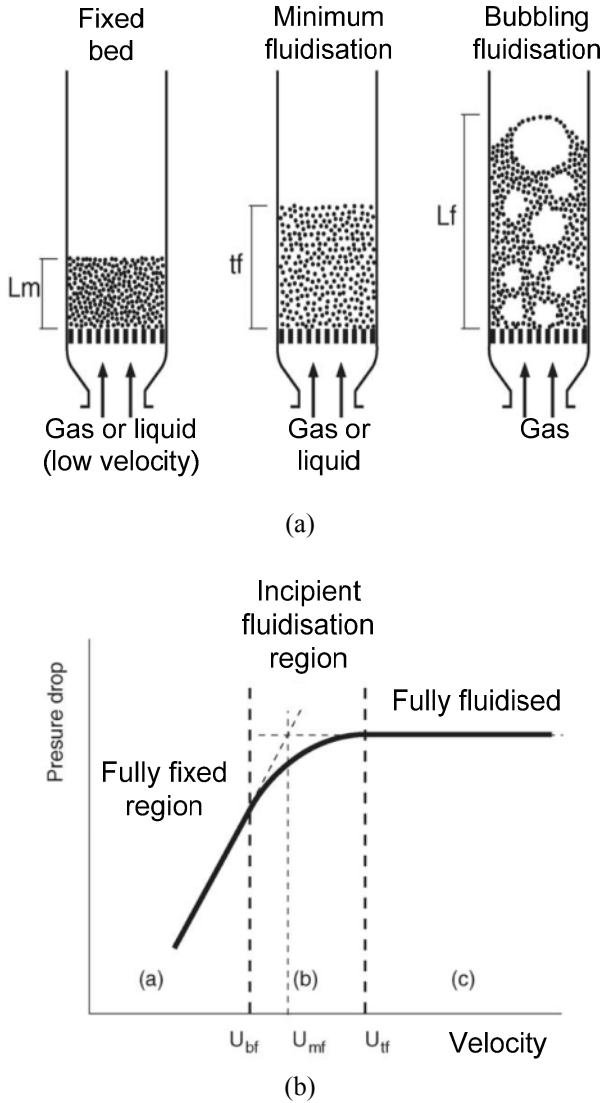


Figure 3.36. Pressure drop-gas velocity relationship and characteristic of fluidised-bed reactors [63]

3.8.3.2 Inner Dense Pyrocarbon Layer (I-PyC)

This pyrocarbon layer has a high density ranging from 1.85 to 2.0 g·cm⁻³ and its thickness is 40 ± 10 μm. It can not only protect the outer SiC layer from detrimental reactions but also protect the buffer layer and the UO₂ kernel from chlorine intrusion during the CVD SiC process with CH₃SiCl₃ as the reactant gas.

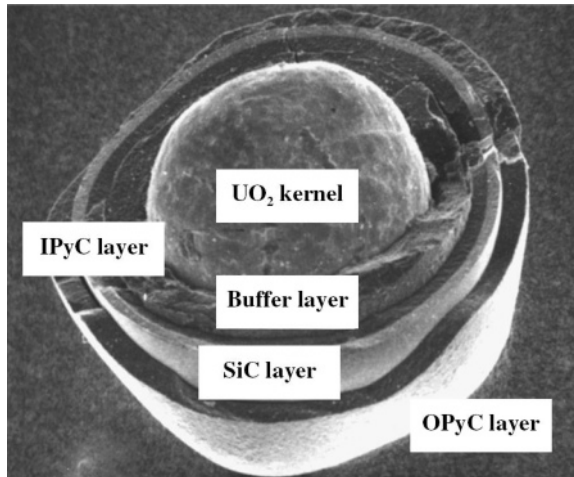


Figure 3.37. Multiple coatings on a UO_2 particle by fluidized bed CVD [67]

3.8.3.3 Dense SiC Layer

The function of the dense SiC layer is to serve as the primary barrier to the release of gaseous and solid fission products. However, it also provides structural rigidity and dimensional stability because of its superior mechanical properties. Its density and thickness are $3.18 \text{ g}\cdot\text{cm}^{-3}$ and $40 \pm 10 \mu\text{m}$ respectively.

3.8.3.4 Dense Isotropic Pyrocarbon Layer (O-PyC)

This layer is as dense as the inner pyrocarbon layer (I-PyC). Both layers are deposited using C_3H_6 as the reactant gas. The function of this layer is to provide a mechanical support for the SiC layer and prevent damage to the inner layers during later manufacture processes. Its density is in the range of 1.85 to $2.0 \text{ g}\cdot\text{cm}^{-3}$ and its thickness is $40 \pm 10 \mu\text{m}$.

3.8.4 Catalyst-assisted Chemical Vapour Deposition Process

3.8.4.1 Whisker Growth

A whisker is a single crystal with a small diameter and large aspect ratio as shown in Figure 3.38a. Its growth mechanism is a complex CVD process which is generally considered to be the vapour-liquid-solid (VLS) process. This mechanism was first proposed by Wagner and Ellis in 1964 [68]. As illustrated in Figure 3.38b, the catalyst is used to form a liquid droplet on the substrate surface at high temperatures. The reactant gases, such as SiO , CH_4 and H_2 , are dissolved in the liquid droplet. When the liquid solution becomes supersaturated with Si and C species, they are precipitated to form the SiC crystal at the solid-liquid interface. As the reactant gases are continuously fed into the liquid droplet from the gaseous

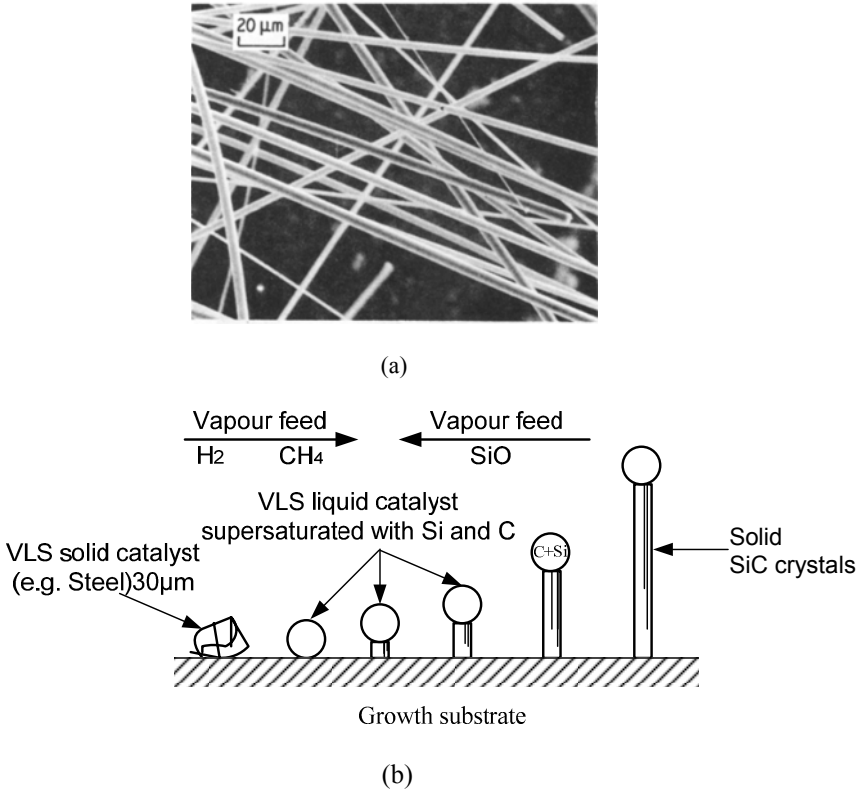


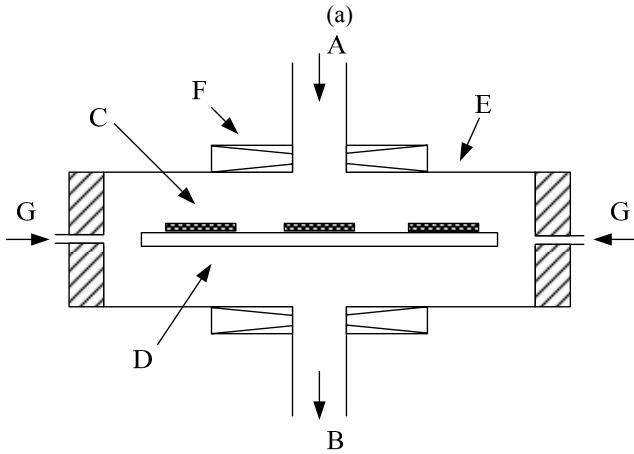
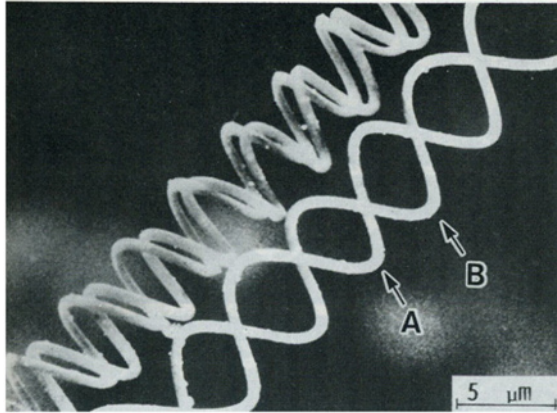
Figure 3.38. SiC whisker and the growth mode [69]: (a) SiC whisker and (b) VLS mechanism

phase, the SiC crystal grows along the preferred direction, hence forming an SiC whisker. In such cases there usually exists a domed droplet at the top of the whisker. Transition metals, such as iron, cobalt and nickel, are usually used as catalysts for SiC whisker growth.

In addition, the vapour-solid (VS) mechanism was proposed to explain whisker growth for some materials. It should be pointed out that the morphology of the crystal growth has a very complex relationship with the catalyst and the processing conditions.

3.8.4.2 Coiled Fibre

Catalyst-assisted CVD processes can also be used to fabricate delicate micro-components. Coiled fibres of carbon and refractory carbides are examples of such components which may be used in functional applications such as microsprings, microsensors and fillers of electromagnetic shielding materials. The microstructure of some coiled fibres is shown in Figure 3.39a. The device for the production of coiled fibre fabrication is shown in Figure 3.39b. A graphite plate substrate is placed at the central part of a horizontal CVD reaction chamber, and a metal



A: source gas inlet (acetylene-thiophene-H₂); B: gas outlet; C: substrate; D: susceptor (graphite plate); E: reaction tube (quartz, 60 mm i.d.); F: heater; G: Ar or N₂ gas inlet

(b)

Figure 3.39. Microstructure of microcoiled fibres: (a) Si₃N₄ coiled fibres [71] and (b) Experimental reactor [72]

powder catalyst listed in Table 3.9 is then uniformly dispersed on the substrate. The reaction chamber is heated by an inductive heating method from the outside. In some cases a metal plate is also used as both substrate and catalyst for fabricating the microcoiled carbon fibres. Some other coiled fibres are also reported in the literature and are listed in Table 3.9.

3.8.5 Combustion Chemical Vapour Deposition

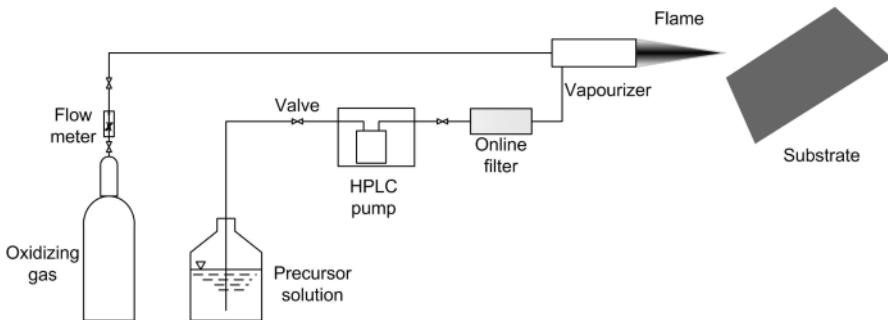
This is an innovative CVD technique developed at the Georgia Institute of Technology in 1995. Combustion chemical vapour deposition (C-CVD) is a special

Table 3.9. Coiled fibres prepared by catalyst-assisted CVD processes [70]

Coils type	Precursors	Catalyst	Temperature (°C)
Carbon	$C_2H_2-H_2-Ar$ -thiophene(C_4H_4S)	Co, Cr, Nb, Ni, Ta, Ti, W, TiC	650–850
SiC	Coked rice husks (SiO) $-H_2-CH_4$	Cr, Fe, Ni	1400–1500
Si ₃ N ₄	SiO ₂ -C-H ₂ -NH ₃ , SiO-H ₂ -NH ₃ , Si ₂ Cl ₆ -H ₂ -NH ₃	Co, Fe	1200–1500
TiC	TiCl ₄ -PCl ₃ -H ₂ -C (graphite substrate)	Pt-Si, Pd-Si	1050–1250
HfC	HfCl ₄ -PCl ₃ -H ₂ -Ar-C (graphite substrate)	PCl ₃	
ZrC	Carbon coils-ZrCl ₄ -H ₂	Zirconization of C coils	1100–1250

deposition method which uses a flame to provide a high-temperature deposition condition. The key to this technique is to deliver the elements to be deposited by combustion of the flammable liquids or vapours which contain the elements. A schematic diagram of the system is presented in Figure 3.40. A combustible solvent, such as toluene, isopropanol, ethanol or methanol, is used to dissolve CVD precursors. This solution is delivered to a mixing device where the oxidising gas such as oxygen can be mixed homogeneously with the solution. This mixture, similar to the fuel and air mixture in a combustion car engine injection system, is injected into the flame in the system, which ignites the combustible mixture. As a result a coating is formed on the substrate.

The parameters affecting the properties and microstructure of the coating in the C-CVD are (1) the solution types and their composition; (2) precursor concentration in the solvent; (3) flow rate of the mixture of solution and the oxidising gas as well as the flow rate of the oxidising gas; (4) the temperature and

**Figure 3.40.** Schematic representation of C-CVD system [73]

stability of the flame; (5) the temperature of the substrate, the distance between the flame and the substrate, substrate moving speed, tilting angle between the substrate and flame, as well as the cooling rate of the coated substrate.

Compared with traditional CVD techniques the C-CVD approach is cheaper because there is no furnace, auxiliary heating or reaction chamber. The process is usually carried out in an environment of atmosphere and a reaction chamber is not required. For a C-CVD process, it is not necessary to heat the substrate in a furnace since the heat from the combustion can provide the necessary energy for the chemical reactions. The substrate is usually heated to some extent by the combustion flame. Therefore, the C-CVD technique is cheaper to implement, and involves fewer problems related to environmental pollution and exhaust handling. Due to the dependence of oxidation combustion the deposited materials are usually oxides. They are divided into several groups: (1) high-temperature ceramics, such as Al_2O_3 , MgO , SiO_2 , spinel (MgAl_2O_4 , NiAl_2O_4 , NiCr_2O_4) etc. (2) glass: silica glasses and (3) superconductors, such as $\text{YBa}_2\text{Cu}_3\text{O}_{7-x}$, $\text{YbBa}_2\text{Cu}_3\text{O}_{7-x}$. In addition, some metals such as Ag, Au, Cu, Ir and Ni have also been successfully produced.

3.8.6 High-temperature Chemical Vapour Deposition Process

In most cases CVD processes take place at relatively low temperatures in the chemical reaction kinetic regime to fabricate uniform thin coatings. CVD processes can also be extended to manufacture bulk monolithic materials (thickness: 25 mm) [23, 74], such as ZnS, ZnSe, CdS, SiC, Si_3N_4 etc. Compared with traditional sintering methods, CVD processes can prepare high-purity and large-area components. In such extended application cases CVD processes occur at relatively high temperatures in the mass transport regime because the high growth rate is much more important than the uniform growth thickness for the deposition of bulk materials.

Figure 3.41a and b shows the schematic of a CVD reactor for ZnS or ZnSe bulk material growth and the monolithic SiC components. The reactant gases (H_2S or H_2Se , Ar) are introduced from the bottom of the reactor by a gas injector. Zinc is placed in a graphite retort which is heated sufficiently for zinc vaporisation, ZnS or ZnSe deposition then takes place on the inner surface of a hollowed graphite mandrel according to the following chemical reactions [23]. The typical deposition parameters for some monolithic materials are listed in Table 3.10.



$$\Delta G = 82.1T - 5.9 T \ln T - 0.62 \times 10^{-2} T^2 - 76400 \text{ (cal}\cdot\text{mol}^{-1}) \quad (3.9)$$



$$\Delta G = 86.4T - 5.95T \ln T - 0.69 \times 10^{-3} T^2 - 85800 \text{ (cal}\cdot\text{mol}^{-1}) \quad (3.11)$$

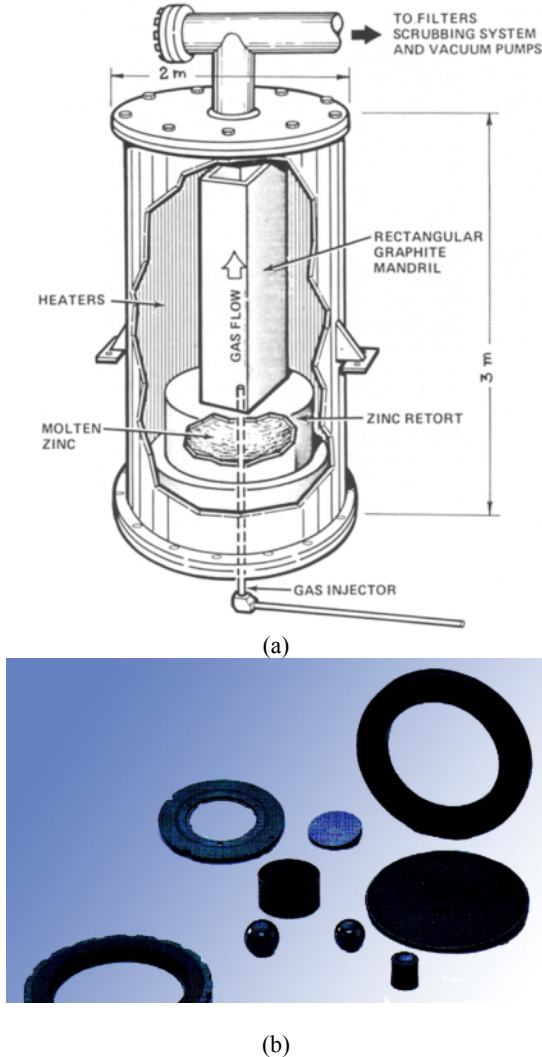


Figure 3.41. High-temperature CVD technique: (a) schematic of the CVD reactor [23] (b) monolithic SiC components [75]

One of the key technical issues is to select suitable material as the substrate. Graphite and silicate glass are widely used because graphite is easily oxidised in air at 700°C and silicate glass can be etched away by HF acid. Sometimes Mo, Ta, W, SiC and Si_3N_4 are also employed due to their superior stiffness at elevated temperatures and inertness to reactant gases.

Table 3.11 compares the property differences of SiC materials prepared by four types of processing methods. CVD processes can fabricate very dense and near-net-shaped SiC components with a very high purity of 99.9995%. However, it is

Table 3.10. CVD processing parameters for ZnS, ZnSe, CdS, SiC and Si [23]

Material deposited	Precursor gases and flow rate (l·min ⁻¹)	Temperature (°C)	Pressure (Torr)	Deposition rate (μm·min ⁻¹)
ZnS	HS2: 0.2–0.4, Zn: 0.2–0.4, Ar: 2.0	730–835	20–40	1.0
ZnSe	HS2: 0.2–0.4, Se: 0.2–0.7, Ar: 2.0	630–730	30–60	1.2
CdS	HS2: 0.2–0.4, Cd: 0.2–0.4, Ar: 2.0	550–650	70–100	1.2
Si	SiHCl3:0.8–1.5, H2: 3.0–9.0, Ar: 2.0	950–1150	100–400	1.25
SiC	CH3SiCl3:0.6–1.2, H2: 2.0–5.0, Ar: 2.0	1250–1400	100–400	1.50

Note: deposition area = 1000 cm²

very difficult to manufacture very dense SiC materials by the traditional methods which include sintering, hotpressing (HPSC) and reaction bonding (RBSC) processes. For these sintering processes, an additive is always used to aid the sintering of the SiC powder, hence leading to low thermal conductivity (50 to 170 W·m⁻¹·K⁻¹). CVD SiC exhibits very low polishability (less than 3 Å RMS) and a relatively high elastic modulus of 466 GPa. These distinct advantages are very important for CVD SiC to be used as an advanced mirror material.

Table 3.11. Property comparison of SiC materials by different methods [75]

Material	Density (g·cm ⁻³)	Thermal conductivity (W·m ⁻¹ ·K ⁻¹)	Coefficient of thermal expansion(×10 ⁻⁶ K ⁻¹)	Elastic modulus (GPa)	Polishability (Å RMS)
CVD SiC	3.21	330	4.0	466	3
RBSC	3.1	120–170	4.3	391	20
HPSC	3.2	50–120	4.6	451	50
Sintered SiC	3.1	50–120	4.5	408	100

References

- [1] French M (1985) *Conceptual design for engineers*, 2nd edn. Design Council, London
- [2] Pahl G, Beitz W (1996) *Engineering design - a systematic approach*, 2nd edn. Springer, London
- [3] Yan XT (2003) A multiple perspective product modelling and simulation approach to enhancing engineering design decision making. *Int J Concurr Eng* 11:221–234
- [4] Borg J, Yan XT, Juster NP (1999) Exploring decisions' influence on life-cycle performance to aid design for Multi-X. *Artifi Intell Eng Des, Anal and Manuf* 13:91–113
- [5] Yan XT, Sharpe JEE (1994) A system simulation platform for mechatronic product design. In: *Proceedings of the European Simulation Multi-Conference*, Barcelona, Spain, pp789–793
- [6] Glocker DA, Shah SI (1995) *Handbook of thin process technology*. IOP
- [7] Pierson HO (1999) *Handbook of chemical vapour deposition (CVD)*, 2nd edn. Noyes, Park Ridge, NJ
- [8] Choy KL (2003) Chemical vapour deposition of coatings. *Prog Mater Sci* 48:57–170
- [9] Ellison A, Zhang J, Peterson J, Henry A, Wahab Q, Bergman JP, Makarov YN, Vorob'ev A, Vehanen A, Janzen E (1999) High temperature CVD growth of SiC. *Mater Sci Eng B61-62*:113–120
- [10] Comfort JH, Reif R (1989) Chemical vapour deposition of epitaxial silicon from silane at low temperature I: very low pressure deposition. *J Electrochem Soc* 136:2386–2398
- [11] Wachtell RL, Seelig RP (1962) Diffusion coating of non-ferrous metals. US Patent 3,037,833
- [12] Vescan L (1995) Introduction and general discussion. In: Glocker DA, Shah SI (eds) *Handbook of thin film process technology*. Institute of Physics, Bristol, UK. B1.0:1–B1.0:12
- [13] Kern W, Ban VS (1978) Chemical vapour deposition of inorganic thin films. In: Vossen JL, Kern W (eds) *Thin film processes*. Academic, New York, pp257–331
- [14] Hitchman ML, Jensen KF (1993) *Chemical vapour deposition: principles and applications*. Academic, New York
- [15] Hopfe V, Grahlert W, Throl O (1999) FTIR based process control for industrial reactors. *J Phys IV* 9:Pr8-995–1002
- [16] Brennfleck K, Scheweis S, Weiss R (1999) In-situ-spectroscopic monitoring for SiC-CVD process control. *J Phys IV* 9:Pr8-1041–1048
- [17] Werner C (1991) Numerical modeling of CVD processes and equipment. *J Phys IV* 2:C2-3–18
- [18] Vescan L (1995) Thermally activated chemical vapour deposition. In: Glocker DA, Shah S I (eds) *Handbook of thin film process technology*. Institute of Physics, Bristol, UK. B1.4:1–B1.0:41
- [19] Leskela M, Ritala M (1999) ALD precursor chemistry: evolution and future challenges. *J Phys IV* 9:Pr8-837–852
- [20] Jones AC, Aspinall HC, Chalker PR (2007) Molecular design of improved precursors for the MOCVD of oxides used in microelectronics. *Surface Coat Technol* 201:9046–9053
- [21] Turgambaeva AE, Bykov AF (1997) Igumenov IK, Routes of thermal decomposition of metal β -diketonates. In: Allendorf MD, Bernard C (eds) *Proceedings of the 14th international conference on chemical vapour deposition/Jointly held with the Euro CVD-11*, Paris, France. Electrochemical Society, Pennington, NJ, pp139–146

- [22] Gorden RG (2000) New liquid precursors for CVD of metal-containing materials. In: Allendorf MD, Hitchman ML (eds) Proceedings of the 15th international symposium on chemical vapour deposition. Toronto, Canada. Electrochemical Society, Pennington, NJ, pp248–259
- [23] Goela JS, Taylor RL (1988) Monolithic material fabrication by chemical vapour deposition. *J Mater Sci* 23:4331–4339
- [24] Boer HJ (1995) Mass flow controlled evaporation system. *J Phys IV5*:C5-961–966
- [25] Ziko JL (1988) Metal-organic chemical vapour deposition: technology and equipment. In: Schuergraf KK Handbook of thin film deposition processes and techniques. Noyes, Park Ridge, NJ, pp234–269
- [26] Vargaftik N B (1983) Handbook of physical properties of liquids and gases, pure substances and mixtures, 2nd edn. Hemisphere, Washington, DC
- [27] Kawahara K, Fukase K, Inoue Y, Taguchi E, Yoneda K (1987) CVD spinel on Si. In: Cullen GW (ed) Proceedings of the 10th international conference on chemical vapor deposition. Electrochemical Society, Pennington, NJ, pp588–602
- [28] Sherman AJ, Tuffias RH, Kaplan RB (1991) Refractory ceramic foams: a novel, new high-temperature structure. *Am Ceram Soc Bull* 70:1025–1029
- [29] Benard ICJ (1988) Handbook of fluid metering, 1st edn. Trade & Technical Press, Morden, Surrey, England, UK
- [30] Siev R, Liptak BG (1993) Mass flowmeters-thermal. In: Liptak BG (ed) Flow measurement. Clinton, Radnor, PA, pp68–72
- [31] Boer IHJ (1999) Precision mass flow metering for CVD applications. *J Phys IV* 9:Pr8-869–876
- [32] Yarwood J (1975) High vacuum technique, 4th revised edn. Chapman & Hall, New York, p103
- [33] Merrick RC (1991) Valve selection and specification guide. Van Nostrand Reinhold, New York, p226
- [34] Stinton DP, Lackey WJ (1985) Simultaneous chemical vapour deposition of SiC-dispersed phase composites. *Ceram Eng Sci Proc* 6:707–713
- [35] Ichijo S, Tamura K, Takano T, Nakao A, Hirahara T (1991) Properties and practical results of tungsten carbide coating produced by low temperature CVD process. *J Phys IV2*:C2-497–504
- [36] Brennfleck K, Reich H (1991) CVD of SiC in large coating vessels. *J Phys IV* 2:C2-467–474
- [37] Bouquet C, Fischer R, Larrieu JM, Uhrig G, Thebault J (2003) Composite technologies development status for scramjet applications. In: Proceedings of 12th AIAA International Space Planes and Hypersonics Systems and Technologies :AIAA-2003-6917, Norfolk, VA
- [38] Bouquet C, Fischer R, Thebault J, Soyris P, Uhrig G (2005) Composite technologies development status for scramjet. In: Proceedings of AIAA/CIRA 13th International Space Planes and Hypersonics Systems and Technologies :AIAA-2005-3431, Capua, Italy
- [39] Jensen KF (1994) Transport phenomena in vapour phase epitaxy reactor. In: Hurlle D T J (ed) Handbook of crystal growth 3. Thin Films and Epitaxy. Elsevier, Amsterdam, pp543–599
- [40] Fotiadis DI, Kieda S (1990) Transport phenomena in vertical reactors for metalorganic vapour phase epitaxy. *J Cryst Growth* 102:411–470
- [41] Incropera FP, Dewitt DP (2001) Fundamentals of heat and mass transfer, 5th edn. Wiley, New York, p408
- [42] Sparrow EM, Eichhorn R, Gregg JL (1959) Combined forced and free convection in a boundary layer flow. *Physics of Fluids* 2:319–328

- [43] Niihara K, Hirai T (1976) Chemical vapor-deposited silicon nitride, Part 1 Preparation and some properties. *J Mater Sci* 11:593–603
- [44] Campbell S A (2001) The science and engineering of microelectronic fabrication, 2nd edn. Oxford University Press, Oxford, p340
- [45] Mironer A (1979) Engineering fluid mechanics. McGraw–Hill, New York
- [46] Munson BR, Young DF, Okiishi TH (2006) Fundamentals of fluid mechanics, 5th edn. Wiley, New York
- [47] Li SJ (1980) Engineering fluid mechanics. China Machine Press, Beijing
- [48] Jiang YZ (1993) Industrial electric furnaces. Tsinghua University Press, Beijing
- [49] Paschkis V, Persson J (1960) Industrial electric furnaces and appliances. Interscience, New York
- [50] Worrall RW, Liptak BG (1993) Thermocouples. In: Liptak BG (ed) Temperature measurement. Clinton, Radnor, PA
- [51] Sherman A (1987) Chemical vapour deposition for microelectronics: principles, technology, and applications. Noyes, Park Ridge, NJ, p155
- [52] Hammond ML (1991) CVD exhaust-safety and environmental sanity. *J PhysIV2:C2-449–458*
- [53] Schuergraf KK (1988) Handbook of thin film deposition processes and techniques. Noyes, Park Ridge, NJ
- [54] Baechler WG (1987) Cryopumps for research and industry. *Vacuum* 37:21–29
- [55] Harris NS (1989) Modern vacuum practice. McGraw–Hill, London
- [56] Silicone Research Group in Chengguang Institute of Chemical Engineering (1986) Silicone monomer and polymer. Chemical Industry Press, Beijing
- [57] Pan ZW, Li HL, Zhang LT (1998) Laser synthesis and crystallization of nanocomposite Si₃N₄ powder. *J Mater Res* 13:1996–2002
- [58] www.specmaterials.com
- [59] Ning XJ, Pirouz P, Lagerlof KPD, DiCarlo J (1990) The structure of carbon in chemically vapor deposited SiC monofilaments. *J Mater Res* 5:2865–2876
- [60] Bhatt RT, Hull DR (1998) Strength-degrading mechanisms for chemically-vapor-deposited SCS-6 silicon carbide fibres in an argon environment. *J Am Ceram Soc* 81:957–964
- [61] Yu JK, Li HL, Shang BL (1994) A functionally gradient coating on carbon fibre for C/Al composites. *J Mater Sci* 29:2641–2647
- [62] Moore AW (1992) Facility for continuous CVD coating of ceramic fibres. In: Besmann TM, Gallois BM, Warren JW (eds) Chemical vapour deposition of refractory metals and ceramics II. Materials Research Society, Pittsburgh, PA, pp269–274
- [63] Vahlas C, Caussat BG, Serp P, Angelopoulos GN (2006) Principles and applications of CVD powder technology. *Mater Sci Eng R53:1–72*
- [64] Geldart D (1986) Gas fluidization technology. Wiley, New York
- [65] Ceankoplis CJ (1993) Transport processes and unit operations, 3rd edn. Prentice Hall, Engelwood Cliffs, NJ
- [66] Helary D, Bourrat X, Dugne O, Maveyraud G, Perez M, Guillemier P (2004) Microstructures of silicon carbide and pyrocarbon coatings for fuel particles for high temperature reactors (HTR), 2nd international topical meeting on high temperature reactor technology. Beijing, China, 22–24 September 2004
- [67] Ueta S, Aihara J, Yasuda A, Ishibashi H, Takayama T, Sawa K (2008) Fabrication of uniform ZrC coating layer for the coated fuel particle of the very high temperature reactor. *J Nucl Mater* 376:146–151
- [68] Wagner RS, Ellis WC (1964) Vapor-liquid-solid mechanism of single crystal growth. *Appl Phys Lett* 4:89–90

- [69] Milewski JV, Gac FD, Petrovic JJ, Skaggs SR (1985) Growth of beta-silicon carbide whiskers by the VLS process. *J Mater Sci* 20:1160–1166
- [70] Motojima S, Hasegawa I, Iwanaga H (1995) Vapour growth of micro-coiled ceramic fibres and their properties. *J Phys IV* 5:C5-1061–1068
- [71] Motojima S, Kawaguchi M, Nozaki K (1991) Preparation of coiled carbon fibres by catalytic pyrolysis of acetylene, and its morphology and extension characteristics. *Carbon* 29(3):379–385
- [72] Motojima S, Hamamoto T, Ueshima N, Kojima Y, Iwanaga H (1997) Preparation and properties of ceramic micro-coils by CVD process. In: Allendorf MD, Bernard C (eds) *Proceedings of the 14th international conference on chemical vapour deposition/Jointly held with the Euro CVD-11*. Paris, France. Electrochemical Society, Pennington, NJ, pp433–439
- [73] Shoup SS, Shanmugham S, Cousins D, Hunt AT (1999) Low-cost combustion chemical vapour deposition of epitaxial buffer layers and superconductor. *IEEE Trans on Appl Superconductiv* 9:2426–2429
- [74] Pickering MA, Goela JS, Burns LE (1995) Chemical vapour deposition furnace and furnace apparatus. US Patent 5,474,613
- [75] Burn L, Haas R (2000) Silicon carbide. *Am Ceram Soc Bull* 79(6):52

Chapter 4 Thermodynamics and Kinetics of Chemical Vapour Deposition

4.1 Introduction

Thermodynamic studies of a CVD process are undertaken to provide a basic understanding of chemical reactions under equilibrium conditions. To ensure a high quality of a CVD coating it is essential to determine the feasibility of a particular CVD reaction first, then select the suitable precursors for the CVD processes. CVD phase diagrams are derived based on the minimisation of Gibbs free energy and are useful in predicting the equilibrium phases present in the chemical reaction system under given processing conditions determined by the deposition temperature, pressure and reactant concentration.

A CVD process is also a non-equilibrium process and typically consists of complex chemical reactions. The kinetics of a CVD system involves many steps which determine the rate of the deposition process. Among them, three important steps are: (1) homogeneous reactions taking place among the gases in a reaction chamber, (2) heterogeneous reactions occurring on the surface of a substrate and (3) mass transportation of the gaseous precursors. The overall deposition rate of the CVD process is limited by the slowest step in the three aforementioned steps. This chapter covers these topics and gives details on these processes.

4.2 Thermodynamics of Chemical Vapour Deposition

4.2.1 Chemical Reaction Feasibility

When a CVD system is proposed for consideration, the first task is to evaluate the feasibility of its underlying chemical reaction. If this reaction is infeasible, an alternative system should be selected and considered. This feasibility can be determined by calculating the Gibbs free energy, ΔG_r , of the reaction under given conditions. A negative ΔG_r implies that the reaction may occur, whereas a positive ΔG_r indicates that the reaction would not take place. If several possible reactions are proposed and all are thermodynamically feasible, the reaction with the most negative ΔG_r should be ideally selected since it leads to the most stable products. The next selection is to determine the other processing parameters, such as depositing temperature, pressure, concentration and so forth.

In order to calculate the Gibbs free energy of a chemical reaction, it is necessary to work out the Gibbs free energy of each reactant and product. The Gibbs free energy $\Delta G_f(T)$ for a given species can be calculated using the following equation [1]:

Table 4.1. Data for the heat capacity of some gaseous species [2]

Substance	a	b×10 ³	c×10 ⁶	d×10 ⁻⁶
SiH ₄	34.39	68.23	-17.79	0.989
SiH ₂ Cl ₂	68.77	36.91	-9.73	-1.546
SiHCl ₃	86.18	20.77	-5.51	-1.488
SiCl ₄	103.91	4.80	-1.43	-1.345
SiCl ₂	56.80	1.68	-0.515	-0.531
H ₂	28.00	1.37	0.927	0.0438
HCl	24.43	8.48	-1.445	0.217

$$\Delta G_f(T) = \Delta H_f^0(298) + \int_{298}^T C_p dT - TS^0(298) - \int_{298}^T (C_p / T) dT \quad (4.1)$$

where $\Delta H_f^0(298)$ is the enthalpy of formation, $\Delta S^0(298)$ is standard entropy and $C_p(T)$ is the heat capacity.

The heat capacity of a gas has a close relationship with the temperature, and the expression is given by [2]

$$C_p = a + bT + cT^2 + dT^{-2} \quad (\text{kJ}\cdot\text{mol}^{-1}\cdot\text{K}^{-1}) \quad (4.2)$$

where a , b , c and d are four different constants. These coefficient values for some gases are listed in Table 4.1.

The thermodynamic data (G , C_p , S , H) for a number of substances are available from some standard sources such as JANAF tables. Entropy and heat capacity are relatively accurate because they can be calculated theoretically and measured by experiments. By contrast, the standard enthalpies of formation are less well known and sometimes must be estimated.

When the free energy of all species is known, the Gibbs free energy of chemical reaction, ΔG_r , can be calculated from the following expression [3]:

$$\Delta G_r = \Sigma \Delta G_f(\text{products}) - \Sigma \Delta G_f(\text{reactants}) \quad (4.3)$$

For a given chemical reaction, the equilibrium constant K_T is related to the Gibbs free energy (ΔG_r) by the following expression:

$$K_T = \exp\left(-\frac{\Delta G_r}{RT}\right) \quad (4.4)$$

where R and T are the perfect gas constant and temperature respectively.

With the equilibrium constant (K_T) of a chemical reaction the partial pressure of each reactant and product can be calculated. The partial pressures of the gaseous species involved in a reaction in equilibrium conditions are related to K_T by the law

of mass action [4]. For a reversible chemical reaction, the general form is expressed as



where a , b , c and d are the mol numbers of the species of A, B, C and D respectively. According to the law of mass action the following equation is obtained:

$$K_T = \frac{p_C^c p_D^d}{p_A^a p_B^b} \quad (4.6)$$

where p_A , p_B , p_C and p_D correspond to the partial pressures of the species of A, B, C and D respectively.

In many cases, when values for entropies of formation (ΔS^0) are not available, the feasibility of a chemical reaction can be roughly determined by using only the values of enthalpy of formation (ΔH). If the chemical reaction is endothermic ($\Delta H > 0$), then an increase in temperature is favourable for the reaction from the left to the right of Equation (4.3). However, if the reaction is exothermic, i.e. $\Delta H < 0$, then the reverse reaction of Equation (4.3) is favoured with an increase in temperature.

The thermodynamic data for many species can be found in references [5–13].

It should be pointed out that these referenced thermodynamic data are obtained by theoretical calculation methods, and the results of the calculations usually fall within a large range. Furthermore, these data may be too approximate or even incorrect in some cases, and it is necessary to determine and detect the species directly by using instruments to measure and validate one's selection and calculation. Therefore, care should be taken when selecting and using these data.

For a given deposit material there usually exist several possible reactions, of which all may be thermodynamically feasible. The reaction with the most negative value should dominate because it leads to the most stable reaction products. For example, in order to co-deposit Si_3N_4 and TiN, two systems of gaseous species are available. The first is $\text{TiCl}_4\text{--SiH}_4\text{--N}_2\text{--H}_2$, where N_2 is used as nitrogen precursor. The chemical reactions are expressed as



The second system consists of Reaction (4.7) and an alternative system to Reaction (4.8) using $\text{SiCl}_4\text{--N}_2\text{--H}_2$ system, and the chemical reaction for Si_3N_4 is



where SiCl_4 is used as an Si-containing precursor instead of SiH_4 . The Gibbs free energy for these three reactions is calculated and shown in Figure 4.1, which shows the dependence of the Gibbs free energy of these three reactions on temperature.

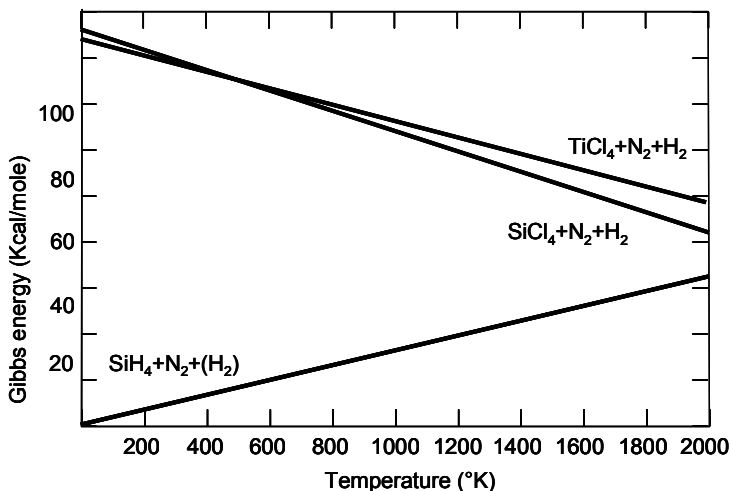


Figure 4.1. Temperature dependence of the Gibbs free energy [14]

Both chemical reactions of Reactions (4.8) and (4.9) aiming to produce Si_3N_4 have a negative Gibbs free energy when the temperature is above 700°C . The Gibbs free energy of Reaction (4.8) is more negative than that of Reaction (4.9) in a temperature range of 0 to 2000 K. The deposition of Si_3N_4 is, hence, favoured by the utilisation of SiH_4 as Si-containing precursor instead of SiCl_4 . Due to its positive gradient, the increasing Gibbs free energy for $\text{SiH}_4\text{-N}_2$ system as shown in Figure 4.1 indicates that the chemical reaction becomes less thermodynamically favourable when the deposition temperature is increased. The production of TiN only becomes thermodynamically feasible when the temperature is more than 750°C . The deposition temperatures required for the CVD of $\text{Si}_3\text{N}_4\text{-TiN}$ co-deposition from $\text{TiCl}_4\text{-SiH}_4\text{-N}_2\text{-H}_2$ gas mixtures should be as low as possible to benefit Si_3N_4 at the same time enabling the deposition of TiN. These results have shown that this co-deposition coating is preferred by using a $\text{TiCl}_4\text{-SiH}_4\text{-N}_2\text{-H}_2$ rather than $\text{TiCl}_4\text{-SiCl}_4\text{-N}_2\text{-H}_2$ system.

An example of using Gibbs free energy is to determine the suitable precursor for a given CVD process. Halides are the most common precursors in CVD processes and could be written in a general form as MX_n . M is a metal element and X is the halogen element of F, Cl, Br or I. As discussed in Chapter 3, the precursor should be stable enough to be transported at relatively low temperatures. However, it must be able to react on the substrate surface at the deposition temperature, so the precursor must not be too stable.

Table 4.2 lists the Gibbs free energy of formation of some halide precursors. It is difficult to generate any general rules or draw any conclusions from the table. There is not a clear cut-off Gibbs formation energy value from the table for the given three variables, namely M , X and n , nor can any Gibbs formation energy trend be identified based on the variation of the three variables of halide precursors. For halides containing a given metal species, it is clear that the stability of a precursor is considerably reduced when X changes from fluoride to chloride, to bromide and to iodide. For example, the ΔG_f value of TiF_3 is $-1143 \text{ kJ}\cdot\text{mol}^{-1}$, the

Table 4.2. Gibbs free energy of some halides at 1000 K [15]

Species	ΔG_f (kJ·mol ⁻¹)	Species	ΔG_f (kJ·mol ⁻¹)	Species	ΔG_f (kJ·mol ⁻¹)	Species	ΔG_f (kJ·mol ⁻¹)
TiCl ₂	-260	TiCl ₄	-642	TiF ₃	-1143	WCl	439
VCl ₂	-242	ZrCl ₄	-755	TiCl ₃	-490	WCl ₄	-239
MnCl ₂	-293	HfCl ₄	-771	TiBr ₃	-381	WCl ₅	-234
FeCl ₂	-187	CrCl ₄	-323	TiI ₃	-204	WCl ₆	-220
CoCl ₂	-137	MoCl ₄	-285	TiCl	49	MoCl ₄	-264
ZnCl ₂	-272	WCl ₄	-239	TiCl ₂	-260	MoCl ₅	-285
				TiCl ₃	-490	MoCl ₆	-170
				TiCl ₄	-642		

values of TiCl₃, TiBr₃ and TiI₃ increase to -490 kJ·mol⁻¹, -381 kJ·mol⁻¹ and -204 kJ·mol⁻¹ respectively.

It is interesting to note that the stability of titanium chloride (TiCl_n) increases significantly with the degree of oxidation indicated by *n*. By contrast, the stability of molybdenum chloride (MoCl_n) generally decreases with the degree of oxidation. Three tungsten-containing chlorides of WCl₄, WCl₅ and WCl₆ almost have the same stability. These observations are very useful in selecting a suitable precursor for a CVD process. Considering the TiN deposition from a TiCl₄-N₂-H₂ reaction system, it is necessary to reduce the deposition temperature if the substrate is very sensitive to the processing temperature. The deposition temperature can be decreased by using a less stable precursor of TiCl₃, which can be formed through the Ti-TiCl₄ chemical reaction.

Figure 4.2 shows the relationship between the Gibbs free energies of formation for some chemical substances and temperature. For Ge-containing species the Gibbs free energy of formation generally decreases with a decrease in the H atom content from GeH₄ to GeH₃Cl, CeH₂Cl₂ and GeHCl₃. GeCl₄ is the most stable species because it has the most negative free energy. Furthermore, these species have a positive temperature dependence on the Gibbs free energy of formation. By contrast, the Gibbs free energies of formation for GeCl and GeCl₂ decrease as the temperature increases from 400 to 1400°C. The Gibbs free energy of formation for HCl is nearly constant within the above temperature range. Si-containing species exhibit a similar tendency.

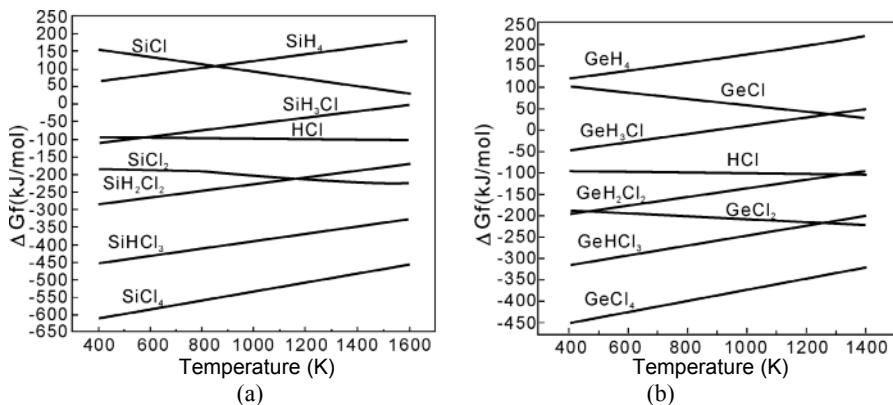


Figure 4.2. Temperature dependence of Gibbs free energy of Ge and Si-containing precursors, data from [16]: (a) ge-containing species and (b) si-containing species

4.2.2 Chemical Vapour Deposition Phase Diagrams

A CVD phase diagram provides important information about the equilibrium compositions of the solid phases present under given conditions of pressure, temperature and input concentration. It is usually constructed either by the equilibrium constant method or the minimisation of Gibbs free energy method. The detailed principles are discussed below.

4.2.2.1 Approaches for Thermodynamic Calculations

For a closed reaction system the determination of the compositions can be calculated with thermodynamic methods under some constraints. The constraints include mass conservation, constant temperature and constant total pressure. Under equilibrium conditions all systems obey the Gibbs phase rule, which relates the number of the species components (n) to the number of phases present (p) and the degree of freedom (f) together. The relationship is expressed by [3]

$$f = n - p + 2 \quad (4.10)$$

The Gibbs phase rule is very useful in predicting the importance of the control variables in a chemical reaction system. These variables include pressure, temperature and composition, as well as the effect on phase equilibrium. It can also be used to predict which way a given reaction will progress when the controlled variables are changed.

Taking the Si–Cl–H system as an example [17], silicon deposition occurs with an appropriate control of the system. It is important to design and determine the control and other variables using the Gibbs phase rule first before a reliable and working system can be established. To apply the Gibbs phase rule for this system Si, Cl and H are considered as three components in the system, hence, $n = 3$. For this CVD process, there are only two phases (gaseous and Si solid), as a result $p =$

2. Applying the Gibbs phase rule gives $f = n = 3$. These three degrees of freedom for this system include the following three control variables: temperature, total pressure and the ratio of chlorine to hydrogen.

Two approaches have been used to calculate and produce a CVD phase diagram [18, 19].

4.2.2.2 The Equilibrium Constant Approach

The equilibrium constant approach is based on Equation (4.6), and it is useful if the chemical reaction is relatively simple, involving a small number of gaseous and solid species. This method requires a knowledge of all chemical reactions and information of species involved, including all the species, chemical reaction paths and their corresponding equilibrium constants.

This method has been applied to some CVD systems. In most cases, however, the chemical reactions are very complex; there exist many gaseous species, such as the reaction intermediates. Consequently, solving the non-linear equations for so many gaseous species becomes very difficult or impossible because there are many unknowns for gaseous species and reaction paths. To deal with such complex situations, free-energy minimisation is generally more suitable, especially for complex chemical systems.

4.2.2.3 Gibbs Free Energy Minimisation Approach

In this approach a chemical reaction is treated as an equilibrium state when the Gibbs free energy of the system reaches a minimal value [20, 21]. The method focuses on Gibbs free energy to predict the deposits produced in a CVD process. It does not require any information about the reactions taking place in the system, based on the understanding that the thermodynamic state changes in the chemical reactions from one state to another are independent of the reaction paths. In addition, the calculation equations of the Gibbs free energy are assumed to be linear, and hence easier to solve.

Under the thermodynamic equilibrium condition the free energy G of a closed system can be expressed as

$$G = \sum_i n_i \mu_i \quad (4.11)$$

where n_i is the mol number of the i th substance and its chemical potential (μ_i) is then defined as

$$\mu_i = \mu_i^0 + RT \ln a_i \quad (4.12)$$

where R is the universal gas constant and T is the temperature in Kelvin. The reactant gas can be treated as an ideal gas, hence, the activity a_i of the i th substance is represented by its partial pressure p_i :

$$p_i = \frac{n_i}{N} P \quad (4.13)$$

where N is the total mol number in the gas phase and P is the total pressure in the system.

For a condensed solid substance its activity is assumed to be equal to unity. Based on the definitions above a dimensionless quantity of G/RT is given by

$$\frac{G}{RT} = \sum_{i=1}^m n_i \left[\frac{\mu_i^0}{RT} + \ln P + \ln \frac{n_i}{N} \right] + \sum_{j=1}^s n_j \left[\frac{\mu_j^0}{RT} + \ln a_j \right] \quad (4.14)$$

where μ_i^0 is the standard chemical potential of the gaseous compound i , μ_j^0 is the standard potential of the condensed compound j and m and s are the numbers of the gaseous species and condensed phases respectively.

The value of (μ^0/RT) in the above equation for a certain substance is calculated using the expression

$$\frac{\mu^0}{RT} = \frac{1}{RT} (G^0 - H_{298}^0) + \frac{\Delta H_f^0(298)}{RT} \quad (4.15)$$

According to the mass balance relations of the chemical reaction system, the following equation is obtained:

$$\sum_i a_{ij}^g n_i^g + \sum_j a_{ij}^c n_i^c = b_j \quad (j=1, 2, \dots, l) \quad (4.16)$$

where a_{ij} represents the number of atoms of the j th element in a molecule of the i th substance, the superscripts c and g over the a_{ij} term denote the condensed phase and gaseous species, respectively; b_j is the total number of mols of the j th element and l is the total number of elements.

According to the principle of Gibbs free energy minimisation the determination of the equilibrium compositions implies obtaining a set of n_i values which lead to a minimal value of G/RT in Equation (4.16). Here, n_i must be a non-negative number.

This method has the advantage of effectively generating and solving linear equations. Many algorithms have been developed to generate CVD phase diagrams based on the above principles and procedures. To calculate a specific phase diagram for a particular CVD process, some computer programs are available, such as SOLGAS, SOLGASMIX, FREEMIN, EKVICALC and EKVIBASE and MELANGE [18].

Due to the fact that CVD is a non-equilibrium process, the investigations indicate that thermodynamic calculations and predictions are sensitive to the accuracy and quality of the original thermodynamic data calculated, which may contain errors and inaccuracies due to system complexity and theoretical assumptions. Therefore, thermodynamic calculations can only provide some indicative information and the final phase diagram should be modified by the experimental results.

4.2.2.4 Some Typical Chemical Vapour Deposition Phase Diagrams

Having introduced theories and the thermodynamic calculation methods it would be useful to show several CVD phase diagrams and their applications in the following section.

Si-C-Cl-H System for Silicon Carbide

Silicon carbide has attracted considerable interest because of its good mechanical and physical properties and chemical inertness. One of the most important applications of SiC is to produce a matrix reinforced by fibres, forming ceramic-matrix composites. These composite materials exhibit much better fracture toughness than monolithic ceramics. Compared with carbon/carbon composites, fibre-reinforced SiC matrix composites possess superior oxidation resistance and mechanical properties. The Si-C-H-Cl system (e.g. methyltrichlorosilane, CH_3SiCl_3) has been used for SiC deposition because it is easy to produce stoichiometric SiC deposits.

Figure 4.3a-d shows the phase diagrams of an Si-C-Cl-H system at temperatures of 1473, 1500, 1600 and 1700 K respectively. A constant total pressure of 10^5 Pa and a ratio of Cl/Si = 3 are used to generate the four diagrams. The gaseous phase equilibrium with all combinations of condensed phases is implicitly shown for all four conditions. Curves are used to mark the boundary between the stable phase fields. For this chemical system, there are no more than two condensed phases in each field.

All of the diagrams in Figure 4.3 have similar profiles and four phase fields with corresponding condensed phases of Si, Si+ β -SiC, β -SiC, β -SiC+C. The first phase field indicates that, at a higher H_2/Si ratio combined with lower C/Si ratio, Si

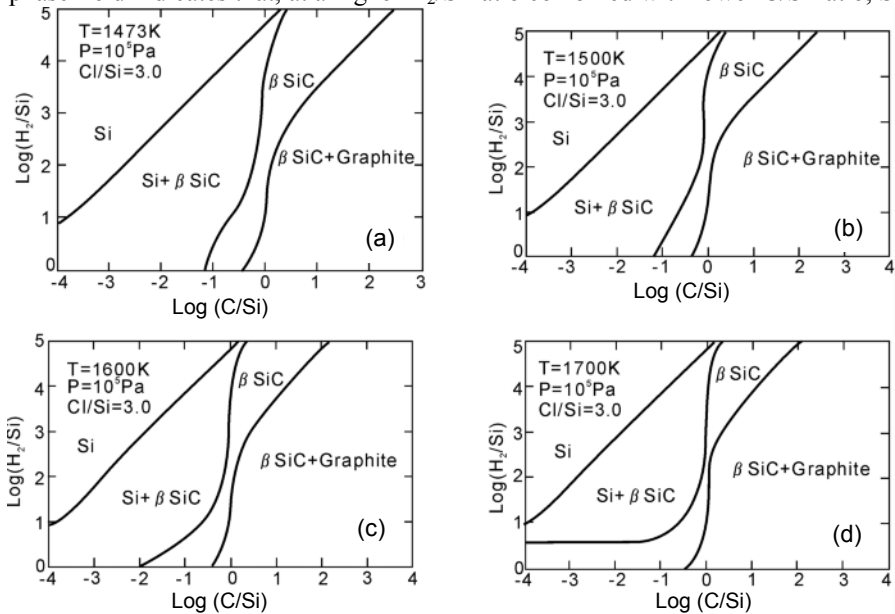


Figure 4.3. CVD phase diagrams of Si-C-Cl-H system in equilibrium with a gas phase [23]

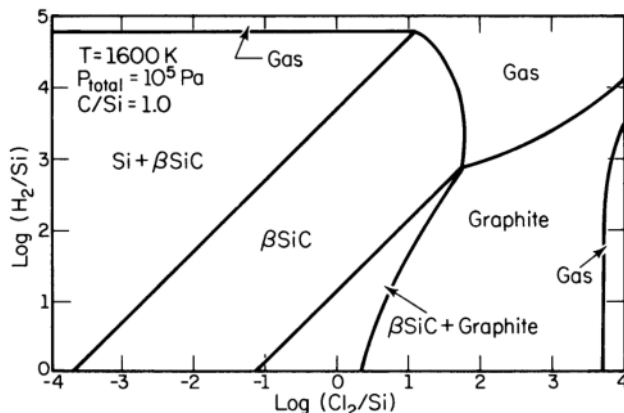


Figure 4.4. CVD phase diagram of Si-C-Cl-H system as a function of H_2/Si and Cl_2/Si ratios [23]

is formed and the area size of the phase field is not influenced by temperature. The second phase field is the Si+ β -SiC, and the area size of this phase field is significantly reduced as the temperature increases from 1472 K to 1700 K. For the β -SiC phase field, the boundary between the β -SiC and the Si+ β -SiC phase fields shifts significantly with increasing temperature, but the boundary position between the β -SiC and the β -SiC+C phase fields barely moves. At low hydrogen content, the β -SiC phase field expands to lower C/Si ratios as temperature increases. The fourth phase field is β -SiC+C, which shows a slightly bigger opening at the top of the field. This implies that the C phase has a greater tendency to co-deposit with β -SiC at higher temperatures and higher H_2/Si ratio. These calculated results are in agreement with the experimental results [23].

Figure 4.4 shows the CVD SiC phase diagram at a temperature of 1600 K, total pressure of 10^5 Pa and C/Si ratio of 1.0. For a given H_2/Si ratio Si+ β -SiC co-deposition takes place at a lower Cl_2/Si ratio. However, C+ β -SiC co-deposition occurs at a higher Cl_2/Si ratio. β -SiC has a relatively large phase field area for a wide range of C/Si and H_2/Si ratios. In many practical cases when a mole ratio of $H_2/CH_3SiCl_3 = 10$ is used, which corresponds to $\text{log}(H_2/Si) = 1$, the phase fields are changed from (Si+ β -SiC) through pure β -SiC, then to (β -SiC+C) with an increasing Cl_2/Si ratio.

Si-N-H System for Silicon Nitride

Silicon nitride (Si_3N_4) has received considerable research and development interest because it has high mechanical properties, electronic properties, low density and corrosive resistance at high temperatures. It can be widely used in structural and functional applications. The CVD process is an effective technique to manufacture silicon nitride materials with ultra-high-purity and unique properties.

Figure 4.5a–c shows the CVD Si_3N_4 phase diagrams of the SiH_4 - NH_3 system at three different pressures. At a pressure of 10^6 Pa there are only two condensed phase fields of Si_3N_4 and Si+ Si_3N_4 . As the pressure is decreased to 10^3 Pa a new

phase field of pure Si appears above 1500°C and at an Si/(Si+N) ratio of 1.0. At the same time both the area size of the Si₃N₄ phase field and the maximum deposition temperature are significantly decreased as shown in Figure 4.5b. As the pressure is decreased further to 10 Pa in Figure 4.5c, the area sizes of both Si₃N₄ and Si+Si₃N₄ phase fields are further reduced while the pure Si phase field is considerably expanded into a lower temperature range. In this case the deposition temperature of pure Si is well below 1300°C at Si/(Si+N) ratio of 1.0.

At these three pressures the vertical boundary between the Si₃N₄ and the Si+Si₃N₄ phase fields is essentially unaffected for most of the temperature range with the Si/(Si+N) ratio fixed at 0.43. The deposition efficiency of the Si₃N₄ phase is as high as 100% and is not influenced by the total pressure. However, the deposition efficiency of Si+Si₃N₄ is obviously decreased with the Si/(Si+N) ratio at the low pressure of 10 Pa. The detailed deposition efficiency values for a particular condition are given in the figures.

If the excessive H₂ is added to the SiH₄-NH₃ system, the shape of the CVD

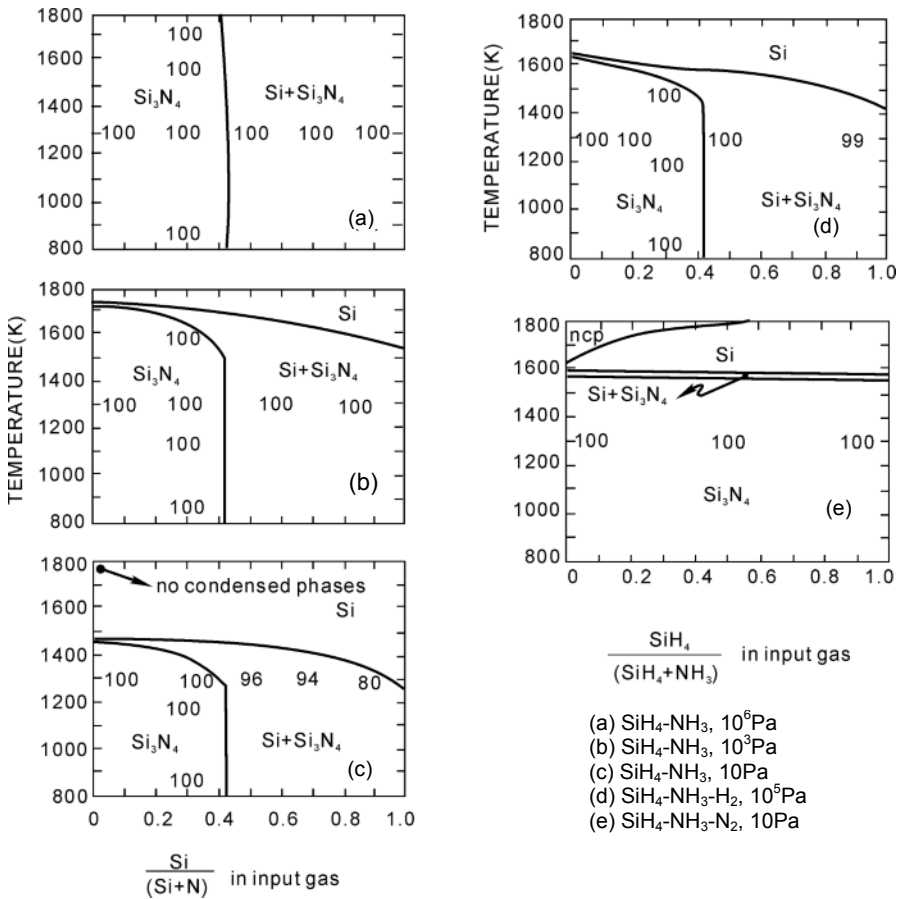


Figure 4.5. CVD phase diagrams for SiH₄-NH₃ system [24]

phase diagram is almost the same as that of the $\text{SiH}_4\text{-NH}_3$ system at a pressure of 10^3 Pa as shown in Figure 4.5d. It is clear that the deposition temperature of the pure Si phase is markedly lowered by the addition of H_2 . Under a pressure of 10 Pa the addition of N_2 to the $\text{SiH}_4\text{-NH}_3$ system results in single-phase Si_3N_4 deposition temperature in an approximate range of 800 to 1560°C regardless of the ratio of $\text{SiH}_4/(\text{SiH}_4\text{-NH}_3)$. One can also find from the diagram that there is another narrow phase field of Si- Si_3N_4 co-deposition located above the pure Si_3N_4 phase field, as shown in Figure 4.5e.

Si-N-Cl System for Silicon Nitride

The CVD phase diagrams of the $\text{SiCl}_4\text{-NH}_3$ system using three pressures are shown in Figure 4.6a–c. The specific deposition efficiency at different conditions is also shown as a number between 2 and 100 in each of the five graphs in Figure 4.6. Compared with the phase diagrams of the $\text{SiH}_4\text{-NH}_3$ system, the $\text{SiCl}_4\text{-NH}_3$ system possesses a much larger phase field area size of pure Si_3N_4 but much lower

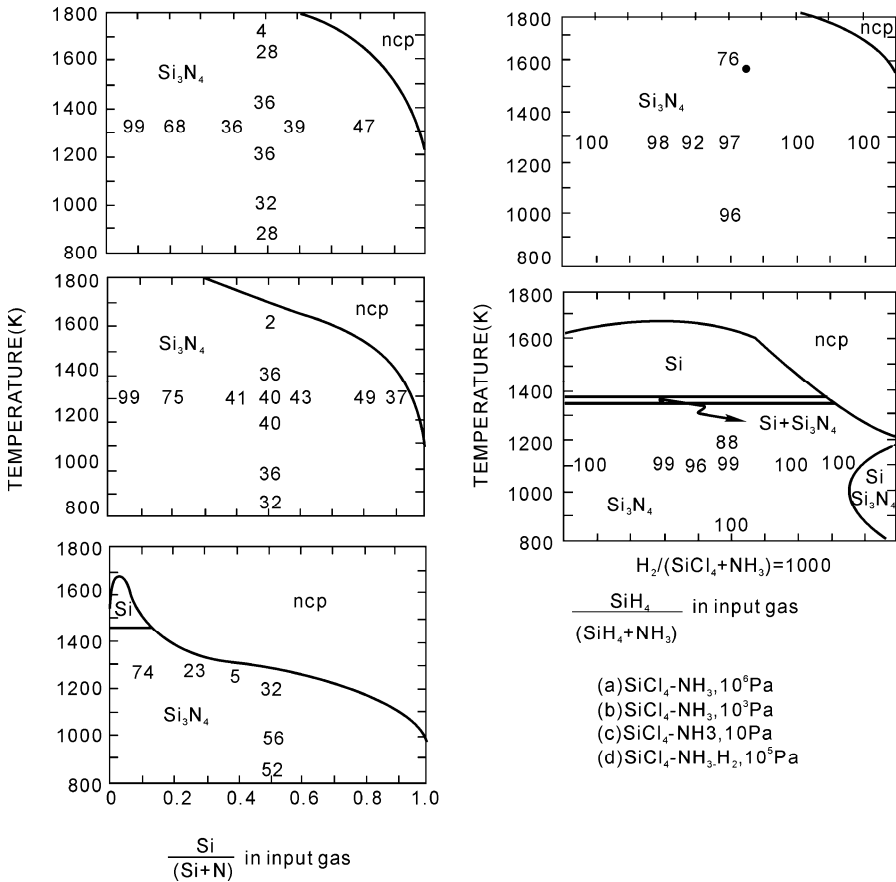


Figure 4.6. CVD phase diagrams for $\text{SiCl}_4\text{-NH}_3$ system [24]

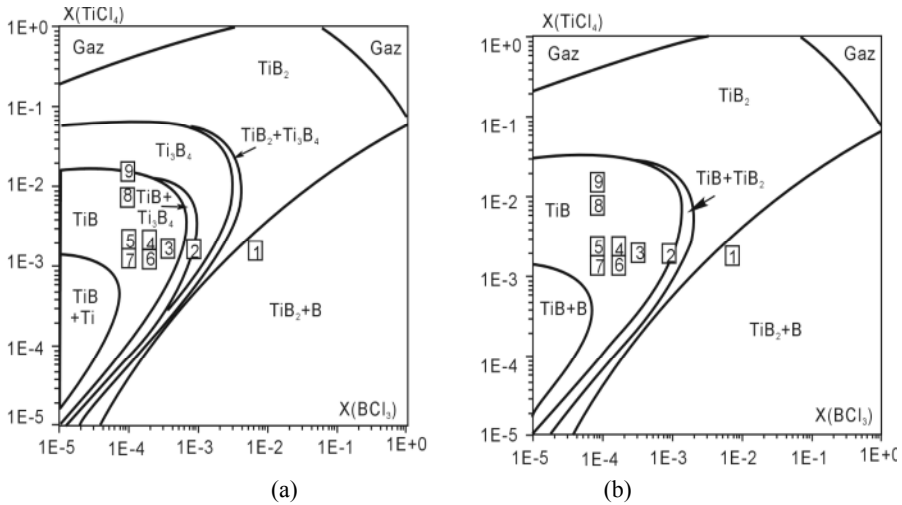


Figure 4.7. CVD phase diagram of $\text{TiCl}_4\text{-BCl}_3$ system [25]: (a) with Ti_3B_4 phase and (b) without Ti_3B_4 phase

deposition efficiency. It can be seen from Figure 4.6a–c, the deposition efficiency ranges from 2 to 99 with majority of the efficiencies falling below 50. This is mainly attributed to the fact that SiCl_4 is much more stable than the reactant gas SiH_4 . However, if H_2 gas is added to the $\text{SiCl}_4\text{-NH}_3$ system, the deposition efficiency is significantly increased. This can be seen from the same deposition efficiency representation in Figure 4.6d–e, which shows a much higher value in the range of 76 to 100 with majority of the values greater than 90. However, the co-deposition of $\text{Si+Si}_3\text{N}_4$ occurs and a new pure Si phase field appears as the pressure decreases.

TiCl₄-BCl₃ System for Titanium Boride

Titanium diboride is an advanced ceramic material with properties similar to those of metals such as high thermal and electrical conductivity. The other distinguishing features of this material are its excellent oxidation resistance and chemical corrosion resistance at elevated temperatures. It can be used as an abrasive and oxidation protection coating as well as the electrode material in aluminium refining. In addition, like other borides it can also be used as a neutron absorber.

The deposition diagram of $\text{TiCl}_4\text{-BCl}_3$ presented in Figure 4.7a is calculated for a CVD process with Ti_3B_4 formed at a temperature of 1500 K. The phase diagram shows seven solid phase fields, namely $\text{TiB}_2\text{+B}$, TiB_2 , $\text{TiB}_2\text{+Ti}_3\text{B}_4$, Ti_3B_4 , $\text{Ti}_3\text{B}_4\text{+TiB}$, TiB and TiB+Ti . At high concentrations of TiCl_4 or TiCl_4 and BCl_3 , there are two gaseous phase fields where no solid deposition takes place because the titanium-and boron-containing species remain dissolved in the gas phase. When the ratio of $\text{BCl}_3/\text{TiCl}_4$ is more than 2, a two-phase field of $\text{TiB}_2\text{+B}$ is generated from the calculation, and the precipitation of boron occurs due to excessive BCl_3 . To the left of the field $\text{TiB}_2\text{+B}$ are five equivalent parallel boundary curves,

defining the six other phase fields. If the ratio of $\text{BCl}_3/\text{TiCl}_4$ is less than 0.001, then partial boundary lines are almost perpendicular to the TiCl_4 axis; hence boundaries between the successive domains are independent of the concentration of BCl_3 in the system. As a consequence, the activity of titanium-containing species is only dependent on the partial pressure of TiCl_4 in H_2 . If Ti_3B_4 is considered to be non-existent as a deposit in this system, Figure 4.7b shows a simplified phase diagram with only five solid phase fields.

$\text{WCl}_4\text{-SiH}_4\text{-H}_2\text{-Ar}$ System for Tungsten Silicide

Refractory metal silicides such as TiSi_2 , TaSi_2 , WSi_2 and MoSi_2 have received considerable attention because of their excellent oxidation resistance at elevated temperatures and their good insulation property due to relatively poor electrical conductivity of polycrystalline silicon (poly-Si). They can be used as an oxidation-resistant coating for carbon/carbon composites, interconnection and gate electrodes in very large-scale integrated circuits.

Figure 4.8 shows six-phase fields of the $\text{WCl}_4\text{-SiH}_4$ system. It is clear that hydrogen has a strong influence on the area size of some phase fields. The area size of four phase fields including W, $\text{W}_5\text{Si}_3\text{+W}$, $\text{W}_5\text{Si}_3\text{+WSi}_2$ and $\text{WSi}_2\text{+Si}$ is much larger than those of the W_5Si_3 and WSi_2 phase fields when there is no hydrogen present. The introduction of the hydrogen partial pressure for the same system has an important consequence: an increased area size of the single-phase deposition domains of WSi_2 and W_5Si_3 and a decreased area size of the W domain. Based on these there is an effective way of changing the resultant solid deposits present in the coating from $\text{W}_5\text{Si}_3\text{+W}$ at point A_1 , to W_5Si_3 at point A_2 and to $\text{W}_5\text{Si}_3\text{+WSi}_2$ at point A_3 as shown in Figure 4.8a–c respectively, for a given concentration in SiH_4 and WCl_4 . From this observation it is interesting to see the significant change of condensed deposits when hydrogen is introduced into the system. This observation can be used as an effective way to modify the deposits to be produced for particular products even with the same level of concentrations of the initial constituents in the system. It can also be seen from the three phase diagrams that the area of the phase field $\text{WSi}_2\text{+Si}$ does not change with the introduction of hydrogen and its pressure change.

$\text{HfCl}_4\text{-BCl}_3\text{-CH}_3\text{SiCl}_3\text{-H}_2$ System for Carbide and Boride Co-deposition

The co-deposited material of $\text{HfB}_2\text{-SiC}$ with a mole ratio of 74% to 26 has shown excellent resistance to oxidation at higher temperatures and thermal shock than their individual constituents alone. Owing to the superior mechanical property of SiC and high oxidation and thermal shock resistances of boride as a result of self-healing behaviour explained in Section 5.6, the $\text{HfB}_2\text{+SiC}$ composite is therefore more suited for high-temperature structural applications.

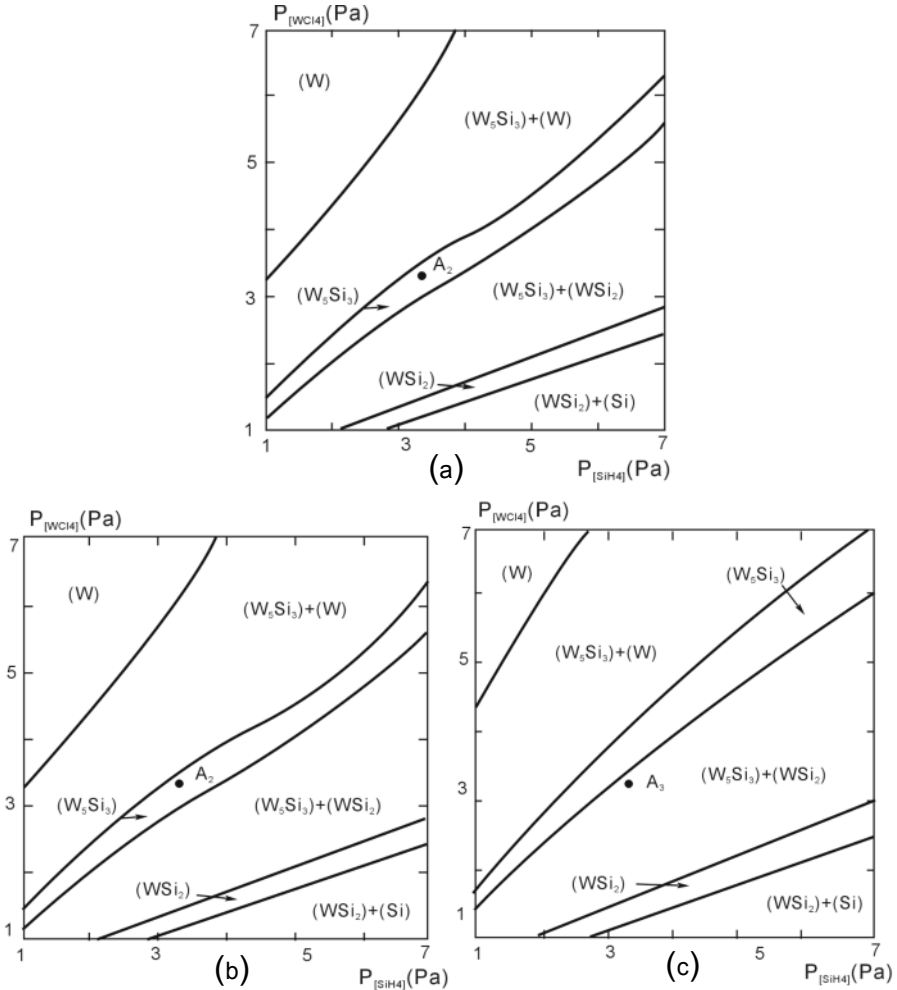


Figure 4.8. CVD phase diagram of WCl_4 - SiH_4 system at 873 K [26]: (a) $P_{tot} = 665$ Pa, $P_{H_2} = 0$ Pa, (b) $P_{tot} = 665$ Pa, $P_{H_2} = 133$ Pa, (c) $P_{tot} = 665$ Pa, $P_{H_2} = 332$ Pa

Figure 4.9a and b shows the solid-phase diagram of the $HfCl_4$ - BCl_3 - CH_3SiCl_3 reactant system at a temperature of 1200 K and a total system pressure of 1 atm. For a particular application the desired CVD region to co-deposit HfB_2 and SiC is located near the MTS corner of the diagram. Using the initial composition ratio (74% HfB_2 and 26% SiC) a simple calculation based on molecule numbers to allow the required co-deposition indicates that point A should be the precursor compositional point, suggesting a chemical composition of 60% BCl_3 , 30% $HfCl_4$ and 10% MTS. From the phase diagram Figure 4.9a, it is clear that point A is not in the HfB_2 +SiC co-deposition phase field. This clearly shows the advantage of using the Gibbs free energy approach to gain insights into the actual chemical reaction and guide the design of a CVD process.

Similar to other phase diagrams, an increase in deposition temperature from 1200 to 1400 K results in shifts of the phase fields as shown in Figure 4.9b and c. When the temperature reaches 1300 K, the HfB_2+SiC phase field shifts to the left side of the diagram, i.e. to lower MTS concentrations. Figure 4.9d shows how the HfB_2+SiC phase field area size becomes smaller and shifts to even lower MTS concentrations, when the temperature increases to 1400 K. Once the temperature is increased to 1600, 1700 and 2000 K respectively, the desired HfB_2+SiC phase field does not exist.

$\text{AlCl}_3\text{-SiCl}_4\text{-CO}_2\text{-H}_2$ System for Mullite

Mullite ($3\text{Al}_2\text{O}_3\cdot 2\text{SiO}_2$) is the only stable solid solution in the $\text{Al}_2\text{O}_3\text{-SiO}_2$ system. It is one of the promising candidate materials for higher-temperature applications because its thermal expansion coefficient is consistent with those of Si_3N_4 and SiC and due to its superior corrosion resistance at high temperatures in oxidising atmosphere. Based on these properties this material can be used as an environment

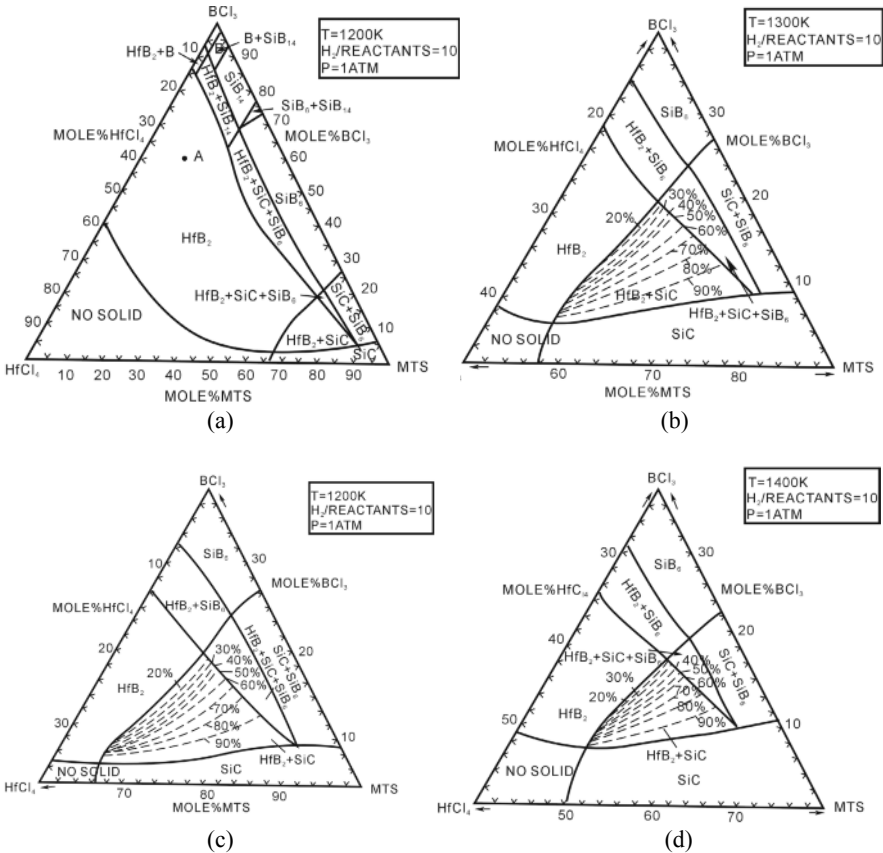


Figure 4.9. CVD phase diagrams of $\text{HfCl}_4\text{-BCl}_3\text{-CH}_3\text{SiCl}_3\text{-H}_2$ system [27]: (a) 1200 K, (b) 1200 K, (c) 1300 K and (d) 1400 K

barrier coating (EBC) for high-temperature components manufactured through CVD processes.

Figure 4.10a shows the CVD phase diagram of the $\text{AlCl}_3\text{-SiCl}_4\text{-CO}_2\text{-H}_2$ system under the following conditions: temperature of 1000°C , total pressure of 75 Torr and $\text{H}_2/(\text{AlCl}_3\text{-SiCl}_4\text{-CO}_2)$ ratio of 5. Pure mullite deposits can only be generated along the boundary line between mullite+ SiO_2 and mullite+ Al_2O_3 phase fields and are always co-deposited with other substances. Along the $\text{AlCl}_3\text{-CO}_2$ line there are three phase fields: mullite+ Al_2O_3 , mullite+ $\text{Al}_2\text{O}_3\text{+C}$ and $\text{Al}_2\text{O}_3\text{+C}$. Along the $\text{SiCl}_4\text{-CO}_2$ line, there are four phase fields: SiO_2 , $\text{SiO}_2\text{+C}$, $\text{SiC+SiO}_2\text{+C}$ and SiC+SiO_2 . The phase fields of the pure oxides (SiO_2 , mullite+ SiO_2 and mullite+ Al_2O_3) are near the CO_2 corner in the diagram. C is co-deposited with some other oxides at the middle concentration of the CO_2 constituent. At the regions of low CO_2 concentration the co-deposition of SiC-oxide takes place. In addition, the phase field area sizes related to SiO_2 are much larger than those related to Al_2O_3 . This is attributed to the fact that the Gibbs free energy of formation of SiO_2 is lower than that of Al_2O_3 .

If the temperature is reduced from 1000 to 800°C , then no mullite deposition occurs and the number of phase fields is increased from 13 to 14, as shown in

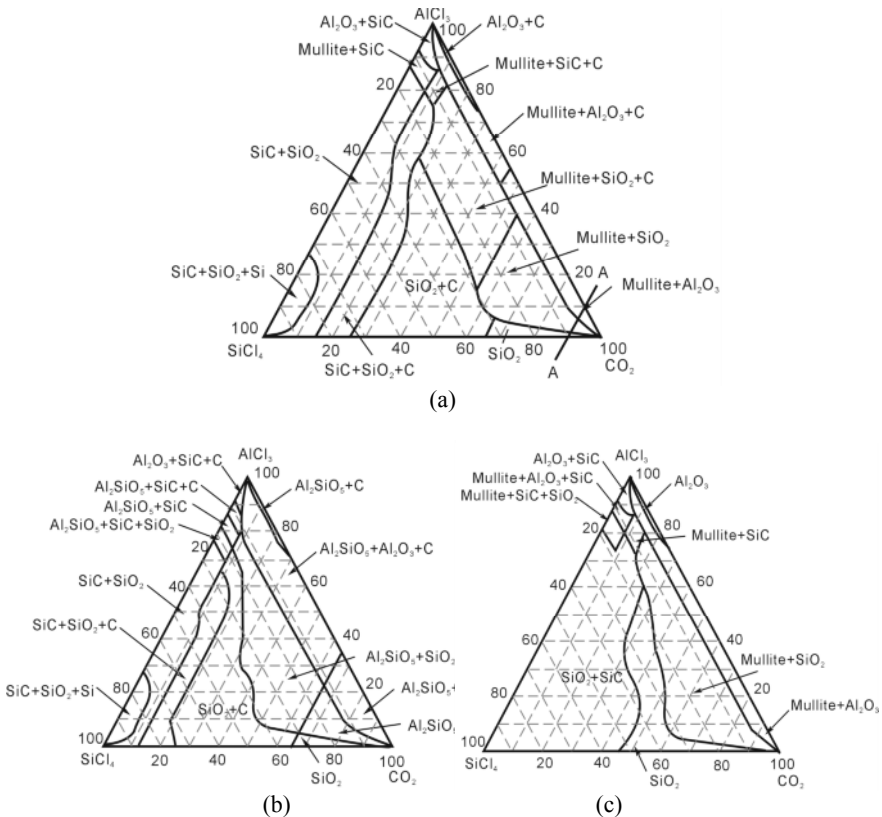


Figure 4.10. CVD phase diagrams of the $\text{AlCl}_3\text{-SiCl}_4\text{-CO}_2\text{-H}_2$ system [28]: (a) 800°C , (b) 1000°C and (c) 1200°C

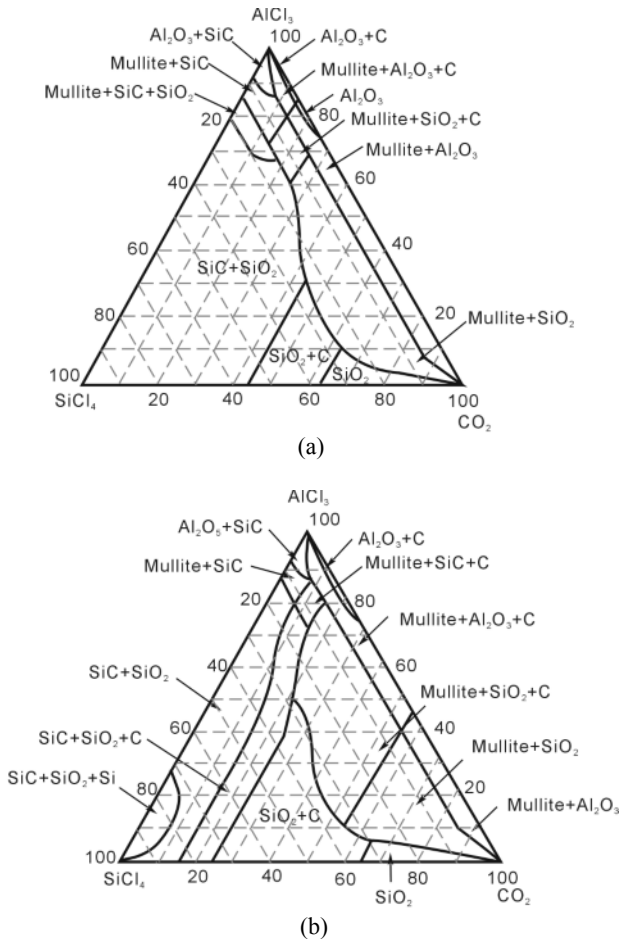


Figure 4.11. CVD phase diagrams of $\text{AlCl}_3\text{-SiCl}_4\text{-CO}_2\text{-H}_2$ system at 1000°C [28]: (a) 2 Torr and (b) 150 Torr

Figure 4.10b. If the temperature is increased from 1000°C to 1200°C , then the number of phase fields decreases from 13 to 9, as shown in Figure 4.10c, but the area sizes of the phase fields related to SiO_2 are further increased and no C deposition takes places. At a temperature of 1000°C the pressure within the reaction system also influences mullite and C in the phase fields. The details of those phase diagrams can be found in Figure 4.11 a and b.

4.3 Kinetics of Chemical Vapour Deposition Process

In a CVD process, there exist a set of complex phenomena which take place both in the gas phase and at the surface of the substrate. These phenomena can generally be divided into the following groups.

4.3.1 Chemical Vapour Deposition Phenomena

4.3.1.1 Gas-phase Phenomena

Homogeneous chemical reactions occur in the bulk gas and within the boundary layer leading to the formation of various intermediates. Reactant gaseous species and intermediates are transported within the boundary layer to the surface of the substrate.

4.3.1.2 Surface Phenomena

The reactant gaseous species and intermediates are adsorbed on the surface of the substrate. First, the adsorbed species migrate to the preferred sites on the surface, then heterogeneous chemical reactions take place to form a solid deposit and to incorporate into the lattice of the substrate.

4.3.1.3 Gas-phase Phenomena

The by-product of the heterogeneous chemical reactions is desorb from the surface of the substrate and transferred out to the boundary layer.

The deposited solid is the final result of all these subprocesses. The rate of the subprocess varies in a wide range. For these sequential reactions or subprocesses the overall deposition rate is controlled by the slowest subprocess. In this section the $\text{CH}_3\text{SiCl}_3\text{-H}_2$ deposition system has been chosen as the system for discussion in both *homogeneous* chemical reactions and *heterogeneous* chemical reactions in order to give a more in-depth understanding of the kinetics of a chosen CVD process.

4.3.2 Homogeneous Chemical Reactions

Homogeneous reactions are defined as chemical reaction taking place completely in the gas phase, whereas heterogeneous reactions occur on a solid surface. Investigations on the homogeneous reactions for a given CVD system are very useful to know the gaseous intermediates generated, as well as the amount and chemistry of these species. On this basis, it is helpful to understand the stoichiometry of the deposits obtained.

Thermodynamic methods can be used to calculate the gaseous species involved in homogeneous reactions. A number of investigations [29, 31] have been conducted on the $\text{CH}_3\text{SiCl}_3\text{-H}_2$ deposition system, focusing on the influence of processing parameters such as temperature, pressure and mol fraction of MTS on the equilibrium compositions of the gaseous species in the gas phase. Papasouliotis and Sotirchos [32] performed a calculation for a $\text{CH}_3\text{SiCl}_3\text{-H}_2$ deposition system, and their work is summarised as follows. The calculations for the gaseous species are listed in Table 4.3. These thermodynamic data (e.g. enthalpy, entropy and standard heat) are mainly obtained from the JANAF thermodynamic tables.

4.3.2.1 Resultant Compounds

Three categories of compounds are considered in the calculations, namely hydrocarbon compounds, chlorine-containing compounds, and silanes and

Table 4.3. Gaseous species considered for the thermodynamic calculations in CH₃SiCl₃-H₂ system [32]

Ar	SiCl	C(g)	CH	C ₃ H ₄	CH ₃ SiH ₃	CH ₃ Cl
H ₂	SiCl ₂	C ₂ (g)	CH ₂	C ₃ H ₄ (py)	(CH ₃) ₂ SiH ₂	CH ₂ Cl ₂
H	SiCl ₃	C ₃ (g)	CH ₃	C ₃ H ₆	(CH ₃) ₃ SiH	CHCl ₃
Cl ₂	SiCl ₄	Si _i (g)	CH ₄	C ₃ H ₈	(CH ₃) ₄ Si	CCl ₄
Cl	SiHCl	Si ₂ (g)	C ₂ H	c-C ₃ H ₆	SiCH ₂	CHCl
HCl	SiHCl ₃	Si ₃ (g)	C ₂ H ₂	c-C ₄ H ₈	SiCH ₃	CCl ₃
SiH	SiH ₂ Cl ₂	SiC(g)	C ₂ H ₃	c-C ₅ H ₈	SiC ₂ H	CCl ₂
SiH ₂	SiH ₃ Cl	Si ₂ C(g)	C ₂ H ₄	c-C ₅ H ₁₀	HSiC ₂ H	CCl
SiH ₃	CH ₃ SiCl ₃	SiC ₂ (g)	C ₂ H ₅	C ₄ H ₁₀	H ₃ SiC ₂ H ₃	C ₂ Cl ₆
SiH ₄	(CH ₃) ₂ SiCl ₂		C ₂ H ₆	C ₅ H ₁₂	H ₂ SiCH ₂	C ₂ Cl ₂
Si ₂ H ₆	(CH ₃) ₃ SiCl			C ₆ H ₁₄	H ₃ SiC ₂ H	
				C ₆ H ₆	H ₂ SiC ₂ H	
				C ₆ H ₅ CH ₃	(CH ₃) ₂ SiH	
				C ₅ H ₉ CH ₃		

organosilicon compounds. The following sections explain the relationship between the control parameters and the resultant species and the key features of each type of compound.

Hydrocarbon Compounds

Figure 4.12 shows the relationship between the equilibrium mol fraction of a gaseous species and the temperature at different pressures. At a pressure of 1 atm methane (CH₄) is the major hydrocarbon species; when the temperature is lower than 1600 K, its amount decreases with a temperature increase. The mol fraction of acetylene (C₂H₂) significantly increases at temperatures below 1400 K until it reaches a maximum value at a temperature of around 1600 K. Four main kinds of hydrocarbon radicals are considered in the present reaction system during the calculations, namely CH₃, C₂H₅, C₂H₃ and CH₂. Among them the amount of methyl radical (CH₃) is much greater than those of the other three kinds of radicals in a temperature range of 1000 to 2000 K, as shown in Figure 4.12a. The CH radical is ignored because of its trace amount (1×10^{-10} at temperatures above 1700 K).

At a reduced pressure of 0.01 atm methane (CH₄) is a dominant hydrocarbon species when the temperature is below 1200 K. Then, acetylene (C₂H₂) becomes dominant when the temperature is increased to 1300 K. It is believed that acetylene is one of the main surface reactive hydrocarbons playing an important role in

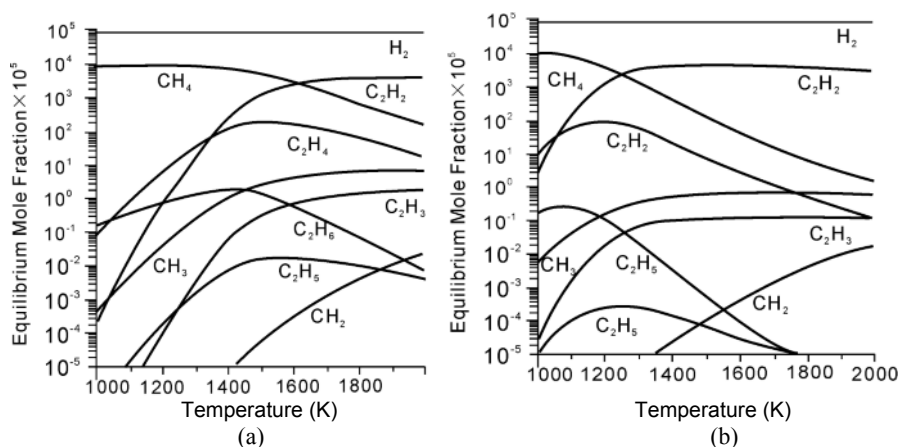


Figure 4.12. Variation of the mol fraction of hydrocarbon species with temperature ($H_2:MTS = 10$) [32]: (a) $P = 1$ atm and (b) $P = 0.01$ atm

carbon deposition. In this lower-pressure case (0.01 atm), the amount of methyl radical (CH_3) is one order of magnitude lower than that at a pressure of 1.0 atm.

Chlorine Containing Compounds

Figure 4.13a depicts the relationships between equilibrium mol fractions of the major silicon and chlorine-containing species with temperature under 1 atm pressure. Both theoretical calculations and experimental studies show that at temperatures below 1200 K, the mol fractions of the stable silicon chloride species ($SiHCl_3$, $SiCl_4$ and SiH_2Cl_2) are higher than those of the radicals ($SiCl_2$, $SiCl_3$). The amount of these stable silicon chloride species decreases with increasing temperature. The radicals of $SiCl_2$ and $SiCl_3$ become the main silicon-containing compounds above 1400 K.

It is also interesting to note that, as illustrated in Figure 4.13a, hydrogen chloride (HCl) and $SiCl_2$ curves are very close to each other with occasional overlapping over the entire temperature range. This indicates that HCl is another major chlorine-containing species. It is well understood by both theoretical and experimental investigations that HCl has a suppressing effect on SiC deposition, as explained in Section 4.3.4.

When the pressure is decreased to 0.01 atm, a graph similar to that shown in Figure 4.13b can be generated. Comparing Figure 4.13a and b it is clear that these two relationship diagrams have similar trends caused by the temperature, but with different profiles and equilibrium model fractions. An important variation is the rapid decrease of the radical ($SiCl_3$) and the stable molecule species ($SiHCl_3$, $SiCl_4$, SiH_2Cl_2 and MTS) when the temperature increases above 1400 K.

Silanes and Organosilicon Compounds

The mol fractions of stable silanes (SiH_4) and silane radicals ($SiHCl$, SiH) at a pressure of 1 atm and 0.01 atm are shown in Figure 4.14a and b respectively. For

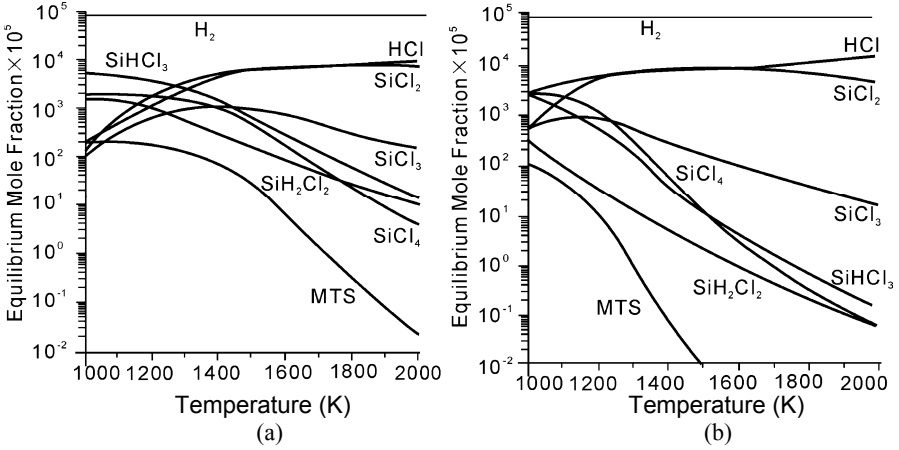


Figure 4.13. Variation of the mol fraction of Si and Cl species with temperature ($H_2:MTS = 10$) [32]: (a) $P = 1$ atm and (b) $P = 0.01$ atm

Figure 4.14 (a), when the temperature is below 1200 K, SiH_4 is the dominant silane species. As temperature increases the mol fractions of the radicals ($SiHCl$, SiH) also increase rapidly as two main species. The equilibrium mol fraction of Si_2H_6 is extremely low and can be ignored in this reaction.

Organosilicon compounds such as $SiCH_2$ radical and Si_2C also exist in this reaction, as shown in Figure 4.14 (a) and (b). The $SiCH_2$ mole fraction increases rapidly with a peak value of 4×10^{-4} at 2000 K when the temperature increases. Similarly, the Si_2C compound exists in slightly larger quantities compared with $SiCH_2$. The influence of temperature on its mol fraction is almost the same as that on $SiCH_2$. The mol fraction of the $SiCH_2$ compound is significantly lower than those of the silicon chloride radicals and acetylene over the entire range of

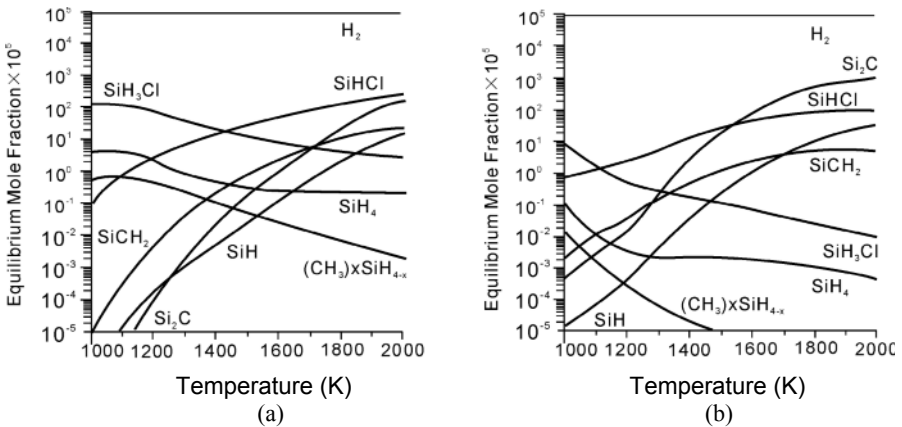


Figure 4.14. Variation of mol fraction of silanes and organosilicon compounds with temperature ($H_2:MTS = 10$) [32]: (a) $P = 1$ atm and (b) $P = 0.01$ atm

Table 4.4. Bonding energy between gaseous molecules [23]

Bond	H-H	Cl-H	Si-Cl	C-C	C-H	C-Cl	Si-H	C-Si	Cl-Cl	Si-Si
Bond energy (kJ·mol ⁻¹)	436	432	359	348	338	329	318	290	243	17

temperature, pressure and composition conditions examined. This indicates that the contribution of this compound to the deposition process can be ignored since, even though its surface reactivity is high, its mol fraction is too low.

Comparing chlorine-containing compounds and silanes and organosilicon compounds shown in Figure 4.14 and Figure 4.13, the mol fractions of stable silanes (SiH₄) and silane radicals (SiHCl, SiH), shown in Figure 4.14a and b at different pressures, are three to four orders of magnitude lower than those of the silicon chlorides (SiCl₂, SiCl₃) shown in Figure 4.13a and b. This indicates that the contributions of silanes and organosilicon compounds to the CVD process are very limited, even though their surface reactivities are high.

4.3.2.2 Chemical Reaction Mechanism

Bonding energies are used to define the degree of linking between chemical elements. Table 4.4 lists the bonding energy between some common elements. For the CH₃SiCl₃ reactant precursor there are three types of Si-C, C-H and Si-Cl bonds corresponding to the bonding energy of 290 kJ·mol⁻¹, 338 kJ·mol⁻¹ and 359 kJ·mol⁻¹ respectively. It is believed that the fission of the weakest Si-C bond is the main pathway for the decomposition of CH₃SiCl₃. Consequently, it is normal that the reactant species do not carry carbon and silicon simultaneously.

As listed in Table 4.5, homogeneous chemical reactions are initiated by the decomposition of CH₃SiCl₃ into radicals of CH₃ and SiCl₃ through the R1 reaction. Then, many chemical reactions take place to form a number of gaseous species containing Si, C, Cl, etc. From the reactions of R2, R5, R6, R9, R11, R13, R15 and R20, H₂ and its radical H are two important reactant species. HCl is formed through the R3 reaction. As indicated in the R4 reaction, HCl can react with SiCl₃ to form more stable SiCl₄ gaseous species because the Gibbs free energy of SiCl₄ is more negative than that of HCl, as indicated in Figure 4.2. The stable CH₄ gaseous species is generated through the reaction of R6 from the CH₃ radical and H₂. It is noted that the radicals play a very important role in the decomposition of the gaseous phase and in the generation of the intermediates. These radicals include H, CH₃, CH₂, C₂H₃, C₂H₅, SiCl₂, SiCl₃, etc. In the proposed mechanism by Papasouliotis and Sotirchos [32] several different reactions, such as R1, R7, R23 and R24, occur in parallel and lead to the generation of the main hydrocarbons (CH₃) in the CH₃SiCl₃-H₂ system. The SiCl₂ and CH₂ radicals are generated by the reactions of R3 and R20 respectively.

Table 4.5. Homogeneous chemical reactions in CH₃SiCl₃-H₂ system [32]

No	Reaction	No	Reaction
R1	CH ₃ SiCl ₃ =SiCl ₃ +CH ₃	R13	C ₂ H ₃ +H=C ₂ H ₂ +H ₂
R2	SiCl ₃ +H ₂ =SiHCl ₃ +H	R14	CH ₃ +CH ₃ =C ₂ H ₅ + H
R3	SiHCl ₃ =SiCl ₂ +HCl	R15	C ₂ H ₅ +H=C ₂ H ₄ + H ₂
R4	SiCl ₃ +HCl=SiCl ₄ +H	R16	C ₂ H ₆ +CH ₃ = C ₂ H ₅ +CH ₄
R5	H ₂ +M=2H+M	R17	C ₂ H ₄ +M= C ₂ H ₂ + H ₂ +M
R6	CH ₃ +H ₂ =CH ₄ +H	R18	C ₂ H ₄ +M= C ₂ H ₃ +H+M
R7	CH ₄ +M=CH ₃ +H+M	R19	C ₂ H ₄ + C ₂ H ₄ = C ₂ H ₅ + C ₂ H ₃
R8	CH ₃ +CH ₃ =C ₂ H ₆	R20	CH ₃ +H=CH ₂ + H ₂
R9	C ₂ H ₆ +H=C ₂ H ₅ +H ₂	R21	CH ₂ +CH ₃ = C ₂ H ₄ +H
R10	C ₂ H ₅ +M=C ₂ H ₄ +H+M	R22	CH ₂ +CH ₂ = C ₂ H ₂ +H+H
R11	C ₂ H ₄ +H=C ₂ H ₃ +H ₂	R23	CH ₂ +CH ₂ =C ₂ H ₂ +H+H
R12	C ₂ H ₃ +M=C ₂ H ₂ +H+M	R24	CH ₂ +CH ₄ =CH ₃ +CH ₃

This theoretical mechanism has been validated by experimental observation. By using a mass spectrometer, both the decomposition of CH₃SiCl₃ and the formation of by-product species can be observed and identified. As shown in Figure 4.15, the values of 16, 36, and 170 of the mass-to-charge ratio (m/z) correspond to CH₄, HCl and SiCl₄ respectively. The free radical of CH₃ is clearly detected.

Free radicals, or radicals, are defined as atomic or molecular species with unpaired electrons on an otherwise open shell configuration. Because a radical has a half-filled orbital, it easily sucks up an electron from another bond, hence exhibiting highly reactive properties and therefore likely to take part in chemical reactions. The first organic free radical is the triphenylmethyl radical, which was identified by Moses Gomberg in 1900 [34]. Radicals play an important role in chemical processes such as combustion, atmospheric chemistry, polymerisation, plasma chemistry, biochemistry, etc. [35].

In some cases radicals can exert a profound effect on chemical reaction kinetics even if their concentration is very low. When a radical interacts with a saturated molecule, the result must contain some species with another radical. This new radical is free to react again. Accordingly, a single radical may initiate a chain of thousands of reactions before it is finally consumed. If the reaction is exothermic, an explosion usually occurs through the formation of radicals. Once a chain reaction is initiated by the radicals, the rate of the subsequent steps is not very dependent on temperature. The reason is that the radicals are so reactive that just a little or no activation energy is required for further reactions. Some examples include the explosion of H₂-O₂, H₂-Cl₂ and SiH₄-O₂. In CVD processes the pyrolysis of the organic parts or organometallic precursors often takes place through radical reactions.

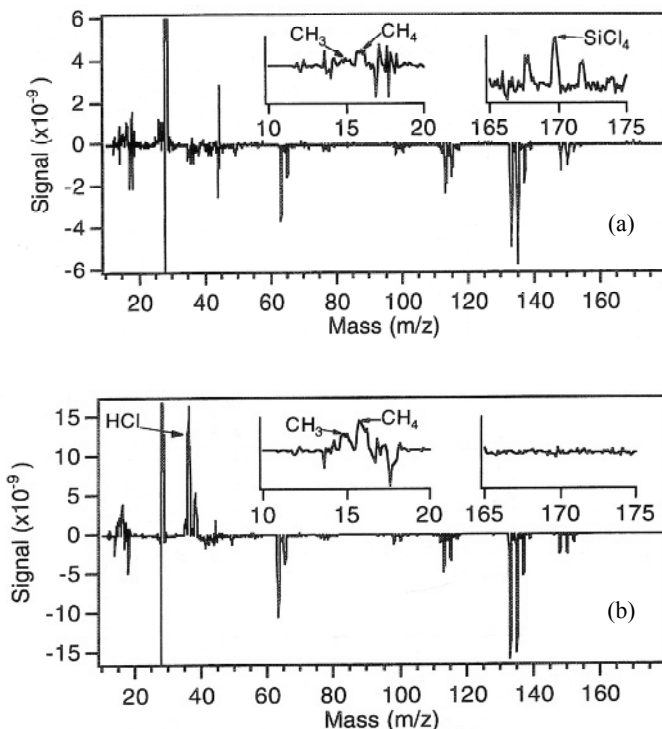


Figure 4.15. Subtracted spectrum of CH_3SiCl_3 decomposition in (a) helium and (b) hydrogen for 58 ms residence time at 1263 K [33]

4.3.3 Heterogeneous Chemical Reactions

Heterogeneous chemical reactions take place on the surface of a substrate and eventually form solid deposits. These reactions are even more complex than those of homogeneous chemical reactions. This section briefly describes the commonly found reactions; the following heterogeneous reactions are reported in the literature and are listed in Table 4.6. These reactions can be divided into three groups: (1) adsorption reactions including SR1, SR2, SR3, SR5 and SR7; (2) reactions occurring between the gaseous species and the surface, such as SR4, SR6 and SR8; (3) solid deposition reactions including SR9, SR10 and SR11. SiC is deposited through SR11 and SR12. In some cases excess C and Si co-deposit with SiC , which correspond to reaction SR9 and SR10 respectively. It is reported that the sticking coefficients for methane and tetrachlorosilane are significantly lower (by more than two orders of magnitude) than those of the other gases [36, 37]. Because these two species (methane and tetrachlorosilane) have very low sticking coefficients on the surface of the substrate, they are assumed not to participate in any deposition reaction. Methyltrichlorosilane is excluded in the deposition reaction because its gas-phase fission takes place almost instantaneously.

Table 4.6. Heterogeneous chemical reactions in MTS-H₂ system [30]

No	Reaction
SR1	$\text{SiCl}_2 + [\text{S}] = [\text{SiCl}_2]_s$
SR2	$\text{C}_2\text{H}_3 + 2[\text{S}] = 2[\text{CH}]_s$
SR3	$\text{C}_2\text{H}_4 + [\text{S}] = 2[\text{CH}_2]_s$
SR4	$[\text{CH}] + \text{H} = [\text{CH}_2]_s$
SR5	$\text{CH}_3 + [\text{S}] = [\text{CH}_3]_s$
SR6	$[\text{CH}_3] + \text{H} = [\text{CH}_2]_s + \text{H}_2$
SR7	$\text{SiCl}_3 + [\text{S}] = [\text{SiCl}_3]_s$
SR8	$[\text{SiCl}_3]_s + \text{H} = [\text{SiCl}_2]_s + \text{HCl}$
SR9	$[\text{CH}_2]_s + \text{H}_2 = \text{C} + 2\text{H}_2$
SR10	$[\text{SiCl}_2]_s + \text{H}_2 = \text{Si} + 2\text{HCl}$
SR11	$[\text{CH}_2]_s + [\text{SiCl}_2]_s = \text{SiC} + 2\text{HCl}$
SR12	$[\text{CH}_3]_s + [\text{SiCl}_3]_s = \text{SiC} + 3\text{HCl}$

4.3.4 Surface Kinetics of Chemical Reactions

Whilst heterogeneous chemical reactions explain a CVD process from a chemical reaction point of view, it is also important to investigate the deposition process from the viewpoint of substrate surface to know how the deposits are formed. Surface reactions of a CVD process usually include the following steps: adsorption of reactant species, decomposition reactions on the surface (heterogeneous reaction), surface migration, incorporation into the lattice of deposited solid species and desorption of by-product gaseous species. Because there are many phenomena involved in a CVD process it is very difficult to extract the features for a single phenomenon from experiments. A simple and common approach is to quantify adsorption and subsequent heterogeneous reactions based on the isotherm adsorption theory, which was first derived by Langmuir in 1918 [38, 39]. This theory is still widely used as the basic theory for the analysis of a CVD process.

The Langmuir model is based on the following assumptions. The large substrate surface can be treated as a finite number of surface sites (N) where gaseous species can be adsorbed. A ratio of the number of sites with gaseous species attached to the total number of sites for adsorption is defined as the surface coverage (θ). The adsorption enthalpy of each site is assumed to be the same for all sites and independent of surface coverage. The adsorbed species do not interact with the other adsorbed species. The adsorption rate (u_{ads}) from the gas phase to the solid surface is proportional to the partial pressure of the gaseous species and the number of vacant sites. The desorption rate (u_{des}) is proportional to the occupied surface sites.

Thus, the following relationship can be established to define the above parameters:

$$u_{ads} = k_{ads}(1 - \Theta)NP \quad (4.17)$$

$$u_{des} = k_{des}\Theta N \quad (4.18)$$

where k_{ads} and k_{des} are the constants for adsorption and desorption respectively.

At equilibrium conditions the number of atoms adsorbed is equal to those desorbed on the substrate. Then the following balance equation can be obtained:

$$k_{ads}(1 - \Theta)NP = k_{des}\Theta N \quad (4.19)$$

The adsorption isotherm for the chemisorbed species, i.e. the equation relating the fraction of occupied sites to the partial pressure in the vapour, p_i , at a fixed temperature, may be written in terms of the rate constants for adsorption and desorption, k_{ads} and k_{des} respectively. Then the Langmuir isotherm adsorption equation can be rewritten as

$$\Theta_i = k_{ads} p_i / (k_{des} + k_{ads} p_i) \quad (4.20)$$

Or it can be simplified as:

$$\Theta_i = k p_i / (1 + k p_i) \quad (4.21)$$

where k is a surface equilibrium constant and equal to the ratio of k_{ads}/k_{des} .

Figure 4.16 shows the relationship between coverage and pressure. If $\Theta_i \ll 1$, i.e. at low surface coverage or with a small adsorption constant (k_{ads}), there is a linear relationship between the coverage and the partial pressure. By contrast, the coverage nearly approaches unity in the case of a high partial pressure or a large adsorption constant. In the intermediate range, the coverage is termed the Freundlich isotherm adsorption and is given by the following equation:

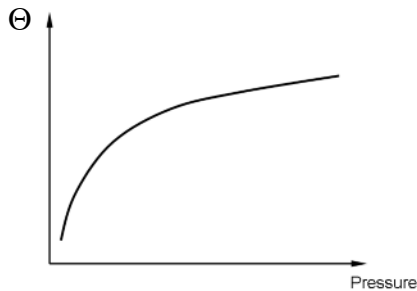


Figure 4.16. Relationship between coverage and pressure

$$\Theta_i = bp_i^{1/n} \quad (4.22)$$

Since chemical adsorption is an exothermic process, the surface coverage decreases with an increase in temperature. The rate of a heterogeneous reaction is proportional to the coverage. As a result the reaction can be treated as a first-order reaction for weakly adsorbed gaseous species. For the strongly adsorbed cases the reaction is the zeroth order because the reaction rate is independent of the partial pressure. For the intermediate case the reaction rate may be a fraction.

The temperature dependence of a heterogeneous reaction is much more complex than that of a homogeneous reaction. For a homogeneous reaction its activation energy can be directly calculated from a plot of reaction rate and temperature, i.e. $\log r - 1/T$ curve. However, the activation energy (E^*) of a heterogeneous reaction is expressed by

$$E^* = E_s^* - \Delta H_{ads} \quad (4.23)$$

where E_s^* is the activation energy of the surface reaction and ΔH_{ads} is the adsorption heat.

When two potential adsorbates, A and B, compete for the same surface sites and both are treated using the Langmuir isotherm, then

$$\Theta_A = k_A p_A / (1 + k_A p_A + k_B p_B) \quad (4.24)$$

and

$$\Theta_B = k_B p_B / (1 + k_A p_A + k_B p_B) \quad (4.25)$$

where Θ_A and Θ_B are the surface coverage of species A and B, p_A and p_B are the partial pressures of species A and B, and k_A and k_B are their corresponding surface equilibrium constants respectively.

These two equations can be used to determine which gas species is to be finally attached to the surface of the substrate, and the one with a higher Θ becomes adsorbates attached to the surface. The reaction rate (k_g) is proportional to the surface coverage for the anion and cation species:

$$r_g = k_{AB} \Theta_A \Theta_B \quad (4.26)$$

For SiC deposition from CH_3SiCl_3 , the adsorption processes are competitive: adsorption of H and SiCl_3 on the C site, as well as Cl and CH_3 on the Si site of the SiC crystal structure. This leads to the general equation of the Langmuir–Hinshelwood isotherm adsorption equation [3]:

$$r_g = k_{AB} k_A p_A k_B p_B / (1 + k_A p_A + k_B p_B)^2 \quad (4.27)$$

The following example illustrates the above competition phenomenon, in which CH_3 can be largely adsorbed on the Si site and SiCl_3 on the C site.

HCl has a bonding energy of $432 \text{ kJ}\cdot\text{mol}^{-1}$, hence it is very difficult to decompose into H and Cl radicals. Nevertheless, absorption between H on C surface atoms and Cl and Si is very easy. This causes competition of absorption to Si by CH_3 and Cl radicals. Similarly, SiCl_3 and H radicals compete for absorption to C. The inhibition effect of HCl on the deposition of a CVD β -SiC process was confirmed by experimental studies [40].

Figure 4.17 shows the deposition kinetics of the $\text{CH}_3\text{SiCl}_3\text{-H}_2$ reaction system. If $\alpha = 3$, then the growth rate almost linearly increases with a pressure increase at temperature of 900°C . A similar trend occurs at a deposition temperature of 1000°C below a critical pressure of 17.5 kPa, then the growth rate becomes constant with pressure increases. This critical pressure is usually considered the saturation pressure for the reactant species. If $\alpha = 5$, there is a linear relationship between the growth rate and the pressure at temperature of 825°C . At temperature of 925°C the profile can be divided into three segments: a steep increase below 4 kPa, a near constant in pressure range of 4 to 10 kPa, then a gentle slope above 10 kPa. The deposition results obtained at 1025°C are much more complex. The growth rate increases below a pressure of 4 kPa, then decreases between 5 and 15 kPa and is nearly constant above 15 kPa. $\alpha = 10$, the pressure dependence of the growth rate becomes much more complex. However, for all temperatures with all α values of CVD processes the growth rate always linearly increases with an increase in pressure below 4 kPa.

Under relatively low pressure, the deposition kinetics of the $\text{CH}_3\text{SiCl}_3\text{-H}_2$ system was systematically investigated by Sones *et al* [42], and their experimental

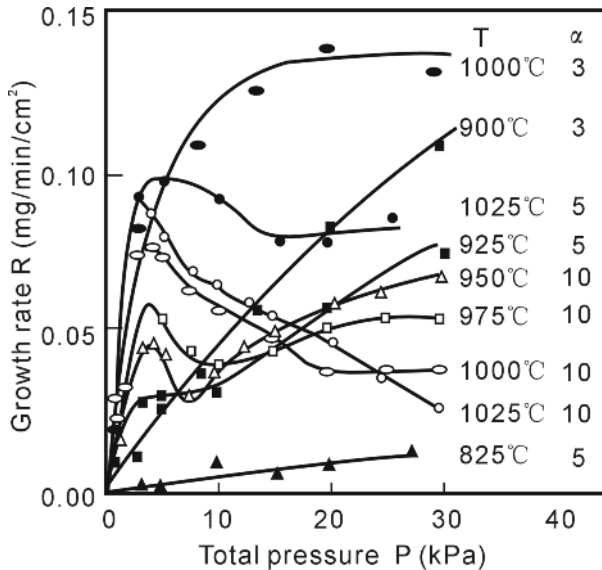


Figure 4.17. Relationship between the growth rate of CVD SiC and the total pressure [41]

results are shown in Figure 4.18. As the temperature increases the growth rate of CVD SiC also increases. The temperature dependence of the growth rate at a low pressure ($p_{MTS} = 0.8$ kPa) becomes less strong than that at high pressure ($p_{MTS} = 4.1$ kPa). In all cases, at different deposition pressures, the curves show a common feature; each curve is composed of two segments of lines joined at a critical temperature around 1570 to 1600 K. Below this critical temperature the growth rate is strongly dependent on temperature and the activation energy is $44.7 \text{ kcal}\cdot\text{mol}^{-1}$ at an MTS partial pressure of 0.08 kPa. This dependence becomes weak and the activation energy decreases to $39.2 \text{ kcal}\cdot\text{mol}^{-1}$ at the same MTS partial pressure when the temperature is higher than 1550 K. This implies that SiC deposition is responsible for different controlling mechanisms at different deposition temperatures.

4.3.5 General Description of Chemical Vapour Deposition Growth Kinetics

In a CVD process, a number of sequential steps are followed, namely mass transport from the bulk gas to the substrate surface, gaseous species absorption and migration on the substrate surface, heterogeneous chemical reaction, lattice incorporation of deposited solid, desorption of by-products and so forth. It is widely recognised that both mass transport and surface reactions play the most important roles in the growth rate of the deposit. If the processing temperature is very high the thermodynamics of the precursor reaction system becomes the third controlling factor. The kinetics of the CVD coating growth is usually represented

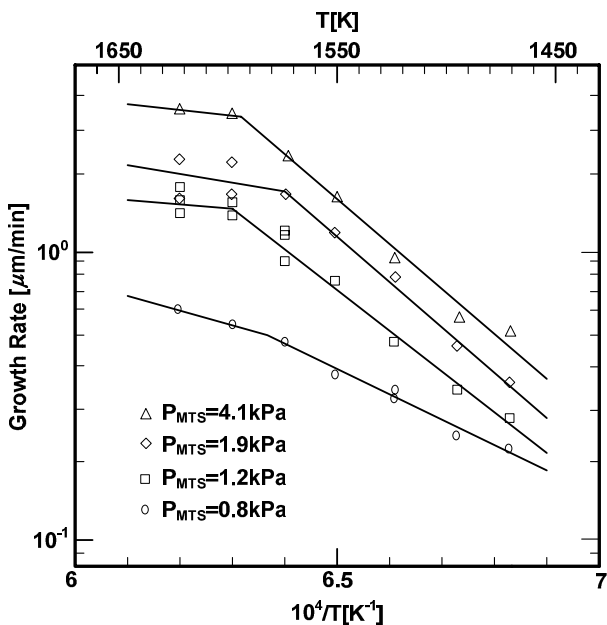


Figure 4.18. Plots of SiC growth rate and temperature of $\text{CH}_3\text{SiCl}_3\text{-H}_2$ system [42]

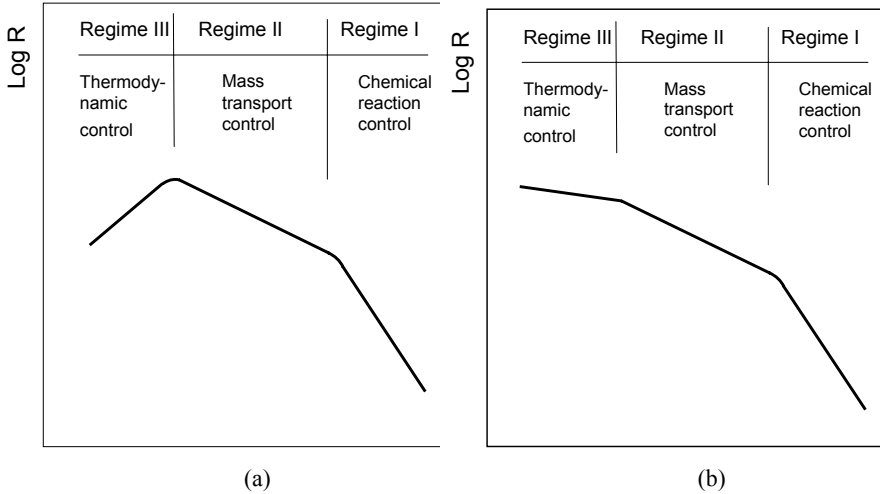


Figure 4.19. Temperature dependence of the deposition rate [43]: (a) exothermic reaction and (b) endothermic reaction

by an Arrhenius plot which shows the relationship between the growth rate and the deposition temperature. As shown in Figure 4.19 the growth kinetics can be distinctly divided into three regimes controlled by chemical surface reaction, mass transfer and thermodynamics respectively.

To understand the temperature dependence of the growth rate Grove [44] proposed a simple model as shown in Figure 4.20. In this model it is assumed that the mass transport of the reactant gaseous species across the boundary layer only depends on the mass diffusion. As a result there is a concentration gradient of the gaseous species. The flux (F_1) of mass transport from the gas phase to the substrate surface is written as [45]

$$F_1 = h_G(C_G - C_S) \quad (4.28)$$

where C_G and C_S are the concentration of reactant gaseous species in the bulk gas phase and at the surface of the substrate respectively. h_G is defined as the mass transfer rate constant and given by

$$h_G = \frac{D}{\delta} \quad (4.29)$$

where D is the diffusion coefficient for the reactant gaseous species and δ is the thickness of the concentration boundary layer.

Assuming that the order of the chemical reaction is one, the flux (F_2) of the reactant gaseous species consumed on the substrate surface through the heterogeneous reactions is represented by

$$F_2 = k_S C_S \quad (4.30)$$

where k_S is the heterogeneous reaction rate constant.

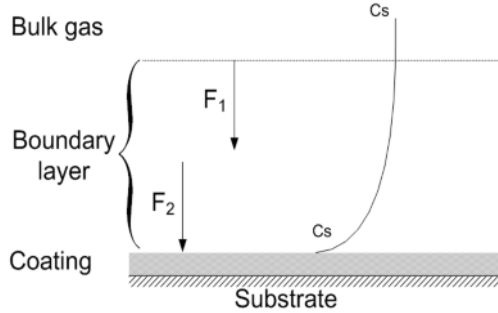


Figure 4.20. Schematic of growth process model [44]

Under steady conditions the flux of reactant gaseous species from the bulk of gas to the surface of the substrate is equal to the flux of the reactant gas consumed on the substrate surface, i.e. $F_1 = F_2$. Then the relationship between C_G and C_S is obtained as

$$C_S = \frac{C_G}{1 + k_S/h_G} \quad (4.31)$$

Regime I: Chemical Reaction Limiting Regime

This regime, shown in Figure 4.19, takes place at relatively low temperatures. It implies that the chemical reaction rate is much lower than that of mass transport, which can be described by $k_S \ll h_G$. In such a case the reactant gaseous species can be sufficiently transported from the bulk gas to the substrate surface. Hence, there exists no concentration gradient in the boundary layer, i.e. $C_G = C_S$. The growth rate (r) of the CVD coating can be expressed by

$$r \sim k_S C_G \quad (4.32)$$

The growth rate significantly increases with a temperature increase because the chemical reaction rate constant (k_S) has a strong dependence on temperature. The thickness of the CVD coatings is relatively uniform since the supply of the reactant gaseous species to the substrate surface is sufficient for consumption through chemical reactions. Accordingly, this regime is usually operated by many CVD processes for coatings and an isothermal/isobaric CVI process for fibre-reinforced ceramic-matrix composites.

Regime II: Mass Transport Limiting Regime

This regime appears at moderate temperatures. Compared with the chemical reaction regime the mass transport rate of the reactant gaseous species is much

lower than that of the chemical reaction, i.e. $h_G \ll k_S$. The coating growth is limited by the mass transport from the bulk gas to the substrate surface. In this case a steep concentration gradient within the boundary layer is generated and the reactant gaseous species are nearly consumed on the substrate surface. The growth rate of the coating is given by

$$r \sim h_G C_G \quad (4.33)$$

Based on fluid mechanics, the thickness of the concentration boundary layer (δ_c) is linked with the Schmidt number and expressed by:

$$\delta_c = a \sqrt{\frac{\mu x}{\rho u}} \quad (4.34)$$

where a is a constant, u , μ and ρ are respectively the velocity, dynamic viscosity and density of the gaseous species, and x is the distance from the leading edge of the substrate.

Combining Equations (4.28), (4.32) with (4.33), the growth rate is expressed as

$$r \sim \frac{DC_G}{\delta} \sim u^{1/2} T^m \frac{p_{react}}{P} \quad (4.35)$$

where p_{react} is the partial pressure of the reactant gaseous species and is proportional to the concentration in the bulk gas (C_G).

In this regime, the temperature dependence of the growth rate becomes mild, which is attributed to the gaseous species diffusivity. The growth rate of the coating increases linearly with the partial pressure increase of the reactant gaseous species (p_{react}), which is confirmed through experimental work as shown in Figure 4.19. The growth rate is inversely proportional to the total pressure in the system. The mass transport rate can be considerably enhanced through a decrease in the total pressure. This is the main reason that most CVD processes are operated at reduced pressures. An increase in the gas velocity in the bulk is useful to reduce the thickness of the boundary layer and, hence, results in a more rapid growth rate of coatings.

For the growth of monolithic materials the high growth rate is much more important than the thickness uniformity from an economical view. The CVD processes are often performed in the mass transport regime. The higher processing temperatures are used for thermal gradient CVI and forced CVI processes in which fast growth rates are needed to ensure the rapid densification of the composites. Further details are discussed in Chapter 5.

Regime III: Thermodynamics Limiting Regime

If the temperature is further increased, the CVD process is controlled by thermodynamics rather than kinetics factors. This regime is divided into two situations as follows.

When the deposition reaction is exothermic ($\Delta H < 0$), the Gibbs free energy (ΔG) becomes less negative as the temperature increases. Therefore, the growth

rate of the coating decreases because the driving force, in terms of ΔG , becomes weaker. It is worth noting that the activity of the species is also considerably enhanced on the substrate surface to form a single crystal. Epitaxial growth, such as GaAs deposition from the Ga-AsCl₃-H₂ system [46, 47], usually occurs in this regime. If the Gibbs energy becomes positive at extreme highly temperatures, the reversible reaction of the deposition process takes place. Hence, the substrate would be etched by the reactant. This etching reaction has been confirmed by the following experimental results. TiB₂ is etched at a high temperature by the reactant gas TiCl₄ and the by-product gas HCl and Si is etched by HCl [48].

When the deposition reaction is endothermic ($\Delta H > 0$), the Gibbs free energy is more negative as the temperature increases. In this case the homogeneous reactions are also significantly enhanced, hence resulting in the formation of powder in the gas phase instead of coating on the substrate surface.

References

- [1] Hunt LP (1987) Thermodynamic equilibria in the Si-H-Cl and Si-H-Br systems. In: Cullen GW (ed) Proceedings of the 10th international conference on chemical vapour deposition, Honolulu, HI. Electrochemical Society, Pennington, NJ, pp112–121
- [2] Hunt LP (1990) Silicon precursors: their manufacture and properties. In: O'Mara WC, Herring RB, Hunt LP (eds) Handbook of semiconductor silicon technology. Noyes, Park Ridge, NJ, pp1–33
- [3] Atkins P, Paula J de (2006) Atkins' physical chemistry, 8th edn. Oxford University Press, Oxford
- [4] Hassell CA, Stasko DJ (2007) Chemistry: principles, patterns and applications. Pearson Education, San Francisco
- [5] Mills KC (1974) Thermodynamic data for inorganic sulphides, selenides and tellurides. Butterworths, London
- [6] Kubaschewski O, Alcock CB (1979) Metallurgical thermochemistry, 5th edn. Pergamon, Oxford
- [7] Stull DR, Prophet H (1986) JANAF Thermochemical Tables, 3rd edn. Parts I and II, American Institute of Physics, U.S. Government Printing Office, Washington, DC
- [8] Pedley JB, Naylor RD, Kirby SP (1986) Thermochemical data of organic compounds, 2nd edn. Chapman & Hall, London
- [9] Gurvich LV, Veyts IV, Alcock CB (eds) (1989) Thermodynamic properties of individual substances, 4th edn. Hemisphere, New York
- [10] Knacke O, Kubaschewski O, Hesselmann K (eds) (1991) Thermochemical properties of inorganic substances. Springer, Berlin Heidelberg New York
- [11] Barin I, Sauer F, Schultze-Rhönhof E, Sheng WS (1993) Thermochemical data of pure substances, 2nd ed. VCH Weinheim, New York
- [12] Lide DR, Kehiaian HV (1994) CRC handbook of thermophysical and thermochemical data. CRC Press, Boca Raton, FL
- [13] Chase MW (1998) NIST-JANAF thermochemical tables, 4th edn, Washington, DC: Published by the American Chemical Society and the American Institute of Physics for the National Institute of Standards and Technology
- [14] Davis AG, van Breda JH, Moretto P, Ordelman J (1995) Development of TiN nanocomposite coatings for wear resistance. J de Physque IV 5:C5-831–840

- [15] Bernard C, Madar R (1992) Thermochemistry in CVD-on the choice of halide gas species. In: Besmann TM, Gallois BM, Warren JW (eds) Chemical vapor deposition of refractory metals and ceramics II. Materials Research Society, Pittsburg, PA, pp3–15
- [16] Tang HP, Vescan L, Luth H (1992) Equilibrium thermodynamic analysis of the Si-Ge-Cl-H system for atmospheric and low pressure CVD of Si_{1-x}Ge_x. *J Cryst Growth* 116:1–14
- [17] Lever RF (1964) *IBM J Res Develop*, p470
- [18] Choy KL (2003) Chemical vapor deposition of coatings. *Prog Mater Sci* 48:57–170
- [19] Leitner J, Vonka P, Mikulec J (1989) Review application of chemical thermodynamics to the description of processes of special inorganic materials preparation. *J Mater Sci* 24:1521–1527
- [20] Eriksson G (1971) Thermodynamic studies of high temperature equilibria. *Acta Chem Scand* 25:2651–2658
- [21] White WB, Johnson SM, Dantzig GB (1958) Chemical equilibrium in complex mixtures. *J Chem Phys* 28:751–755
- [22] Vescan L (1995) Thermally activated chemical vapour deposition. In: Glocker DA, Shah SI (eds) *Handbook of thin film process technology*. Institute of Physics, Bristol, UK, B1.4:1–39
- [23] Fischman GS, Petuskey WT (1985) Thermodynamic analysis and kinetic implications of chemical vapour deposition of SiC from Si-C-Cl-H gas systems. *J Am Ceram Soc* 68:185–190
- [24] Kuta AJ, Davis RF (1983) Thermodynamic calculations for the chemical vapor deposition of silicon nitride. *J Am Ceram Soc* 66:551–558
- [25] Nadal M, Grenet T, Teyssandier F (1993) Titanium borides deposited by chemical vapor deposition thermodynamic calculation and experiments. *J Phys IV* 2:C3-511–518
- [26] Thomas N, Dutron A M, Vahlas C, Bernard C, Madar R (1995) Influence of hydrogen pressure on the properties of CVD tungsten silicide films. *J Electrochem Soc* 142: 1608–1614
- [27] Lackey W J, Smith AW, Dillard DM, Twait DJ (1987) Co-deposition of dispersed phase ceramic composites. In: Cullen GW (ed) *Proceedings of the 10th international conference on chemical vapor deposition*. Electrochemical Society, Pennington, NJ, pp1008–1027
- [28] Mulpuri PD, Sarin VK (1996) Synthesis of mullite coatings by chemical vapor deposition. *J Mater Res* 11:1315–1324
- [29] Yeheskel J, Agam S, Dariel M S (1990) Mass spectrometric study of SiC CVD from MTS (CH₃SiCl₃) and hydrogen. In: Spear K E, Cullen G W (eds) *Proceedings of the 11th international conference on chemical vapour deposition*, Seattle, WA. Electrochemical Society, Pennington, NJ
- [30] Sotirchol SV, Papisoulitis GD (1992) Kinetic modeling of the deposition of SiC from methyltrichlorosilane. In: Besmann T M, Gallois B M, Warren J W (eds) *Chemical vapor deposition refractory metals and ceramics II*. Materials Research Society, Pittsburgh, PA, pp35–40
- [31] Allendore MD, Osterheld TH (1995) Modeling the gas-phase chemistry of silicon carbide formation. In: Gallois BM, Lee WY, Pickering MA (eds) *Chemical vapour deposition of refractory metals and ceramics III*. Materials Research Society, Pittsburgh, PA, pp39–44
- [32] Papisoulitis GD, Sotirchos SV (1994) On the homogeneous chemistry of the thermal decomposition of methyltrichlorosilane: thermodynamic analysis and kinetic modelling. *J Electrochem Soc* 141:1599–1611

- [33] Osterheld TH, Allendorf MD (1995) The decomposition of methyltrichlorosilane in hydrogen and helium. In: Gallois BM, Lee WY, Pickering MA (eds) Chemical vapour deposition of refractory metals and ceramics III. Materials Research Society, Pittsburgh, PA, pp27–32
- [34] Stirling CJM (1965) Radicals in organic chemistry. Oldbourne, London
- [35] Isaacs N (1995) Physical organic chemistry, 2nd edn. Longman, Essex, UK
- [36] Mogab CJ, Leamy HJ (1974) Conversion of Si to epitaxial SiC by reaction with C₂H₂. *J Appl Phys* 45:1075–1084
- [37] Stinespring CD, Wormhoudt JC (1989) Surface studies relevant to silicon carbide chemical vapour deposition. *J Appl Phys* 65:1733–1742
- [38] Adamson AW, Gast AP (1997) Physical chemistry of surface, 6th edn. Wiley, New York
- [39] Thomas JM, Thomas WJ (1997) Principles and practice of heterogeneous catalysis. VCH, Weinheim
- [40] Besmann TM, Sheldon BW, Moss TS, Kaster MD (1992) Depletion effects of silicon carbide deposition from methyltrichlorosilane. *J Am Ceram Soc* 75:2899–2903
- [41] Loumagne F, Langlais F, Naslain R (1995) Experimental kinetic study of the chemical vapour deposition of SiC-based ceramics from CH₃SiCl₃/H₂ gas precursor. *J Cryst Growth* 155:198–204
- [42] Sone H, Kaneko T, Miyakawa N (2000) In situ measurements and growth kinetics of silicon carbide chemical vapor deposition from methyltrichlorosilane. *J Cryst Growth* 219:245–252
- [43] Vescan L (1995) Introduction and general discussion. In: Glocker DA, Shah SI (eds) Handbook of thin film process technology. Institute of Physics, Bristol, UK, B1.0:1–12
- [44] Grove AS (1967) Physics and technology of semiconductor devices. Wiley, New York
- [45] Hitchman ML, Kane J, Widmer AE (1979) Polysilicon growth kinetics in a low pressure chemical vapour deposition reactor. *Thin Solid Films* 59:231–247
- [46] Reep DH, Ghandhi SK (1983) Morphology of organometallic CVD grown GaAs epitaxial layers. *J Cryst Growth* 61:449–457
- [47] Reep DH, Ghandhi SK (1983) Deposition of GaAs epitaxial layers by organometallic CVD. *J Electrochem Soc* 130:675–680
- [48] Choy K L, Derby B (1991) The CVD of TiB₂ protective coating on SiC monofilament fibres. *J Phys IV2*:C2-697–703

Chapter 5 Chemical Vapour Infiltration

5.1 Introduction

Chemical vapour infiltration (CVI) was initially proposed and developed by Bickerdike [1] in 1962 to increase the density of porous carbon. The earliest patent was to infiltrate the porous alumina preform with chromium carbide by Jenkins [2] in 1964. CVI was then described for the densification of C/C composites by Kotlensky in 1973 [3]. CVI techniques have been widely investigated since. In the early 1970s Professor Fitzer's group [4] at Karlsruhe University started to investigate SiC CVI for fibre-reinforced composites. Meanwhile, Professor Naslain's group [5] at Bordeaux University began the development of an isothermal isobaric CVI (I-CVI) technique to fabricate carbon-fibre-reinforced silicon carbide composite aimed improving the oxidation resistance of C/C composites. In 1984 a forced CVI (F-CVI) technique was demonstrated by Professor Lackey's group [6] at Oak Ridge National Laboratory, USA. The commercialisation of the I-CVI technique for ceramic-matrix composites was first carried out at Societe Europeenne de Propulsion (SEP), France and at Du Pont, USA.

CVI technology is considered an extension of CVD technology. CVD is a process in which the coating is deposited on a completely dense solid surface at high temperatures from gaseous precursors. CVD has been successfully used to fabricate special coatings and thin-film electronic devices since the 1960s. CVI processes are special applications of CVD and the deposition takes place within porous preforms relying on a standard CVD reaction. This CVD coating penetrates and grows into the porous structure in a continuous layer-by-layer manner, forming the composite matrix. CVI, therefore, is a way of fabricating a new type of structural material which has many advantages. Similar to the CVD model, Fitzer [7] proposed a model for the CVI process as shown in Figure 5.1. The CVI process typically consists of the following steps:

1. gaseous precursors penetrate into the boundary layer from the bulk gas;
2. gaseous species are transported by diffusion into the pores within the fibre preform;
3. gaseous species are adsorbed onto the inner surface of the pore;
4. chemical reactions take place and coating forms on the fibre surface;
5. volatile by-products are desorbed from the surface;
6. gaseous by-products are transport outwards by diffusion; and
7. gaseous by-products return to the bulk gas through the boundary layer.

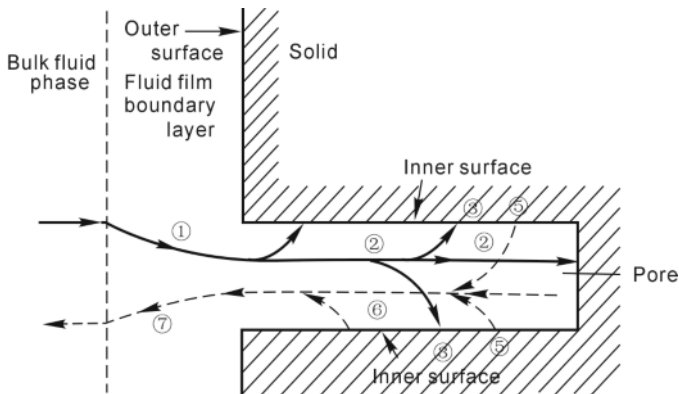


Figure 5.1. A CVI model [7]

Compared with conventional techniques for fabricating ceramic-matrix composites, such as hot pressing (HP), reactive melt infiltration (RMI) and polymer impregnation and pyrolysis (PIP), CVI techniques have distinct advantages, which can be summarised as follows [8, 9]:

5.1.1.1 Near-net-shape Process

During the densification process the preforms are usually placed in the reaction chamber at a reduced pressure. As there is no pressing or other mechanical forces exerted on the fibre preform during the densification process the final shape of the preform is very close to the desired shape and there is no large amount of material to be further removed by the machining method. The starting preforms therefore can be very complex in terms of shapes as this should represent the final finished target component.

5.1.1.2 Minimal Mechanical Damage to the Fibres

Damage to the fibres can easily happen if the component is exposed in an environment with high temperatures and mechanical loads. CVI processes normally take place at relatively low temperatures, typically in a range of 900 to 1100°C. This temperature is contrasted to high processing temperatures, usually above 2000°C when a traditional sintering method is employed to fabricate the high-temperature SiC-matrix material. Using the CVI technique, SiC material can be easily deposited at 1000°C via the following chemical reaction:



In such conditions the brittle ceramic fibres, such as Nicalon SiC and Al₂O₃ fibres, remain undamaged during the CVI process. However, conventional techniques for the fabrication of ceramic-matrix composites such as hot pressing take place at extremely high temperatures (2000°C) and under high mechanical stresses (30 MPa), which usually severely damage the fibres.

Moreover, the service temperature of CVI materials can be much higher than CVI processing temperatures. The reason for this advantageous feature is that the ceramic matrix produced by CVI is much purer than that obtained with the hot-pressing method, in which sintering additives are generally needed.

5.1.1.3 *Variety of Ceramic-matrix Materials*

Through many research and development studies CVI processes have already been established as good ways of fabricating a wide variety of ceramic-matrix materials including boride (e.g. SiB_2 , SiB_6 , TiB_2 , ZrB_2), carbide (e.g. SiC , B_4C , HfC , TiC etc.), nitride (BN , Si_3N_4 etc.), oxide (Al_2O_3 , ZrO_2 etc.) and silicide (e.g. TiSi_2 , MoSi_2). Owing to their superior mechanical properties fibre-reinforced SiC and related matrix composites have been widely produced on an industrial scale, mainly for applications in the aeronautic and space fields. It is expected that the number of composite components produced by CVI techniques will increase and more materials will become available.

5.1.1.4 *A Flexible Fabrication Technique for Smart and Delicate Microstructures*

One of the outstanding advantages of CVI processes over other CVD approaches is its suitability to deposit nanometre-scale coatings ($10^1\text{--}10^2$ nm) as an interphase on the surface of individual fibres within a preform. This is expected to be of particular importance and interest in the fabrication of tough ceramic-matrix composites. The interface is the key to controlling the mode of crack propagation between the fibre and the matrix. According to recently developed theories of interface fracture, the path of a crack can be deflected along the interface, caused by the pull-out of the fibre, thereby increasing the required total work of fracture. The ability to deposit a multilayered matrix is used to produce self-healing ceramic-matrix composites which allow for a long service lifetime in an oxidation atmosphere.

The main drawback of the CVI techniques is the long processing time of infiltration, normally in the range of a hundred hours. This is coupled with a very slow rate of deposition associated with a relatively low conversion efficiency of the precursor. To address this deficiency new manufacturing approaches have been explored to develop rapid infiltration techniques and so far most of these attempts remain as research work being investigated in laboratories. Another potential problem is that CVI composites exhibit some residual open porosity. This would be a drawback for applications where gas or liquid tightness is strictly required.

According to the controlling parameters used in the process, CVI approaches can be classified into five typical categories [9]: isothermal/isobaric CVI (I-CVI), forced-flow CVI (F-CVI), thermal gradient/isobaric CVI (TG-CVI), pulsed CVI (P-CVI) and liquid immersion CVI (LI-CVI). There are more than ten CVI techniques if a particular method is coupled with plasma, microwave or a catalyst to enhance the process [10]. Some representative techniques are discussed in this chapter as follows.

5.2 Isothermal and Isobaric Chemical Vapour Infiltration

5.2.1 General Description

Isothermal and isobaric CVI (I-CVI), a relatively easy and the oldest hot-wall technique, is still widely used in research and in industry. The key feature of this approach is that both temperature and pressure are kept constant during the infiltration process. Because of this its main advantage is good consistency of the finished product due to strict yet easy thermal and pressure parameter control. In particular a large number of complex preforms can be densified simultaneously, as shown in Figure 5.2.

For the infiltration of SiC methyltrichlorosilane (MTS with a molecular formula of CH_3SiCl_3) is employed as the precursor, which is carried using a hydrogen bubbling method. The normal processing conditions include a temperature of 1000°C , an H_2/MTS mol ratio of 10 with Ar often used as dilute gas. Usually the process is performed at a reduced pressure of 10 to 30 kPa. The reasons for using reduced pressures in I-CVI are (1) to enable higher gas-phase diffusivity, leading to more uniform distributions of density and microstructure within the composites, and (2) to reduce or eliminate undesirable gas nucleation and the formation of deleterious by-products, such as tar and soot in the case of carbon CVI. The temperature of the working zone is measured and controlled by a thermocouple and its driven actuator to control the heating elements of the system. The pressure is measured by a pressure gauge and controlled by a throttle valve on the vacuum system.

5.2.2 Isothermal and Isobaric Chemical Vapour Infiltration Process Model

For I-CVI processes, the driving force for mass transport is the concentration gradient of the reactant gaseous species as shown in Figure 5.3. During the densification process the precursor gases flow over the preforms at a reduced pressure. Then they diffuse into the porous and fibrous preforms, react and form a

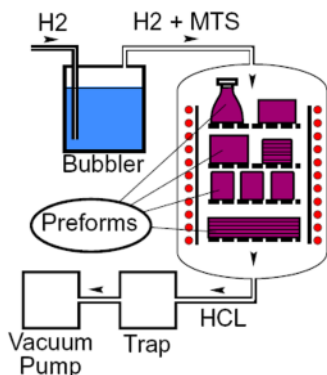


Figure 5.2. I-CVI schematic diagram of hot-wall infiltration chamber for SiC-matrix composites [11]

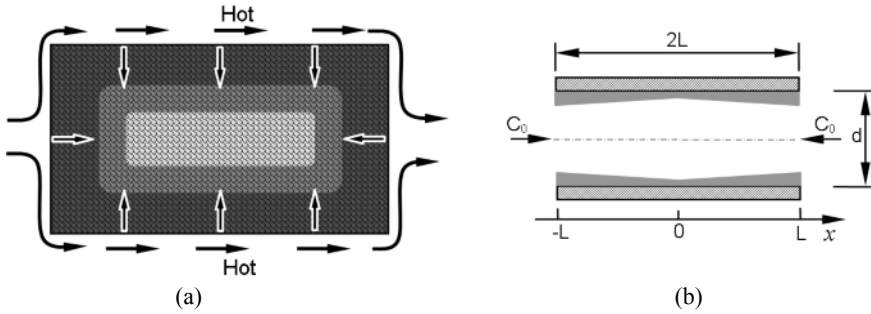


Figure 5.3. I-CVI model: (a) overall model and (b) one-dimensional model

ceramic matrix on the surfaces of the fibres. Therefore, the densification occurs preferentially near the outer surface of the preform because the concentrations of the reactant gases are at their maximum values near the outer surface and decrease along the infiltration direction of the preform. The primary objectives of the I-CVI processes are to maximise the densification rate and minimise the density gradients within the composite so that the mechanical properties of the finished product are consistent throughout its structure. Unfortunately, there is an inherent competition between the deposition reaction and the mass transport of the gaseous species [9]. Rapid deposition reactions result in severe density gradients from the external region to the interior region of the preform, which slows down the deposition rate. An alternative slow-deposition reaction leads to a denser composite but at the cost of an uneconomically long densification time.

Fibre preforms generally have a complex pore size distribution, which may consist of several size ranges, depending on the architecture of the preform. For two-dimensional (2-D) preforms with carbon cloth stacked together the fibres with a diameter of 5~15 μm are arranged in bundles of 500 to 3000 or more fibres. The typical pore sizes between individual fibres are the smallest, on the order of 1 to 10 μm . Pores between the fibre bundles are much larger, up to several hundred, micrometres, and pores between layers of cloth are similar or slightly larger.

To understand the I-CVI process, a one-dimensional model is widely used to demonstrate the principle as shown in Figure 5.3b. Based on this simple schematic diagram, it is possible and essential to establish its process model under steady conditions. A mass-conservation equation model is established based on the fundamental conservation of matter as this lies at the heart of all CVI processes. Under steady conditions the governing transport-reaction equation is written as [12–14]

$$D_e \frac{d^2C}{dx^2} + u \frac{dC}{dx} = rS \quad (5.2)$$

where C is the concentration of a chemical species, D_e is the efficient diffusivity, u is the gas velocity in the x -direction, r is the mol deposition rate per unit of solid surface area and S is the solid surface area per unit volume.

The two terms on the left-hand side of this equation are the net fluxes of the gaseous species into a specific volume by diffusion and convection respectively;

the term on the right-hand side is the deposit production through chemical reactions within the specific volume.

For isothermal/isobaric CVI processes there is no forced flow, i.e. the convection term cannot be taken into consideration. Assuming the first-order reaction, Equation (5.2) becomes

$$D_e \frac{d^2C}{dx^2} = \frac{4}{d}kC \quad (5.3)$$

where k is the first-order reaction constant and d is the diameter of the pore.

The associated boundary conditions for the problem may be explained in the following physical sense. At the exterior surface of the pore the reactant concentration equals the bulk concentration of the gaseous species; at the central cross-section of the pore, considering the symmetric demand, there is no reactant concentration gradient, i.e.

$$X = 0, C = C_0 \quad (5.4)$$

$$X = L, \frac{dC}{dx} = 0 \quad (5.5)$$

Solving Equation (5.3) gives the concentration profile, $C(x)$, of the precursor species along the pore expressed by

$$C(x) = C_0 \frac{\cosh\left(\theta \frac{x}{L}\right)}{\cosh \theta} \quad (5.6)$$

where θ is called the Thiele number. θ is a dimensionless parameter and is defined as the ratio of the chemical reaction rate to the mass transfer rate [15]. Furthermore, θ^2 is known as the second Damkijhler number (Da_{II}).

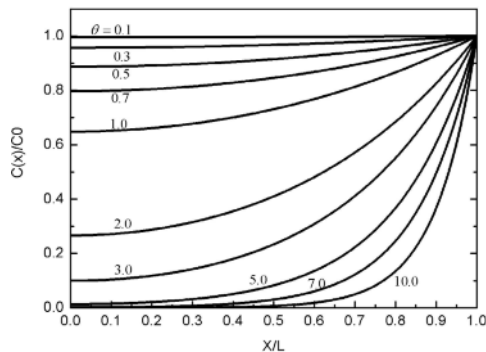


Figure 5.4. Influence of θ number on concentration profile

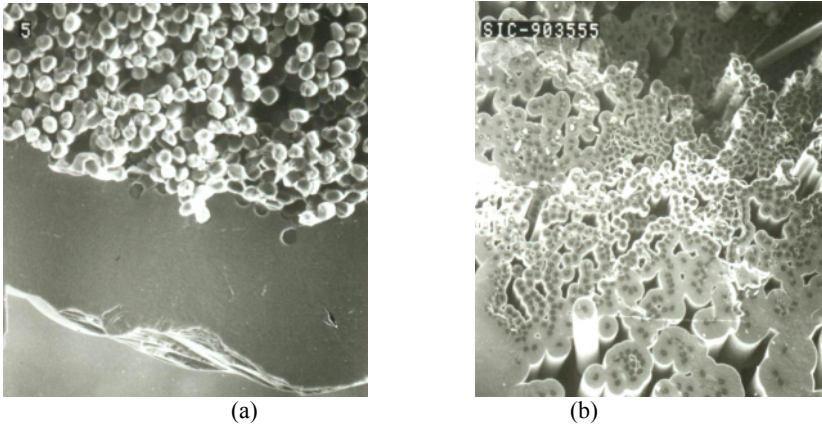


Figure 5.5. The influence of θ on SiC infiltration: (a) uniform infiltration at small θ and (b) poor infiltration at large θ

$$\theta = \left(\frac{4kL^2}{dD_e} \right)^{1/2} \quad (5.7)$$

The relationship between the θ value and the concentration is illustrated in Figure 5.4. It is clear that the concentration of the precursor gas decreases with the distance from the opening of the pore. The curve of the concentration distribution is relatively flat when θ is small. However, the curve becomes very steep when the value of θ is greater than 1. Based on the kinetic discussion in Section 4.3.4, the densification process is changed from the chemical reaction regime to the mass transport regime with an increase of the θ value. For the large θ case densification only occurs near the external region of the pore but much poorer densification in the interior region. For small values of θ (< 0.5) the deposition takes place in a kinetics limited region and the infiltration is relatively uniform, which is determined by the uniform distribution of $C(x)/C_0$ along the pore depth.

According to Equation (5.7) the increase in processing temperature and preform thickness leads to larger values of θ and poor density uniformity. As stated previously, CVI processes preferably operate in a chemical-reaction-controlled regime where the ratio of k/D is small. For Fick diffusion, discussed in Section 2.3.1, the diffusivity D is inversely proportional to the pressure and thus operates at lower pressures. Furthermore, coarser pore structures correspond to more uniform deposition. Figure 5.5 shows the microstructures of C/SiC composites prepared at different θ numbers.

As reported by Fedou [16] on SiC infiltration into a pore 10 mm deep and 34 μm in diameter, at a pressure of 20 kPa and with an $\text{H}_2/\text{CH}_3\text{SiCl}_3$ ratio of 5, the temperature has a significant influence on densification, as shown in Figure 5.6. At temperatures of 950°C, 1050°C and 1100°C, the thickness of an SiC deposit decreases considerably along the depth of the pore in each case. As the processing temperature increases, the profile of the deposit thickness becomes much steeper.

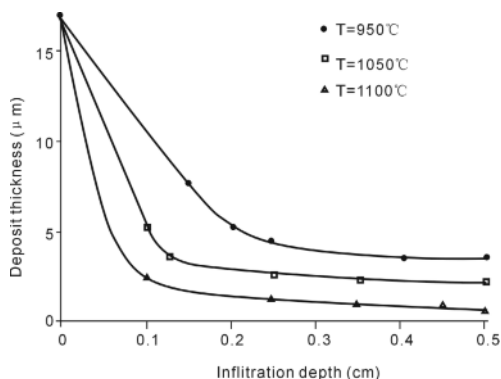


Figure 5.6. Influence of temperature on the thickness profile of SiC infiltration [16]

The figure also shows that the deposition gradient exists under any conditions. These experimental results agree with the theoretical calculations from the one-dimensional model discussed in Equation (5.6). In order to obtain uniformly dense composite material machining is necessary to open the blocked openings for further infiltration.

For I-CVI processes the overall densification kinetics of a preform with initial density (ρ_0) follows an exponential pattern to a “final” density value (ρ_f) as shown in Figure 5.7, which can be expressed as follows [10]:

$$\rho(t) = \rho_o + (\rho_f - \rho_o)[1 - \exp(t / \tau)] \tag{5.8}$$

where τ is the time constant of the process, which decreases with increasing temperature according to the Arrhenius relationship in the chemical reaction limited regime.

The way to achieve the final required density is through several approximately exponential infiltration steps as shown in Figure 5.7. For I-CVI processes, the

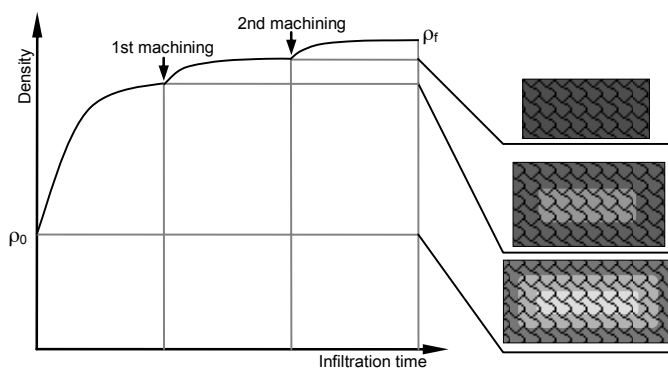


Figure 5.7. Plot of the density of a thick preform against time in an I-CVI process

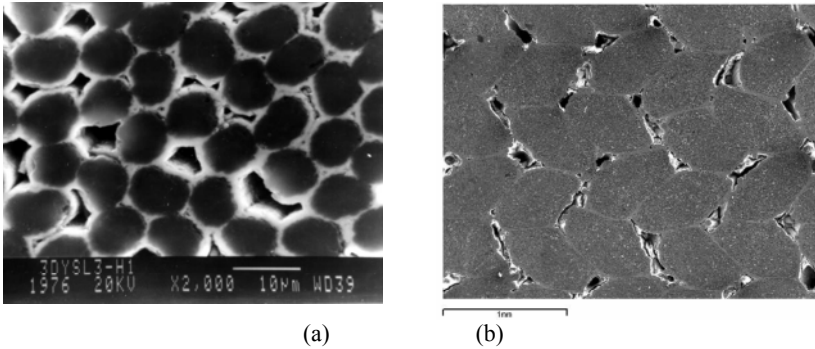


Figure 5.8. Two kinds of residual pores within the composites by I-CVI: (a) small pores within the bundle and (b) large pores between bundles

diffusion of the gaseous precursors leads to a concentration gradient along the pore, thereby causing blockage of pores due to deposition of a layer of impermeable coating near the opening of the pore. Consequently, the infiltration process must be interrupted to grind off the outer dense layer to enable the reactant gases to penetrate into the interior of the preform. For economical reasons, the infiltration process is normally terminated when the porosity of the composites reaches around 10 to 15%. Figure 5.8 shows the typical microstructures of 3-D C/SiC composites. The residual pores include the small pores among the fibres within one fibre bundle and the large pores among the fibre bundles.

From an economical point of view the overall conversion efficiency of the precursor is another important parameter for cost considerations. This efficiency is defined as the ratio of infiltrated mass to the precursor mass introduced into the reaction chamber. Investigations indicate that the conversion efficiency is dependent on the mass transport method, residual time of the precursor, pressure and temperature, etc. As shown in Figure 5.9 the conversion efficiency of propylene (C_3H_6) increases with an increase in residence time but decreases with the partial pressure of the precursor gas. In particular, it is worth noting that the conversion efficiency in the I-CVI process is rather low and generally is in the range of 0.78 to 2.14% [17].

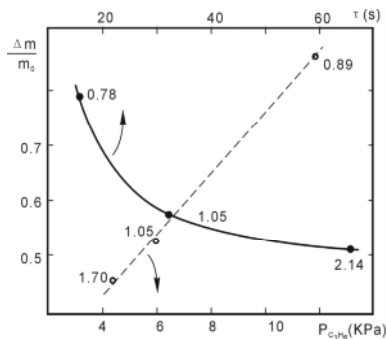


Figure 5.9. Dependence of mass gain on partial pressure and residence time [17]. Note: The numbers next to the data points are conversion efficiencies of C_3H_6

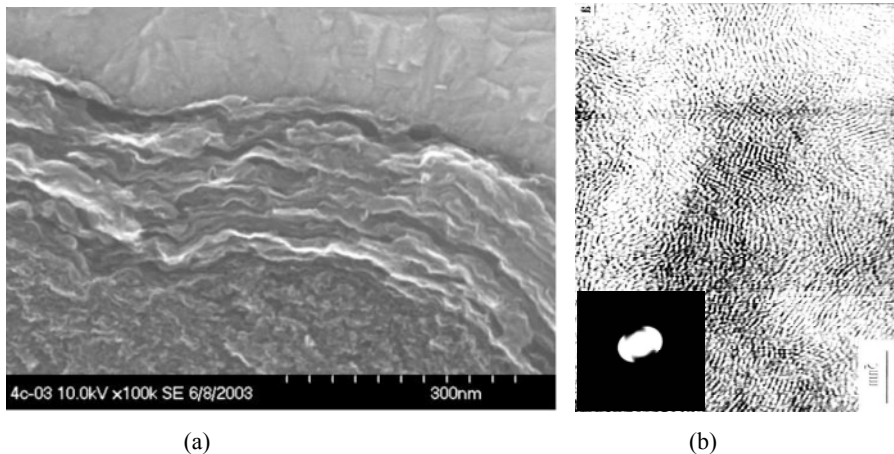


Figure 5.10. PyC interphase in the C/SiC composites [24]: (a) SEM image and (b) TEM image

5.2.3 Characteristics of Fibre-reinforced Ceramic-matrix Composites

In recent years fibre-reinforced ceramic-matrix composites have been designed and manufactured as very interesting structural materials because of their higher performance at elevated temperatures compared with super-alloys and higher fracture toughness compared with monolithic ceramics. They can be used as component materials in ultra-high-temperature environments, such as advanced aero-engines, scramjet and a thermal protection system for the space shuttle. To date, for example, both carbon-fibre- and silicon-carbide-fibre-reinforced silicon carbide composites (C/SiC and SiC/SiC) have been well developed to serve these purposes.

It is well recognised that the interphase plays a very important role in ceramic-matrix composites [18–21]. The material becomes much tougher if the bonding between the fibre and matrix is neither too strong nor too weak. The interfacial bonding could be tailored with the interphase layer between the fibre and the matrix. The interphase usually performs several key functions: load transfer, matrix crack deflection (mechanical fuse function) and diffusion barrier. The best interphase materials might be those with a layered crystal structure [22, 23], such as hexagonal carbons (pyrocarbons, or PyC), hexagonal boron nitride and multilayered microstructure (such as PyC/SiC/..., BN/SiC/...).

Figure 5.10 shows the microstructure of a pyrocarbon interphase in C/SiC composites.

Figure 5.11 shows the typical failure behaviour of 3-D C/SiC composites, which is quite different from that of monolithic ceramics. The present composite materials exhibit a non-catastrophic failure behaviour and a remarkable failure displacement of around 1.2 mm.

In general the strength of monolithic ceramics decreases significantly at elevated temperatures due to the softening and sliding of a glass phase at the grain

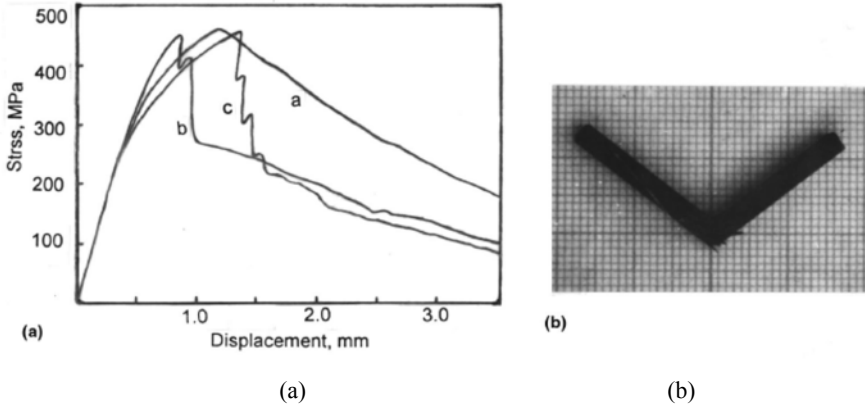


Figure 5.11. Fracture behaviour of 3D C/SiC composite from RT to 1600°C [24]: (a) stress-displacement curve and (b) fracture surface

boundary. For C/SiC composites fabricated with CVI there is no glass phase in materials. Hence, the flexural strength of the composites does not decrease at temperatures up to 1600°C. The average value of flexural strength is 441 MPa at room temperature, 450 MPa at 1300°C, and 447 MPa at 1600°C. However, the failure behaviour of the composites varies with temperature. This is caused by the thermal stress variation in the composites, which results from the differences in thermal expansion coefficients between the fibre and the matrix. The T300 carbon fibre by Toray Carbon Co., Japan, is an anisotropic material and usually characterised by two thermal expansion coefficients (TECs) [25], a radial TEC ($7.0 \times 10^{-6} \text{ K}^{-1}$) and a longitudinal TEC (0.1 to $1.1 \times 10^{-6} \text{ K}^{-1}$). The TEC of a CVI SiC matrix is $4.8 \times 10^{-6} \text{ K}^{-1}$ [26]. The interfacial bonding changes from tensile stress to compressive stress as the testing temperature increases to 1300°C, resulting in different failure behaviours of the composites, as shown in graphs a–c in Figure 5.11.

The toughening mechanism of fibre-reinforced ceramic-matrix composites is due to the pull-out phenomenon of the fibre from the matrix. For 3-D C/SiC composites three kinds of pull-out are observed from the fracture, namely the fibre pull-out, the fibre cluster pull-out and the bundle pull-out illustrated in Figure 5.12a, b and c respectively.

The Weibull modulus (m), an important parameter to determine the reliability of materials, is characterised by the scattering range of the material properties. A large value of m implies high uniformity of mechanical properties, while a small m represents a large scattering range. Figure 5.13 shows the result of a Weibull plot of $\ln(1/F)^{-1}$ versus $\ln\sigma$. It is clear from the figure that the flexural strength of 3-D C/SiC composites also obeys a Weibull distribution. The result is consistent with that of a SiC/TiAl composite [27, 28]. The slope gradient corresponding to the Weibull modulus m in Figure 5.13 is as high as 23.3.

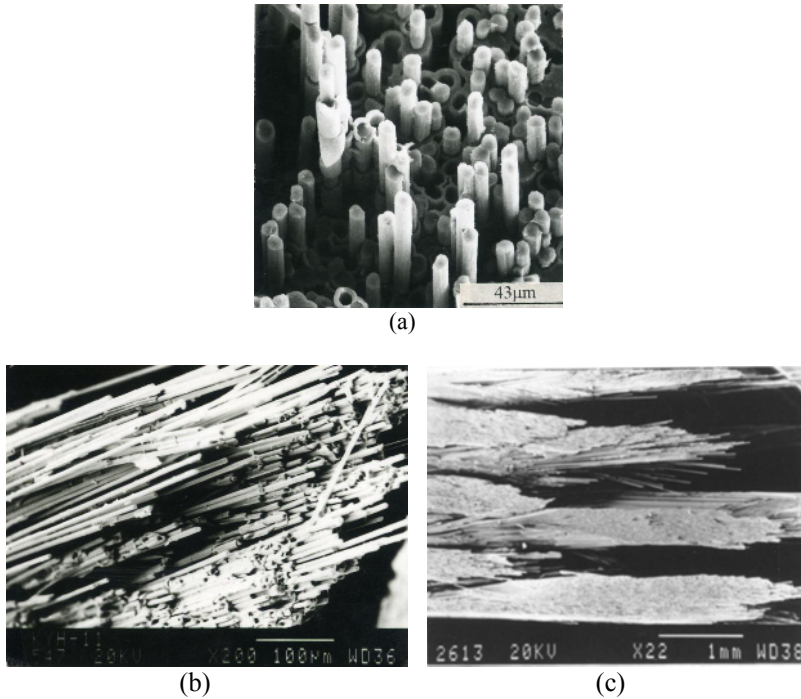


Figure 5.12. Fracture surface of 3D C/SiC composites [24]: (a) fibre pull-out, (b) fibre cluster pull-out and (c) bundle pull out

The equations for monolithic ceramics together with the experimental results of the notched specimen are used to determine the fracture toughness (represented as K_{IC}) of the 3-D C/SiC composites created with the single edge notched beam (SENB) method. Its value is calculated as $20.3 \text{ MPa}\cdot\text{m}^{1/2}$, which is much higher than that of monolithic ceramic materials ($3 \text{ to } 5 \text{ MPa}\cdot\text{m}^{1/2}$). It should be noted that

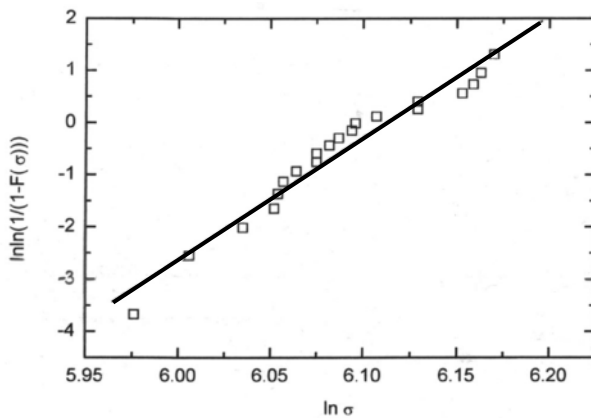


Figure 5.13. Weibull plot for flexural strength of 3D C/SiC composites [24]

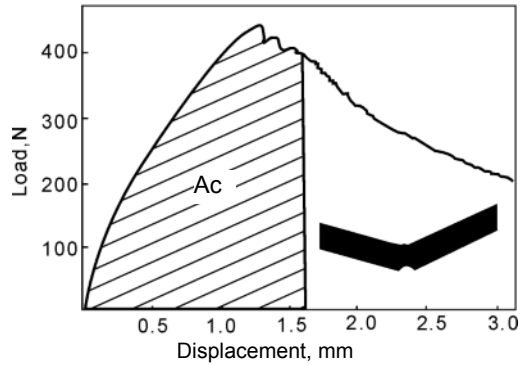


Figure 5.14. Failure behaviour of 3-D C/SiC composite sample with a notch [24]

this value of K_{IC} could not represent the real toughness of present composite materials. The reason for this is that fracture toughness is based just on the linear elastic mechanics for brittle materials, which is not valid and applicable for composites with substantial non-linear behaviour as shown in Figure 5.14.

Instrumented Charpy impact tests on unnotched samples are conducted to determine the energy absorbing capability and dynamic fracture behaviour of the C/SiC composites. The dynamic fracture toughness (α_k) is calculated using the following equation:

$$\alpha_k = \frac{\Delta W}{bh} \quad (5.9)$$

where ΔW is the absorbed energy of materials during impact testing and b and h are the thickness and width of a specimen respectively.

For 3-D C/SiC composite materials the value of α_k is $62 \text{ kJ}\cdot\text{m}^{-2}$, which could be comparable to that of a super-alloy ($\alpha_k = 80\sim 160 \text{ kJ}\cdot\text{m}^{-2}$). The impact fracture

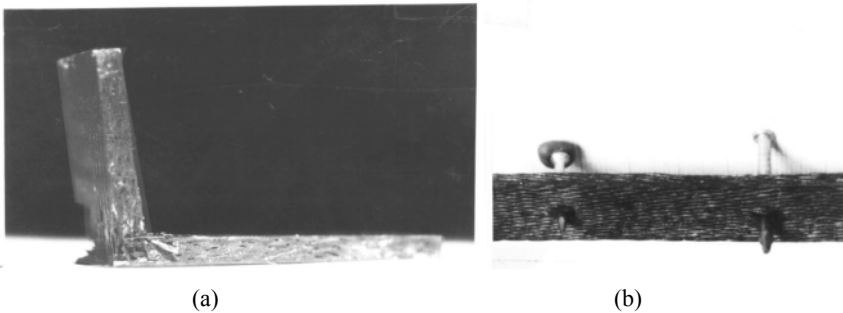


Figure 5.15. Impact fracture surface of C/SiC composites [24]: (a) after Charpy impact test and (b) after the nails penetrated test

surface is shown in Figure 5.15. It is worthwhile to note that the materials are still connected together, not broken into pieces, after the impact tests. In addition, the composites could also be penetrated by a steel nail without any severe fracture, as shown in Figure 5.15b, showing a strong reliability. Overall, C/SiC composite materials exhibit excellent toughness characterised by insensitivity to cracks, non-catastrophic failure behaviour and high reliability.

5.2.4 Isothermal and Isobaric Chemical Vapour Infiltration Applications

As a well-established and relatively well-understood technique I-CVI is still widely used in both the laboratory and industry. Uniform temperatures and pressures within the reactors can be easily realised in practice and make it suitable for industrial manufacturing. So far, very large reactors (up to 2500 mm in diameter) have been successfully designed and developed for densification of C/C, SiC and other refractory composites [29].

I-CVI has been widely used to manufacture carbon/carbon braking disks since the 1960s. In a common application as shown in Figure 5.16, multicylindrical carbon brake disk preforms, typically 550 mm in outer diameter and 20 to 30 mm in thickness, are placed in a hot-wall reactor at a temperature of 1000°C and exposed to the CH₄ precursor at a pressure of 1 to 30 kPa [29].

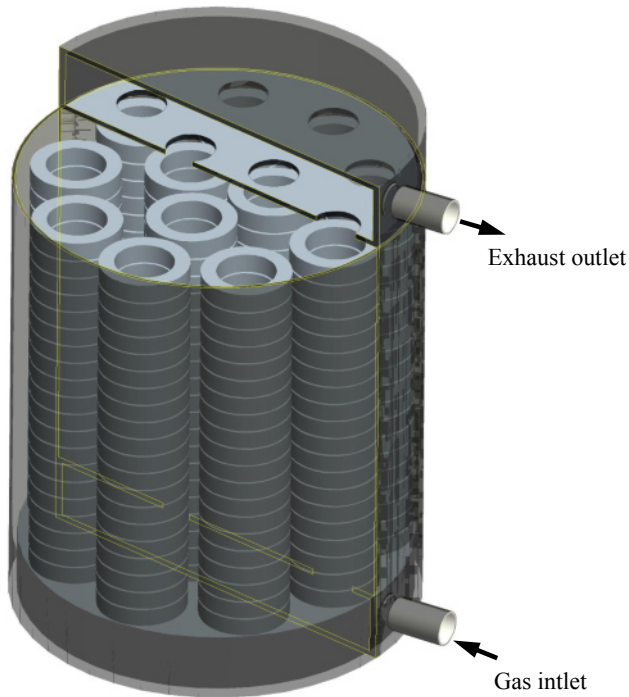


Figure 5.16. A large I-CVI reaction chamber for C/C braking disk densification

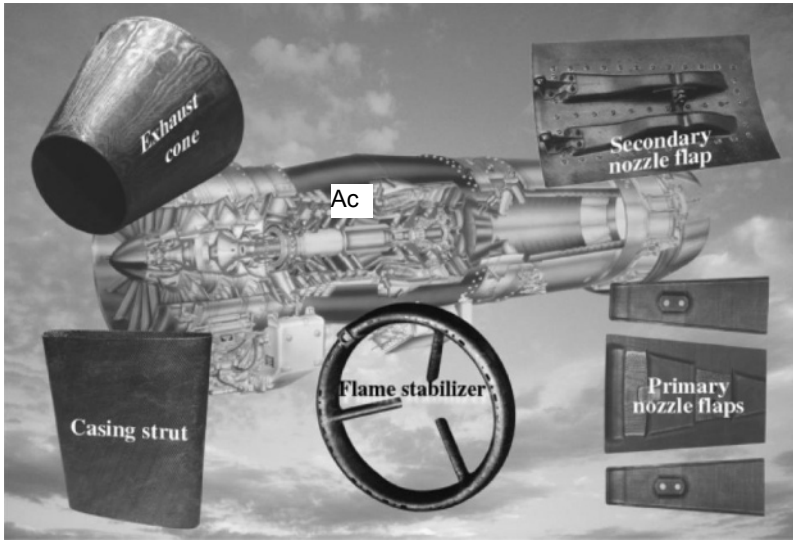


Figure 5.17. Potential applications of SiC-matrix components in aero-engines [33]

Due to the excellent aforementioned properties, fibre-reinforced ceramic-matrix composites have been identified as improving the thrust-to-weight ratio of higher performance aero-engines. Some typical projects include integrated high-performance turbine engine technology, high-speed civil transport, propulsion system in high-speed research (HSR), the continuous fibre ceramic composite programme in USA [30], the novel ceramic composites project in European as well as the research institute of advanced material gas generator in Japan [31]. The potential applications are nozzle flaps, exhaust cone, flame stabiliser, combustion liners and turbines. As presented in Figure 5.17 C/SiC flaps have been manufactured using an I-CVI technique in volume production by a company called Snecma and they have been successfully used in M-88 aero-engines for Rafale fighters since 1996. By using C/SiC composites the flaps save 50% of the weight compared with the original material super-alloy Inconel 718 [32, 33]. C/SiC and SiC/SiC composites have also been demonstrated for use in thermal protection systems for the space shuttle and scramjet engines [34].

5.3 Thermal Gradient and Forced Flow Chemical Vapour Infiltration

5.3.1 General Description

In a forced flow CVI (F-CVI) process, the precursor gases are allowed to flow through the fibre preform, rather than relying on diffusion transport as with I-CVI processes. An F-CVI process offers the advantages of much reduced processing

time, improved infiltration efficiency and hence economics, especially for components with thick sections.

A schematic diagram of F-CVI equipment is shown in Figure 5.18 [6]. The fibrous preform is placed in a water-cooled metal holder which cools the bottom and sides surrounding the preform to prevent undesirable deposition there. The top of the preform is heated by a heating element. As a result the temperature gradient is built up within the preform. The precursor gases are forced to flow through the preform from the cold surface to the hot surface. The back pressure of the precursor gases is in a range of 0.1 to 0.2 MPa. In this case a pressure gradient has

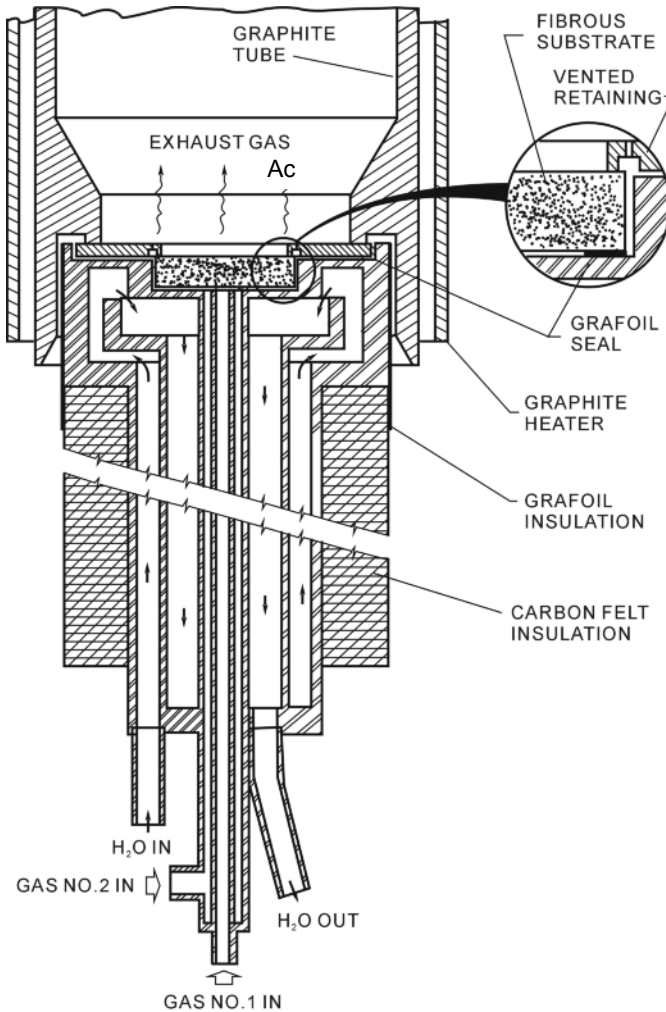


Figure 5.18. Schematic of F-CVI process for plate preform [6]

the opposite direction to the temperature gradient. The infiltration occurs progressively from the top to the bottom of the preform.

Grafoil is used to seal the gaps between the preform and the holder. When the top surface region becomes dense, the gases flow up into the preform, then penetrate radially through the preform to the annular void space around the preform and finally flow out through the vented retaining ring.

The F-CVI process can also be used to infiltrate tubular preforms radially by creating a thermal gradient from the inside of the tube to the outside. As shown in Figure 5.19, the outside of the preform is heated while the cold water is circulated through the stainless steel injector to cool the inside of the preform. The precursor gases flow up in the gas guide pipe which is connected to the gas distributor. The gases are then forced to flow radially through a number of holes on the distributor and further penetrate uniformly through the preform along the longitudinal direction. The preform is supported by the mandrel. The gases are finally guided to the reactant gas outlet after passing the mandrel.

In order to demonstrate the ease of scaling this process to fabricate much larger work pieces Besmann *et al.* [36] developed a large F-CVI system at the Oak Ridge National Laboratory, USA, as shown in Figure 5.20. The furnace shell and lid are water-cooled. The top lid needs to be raised by pneumatic lifters. There are two

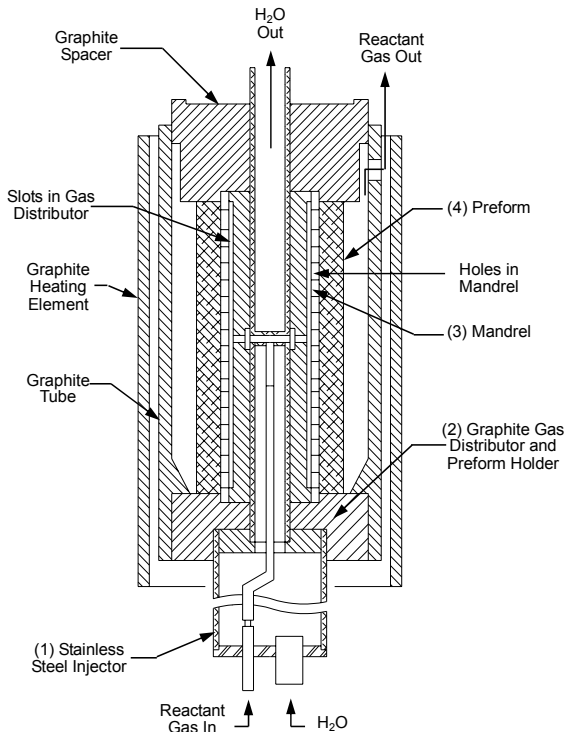


Figure 5.19. Schematic of F-CVI process for tubular preform [36]

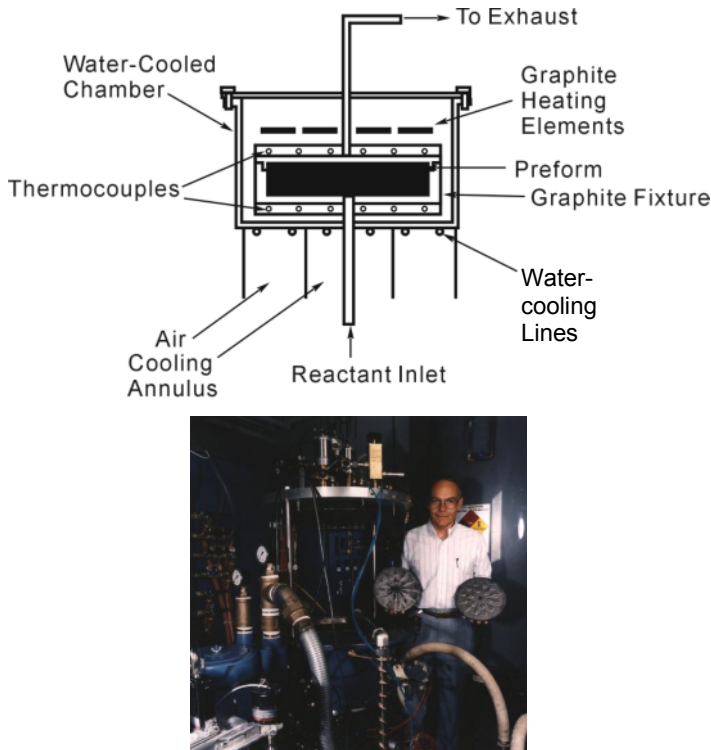


Figure 5.20. F-CVI furnace for large-scale component fabrication [37]

concentric heating elements which are controlled independently and, therefore, allow good radial temperature uniformity. The radial temperature difference can be controlled to less than 10°C . The fibre preform is placed in the fixture. The fixture also acts as a reaction chamber with a good seal to prevent precursor gases leaking out of the fixture. The reactant gas is introduced by an inlet fitted into the bottom of the fixture, while the exhaust exits the fixture through a graphite tube and then to the metal exhaust line. The effective working capacity of the fixture is 300 mm in diameter and 24 mm thick.

The bottom surface of the F-CVI chamber is cooled either with a water-cooled plate or with forced air. A baffle is designed to direct the air flow to varying degrees into the inner or outer annulus, thus controlling the lower surface radial gradient. Thermocouples are placed above and below the preform fixture to measure the temperatures, which are maintained by controlling power to the heating elements based on the signals from the control thermocouples on the hot side and the positioning of the air flow baffle on the cool side. The size of the preform reported in the researchers' work is 246 mm in diameter and 12.7 mm thick with a 12.7-mm-diameter central hole. The fibre volume fraction of the preform is 33%. During the infiltration process the flow rates of CH_3SiCl_3 and H_2 are $5 \text{ g}\cdot\text{min}^{-1}$ and $5 \text{ l}\cdot\text{min}^{-1}$ respectively; the hot surface temperature of the preform is 1200°C and an infiltration time of 40 h is required for each run.

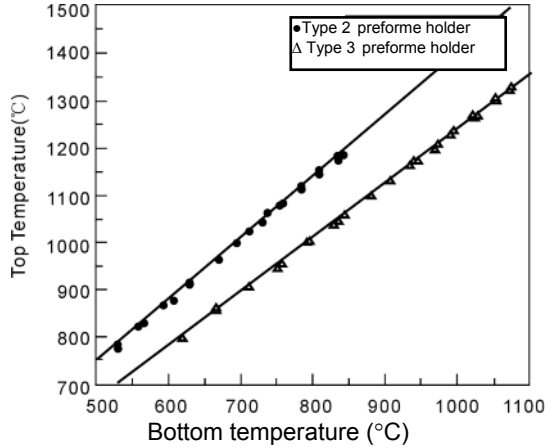


Figure 5.21. Temperature profile within the preform for F-CVI process [38]

The temperature gradient is dependent on the configuration of the preform holder which determines the cooling effect. For a fibre preform with a thickness of 8 mm the temperature profiles are measured at the top and the bottom of the preform without infiltration, as shown in Figure 5.21. The temperature differences between the top surface and bottom surface of the preform are around 350°C and 250°C, corresponding to preform holders 2 and 3 respectively.

In contrast to the I-CVI technique, processing parameters must be adjusted during the F-CVI process. An example for F-CVI C/C is given by Vaidyaraman *et al.* [38]. The pressure above the preform is atmospheric pressure (or slightly higher than atmospheric pressure). At the initial infiltration stage, the pressure in the precursor supply line is 3.4 kPa above atmospheric pressure. This pressure gradient forces the precursor gases to flow through the preform. The reagent gas first comes in contact with the cooler side of the preform then flows up through the preform to the hot side. As the infiltration progresses, it is necessary to increase the back pressure in the supply line because the preform becomes denser. A higher pressure is required to force the gases to flow through it. The infiltration process typically ends when the back pressure on the cold side of the preform increases about 170 kPa.

5.3.2 Forced-Flow-Chemical Vapour Infiltration Model

For the F-CVI process shown in Figure 5.22a a temperature gradient is applied across the preform thickness and the precursor gases are forced to flow through the preform from the cold to the hot surface. It is desirable to obtain uniform deposition throughout the preform; this can be accomplished by choosing and controlling the precursor pressure and processing temperature. A high precursor concentration on the cold side compensates the lower temperature, and a lower concentration at the hot side offsets the higher temperature combining these results in a uniform deposition along the thickness of the preform.

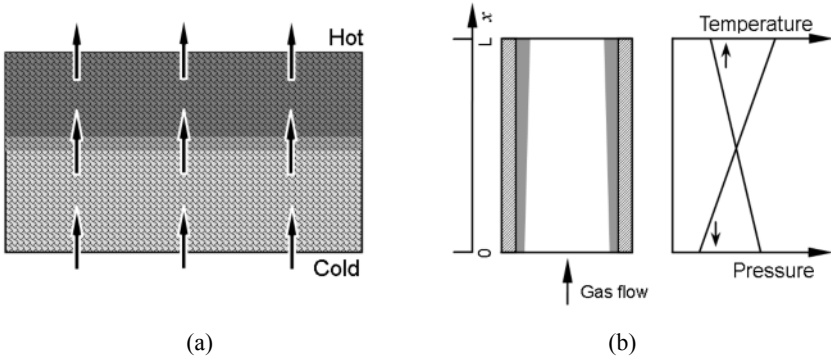


Figure 5.22. F-CVI model: (a) overall model (b) one-dimensional model

In practice a faster deposition process occurs in the hot region of the preform compared with the cold region of the preform. Figure 5.22b shows the effect of coating thickness on temperature. In addition, the temperature gradient helps to prevent the formation of an impermeable skin. This is due to the fact that the preform is exposed to the precursor gases in the low temperature region first. This approach allows the process to be conducted at much higher temperatures (around 200°C) than I-CVI processes, thereby further reducing the processing time significantly. F-CVI also offers greater flexibility in the selection of processing conditions. It is not essential to use low temperatures, pressure and precursor concentration as in I-CVI processes. Consequently, there is a wider range of selection of the conditions under which deposits possessing the required microstructure and properties can be obtained.

By forcing the precursor gases through the preform, the diffusion term in Equation (5.2) can be neglected, and the governing transport-reaction equation is rewritten as

$$u \frac{dC}{dx} = RS \tag{5.10}$$

The associated boundary conditions are given by

$$x=0, C=C_0 \tag{5.11}$$

The concentration of the precursor along the pore can then be obtained as

$$C(x) = C_0 \exp\left(-Da_1 \frac{x}{L}\right) \tag{5.12}$$

where the cold surface of the preform is at $x = 0$; the concentration of the precursor gases depends on the dimensionless parameter, Da_1 :

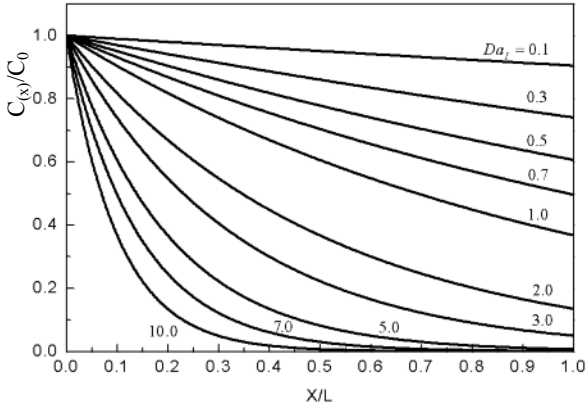


Figure 5.23. Relationship of Da_1 number and concentration distribution

$$Da_1 = \frac{kSL}{u} \quad (5.13)$$

where Da_1 is called the first Damkijhler number. It represents the ratio of chemical reaction rate to the convective mass transfer rate.

As shown in Figure 5.23, the concentration profile of the precursor gas is related to the value of Da_1 . The concentration gradient of the precursor gas becomes steeper with increasing Da_1 . Due to complex coupling effects between the pressure and temperature of F-CVI it is very difficult to model this phenomenon. A large body of research work has been undertaken under isothermal conditions to simplify the simulation. Under isothermal conditions the concentration profile represents the deposition gradient. In such a case densification always occurs more rapidly at the precursor gas entrance region of the preform.

In order to obtain a uniform infiltration, Da_1 should be as small as possible. Processing conditions must include a large gas velocity (large pressure gradient) and large pore diameter, but with a short pore length (preform thickness). Moreover, the increase in the gas velocity through the increase of the total gas flow rate will enhance both uniform and rapid matrix deposition. Hence, the suitable selected processing parameters can achieve the maximal densification rate and the minimal density gradient. This is a distinguishing feature aided by the use of forced gas flow, which is different from that of I-CVI techniques based on mass diffusion.

F-CVI processes take place far from the thermodynamic equilibrium. The dimensionless Peclet number, Pe , is used to describe this process [39]:

$$Pe = \frac{uL}{D} \quad (5.14)$$

The Peclet number means the ratio of the mass transfer rate by convection mechanism into the pore to the mass transport rate by a diffusion mechanism. At

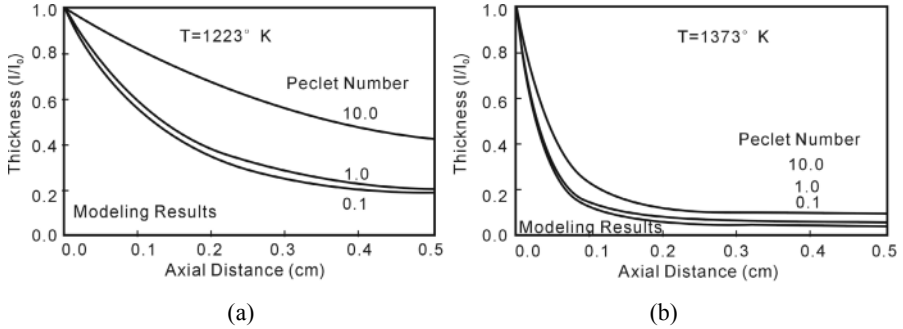


Figure 5.24. Forced-flow effect on the infiltration profile [39]: (a) at 1223°K and (b) at 1373°K

low Pe numbers the mass transfer is dominated by a diffusion mechanism, whereas at large Pe numbers convection is dominant.

Figure 5.24 shows the simulated results of F-CVI under isothermal conditions. The forced effect on infiltration is very limited if the Pe number is small. Uniform infiltration is obtained when the Pe number reaches 10 at relatively the low temperature of 1223°K. The reason is the convective flow can force much more gaseous species to penetrate deeply into the pores of the preform. However, the influence becomes minimal at high temperatures (1373°K) even for high a Pe number (10.0).

5.3.3 Characteristics of Forced-Flow-Chemical Vapour Infiltration Composites

For an I-CVI process the surfaces of preforms require grinding in several stages during a complete process in order to open the blocked channels or pores in the outer region of the preform for further infiltration. In contrast, F-CVI is a one-step

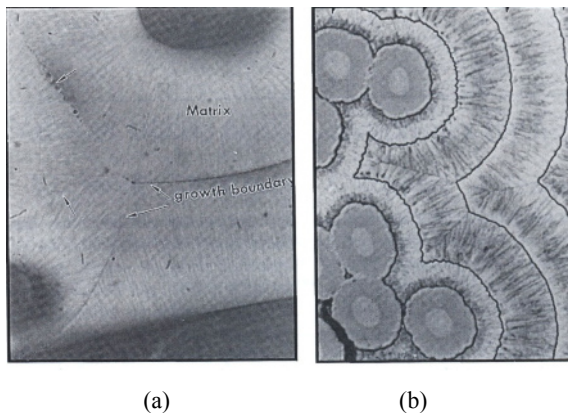


Figure 5.25. Microstructure comparison between I-CVI and F-CVI processes [40]: (a) F-CVI and (b) I-CVI

processing method, which implies that the infiltration of the composites could be realised in only one run. Figure 5.25 shows the microstructures obtained by F-CVI and I-CVI techniques respectively. In both cases, SiC is deposited on the fibre surface, then grows radially until it meets another growing deposit. Multistage infiltration in an I-CVI process results in a multilayered structure, which is very similar to the growth rings of a tree.

It has been reported [40] that the infiltration rate of F-CVI can reach 1 mm per hour, while the infiltration rate of I-CVI techniques is much slower, around 1 mm per day. Figure 5.26 shows the density distribution of a large disk fabricated using a F-CVI technique for 40 h. The dimension of the SiC/SiC composite disk is 264 mm in diameter and 12.7 mm thick. The results indicate that the relative densities (real density/theoretical density) of the interior region are high, around 90%. However, the relative density of both exterior parts is lower (about 80%) than that of the central part.

Investigations reveal that the precursor conversion efficiency is dependent not only on the nature of the precursor but also on the processing conditions such as

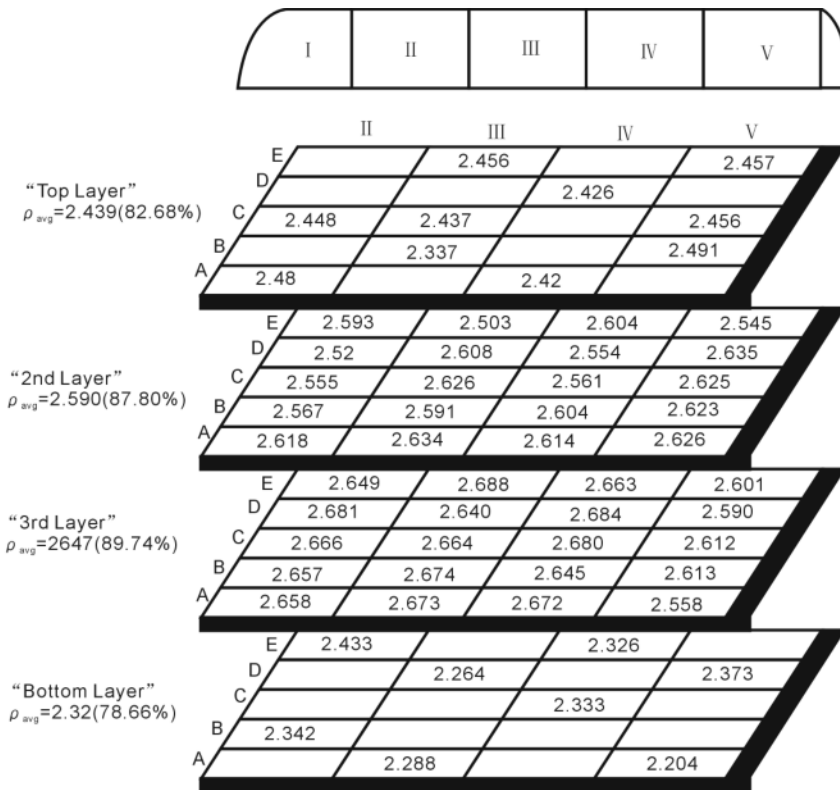


Figure 5.26. Density distribution within a large Nicalon/SiC disk [37]

mass transport method, temperature and pressure of the process, etc. The precursor conversion efficiency in F-CVI processes is much higher than that in I-CVI techniques [38]. For the F-CVI process the observed conversion efficiencies are 5~24% for C_3H_6 , 3~14% for C_3H_8 , and 10~15% for CH_4 . However, the efficiency is typically 0.8~1.5%, reported for isothermal and isobaric CVI techniques.

5.4 Thermal Gradient Chemical Vapour Infiltration

5.4.1 General Description

Both experimental and simulated results of CVI processes reveal that the infiltration rate could be significantly increased with temperature gradient, even as low as 5%, exerted along the thickness of the preform [41]. The direction of the temperature gradient is opposite to that of the concentration gradient of the precursor. Under such conditions an in-depth infiltration is favoured and the densification front moves from the inner sections of the pore towards its entrance. As a result, a complete infiltration is achieved without any early pore sealing.

As shown in Figure 5.27 the I-CVI process is performed in a hot-wall reactor, in which both the heat and mass are transferred from the outer region to the inner region of the preform. As a result it leads to a severe density gradient and forms an impermeable “skin” which impedes the further densification of the inner part of the preform. However, thermal gradient CVI (TG-CVI) is a cold-wall technique, although the densification is also dependent on the mass diffusion. A temperature gradient can be deliberately established across the fibre preform. Unlike the I-CVI model, TG-CVI has a mobile infiltration front within the preform, caused by a

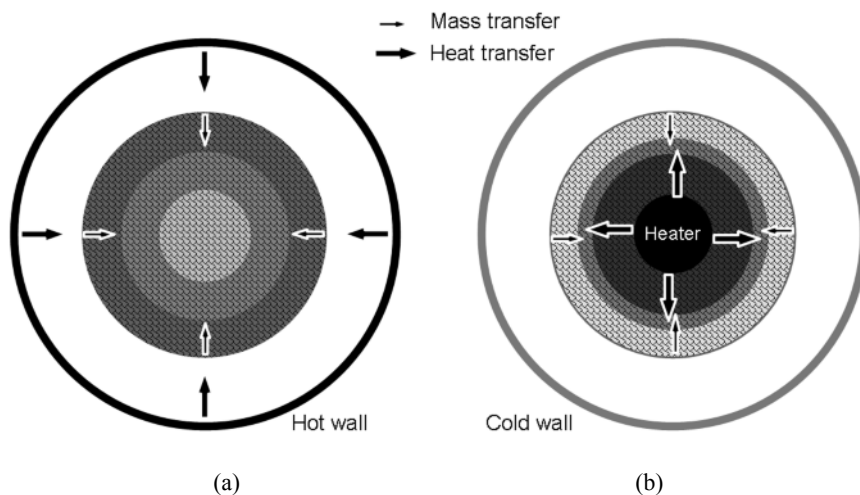


Figure 5.27. Schematic comparison of the I-CVI and TG-CVI techniques: (a) I-CVI and (b) TG-CVI

temperature gradient as shown in Figure 5.27. The direction of the mass transport is opposite to that of the heat transfer. In this case, there is no coupling between the mass transport and chemical reactions [42]. Therefore, the chemical reactions take place in the exact position needed at relatively high temperatures. In this way, the infiltration front moves progressively from the interior region to the exterior region within the fibre preform. If there is a steep temperature gradient, the infiltration rate of TG-CVI is about one or two orders of magnitude larger than that of isothermal/isobaric CVI. TG-CVI is especially suitable for the fabrication of annular and cylindrical preforms.

5.4.2 Some Typical Thermal Gradient/Isobaric Chemical Vapour Infiltration Techniques

5.4.2.1 Inductive Heating Thermal Gradient Chemical Vapour Infiltration

Since its inception, the TG-CVI technique has received considerable attention. During the 1970s this method was developed to manufacture carbon/carbon composites in rocket components reported by Buckley [43] and Stoller *et al.* [44]. As shown in Figure 5.28 the carbon fibre preform is placed over a conical graphite substrate, which is also used as induction susceptor to heat the preform. As reported by Lieberman *et al.* [45] the free space between the sleeve and the preform is about 25 mm. At the beginning of the infiltration stage the carbon preform does not couple electromagnetically to the coil because its density is very low, $0.14 \pm 0.02 \text{ g/cm}^3$. As a result the pyrocarbon is only deposited on the surface of the preform very close to the susceptor and the deposition front moves outwards radially through the preform as the densified preform becomes inductively heated.

The TG-CVI process takes place at a temperature of 1325°C (mandrel temperature) and pressure of 630 Torr. Methane is used as precursor gas and its

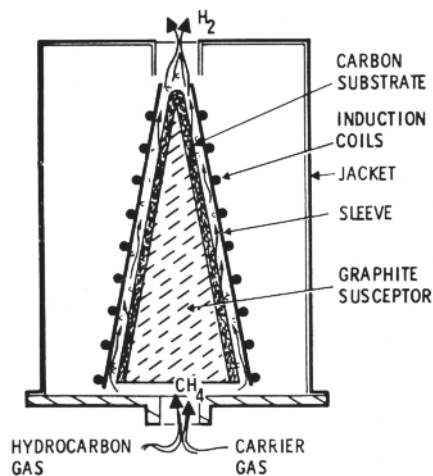


Figure 5.28. Schematic diagram of TG-CVI for conical component [43]

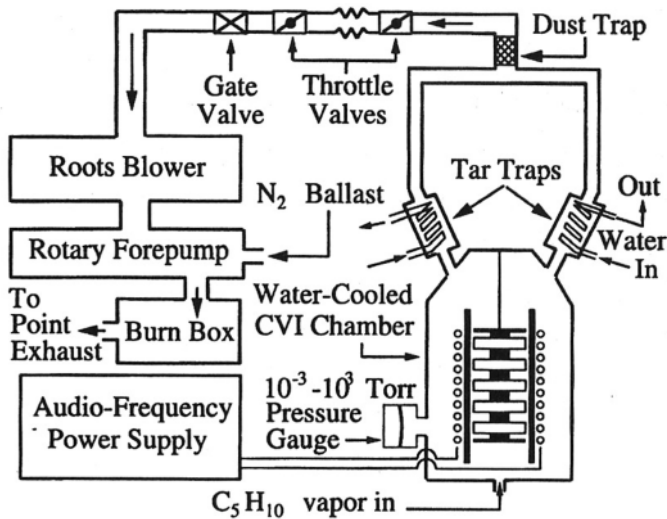


Figure 5.29. Schematic of TG-CVI system developed by AlliedSignal [10]

flow rate is $61 \text{ l}\cdot\text{min}^{-1}$. Argon is used as diluent gas at a flow rate of $205 \text{ l}\cdot\text{min}^{-1}$. This process has a disadvantage of forming soot, due to the combination of very high temperature and high pressure caused by homogenous nucleation in the gaseous phase. There is a density gradient from the inner region (1.74 to $1.84 \text{ g}\cdot\text{cm}^{-3}$) towards the outer region (1.87 to $1.89 \text{ g}\cdot\text{cm}^{-3}$) of the cross-section of the carbon/carbon composites.

In order to infiltrate thick carbon preforms within a short time in one processing cycle, a novel TG-CVI method was developed by AlliedSignal, Inc. [46], USA. As shown in Figure 5.29 the carbon preform disks are heated by the induction method. The preforms are fabricated with non-woven PAN carbon fibres and have a relatively high density in the range 0.4 to $0.6 \text{ g}\cdot\text{cm}^{-3}$. The size of the carbon preform disks is 108 mm (outer diameter, o.d.) \times 44 mm (inner diameter, i.d.) \times 30 mm (thickness). Carbon fibre preform disks are placed around a mandrel (molybdenum or alumina) and spaced about 10 mm apart. In this case the preforms with high density can couple with the electromagnetic field. Hence, an electrically conductive mandrel is not required for heating. A quartz tube inserted between the carbon preform disks and the inductive coil is used as a flow channel for the precursor gases. The temperatures are measured with Pt-Rh/Pt thermocouples inserted into the disks as well as with a pyrometer through a sapphire window. The processing parameters are defined as follows: power and frequency of induction power supply: 8.8 to 13.2 kW , 4.9 to 8.6 kHz ; total pressure: 20 to 100 Torr and cyclopentane (C_5H_{10}); flow rate: 170 to $540 \text{ ml}\cdot\text{min}^{-1}$.

This TG-CVI technique allows significantly higher deposition temperatures, around 200°C higher than that of I-CVI techniques. The infiltration process is normally monitored and controlled in real time. The precursor conversion

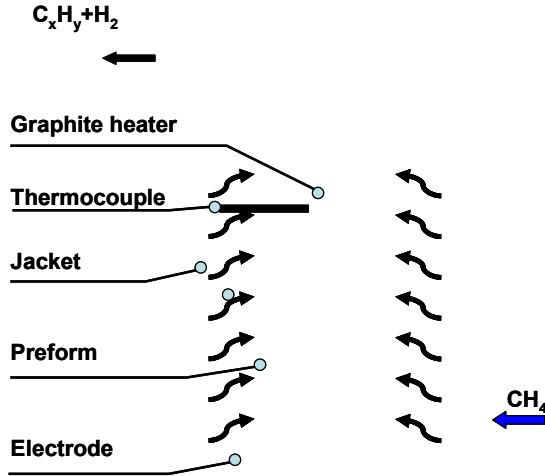


Figure 5.30. Schematic diagram of resistant heating TG-CVI [48]

efficiency is typically 20 to 30% [47]; but very little tar and no soot are produced during the infiltration process. The desirable rough-laminar carbon microstructure is obtained. This technique, therefore, has significant scale-up potential and economic competitiveness in being applied to other materials and wider applications.

5.4.2.2 Resistant Heating Thermal Gradient Chemical Vapour Infiltration

In this approach conductive and refractory materials (e.g. C, Mo or W) are used as the heating element and located at the centre of the preforms. Large electric currents with low voltage flow through the heating element. Hence, a temperature gradient is established with an inside-out direction along the radial direction of the preforms. Figure 5.30 shows the principle of such a resistant heating TG-CVI system with its detailed constituent components.

The following discussion describes a specific example with more detailed information to illustrate the design and operation of such a system [48]. The density of the carbon fibre preform in this case is $0.6 \text{ g}\cdot\text{cm}^{-3}$ and its size is 160 mm (o.d.) \times 80 mm (i.d.) \times 25 mm (thickness). Carbon fibre preforms are stacked vertically and kept tightly together by a mechanical clamp. Natural gas (mainly containing CH_4 : 98%) is used as the precursor gas for infiltration. During the process the densification only occurs in a narrow region where the temperature is sufficiently high for the pyrolysis of the hydrocarbon gas. The temperature gradient within the preform depends on several factors including the heating power, electrical resistance of the heater, the thermal conductivity of the preforms and the cooling of the gas flow along the exterior surface of the preforms. The

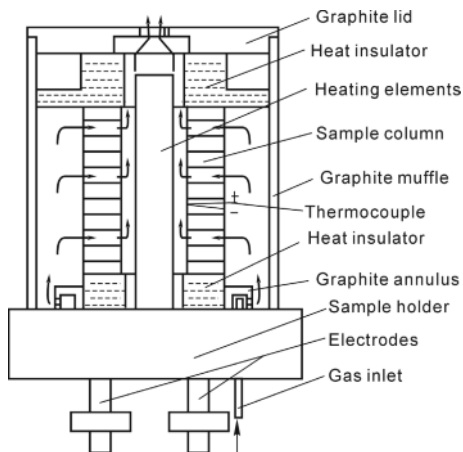


Figure 5.31. Schematic diagram of directional-flow TG-CVI [49]

thermocouple is inserted into the preforms to measure the temperature. The deposition temperature is kept constant by controlling the electrical power supply. During the TG-CVI process the thermocouple is progressively being pulled outwards. The pulling speed of the thermocouple is equal to the moving speed of the deposition front, which is controlled at around $0.25 \text{ mm}\cdot\text{h}^{-1}$. A schematic diagram of this process is presented in Figure 5.30.

Directional-flow TG-CVI was developed to increase the density uniformity, prevent the formation of a dense crust on the surface of preforms and improve the conversion efficiency of the precursor. In such a developed solution, the precursor gases are only allowed to flow into the carbon preforms in the direction of predefined paths as shown in Figure 5.31.

During the densification process, the preform can be distinctly divided into three zones as shown in Figure 5.32a: the completely deposited zone or C/C composites, the depositing zone and the as-prepared porous preform zone. In Figure 5.32b, there is a steep temperature gradient within the depositing zone, as illustrated in the corresponding density gradients of the preforms. Due to the dynamic nature of the depositing process it is a common practice to link the density gradients to the temperature gradient.

Figure 5.33 shows the microstructure characteristics of C/C composites fabricated by the TG-CVI process. The rough laminar pyrocarbon (RL) is located near the heating source at position 1 in Figure 5.32b and the corresponding microstructure is shown in Figure 5.33a. A mixture of smooth laminar and isotropic structure pyrocarbon (SL+ISO) at position 2 is formed and its microstructure is shown in Figure 5.33b. At and near the depositing zone, the pyrocarbon has a smooth laminar structure (SL), and the related microstructures are shown in Figure 5.33c and d. The structure characteristic of the pyrocarbon is dependent on the deposition temperature, the concentration and nature of the precursor as well as those of intermediates. During the TG-CVI process the width of the depositing zone (δ) depends on the deposition temperature (T_d), the

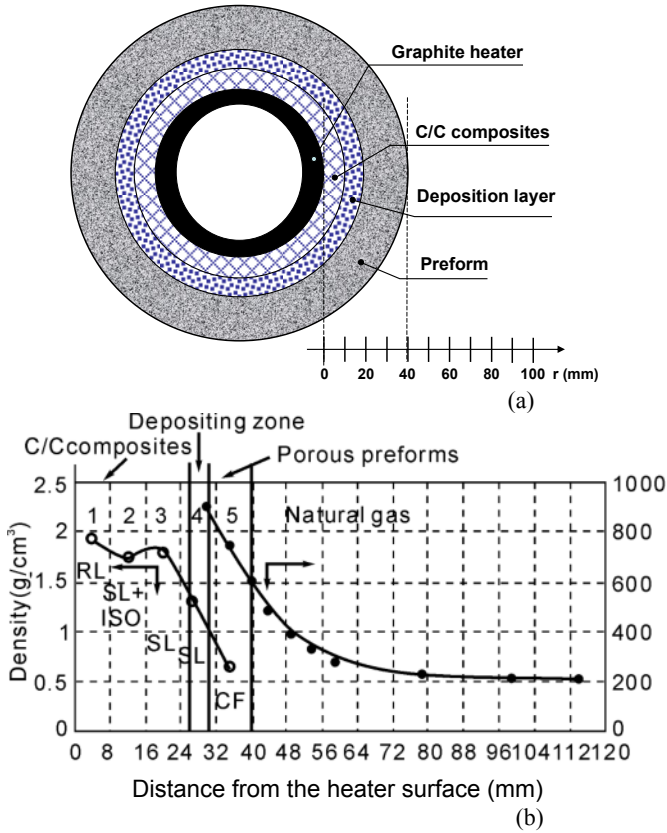


Figure 5.32. Schematic of deposition process and the relationship of distance vs density [48]: (a) different zones and (b) profiles of density and temperature

minimum deposition temperature (T_{min}), and the temperature gradient ∇T within the preform. The relationship is empirically given by [49]

$$\delta = \frac{T_d - T_{min}}{\nabla T} \quad (5.15)$$

For a given thermal gradient higher deposition temperatures result in a wider depositing zone. In this case the pores are very easily trapped within the composites because of the complex architecture of the preforms and a bottleneck effect for the bottle-shaped pores; this produces poor infiltration for these pores. A relatively low deposition temperature and steep thermal gradient give rise to high density and uniform densification.

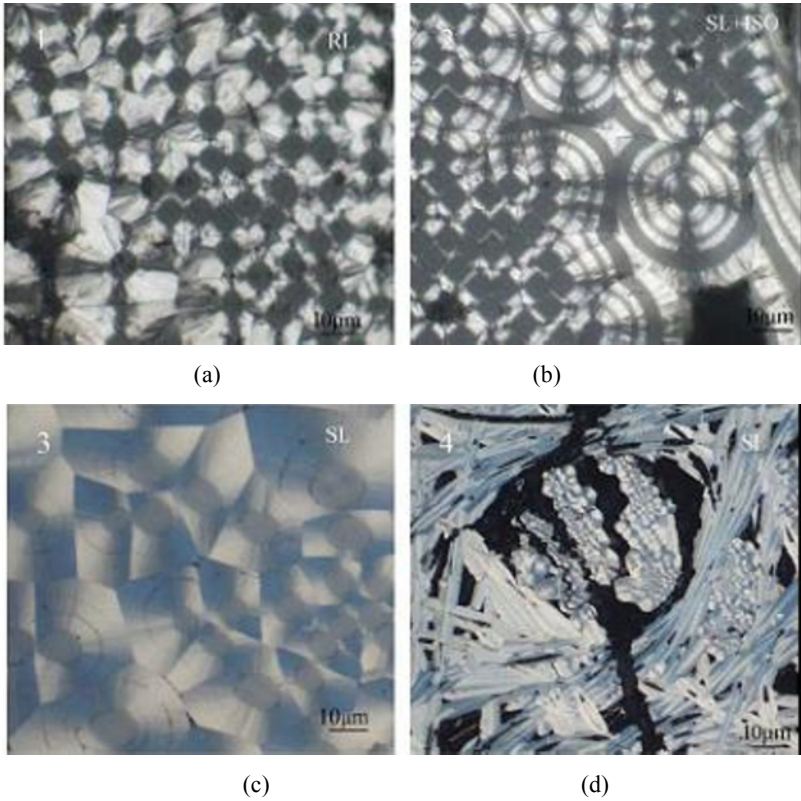


Figure 5.33. Microstructure characteristics of pyrocarbon at the radial cross-section of a preform [48]: (a) RL pyrocarbon at position 1, (b) SL+ISO pyrocarbon at position 2, (c) SL pyrocarbon at position 3 and (d) SL pyrocarbon at position 4

5.4.2.3 Heaterless Thermal Gradient Chemical Vapour Infiltration

For a thick plate carbon preform a steep temperature gradient could be established across the thickness by passing an electric current through it rather than by using a heating element, as shown in Figure 5.34. This kind of method is also called heaterless CVI (HT-CVI) [50, 51]. In this case the highest temperature is at the centre while the lowest temperature is located on the outside surface of the preform. In order to build a steep thermal gradient, some additional methods are used to cool the outer surface of the preform.

As shown in Figure 5.34 a carbon fibre preform with dimensions $380 \times 120 \text{ mm} \times 7 \text{ mm}$ is directly connected to electrodes by passing through an electric current. Due to the low electric resistance of the carbon preform, it is necessary to use an electric power source with a large electric current (0.45 to 1.10 kA) but at a low voltage (40 to 25 V). The heat generated by the current is proportional to the power of the electric current, hence a large electric current significantly increases the heat produced. After the preform (with a density of $0.6 \text{ g}\cdot\text{cm}^{-3}$) is infiltrated

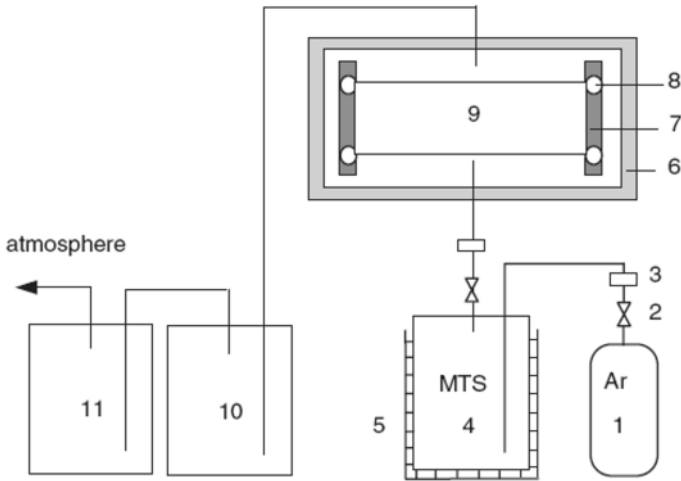


Figure 5.34. Schematic of heaterless TG-CVI process [51]: 1: Ar, 2: shut-off valve, 3: mass flow controller, 4: methyltrichlorosilane (MTS), 5: thermostat bath, 6: water-cooled wall, 7: graphite electrode, 8: graphite bolt, 9: fibre preform, 10: NaOH trap, 11: H₂O trap

with CH₃SiCl₃ and H₂ for 25 h, the density of the C/SiC composite reaches 2.32 g·cm⁻³. Figure 5.35 shows that the SiC matrix is well infiltrated into the large pores, between the plies and small pores among the individual fibres. From the micrographs, the SiC infiltration rate is calculated with the SiC coating thickness divided by the infiltration time. The maximum infiltration rate within the inter-fibre pores is as high as 0.33 μm·h⁻¹.

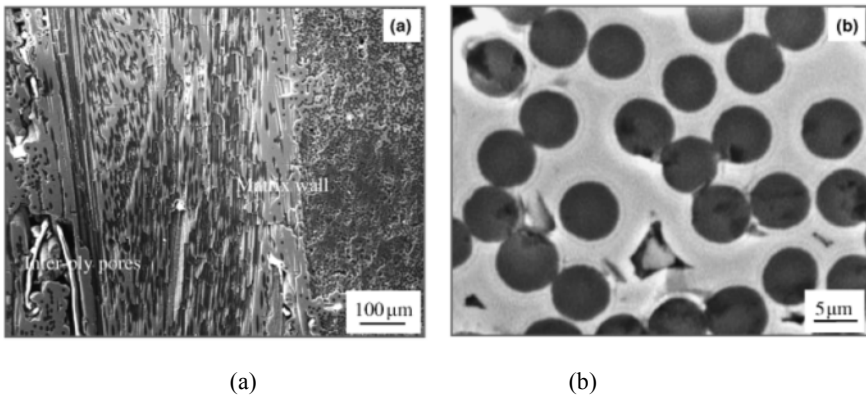


Figure 5.35. Structure characteristics of HT-CVI C/SiC composites [51]: (a) macro-structure and (b) microstructure

5.4.3 Temperature Profile Within the Preform

As mentioned above both exterior and interior heating sources are methods for creating a temperature gradient within a preform. If the preform is heated with an exterior heating source, the temperature profile within the preform could be treated as a linear distribution according to the Fourier law of heat transfer in Section 2.3. If the preform is heated by itself (as in Section 5.4.2.3), however, the situation of interior heating source is much more complex.

Here we consider a cylinder model as shown in Figure 5.36a. In order to simplify the calculation some reasonable assumptions are made as follows:

1. the cylinder has a large aspect ratio, i.e. $L \gg 2R$,
2. both the electric conductivity and thermal conductivity remain constant within the whole temperature range and
3. the outer surface temperature of the cylinder is maintained at constant temperature (T_0).

In steady conditions, the following relation can be established according to the energy balance [12]:

rate of thermal energy in across surface at r	+	rate of thermal energy in across surface at $r+dr$	=	rate of thermal production by electrical heating
--	---	--	---	--

The relationship is written as

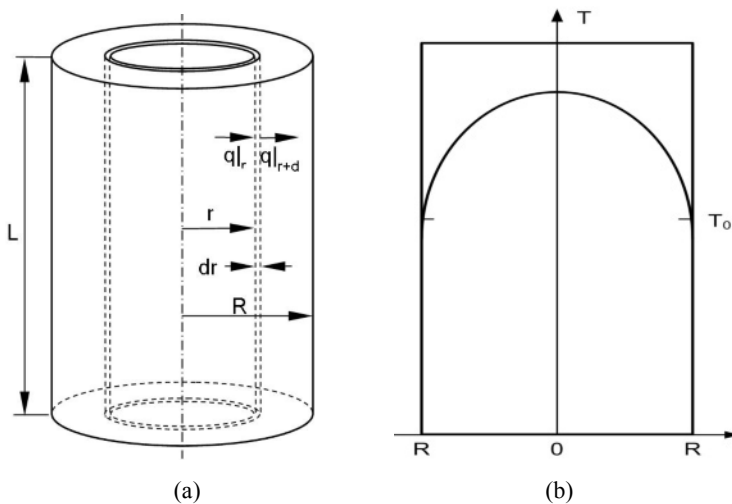


Figure 5.36. Cylinder model for temperature calculation [12]: (a) a cylinder model (b) temperature distribution

$$(2\pi r dr L) \dot{q} + 2\pi r L q|_r = 2\pi(r + dr)Lq|_{r+dr} \quad (5.16)$$

where \dot{q} is the rate of heat production per unit volume. For resistant heating methods, \dot{q} is given by

$$\dot{q} = \frac{I^2}{k_e} \quad (5.17)$$

where k_e is the electric conductivity and I is the electric current.

Here \dot{q} can be treated as a constant; then the following expression can be obtained:

$$\frac{d}{dr}(rq) = \dot{q} r \quad (5.18)$$

Using the Fourier law of heat transfer:

$$q = -\alpha \frac{dT}{dr} \quad (5.19)$$

where α is the thermal conductivity.

By substituting Equation (5.19) into Equation (5.18) the following expression can be obtained:

$$\frac{d}{dr}\left(r \frac{dT}{dr}\right) = -\frac{\dot{q} r}{\alpha} \quad (5.20)$$

$$\frac{dT}{dr} = -\frac{\dot{q} r}{2\alpha} + \frac{C_1}{r} \quad (5.21)$$

After further integration this gives

$$T = -\frac{\dot{q} r^2}{4\alpha} + C_1 \ln r + C_2 \quad (5.22)$$

Because the flux of heat production is equal to the flux of heat dissipation at the surface, the associated boundary conditions can be written as

$$\dot{q} \pi R^2 L = -2\pi \alpha R L \left. \frac{dT}{dr} \right|_{r=R} \quad (5.23)$$

$$r=R, T=T_0 \quad (5.24)$$

Equation (5.23) becomes

$$\left. \frac{dT}{dr} \right|_{r=R} = -\frac{\dot{q} R}{2\alpha} \quad (5.25)$$

By comparing Equation (5.20) with Equation (5.25), $C_1=0$. According to other boundary conditions, $T=T_0$ at $r=R$, the integral constant of C_2 is found to be

$$C_2 = T_0 + \frac{\dot{q} R^2}{4\alpha} \quad (5.26)$$

Hence, Equation (5.22) becomes

$$T = T_0 + \frac{\dot{q} R^2}{4\alpha} \left[1 - \left(\frac{r}{R} \right)^2 \right] \quad (5.27)$$

Equation (5.28) expresses the relationship between temperature (T) and position (r) along the radial direction of the preform. It is a parabolic profile from the central axis of the cylinder, as shown in Figure 5.36b.

5.5 Liquid-immersion Chemical Vapour Infiltration

5.5.1 General Description

The discussion in Section 5.4 clearly indicates that a temperature gradient has a significant influence on the densification of the preform. In order to increase the densification rate and improve the density, it is necessary to establish a very steep thermal gradient within the preform. In 1984 Houdayer *et al.* [52] described a method for rapid densification by immersing the preform into a liquid precursor at high temperatures to fabricate the C/C composites. This densification process is also called liquid-immersion CVI (LI-CVI).

As shown in Figure 5.37 the preform is placed on a graphite mandrel, which is immersed in a liquid precursor. The mandrel is located at the lower part of the reactor, which has an opening through which a shaft is connected to a motor. The motor outside the reactor in turn rotates the graphite mandrel in the liquid precursor. The graphite mandrel is also used as a heating element coupled with the electromagnetic field from the induction coils. The infiltration temperature generated is in the range 1000 to 1300°C, which is sufficiently high to cause the liquid precursor to be vaporised. The vaporised precursor gases penetrate into the preform and then pyrolysed to form pyrocarbon deposited on the fibre surface. There are two outlet ports located at the upper position of the reactor. One is used to introduce the liquid precursor and the other to introduce inert gas for expelling the air contained inside before the infiltration process commences. At the top of the reactor there is a water-cooling condenser to separate the unconsumed vaporised liquid precursor from exhaust gases.

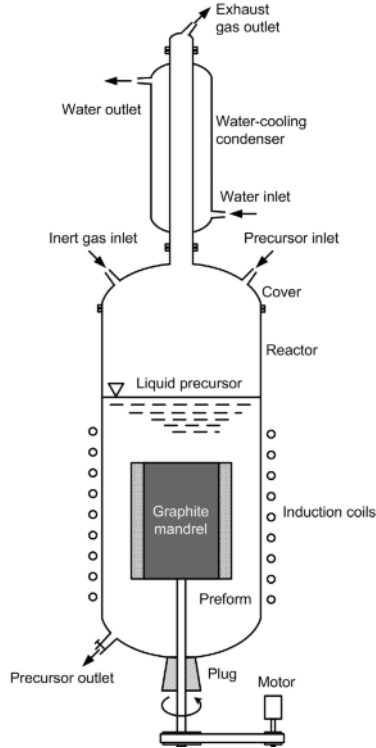


Figure 5.37. Illustration of liquid-immersion CVD reactor [52]

In this technique cyclohexane (C_6H_{12}) is selected as a liquid precursor because of its suitable boiling point, low toxicity and low cost. In addition, some other hydrocarbons also exhibit infiltration properties similar to those of cyclohexane,

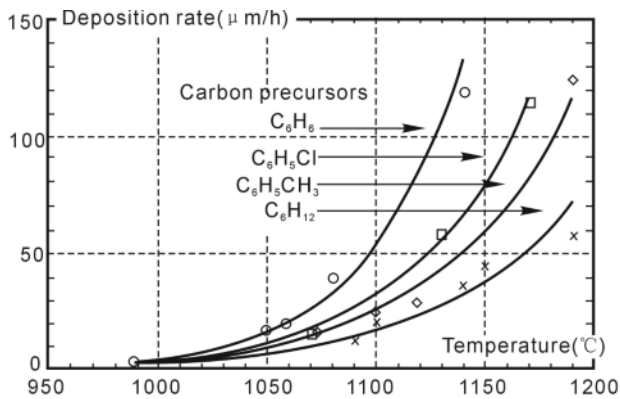


Figure 5.38. Deposition rate comparison of several carbon precursors [42]

Table 5.1. Some commonly used precursors and the corresponding materials deposited [10]

Deposit	Liquid precursor
C	C ₅ H ₁₀ , C ₆ H ₁₂ , C ₆ H ₆ , C ₆ H ₅ CH ₃ and C ₆ H ₅ Cl, gasoline, etc.
BN	Trichlorobozaine (B ₃ N ₃ Cl ₃ H ₃), borazine (B ₃ NH ₆)
SiC	Methyltrichlorosilane CH ₃ SiCl ₃ , dimethyldichlorosilane (CH ₃) ₂ SiCl ₂ , and methylchlorosilane ((CH ₃) ₂ SiHCl ₂)
SiC–Si ₃ N ₄	Tris-n-methyl-amino-silane, silazane
SiO ₂	Si(OC ₂ H ₅) ₄

including C₆H₅CH₃, C₆H₆ and C₆H₅Cl. As illustrated in Figure 5.38, both aromaticity and the presence of halogen in the above precursors increase the conversion efficiency and the yield. Some commonly used precursors for other deposit materials are listed in Table 5.1.

For the liquid-immersion CVI process a very steep thermal gradient is established within the preform at the initial infiltration, ranging from 400 to 500°C·min⁻¹. This then decreases because the parts successively densified reach a temperature closer to that of the heating element. As the temperature is increased from 900 to 1200°C, the densification rate is significantly increased from 0.02 g·min⁻¹ to 1.25 g·min⁻¹, as listed in Table 5.2. However, undesirable deposition behaviour occurs if the temperature is further increased; the preforms become less dense in the inner region than in the outer region. In such cases, regions far from the susceptor reach a temperature higher than that of hydrocarbon pyrolysis, thus leading to densification at the outer regions or extremes of the preform before the intermediate regions are completely infiltrated.

5.5.2 Model of Liquid-immersion Chemical Vapour Infiltration

Based on experimental results an overall model of the LI-CVI process is proposed by Rovillain [42], as shown in Figure 5.39. Starting from the centre of the heating element the reactor is divided into five zones, each of them characterised by a specific function.

Zone I: Heating Resource

The first zone is characterised by its function of generating sufficient heat for the CVI process. This heating source is also required to maintain a constant temperature (T) during the CVI process. The heating source initially includes only

Table 5.2. Relationship between densification rate and processing temperature [53]

Temperature (°C)	900	1000	1050	1100	1200
Densification rate (g·min ⁻¹)	0.02	0.10	0.25	0.45	1.25

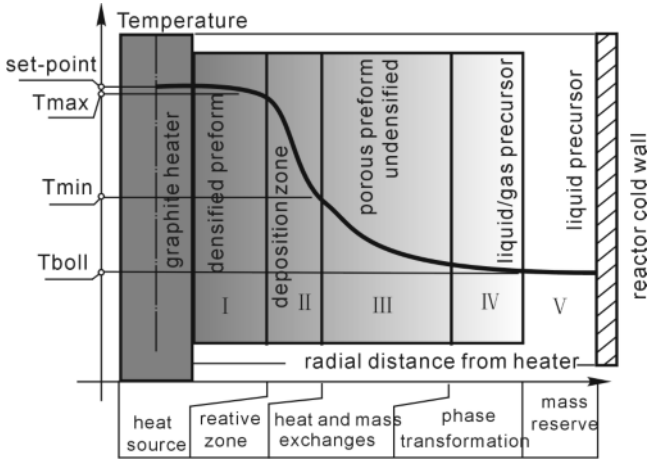


Figure 5.39. LI-CVI process model of [42]

the graphite heater, but as the preform is gradually densified and becomes C/C composites this also becomes a part of the heating source. The heat is transferred outwards by a thermal conductive mechanism to the adjacent zones. Within this zone the temperature gradient is very small.

Zone II: Reactive Zone

The reactive zone is the region where chemical vapour infiltration takes place through many complex chemical reactions. The reactive zone is narrow. There is a very steep thermal gradient within this zone to facilitate the infiltration process. In Figure 5.39 T_{max} and T_{min} are the maximum temperature and minimum temperature for deposition respectively.

The pyrolysis of the precursors is a complex process and it produces a large number of intermediate species. The composition of the exhaust gases can be analysed by gas phase chromatography. The by-products listed in Table 5.3 are generally the same within temperature range of 1000 to 1350°C when cyclohexane

Table 5.3. Exhaust gas analysis results by GPC (mol%) [53]

T(°C)	H ₂	CH ₄	C ₂ H ₂	C ₂ H ₄	C ₂ H ₆	C3	C4	C ₆ H ₁₂
1000	21.1	11.6	0.5	31.1	5.2	6.9	18.1	5.5
1100	36.2	12.8	2.5	27.7	1.0	4.5	ND	7.5
1250	49.1	13.3	4.5	16.5	0.4	1.2	ND	ND
1350	45.3	13.1	4.0	21.4	0.6	1.7	ND	ND

Note: (1) C₆H₁₂ is used as the liquid precursor; (2) C3 and C4: undetermined C3 and C4, species; (3) ND: non-detected products.

is utilised as the liquid precursor. However, their relative proportions depend on the processing temperature. The amount of hydrogen and the lightest hydrocarbons (mainly methane and ethylene) is increased as the temperature increases. By contrast, the proportion of the heaviest gaseous compounds, especially C3 and C4 species and cyclohexane, becomes less and less important as the processing temperature is increased above 1250°C. These studies clearly reveal that, as expected, cyclohexane is firstly vaporised and then decomposed in a great number of compounds.

Zone III: Heat and Mass Exchange Zone

This is the area within the porous preform where the complex heat and mass exchanges occur. In this multiphase system the heat is transferred outwards through convective and radiation mechanisms. The precursor gases are supplied from the outside towards the reactive zone while the exhaust gases are transferred in the reverse direction after the chemical reactions.

Zone IV: Phase Transformation Zone

The liquid precursor is transformed into gaseous reactants and the function of this zone is to ensure a sufficient liquid-to-gas-phase transformation. The liquid precursor is vaporised on the outer surface of the preform where the temperature is maintained just above the boiling point of the liquid precursor. In this case the boiling point refers to the temperature at atmospheric pressure for a given hydrocarbon.

Zone V: Mass Reserve Zone

The outside zone is used to store the reserve liquid precursor in a mass reservoir, which surrounds the preform in a fully immersed manner. Outside of the preform the liquid forms a ‘turbulent’ boiling fluid with many bubbles due to cavitation and the outgoing gases. The cavitation phenomenon is a two-phase process in which bubbles or voids in the heated liquid precursor are formed.

The in-depth model of the deposition process is another important aspect of gaining a deep understanding of an LI-CVI process as well as a TG-CVI process. Under a strong thermal gradient the relationship between the deposition rate on a fibre (u_{dep}) and the densification rate inside the preform (u_{front}) can be calculated by using the one-dimensional model [42].

As shown in Figure 5.40, the regularly arranged fibres are perpendicular to the reaction front. The spacing between fibres is d and the deposition location along the fibre is f . Based on experimental observation both u_{dep} and u_{front} can be expressed as

$$u_{dep} = k \exp\left(-\frac{E_a}{RT}\right) \quad (5.29)$$

$$u_{front} = \frac{df}{dt} \quad (5.30)$$

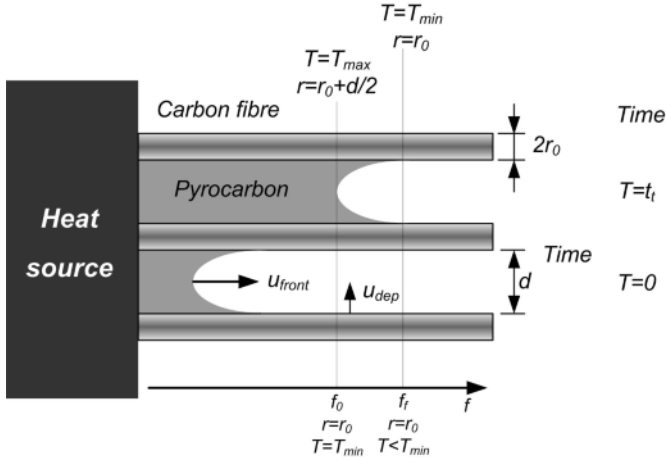


Figure 5.40. One-dimensional model for LI-CVI process [42]

As the deposition advances the fibre becomes thicker and thicker. The radius of the coated fibre is then expressed as

$$r = r_0 + \int_0^t u_{dep} dt = r_0 + \int_{f_0}^{f_f} u_{dep} \frac{df}{u_{front}} \quad (5.31)$$

At t_f the coated fibre radius is $r = r_0 + d/2$, and the front location is f_f . Then we can obtain

$$u_{front} = \frac{2}{d} \int_{f_0}^{f_f} u_{dep} df \quad (5.32)$$

Considering that the temperature gradient is constant in the thickness of the densification front the precursor starts to be pyrolysed between the deposition temperature T_{max} and the lowest temperature T_{min} . Then the front densification rate is the function of T_{max} and temperature gradient ∇T . This is expressed as

$$u_{front} = \frac{2}{d} \int_{T_{min}}^{T_{max}} u_{dep} \frac{df}{dT} dT = \frac{2k}{d|\nabla T|} \int_{r_{min}}^{r_{max}} \exp\left(-\frac{E_a}{RT}\right) dT \quad (5.33)$$

where R is the perfect gas constant, k is the chemical reaction constant and E is the active energy of the chemical reaction.

5.6 Pulsed Chemical Vapour Infiltration

5.6.1 General Description

For most reactions in CVD processes the volume of the by-products is larger than those of the reactant gases, as exemplified by Equation (5.1); therefore, fresh reactant gases have to penetrate through the outgoing stream of by-product gases in order to reach new areas, at deeper locations, for further deposition. This is the main cause of the long densification time and relatively high residual porosity.

Based on pulsed CVD (P-CVD) by Bryant [55] in 1976 Sugiyama [56, 57] proposed the pulsed CVI method (P-CVI). The aim is to accelerate the in-diffusion of fresh precursor species and the out-diffusion of the by-products to and from the pores of the preform and thereby reduce the total infiltration time and density gradient along the thickness of the composites. The instantaneous introduction of precursor gases ensures the uniformity of the precursor gas composition along the depth of the pores within the preform and leads to uniform dense composites.

The typical system architecture for a P-CVI process is shown in Figure 5.41. For silicon carbide infiltration hydrogen gas after a purification process is mixed with argon and then bubbled through a CH_3SiCl_3 liquid precursor. The precursor gases are then accumulated in a reservoir from which the gases are fed into the reaction chamber instantaneously during the gaseous reactant injection phase of the P-CVI cycle. This is controlled by the electromagnetic valve at a preset pressure. Then, the inlet electromagnetic valve is closed for the second phase of the cycle, deposition, and the gases are kept in the chamber for a given time to allow the SiC deposition process to occur. Finally the outlet electromagnetic valve is opened to evacuate the deposition chamber and all by-products are purged for a new cycle. This is the last phase of the cycle evacuation. The total volume of the pipes, dead spaces and reaction chamber is minimised to satisfy the requirements of high gas yield and short evacuation time.

The above three-phase (namely gaseous reactant injection, deposition and evacuation) cycle is repeated for the whole duration of the P-CVI process until a product is finished. The inlet and outlet valves opening and closing are typically controlled with a computer system.

5.6.2 Model

As described above P-CVI works on the principle of alternative injection of reactant gases, deposition and evacuation of CVI exhaust gases. This is required to rapidly transport reactant species into, and by-product gases out of, the preform at isothermal conditions. For each cycle the detailed sequence generally consists of the following essential and sequential steps, as shown in Figure 5.42:

1. rapidly injecting the precursor into the fully evacuated CVI chamber at a predetermined pressure,
2. holding the precursor gases for a preset period (also known as duty cycle) during which deposition occurs under a designed condition at a preset pressure and temperature, and

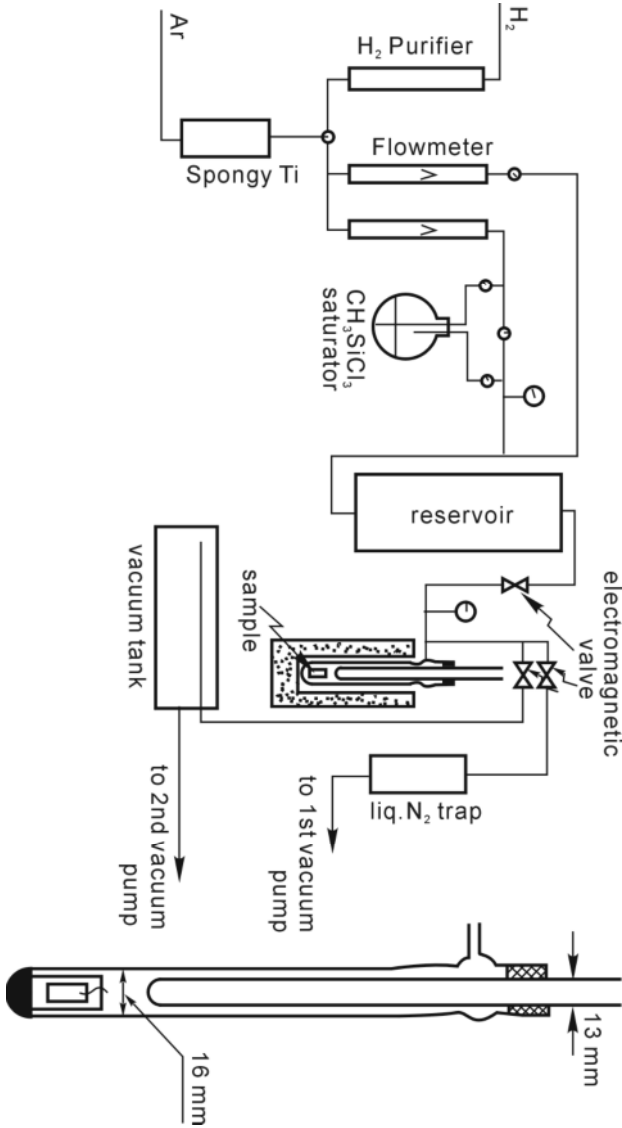


Figure 5.41. Apparatus for pulsed CVD of SiC [57]

3. rapidly evacuating the by-product gases from the reaction chamber.

Depending on the requirement of the vacuum level generated during the evacuation phase sometimes it is necessary to introduce a period of time in the cycle to purge the exhaust gases further to ensure a thorough evacuation. During this process the inlet valve is fully closed and the outlet valve is kept open.

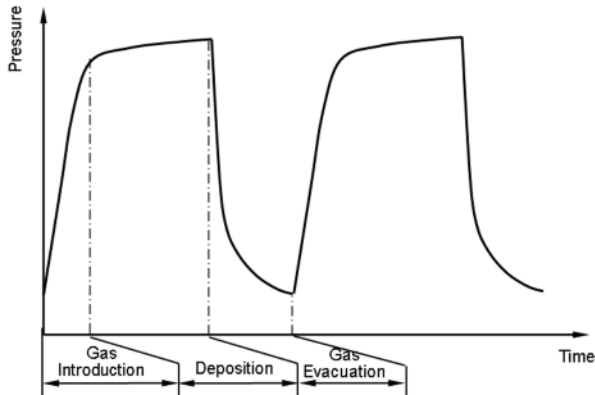


Figure 5.42. Elementary sequences for a P-CVI process

At each cycle or pulse the reactor is first evacuated at a reduced level pressure, 0.05 to 0.1 kPa, at the end of the previous cycle. The precursor gases are injected into the reactor within a pressure range of 1~10 kPa within a few seconds. Then the reactor is sealed off for infiltration for a period of holding time (t_h), which can be easily controlled in a wide range, typically from 0.2 to 120 s. Each pulse ends with the evacuation stage which takes a few seconds. These steps are repeated many times.

The P-CVI processing parameters include the deposition temperature and pressure, precursor injection time, holding time, evacuation time and the number of pulses.

The overall model of a P-CVI process is as shown in Figure 5.43. During a P-CVI process the mass transport of gaseous species can be divided into two stages. In the first stage mass transport takes place by forced convection within a very short period of a few hundredths or tenths of a second. In the second stage of the duty cycle the mass transport is dominated by the diffusion from the free space of the reaction chamber into the pores of the fibre preform. The temperature is kept

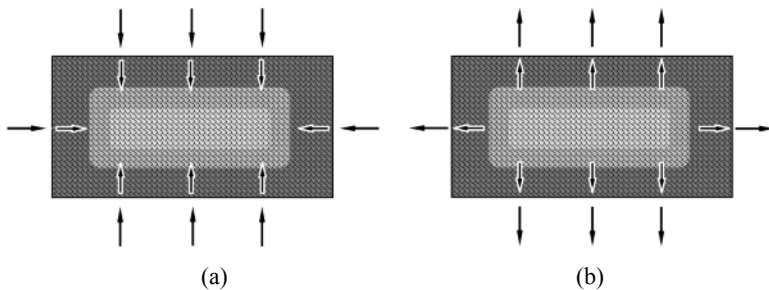


Figure 5.43. Overall model of a P-CVI process: (a) during gas introduction and (b) during gas evacuation

constant throughout the whole process. Accordingly, this process can be considered another form of I-CVI process operated within a very short time and regularly interrupted by a number of pulses. In other words, P-CVI is transformed into I-CVI if the duty cycle is increased from a few seconds to a few hours.

5.6.3 Applications

At the initial development period of the P-CVI process it was considered a novel way to increase the densification rate and to minimise the density gradient of the composites. However, this technique is difficult to scale up because it is very difficult, or impossible, to evacuate a large reaction chamber within a very short time. In spite of that, this approach provides some useful information to understand the infiltration mechanisms and to tailor the materials according to the requirements [58]. For example, the residence time of the reactant gases in a P-CVI process can be accurately controlled. Hence, it is helpful to understand the influence of homogeneous reactions and evolution of the reactant gases on the microstructure characteristics of the deposit. Furthermore, multilayered materials can be fabricated if different precursors are alternately introduced into the reaction chamber. Multilayered deposits of $(\text{PyC-SiC})_n$ are prepared in this way; pyrocarbon (PyC) and silicon carbide (SiC) are deposited from hydrocarbon gas (C_xH_y) and methyltrichlorosilane (MTS-H_2) respectively. The thickness of the sublayer can be elaborately fabricated in a large-scale range by controlling the processing parameters of temperature, pressure and holding time.

One of the distinct applications of the P-CVI technique is fabricating highly engineered composites with a multilayered interphase and matrix, which exhibit self-healing behaviour in an oxidising environment. Figure 5.44a shows the microstructure of a composite which has a self-healing matrix consisting of four sequences—S1, S2, S3 and S4. Each sequence includes four sublayers of $\text{C(B)/B}_{13}\text{C}_2/\text{C(B)/SiC}$. Both S1 and S2 are located in the inner region and have a very thin thickness of 1 μm . By contrast, the S3 and S4 sequences are located in the outer region and their thicknesses are 4 μm and 6 μm respectively. It is interesting to note that the multistep pull-out of the fibre from the matrix is observed from the fracture surface as shown in Figure 5.44b and c.

The boron-doped pyrocarbon sublayer of C(B) is used as the mechanical fuse which ensures crack deflection and fibre pull-out. A hydrocarbon (C_xH_y) and BX_n ($\text{X}=\text{F}$ or Cl) are used as reactant precursors to deposit the C(B) layer. Both B_{13}C_2 and SiC are employed as the glass former to improve the oxidation resistance of the composite. B_{13}C_2 is deposited with the same precursors as for C(B) but in different conditions. CH_3SiCl_3 and H_2 are used as the precursor gases for the SiC deposition.

Figure 5.45 shows examples of the self-sealing behaviour of this composite. The $\text{B}_2\text{O}_3\text{-SiO}_2$ glass is formed at high temperature after boron carbide (B_{13}C_2) and silicon carbide (SiC) are oxidised in the oxidising atmosphere. The glass has sufficient fluidity and can fill the microcracks and defects within the composite. The incoming oxygen is consumed by *in-situ* reactions with boron carbide and silicon carbide such that the oxygen transport access is efficiently blocked off by

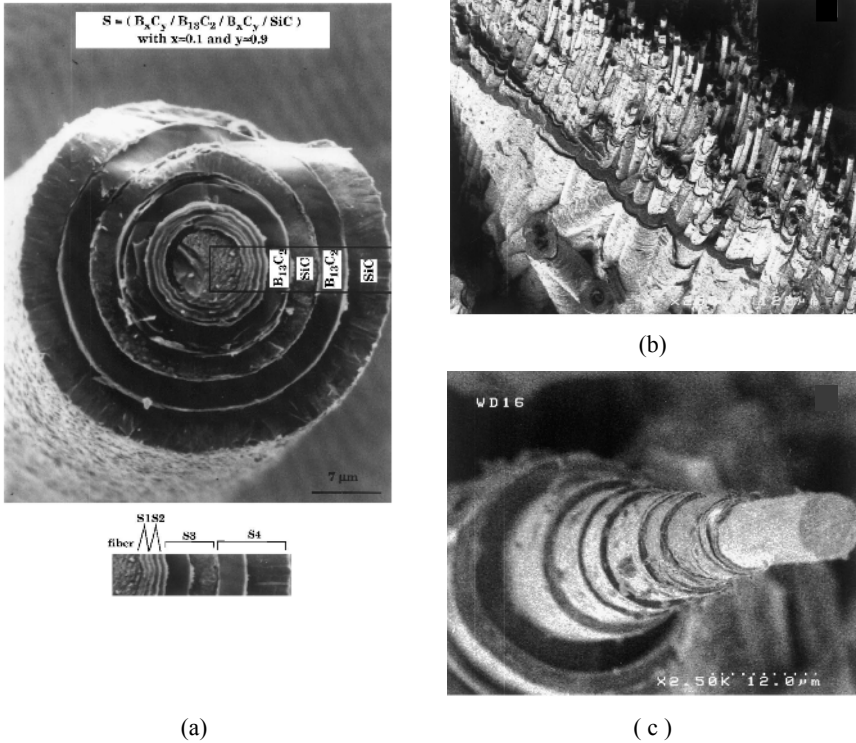


Figure 5.44. SEM graphs of multilayered matrix composite by P-CVI: (a) details of four sequences on a single fibre [23], (b) fracture surface of 2.5-D C/SiC composite [59], (c) fracture surface of a single fibre [59]

$B_2O_3-SiO_2$ glass. Hence, the oxidation resistance of the composite is greatly improved by the multilayered matrix.

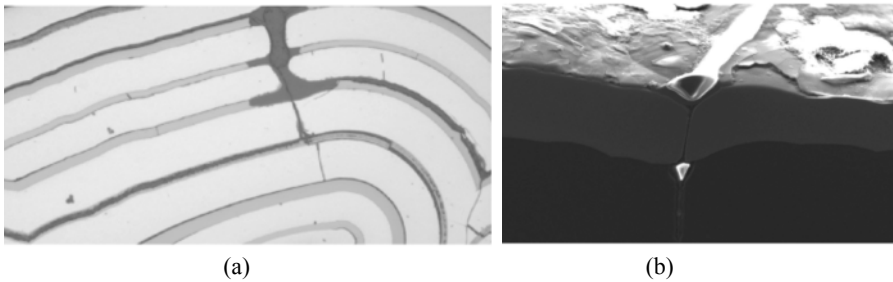


Figure 5.45. Self-sealing composites [33]: (a) self-sealing sequences and (b) glass-filled cracks

5.7 Chemical Vapour Composite

The chemical vapour composite (CVC) process was developed by ThermoTrex Corporation [60, 61] to fabricate materials by simply mixing reinforcement elements such as particles, whiskers and fibres with precursor gases, which are then transported and co-deposited on a substrate. A schematic of a CVC SiC reactor is shown in Figure 5.46. One distinct advantage of this technique is flexibility in controlling the variation of density, geometry and composition of the reinforcement during deposition. The process can fabricate composite components to the net shape (± 0.013 mm) on a machined substrate in a single run.

The advantages of the CVC process are as follows: fast growth rate of the composites (about 100 times faster than conventional techniques because the precursor gases need not infiltrate into a preform), no need for expensive fibre preforms, possible to use high modulus fibres in the composites and high accuracy of deposited composites without further machining. However, the CVC technique also suffers the weakness of having a low fibre volume fraction in the composites and using only short fibre, resulting in inferior mechanical properties of the composites.

During CVC processing, a CH_3SiCl_3 precursor is bubbled and delivered by the H_2 carrier gas. Then the reactant gases and reinforcements are mixed together and injected onto the graphite substrate, which is heated at a preset temperature. Like a CVD process, a CVC process can essentially produce a uniform layer of deposit onto the surface of the substrate. Hence, it allows the geometry of the base

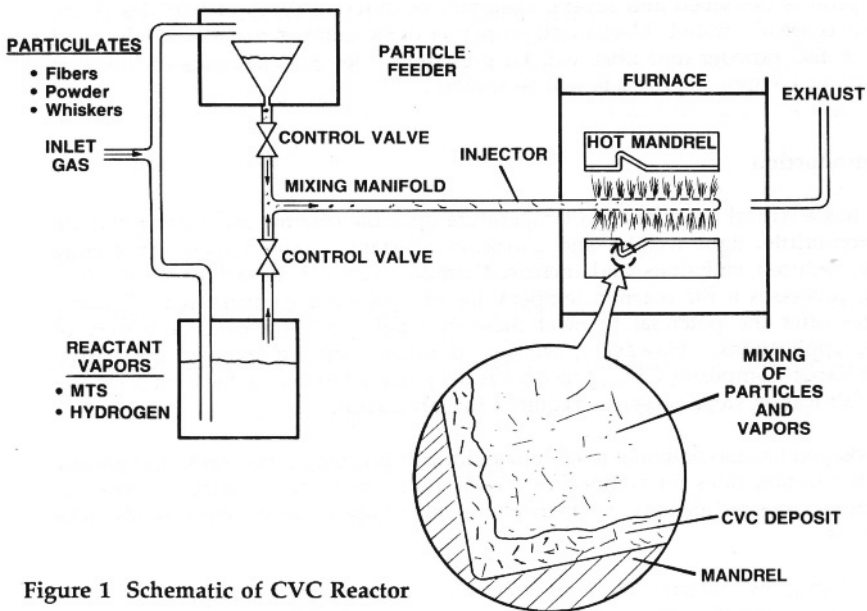


Figure 1 Schematic of CVC Reactor

Figure 5.46. Schematic of CVC SiC reactor [60]



(a)



(b)

Figure 5.47. Microstructure of C/SiC (a) and some components (b) by the CVC technique [60]

component substrate to be replicated. Figure 5.47a shows the microstructure of the components fabricated by the CVC technique. Figure 5.47b shows some typical examples of the components produced by using the CVC technique. It can be seen that components in a range of complex shapes have been manufactured.

References

- [1] Bickerdike RL, Brown ARG, Hughes G, Ranson H (1962) In: Mrosowski S, Studebaker MC, Walker PL (eds) Proceedings of 5th conference on carbon, vol 1. Pergamon, New York, p575
- [2] Jenkins WC (1964) Method of depositing metals and metallic compounds throughout the pores of a porous body. US Patent 3,160,517
- [3] Kotlensky WV (1973) Deposition of pyrolytic carbon in porous solid. In: Walker PL Jr, Thrower PA (eds) Chemistry and physics of carbon. Dekker, New York, vol 9, pp173–262:

- [4] Fitzer E, Hegen D, Strohmeier H (1979) Chemical vapor deposition of silicon carbide and silicon nitride and its application for preparation of improved silicon ceramics. In: Sedgwick TO, Lydtin H (eds) Proceedings of the 7th international conference on chemical vapour deposition. Electrochemical Society, Pennington, NJ, pp525–535
- [5] Christin F, Naslain R, Bernard C (1979) A thermodynamic and experimental approach of silicon carbide CVD. Application to the CVD-infiltration of porous carbon composites. In: Sedgwick TO, Lydtin H (eds) Proceedings of the 7th international conference on chemical vapour deposition. Electrochemical Society, Pennington, NJ, pp499–514
- [6] Caputo AJ, Lackey WJ (1984) Fabrication of fibre-reinforced ceramic composites by chemical vapor infiltration. *Ceram Eng Sci Proc* 5:654–667
- [7] Fitzer E, Fritz W, Schoch G (1991) The chemical vapor impregnation of porous solids, modeling of the CVI-process. *J de Physique IV* 2:C-2-143–150
- [8] Naslain R (1992) CVI composites. In: Warren R (ed) *Ceramic-matrix composites*. Chapman & Hall, New York, pp199–244
- [9] Besmann TM, Sheldon BW, Lowden RA, Stinton DP (1991) Vapor-phase fabrication and properties of continuous-filament ceramic composites. *Science* 253:1104–1109
- [10] Golecki I (1997) Rapid vapor-phase densification of refractory composites. *Mater Sci Eng R*20:37–124
- [11] Christin F (2002) Design, fabrication and application of thermostructural composites (TSC) like C/C, C/SiC, and SiC/SiC composites. *Adv Eng Mater* 4:903–912
- [12] Bird RB, Stewart WE, Lightfoot EN (1960) *Transport Phenomena*. Wiley, New York
- [13] Kalidindi SR, Desu SB (1990) Analytical model for the low pressure chemical vapor deposition of SiO₂ from tetraethoxysilane. *J Electrochem Soc*137:624–628
- [14] Starr TL (1992) Advance in modeling of the chemical vapor infiltration process. In: Besmann TM, Gallois BM, Warren JW (eds) *Chemical vapor deposition of refractory metals and ceramics II*. Materials Research Society, Pittsburgh, PA, pp207–214
- [15] Thomas JM, Thomas WJ (1997) *Principles and practice of heterogeneous catalysis*, VCH, Weinheim
- [16] Fedou R, Langlais F, Naslain R (1990) On the modeling of the chemical vapor infiltration of SiC-based ceramics in a straight cylindrical pore. In: Spear KE, Cullen GW (eds) Proceedings of the 11th international conference on chemical vapour deposition. Electrochemical Society, Pennington, NJ, pp513–524
- [17] Marinkovic S, Dimitrijevic S (1985) Carbon/carbon composites prepared by chemical vapour deposition. *Carbon* 23:691–699
- [18] Clegg WJ, Kendall KMN, Alford N, Button TW, Brichall JD (1990) A simple way to make tough ceramics. *Nature* 347:455–457
- [19] Evans AG (1990) Perspective on the development of high-toughness ceramics. *J Am Ceram Soc* 73:187–206
- [20] Dugne RO, Guette A (1991) Boron nitride interphase in ceramic-matrix composites. *J Am Ceram Soc* 74:2482–2488
- [21] Tressler RE (1999) Recent developments in fibres and interphases for high temperature ceramic matrix composites. *Composites A*30:429–437
- [22] Brennan JJ (1990) Interfacial studies of chemical-vapour-infiltrated ceramic matrix composites. *Mater Sci Eng A*126: 203–223
- [23] Naslain R, Pailler R, Bourrat X, Bertrand S, Heurtevent F, Dupel P, Lamouroux F (2001) Synthesis of highly tailored ceramic matrix composites by pressure-pulsed CVI. *Solid State Ion* 141-142:541–548

- [24] Xu YD, Cheng LF, Zhang LT, Yin HF, Yin XW (2001) Mechanical properties of 3D fibre reinforced C/SiC composites. *Mater Sci Eng A* 300:196–202
- [25] Lamouroux F, Bourrat X, Naslain R (1993) Structure/oxidation behavior relationship in the carbonaceous constituents of 2D-C/PyC/SiC composites. *Carbon* 31:1273–1288
- [26] Lackey J, Hanigofsky JA, Freeman GB, Hardin RD, Prasad A (1995) Continuous fabrication of silicon carbide fibre tows by chemical vapor deposition. *J Am Ceram Soc* 78:1564–1570
- [27] Ochiai S, Hojo M, Tanaka M (1999) Mechanical interactions between fibre and cracked coating layer and their influences on fibre strength. *Composites A* 30:451–461
- [28] Naslain R, Lamon J, Pailler R, Bourrat X, Guette A and Langlais F (1999) Micro/minicomposites: a useful approach to the design and development of non-oxide CMCs. *Composites A* 30:537–547
- [29] Morgen P (2005) Carbon fibres and their composites. Taylor & Francis, London, p565
- [30] Bouquet C, Fischer R, Thebault J, Soyris P, Uhrig G (2005) Composite technologies development status for scramjet. In: Proceedings of AIAA/CIRA 13th International Space Planes and Hypersonics Systems and Technologies :AIAA-2005-3431, Capua, Italy
- [31] Ohnabe H, Masaki S, Onozuka M, Miyahara K, Sasa T (1999) Potential application of ceramic matrix composites to aero-engine components. *Composites A* 30:429–437
- [32] Naslain R, Christin F (2003) SiC-matrix composite materials for advanced jet engines. *MRS Bull.* 28:9:654–658
- [33] Christin FA (2005) A global approach to fibre nD architectures and self-sealing matrices: from research to production. *Int J Appl Ceram Technol* 2:97–104
- [34] Bouquet C, Fischer R, Larrieu JM, Uhrig G and Thebault J (2003) Composite technologies development status for scramjet applications. In: Proceedings of 12th AIAA International Space Planes and Hypersonics Systems and Technologies :AIAA-2003-6917, Norfolk, VA
- [35] Caputo AJ, Lackey WJ (1984) Fabrication of fibre reinforced ceramic composites by chemical vapour infiltration. *Ceram Eng Sci Proc* 5:654–667
- [36] Stinton DP, Lowden RA, Besmann TM (1992) Fibre-reinforced tubular composites by chemical vapour infiltration. In: Besmann TM, Gallois BM, Warren JW (eds) Chemical vapour deposition of refractory metals and ceramics II. Materials Research Society, Pittsburgh, PA, pp233–238
- [37] Besmann TM, McLaughlin JC, Lin HT (1995) Fabrication of ceramic composites: forced CVI. *J Nucl Mater* 219:31–35
- [38] Vaidyaraman S, Lackey WJ, Freeman GB, Agrawal PK, Langman MD (1995) Fabrication of carbon-carbon composites by forced flow-thermal gradient chemical vapour infiltration. *J Mater Res* 10:1469–1477
- [39] Tsai CY, Desu SB (1992) Contribution of gas-phase reactions to the deposition of SiC by a forced-flow chemical vapor infiltration process. In: Besmann TM, Gallois BM, Warren JW (eds) Chemical vapour deposition of refractory metals and ceramics II. Materials Research Society, Pittsburgh, PA, pp227–232
- [40] Snead LL, Jones RH, Kohyama A, Fenici P (1996) Statue of silicon carbide composites for fusion. *J Nucl Mater* 233-237:26–36
- [41] Gupte SM, Tsamopoulos JA (1989) Densification of porous materials by chemical vapor infiltration. *J Electrochem Soc* 136:555–561
- [42] Rovillain D, Trinquocoste M, Bruneton E, Derre A, David P, Delhaes P (2001) Film boiling chemical vapor infiltration: an experimental study on carbon/carbon composites materials. *Carbon* 39:1355–1365

- [43] Buckley JD (1988) Carbon-carbon: a overview. *Am Ceram Soc Bull* 67:364–368
- [44] Stoller HM, Frye ER (1972) *SAMPE*. Q3:10–12
- [45] Lieberman ML, Curlee RM, Brannten FH, Noles GT (1975) CVD/PAN preform carbon/carbon composites. *J Comp Mater* 9:337–346
- [46] Golecki I, Morris RC, Narasimhan D (1994) Method of rapid densifying a porous structure. US Patent 5,348,774
- [47] Golecki I (2003) Industrial carbon chemical vapor infiltration (CVI) processes. In: Delhaes P (ed) *Fibre and composites*. Taylor & Francis, London, pp112–138
- [48] Zhao JG, Li KZ, Li HJ, Wang C (2006) The influence of thermal gradient on pyrocarbon deposition in carbon/carbon composites during the CVI process. *Carbon* 44:786–791
- [49] Tang ZH, Qu DN, Xiong J, Zou ZQ (2003) Effect of infiltration conditions on the densification behavior of carbon/carbon composites prepared by a directional-flow thermal gradient CVI process. *Carbon* 41:2703–2710
- [50] Tang SF, Deng JY, Wang SJ, Liu WC (2007) Fabrication and characterization of C/SiC composites with large thickness, high density and near-stoichiometric matrix by heaterless chemical vapor infiltration. *Mater Sci Eng A* 465:290–294
- [51] Tang SF, Deng JJ, Du HF, Liu WC, Yang K (2005) Fabrication and microstructure of C/SiC composites using a novel heaterless chemical vapor infiltration technique. *J Am Ceram Soc* 88:3253–3255
- [52] Houdayer M, Spitz J, Tran-Van D (1984) Process for the densification of a porous structure. US Patent 4,472,454.
- [53] Bruneton E, Narcy B, Oberlin A (1997) Carbon-carbon composites prepared by a rapid densification process I: Synthesis and physico-chemical data. *Carbon* 35:1593–1598
- [54] Vignoles GL, Goyheneche JM, Sebastian P, Puiggali JR, Lines JF, Lachaud J, Delhaes P, Trinqucoste M (2006) The film-boiling densification process for C/C composite fabrication: from local scale to overall optimization. *Chem Eng Sci* 61:5636–5653
- [55] Bryant WA (1976) Producing extended area deposits of uniform thickness by a new chemical vapour deposition technique. *J Cryst Growth* 35:257–261
- [56] Sugiyama K, Nakamura T (1987) Pulse CVI of porous carbon. *J Mater Sci Lett* 6:331–333
- [57] Sugiyama K, Yamamoto E (1989) Reinforcement and antioxidizing of porous carbon by pulse CVI of SiC. *J Mater Sci* 24:3756–3762
- [58] Dupel P, Bourrat X, Pailler R (1995) Structure of pyrocarbon infiltration by pulse-CVI. *Carbon* 33:1193–1204
- [59] Lamouroux F, Bertrand S, Pailler R, Naslain R, Cataldi M (1999) Oxidation-resistant carbon-fibre-reinforced ceramic-matrix composites. *Composites Sci Technol* 59:1073–1085
- [60] Reagan P (1993) Chemical vapor composites (CVC). *J de Physique IV* 2:C3-541–548
- [61] Reagan P, Scoville AN, Leaf R (1992) Method of forming composite articles from CVD gas streams and solid particles of fibre. US Patent 5,154,862

Chapter 6 Microstructure Evolution and Process Control

6.1 Introduction

A CVD process is very complex, many ignore chemical reactions and involves. To this day, it is still very difficult or impossible to identify the reactant species and reaction paths during a CVD process at high temperature by experimental methods. Meanwhile, various physical and chemical phenomena are involved in the deposition process. For a CVD process, these phenomena include [1]: (1) heat transfer from the heating element to the substrate to activate the chemical reactions, (2) mass transport in the bulk gas and boundary layer, (3) adsorption and migration of the reactant gaseous species on the surface of the substrate, as well as the desorption of the by-product gaseous species, and (4) solid product formation from the homogeneous and heterogeneous chemical reactions. Furthermore, the situation becomes much more complex because these phenomena are always interacting with each other.

For each phenomenon, there are also many elements involved which determine the behaviour of each phenomenon. These phenomena are described by a wide range of characteristic time and length values. For the case of CVI fabrication of fibre-reinforced ceramic-matrix composites, the diameter of a molecule and the thickness of the interfacial phase are about 10^{-1} nm and 10^2 nm respectively, whilst the sizes of the substrate/component and the reaction are around 1 m. In addition, elementary chemical reactions occur in a time range of 10^{-5} to 10^{-4} s, the time for heat transfer and mass transfer is around 1 s to 10 min. By contrast, the total densification time for one CVI run is as long as approximately 10^2 h. In such cases, it is necessary to establish multiscale models to understand and optimise a CVD process.

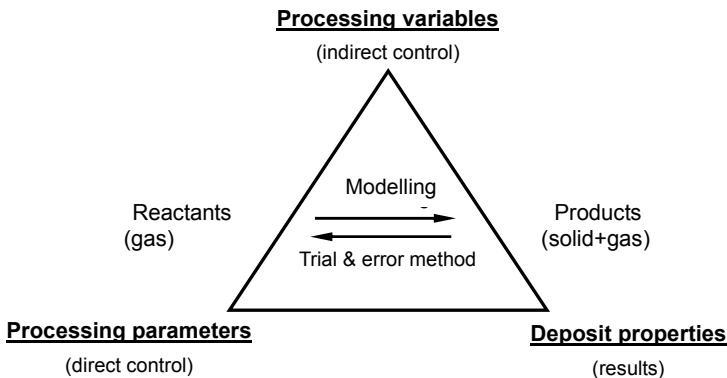


Figure 6.1. Relationships among the processing parameters, variables and properties of the deposit [2]

Table 6.1. CVD parameters, variables and properties [2]

Processing parameters (direct)	Processing variables (indirect)	Deposit properties (results)
Temperature	Temperature field	Microstructure
Flow rate	Velocity field	Characteristics
Pressure	Concentration field	Chemical composition
Deposition time	Supersaturation	Thickness uniformity
Nature of precursor	Sticking coefficient	Crystalline nature
Reaction geometry	A/V ratio	Deposition defects
Substrate/preform geometry	Residence time	Residual stress
Orientation of	Coefficient of drag	Density distribution
Substrate/preform		Growth rate

For any CVD process, the two key issues to be addressed are increasing the deposition rate and improving the quality of the matrix deposit. In order to obtain materials with desirable properties, it is necessary to strictly control the processing parameters. A phenomenological approach is usually used to establish the relationships among processing parameters, processing variables and properties of the deposit. A framework was proposed by Spear [2], as shown in Figure 6.1.

As listed in Table 6.1, some parameters such as temperature, pressure, flow rate, etc. are considered processing parameters because they can be directly used to control a CVD process and to determine the microstructure and properties of the deposit. The processing variables include temperature field, velocity field and so forth, which are the results of the system response. These are known as indirectly controlling parameters which are very important for understanding the deposition mechanism.

This chapter describes the theory of the microstructure evolution of the deposits and some control methods of a CVD process and the relationship between microstructures and processing parameters.

6.2 Microstructure Evolution of Chemical Vapour Deposition Deposits

6.2.1 Film Formation and Structure Zone Model

Thin-film formation is described as a sequential process which includes nucleation, coalescence and subsequent thickness growth, whereby all states can be influenced by deposition parameters, such as temperature, pressure, gas flow rate, etc. [3, 4]. For physical vapour deposition (PVD) processes, significant works have been published and progress made in understanding the microstructure evolution of the films. In the atomistics of growth processes, there exists much in common between CVD and PVD. Theories from PVD processes can thus be used to analyse the microstructure evolution of CVD processes [5, 6].

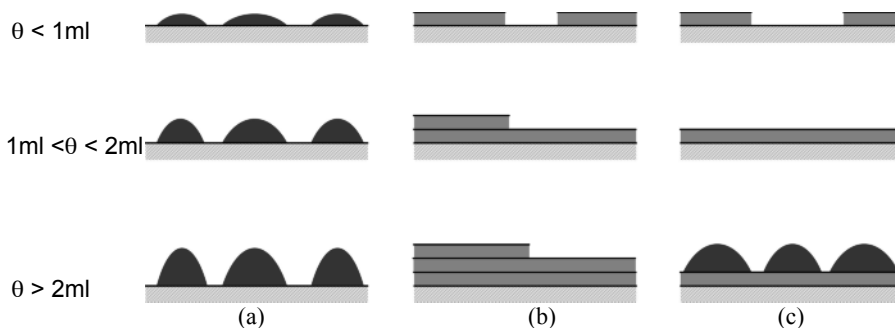


Figure 6.2. Three types of growth mode (θ : coverage, ml: monolayer): (a) 3-D island mode, (b) 2-D layer mode and (c) island-layer mode

At the initial stage of film deposition, a sufficient number of gaseous species are condensed to establish a permanent residence on the surface of the substrate. The model of film formation can be categorised into three basic types, which are illustrated schematically in Figure 6.2. This work was first realised by Bauer [7] and the details of these categorisations are described as follows.

6.2.1.1 Three-dimensional Island Mode (Volmer–Weber Mode)

This occurs when stable clusters small, form on the substrate surface and grow in three dimensions to form separate islands. This happens when the bonding between atoms in the clusters is much greater and stronger than that between the atom and the substrate. Many systems of metals on the insulators of micro-electronic devices display this mode of growth, such as silicon growth on a SiO_2 substrate reported by Bloem [8].

6.2.1.2 Layer-by-layer Mode (Frank–Van Der Merwe Mode)

This is a kind of two-dimensional growth mode, and layers of the deposit grow on the surface of another layer. In this case, the atomic bonding between the substrate surface and the film is greater than that between atoms of adjacent film layers. The homoepitaxial growth of Si thin film on Si substrate belongs to this mode.

6.2.1.3 Layer Plus Island Mode (Stanski–Krastanov Mode)

This is an intermediate combination of the two growth modes mentioned above. The substrate is first covered with one or a few monolayers grown in Frank–van der Merwe mode, then some three-dimensional islands are formed on the surface in the Volmer–Weber growth mode. This mode is a transition from two-dimensional growth to three-dimensional growth and has been observed in metal–metal and metal–semiconductor systems.

In order to characterise the morphology of deposit, several models have been proposed; the structure zone model (SZM model) was first proposed by Movchan and Demchishin in 1969 [9]. Based on the observation of the microstructure characteristics of Ti, Ni, W, ZrO_2 and Al_2O_3 coatings by electron beam evaporation, they established the structure zone model in terms of three zones, which was used to describe the relationship between the morphology and the processing

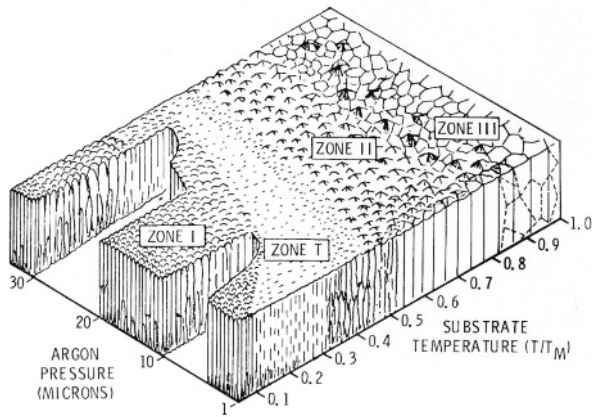
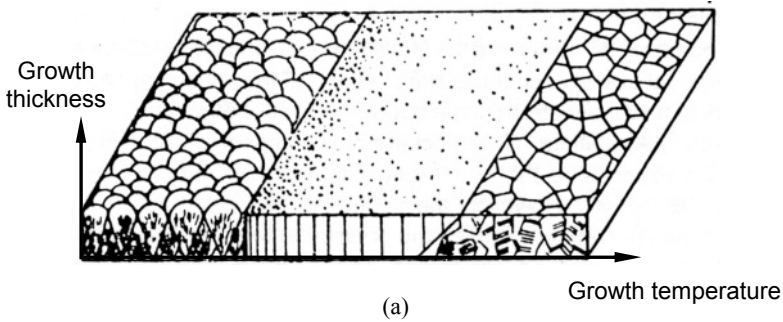


Figure 6.3. Structure zone model: (a) Movchan and Demchishin model [9] and (b) Thornton model [11]

temperature parameter (T/T_m). Here, T is the substrate temperature and T_m is the coating-material melting point. Later, Thornton [10, 11] introduced a second parameter of sputtering gas pressure and a transition zone (T_{trans}) between zones I and II. As shown in Figure 6.3, each zone has its own distinct characteristic structures and deposit properties.

(i) Zone I ($T/T_m < 0.3$)

This zone is characterised by a lower T/T_m ratio and consists of tapered crystals with domed tops which are separated and have voided boundaries. The internal structure of the crystals is poorly constructed and the crystal defect (e.g. dislocation) density is very high. The size of the crystallite increases with an increase in the T/T_m ratio. This dependence implies that there is very little surface diffusion. Accordingly, the metals fabricated by PVD techniques exhibit great hardness but weak lateral strength. This zone is associated with coating-flux shadowing that is not overcome by atom surface diffusion.

(ii) Zone T_{trans} (conical columnar structure)

The T_{trans} zone is a transitional zone between zones I and II. The coating in this zone consists of dense arrays of poorly defined fibrous grains without a voided boundary. At relatively high temperatures, surface diffusion becomes very evident; however, grain boundary diffusion is strongly limited. Grain coarsening occurs during coalescence of the small islands which have a high surface-area-to-volume ratio. During the coarsening process, the orientation of the crystal is determined by the T/T_m ratio; thus crystallites are nearly random or only weakly textured. In this case, there is a wide distribution of grain sizes.

(iii) Zone II ($0.3 < T/T_m < 0.5$)

The coating grown in this zone at higher substrate temperatures consists of columnar grains separated by distinct, dense and intercrystalline boundaries. The deposit has a smooth surface. The size of the grain is further increased with an increase in the T/T_m ratio and may extend through the coating thickness if the processing temperature is sufficiently high. If it is, the mechanical properties of the metallic deposits by the PVD processes are comparable to those of the cast metals.

This zone is characterised by high substrate temperatures at which both surface and grain boundary diffusion occur at significant levels. A homogeneous structure is obtained through the film thickness and is composed of columnar grains from the bottom to the top of the film. The grain boundaries are nearly perpendicular to the surface of the substrate.

(iv) Zone III ($0.5 < T/T_m < 1$)

This one consists of equiaxed grains with a high density, resulting in a bright surface. The surface diffusion, grain boundary diffusion and bulk diffusion are all operative. Therefore, secondary recrystallization of the deposits occurs and the degree of texture is considerably enhanced. The equiaxed grains obtained imply that the crystal growth of the deposits is regularly blocked.

Active energies for surface, grain boundary and bulk diffusion are typically in the ratio of 1:2:4. Here, surface diffusion occurs with active energy in the range 0.1 to 0.3 eV, and the bulk diffusion occurs with activation energies above 0.3 eV [3]. During island coalescence, there is a strong driving force for coarsening through surface atom diffusion and grain boundary (GB) movement, which is due to the free energy decrease as discussed by the classical theory of crystal growth. The islands with lower free energy atoms consume the islands with high free energy, resulting in a new larger island as the system attempts to minimise the overall surface energy.

6.2.2 Microstructure Characteristics of Chemical Vapour Deposition Deposits

6.2.2.1 Influence of Supersaturation and Temperature on Deposit Microstructure

For a CVD process, the depositing parameters affect the nucleation and growth modes which in turn influence the microstructure and properties of the deposited material. The driving force of the nucleation is the supersaturation in the CVD reaction system. The supersaturation in the gaseous reactions can be analogous to the supercooling in the solidification process for metal materials. For a general chemical reaction,



Supersaturation is defined as the ratio of the product of the gas-phase partial pressures in the real state to the product of the corresponding equilibrium partial pressures and is expressed by [12]

$$\gamma = \frac{P_A^a P_B^b P_D^d}{P_{Ae}^a P_{Be}^b P_{De}^d} \tag{6.2}$$

where p_A , p_B and p_D are the partial pressure of gases A, B and D in the real state respectively; p_{Ae} , p_{Be} and p_{De} are the partial pressures of gases A, B and D in the equilibrium state respectively.

According to the processing conditions of a CVD process, supersaturation can be divided into two categories, bulk supersaturation and local supersaturation [13]. If a CVD process occurs in the chemical reaction control regime discussed in Section 4.3.4, it is reasonable to assume that the compositions of a gas on the substrate surface equal that in the bulk gas. Accordingly, the expression of supersaturation in Equation (6.2) is used for calculation. However, if a CVD process occurs in the

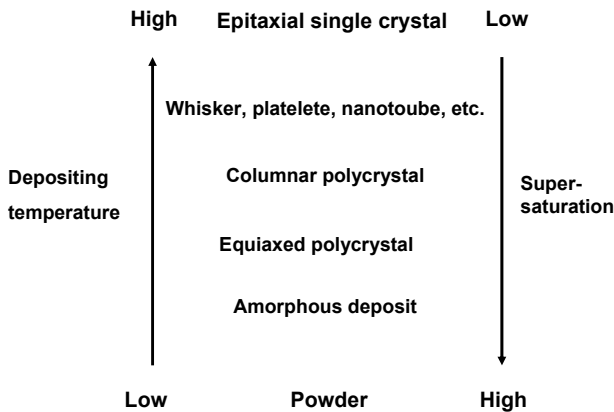


Figure 6.4. Relation of supersaturation and temperature to morphology [15]

mass transport regime, a significant concentration gradient will exist within the boundary layer near the substrate surface. In this case, the local supersaturation is difficult to calculate and it is considerably lower than that of the bulk gas.

Based on the observations of PVD, Blocher established morphological dependence on supersaturation and temperature as shown in Figure 6.4. According to Bryant's investigation [14], the same sort of dependence exists for CVD materials [15].

Epitaxial Growth

Materials with an epitaxial structure have been widely used in semiconductor and superconductor applications. Epitaxial growth occurs at a relatively high depositing temperature but with a low supersaturation. For example, the 4H-SiC epitaxial growth from $\text{SiH}_4\text{-C}_3\text{H}_8$ gases is conducted at 1700 to 1900°C [16], whilst the β -SiC polycrystal growth from $\text{CH}_3\text{SiCl}_3\text{-H}_2$ gases is fabricated at a temperature of around 1000°C. Such deposits exhibit the same orientation as the substrate material and perfect crystal structure because the atoms have sufficient activities for surface diffusion, grain diffusion and bulk diffusion. Therefore, the nucleation and growth of the deposit take place in the particles' preferred orientation, which has the minimal interfacial free energy among all orientations. The epitaxial growth of a single crystal is usually performed at reduced pressure.

Whiskers/Platelets/Nano-Belts/Nano-Tubes/Coiled Fibres

A whisker is fabricated according to the vapour-solid or vapour-liquid-solid mechanisms with the aid of certain special catalysts [17]. It involves nucleation at preferred locations such as the terrace, ledge and kink on a substrate surface, and defects in crystal structures developed along a special direction of impingement of nuclei. Two-dimensional and three-dimensional microstructures have also been

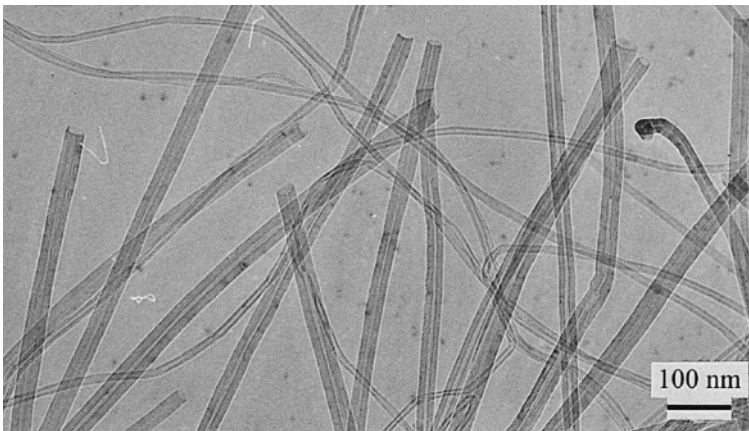


Figure 6.5. Carbon nanotubes by chemical vapour deposition [18]

successfully produced, including platelets, nanobelts, nanotubes in Figure 6.5 [18] as well as microcoiled fibres [19]. However, the formation mechanisms of these unique microstructures are very complex and further research should be carried out on these topics.

Polycrystal Growth

Both columnar and equiaxed microstructures are obtained from polycrystal growth. Columnar microstructure is composed of columnar grains of preferred orientation that grow from the first nucleated location on a substrate surface. The microstructure is attributed to high supersaturation and low temperature and hence more limited diffusion. A columnar microstructure is suitable for high-temperature structural applications, such as thermal barrier coatings. Figure 6.6 shows the typical columnar CVD SiC microstructure in C/SiC composites.

An equiaxed microstructure is comprised of small randomly oriented grains. Deposited materials with an equiaxed microstructure have superior mechanical properties according to the Hall–Petch equation [20]. They are desirable for structural applications. Such a microstructure is formed at an even higher supersaturation which ensures a sufficient amount of nuclei generated from the heterogeneous reaction on the substrate surface. The lower depositing temperature significantly limits surface diffusion and restrains the migration of atoms to preferred crystal lattice sites.

Amorphous Deposit

If the depositing temperature is sufficiently low, an amorphous deposit structure is formed because the atoms absorbed on the substrate surface are strictly constrained to the specific location, thus no further migration takes place. Two examples are amorphous silicon (a-Si:H) and silicon carbide (a-SiC:H) films with a high

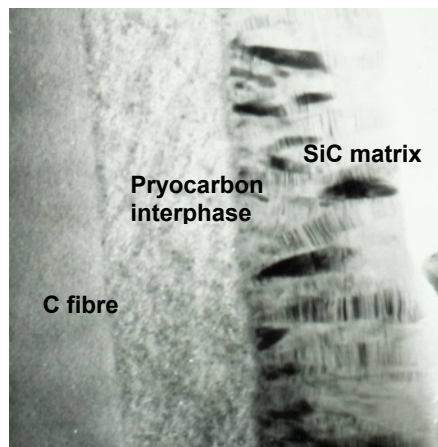


Figure 6.6. Columnar SiC in carbon-fibre-reinforced silicon carbide composites [18]

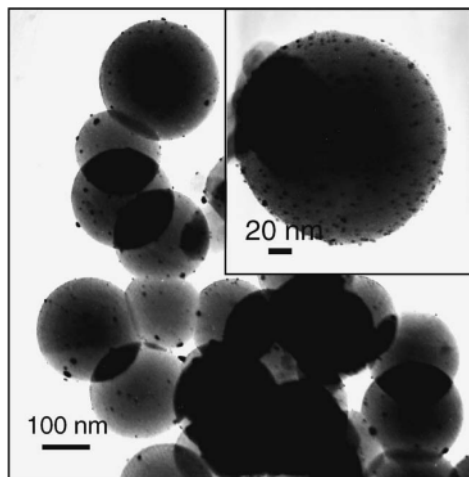


Figure 6.7. CVD Pt nanoparticles from $\text{Pt}(\text{CH}_3)_2(\text{cod})$ deposited on C nanospheres [23]

hydrogen content [21, 22]. In order to decrease deposition temperature to approximately 300°C (less than the melting point of a polymer), it is necessary to use some enhancement methods such as plasma. Amorphous deposits have been extensively used in transistors, memory switches and solar energy conversion devices because of their wide band gap and optical energy gap.

Powder

At sufficiently high supersaturation and very low temperature, the frequency of molecular collisions within the gas phase is great enough to cause homogeneous nucleation and growth of powder-like product. Up to the present, CVD has been an important technique for manufacturing superfine powders as discussed in Section 3.7.1, or surface modification of functional powders as shown in Figure 6.7.

6.2.2.2 Microstructure of Chemical Vapour Deposition SiC

Figure 6.8 shows the X-ray diffraction (XRD) patterns of CVD SiC deposited in a temperature range of 1000 to 1300°C . Detailed analyses of the X-ray results indicate that the deposits are pure silicon carbide mainly composed of β -SiC (cubic 3C crystal structure) with a small amount of α -SiC (hexagonal 4H crystal structure). It is clear from the figure that the diffraction angles of 35.6° , 41.3° , 60.1° , 72.1° and 75.5° correspond to β -SiC and the diffraction angle of 33.7° corresponds to α -SiC. As the deposition temperatures decrease, the deposits become poorly crystallised because the diffraction peaks become broader or its intensity shown in Y axis become lower. At the deposition temperature of 1000°C , the deposits are in a quasi-amorphous state.

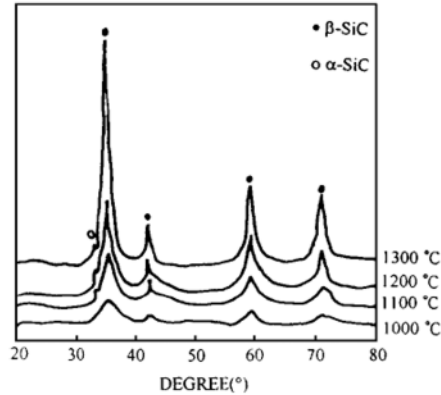


Figure 6.8. XRD patterns of CVD SiC at various temperatures [24]

Figure 6.9 shows the microstructures of CVD SiC grown at different parameters on a graphite substrate. The images on the left-hand side show a cross-section of the deposit at different temperatures, whereas the images on the right-hand side show the surface morphology of the corresponding coatings. At relatively low deposition temperatures (1000°C), the deposits are composed of a large number of spherical particles forming a cloud cluster-like structure with a smooth domed top. It should be pointed out that each particle is an aggregate consisting of a large number of nanometer SiC crystallites rather than one single crystallite. Among these particles, coalescence is clearly observed. As the deposition temperature is increased to 1100°C , the particles become larger than those deposited at 1000°C . From the microstructure cross-section, it is observed that the deposited film becomes denser. When the deposition temperature is higher than 1200°C , the size of particles is increased and the deposits become even denser.

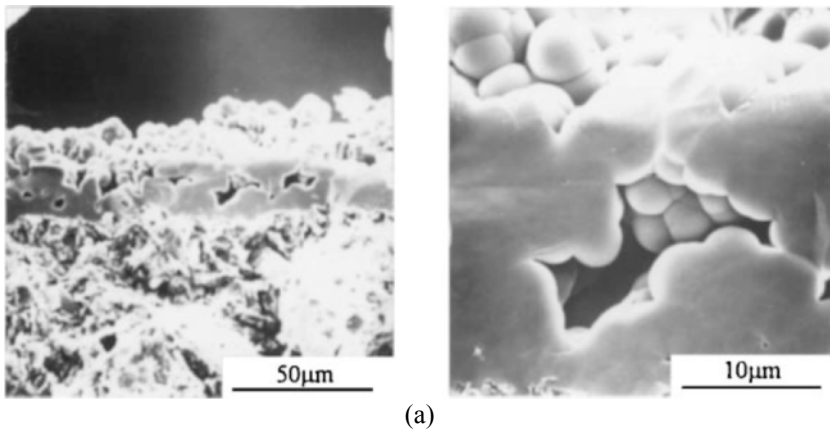
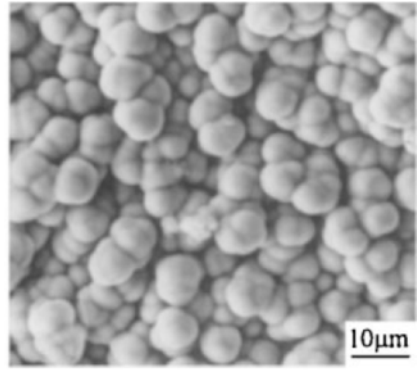
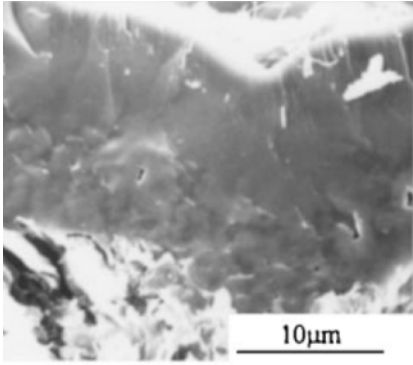
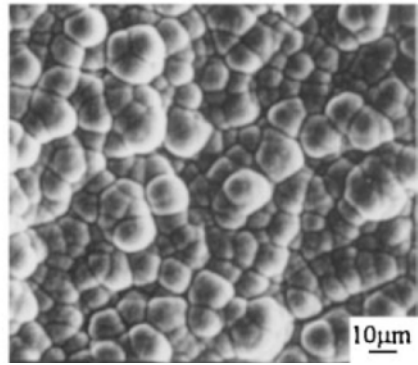
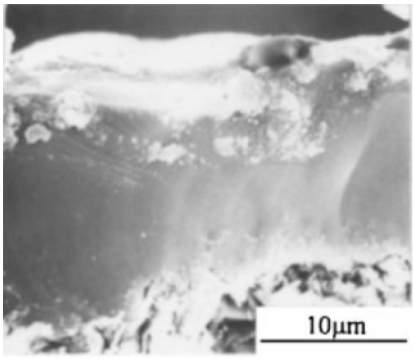


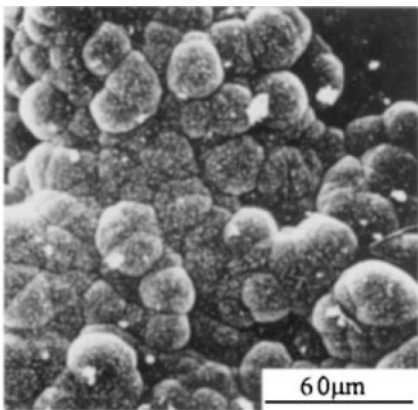
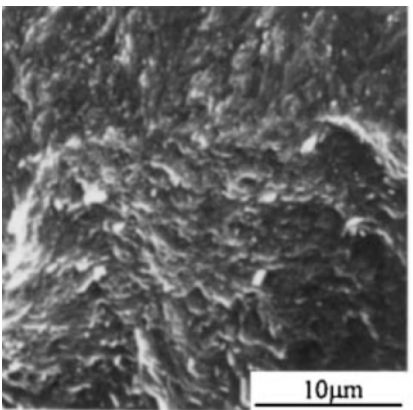
Figure 6.9. Microstructures of CVD SiC grown on graphite substrate [24]: (a) $T_{dep}=1000^{\circ}\text{C}$, (b) $T_{dep}=1100^{\circ}\text{C}$, (c) $T_{dep}=1200^{\circ}\text{C}$ and (d) $T_{dep}=1300^{\circ}\text{C}$



(b)



(c)



(d)

Figure 6.9. (continued)

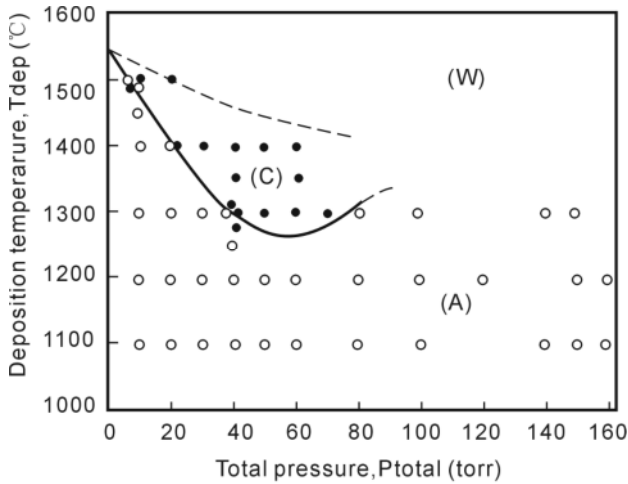


Figure 6.10. Effect of the deposition temperature and total pressure (P_{tot}) on the structure of Si_3N_4 [25]

6.2.2.3 Microstructure of Chemical Vapour Deposition Si_3N_4

As shown in Figure 6.10, both amorphous and crystalline Si_3N_4 deposits can be obtained from $\text{SiCl}_4\text{-NH}_3$ systems. These crystal structures depend markedly on the deposition temperature (T_{dep}) and the total pressure (P_{tot}) within the reaction chamber. At temperatures below 1200°C , amorphous deposits are formed over the whole range of pressures (region A). The maximum thickness of an amorphous deposit is 4.2 mm. At 1300°C , the deposit is amorphous at P_{tot} below 40 Torr and above 75 Torr, whilst a crystalline structure is formed at P_{tot} between 40 and 75 Torr. At 1400 and 1500°C , crystalline deposits are obtained between 20 and 60 Torr and between 5 and 10 Torr respectively (region C). The maximum thickness of the crystalline deposit is 4.6 mm.

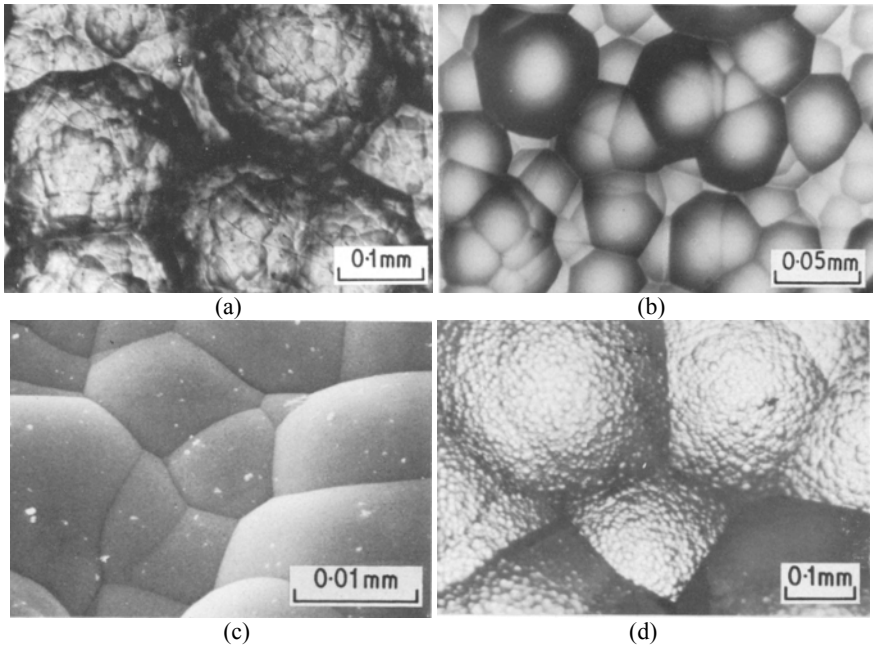
According to the morphological characteristics, the amorphous deposits of Si_3N_4 may be divided into three types:

Pebble Structures

Figure 6.11a shows a typical surface structure formed at a relatively low temperature (1200°C) and low pressure (10 Torr). Only the primary pebble structure can be observed in the deposits.

Large Primary Cone Structures

Figure 6.11b shows cone structures formed at a temperature higher than 1300°C and total pressures at 30 Torr, which corresponds to region A in Figure 6.10. In this case, large primary cones are composed of secondary cones.



(a) pebble structure, (b) large primary cone structure, (c) and (d) large primary and second cone structure

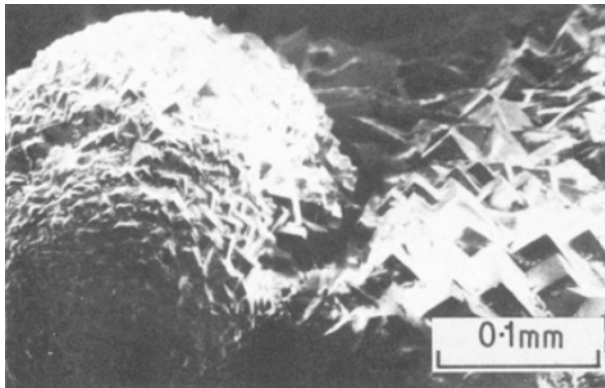
Figure 6.11. Morphology of amorphous Si_3N_4 [25]: (a) 1200°C, 10 Torr (b) 1300°C, 30 Torr (c) 1400°C, 20 Torr and (d) 1400°C, 20 Torr

Large Primary Cones and Second Cone Structures

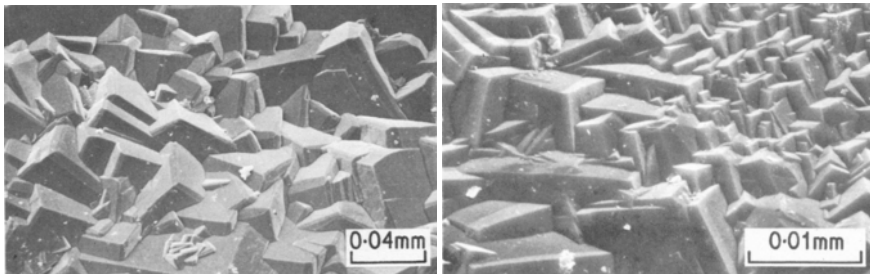
Figure 6.11c and d indicate the third typical surface structure which is found in amorphous deposits prepared at a deposition temperature of 1400°C and pressure of 20 Torr. Large primary cones containing numerous small secondary pebble-like cones were formed. The surface of secondary cones is smooth and similar to that in Figure 6.11a.

The crystalline deposits show remarkable brightness resulting from a preferred orientation of grains. Surface structures of crystalline deposits are significantly different from those of amorphous deposits. The microstructure characteristics of the crystalline deposits are strongly dependent on the deposition conditions, as shown in Figure 6.12a–c.

At a deposition temperature of 1300°C, surface structures vary with the total pressure. At a total pressure of 50 Torr, growth cones are observed (two cones in Figure 6.12a) and each cone consists of a number of small crystals which have well-defined corners (around 90°). At a total pressure of 60 Torr Figure 6.12b, no growth cones are found and the whole surface is made up of well-grown crystals with clear prominent profiles. The surface of each crystal is very smooth. It is



(a)



(b)

(c)

Figure 6.12. Morphology of crystalline Si_3N_4 [25]: (a) 1300°C, 50 Torr, (b) 1300°C, 60 Torr obvious from Figure 6.12b that faceted growth occurs and that each grain has nearly the same orientation. At 1400°C and 50 Torr, Figure 6.12c reveals a different type of crystal growth in which another crystal face exists at the edge of almost each small crystal.

As calculated by Lespiaux *et al.* on a $\text{CH}_3\text{SiCl}_3\text{-H}_2$ system, supersaturation in a CVD SiC process is extremely high (more than 10^4) [12], and the nucleation and growth of the film take place at a state which is far from thermodynamic equilibrium. The morphology of the film produced in this condition can be explained by the theory of dissipative structure by Prigogine [26]. The growth mode of a CVD film is controlled not only by interface energies but also by supersaturation. Under such circumstances, the self-assembly or self-organisation of crystals is one of the key characteristics in Prigogine's theory. Self-organisation is a process of attraction and repulsion in which the internal organisation of a system, normally an open system, increases in complexity without being guided or managed by an outside source.

Cauliflower structures and conical structures are usually observed from the CVD processes as shown in Figure 6.13. Generally speaking, the former is formed by a competition between randomly branching structures, and the conical-like column is the result of continuous and inherent competition in the evolution of the

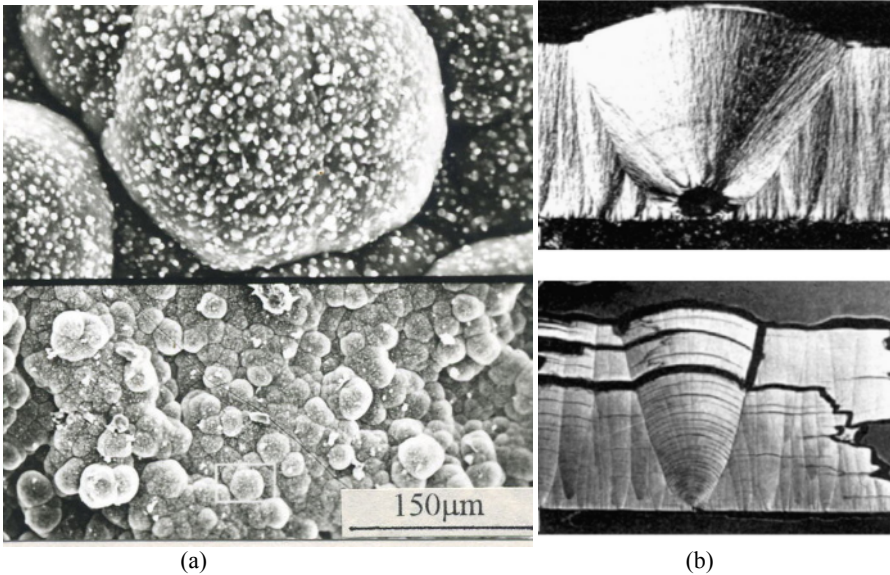


Figure 6.13. Fractal structures in CVD deposits: (a) cauliflower structure and (b) conical structure [28]

physical structure [27]. The large columns are seen to be parabolic-like in profile with an internal structure consisting of small columns. Both kinds of deposits show the feature of self-similarity and are fractal structures which could be found in natural plants, such as lotus leaves. However, the evolution mechanisms for the structures are not yet understood.

6.3 Quantitative Control of Chemical Vapour Deposition Process Parameters

6.3.1 Quantitative Control Method Based on Chemical Reaction Mechanism

6.3.1.1 Free Volume Fraction and Critical Residence Time

From the CVD mechanism shown in Figure 6.14, the chemical reactions in the gas phase are much more complicated because the precursor often undergoes complex homogeneous gas-phase reactions, which result in many complex intermediate species. At the same time, the homogeneous reactions compete with heterogeneous surface reactions. The residence time, which is the duration of reactant gases flowing through the reaction, has a strong influence on the interactions of these reactions for the CVD processes.

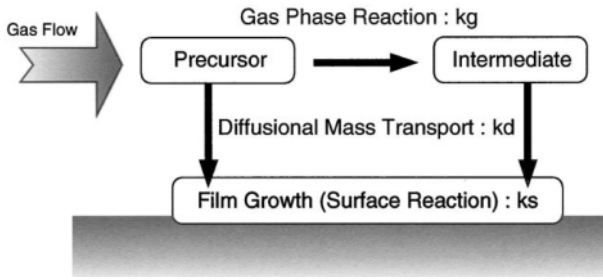


Figure 6.14. Simplified reaction mechanism of a CVD process [29]

Chemical Vapour Deposition WSi_x from WF_6 - Si_2H_6

In order to identify the reaction scheme, tubular reaction experiments were used to analyse the compositions of WSi_x film from WF_6 and Si_2H_6 systems by Saito and Shimogaki *et al.* [30–32]. Figure 6.15a shows that the content of Si in the deposit of WSi_x increases significantly with an increase in the axial distance if the deposition temperature is higher than $180^\circ C$. Based on these results, the consecutive reaction model shown in Figure 6.15b was developed. It is assumed that the initial reaction forms WSi_2F_5 , followed by consecutive Si_2H_6 insertion reactions to form $WF_{6-x}(SiH_3)_x$ as the residence time increases.

Chemical Vapour Deposition Cu_2O from CuI - O_2

Figure 6.16 shows an example of CVD Cu_2O from CuI - O_2 . Initially, a dense film is formed as the growth rate increases due to an increase in the axial position. The

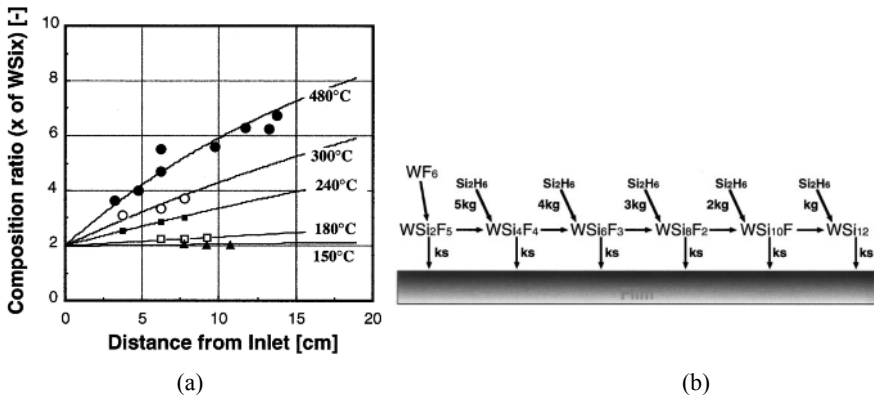


Figure 6.15. CVD from WF_6 - Si_2H_6 in tubular reaction [29]: (a) WSi_x CVD film composition profile and (b) reaction mechanism of WSi_x deposition

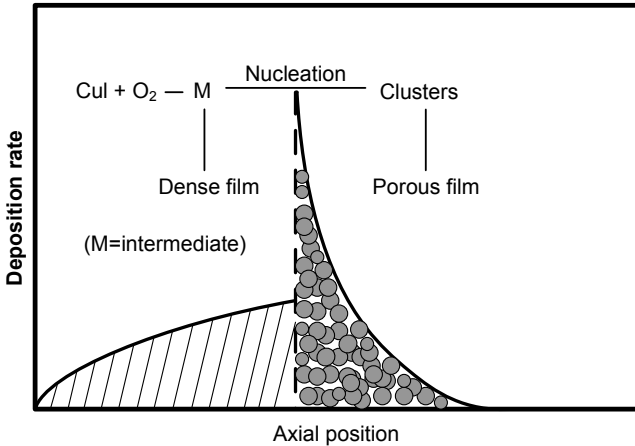


Figure 6.16. Schematic of Cu_2O deposition mechanism from CuI-O_2 system [33]

gas-phase homogeneous reactions form intermediate products that control the growth process. The deposition rate increases suddenly such that the film formed becomes porous if the film is located at a critical distance from the reaction inlet. The diameter of molecular cluster is about 1 to 2 nm, which is significantly larger than that of an intermediate molecule. This indicates that the growth mode has been changed from intermediate-molecule-based deposition to cluster-based growth. From this it can be concluded that homogeneous nucleation causes the shift from chemical-reaction-limited to mass-diffusion-limited film growth, and consequently from a dense to porous film.

Chemical Vapour Deposition Pyrolytic Carbon from CH_4

As another example, Huttinger [34, 35] has developed a synthesis reaction model based on experiments. This section introduces the work to illustrate the complex reactions and demonstrates the relationship between the chemical reactions and residence time.

For the CVD process of pyrolytic carbon from methane, the elementary reaction processes are illustrated in Figure 6.17. The following assumptions are made to discuss this scheme:

- The substrate inside a tubular reaction is heated from the outside of the wall.
- The methane temperature before entering the deposition zone is assumed to be too low to activate any chemical reactions. It is heated to the reaction temperature immediately once it enters the deposition zone.

The primary reaction of methane is the formation of the methyl radical CH_3 , indicated as C1 species, according to the following reaction [34, 36]:

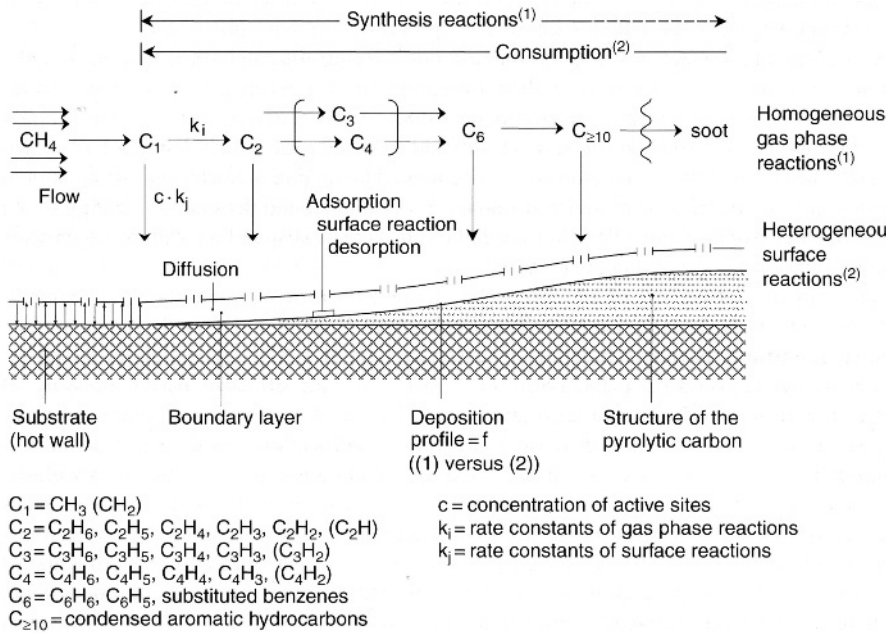


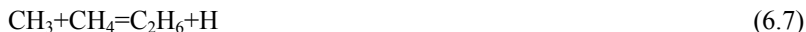
Figure 6.17. Scheme of elementary reactions in pyrocarbon deposition from CH₄ [35]



where CH₄* is the excited molecule and M is the inert gas molecule. Equation (6.3) determines the chemical reaction rate due to the high bond dissociation energy of the C–H bond.

Though methane exhibits a very low sticking coefficient, the methyl radical is supposed to be the first species that can be chemically absorbed on a substrate surface. Chemisorption takes place on an available free active site on the growing substrate surface. If such a site is not available, the methyl radical undergoes gas-phase reactions. Synthesis reactions with CH₃ become the considerations of the above reactions. Possible reactions are expressed in the equations below, and their reaction products are C₂H₆, C₂H₅, C₂H₄, C₂H₃ and C₂H₂, summarised as C₂ species.





The species in the above equations have the same reaction possibilities as discussed in the case of methyl radicals (CH_3). In relation to chemisorption, species with a high carbon/hydrogen ratio such as acetylene or vinyl radical react more easily. Acetylene shows a particularly strong capability of chemisorption and can even form a complex surface of carbon/hydrogen (C(H)) for blocked carbon edge atoms. On the other hand, such species are also highly reactive in homogeneous gas-phase reactions. Consequently, there is a competition between chemisorption and homogeneous gas-phase reactions of C_2 species, which has become a focus of study for the methyl radical.

As shown in Figure 6.17, the longer the residence time is, especially after the formation of C_4 species, the more likely the C_6 species or even soot will be formed. C_6 species may include benzene, a phenyl radical, or similar six-membered ring species. If the methane stays in the reaction long enough, the reaction sequence in the gas phase is terminated with C_6 species as shown in the following equations:





As polynuclear aromatic hydrocarbons show a high tendency towards undesired gas-phase nucleation and soot formation, they should be avoided by choosing a suitable critical residence time and other appropriate processing parameters.

After a certain residence time or reaction length the deposition profile shows a decrease in the layer thickness because of the consumption of carbon from the gas phase used in the initial range of the deposition zone. Carbon concentration, which is defined as gas-phase concentration, gradually decreases as CVD takes place from the time that the methane enters the deposition space.

The above gas-phase reaction is a polymerisation process which causes deviation from linear kinetics. Long residence-time performance is essential in large industrial reactions for forming hard coatings, where the residence time of the feed precursor is measured in minutes, whereas typical residence times for small tubular reactions is on the order of 1 s or less.

Residence time (t_r) is defined as the average time that a gas stays in the reaction chamber and is given by [37]

$$t_r = \frac{V_f}{F_{vap} \times (T/T_0) \times (P/P_0)} \quad (6.23)$$

where F_{vap} is the precursor flow rate expressed in standard conditions at a pressure of 1 atm and a temperature of 25°C, in standard cubic centimetre per minute (scm, ml·min⁻¹). P and T are the mean pressure and temperature in the reaction chamber respectively. V_f is the free volume within the reaction chamber.

From the above three examples, it is clear that when the chemical reactions reach a certain stage or are at a certain distance, there will be a significant change in the state of the depositions. For CVD WSi_x from the WF₆-Si₂H₆ system as shown in the first case, when the distance of the substrate is beyond a critical value, the content of Si in the deposit of WSi_x is significantly increased. For case 2, where Cu₂O is formed from CuI-O₂, an increase in the axial position results in a change of dense film to porous film. For the third case in 3, once the residence time reaches a certain level, undesired gas-phase nucleation and soot formation take place for polynuclear aromatic hydrocarbons. All these indicate that residence time at a critical level is a key consideration in the design of CVD processing parameters. Though it appears for cases 1 and 2 that distance is a key factor, they are ultimately linked to the residence time and have been used as a more convenient measure to determine the residence time.

6.3.1.2 Deposition Pressure and Surface Area and Free Volume Ratio

As discussed in Chapter 4, both homogeneous and heterogeneous chemical reactions occur in a CVD process. Within porous fibre preforms, two types of reactions are competing or interacting with each other, thereby influencing the deposition rate within the preform. Based on these understandings, Huttinger [34] proposed that a ratio called the A/V ratio should be considered as an important parameter for CVI processes. Here, A and V stand for the surface area and free volume within the porous preform, respectively. In order to investigate the influence of the A/V ratio on deposition kinetics, a special small reaction is designed and shown in Figure 6.18a. Cordierite ceramic honeycomb is used as the deposition substrate and placed into the deposition chamber made of alumina ceramic. The honeycomb structure is made of orderly arranged small pores, and this structure is used to simulate a fibre preform. Four types of ceramic honeycombs are used, and their cross-sections are shown in Figure 6.18b. Their A/V values are 0.79, 1.6, 3.2 and 7.4 mm⁻¹ respectively.

Figure 6.19a shows the relationship between the deposition rate and pressure under different A/V ratios. At the low part of the honeycomb substrate, the deposition rate increases as the pressure increases below 20 kPa for all A/V ratios, then remains nearly constant between pressures of 20 to 30 kPa. It increases linearly above pressures of about 30 kPa. These different deposition rates are a result of the different deposition mechanisms in terms of the dominance of homogeneous and heterogeneous reactions under certain conditions. Under a lower

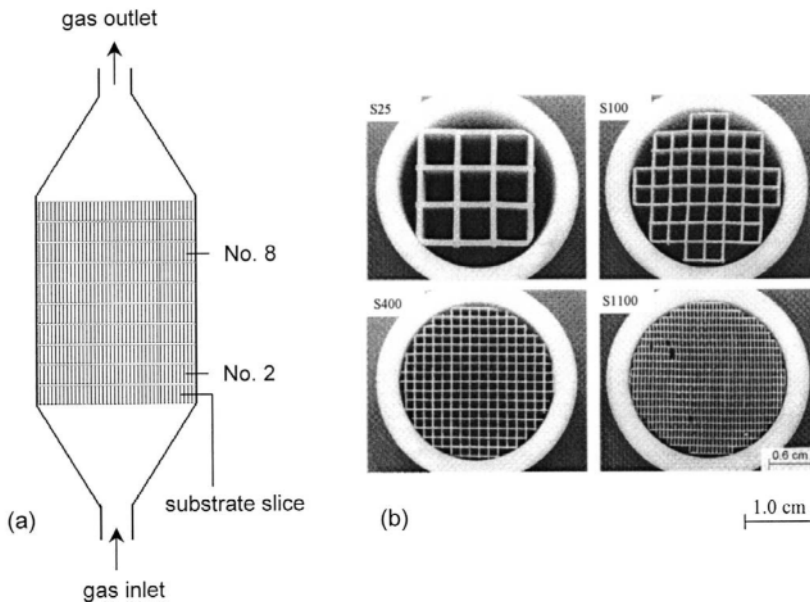


Figure 6.18. Schematic of the deposition reaction [38]: (a) arrangement of substrate slices and (b) cross-sections of substrates

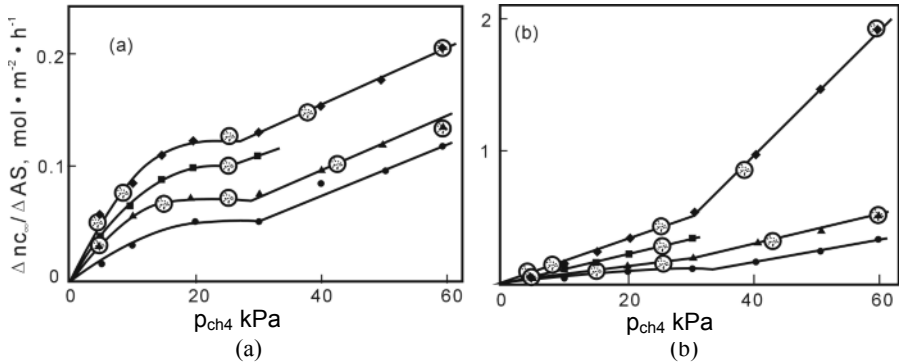


Figure 6.19. Deposition rates as a function of methane pressure at a temperature of 1100 °C and various A/V ratios, $[A/V]$ ratios of the substrates of 0.79 mm⁻¹ (◆), 1.6 mm⁻¹ (■), 3.2 mm⁻¹ (▲) and 7.4 mm⁻¹ (●) [38]: (a) lower part of the substrate and (b) upper part of the substrate

pressure, the absorption of the precursor is dominant, which implies the heterogeneous reactions on the surface play a much more important role in the deposition process. The amount of the adsorbed species on the substrate increases with pressure according to the Langmuir–Hinshelwood isothermal adsorption discussed in Section 4.3. The deposition rate in a pressure range of 20 to 30 kPa corresponds to the saturated pressure. If the pressure is further increased, the absorption is not the only decisive factor for the deposition. In such a case, homogeneous reactions are also enhanced to form large gaseous species in the gaseous phase, hence the deposition rate is also further increased. The pore volume increases with a decrease in the A/V ratio. For the case of a bigger pore volume, it is more likely for the homogeneous reactions to form species with large structures (such as polycyclic aromatic hydrocarbons), hence resulting in more rapid deposition. At the upper part of the honeycomb substrate of the down stream, the deposition rate exhibits similar behavior. However, the deposition rate in the upper part of the chamber is one order of magnitude higher than that in the lower part. This implies that the role of homogeneous reactions becomes much more significant in the down stream region or the upper part of the chamber as shown in Figure 6.19b.

6.3.1.3 Sticking Coefficient

Only when the gaseous species are adsorbed on the substrate surface can heterogeneous chemical reactions take place. The amount of the gaseous species adsorbed on the substrate surface mainly depends on the sticking coefficient. The sticking coefficient (S_c) is defined as the ratio of the number of gaseous molecules and radicals in the gas phase colliding with the substrate surface and being chemisorbed for heterogeneous reaction to the total number of gaseous species hitting the substrate surface. The expression is written as [39, 40],

$$S_c = c \cdot f(\theta) \exp\left(-\frac{E_a}{RT}\right) \quad (6.24)$$

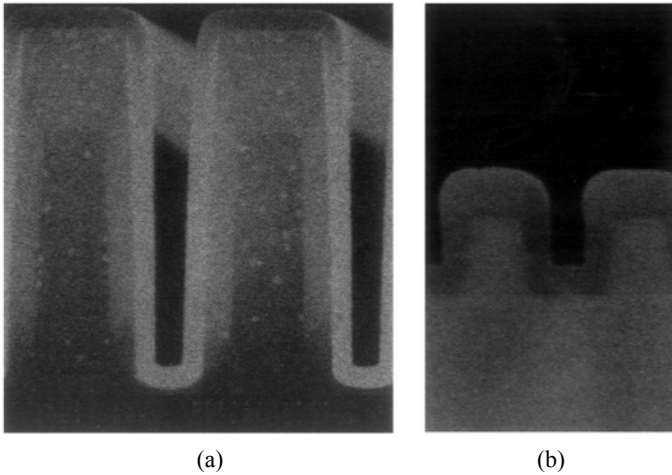


Figure 6.20. Typical coverage profiles by species with different Sc [29]: (a) $Sc = 0.001$ for TEOS and (b) $Sc = 0.5$ for $\text{SiH}_4\text{-O}_2$

where c is the condensation coefficient, $f(\theta)$ is the fraction of available surface related to the coverage θ , and E_a is the activation energy of adsorption. R and T are the gas constant and temperature, respectively.

The Sc has received considerable research interest since the very early stages of fluid dynamics research, but it is still very difficult to analyse the sticking coefficients for different gaseous conditions and to determine their values [41,42]. Generally speaking, the Sc of active radicals is higher than that of the stable species. This coefficient is dependent not only on the nature of the species, but also on the processing conditions (such as temperature). Table 6.2 lists the relationship between Sc and temperature. The data are determined by the direct Monte Carlo simulation based on the experimental results. As the temperature increases, the coefficient significantly decreases from 0.50 to 0.08.

For the infiltration of a pore with a large aspect ratio, a small Sc implies the entire surface of the deep pore can be uniformly coated. The reason is that the reactant gaseous species are easily transported to the bottom of the pores by

Table 6.2. Sticking coefficient of $\text{SiH}_4\text{-O}_2$ at different temperatures [43]

Temperature (°C)	573	673	723
Sticking coefficient	0.50	0.24	0.08

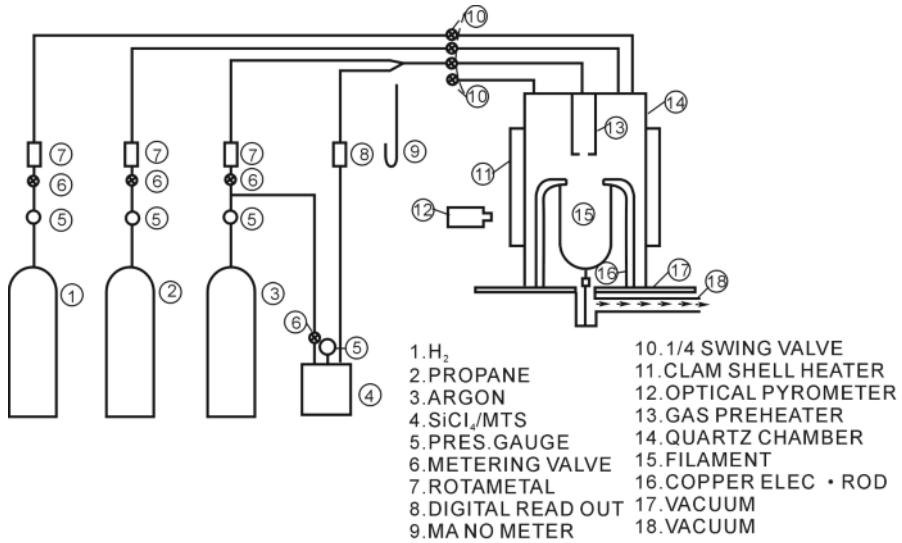


Figure 6.21. Schematic for CNTD-SiC process [44]

multiple reflections inside the wall of a pore. For a large Sc , however, the deposition takes place preferentially at the opening of the pore, hence resulting in poor infiltration. This is due to the fact that reactant species have a tendency to attach to the opening part of the pore.

The Sc of the tetraethyl orthosilicate ($\text{Si}(\text{OC}_2\text{H}_5)_4\text{-TEOS}$) and $\text{SiH}_4\text{-O}_2$ are 0.001 and 0.5 respectively. For SiO_2 deposition from TEOS, the deposition thickness is very uniform from the opening to the bottom of a micro-trench. However, the SiO_2 coating from $\text{SiH}_4\text{-O}_2$ at the outer location of the trench is markedly thicker than that in depth of the microtrench, even if the aspect ratio of the microtrench is much smaller than that for TEOS, as shown in Figure 6.20.

6.3.2 Experimental Basis for Quantitative Control Parameters

6.3.2.1 Preheat Temperature

For a cold-wall reaction with small heating source, preheating the precursor gases is preferred and important in order to obtain thick coatings with a smooth outer surface and fine crystal structure. This is normally realised by using a separately designed heater system. By contrast, precursor gases in a hot-wall reaction are always preheated before being transferred to the surface of the substrate, as mentioned in Section 3.4.

A representative example is to deposit a CVD a SiC thick coating on a tungsten wire. This CVD system, developed by Chemetal Corporation [44, 45], USA, uses tungsten wire with a diameter of 500 μm and a length of 200 mm as a substrate. The wire is directly heated by passing an electric current through it. For SiC deposition, a mixture of CH_3SiCl_3 , H_2 and Ar is employed as the precursor gases.

These gases are preheated to the preset temperature in a clamshell heater before they reach the surface of the tungsten wire. The CVD process is operated within a quartz chamber as shown in Figure 6.21.

Figure 6.22a and b compare the morphology difference of the coating surface formed by conventional CVD and controlled nucleation thermochemical deposition (CNTD), which is a proprietary CVD technique. If the precursor gases are preheated, the coating surface is very smooth. However, the coating comprises a number of irregular aggregates and its surface is very rough if the conventional CVD technique is used. From a cross-sectional view, the coarse columnar structure is observed in the conventional coating shown in Figure 6.22c. For CNTD coating, the equiaxed SiC grains are very fine and their crystal sizes range from 10 to 100 nm as observed using TEM, as shown in Figure 6.22d.

The effect of preheating on growth modes and surface finishes can be explained by the nature and amount of intermediates through homogeneous reactions. If the precursor gases are not preheated, there are not enough active

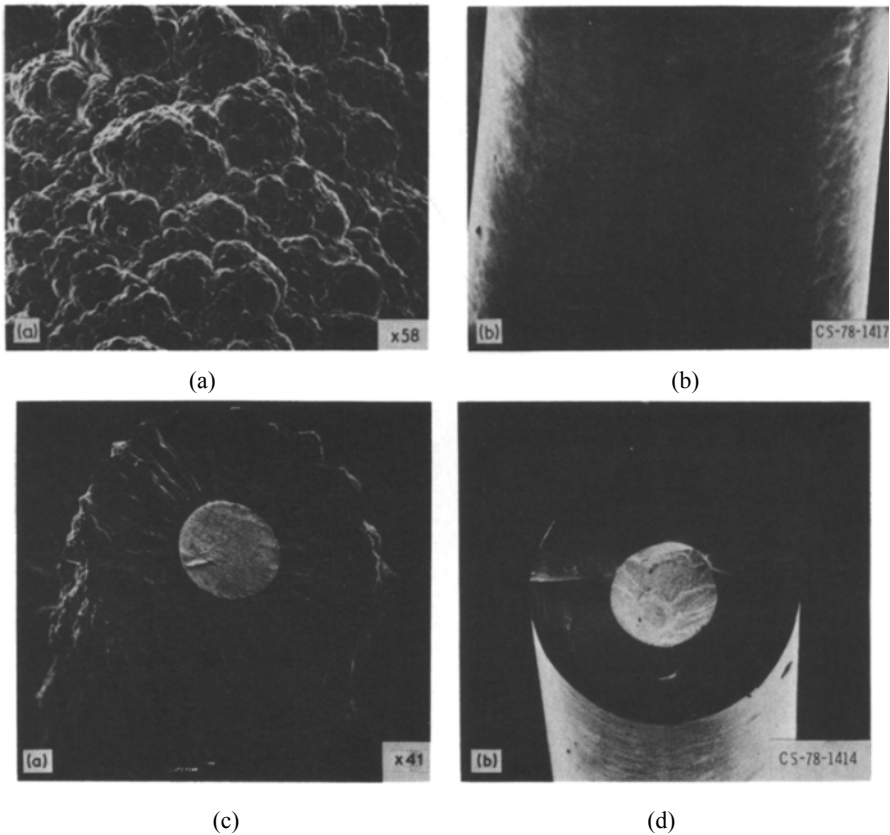


Figure 6.22. Microstructure of CVD SiC coating by different CVD methods [44]: (a) surface morphology by conventional CVD, (b) surface morphology by CNTD, (c) cross-section structure by conventional CVD and (d) cross-section structure by CNTD

intermediates being adsorbed onto the preferred sites (such as terrace, ledge and kink) on the substrate surface. In this case, the growth of the deposit takes place along the preferred orientation from those sites, which results in the formation of a columnar structure with coarse grains. This is very similar to the cave crystal formation process, where CaCO_3 water-containing runs along the rough ceiling surfaces to the lowest projected points to form drops at a low flow rate. In the course of dripping over this gradually expanding columnar structure, CaCO_3 is deposited on the surface to form a large columnar structure, which is called a cave crystal. If the precursor gases are preheated adequately, then enough active intermediates will be produced from homogeneous reactions. These intermediates can cover the substrate completely and be adsorbed on the substrate surface to ensure a uniform heterogeneous reaction to form the deposit with a smooth surface. In this case, the equiaxed fine grains are deposited rather than the coarse columnar grains.

6.3.2.2 Depositing Time

A number of attempts have been made and methods have been developed to improve the deposit thickness uniformity as shown in Figure 6.23. These methods include periodically reversing the gas flow direction, rotating the substrate, combining gas flow reversal and substrate rotation, stirring the gas, periodically repositioning the substrate, imposing a temperature gradient over the length of the substrate and tilting the substrate to increase its downstream projection into the boundary layer [14].

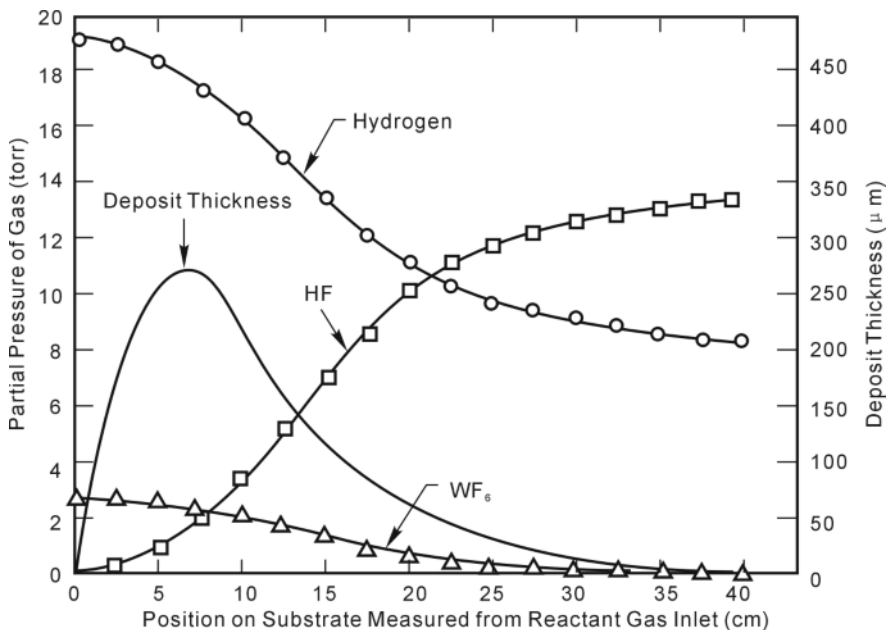


Figure 6.23. Gas composition and deposition thickness profile through the CVD process [46]

Table 6.3. Process parameters for P-CVD [46]

Deposition temperature	640°C
Nominal pressure during deposition	15 Torr
Nominal pressure during evacuation	2 Torr
Cycle time	10 s coat, 5 s exhaust
H₂/WF₆ ratio	6

Bryant [46] developed a novel method to fabricate a complex and large component with uniform thickness. Investigations reveal that the deposit thickness is largely dependent on the composition distribution of the reactant gases along the substrate. Figure 6.23 shows the composition variation of gases within a reaction chamber for a tungsten deposition from a tungsten fluoride and hydrogen system. As the distance to the gas inlet increases, the partial pressures of both reactant gases (WF₆ and H₂) are decrease; however, the partial pressure of the by-product of HF is increased significantly. As a result, the thickness of the deposit (W) is increased initially and reaches a maximum value at a distance of around 70 mm from the inlet. The thickness then decreases with distance, corresponding to the decrease of the partial pressures of the reactant gases. Pulsed chemical vapour deposition (P-CVD) was proposed to solve the reactant depletion problem and to lead to W deposit with uniform thickness along the length.

As indicated in Section 5.6 (pulsed CVI process), deposition time is a critical process parameter to control layer thickness uniformity and deposition quality. Unlike other traditional methods, the distinguished feature of P-CVD is that reactant gases are introduced in pulses, rather than in a continuous flow manner, into a previously evacuated deposition chamber at a high velocity. Tungsten deposition is conducted by repeated cycles of gas injection followed by chamber evacuation, forming pulses of gas injection into the chamber. Such a pulsing technique avoids the problem of gas composition and concentration being dependent on the position on the substrate. Instead, in pulsing, gas concentration varies as a function of time but in the same manner for every portion of the substrate. Details of the process parameters and techniques can be found in Table 6.3.

A tapered tungsten tube produced by the CVD process is shown in Figure 6.24a. Its as-deposited length is 1070 mm. The wall thickness is 0.75 mm and varies within the limits of ± 0.025 mm. The inner wall surface finish is 8 rms, equivalent to the finish of the mandrel. The outer wall surface finish is about 250 rms, which is a typical value associated with fluoride-produced CVD tungsten.

The microstructure of the tube taken in a direction normal to the growth direction is shown in Figure 6.24b. The multi-layer columnar grain structure in this figure is the result of cyclically interrupted deposition because of P-CVD. The deposition rate is calculated to be $30 \mu\text{m}\cdot\text{h}^{-1}$. This is well below the deposition rate of $125 \mu\text{m}\cdot\text{h}^{-1}$ normally achieved with the same parameters of temperature and

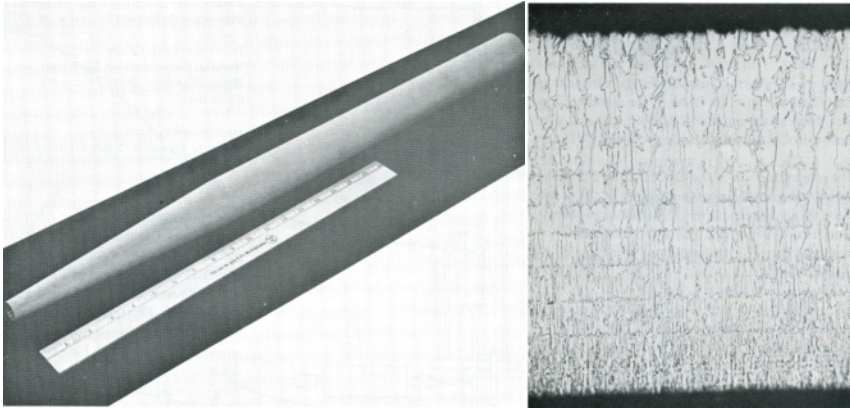


Figure 6.24. Tungsten tapered tube produced by pulsed CVD [46]: (a) a tube 1070 mm long and 0.75 mm thick (b) microstructure of W deposit

pressure when a non-interrupting flow-through process is used. The discrepancy in deposition rates can be attributed to two facts: (1) no deposition occurs during the part of each cycle used for the chamber evacuation and (2) little tungsten deposition occurs during the gas introduction phase of the deposition cycle. The latter conclusion is substantiated by the experimental observation that for each cycle the system pressure only increases for about 3 or 4 s from the time of gas injection. Increasing pressure from 10 to 80 Torr is effective for increasing the deposition rate of tungsten because there is more precursor supply for the deposition. The same increase is also observed by increasing the temperature from 640 to 750°C.

6.3.2.3 Influence of Temperature and Pressure on the Microstructure

It is well established that three types of pyrocarbon can be obtained by CVD processes, namely smooth laminar (SL) structure, rough laminar (RL) structure and isotropic (ISO) structure pyrocarbon. Their structural characteristics were first identified from optical observations by Lieberman and Pierson [41] in the 1970s.

Table 6.4. Physical and structural characteristics of three types of pyrocarbon [47]

	ISO	SL	RL
Density (g/cm ³)	1.5–1.8	1.7–1.9	2.0–2.1
Extinction angle (°)	<4	12~18	>18
Diamagnetic anisotropy	Very weak	Weak	Strong
TEM experiments	Micropores	Flattened pores	No pores
Graphitizability	No	Partial	Yes
D (002) after HTT at 2800°C (nm)	0.344	<0.344	0.337

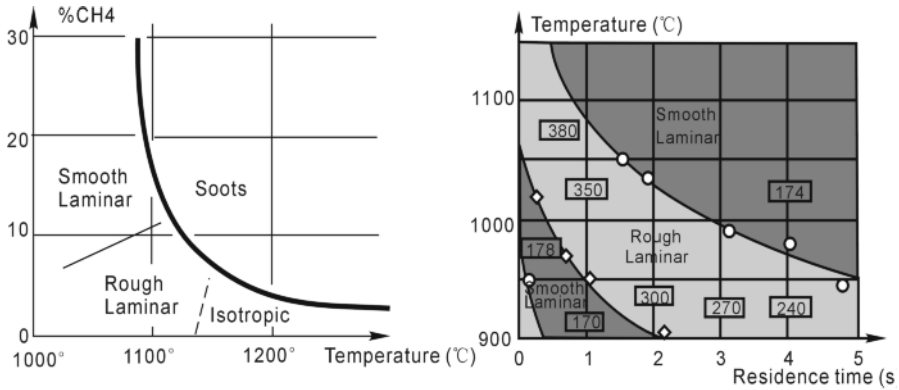


Figure 6.25. Microstructure characteristics of CVD pyrocarbon [47]: (a) influence of precursor partial pressure and temperature and (b) influence of residence time and temperature

Further investigation revealed some more differences among these three pyrocarbons, as listed in Table 6.4. A mixture of three types of pyrocarbons is always obtained in a CVD process. Of these, it is more desirable to produce RL pyrocarbon because of its high density, dense microstructure and good graphitizability. These advantages result in the superior friction behaviour for applications such as carbon/carbon braking discs and ablation resistance for thrust liners of a solid rocket engine.

For the CH₄-N₂ deposition system, the relationship between pyrocarbon structure and processing parameters is well established, as shown in Figure 6.25a. SL pyrocarbon is deposited at a high pressure of CH₄ precursor but a low temperature of less than 1100°C. By contrast, ISO pyrocarbon is obtained at a low pressure of CH₄ precursor but a high temperature of more than 1150°C. RL pyrocarbon is formed and deposited at the middle range of temperature and pressure, i.e. middle pressure and middle temperature. Soots are produced at both high temperature and high precursor pressure by homogeneous nucleation in the gas phase. In addition, the residence time of the precursor in the reaction zone plays an important role in the microstructure formation of the pyrocarbon. At a deposition temperature of 1000°C, the pyrocarbon microstructure is changed from SL to rough laminar then to SL structure as the residence time increases, as shown in Figure 6.25b.

6.3.3 Quantitative Control Parameters on the Basis of Fluid Mechanics Consideration

Preforms placed in a reaction chamber are subject to gas flow and allow deposition. The gas flow patterns are governed by pressure and velocity and have a significant influence on the rate and quality of the deposit. It is essential to have a good understanding of the impact of gas flow patterns on a CVD process. This enables a suitable design solution to both preforms and gas channelling systems,

including the location of preforms in the chamber and some gas flow guides if necessary, such that a high-quality deposition is achieved with a higher deposition rate. The key to achieving this is to minimise the pressure drag force.

Drag reduction of an object moving relative to its surrounding gas or fluid is a focal research point in design and analysis of such an object, such as an aircraft or a boat. Such a drag mainly depends on the shape of the object for a given flow. Rain droplets are good examples of the shape with the smallest drag coefficient when they fall in air. Their shape possesses excellent aerodynamics with a rounded front and a slim rear. This type of aerodynamic form is critical to any object when it travels in a fluid, whether a high-speed aircraft or a fish swimming in water. By designing and arranging the preforms in a reaction chamber, it is possible for them to present the smallest possible drag coefficient and reduce the residence time of the precursor gases within the reaction chamber.

6.3.3.1 Boundary Layer Separation

For a flat plate in a gas stream flow, arranged with its flat surface aligning along the flow direction, the streamline pattern is hardly affected by the presence of the thin boundary layer of the plate and remains nearly straight and parallel. The uniform pressure of the outside boundary layer does not affect the streaming flow which is impressed on the boundary layer flow. As a consequence there are no pressure variations either across or along the boundary flow. For a part with a curved surface or profile, the streamline flow and the pressure change are different from those of a flat plate [48]. The fundamental difference between flow over a flat plate and flow over a curved surface is the pressure variation caused by the curved surface. The flow is commonly divided into three zones, as shown in Figure 6.26, determined by the pressure change.

Pressure Decrease Zone

In the case where a gas flows over the front portion of a curved surface or a convex curve surface, the flow outside the boundary layer accelerates. The boundary layer over most of the front portion remains fairly thin and has a uniform streamline pattern over this portion. According to the Bernoulli equation [48], accelerated flow results in a pressure decrease in the vicinity of the front portion area. In this zone, the pressure gradient is positive, i.e. the direction of pressure gradient is the same as the flow direction. The positive pressure gradient is helpful to push the flow within the boundary layer forwards. The variations of velocity and pressure are expressed as

$$\partial u_x / \partial x > 0 \quad (6.25)$$

$$\partial P / \partial x < 0 \quad (6.26)$$

Top Point

At the top point of the curved surface, the flow is accelerated to the maximum value, however, the pressure reaches the minimum value. This means

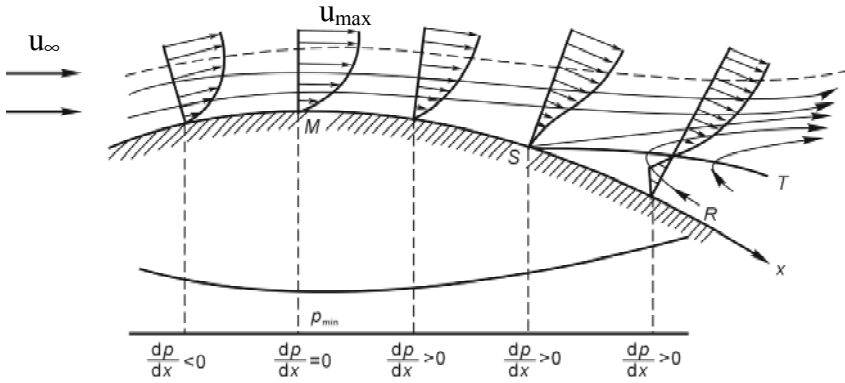


Figure 6.26. Boundary layer separation of a flow over a curved surface

$$\partial u_x / \partial x = 0 \quad (6.27)$$

$$\partial P / \partial x = 0 \quad (6.28)$$

Pressure Increase Zone

In the flow over the back portion of the curved surface as shown in Figure 6.26, the flow begins to decelerate, causing in the pressure of the outside flow. The flow in the boundary layer also decelerates because of the viscous resistance within the boundary layer and reverse pressure gradient outside the boundary layer. Finally, at some location along the back side of the curved surface, part of the boundary layer flow stalls, or comes to rest. The increasing pressure then causes this stalled flow to reverse direction and flow back along the curved surface. This phenomenon is called boundary layer separation and the region of reversed eddying flow is called the wake.

In this zone, the velocity and pressure variations are expressed as

$$\partial u_x / \partial x < 0 \quad (6.29)$$

$$\partial P / \partial x > 0 \quad (6.30)$$

6.3.3.2 Profile Drag Coefficient

The separated boundary layer and wake displace the outside streamline pattern, which causes the pressure distribution to be significantly altered. Boundary layer separation causes a force on the body called drag force. The drag coefficient is defined as the ratio of total profile drag force divided by the flow pressure and projected area of an object and is expressed as [49]

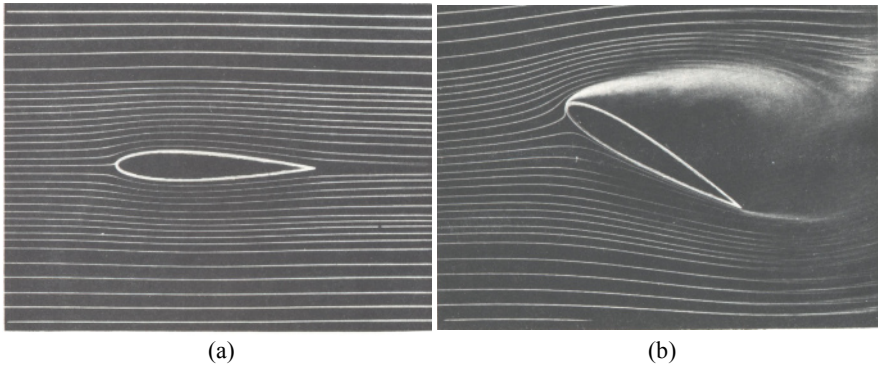


Figure 6.27. Orientation of an airfoil on the drag force [50]: (a) zero angle of attack and (b) large angle of attack

$$C_D = \frac{F_D}{A_p \rho u_0^2 / 2} \quad (6.31)$$

where A_p is the projected area of a body, ρ is the fluid density, u_0 is the free stream velocity, and F_D is the drag force usually determined by experiments.

The drag coefficient (C_D) can be determined if the pressure and shear stress distribution around a body are known. The drag coefficient can also be calculated if the total drag is measured, for example, by means of a force dynamometer in a wind tunnel. Then C_D is calculated using the above equation.

The drag force contributed by pressure drag and friction drag to the profile drag strongly depends upon the shape of the body and its orientation with respect to the flow of the fluid. For instance, if an airfoil is placed in a fluid stream with zero angle of attack, as shown in Figure 6.27a, the pressure drag is negligible, because even though the pressure recovery is incomplete, the resulting pressure difference acts on a very small frontal area (perpendicular to the flow). The skin friction drag, however, is substantial, owing to the formation of the boundary layer on the surface of the airfoil. If the angle of attack is large as shown in Figure 6.27b, the drag force also becomes very large due to the pressure difference, whereas the skin friction drag is negligible.

The drag coefficient is not only related to the shape and orientation of an object, as shown in Figure 6.28, it is also affected by the Reynolds number (Re) of the flow gas. This can be explained by inserting this statement into the definition of Reynolds number in Equation (2.58). The thickness of the boundary layer is decreased as the Reynold number increases, therefore reducing the contribution of the velocity boundary layer to the drag force.

6.4 Numerical Design and Analysis Techniques for Flow Field

Expanding on the introduction of a proposed engineering design approach in Chapter 3, this section describes a specific and effective approach to facilitating the design of a CVD or CVI system and its associated process control parameters. As an effective and rapid evaluation method, computational fluid dynamics (CFD) has developed significantly and has been widely used in recent years [51, 52]. Whilst there are many commercially available CFD software tools, such as CFX, PHOENICS, I-DEAS-ESC, FLUENT, FLOW3D and STAR-CD; their applications have been fully explained in other publications. Therefore the focus of this section is not to give a full theoretical introduction to the technique. This section aims to give a brief introduction to CFD theory and problem solving techniques and, more importantly, how one can use the techniques effectively in a real CVD system design. Some example CFD uses in solving CVD problems are also demonstrated.

CFD-based techniques date back to the early 1960s, and the first commercial CFD software became available in the early 1980s. Since then, research and development into CFD has transformed the techniques from a theoretical approach

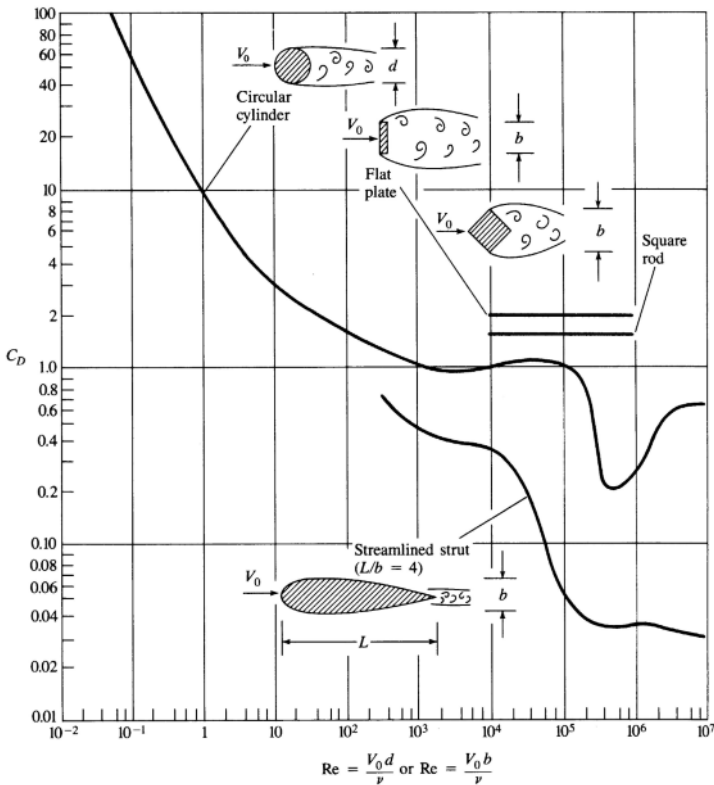


Figure 6.28. Drag coefficient vs. Reynolds number for two-dimensional bodies [49]

into a very effective and useful tool for many practical engineering problems. This is especially the case over last 10 years due to significant improvements in the computer user interface, as well as to rapid advancement in computational powers of personal computers. This effectively enables many engineers and graduates to model a particular system involving physical phenomena such as single or multiphase fluid/gas flow, flow turbulence, chemical reactions and radiative heat transfer that cover aerospace, chemistry, marine meteorology and a wide range of industrial and non-industrial application areas. Complex applications such as gas flow in a CVD system, aero dynamic race car design, aerofoil design in aeronautics, rocket modelling and simulation in aerospace drag simulation in automobile design, jet and thermal flow in engine design, and lava flow simulation in earthquake study can all make use the CFD methodology. This is because complex geometric representations of components or systems have been significantly improved. The performance of problem solving and visualisation have also been greatly enhanced.

Similar to other computer simulation techniques, CFD-based tools enable CVD system designers to undertake many what-if scenario studies to evaluate and assess the impact of design decisions on a system and on components manufactured by CVD or CVI in a virtual computer environment. This can greatly reduce the cost and time associated with traditional trial-and-error methods used in designing such sophisticated CVD systems and their process control parameters. For studies of complex multiphysics processes such as those taking place in a CVD process, CFD can provide an ideal environment in which many multiphysics phenomena can be investigated. This in turn reduces the cost associated with system design and process parameter determination by experiments. It can potentially help designers come up with a CVD design solution which can produce correctly deposited components the first time. Hence, CFD enables designers to study system behaviours without real difficulty and without the use of costly experiments. It can form an integral part of a powerful computer-aided CVD design and evaluation environment.

6.4.1 Governing Conservation Partial Equations Used in Computational Fluid Dynamic Approach

Gas flow in a reaction is considered to follow the principles of conservation of momentum, energy, and total mass. These parameters are used to simulate flow behaviour through numerical solutions of differential equations. The general derivation and form of these equations are given in standard references [53–55], and these principles and related equations are briefly introduced below.

Conservation of Mass Equation

Within CFD, mass is conserved, that is the rate at which mass enters a volume element equals that mass leaving the element in any steady state process. The mass continuity equation is important and is hence developed by formulating the relationship between the mass flowing into and out of a stationary volume element:

$$\text{Rate_of_mass_accumulation} = \text{Rate_of_mass_in} - \text{Rate_of_mass_out} \quad (6.32)$$

The above relationship defines the physical principle of continuity – mass conservation. A more concise mathematical representation of the mass conservation principle is given for a flow with a density of ρ and flowing at a speed of u by

$$\frac{\partial \rho}{\partial t} + \nabla \cdot (\rho \vec{u}) = 0 \quad (6.33)$$

where ∇ is the vector elementwise differential operator, known as the ‘del’ or ‘nabla’ operator.

Assume there is an incompressible fluid flow with a constant density ρ ; the above equation can then be simplified as a very important special form of the continuity equation

$$\nabla \cdot (\vec{u}) = 0 \quad (6.34)$$

Conservation of Momentum Equation

For a CFD volume element, conservation of momentum can be expressed by the following statement:

$$R_{m_a} = R_{m_in} - R_{m_out} + S_f \quad (6.35)$$

where R_{m_a} is the rate of momentum accumulation, R_{m_in} is the rate of momentum in, R_{m_out} is the rate of momentum out, and S_f is the sum of forces acting on the system.

Mathematically, the above can be expressed by the well-known Navier–Stokes equation as

$$\rho \frac{D\vec{u}}{Dt} = -\nabla p - \nabla \cdot (\vec{\tau}) + \rho \vec{g} \quad (6.36)$$

where the left-hand side represents acceleration multiplied by density or the mass per unit volume. The right-hand side is the summation of various forces on the element per unit volume from the pressure force ∇p , viscous force $\nabla \cdot (\vec{\tau})$ and gravity $\rho \vec{g}$, respectively. In a physical sense, the Navier–Stokes equation is another form of Newton’s second law.

Here the partial time derivation, $\partial/\partial t$, describes how the variable (concentration, velocity and temperature) changes with time at a fixed position. Substantial time derivation, D/Dt , is a special kind of total time derivation computed by an observer floating downstream with the fluid. In this form the equation of motion states that a

small volume element moving with the fluid accelerates because of the forces acting upon on it.

For constant density gases with constant viscosity, Equation (6.36) can be simplified as

$$\rho \frac{D\vec{u}}{Dt} = -\nabla p + \mu \nabla^2 \cdot (\vec{u}) + \rho \vec{g} \quad (6.37)$$

where ∇^2 is the Laplace operator.

Conservation of Energy Equation

The conservation of energy is also called the First Law of Thermodynamics and is based on the concept that energy can be neither created nor destroyed. This conservation of energy defines the relationship between the energy involved in an isolated system and work (the mechanical energy) the system does on its surroundings. The differential equation of energy can be derived according to the physical principle of mass conservation:

$$R_{e_a} = R_{e_in} - R_{e_out} + R_{ew} \quad (6.38)$$

where R_{e_a} is the rate of energy accumulation, R_{e_in} is the rate of energy in, R_{e_out} is the rate of energy out, and R_{ew} is the rate of external work done by the system on its surroundings.

The energy within a system includes potential energy, kinetic energy and internal energy. Under steady conditions, the mathematical equation for an incompressible fluid with constant properties is expressed by

$$\frac{DT}{Dt} = \alpha \nabla^2 T + \dot{q} + \mu \Phi \quad (6.39)$$

where T is the temperature, \dot{q} is the rate of heat generation per unit volume, α and μ are the thermal diffusivity and viscosity coefficients respectively, and Φ is the friction heat resulting from viscous force.

If there is no interior heating source within the system, \dot{q} becomes zero. Moreover, the viscous dissipation term ($\mu\Phi$) is generally negligible except where extremely large velocity gradients exist in a system. As a result, the latter terms of the right side of Equation (6.39) can be omitted and the equation can be rewritten as

$$\frac{DT}{Dt} = \alpha \nabla^2 T \quad (6.40)$$

The above conservation equations can be used to work out the profiles of concentration, temperature and velocity within the reaction chamber of a CVD process. For the most commonly used isothermal CVD systems, it is understood that the temperature and gas concentration has less influence on CVD processes than velocity. Therefore, the next section focuses on the velocity of CVD systems.

6.4.2 Computational Fluid Dynamics in Chemical Vapour Deposition

Computational fluid dynamics (CFD) is essentially a computer-based numerical analysis approach for fluid flow, heat transfer and related phenomena. CFD techniques typically consist of the following five subprocesses: geometrical modelling, geometry discretisation, boundary condition definition, CFD-based problem solving, and post-processing for solution visualisation.

6.4.2.1 Geometrical Modelling

The geometric representation of a solid object such as a CVD reaction chamber or any substrates inside the chamber can be represented unambiguously using solid modelling techniques, which is also known as volume modelling as it deals with the three-dimensional (3-D) volume of these solid objects. Within these techniques, a solid object can be represented by boundary representation (B-Rep) as a volume contained in a set of faces together with topological information which defines the relationships between the faces, vertices and edges and how they are joined together. This technique can represent a wide range of solid objects and can employ the *intersection*, *union* and *difference* techniques between two arbitrary shapes overlapping in a 3-D space to represent complex objects.

Three-dimensional objects can also be represented by so-called primitives in a constructive solid geometry (CSG) representation. These primitives are the essential building blocks of more complex shapes and include simple shapes: cuboids, cylinders, prisms, pyramids, spheres, cones and so forth. Boolean operators include *Union* to add a new primitive into an existing shape, *Cut* to subtract a particular shape from an existing shape, and *Intersect* to generate the overlapped volume. Building on these operations, complicated geometry can be created using basic objects. As each basic object contains necessary information, the processing of compound shapes is usually simpler and less demanding compared with the B-Rep methods. For CVD system modelling, some system components are of regular shapes and hence can be easily modelled using this method. Figure 6.29 shows an example of the chamber and substrates model created using this basic technique.

Wireframe models are also used in many applications and are visual representations of a physical object which only specify and display straight or curved edges at the point of intersection of two faces. Edges are connected to each other with vertices. A wireframe model is represented by tables defining edges and points. The start point and end point of each edge are stored in the edge table. An edge may be a line or a curve. The coordinates of each point are stored in the point table. A wireframe model is stored in a computer as a data structure, using very small data space. Wireframe representation is particularly useful for mesh representation in CFD and finite element analysis (FEA) techniques.

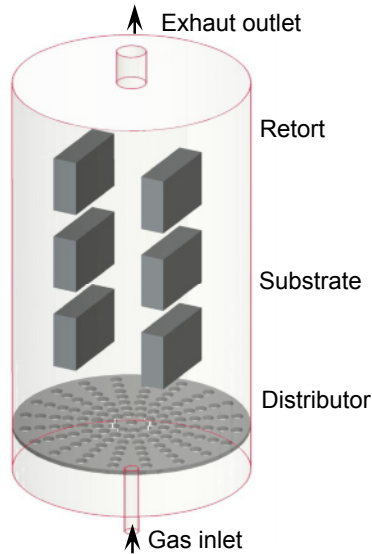


Figure 6.29. A typical solid model constructed using CSG method for a CVD system

It is also worth mentioning that 3-D objects can be simplified into 2-D structures. This simplification can reduce significantly the requirement for computational power hence much quicker for these problems.

6.4.3 Geometry Discretisation and Mesh Generation

Geometry using the above techniques is the first step. Trying to produce a single-solution method for any defined geometry and different types of flow is impractical, if not impossible, with current technology. The key with the numerical approach used in CFD is to divide the whole flow space or domain into many smaller and easy to understand subdomains (also called element or control volumes), which is known as the geometry discretisation and mesh generation process. The basis for this is that, though it is difficult to derive a single generic analytical solution to a complex problem, it is possible to develop solutions to smaller and well-understood elements within the fluid dynamic domain. For each of these well-understood types of elements, it is possible and relatively easier to derive a set of partial differential or integral-differential equations for the elements and use the required boundary conditions for each element to find solutions to the problem. During this process, it is reasonable and accurate enough to simplify the exact conservation laws for a given type of element. It is therefore often the case that a solution in the form of a particular set of equations is usually derived for a particular type of element. This approach hence ensures that the solution and computational efficiency can be optimised as general purpose tools, but they are usually not optimum for any one application.

The constituent subprocesses of discretisation consist of mesh generation (determining the types of mesh elements), space discretisation and time discretisation.

6.4.3.1 Mesh Generation Strategy

Once a solid object is modelled either in 2-D or 3-D, the next stage of the CFD working principles is to generate mesh elements for the volumetric space where a fluid flows. This effectively divides the whole volume space, often referred to as a domain, into a large number of so-called small elements which are more solvable. The volume space or domain is divided into fine, non-overlapping elements or cells, also called grids, which govern the accuracy of a CFD solution. Generally the finer the grids are, the better the solution accuracy. From a mathematical modelling point of view, this essentially transforms in most cases the partial differential equations of a complex fluid system into a set of algebraic equations, which are much easier to solve.

The above process of generating elements and linking them through nodes is called discretisation or, more commonly, meshing. Unlike a structural FEA approach, CFD meshing deals with the flow space between geometric boundaries. The meshing process of a computer system effectively relies on the system to recognise the 'space', sometimes requiring the help of a user, to discretise them into many smaller elements which are determined by the definition of the element sizes. As a general guideline, the smaller the elements are, the larger the number of elements created for a system, and the longer it takes to solve a problem. From design feasibility study point of view, it is advisable that each design session start with a larger element size first in meshing and then go through the whole CFD process first so that a working solution is achieved before a refined solution can be generated. This approach can reduce the effort required to give a rough solution and avoid many scenarios where an inability to solve a particular problem is more likely to be caused by mistakes in the model and in boundary condition definitions, rather than in meshing.

For CFD discretisation, some methods are available in commercial systems. These common methods include finite difference (FD), finite volume (FV) and finite element (FE) methods. Each of them takes a different approach in approximating the differential equations essentially based on the Navie–Stokes equation. Their underlying approaches are similar and they all approximate differential equations by a system of algebraic equations for the variables in some set of discrete locations in space and time.

Depending on the methods used, there are potentially three types of meshes which can be generated during a meshing process, namely structured, block-structured and arbitrary or unstructured meshes. In a structured mesh, gridlines are used to represent the domain; these gridlines do not cross and only intersect with other family gridlines once, as shown in Figure 6.30a. Each mesh element is represented in Cartesian coordinates, as the mesh topology is equivalent to a Cartesian grid. A structured mesh is characterised by a mesh element arrangement where all interior nodes of the mesh have an equal number of adjacent elements. The most common meshes generated by a structured grid generator are typically

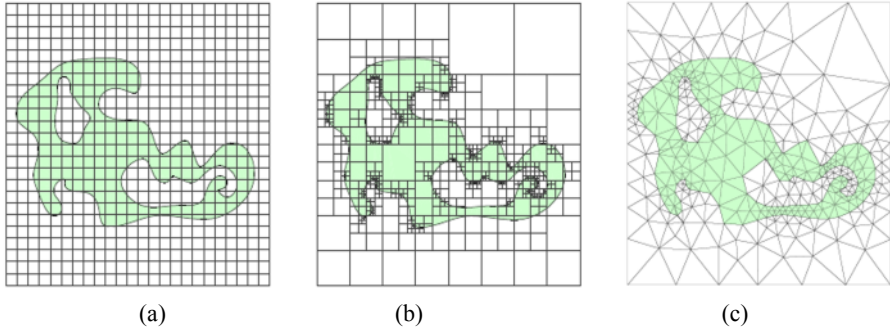


Figure 6.30. Examples of meshing methods: (a) structured, (b) block-structured and (c) unstructured

quadrilateral or hexahedral meshes. These mesh elements are only created for simple domains; other meshing techniques are required for more complex domains.

Block-structured meshes are an improvement over structured meshes as this approach allows the generation of a variable element number or element density in different blocks of the whole domain. Block structures are arranged in multiple levels based on the topology of the subdomain within the solution domain. On the top or coarse level of such a hierarchical structure, the whole domain is divided into blocks, which are a relatively large solution subspace of the domain. The structure of this subspace may not be regular and this subspace may or may not overlap with the block or subspace at a higher level of the hierarchy. At the next low or fine level, a particular structure grid with a particular resolution is defined for each block. It is also necessary to undertake special treatments for block interfaces due to the above meshing difference. For some blocks, a lower level division is required to refine the mesh elements further to improve the accuracy of the CFD numerical analysis.

Unstructured meshes, as shown in Figure 6.30c, refer to the mesh elements generated by dividing an arbitrary solution domain boundary into a number of elements or control volume which may have any shape. There is no restriction on the element definitions. The most commonly generated element shapes are triangle or quadrilateral shapes in a 2-D domain, or tetrahedral or hexahedra shape in a 3-D domain. Unstructured mesh generation allows any number of elements to meet at a single node. This type of meshing increases the complexity of the data structures representing the meshes and can cause difficulties in computational implementation as the sparse matrix used in the analysis can require significant computer memory and may require the development of many special algorithms. On the other hand, due to their flexibility, these meshes are ideally suited for arbitrary domains and are amenable to adaptive mesh refinement.

6.4.3.2 Space Discretisation Method

With an accurate flow space or domain defined in terms of its geometry and a strategy for discretisation determined, it is necessary to select a suitable specific discretisation method before a problem can be solved. Having studied the field of

fluid flow and dynamics for decades, researchers have developed a good set of mathematical solutions to different types of discretisation problems. Each of these methods takes a different approach in approximating the differential equations essentially based on Navier–Stokes equations. All these discretisation methods approximate differential equations by a system of algebraic equations and only calculate the required variable values at these discrete locations in space and time. Due to the fact that these methods were developed for different problems, one method is therefore more suitable to the class of problems it was intended than others. In addition, the conservation equations can be written for different coordinate systems e.g. Cartesian, cylindrical, spherical, curvilinear orthogonal or non-orthogonal coordinate systems. For CFD space discretisation, there are a number of techniques and associated methods developed and available in commercial systems. The most important of these are finite difference (FD), finite volume (FV) and finite element (FE) methods as shown in Figure 6.31a–c respectively.

An FD-based method is a simple and straightforward method used and developed as a first approach to tackling the fluid flow problems using computers. The FD methods usually utilise Cartesian gridlines spaced out to represent the flow space, and the methods calculate the values of the relevant fluid dynamic parameters of interest for a number of gridline intersections points. In solving partial differentiation equations of a fluid system, this method essentially uses the linear combinations of the original function values at the gridline intersection points rather than their derivatives. This approximation enables the approach to simplify many complex partial differentiation calculations. Due to the simple gridline representations and the aforementioned approximation, their use is therefore largely restricted to the flow problems involving simple Cartesian geometries. FD has mostly been applied to structured or block-structured grids and meshes. FD methods utilise the differential form of the conservation equation.

In an FV method, the whole solution domain is subdivided into a finite number of contiguous control volumes. The computational node is located at the centroid of each control volume, whereas the node is located at the grid in the FD method. The FV method uses the integral form of the conservation equation

$$\int_S f dS = \sum_k \int_{S_k} f dS \quad (6.41)$$

This method is a widely adopted approach used most often in commercially available software systems. It is a method to represent, solve and evaluate partial differential equations as algebraic equations for the divided discrete volumes. In this approach, a small volume surrounding each node point on a mesh is defined and studied to calculate the relevant information such as the flow rate, temperature, etc. of this particular node using the ‘finite volume’. Applying the laws of conservation of mass, energy and momentum, the flux in terms of these three properties entering a given volume is always assumed to be identical to that leaving the adjacent volume. Based on this, starting from the volume element which is fully constrained and defined by the initial known boundary conditions,

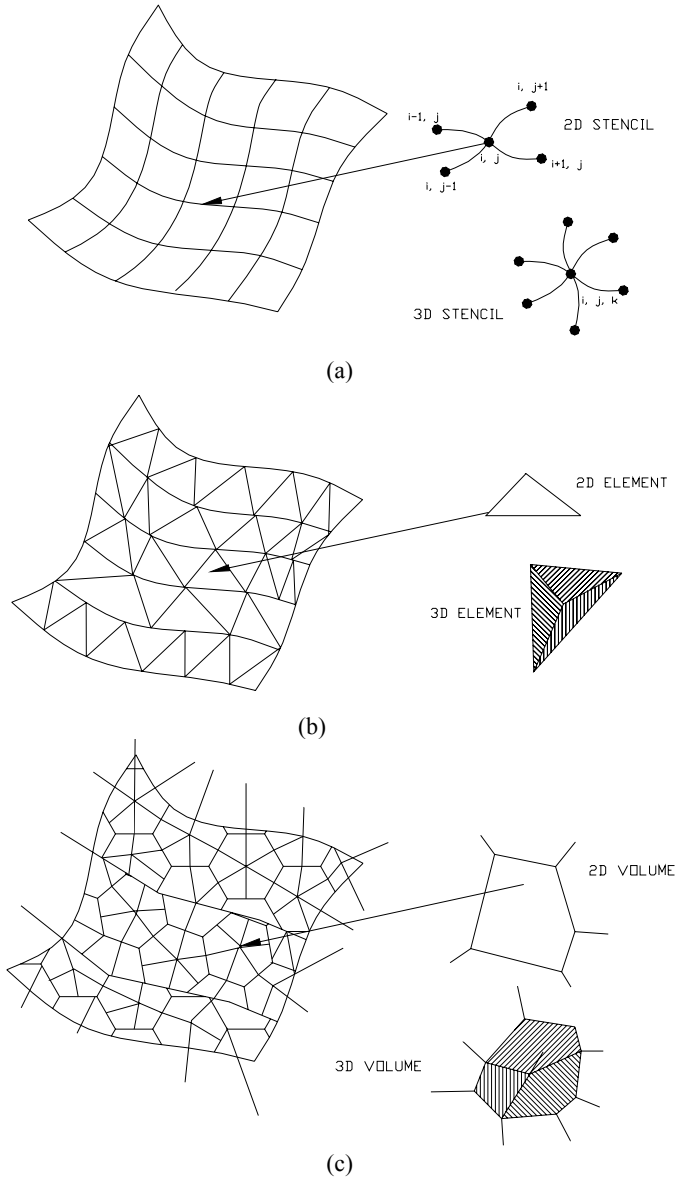


Figure 6.31. Examples of (a) FD, (b) FV and (c) FE meshing elements

the calculation of each element can be carried out and relevant information can be obtained.

The FE approaches used in CFD originate from structural mechanics and is similar to the FV method. A domain is divided into many discrete control volumes or finite elements. These elements are generally unstructured meshes. The most commonly used 2-D elements are triangles or quadrilaterals, whereas for 3-D

meshing, tetrahedra or hexahedra are the most commonly generated meshes. In an FE method, weighting functions have to be selected, and this is the key distinguishing feature of an FE method compared with FV methods. For a given governing partial differential equation based on Navier–Stokes equations, it is possible to approximate it with a high-order polynomial equation. As this is an approximation, there is an error normally defined by a residual function. To accurately represent the original conservation law represented by a partial differentiation equation, an FE approach in CFD now involves solving the problem of selecting the best solution with the minimum residual value, or ideally zero value for the residual.

6.4.3.3 Time Discretisation

Once a domain is discretised in terms of its space or geometry definitions for a given problem, it is also necessary to discretise the time – a process of determining the timing step value, as the computer based CFD analysis is essentially a discrete simulation technique. From conservation law equations, it is clear that all variables such as mass, momentum and energy vary in time, and the purpose of CFD analysis of a CVD process is to determine the performance of the system at any time. Depending on the problem, the time discretisation technique may vary. As the space and time variables are independent of each other, they can be discretised independently to obtain a sequence of normally non-linear algebraic systems.

For simple problems with simple geometries, the global time step for solving the conservation equations are normally set to be a constant step size determined by the stability constraint on the finest grid. The stability constraint refers to the step size at which the level of numerical errors, caused by the roundoff due to final precision of variable values represented in computers, should not be allowed to grow unboundedly.

For complex mesh types such as unstructured or block-structured meshes, it is necessary to adopt a ‘time-step-refined’ approach, where different suitably defined time step sizes are employed for each mesh level [56]. Typically, this requires *recursive* integration on the various mesh levels, starting with the coarsest level (at a time step determined by the stability constraint of the mesh level itself), followed recursively by the integration of its child mesh levels, which are processed more often but at their (smaller) stability constrained time steps. Generally, this multilevel time stepping approach is commonly known as *subcycling*, which can be further improved by more rigorously defined methods using partitioned multirate time stepping [57], in which time step sizes are defined using more rational rules linking to the mesh types and mesh elements.

6.4.4 Boundary and Initial Conditions

For any given fluid dynamics problem, CFD-based simulation is normally used to evaluate the behaviour of a system for a limited domain or a bounded space. It is therefore important to define the fluid behaviour at the boundaries of this domain so the CFD analysis can be confined in a domain. Initial values of some flow properties should also be defined and can also be found from the understanding of the flow by investigating its initial definitions either when a steady state flow is

fully developed or by giving dynamic values or a data table to define a function of the initial flow process.

6.4.4.1 Boundary Conditions

For CFD analysis of CVD systems, it is important to define correct boundary conditions for conservation equations. Typical example attributes of boundary conditions used in flow and heat transfer simulations are velocity, gas concentration, and temperature of the boundary areas. If an inlet boundary is selected such that it contains too many unknown initial values for the problem, one should extend the boundary area to as far as a bound where all initial variable values are known. In assigning the initial values of the boundary areas, it is a common practice to make the following assumptions [58, 59].

For solid walls, no-penetration and no-slip are typically applied to the momentum equation. Boundary conditions such as velocity, pressure and temperature at the inlet are usually known and specified, whereas their counterparts at the outlet are derived from assumptions of no-stress or fully developed and simulated flow. The thermal wall boundary conditions influence the flow significantly. Simple assumptions of constant wall temperature, insulated side walls and constant wall heat transfer flux have been used extensively for simple applications. More specifically, the following assumptions are normally made for a retort as shown in Figure 6.29 (the directions of the velocity in the following description refer to a cylindrical coordinate system in this figure).

On the walls, the normal and tangential velocities are assumed to be zero:

$$u_r = 0, u_\theta = 0, u_z = 0, T = \text{const}, P = \text{const} \quad (6.42)$$

At the inlet, the fluid has only an axial velocity according to either a parabolic or plug flow inlet profile:

$u_r = 0, u_\theta = 0; T = \text{constant}, P = \text{constant}, u_z = \text{constant}$ (for plug flow) or a predefined velocity profile,

$$u_z = 2u_0 \left[1 - \left(\frac{r}{R} \right)^2 \right], 0 \leq r \leq R \text{ for the parabolic inlet profile} \quad (6.43)$$

The outlet of the reaction chamber is assumed to be long enough that the velocity and temperature fields are fully developed:

$$\frac{\partial u_z}{\partial z} = 0, \frac{\partial u}{\partial z} = 0, \frac{\partial u_z}{\partial z} = 0, \frac{\partial T}{\partial z} = 0 \quad (6.44)$$

6.4.4.2 Initial Conditions

The initial flow attribute values are essential for the CFD solver to start the calculation with some known values in order to derive the fully understood element by working out all required flow property parameter values. For a CVD system, these initial values include the gas inlet speed, temperature and pressure and the

temperature of the chamber wall and the substrates. The inlet initial gas flow properties are given as:

$$T = T_0, P = P_0, u = u_0 \quad (6.45)$$

As a first approach, the wall and substrate temperatures are assumed to be given. The initial conditions of the chamber wall and the substrates are also assumed to be given:

$$T = T_w \text{ (on the wall)}, T = T_s \text{ (on the substrate)} \quad (6.46)$$

In addition, the variable values for physically non-negative attributes such as density must always be positive or meaningful for other values to be in a sensible range, e.g. concentration between 0 and 100 %.

6.4.5 Iterative Problem Solving Strategy

Depending on the space discretisation techniques used, the set of equations to be solved may be different, but for FD- and FV- based methods, the discretisation results in a set of linear or non-linear algebraic equations. These depend on the nature of these partial differential equations and how they are derived. For linear equations, it is well known that a Gauss elimination method can be used as a basic method to solve them. Further details of the Gauss method can be found in [60].

The Gauss elimination method can equally be used to solve any set of algebraic equations. However, this method is often expensive to use as there are still a large number of elements in the triangular matrices to use a direct method to solve them. Furthermore, the algebraic systems to be solved are very large and may contain millions of unknowns. For many such problems, these matrices are sparse, and most of the matrix coefficients are equal to zero. Gauss elimination methods are not effective for these problems. This brings about the necessity of employing iterative methods even sometimes for linear problems.

For non-linear algebraic equations and sometimes for linear problems as discussed above, an iterative method must be used, in which an initial solution is estimated or guessed and it in turn is used in the equations to systematically improve its accuracy. Non-linear problem solving techniques can be classified into two broad groups: Newton-like methods and global solving methods. Newton-like methods are effective and efficient in solving non-linear problems provided the initial estimated solution is available and closer to the final solution. Otherwise, they may fail to solve the problem completely. Global methods, on the other hand, can guarantee to derive an existing solution by searching all solution spaces. It is therefore not an efficient and fast approach to finding solutions. Whichever methods are used, this iteration process continues until, under an ideal situation in most cases, the solution gradually approaches the target solution, in which case the solution converges.

Assume that a solution after the n th iteration is represented as Φ_n which contains a set of values of interest (e.g. temperature, velocity, etc.) for all elements

of a domain. The converged solution can be represented by Φ , and the residual after the n th interaction can be expressed as:

$$\epsilon_n = \Phi - \Phi_n \quad (6.47)$$

The purpose of interactive calculation is to drive the residual error ϵ_n to zero. The process of deriving a solution Φ_n which is close to the problem solution is called a converging process. In a typical interactive problem solving process, there are two levels of iteration, namely outer iterations and inner iterations. During outer iterations, the coefficients of the discrete problems are recalculated and updated for more accurate representations of these coefficients, using the solution values of the fluid flow system from the previous iteration. During these calculations, Newton-like methods are used to eliminate the non-linearities of the fluid problem such as those defined in previous sections. Coupled equations are also segregated so that these governing equations of the fluid system can be solved. For the inner iterations, linear equations or subproblems are solved by an iterative method, such as conjugate gradients introduced by Golub and van Loan [61], biconjugate gradients proposed by Fletcher, or a strategy-based multigrid approach [60]. If direct solvers such as Gaussian elimination are to be used, they require large and expensive computer resources both in terms of memory required and time taken. It is therefore common to use iterative approaches to solve these problems.

During the course of interactive problem solving, it is important to know when to stop the iteration if the solution converges. This has a great impact on the solution accuracy as well as problem solving efficiency. The ultimate factor determining this is the errors produced at the end of each iteration during the problem solving. If these errors reach an acceptable level, the numerical problem solving can be stopped. Otherwise the iterative problem solving carries on until an acceptable solution is found, or unless the problem solution is not converging. The solution errors come from each part of the process used to produce numerical solutions, as detailed in the following sources: (1) modelling errors: these define the difference between the actual flow and the exact solution of the mathematical model; these errors include geometrical representational errors from geometric models of a physical fluid flow system; (2) discretisation errors: these are defined as the difference between the exact solution derived from the equations of the laws of conservation of mass, momentum and energy and the converged solution of the discretised system; and (3) iteration errors; these are the difference between the exact solution of the algebraic equation systems and that from a solution after so many iterations.

Using the above errors in a CFD interactive problem solving process, it is necessary and possible to check the residuals, relative solution changes and other indicators to make sure that the solutions converge after certain iterations. Computer algorithms have been implemented based on these indicators to stop the calculations once a certain level of errors is reached based on the calculations of the above three types of residual errors. Using a CFD software system in this process is relatively easy and simple and all that is normally required is patience to see the results. Depending on the complexity of the problem, solving can take hours

if not days before it finishes. In some cases, the results of the problem solving may not produce the expected results due to a number of reasons, including wrong initial or boundary conditions defined, meshes are too coarse, or elements are too small for the computer to solve. It is important to read the error message from the software system to rectify any problems in the model or initial specifications.

6.4.6 Postprocessing and Visualisation

The main function of postprocessing and visualisation in CFD is to process the simulation results derived from the computed flow field and externalise them in a suitable and comprehensible format. Any deficiency identified at this stage can be eliminated without incurring any costs associated with physically building these systems. More specifically, postprocessing deals with the calculation of derived parameter quantities for velocity and stream function in a fluid flow system. These can help CVD system designers and process engineers to identify suitable process control parameters such as drag, total mass and lift to ensure constant flow velocity can be established by adjusting inlet initial reactant gas control parameters, such as pressure, temperature, etc. For delicate coating applications, a slight mismatch of gas velocity to the required one may cause the whole process to be substandard and the products coated may not achieve the expected behaviour.

Visualisation is a process of converting all data for one parameter or a set of parameters of interest into a more visual graphical representation to help users of the CFD systems to quickly visualise the results. The format of this visual externalisation of the results can be in one dimension, showing a number of values of a particular system performance parameter in a series of line segments in a chosen colour and line types (solid line, dashed lines, dotted line, etc.). In a 2-D representation of function values, two sets of data are used to form a 2-D curve, which could represent streamlines of a flow, isobaric contours showing the areas where the pressures are the same. Alternatively, colour diagrams are used to indicate the different levels of functional parameter values using different colours which normally have an indicative value besides the colour diagrams.

For 3-D representations, similar functional parameter values can be shown for a 3-D feature, such as surfaces, volumes and cut planes. To represent the magnitude of the functional parameter values, arrows can also be used to give a less scattered representation. Arrow plots are usually used to represent the flow directions and vortexes formed and they are particularly suitable for representing flow directions within the solution domain as these arrows can give clear directional information.

6.4.7 Some Computational fluid dynamics Application Examples

6.4.7.1 *Influence of the Number and Arrangements of Components on the Flow Field*

A CFD technique can be used to evaluate the behaviour of a CVD system. Here some examples are given to show its applications and effectiveness to understand how systems work and how to design a process for a system. Figure 6.32 shows the simulation results of flow patterns and gas distribution inside a reaction chamber

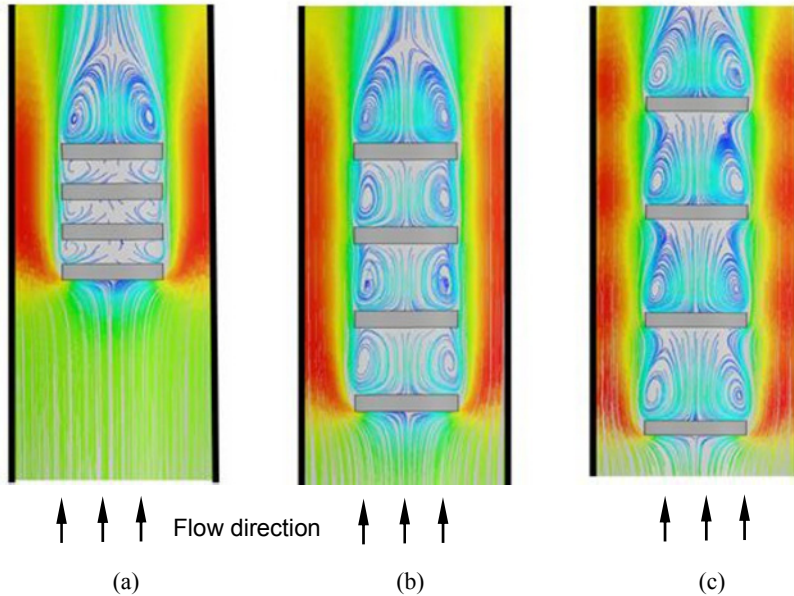


Figure 6.32. Flow velocity profile of stream lines around the components horizontally arranged in the reaction chamber: (a) 50 mm, (b) 100 mm and (c) 150 mm

where the components are arranged in 4×1 (four components arranged vertically in one column). The components to be deposited are arranged horizontally and the distance between the components is changed from 50 mm to 100 mm and then 150 mm. Assume that the plug gas flow is introduced into the reaction chamber from the bottom. The flow approaches the first component at the bottom of the chamber and is diverted horizontally and then squeezed into the gaps between the components and chamber wall. The flow velocity along this circumferential ring, which is also called a main stream flow, is much faster than that in the other areas as indicated by the densities of the stream lines. Between the components, the gas flow is very slow and there are some recirculations as shown in Figure 6.32.

When the reactant precursor gases flow passing the sides of the components, their velocities increase as they pass through a narrow gap. After passing through the narrowest area, they form vortexes or recirculations as the velocity decreases. When the distance is 50 mm, there is a stagnant flow area between the components, as shown in Figure 6.32a. When the distance between components is increased to 100 mm and 150 mm as in Figure 6.32b and c, there are recirculations between the components. The recirculation leads to the longer residence time of the gases between the components. This in turn results in poor deposition quality because the exhaust gases cannot be removed in time and the reactant gases cannot be delivered onto the surface of the substrate. Meanwhile, the quality of the deposition on the central area of a component varies significantly on the sides of the component as they experience different flow velocities of the reactant precursor gases. It is clear that the arrangements and the number of components in a reaction

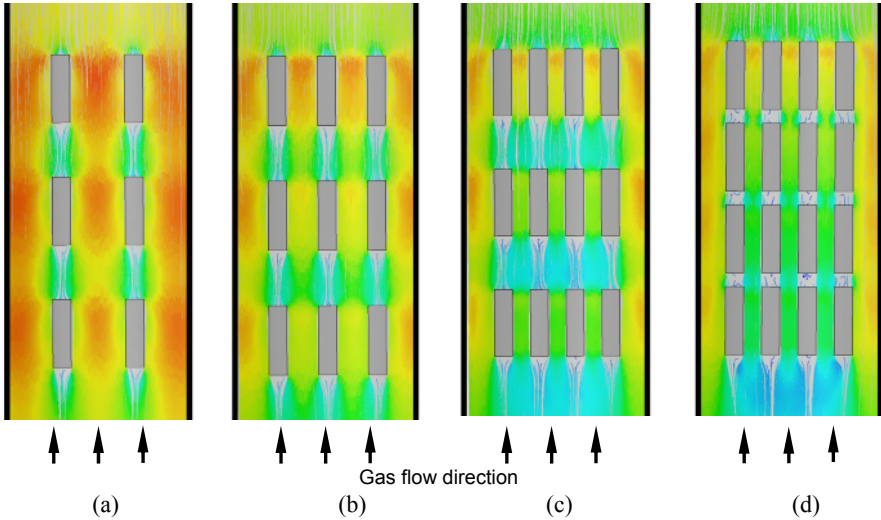


Figure 6.33. Flow velocity profile around the components vertically arranged in the reaction chamber: (a) 2×3 , (b) 3×3 , (c) 4×3 and (d) 4×4

chamber has a significant impact on the gas flow patterns and the deposition quality.

As shown in Figure 6.33, the components are arranged in 3×2 (three components arranged vertically in two columns), 3×3 , 4×3 and 4×4 layouts. When the components are arranged vertically, the flow becomes much less restrictive and several main stream flows can be formed depending on the number of columns of the components. The number of components in each row also determines the flow pattern and the smoothness of the main stream flows. Figure 6.33 shows four different arrangements of components and their gas flow simulation results. As the number of columns increases, the gas flow becomes smoother and the quality of gas flow also improves with more constant flow speed. This can be explained by the decreases in free volume within the reaction chamber according to Equation (6.23). As the free volume decreases, the residence time becomes shorter, hence leading to the better deposition quality. In addition, the free convection of the gas flow can also be eliminated as the characteristic distance decreases according to Equation (2.64).

From the simulation results it can also be seen that residence time is not only dependent on the free volume but also on the arrangements of the components within a reaction chamber. This observation through simulation results is not reflected in Equation (6.23).

6.4.7.2 Optimisation Design of Flow Profile for Components with Complex Shape

For simple components such as plates and flat disks, the above simple change of arrangements is effective and can be optimised to ensure an approximately constant flow velocity, which in turn ensures uniform deposition. For components with complex shapes, such as domed components as shown in Figure 6.34, it is

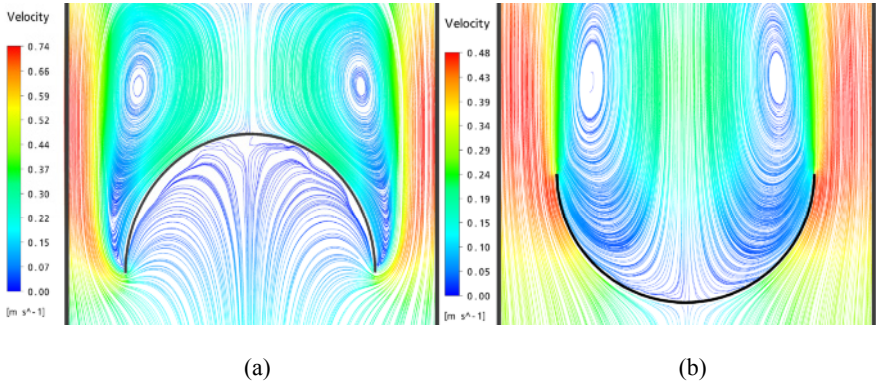


Figure 6.34. Flow profile around dome-shaped component: (a) Facing downstream and (b) Facing upstream

important to study the arrangement of such components inside the chamber. In many cases, there exist stagnant gas flow behaviours in some parts of the component and it is therefore necessary to design a gas flow guidance device to ensure a relatively smooth and constant precursor gas flow passing through the components. This approach depends on the shape of the components and has to be dealt with in a case-by-case manner. Simulation based on CFD can facilitate a rapid evaluation of gas flow velocity of such components in a predefined chamber and help designers and manufacturers to decide how they can produce high-quality CVD components. The following section shows a CFD simulation analysis and the design of a sample product.

Taking a domed component as an example, the precursor gases inside the

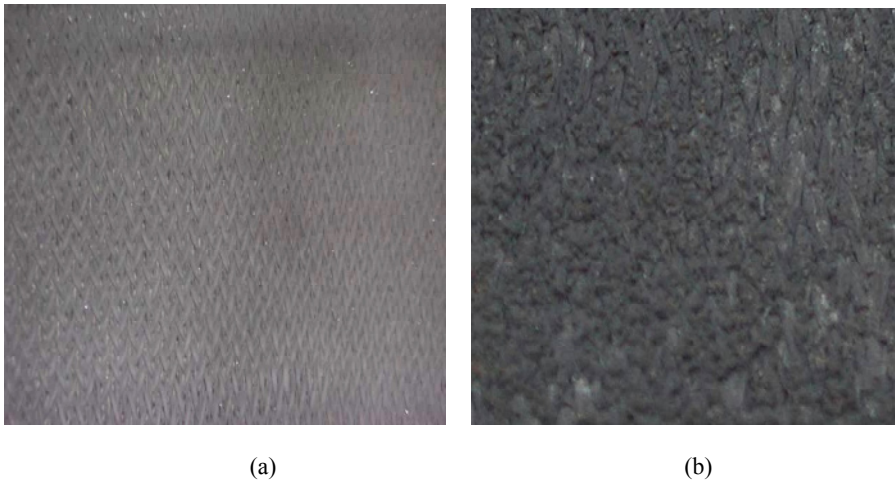


Figure 6.35. Deposition quality comparison of both sides of a dome-shaped component corresponding to the arrangement of Figure 6.34b: (a) Smooth outside of the component (b) Coarse inside

component tend to be trapped if the component is placed as shown in Figure 6.34a. Near the centre of the dome underside is a stagnant gas flow area and the velocity near the circumference of the upper side is also very slow. These two types of gas flows on the same component can lead to poor and uneven deposition on the surface of the component. When the component is arranged upside down as shown in Figure 6.34b, there is a more consistent gas velocity near the underside of the component. On the upper side, there are severe recirculations. These contrasting flows on both sides of the component result in clearly different qualities of deposition. As the underside of the component experiences more consistent precursor gas flow, the deposition quality is much better than that at the top side of the component.

Figure 6.35 shows the deposition quality on both sides of a domed component when it is placed in Figure 6.34b for deposition. The component is a fibre preform prepared by the 3-D braiding method. The outside of the component is smooth whereas the inside is very coarse.

It is clear that it is impossible to solve the poor deposition quality problem by simply arranging the orientation of the complex shaped components. Based on the above simulation results and applying the principle of minimising the residence time inside the reaction chamber, techniques on the process design and associated tools have been developed to solve the above problems. Central to these techniques is the introduction of a gas flow guidance tool according to the geometric shape of the complex components. These guidance tools are designed to force and optimise the gas flow consistently around the component to be deposited. Such a design of a gas flow guidance tool for the domed component is as shown in Figure 6.36. The reactant precursor gases can only flow following the directions indicated by the arrows as no other flow path is allowed.

Once again, a CFD-based simulation tool can be used to evaluate the effect of such a design. Figure 6.37 shows the simulation results and effects of three such gas flow guidance tools, where the distance between the component deposition surface and the guidance tool inner surface is about 30 mm and the opening angle of the guidance tool varies from 30° , 60° and 90° . The precursor gases are introduced into the centre of the domed part of the component where they are

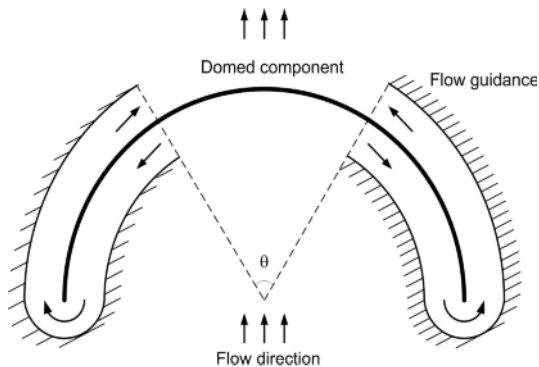


Figure 6.36. Schematic diagram of a domed component with flow guidance tool

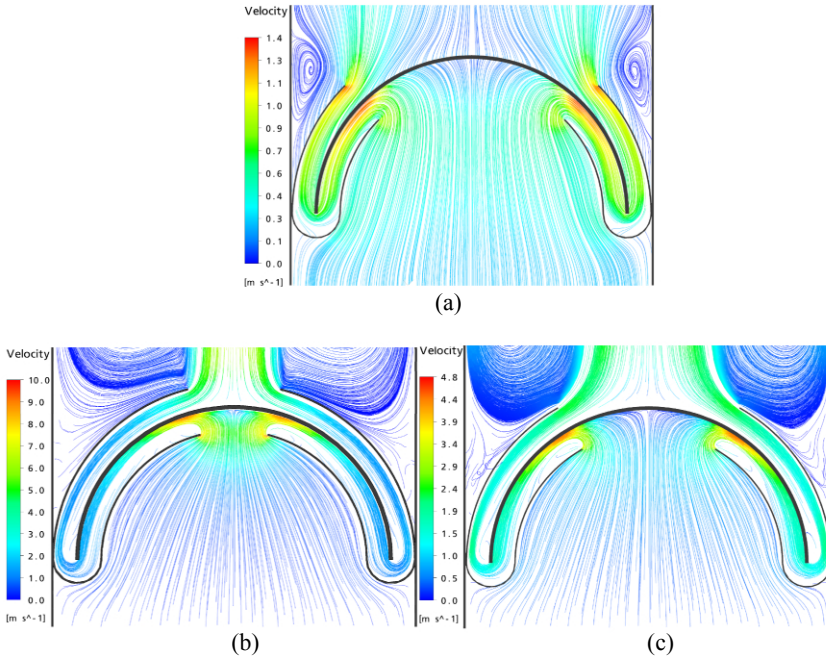


Figure 6.37. Velocity profile of stream lines by complex guidance tool with a distance of 30 mm between the component and the tool: (a) $\theta = 90^\circ$, (b) $\theta = 60^\circ$ and (c) $\theta = 30^\circ$

forced to flow downwards inside the channel between the component and the flow guidance. Then, the gases change direction after they reach the bottom edge of the component, thereafter upwards along the component surface.

By introducing such a flow guidance tool, it is clear from the simulation results that there is neither a stagnant gas flow area nor recirculations in any part of the component surface. This effectively solves the problems encountered in the arrangements shown in Figure 6.34a and b. Therefore, uniform deposition on both sides of the component can be ensured and the deposition quality can be significantly improved.

Figure 6.37 shows the comparative evaluation and some simulation results of three scenarios when the θ angle as defined in Figure 6.36 is 90° (a), 60° (b) and 30° (c). When θ is 90° , the component experiences much slower average gas velocity ranging from 0 to 1.4 m s^{-1} . When θ is decreased to 60° , the average velocity is increased, as does the velocity range across the component surface. When θ is further reduced to 30° , the velocity over the whole component surface increases significantly to a range of 1.5 to 8 m s^{-1} . The stagnant flow area has also been reduced compared with the other two scenarios. These results clearly show the difference in velocity and its profile without the need for experiments. The actual effects of the gas guidance tool on the deposition quality require further experimental confirmation.

References

- [1] Vignoles G, Goyheneche J, Sebastian P, Puiggali JR, Lines JF, Lachaud J, Delhaesc P, Trinquecostec M (2006) The film-boiling densification process for C/C composite fabrication: from local scale to overall optimization. *Chem Eng Sci* 61:5636–5653
- [2] Spear KE, Dirks RR (1990) Predicting the chemistry in CVD system. In: Besmann T M, Gallois B M (eds) *Chemical vapour deposition of refractory metals and ceramics*. Materials Research Society, Pittsburgh, PA, pp19–30
- [3] Kaiser N (2002) Review of the fundamentals of thin-film growth. *Appl Opt* 41:3053–3060
- [4] Petrov I, Barna PB, Hultman L, Greene JE (2003) Microstructural evolution during film growth. *J Vac Sci Tech A* 21:S117–S128
- [5] Winand R (1994) Electrodeposition of metals and alloys—new results and perspectives. *Electrochim Acta* 39:1091–1105
- [6] Landolt D (2002) Electrodeposition science and technology in the last quarter of the twentieth century. *J Electrochem Soc* 149:S9–S20
- [7] Bauer E (1958) Phänomenologische theorie der kristallabcheidung an obernflächen, I-II. *Z Kristallogr* 110:372–394
- [8] Bloem J (1980) Review: nucleation and growth of silicon by CVD. *J Cryst Growth* 50:581–604
- [9] Movchan BA, Demchishin AV (1969) Investigations of the structure and properties of thick Ni, Ti, W, Al₂O₃ and ZrO₂ vacuum condensates. *Phys Met Metallogr (USSR)* 28:83–90
- [10] Thornton JA (1977) High rate thick film growth. *Annu Rev Mater Sci* 7:239–260
- [11] Thornton JA (1974) Influence of apparatus geometry and deposition conditions on the structure and topography of thick sputtered coatings. *J Vac Sci Technol* 11:666–669
- [12] Hwang NM, Yoon DY (1994) Driving force for deposition in the chemical vapour deposition process. *J Mater Sci Lett* 13:1437–1439
- [13] Lespoux D, Langlais F, Naslain R (1995) Correlations between gas phase supersaturation, nucleation process and physico-chemical characteristics of silicon carbide deposited from Si-C-H-Cl system on silica substrate. *J Mater Sci* 30:1500–1510
- [14] Bryant WA (1977) Review: the fundamentals of chemical vapour deposition. *J Mater Sci* 12:1285–1306
- [15] Blocher JM (1974) Structure/property/process relationships in chemical vapour deposition CVD. *J Vac Sci Technol* 11:680–686
- [16] Nakashima S, Matsunami H (eds) (1995) *Silicon carbide and related materials*. Institute of Physics, Bristol, UK
- [17] Wagner RS, Ellis WC (1964) Vapor-liquid-solid mechanism of single crystal growth. *Appl Phys Lett* 4:89–90
- [18] Pan ZW, Xie SS, Chang BH *et al.* (1999) Direct growth of aligned open carbon nanotubes by chemical vapour deposition. *Chem Phys Lett* 299:97–102
- [19] Motojima S, Ueno S, Hattori T, Goto K (1989) Growth of regularly coiled spring-like fibers of Si₃N₄ by iron impurity-activated chemical vapor deposition. *Appl Phys Lett* 54:1001–1003
- [20] Callister W d Jr (2007) *Materials science and engineering: an introduction*, 7th edn. Wiley, New York
- [21] Spencer MG ed, (1994) *Silicon carbide and related materials*. Institute of Physics, Bristol, UK
- [22] Nakashima S, Matsunami H (eds) (1995) *Silicon carbide and related materials*. Institute of Physics, Bristol, UK

- [23] Vahlas C, Caussat BG, Serp P (2006) Principles and applications of CVD powder technology. *Mater Sci Eng R53*:1–72
- [24] Xu YD, Cheng LF, Zhang LT, Zhou WC (1999) Morphology and growth mechanism of silicon carbide chemical vapor deposited at low temperature and normal atmosphere. *J Mater Sci* 34:551–55
- [25] Niihara K, Hirai T (1976) Chemical vapour-deposited silicon nitride: Part 1: Preparation and some properties. *J Mater Sci* 11:593–603
- [26] Nicolis G, Prigogine I (1977) Self-organization in non-equilibrium systems. Wiley, New York
- [27] Messier R, Yehoda J E (1985) Geometry of thin-film morphology. *J Appl Phys* 58:3739–3746
- [28] Coffin LF (1964) Structure-property relations for pyrolytic graphite. *J Am Ceram Soc* 47:473–478
- [29] Komiyama H, Shimogaki Y, Egashira Y (1999) Chemical reaction engineering in the design of CVD reactors. *Chem Eng Sci* 54:1941–1957
- [30] Saito T, Shimogaki Y, Egashira Y *et al.* (1992) Conformal deposition of WSi_x films on micron-sized trenches: the reactivity of film precursors. *Appl Phys Lett* 61:764–765
- [31] Saito T, Oshima K, Shimogaki Y, Egashira Y, Komiyama H (1993) A kinetic study of CVD- WSi_x processes—the comparison of WF_6/SiH_4 and WF_6/Si_2H_6 processes. In: Jensen K N, Cullen G W (eds) Proceedings of the 12th international conference on chemical vapour deposition. Honolulu, HI, Electrochemical Society. Pennington, NJ, pp238–243
- [32] Saito T, Shimogaki Y, Oshima K, Egashira Y, Sugawara K, Takahiro K, Nagata S, Yamaguchi S, Komiyama H (1994) Gas phase chemistry determining silicon contents in CVD WSi_x process. Materials Research Society Conference Proceedings 9. Advanced Metallization for ULSI Applications in 1994, pp475–479
- [33] Hong LS, Komiyama H (1991) Chemical vapor deposition of CuO_x films by CuI and O_2 : role of cluster formation on film morphology. *J Am Ceram Soc* 74:1597–1604
- [34] Huttinger KJ (1998) CVD in hot wall reactions—the interaction between homogeneous gas-phase and heterogeneous surface reactions. *Chemical Vapor Deposition* 4:151–158
- [35] Huttinger KJ (2003) Fundamentals of chemical vapour deposition in hot wall reactors. In: P Delhaes (ed) *Fibres and Composites*. Taylor & Francis, London, pp75–86
- [36] Benzinger W, Becker A, Huttinger KJ (1996) Chemistry and kinetics of chemical vapour deposition of pyrocarbon: I. Fundamentals of kinetics and chemical reaction engineering. *Carbon* 34: 957–966
- [37] Feron O, Langlais F, Naslain R, Thebault J (1999) On kinetic and microstructural transitions in the CVD of pyrocarbon from propane. *Carbon* 37: 1343–1353
- [38] Hu ZJ, Zhang WG, Huttinger KJ, Reznik B, Gerthsen D (2003) Influence of pressure, temperature and surface area/volume ratio on the texture of pyrolytic carbon deposited from methane. *Carbon* 41:749–758
- [39] Thomas J M, Thomas W J (1997) Principles and practice of heterogeneous catalysis. VCH, Weinheim
- [40] Adamson AW, Gast AP (1997) Physical chemistry of surfaces. Wiley, New York
- [41] Lieberman ML, Pierson HO (1974) Effect of gas phase conditions on resultant matrix pyrocarbons in carbon/carbon composites. *Carbon* 23:233–241
- [42] Delhaes P (2002) Chemical vapour deposition and infiltration processes of carbon materials. *Carbon* 40:641–657

- [43] Watanabe K, Komiyama H (1990) Micro/macrocavity method applied to the study of the step coverage formation mechanism of SiO₂ films by LPCVD. *J Electrochem Soc* 137:1222–1227
- [44] Dutta S, Rice RW, Graham HC, Mendiratta MC (1980) Characterization and properties of controlled nucleation thermochemical deposition (CNTD)-silicon carbide. *J Mater Sci* 15:2183–2191
- [45] Holz RA (1980) Deposition method and products. US Patent 4,239,819
- [46] Bryant WA (1976) Producing extended area deposits of uniform thickness by a new chemical vapour deposition technique. *J Cryst Growth* 35:257–261
- [47] Delhaes P (2002) Review: chemical vapor deposition and infiltration processes of carbon materials. *Carbon* 40:641–657
- [48] Douglas JF, Gasiorek JM, Swasfield JA, Jack LB (2005) *Fluid mechanics*, 5th edn. Pearson, London
- [49] Munson BR, Young DF, Okiishi TH (2006) *Fundamentals of fluid mechanics*, 5th edn. Wiley, New York
- [50] Mironer A (1979) *Engineering fluid mechanics*. McGraw–Hill, New York, pp287–288
- [51] Ferziger JH, Peric M (2002) *Computational methods for fluid dynamics*, 3rd edn. Springer, Berlin Heidelberg New York
- [52] Anderson JD Jr (1995) *Computational fluid dynamics: the basics with applications*. McGraw–Hill, New York
- [53] Bird RB, Stewart WE, Lightfoot EN (1960) *Transport phenomena*. Wiley, New York
- [54] Incropera FP, Dewitt DP, Bergman TL, Lavine AS (2007) *Fundamentals of heat and mass transfer*, 6th edn. Wiley, New York
- [55] Thomson WJ (2000) *Introduction to transport phenomena*. Prentice Hall, Engelwood Cliffs, NJ
- [56] Berger M, Oliger J (1984) Adaptive mesh refinement for hyperbolic partial differential equations. *J Comput Phys* 53:484–512
- [57] Gunther M, Kværno A, Rentrop P (2001) Multirate partitioned Runge–Kutta methods. *BIT* 41:504–514
- [58] Jensen KF (1993) Fundamentals of chemical vapour deposition. In: Hitcham ML, Jensen KF (eds) *Chemical vapour deposition: principles and applications*. Academic, San Diego, CA, pp31–90
- [59] Fotiadis DI, Kieda S (1990) Transport phenomena in vertical reactors for metalorganic vapour phase epitaxy. *J Cryst Growth* 102:411–470
- [60] Fletcher R (1976) Conjugate gradient methods for indefinite systems. *Lecture Notes in Mathematics*, vol 506. Springer, Berlin Heidelberg New York
- [61] Golub GH, Van Loan C (1990) *Matrix computations*. Johns Hopkins University Press, Baltimore, MD

Appendix A Conversion Factors for Pressure Units

As pressure is an important parameter in any CVD system, it is useful to know the pressure conversion from one representation system to another. This appendix lists commonly used conversions of a pressure represented in different unit systems, e.g ISO unit, imperial units and so forth.

Table A.1. Pressure conversion factors table 1

	Pascal (Pa)	Torr (mmHg)	Microns of mercury (μHg)	Dyne per Square cm (μbar)
1 Pa (1N/m ²)	1	7.50062×10^{-3}	7.50062	10
1 μHg	0.133322	10^{-3}	1	1.33322
1 Torr (1mmHg)	133.322	1	10^3	1333.22
1 dyn/cm ² (1 μbar)	10^{-1}	7.50062×10^{-4}	7.50062×10^{-1}	1
1 mbar	10^2	7.50062×10^{-1}	7.50062×10^2	10^3
1 bar	10^5	750	7.50062×10^5	10^6
1 atm	101325	760	760×10^3	1013.25×10^3
1 lb/in ² (psi)	6895	51.715	51.715×10^3	6.895×10^4

Table A.2. Pressure conversion factors table 2

	Pascal (Pa)	Millibar (mbar)	Standard atmosphere (atm)	lb/in² (psi)
1 Pa (1N/m ²)	1	10^{-2}	9.86923×10^{-6}	1.450×10^{-4}

Table A.2 (continued)

1 μHg	0.133322	1.33322×10^{-3}	1.31579×10^{-6}	1.934×10^{-5}
1 Torr (1 mmHg)	133.322	1.33322	1.31579×10^{-3}	1.934×10^{-2}
1 dyn/cm^2 (1 μbar)	10^{-1}	10^{-3}	9.86923×10^{-7}	1.450×10^{-5}
1 mbar	10^2	1	9.86923×10^{-4}	1.450×10^{-2}
1 bar	10^5	10^3	9.86923×10^{-1}	14.5
1 atm	101325	1013.25	1	14.696
1 lb/in^2 (psi)	6895	68.95	6.805×10^{-2}	1

Appendix B Vapour Pressure of Precursors

The following table provides useful information on the pressures of commonly used precursor gases. They can be used as a guideline to CVD process design and deposition tank system design.

Table B.1. Vapour pressure constants for some precursors

Precursor	A	B	Temperature	Pressure	Ref
Al(CH ₃) ₃	7.3147	1534.1	17–100°C	lgP(Torr)=A–B/(T–53)	[1]
Al(C ₂ H ₅) ₃	10.784	3625	110–140°C	Torr	[1]
Al ₂ (CH ₃) ₆	10.48	2780		Torr	[2]
AsH ₃	7.56	978.2		Torr	[2]
As(CH ₃) ₃	7.7119	1563		Torr	[1]
As(C ₂ H ₅) ₃	8.15	2138		Torr	[2]
H ₂ AsC(CH ₃) ₃	7.24	1509		Torr	[2]
[Me ₂ Au(OAc)] ₂	14.2	5280	18–59°C	Torr	[3]
[Me ₂ Au(piv)] ₂	15.3	5700	22–50°C	Torr	[3]
Ba ₃ (thd) ₆	21.22	10900		Torr	[4]
Bi(CH ₃) ₃	7.628	1816		Torr	[1]
BiPh ₃	10.5	5090	373–393 K	Pa	[5]
Ca(thd) ₂	16.2	8500	453–483 K	Pa	[5]
Cd(CH ₃) ₂	7.764	1850		Torr	[1]
Cu(thd) ₂	11.5	6010	398–413 K	Pa	[5]
Ga(CH ₃) ₃	8.07	1703		Torr	[1]
Ga(C ₂ H ₅) ₃	8.224	2222	50–80°C	Torr	[1]

Table B.1 (continued)

$\text{Ga}(\text{CH}_3)_3 \cdot \text{As}(\text{CH}_3)_3$	9.114	2458		Torr	[1]
HfCl_4	11.663	5170	476–681 K	Torr	[6]
$3\text{HfCl}_4 \cdot 2\text{POCl}_3$	7.134	4480		Atm	[7]
$\text{Hg}(\text{CH}_3)_2$	7.575	1750	20.5–78.7°C	Torr	[1]
$\text{In}(\text{CH}_3)_3$	10.52	3014		Torr	[1]
$\text{In}(\text{C}_2\text{H}_5)_3$	8.94	2815		Torr	[2]
$\text{In}(\text{CH}_3)_3 \cdot \text{P}(\text{CH}_3)_3$	6.9534	1573		Torr	[1]
$\text{Ir}(\text{acac})_3$	25.88	15391	110–200°C	atm	[8]
$\text{Ir}(\text{acac})(\text{cod})$	13.19	5840	335–370 K	Torr	[9]
$\text{Ir}(\text{MeCp})(\text{cod})$	17.43	6510	293–309 K	Torr	[9]
$\text{Ir}(\text{MeCp})(\text{cod})$	11.31	4600	311–329 K	Torr	[9]
$\text{Mg}(\text{C}_5\text{H}_5)_2$	$\lg P(\text{Torr}) = 25.14 - 2.18 \ln T - 4198/T$				[1]
PH_3	7.24	809.4		Torr	[2]
$\text{P}(\text{CH}_3)_3$	7.7329	1512		Torr	[1]
$\text{P}(\text{C}_2\text{H}_5)_3$	7.86	2000	18–78.2°C	Torr	[1]
$\text{H}_2\text{PC}(\text{CH}_3)_3$	7.59	1539		Torr	[2]
$\text{Pd}(\text{acac})_2$	22.05	13425	74–180°C	atm	[8]
$\text{Pt}(\text{acac})_2$	20.19	12737	59–180°C	atm	[8]
$\text{Pt}(\text{hfa})_2$	21.974	10496		mbar	[10]
$\text{Rh}(\text{acac})_3$	22.97	14290	75–210°C	atm	[8]
$\text{Rh}(\text{allyl})_3$	10.41	3069	34–42°C	Torr	[11]
$\text{Rh}_2\text{Cl}_2(\text{CO})_4$	9.42	3026	50–53°C	Torr	[11]
$\text{Rh}(\text{CO})_2(\text{acac})$	12.07	4425	58–65°C	Torr	[11]

Table B.1 (continued)

$\text{Sb}(\text{CH}_3)_3$	7.728	1709		Torr	[1]
$\text{Se}(\text{C}_2\text{H}_5)_2$	7.91	1924		Torr	[2]
$\text{Si}(\text{OC}_2\text{H}_5)_4$	10.5348	2429.55	323–441 K	Pa	[12]
CH_3SiCl_3	7.505	1570		Torr	[13]
$\text{Sn}(\text{CH}_3)_4$	7.495	1620	18–78.9°C	Torr	[1]
$\text{Sn}(\text{CH}_3)_2\text{Cl}_2$	8.938	2795		Torr	[14]
$\text{Sr}(\text{thd})_2$	16.3	9100	493–513 K	Pa	[5]
$\text{Te}(\text{CH}_3)_2$	7.97	1865		Torr	[1]
$\text{Te}(\text{C}_2\text{H}_5)_2$	7.99	2093		Torr	[1]
$(\text{C}_5\text{H}_5)_2\text{TiCl}_2$	13.22	6500		Torr	[15]
$\text{Zn}(\text{CH}_3)_2$	7.802	1560		Torr	[1]
$\text{Zn}(\text{C}_2\text{H}_5)_2$	8.28	2190		Torr	[1]
$\text{Zr}(\text{thd})_4$	7.659	3687		Torr	[16]
ZrCl_4	11.741	5390	480–689 K	Torr	[6]
$3\text{ZrCl}_4 \cdot 2\text{POCl}_3$	7.078	4480		Atm	[7]
ZrI_4	12.05	6455		Torr	[6]

Note:

Vapour pressure is calculated with Equation (2.70) expressed by

$$\ln P = A - \frac{B}{T}$$

where A and B are two constants as listed in Table B.1.

Table B.2. Relationship between temperature and vapour pressure of Si-containing precursors [17]

This is the first part of a table showing the relationship between the temperature and vapour pressure of Si-containing precursors at a pressure of 1, 5, 10, 20 and 40 Torr. The second table Table B.3 on the next page shows the same relationship at a pressure of 60, 100, 200, 400 and 700 Torr.

Precursor	P_{vap} (Torr)				
	1	5	10	20	40
	$T(^{\circ}\text{C})$				
HSiCl₃	-80.7	-62.6	-53.4	-43.8	-32.9
SiCl₄	-63.5	-44.1	-34.4	-24.0	-12.1
CH₃SiH₂Cl	-95.0	-79.2	-71.0	-62.0	-53.7
CH₃SiHCl₂	-75.0	-56.9	-47.8	-37.7	-26.2
CH₃SiCl₃	-60.8	-40.7	-30.7	-19.3	-7.0
(CH₃)₂SiCl₂	-53.5	-33.8	-23.8	-12.7	-0.4
(CH₃)₃SiCl	-62.8	-43.6	-34.0	-23.2	-11.4
(CH₃)₄Si	-83.8	-66.7	-58.0	-48.3	-37.4
C₂H₅SiCl₃	-	-	-1.6	9.7	22.3
(C₂H₅)₂SiCl₂	-	-	21.0	33.7	47.9
(C₂H₅)₃SiCl	-	-	32.0	45.5	60.2
CH₃C₆H₅SiCl₂	35.7	63.5	77.4	92.4	109.5
C₆H₅SiCl₃	33.0	60.4	75.3	89.8	105.9
(C₆H₅)₂SiCl₂	109.6	142.4	158.4	175.2	194.0
(C₆H₅)₃SiCl	-	-	210.0	-	-

Table B.3. Relationship between temperature and vapour pressure of Si-containing precursors [17]

Precursor	$P_{\text{vap}}(\text{Torr})$				
$T(^{\circ}\text{C})$	60	100	200	400	760
HSiCl₃	-25.8	-16.4	-1.8	14.5	31.8
SiCl₄	-4.8	5.4	21.0	38.4	56.8
CH₃SiH₂Cl	-45.2	-36.4	-22.9	-7.8	8.7
CH₃SiHCl₂	-18.9	-9.0	6.2	23.7	41.9
CH₃SiCl₃	1.0	12.1	28.1	47.0	66.4
(CH₃)₂SiCl₂	7.4	17.5	33.9	51.9	70.3
(CH₃)₃SiCl	-4.0	6.0	21.9	39.4	57.9
(CH₃)₄Si	-30.0	-20.9	-6.5	10.0	27.0
C₂H₅SiCl₃	30.6	41.5	58.4	77.9	98.8
(C₂H₅)₂SiCl₂	56.9	69.1	87.5	108.4	130.4
(C₂H₅)₃SiCl	69.5	82.3	101.6	126.6	146.3
CH₃C₆H₅SiCl₂	120.0	134.2	155.5	180.2	205.5
C₆H₅SiCl₃	116.3	130.3	151.5	175.5	201.0
(C₆H₅)₂SiCl₂	205.9	222.2	246.8	274.8	304.4
(C₆H₅)₃SiCl	-	-	-	-	378.0

Appendix C Chemical Vapour Deposition Materials and Their Corresponding Precursors

This appendix provides useful guidelines on the materials to be deposited and the precursor gases that should be used. As much as possible, the deposit–precursor gas pairs have been identified and compiled. A comprehensive list of these pairs are provided here for reference purposes. It is intended to be a guideline, and detailed research and investigations on both deposition processes and deposits are required to generate desirable deposit.

Table C.1. Metallic and non-metallic element deposit–precursor pairs used in CVD processes

Deposit	Precursor	Note
Ag	AgF-Si, Ag-SiO ₂ , Ag(piv)	piv: (CH ₃) ₃ CCOO
	[(n-Bu ₃ P)Ag(piv)] ₂	Bu: C ₄ H ₉
Al	AlH(CH ₃) ₂ , Al(CH ₃) ₃ , Al(C ₂ H ₅) ₃	Me: CH ₃ , Et: C ₂ H ₅
	(C ₄ H ₉) ₃ Al, AlI ₃ , Al(acac) ₃	acac: C ₅ H ₇ O ₂
As	AsH ₃ , AsCl ₃ -H ₂	
Au	AuCl(PF ₃)-N ₂ -H ₂ , (CH ₃) ₃ PAuCH ₃	Me: CH ₃
	AuCl ₃ , MeAu(acac)	
B	BCl ₃ -H ₂ , BBr ₃ -H ₂ , B ₂ H ₆ , BMe ₃	
Be	Be(C ₄ H ₉) ₂ , BeI ₂ -H ₂	
Bi	BiCl ₃ -H ₂ , BiH ₃ -H ₂ , Bi(Me) ₃ -C ₆ H ₅ Me	
C	CH ₄ , C ₃ H ₈ , CH ₄ -C ₃ H ₈	Alkane
	C ₃ H ₆	Alkene
	C ₂ H ₂	Alkyne
	C ₅ H ₁₀ , C ₆ H ₁₂	
	C ₆ H ₆ , C ₆ H ₅ CH ₃ , C ₆ H ₅ Cl	Benzene and derivatives
Cd	Cd(CH ₃) ₂ , Cd(acac) ₂	
Ce	Ce(acac) ₃	
Co	Co(CO) ₃ NO, Co ₂ (CO) ₈ , CoCp ₂	Cp: C ₅ H ₅
	Co(acac) ₃ , CoI ₂ , CoCl ₃ -H ₂	

Table C.1. (continued)

Cr	CrI ₂ , CrCl ₂ -H ₂ , CrO ₂ Cl ₂ -H ₂	
	Cr(C ₆ H ₆) ₂ , Cr(CO) ₆ -H ₂	
Cr-Al	CrCl ₃ -AlCl ₃ -H ₂	
Cr-Fe	CrCl ₃ -Fe-H ₂	Fe as substrate
Cu	CuCl ₂ -H ₂ , Cu(OC ₄ H ₉) ₄	
	Cu(acac) ₂ , Cu(dpm) ₂ -H ₂	dpm: C ₁₁ H ₁₉ O ₂
	Cu(etob) ₂	etob: C ₈ H ₁₃ O ₂
	Cu(hfac) ₂ -H ₂	hfa/hfac: C ₅ F ₆ HO ₂
	Cu(hfac)(cod)	cod: C ₈ H ₁₂
	Cu(hfac)(dmb)	dmb: C ₆ H ₁₂
	Cu(hfa)VTMS	VTMS: SiC ₅ H ₁₂
	Cu(pta) ₂ -H ₂	pta: C ₈ F ₃ H ₁₀ O ₂
	Cu(pva) ₂ -H ₂	pva: C ₈ H ₁₃ O ₂
	Cu(tfa) ₂ -H ₂	tfa/tfac: C ₅ H ₄ F ₃ O ₂
Fe	Fe(CO) ₅ , FeCl ₃ -H ₂ , FeI ₂	
Fe-Ni	Fe(CO) ₅ -Ni(CO) ₄	
Ge	GeH ₄ , GeI ₂ , GeMe ₂	
P doped Ge	GeH ₄ -PH ₃ -He	
Hf	HfCl ₄ -H ₂ , HfBr ₃ -H ₂ , HfI ₄	
In	InCp	
Ir	Ir(allyl)I ₃ , Ir(acac) ₃ , Ir(acac)(cod)	allyl: C ₃ H ₅
	Ir(MeCp)(cod)	Cp: C ₅ H ₅
Mg	MgCp ₂	
Mo	MoF ₅ -H ₂ , MoCl ₆ -H ₂ , Mo(CO) ₆ -H ₂	
	MoO ₂ Cl ₂ -H ₂ , Mo(C ₆ H ₆) ₂	
Mn	Mn(CO) ₆	
Nb	NbF ₅ -H ₂ , NbCl ₅ -H ₂ , NbBr ₅ -H ₂ , NbI ₅	
	NbBr ₅ -H ₂ , NbI ₅ -H ₂	
Nb-Ge	NbCl ₅ -GeCl ₄ -H ₂	
Ni	Ni(C ₂ H ₅) ₂ -H ₂ , Ni(CO) ₄ -H ₂	
	Ni(acac) ₂ -H ₂ , Ni(tfa) ₂ -H ₂	
	Ni(thd) ₂ -H ₂	
	Ni(MeCp) ₂ -H ₂ , Ni(Cp) ₂ -H ₂	

Table C.1 (continued)

Os	OsCl ₄ -H ₂ , OsO ₄ , Os(CO) ₃ Cl ₂	
Pb	PbEt ₂	
Pd	PdCl ₂ -H ₂ , Pd(acac) ₂ , Pd(hfa) ₂	
Pt	Pt(CO) ₂ Cl ₂ , Pt(acac) ₃ , Pt(hfa) ₂	
	(CH ₃ NC) ₂ Pt(CH ₃) ₂ , Pt(PF ₃) ₄	
	Pt(C ₅ H ₅)(CH ₃) ₃	
Pu	PuCp ₂	
Re	Re ₂ (CO) ₁₀	
	ReF ₆ -H ₂ , ReCl ₅ -H ₂ , ReOCl ₄ -H ₂	
Rh	Rh ₄ (CO) ₁₂ , Rh(CO) ₂ (acac)	
	Rh(allyl) ₃ , Rh(acac) ₃ , Rh(tfa) ₃	
	RhCl(PF ₃) ₂ -N ₂ -H ₂	
Ru	Ru(C ₅ H ₅) ₂ -H ₂ , Ru ₃ (CO) ₁₂	
	Ru(EtCp) ₂ -N ₂	
	Ru(acac) ₃ , Ru(thd) ₂ (cod)	thd: C ₁₁ H ₁₉ O ₂
Sb	SbCl ₃ -H ₂ , SbH ₃ -H ₂	
Si	SiH ₄ -H ₂ , Si ₂ H ₆	
	SiCl ₄ -H ₂ , SiHCl ₃ -H ₂ , SiH ₂ Cl ₂	
a:Si:H	SiH ₄ -H ₂ (assisted by plasma)	Hydrogenated amorphous Si
B-doped Si	SiH ₄ -BCl ₃ -H ₂	
Si-Ge	SiH ₄ -GeH ₄ -H ₂	
Sn	Sn(CH ₃) ₄ , Sn ₂ (C ₂ H ₅) ₆ , SnCl ₄ -H ₂	
Ta	TaCl ₅ -H ₂ , TaI ₄	
Ta-Nb	TaCl ₅ -NbCl ₅	
Ti	TiCl ₄ -Mg, TiBr ₄ -H ₂ , TiI ₄	
Ti-Ta	TiCl ₄ -TaCl ₅ -H ₂	
Ti-Fe	TiCl ₄ -Fe-H ₂	Fe as substrate
Th	ThI ₄	
U	UI ₄	
V	VF ₆ -H ₂ , VCl ₄ -H ₂ , VI ₂	
W	W(CO) ₆ -H ₂ , WCl ₆ -H ₂ , W(PF ₃) ₆	
	WF ₆ -H ₂ , WF ₆ -Si, WF ₆ -SiH ₄	
	WH ₂ (iPrCp) ₂ -H ₂ , WH ₂ (EtCp) ₂ -H ₂	i-Pr: C ₃ H ₇

Table C.1 (continued)

W-Mo	WCl ₆ -MoCl ₅ -H ₂ , WF ₆ -MoF ₆ -H ₂	
W-Mo-Re	WF ₆ -MoCl ₆ -ReF ₆ -H ₂	
	WCl ₆ -MoCl ₅ -ReCl ₅ -H ₂	
W-Re	WF ₆ -ReF ₆ -H ₂	
W-Th	WF ₆ -Th(fod) ₄	fod: C ₁₀ H ₁₀ F ₇ O ₂
Zn	ZnMe ₂ , ZnEt ₂	
Zr	ZrI ₄ , ZrCl ₄ +Mg	
Y-Al-Ni	AlCl ₃ -YCl ₃ -Ni-H ₂	Ni as substrate

Table C.2. Boride

Fe ₂ B	Fe-BBr ₃	Fe as substrate
HfB ₂	HfCl _x -BCl ₃ -H ₂	
LaB ₆	LaCl ₃ -B ₂ H ₆ , LaCl ₃ -B ₅ H ₉	
	LaCl ₃ -B ₁₀ H ₁₄	
MoB	MoCl ₅ -BCl ₃	
NbB ₂	NbCl ₅ -B ₂ H ₆ , NbCl ₅ -B ₅ H ₉	
	NbCl ₅ -B ₁₀ H ₁₄ , NbBr ₅ -BBr ₃	
	NbCl ₅ -BCl ₃ -H ₂ , NbCl ₅ -BBr ₃ -H ₂	
Si _x B _y	SiCl ₄ -B ₂ H ₆ -H ₂ , SiCl ₄ -BCl ₃ -H ₂	SiB ₄ , SiB ₆
TaB ₂	TaBr ₅ -BBr ₃	
	TaCl ₅ -B ₂ H ₆ , TaCl ₅ -B ₅ H ₉	
	TaCl ₅ -B ₁₀ H ₁₄	
TiB ₂	TiCl ₄ -BCl ₃ , TiCl ₄ -B ₂ H ₆	
	TiCl ₄ -BBr ₃ -H ₂	
	TiCl ₄ -B ₅ H ₉ , TiCl ₄ -B ₁₀ H ₁₄	
	TaCl ₅ -BBr ₃ -H ₂ , TaCl ₅ -BCl ₃ -H ₂	
WB	WCl ₆ -BCl ₃ -H ₂	
ZrB ₂	ZrCl ₄ -BCl ₃ -H ₂	
	ZrCl ₄ -B ₂ H ₆ , ZrCl ₄ -B ₅ H ₉ , ZrCl ₄ -B ₁₀ H ₁₄	

Table C.3. Carbide

B ₄ C	BCl ₃ -CH ₄	
Cr ₇ C ₃	Cr(C ₆ H ₅)(C ₃ H ₇) ₂ -Ar	
Cr ₃ C ₂	Cr(CO) ₆ -CH ₄ -H ₂	
Cr _x C _y	Cr(C ₆ H ₆) ₂ -H ₂	Cr ₃ C ₂ , Cr ₇ C ₃
	bis-ethyl-benzene-chromium	Cr ₃ C ₂ , Cr ₇ C ₃
Cr ₂ (N,C) ₂	Cr(C ₆ H ₆) ₂ -NH ₃ , Cr(C ₆ H ₆) ₂ -N ₂ H ₂	
Fe _x C _y	Fe(CO) ₅ -C ₂ H ₂ , Fe(CO) ₅ -C ₂ H ₄	Fe ₃ C, Fe ₇ C ₃
HfC	HfCl ₄ -CH ₄ -H ₂ , HfCl ₄ -CH ₃ Cl-H ₂	
Mo _x C _y	MoCl ₅ -CH ₂ I ₂ -H ₂	Mo ₂ C, δ-MoC _{1-x}
NbC	NbCl ₅ -CCl ₄ -H ₂	
SiC	SiH ₂ Cl ₂ -C ₄ H ₁₀ -H ₂ , CH ₃ SiCl ₃ -H ₂	
	H ₄ Si ₂ (Me) ₂ , (Me) ₂ SiCl ₂ -H ₂ , Si ₂ (Me) ₆	
	SiCl ₄ -C ₆ H ₁₄ -H ₂	SiC epitaxial growth
a:Si _{1-x} C _x -H	SiHCl ₃ -C ₃ H ₈ -H ₂ , SiH ₄ -CH ₄ -H ₂	Hydrogenated amorphous SiC assisted by plasma
	SiH ₄ -C ₂ H ₂ -H ₂ , SiH ₄ -C ₃ H ₈ -H ₂	
TaC	TaCl ₅ -CH ₄ -H ₂ , TaCl ₄ -CH ₃ Cl-H ₂	
	Ta-CH ₄	Ta as a substrate
TiC	TiCl ₄ -CH ₄ , TiCl ₄ -C ₂ H ₂ -H ₂	
	Ti[CH ₂ (CH ₃) ₃] ₄ , Cp ₂ TiCl ₂	
VC	VCl ₂ -CH ₄ -H ₂ , V(C ₅ H ₅) ₂	
WC	WF ₆ -CH ₄ -H ₂	
	WCl ₆ -C ₃ H ₆ -H ₂ , WCl ₆ -C ₃ H ₈ -H ₂	
ZrC	ZrCl ₄ -CH ₄ -Ar, ZrBr ₄ -CH ₄ -Ar	

Table C.4. Nitride

AlN	AlCl ₃ -NH ₃ -H ₂ , AlBr ₃ -NH ₃ -H ₂	
	Al(CH ₃) ₃ -NH ₃ , Al ₂ (NMe ₂) ₆	
	[(CH ₃) ₂ AlN ₂] ₃ , [(C ₂ H ₅) ₂ AlN ₃] ₃	
	N ₃ Al[(CH ₂) ₃ NMe ₂] ₂	
BN	BF ₃ -NH ₃ , BCl ₃ -NH ₃ , B ₃ N ₃ H ₆ -Ar	
	B ₂ H ₆ -NH ₃ , B ₃ N ₃ Cl ₃ H ₃	
	B(C ₂ H ₅) ₃ -NH ₃	
	(CH ₃) ₂ NHBH ₃ -N ₂ -Ar	
	H ₃ B ₃ N ₃ (CH ₃) ₃ -NH ₃ -H ₂	
BN _x :H	B ₃ N ₃ H ₆ -He	Hydrogenated BN
CN _x	CCl ₄ -N ₂ -H ₂ -Ar, C ₂ H ₂ -N ₂ O-NH ₃	
	C ₃ N ₃ Cl ₃ -C ₅ H ₁₃ N ₃	
GaN	GaCl ₃ -NH ₃	
	GaMe ₃ -NH ₃ -H ₂ , GaEt ₃ -NH ₃ -H ₂	TMG: Ga(CH ₃) ₃
	Ga(Et) ₃ -	
	H ₂ NNH ₂ (N ₃)Ga[(CH ₂) ₃ NMe ₂] ₂	

Table C.4 (continued)

Ga _{1-x} In _x N	Ga(Me) ₃ -In(Me) ₃ -NH ₃	
Mg-doped GaN	Ga(CH ₃) ₃ -NH ₃ -Cp ₂ Mg-H ₂	
Hf ₄ N ₃	HfCl ₄ -N ₂ -H ₂ , HfI ₄ -NH ₃ -H ₂	
	Hf(NMe ₂) ₄ , Hf(NEt ₂) ₄ , Hf(NEtMe) ₄	
InN	N ₃ In[(CH ₂) ₃ NMe] ₂	
InGaN	In(CH ₃) ₃ -Ga(CH ₃) ₃ -NH ₃ -H ₂	
Nb _x N _y	NbF ₅ -NH ₃ , NbCl ₄ -N ₂ -H ₂ -Ar	Nb ₂ N, Nb ₄ N ₃ , NbN
	NbCl ₅ -NH ₃ , Nb(NMe ₂) ₅ -NH ₃	
	NbN(NEt ₂) ₅ -NH ₃	
ScN	Sc-HCl-NH ₃ -H ₂	
Si ₃ N ₄	CH ₃ SiCl ₃ -NH ₃ , SiCl ₄ -NH ₃ -H ₂	
	Si(CH ₃) ₄ -NH ₃ , HSiCl ₃ -NH ₃ -N ₂	
	SiH ₄ -NH ₃ , SiH ₄ -H ₂ , SiH ₂ Cl ₂ -NH ₃	
	HSiCl ₂ -NH ₃ -H ₂	
	SiH ₃ NH ₂ -NH ₃	MSA: monosilylamine
	(SiH ₃) ₂ NH-NH ₃	DSA: disilylamine
	(SiH ₃) ₃ N-NH ₃	TSA: trisilylamine
SiN _x	(Me ₂ N) ₃ SiH	TDMAS
SnN	Sn(NEt ₂) ₄ -NH ₃	
TaN	Ta(Nt-Bu)(NEt ₂) ₃ -NH ₃ -N ₂	
	Ta(NEt ₂) ₅ -NH ₃ -N ₂	
	Ta(NCMe ₃)(NetMe) ₃ -N ₂	
Ta _x N _y	TaCl ₅ -N ₂ -H ₂	Ta ₂ N, TaN, Ta ₃ N ₅
TiN	TiCl ₄ -N ₂ -H ₂ , TiCl ₄ -NH ₃ -H ₂ , TiI ₄ -NH ₃	
	Ti[NMe ₂] ₄ -NH ₃ , Ti(NMe ₂) ₄ -N ₂ -Ar	TDMAT: Ti(NMe ₂) ₄
	Ti[N(C ₂ H ₅) ₂] ₄ -NH ₃	TDEAT
VN	VCl ₄ -N ₂ -H ₂ -Ar	δ-VN, β-VN
WN _x	Cl ₄ (CH ₃ CN)WN-i-Pr,	
	Cl ₄ (CH ₃ CN)WN-t-Bu	
	W(Nt-Bu) ₂ (NMe ₂) ₂ -NH ₃ -N ₂	
YN	Y-HCl- NH ₃ -H ₂	
YbN	Yb-HCl- NH ₃ -H ₂	
ZrN	ZrCl ₄ -N ₂ -H ₂ , ZrBr ₄ -NH ₃ -H ₂	
	Zr(NMe ₂) ₄ -NH ₃	

Table C.5. Oxide

AlPO ₄	AlCl ₃ -PO(Ome) ₃	
Al ₂ O ₃	AlCl ₃ -CO ₂ -H ₂ , AlCl ₃ -H ₂ O, AlCl ₃ -O ₂	
	AlR ₃ -O ₂ , AlR ₃ -H ₂ O, AlR ₃ -N ₂ O	R: Me, Et
	Al(OC ₃ H ₇) ₃ -O ₂ -N ₂ , Al(OC ₃ H ₇)(CH ₃) ₂	

Table C.5 (continued)

Al ₂ O ₃	Al(acac) ₃ -O ₂ , Al(thd) ₃ -O ₂ -Ar	thd: C ₁₁ H ₁₉ O ₂
	Alkyl ₂ Alacac-O ₂ , Alkyl ₂ Alacac-H ₂ O	
	R ₂ Al(acac)-O ₂	R: Me, Et or Bu
Al ₂ O ₃ -La ₂ O ₃	La(thd) ₃ -Al(acac) ₃ -O ₂ -Ar	
3Al ₂ O ₃ ·2SiO ₂	AlCl ₃ -SiCl ₄ -CO ₂ -H ₂ , [Al(OsiEt ₃) ₃] ₂	Mullite: 3Al ₂ O ₃ ·2SiO ₂
	AlCl ₃ -SiCl ₄ -N ₂ O-H ₂	
Al _x Ti _y O _z	AlCl ₃ +Ti(OC ₃ H ₇) ₄	
BaTiO ₃	Ba(C ₅ tBu ₃ H ₂) ₂ -Ti(OC ₃ H ₇) ₄ -H ₂ O	
(Ba, Sr)TiO ₃	Ba(thd) ₂ -Sr(thd) ₂ -Ti(thd) ₂ (i-PrO) ₂	
B ₂ O ₃	B ₂ H ₆ -O ₂ -N ₂	
Bi _x O _y	BiI ₃ -O ₂ , Bi(acac) ₃ -O ₂	Bi ₂ O ₃ , Bi ₂ O _{2.33}
Bi ₃ FeO ₃	Bi(C ₆ H ₅) ₃ -Fe(thd) ₃	
Bi _{4-x} La _x Ti ₃ O ₁₂	Bi(Ph) ₃ -La(thd) ₃ -Ti(dmae) ₄	
Bi _{4-x} Y _x Ti ₃ O ₁₂	Bi(Ph) ₃ -Y(thd) ₃ -Ti(dmae) ₄	
CeO ₂	Ce(thd) ₄ -O ₂	
Co ₃ O ₄	Co(acac) ₂ -O ₂ , Co(thd) ₂ -O ₃	
Cr ₂ O ₃	Cr(CO) ₆ -O ₂	
	CrO ₂ Cl ₂ -H ₂ O, CrO ₂ Cl ₂ -MeOH	CrO ₂ Cl ₂ : chromyl chloride
	Cr(acac) ₃ -CO ₂ , Cr(acac) ₃ -H ₂ O	
CuO	CuI ₂ -O ₂ , Cu(CH ₃ COO) ₂ -O ₂	
CuCrO ₂	Cu(acac) ₂ -Cr(acac) ₃ -O ₂	
(Cu _{1-x} Zn _x)Fe ₂ O ₄	Cu(acac) ₂ -Zn(acac) ₂ -Fe(acac) ₃ -O ₂	
EuFeO ₃	Eu(thd) ₃ -Fe(thd) ₃	
Fe ₂ O ₃	FeCl ₃ -H ₂ O, Fe(C ₅ H ₅) ₂ -O ₂ -Ar	
	Fe(acac) ₃ , Fe(tfa) ₃ -O ₂	
Fe ₂ O ₃ -Fe ₃ O ₄	Fe(OC ₄ H ₉) ₃	
Fe ₂ O ₃ -ZrO ₂	Fe(acac) ₃ -Zr(thd) ₄ -O ₂	
Fe ₂ O ₃ -Y ₂ O ₃ -ZrO ₂	Fe(acac) ₃ -Y(acac) ₃ -Zr(thd) ₄ -O ₂	
HfO ₂	HfCl ₄ -CO ₂ , Hf(OtBu) ₄ , Hf(acac) ₄ -O ₂	
	(RCp) ₂ Hf(OR') ₂	R: Si(CH ₃) ₃ , R' : Me, Et
	Hf(NR ₂) ₄ -O ₂	R: Et, Me
Hf _x Al _y O _z	HfCl ₄ +Al(OC ₂ H ₅) ₃	
Hf _x Ti _y O _z	HfCl ₄ +Ti(OC ₃ H ₇) ₄	
In ₂ O ₃	In(acac) ₂	
La _{0.7} Ca _{0.3} MnO ₃	Ca(thd) ₂ -Mn(thd) ₃ -La(thd) ₃	
LaFeO ₃	La(thd) ₃ -Fe(thd) ₃	
La _{1-x} Pb _x MnO ₃	La(thd) ₃ -Pb(thd) ₂ -Mn(thd) ₃ -O ₂	
La _{1-x} Sr _x CoO ₃	La(thd) ₃ -Sr(thd) ₂ -Co(thd) ₂	
(LaPr) _{0.7}	La(thd) ₃ -Pr(thd) ₃ -Sr(thd) ₂	
(CaSr) _{0.3} MnO ₃	-Ca(thd) ₂ -Mn(thd) ₃	
LiNbO ₃	LiN(SiMe ₂ Et) ₂ -Nb(Net) ₃ -O ₂	

Table C.5 (continued)

MgAl ₂ O ₄	MgCl ₂ -AlCl ₃ -CO ₂ -H ₂	Spinel: MgAl ₂ O ₄
	Mg(Cp) ₂ -Al(Et) ₃ -H ₂ O	
MgO	Mg(thd) ₂ -H ₂ O, Mg(Cp) ₂ -H ₂ O	
MgTiO ₃	Ti(OiPr) ₄ -Mg(CpMe) ₂ -O ₂	
MoO ₃	Mo(CO) ₆ -O ₂	
Nb ₂ O ₅	NbOCl ₃ -O ₂ , Nb(OC ₂ H ₅) ₅	
Nb _x Al _y O _z	Nb(OC ₂ H ₅) ₅ -AlCl ₃	
Nb _x Ta _y O _z	Nb(OC ₂ H ₅) ₅ -Ta(OC ₂ H ₅) ₅	
NdFeO ₃	Nd(thd) ₃ -Fe(thd) ₃	
NdNiO ₃	Nd(thd) ₃ -Ni(thd) ₃	
NiFe ₂ O ₄	Ni(acac) ₂ -Fe(acac) ₃	
PbO	Pb(acac) ₂ -O ₂ , Pb(C ₆ H ₅) ₂ -O ₂	
PbMnO ₄	Pb(thd) ₂ -Mn(thd) ₃ -O ₂	
PbTiO ₃	Pb(thd) ₂ -Ti(OC ₃ H ₇) ₂ (thd) ₂ -O ₂	
	Pb(C ₂ H ₅) ₄ -Ti(OC ₃ H ₇) ₄	
PbZn _x Ti _{1-x} O ₃	PbEt ₄ -Zn(Obut) ₄ -Ti(OPri) ₄ -N ₂ -O ₂	PZT
Pb(Zr,Ti)O ₃	Pb(thd) ₂ -Zr(tmhd) ₄ -Ti(OC ₃ H ₇) ₄	tmhd: C ₁₁ H ₁₉ O ₂
	Pb(C ₂ H ₅) ₄ -Zr(OC ₄ H ₉)-Ti(OC ₃ H ₇) ₄	
Pr ₂ O ₃	Pr(hfa) ₃	
Pr _{0.7} Ca _{0.3} MnO ₃	Pr(thd) ₃ -Ca(thd) ₂ -Mn(thd) ₃	
PrNiO ₃	Pr(thd) ₃ -Ni(thd) ₃	
Sb ₂ O ₃	Sb(NbuO) ₃	
Sb ₆ O ₁₃	Sb(OC ₂ H ₅) ₃ -O ₂	
SBT	Sr(tmhd) ₂ -Bi(C ₆ H ₅) ₃ -Ta(OC ₂ H ₅) ₅	
Sc ₂ O ₃	Sc(acac) ₃	
Si _x N _y O _z	SiH ₄ -NH ₃ -O ₂ , SiH ₄ -O ₂ -N ₂ -Ar, SiH ₄ -N ₂ O	
	SiH ₄ -CO ₂ -NH ₃ -H ₂ , SiCl ₂ H ₂ -N ₂ O	
	SiCl ₂ H ₂ -NH ₃ -N ₂ O, Si(Oet) ₄ -SiH ₂ Cl ₂ -NH ₃	
SiO ₂	SiBr ₄ -H ₂ -NO, SiCl ₄ -H ₂ -NO	
	SiCl ₄ -CO ₂ -H ₂ , SiH ₂ Cl ₂ -N ₂ O	
	Si(OC ₂ H ₅) ₄ , SiH ₄ -O ₂ , SiH ₄ -CO ₂ -H ₂	
SmNiO ₃	Sm(thd) ₃ -Ni(thd) ₃ -O ₂ -Ar	
SnO ₂	SnCl ₄ -H ₂ O, SnR ₄ -H ₂ O	R: Me, Et
	Sn(CH ₃) ₂ Cl ₂ -O ₂ , Sn(CH ₃) ₂ Cl ₂ -H ₂ O	DMTC: dimethyltin dichloride
	CH ₃ SnCl ₃ -O ₂ , SnR ₄ -O ₂	R: Me, Et
	(C ₄ H ₉) ₂ Sn(OOCH ₃) ₂ -O ₂ -H ₂ -N ₂	
	C ₄ H ₉ SnCl ₃ -O ₂ , Sn(Me) ₄ -O ₂ Me ₂ SnEt ₂ -O ₂	
Pt-doped SnO ₂	SnEt ₄ -Pt(hfa) ₂ -O ₂	

Table C.5 (continued)

SrRuO ₃	Sr(thd) ₂ -Ru(acac) ₃	
SrTiO ₃	Sr(CpiPr ₃ H ₃) ₂ -Ti(OC ₃ H ₇) ₄ -H ₂ O	Cp: C ₅ H ₅ , iPr: C ₃ H ₇
SrTiO ₃	Sr(dpm) ₂ -Ti(iPrO) ₄	dpm: C ₁₁ H ₁₉ O ₂
Ta ₂ O ₅	Ta(OC ₂ H ₅) ₅ -O ₂ , TaCl ₅ -CO ₂ -H ₂	
	TaCl ₅ -H ₂ O, TaCl ₅ -O ₂ , Ta(Oet)(dmae)	
	TaCl ₅ +Ta(OC ₂ H ₅) ₅ , TaI ₅ -H ₂ O ₂	
TaO _x N _y	Ta(Oet) ₅ -NH ₃	
Ta _x Ti _y O _z	Ta(OC ₂ H ₅) ₅ -Ti(OC ₃ H ₇) ₄	
ThO ₂	Th(tfa) ₄	tfa: C ₉ F ₁₄ HO ₂
Ti _x Al _y O _z	ZrCl ₄ +Al(OC ₂ H ₅) ₃	
TiO ₂	Ti(dpm) ₂ (OC ₃ H ₇) ₂ -O ₂ , TiI ₄ -H ₂ O	mpd : C ₆ H ₁₂ O ₂
	Ti(mpd)(dmae) ₂ , Ti(Obu) ₄ -O ₂ , TiI ₄ - H ₂ O ₂	dmae: C ₄ H ₁₀ O
	Ti(C ₃ H ₇) ₄ -H ₂ O, Ti(OC ₃ H ₇) ₄ -O ₂	
	TiCl ₄ -O ₂ , TiI ₄ -H ₂ O, TiI ₄ +Ti(OC ₃ H ₇) ₄	
V ₂ O ₅	VO(OiPr) ₃	
W-doped VO ₂	W(OC ₂ H ₅) ₆ -VCl ₅ -H ₂ O	
V _x O _y	VCl ₄ -H ₂ O, VO(OC ₃ H ₇), VO(acac) ₂ - O ₂	V ₂ O ₃ , VO ₂ , V ₂ O ₅
	VO(dpm) ₂ -O ₂ , VO(fod) ₂ -O ₂	fod: C ₁₀ F ₇ H ₁₀ O ₂
	VO(hfa) ₂ -H ₂ O-Ar	
WO ₃	W(CO) ₆ -O ₂ -Ar, WF ₆ -H ₂ O	
WO ₃ -MoO ₃	Mo(CO) ₆ -W(CO) ₆ -O ₂	
YBa ₂ Cu ₃ O _{7-x}	Y(thd) ₃ -Ba(thd) ₂ -Cu(thd) ₂	
YFeO ₃	Y(thd) ₃ -Fe(thd) ₃	
Y ₂ O ₃	YCl ₃ -H ₂ O, Y(thd) ₃	
ZnO	(C ₃ H ₅ O ₂) ₂ Zn, ZnR ₂ -H ₂ O	R: Me, Et
	Zn(CH ₃ COO) ₂ -H ₂ O	
Lu doped ZnO	Lu(acac) ₃ -Zn(acac) ₂ -O ₂	
ZnFe ₂ O ₄	Zn(acac) ₂ -Fe(acac) ₃	
ZnCr ₂ O ₄	Zn(acac) ₂ -Cr(acac) ₃ -O ₂	
ZrO ₂	Zr(acac) ₄ -O ₂ , Zr(acac) ₄ -CO ₂ , ZrI ₄ - O ₂	
	ZrCl ₄ -H ₂ -CO ₂ -HCl, Zr(thd) ₄ -O ₂	
	ZrCp ₂ Cl ₂ -O ₃ , ZrOCl ₂ ·8H ₂ O	
ZrO ₂ -CeO ₂	Ce(thd) ₄ -Zr(OC ₃ H ₇) ₃ -O ₂ -N ₂	CeO ₂ stabilised ZrO ₂
Zr _x Si _y O _z	ZrCl ₄ + Si(OC ₂ H ₅) ₄ , ZrCl ₄ + Si(O ⁿ Bu) ₄	

Table C.5 (continued)

Zirconium tin titanate (ZTT)	$Zr(\text{Net}_2)_4\text{-Sn}(\text{Net}_2)_4\text{-Ti}(\text{Net}_2)_4$	Et: C_2H_5
	$Zr(\text{Nme}_2)_4\text{-Sn}(\text{Nme}_2)_4\text{-Ti}(\text{Nme}_2)_4$	Me: CH_3
	$Zr(\text{BuO})_4\text{-Sn}(\text{BuO})_4\text{-Ti}(\text{BuO})_4$	Bu: C_4H_9
$\text{ZrO}_2\text{-Y}_2\text{O}_3$	$Zr(\text{dpm})_4\text{-Y}(\text{dpm})_3\text{-O}_2$	Y_2O_3 stabilised ZrO_2
	$Zr\text{Cl}_4\text{-YCl}_4\text{-O}_2, Zr(\text{thd})_4\text{-Y}(\text{thd})_3$	
$\text{ZrO}_2\text{-Y}_2\text{O}_3\text{-CeO}_2$	$Zr\text{Cl}_4\text{-YCl}_3\text{-CeCl}_3\text{-H}_2\text{O}$	

Table C.6. Oxide glass

AISG	Aluminosilicate glass	
	$\text{SiH}_4\text{-PH}_3\text{-B}_2\text{H}_6\text{-O}_2\text{-N}_2$	
	$\text{AlCl}_3\text{-SiCl}_4\text{-CO}_2\text{-H}_2$	
	$\text{Al}(\text{CH}_3)_3\text{-SiH}_4\text{-O}_2\text{-N}_2$	
AsSG	Arsenosilicate glass	
	$\text{Si}(\text{OC}_2\text{H}_5)_4\text{-AsCl}_3\text{-O}_2$	
	$\text{Si}(\text{OC}_2\text{H}_5)_4\text{-AsCl}_3\text{-CO}_2$	
	$\text{SiH}_4\text{-AsCl}_3\text{-O}_2, \text{SiH}_4\text{-AsH}_3\text{-O}_2$	
BPSG	Borophosphosilicate glass	
	$\text{SiH}_4\text{-B}_2\text{H}_6\text{-PH}_3\text{-O}_2$	
	$\text{Si}(\text{Oet})_4\text{-TMB-TMP-O}_2$	TMB: $(\text{CH}_3\text{O})_3\text{B}$
	$\text{Si}(\text{Oet})_4\text{-TMB-TMP-O}_3$	TMP: $\text{CH}_3\text{O}_3\text{PO}$
BSG	Borosilicate glass	
	$\text{SiH}_4\text{-B}_2\text{H}_6\text{-O}_2$	
	$\text{Si}(\text{OC}_2\text{H}_5)_4\text{-B}(\text{OCH}_3)_3\text{-P}(\text{OCH}_3)_3\text{-O}_3$	
PSG	Phosphosilicate glass	
	$\text{SiCl}_4\text{-POCl}_3\text{-H}_2\text{O}, \text{SiH}_4\text{-PH}_3\text{-O}_2$	
	$\text{SiBr}_4\text{-PH}_3\text{-O}_2, \text{Si}(\text{OC}_2\text{H}_5)_4\text{-PO}(\text{OCH}_3)_3\text{-O}_2$	

Table C.7. Silicide

FeSi_2	$\text{FeCl}_3\text{-SiH}_4\text{-H}_2\text{-Ar}$	
MoSi_2	$\text{MoF}_6\text{-SiH}_4$	
	$\text{MoCl}_5\text{-SiH}_4\text{-H}_2, \text{MoCl}_5\text{-SiCl}_4\text{-H}_2$	
NbSi_2	$\text{NbCl}_5\text{-SiH}_4\text{-H}_2$	
Ta_xSi_y	$\text{TaCl}_5\text{-SiH}_4$	$\text{TaSi}_3, \text{TaSi}_2$
TiSi_2	$\text{TaCl}_4\text{-SiH}_4, \text{TaCl}_4\text{-SiH}_2\text{Cl}_2$	
	$\text{TiCl}_4\text{-SiCl}_4\text{-H}_2$	
WSi_x	$\text{WF}_6\text{-SiH}_4, \text{WF}_6\text{-Si}_2\text{H}_6, \text{WF}_6\text{-SiH}_2\text{Cl}_2$	
	$\text{WCl}_6\text{-SiH}_4$	

Table C.8. Sulfide and other components

AlAs	AlCl ₃ -AsH ₃ , AlR ₃ -AsH ₃	R: Me, Et
GaAs	Ga(CH ₃) ₃ -AsH ₃ , GaCl ₃ -AsH ₃	
ScAs	Sc-HCl-AsH ₃ -H ₂	
CaF ₂	Cd(thd) ₂ -NH ₄ F	
SrF ₂	Sr(thd) ₂ -NH ₄ F	
CoGa	(CO) ₄ CoGaEt ₂ (Nme ₃)	
SiGe	SiH ₄ -GeH ₄	
CoIn	[(CO) ₄ Co] _{3-a} In[CH ₂ CH ₂ CH ₂ N(CH ₃) ₂] _a	a=1,2
BP	B ₂ H ₆ -PH ₃	
CoP	Co(CpMe) ₂ -PH ₃	
GaP	Ga(CH ₃) ₃ -PH ₃	
InGaAsP	In(CH ₃) ₃ -Ga(CH ₃) ₃ -H ₂ AsC(CH ₃) ₃ -H ₂ PC(CH ₃) ₃	
ScP	Sc-HCl-PH ₃ -H ₂	
SnP _x	SnCl ₄ -PCy _x H _{3-x} (x=1,2,3)	(x=1.33, 1.0, 0.66, 0.4)
BaS	Ba(thd) ₂ -H ₂ S	
CaS	Cd(thd) ₂ -H ₂ S	
CdS	Cd-Te, Cd _(v) -H ₂ S-H ₂ , Cd[S ₂ CN(C ₂ H ₅) ₂]	
Co ₉ S ₈	Co[(C ₂ H ₅) ₂ NCS ₂] ₃ -[(CH ₃) ₃ C] ₂ S ₂ -Ar	
Cu ₂ S	Cu[S ₂ CN(C ₂ H ₅) ₂]	
Cu _x S	Cu(thd) ₂ -H ₂ S	Cu ₉ S ₅ , Cu _{1.96} S, Cu ₃₁ S ₁₆
FeS _{1+x}	Fe[(C ₂ H ₅) ₂ NCS ₂] ₃ -[(CH ₃) ₃ C] ₂ S ₂ -Ar	TBDS: tert-butyl disulfide
	Fe(acac) ₃ -(C ₄ H ₉) ₂ S ₂ -H ₂ , Fe(acac) ₃ -H ₂ S-H ₂	
MgS	Mg(thd) ₂ -H ₂ S	
MoS ₂	MoCl ₅ -H ₂ S-H ₂ , Mo(CO) ₆ -H ₂ S	
MnS	MnPh(Et ₂ HNCS ₂) ₃ -[(CH ₃) ₃ C] ₂ S ₂ -Ar	
PbS	(Me) ₄ Pb-H ₂ S, Pb(OBu) ₂ -H ₂ S	
	Pb(thd) ₂ -H ₂ S	
Sn _x S _y	SnBr ₄ -H ₂ S	SnS ₂ , SnS, SnS ₃
Zn-Eu-S	ZnPh(S ₂ CNEt ₂) ₂ -EuPh(S ₂ CNEt ₂) ₂	
ZnO _{1-x} S _x	Zn(Me) ₂ -H ₂ S-O ₂	
ZnS	Zn-S, Zn _(v) -H ₂ S-H ₂ , ZnR ₃ -H ₂ S-H ₂	R: Me, Et
	ZnS _(v) -HCl-H ₂ , Zn(CH ₃) ₂ -(C ₄ H ₉) ₂ S ₂	
As _x Se _{1-x}	H ₂ Se-AsH ₃	0<x<0.4
PbSe	(CH ₃) ₄ Pb-H ₂ Se-H ₂	
SrS _{1-x} Se _x	Sr(thd) ₂ -H ₂ S-Se _(v) -N ₂	
ZnSe	Zn-Se, Zn _(v) -H ₂ Se-H ₂ , ZnSe _(v) -HBr-H ₂	
	(C ₂ H ₅) ₂ Zn-H ₂ Se-H ₂ , Zn(CH ₃) ₂ -(C ₄ H ₉) ₂ Se	
	H ₂ Se-Zn _(v) -H ₂ -Ar, Zn-Se(Et) ₂	
CdTe	Cd(CH ₃) ₂ -Te(CH ₃) ₂	

Table C.8 (continued)

PbTe	$(C_2H_5)_2Pb-(CH_3)_2Te-H_2$	
Si-As-Te	$Si_{(v)}-As_{(v)}-Te_{(v)}-H_2-He$	
ZnTe	$Zn-Te, Zn(Me)_2-Te(Et)_2, Zn(Et)_2-Te(Et)_2$	

Table C.9. Co-deposition

AlN-Si ₃ N ₄	$AlCl_3-SiCl_4-NH_3-N_2, AlCl_3-SiH_4-N_2$	
BN-AlN	$BCl_3-AlCl_3-NH_3$	
HfB ₂ -SiC	$HfCl_4-BCl_3-CH_3SiCl_3$	
Ir-Al ₂ O ₃	$Ir(acac)_3-Al(acac)_3-H_2$	
SiC-C	$SiCl_4-C_3H_8-H_2$	
	$CH_3SiCl_3-C_2H_2-N_2-H_2$	
SiC-CrSi ₂	$CH_3SiCl_3-CrCl_4-H_2$	
SiC-Mo ₄ SiC	$CH_3SiCl_3-MoCl_5-H_2$	
SiC-TiC	$SiH_2Cl_2-C_4H_{10}-TiCl_4-H_2$	
	$SiCl_4-TiCl_4-CCl_4-H_2$	
SiC-TiSi ₂	$CH_3SiCl_3-TiCl_4-H_2$	MTS: CH_3SiCl_3
SiC-TiSi ₃ C ₂	$CH_3SiCl_3-TiCl_4-H_2$	
Si ₃ N ₄ -C	$SiCl_4-NH_3-H_2-C_3H_8$	
Si ₃ N ₄ -BN	$SiCl_4-NH_3-B_2H_6-H_2$	
Si ₃ N ₄ -TiN	$SiCl_4-TiCl_4-NH_3-H_2$	
TiB ₂ -TiC	$TiCl_4-n-C_7H_{16}-BCl_3-H_2$	
	$TiCl_4-C_6H_6-BBr_3-H_2$	
TiN-AlN	$TiCl_4-AlCl_3-NH_3-H_2$	
TiN-MoS ₂	$Ti((CH_3)_2N)_4-NH_3-MoF_6-H_2S$	
TiN-Ti _x Si _y	$TiCl_4-SiH_2Cl_2-N_2-H_2, TiCl_4-SiH_4-N_2-H_2$	
	$TiCl_4-SiCl_4-N_2-H_2$	

Table C.10. Complex compound

Al-Ni	$AlCl_3-Ni-H_2$	Ni as substrate
B-C-N	$C_2H_2-BCl_3-NH_3-N_2, N(Et_3BH_3)-NH_3$	
	$NEt_3BH_3-NH_3, B(OMe)_3-NH_3-N_2$	
B-Si-C	$CH_3SiCl_3-CH_4-BCl_3-H_2$	
Cr ₃ (C, N) ₂	$Cr(NEt_2)_4$	$Cr_3(C_{0.8}N_{0.2})_2$
Cr-Si-C	$CrCl_4-CH_3SiCl_3-H_2, Cr[CH_2SiMe_3]_4$	
Mo-Si-C	$MoCl_5-CH_3SiCl_3-H_2$	
Re-Si-N	$ReCl_5-SiH_4-NH_3-H_2-N_2$	
Si-B-C	$BCl_3-C_3H_8-H_2$	
SiBCN	$Si(NMe_2)_3NHB(NMe_2)_2$	
Si-N-C	$Si(CH_3)_4-NH_3-H_2, Si_2NH(CH_3)_6-NH_3$	HMDS: $Si_2NH(CH_3)_6$
	$C_3N_3Cl_2N(Si(CH_3)_3)_2$	
Si-O-C-N	$SiCl_4-C_2Cl_3-NH_3-H_2O$	

Table C.10 (continued)

SiC _x N _y	Si(CH ₃) ₄ -NH ₃ -N ₂	
Ta-Si-N	TaCl ₄ -SiH ₄ -NH ₃ -H ₂ -N ₂	
Ti _{1-x} Al _x N	TiCl ₄ -AlCl ₃ -N ₂ -H ₂	Enhanced by plasma
Ti-B-N	TiCl ₄ -BCl ₃ -N ₂ -H ₂	
Ti-C-N	TiCl ₄ -(CH ₃) ₂ NH, TiCl ₄ -CH ₃ CN	CH ₃ CN: acetonitrile
	TiCl ₄ -CH ₄ -N ₂ -H ₂ , Ti(NMe ₂) ₄	
Ti(O,C,N)	Ti(OC ₃ H ₇) ₄ -N ₂ -H ₂ -Ar, TiCl ₄ -CH ₄ -CO ₂ -H ₂	
Ti-Si-C	TiCl ₄ -SiCl ₄ -CH ₄ -H ₂ , TiCl ₄ -CH ₃ SiCl ₃ -H ₂	
	TiCl ₄ -SiH ₂ Cl ₂ -C ₄ H ₁₀ -H ₂	
Ti-Si-C-N	TiCl ₄ -SiCl ₄ -CH ₄ -N ₂ -H ₂	Enhanced by plasma
Ti-Si-N	TDMAT-NH ₃ -SiH ₄ , TiCl ₄ -SiH ₄ -NH ₃ -H ₂ -N ₂	TDMAT: Ti(NMe ₂) ₄
	Ti(NMe ₂) ₄ -SiH ₄ -NH ₃	
Ti-W-C	TiCl ₄ -W(CO) ₆ -CH ₄ -H ₂ -Ar	
W-Si-N	WCl ₅ -SiH ₄ -NH ₃ -H ₂ -N ₂	
Zr-B-N	ZrCl ₄ -BCl ₃ -N ₂ -H ₂	

Table C.11. Abbreviations

Abbreviation	Full Name	Formula
Ac	Acetate	OCCH ₃
aa/acac	Pentane-2,4-dionate, acetylacetonate	C ₅ H ₇ O ₂
Allyl	Allyl	C ₃ H ₅
BBC	Bis-benzene chromium	Cr(C ₆ H ₆) ₂
i-Bu	Iso-butyl	C ₄ H ₉ : CH ₂ CH(CH ₃) ₂
s-Bu	Sec-butyl	C ₄ H ₉ : CH(CH ₃)(CH ₂ CH ₃) ₂
t-Bu	Tert-butyl	C ₄ H ₉ : CH(CH ₃) ₂
Cp	Cyclopentadienyl	C ₅ H ₅
cod	Cyclooctadiene	C ₈ H ₁₂
dbm	1,3-diphenylpropane-1,3-dionate, dibenzoylmethane	C ₁₅ H ₁₁ O ₂
dhd	1,1-dimethylhexane-3,5-dionate	C ₈ H ₁₃ O ₂
dmae	N, N' dimethylaminoethoxide	C ₄ H ₁₀ O
dmb	3,3-dimethyl-1-butene	C ₆ H ₁₂
dmhd	Dimethyl-heptandionate	C ₇ H ₁₁ O ₂
dpm	Dipivaloylmethanate	C ₁₁ H ₁₉ O ₂
Et	Ethyl	C ₂ H ₅
etob	Ethylacetoacetate	C ₈ H ₁₃ O ₂
fod	6,6,7,7,8,8-heptafluoro-2,2-dimethyl-3,5-octandion	C ₁₀ F ₇ H ₁₀ O ₂

Table C.11 (continued)

hfa/hfac	1,1,1,5,5,5-hexafluoropentane-2,4-dionate, hexafluoroacetylacetonate	$C_5F_6HO_2$
HMDS	Hexamethyl disilyamine	$Si_2NH(CH_3)_6$
Me	Methane	CH_3
mhd	6-methylheptane-2,4-dionate	$C_8H_{13}O_2$
mpd	2-methylpentane-2,4-diolate	$C_6H_{12}O_2$
MTS	Methyltrichlorosilane	CH_3SiCl_3
	Pentadienyl	C_5H_7
Ph	Phenyl	C_6H_5
Piv	Pivalate	$(CH_3)_3CCOO$
i-Pr	Iso-propyl	C_3H_7 : $CH(CH_3)_2$
i-PrO	Iso-propoxide	C_3H_7O
pta	Pivaloyltri fluoracetate	$C_8F_3H_{10}O_2$
pva	Pivaloylacetate	$C_8H_{13}O_2$
tdf	1,1,1,2,2,3,3,3,7,7,8,8,9,9,9- tridecafluorononane-4,6-dionate	$C_9F_{14}HO_2$
tfa/tfac	1,1,1-trifluoropentane-2,4-dionate, Trifluoroacetylacetonate	$C_5F_3H_4O_2$
tdeat	Tetrakis(diethylamino)titanium(IV)	$Ti[(C_2H_5)_2N]_4$
tdmat	Tetrakis(dimethylamino)titanium(IV)	$Ti[(CH_3)_2N]_4$
thd/dmp/tmhd	2,2,6,6-tetramethyl-3,5- heptandionate	$C_{11}H_{19}O_2$
TEOS	Tetraethyl orthosilicate	$Si(OC_2H_5)_4$
VTMS	Vinyltrimethylsilyl	SiC_3H_{12}

Appendix D Chemical Vapour Deposition Phase Diagram Collection

In addition to the phase diagrams shown and explained in the main text, this appendix provides further useful phase diagrams of five main types of materials: borides, carbides, nitrides, oxides and silicides. These can provide initial useful information about the conditions and chemical reactions of a system for anyone who wishes to deposit them.

D.1 Chemical Vapour Deposition Phase Diagrams for Borides

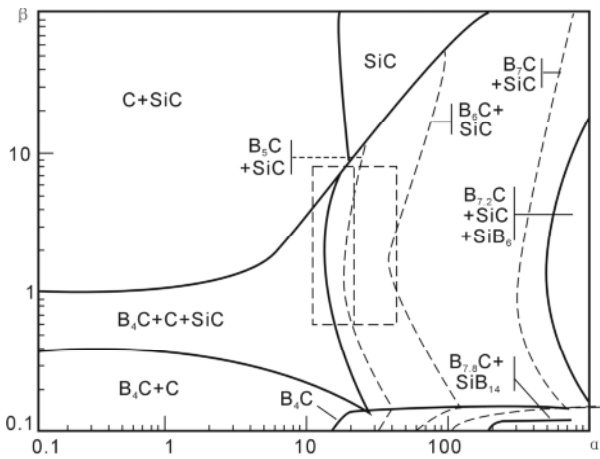


Figure D.1. CVD phase diagram of MTS-BCl₃-H₂ system (40Pa, 1127°C, $\alpha = \text{H}_2/\text{MTS}$, $\beta = \text{MTS}/\text{BCl}_3$) [18]

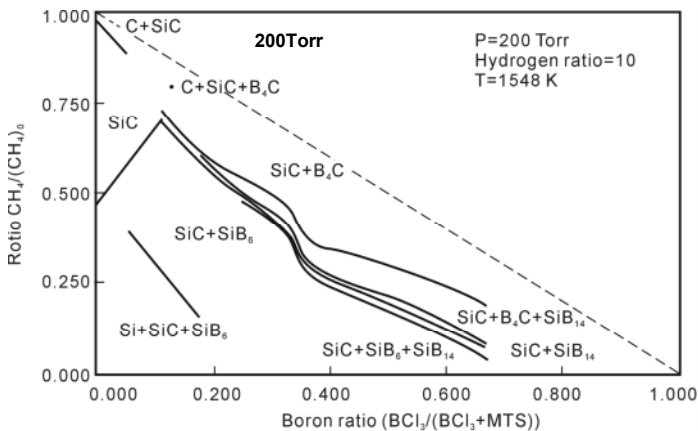


Figure D.2. CVD phase diagram of BCl₃-CH₃SiCl₃-H₂ system [19]

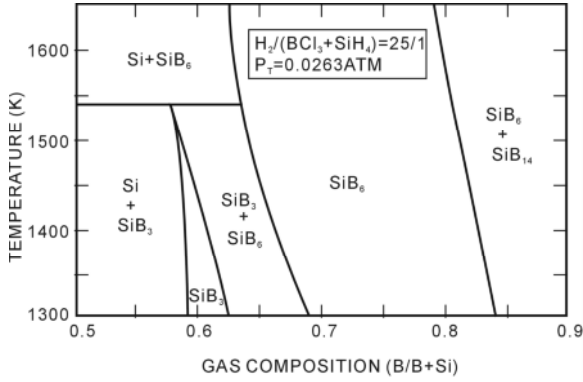


Figure D.3. CVD phase diagram of SiH₄-BCl₃-H₂ system [20]

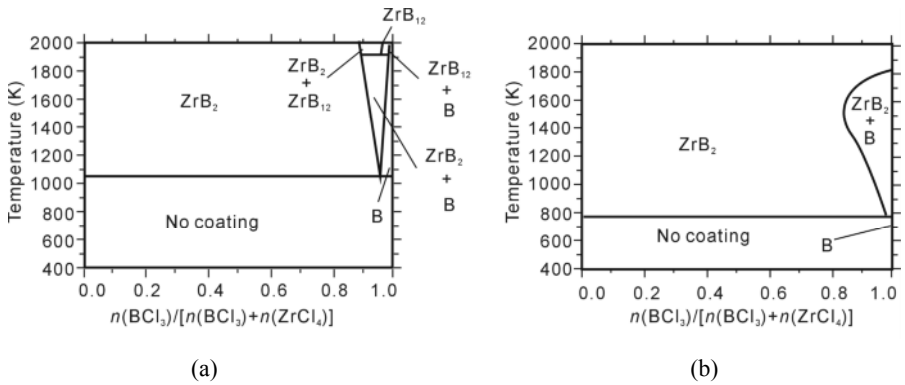


Figure D.4. CVD phase diagram of Zr-B-H-Cl system for H/Cl = 1: (a) $P = 10^5$ Pa and (b) $P = 10^2$ Pa [21]

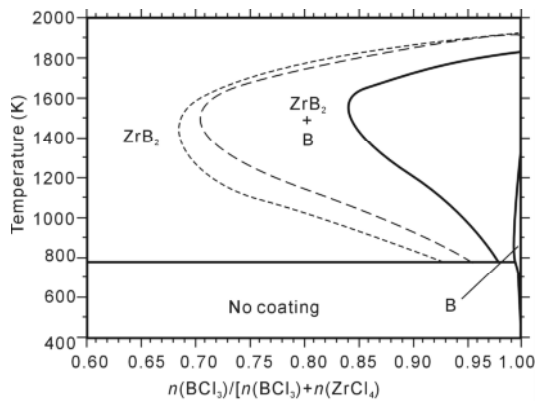


Figure D.5. Effect of H/Cl ratio on CVD deposition diagram of Zr-B-H-Cl systems $P = 10^2$ Pa. Solid line: H/Cl = 5 and dotted line: H/Cl = 10 [21]

D.2 Chemical Vapour Deposition Phase Diagrams for Carbides

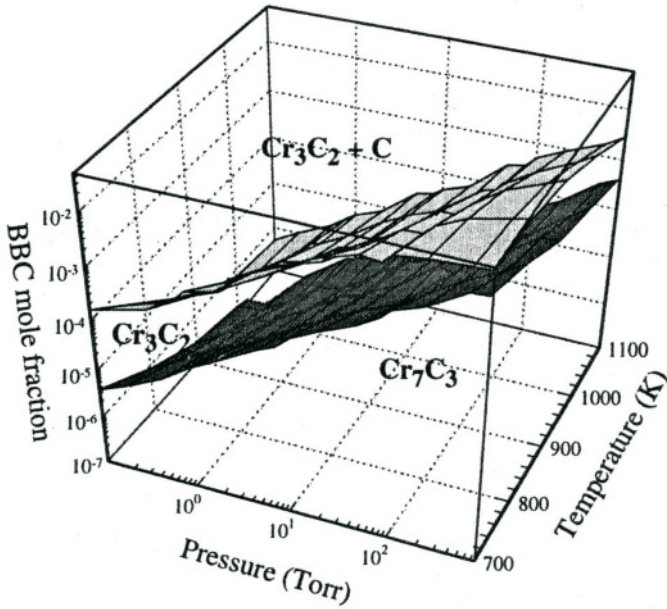


Figure D.6. CVD phase diagram of $\text{Cr}(\text{C}_6\text{H}_6)_2\text{-H}_2$ system (BBC: $\text{Cr}(\text{C}_6\text{H}_6)_2$) [22]

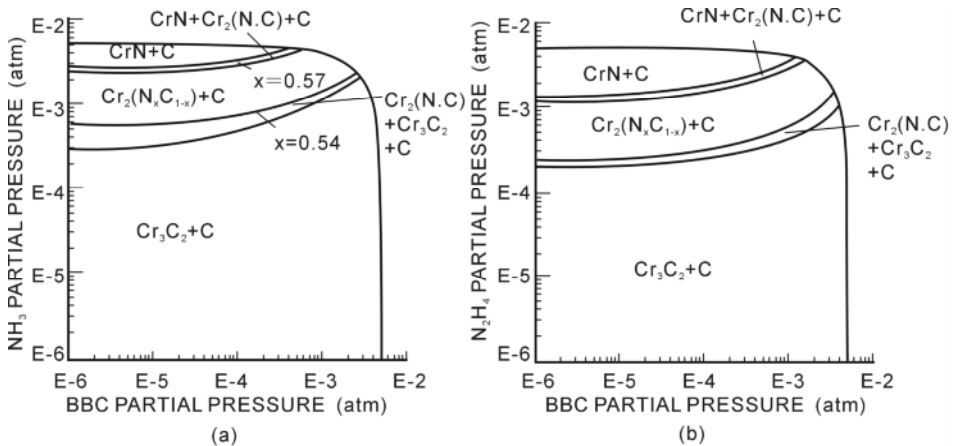


Figure D.7. CVD phase diagrams at 527°C , 5×10^{-3} atm: (a) $\text{Cr}(\text{C}_6\text{H}_6)_2\text{-NH}_3\text{-He}$ system and (b) $\text{Cr}(\text{C}_6\text{H}_6)_2\text{-N}_2\text{H}_4\text{-He}$ system [23]

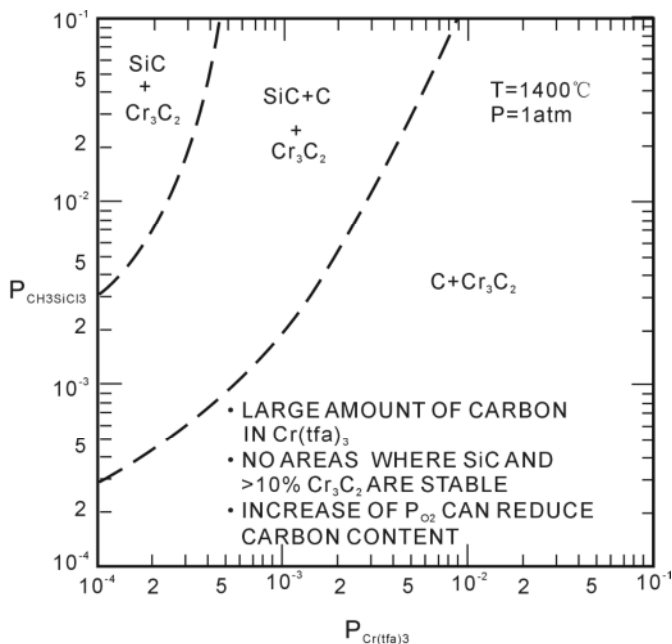


Figure D.8. CVD phase diagram of $\text{CH}_3\text{SiCl}_3\text{-Cr(tfa)}_3$ system [24]

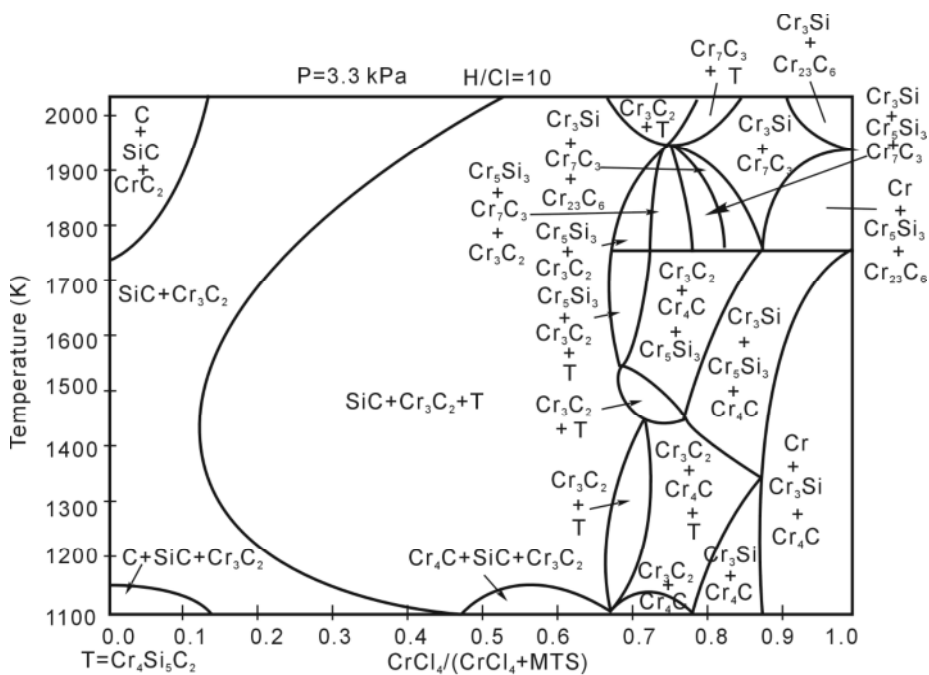


Figure D.9. CVD phase diagram of $\text{CH}_3\text{SiCl}_3\text{-CrCl}_4\text{-H}_2$ system [25]

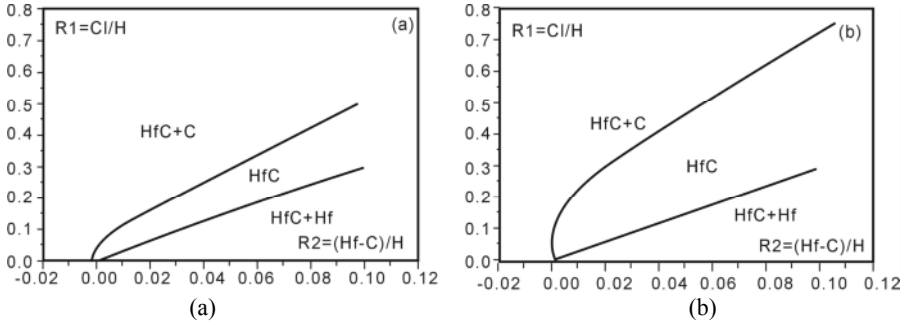


Figure D.10. CVD phase diagram of Hf-C-Cl-H system at 1700 K: (a) 1 atm and (b) 0.01 atm [26]

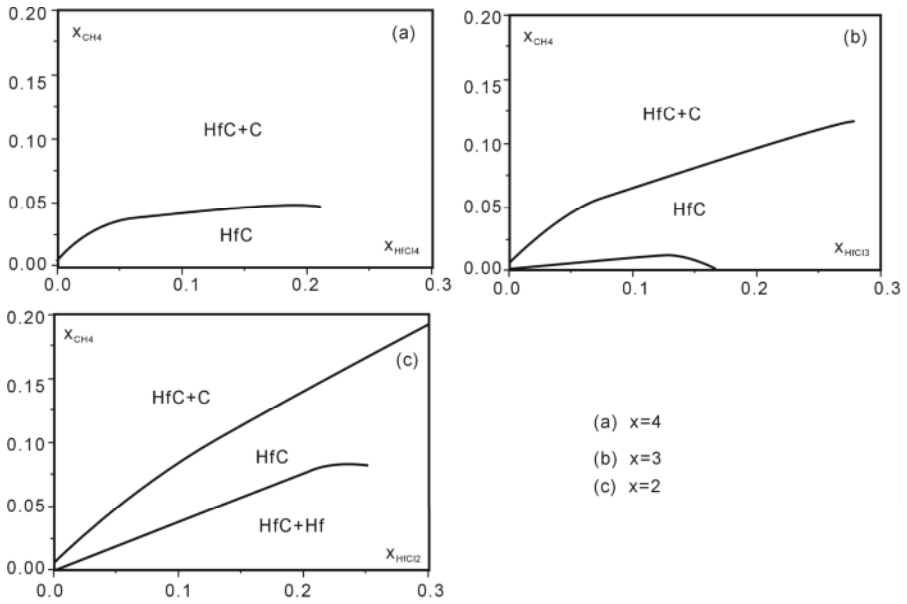


Figure D.11. CVD HfC diagram of $HfCl_x-CH_4-H_2$ system at 1700 K, 1 atm [26]

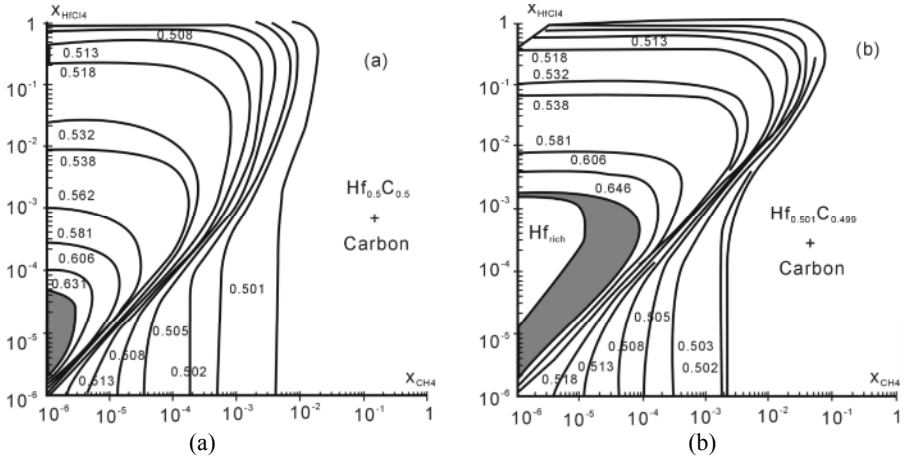


Figure D.12. CVD phase diagram of $\text{HfCl}_4\text{-CH}_4$ at 1 atm: (a) 1400 K and (b) 2000 K. Grey area is the two-phase domain of $\text{Hf}_{\text{rich}}+\text{Hf}_x\text{C}_{1-x}$ [26]

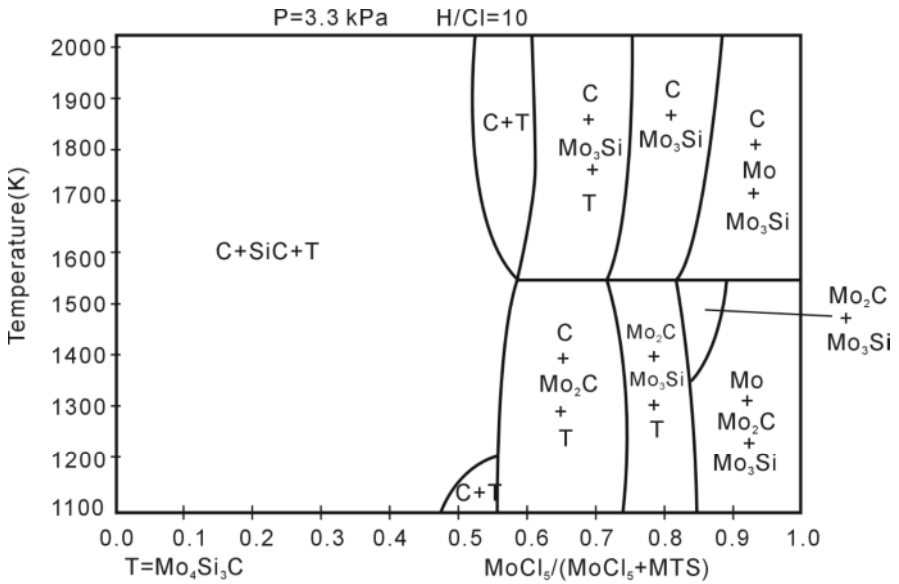


Figure D.13. CVD phase diagram of $\text{CH}_3\text{SiCl}_3\text{-MoCl}_3$ system in H_2 [25]

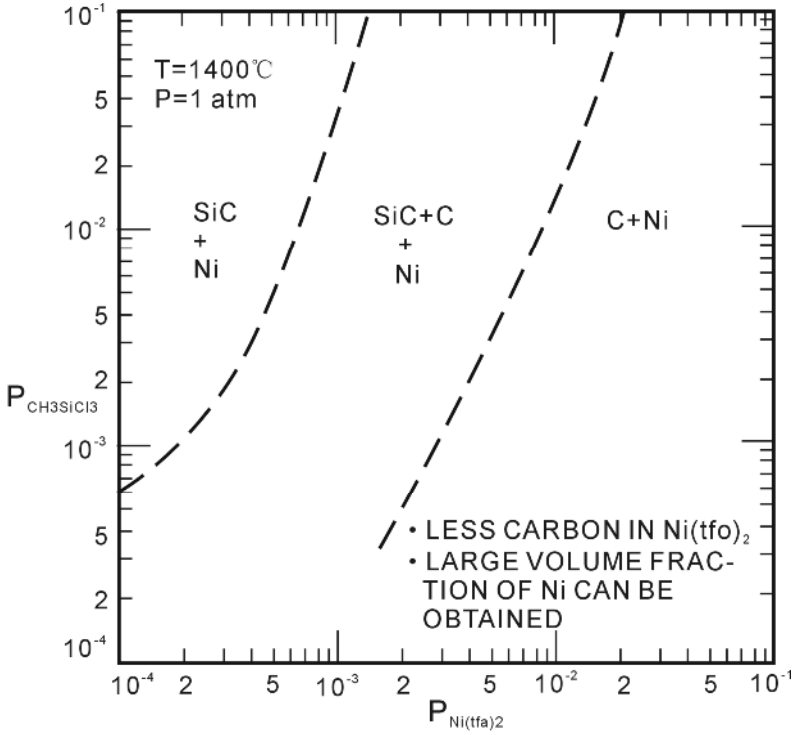


Figure D.14. CVD phase diagram of $\text{CH}_3\text{SiCl}_3\text{-Ni}(\text{tfa})_2$ system [24]

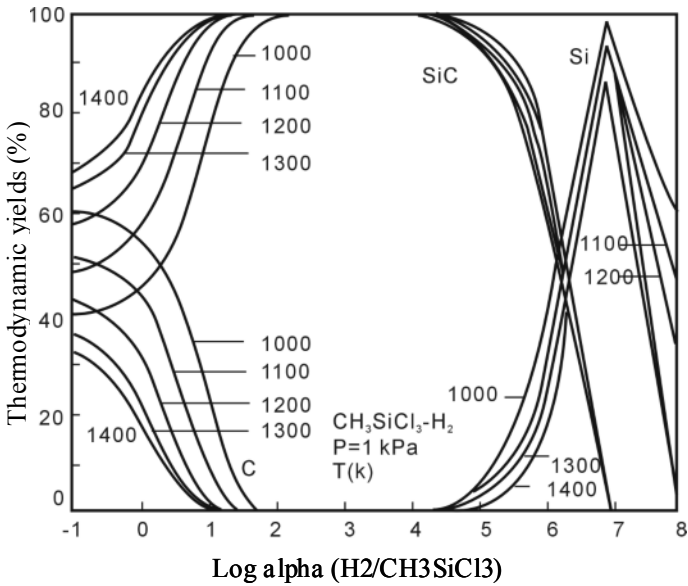


Figure D.15. CVD phase diagram of $\text{CH}_3\text{SiCl}_3\text{-H}_2$ system [27]

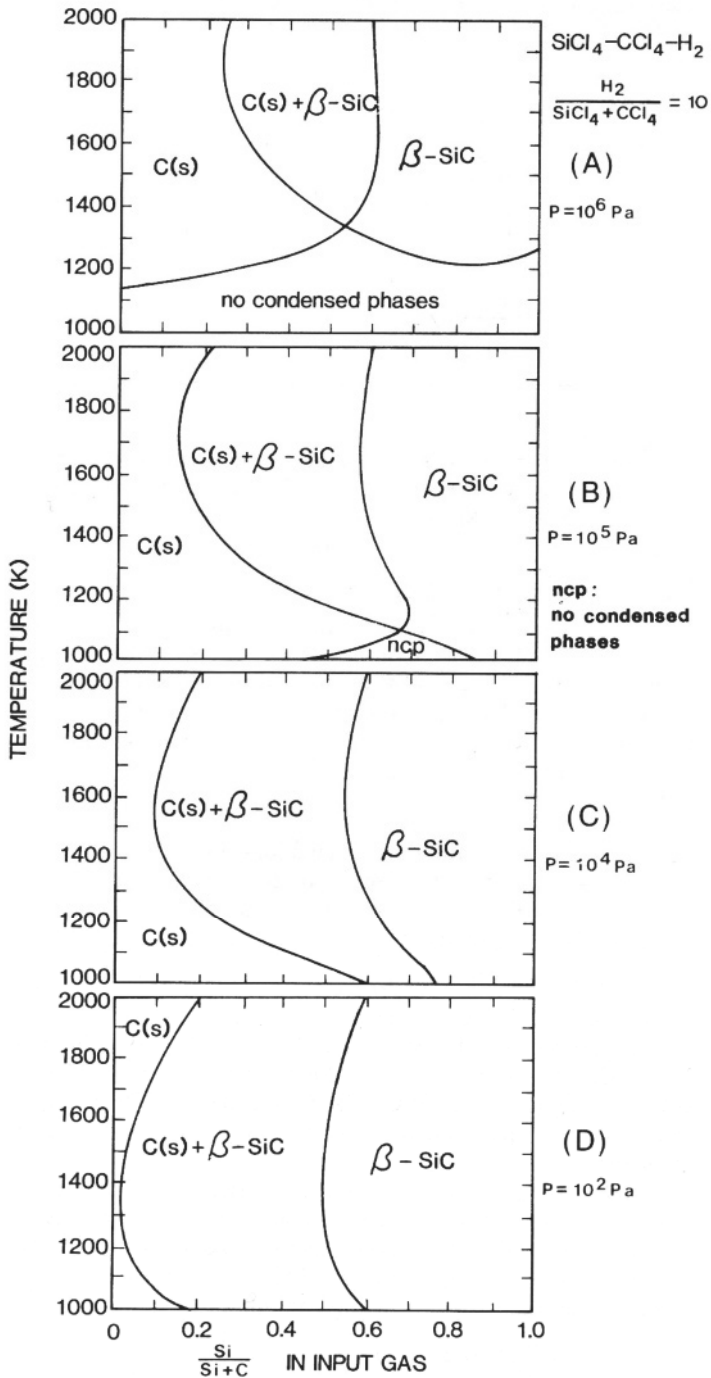
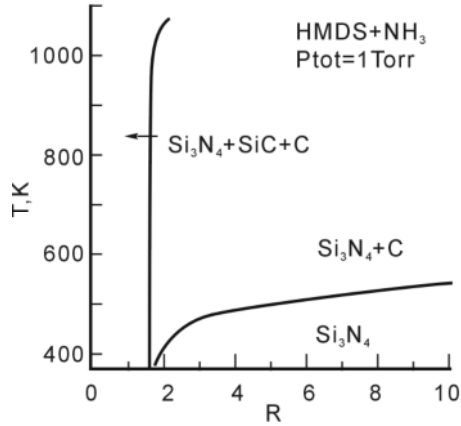
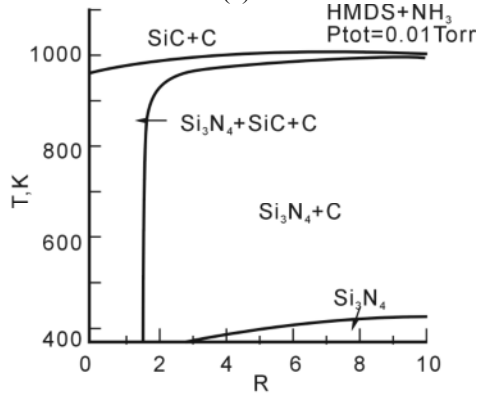


Figure D.16. CVD phase diagram of $\text{SiCl}_4\text{-CCl}_4\text{-H}_2$ with $\text{H}_2/(\text{SiCl}_4 + \text{CCl}_4) = 10$ [28]



(a)



(b)

Figure D.17. CVD phase diagram of Si₂NH(CH₃)₆-NH₃ system [29]: (a) 1 Torr, (b) 0.01 Torr; $R = [\text{NH}_3]/[\text{HMDS}]$, HMDS: Si₂NH(CH₃)₆

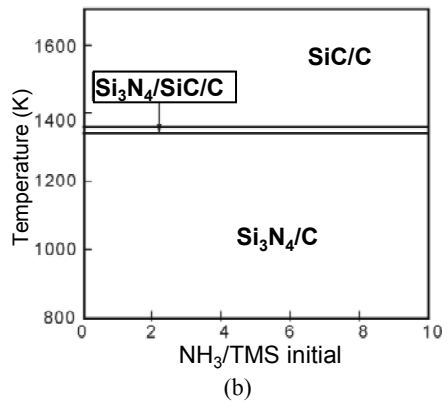
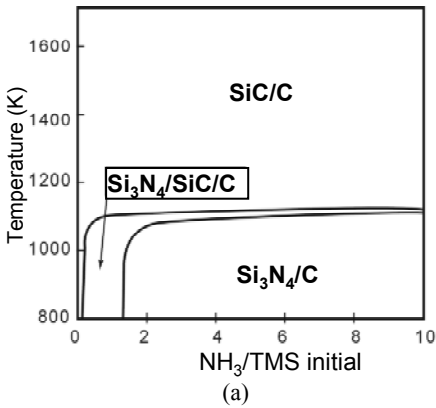


Figure D.18. CVD phase diagram of Si(CH₃)₄-NH₃ system at 4 Torr, N/Si = 10 [30]: (a) in H₂ and (b) in N₂ (TMS: tetramethylsilane, Si(CH₃)₄)

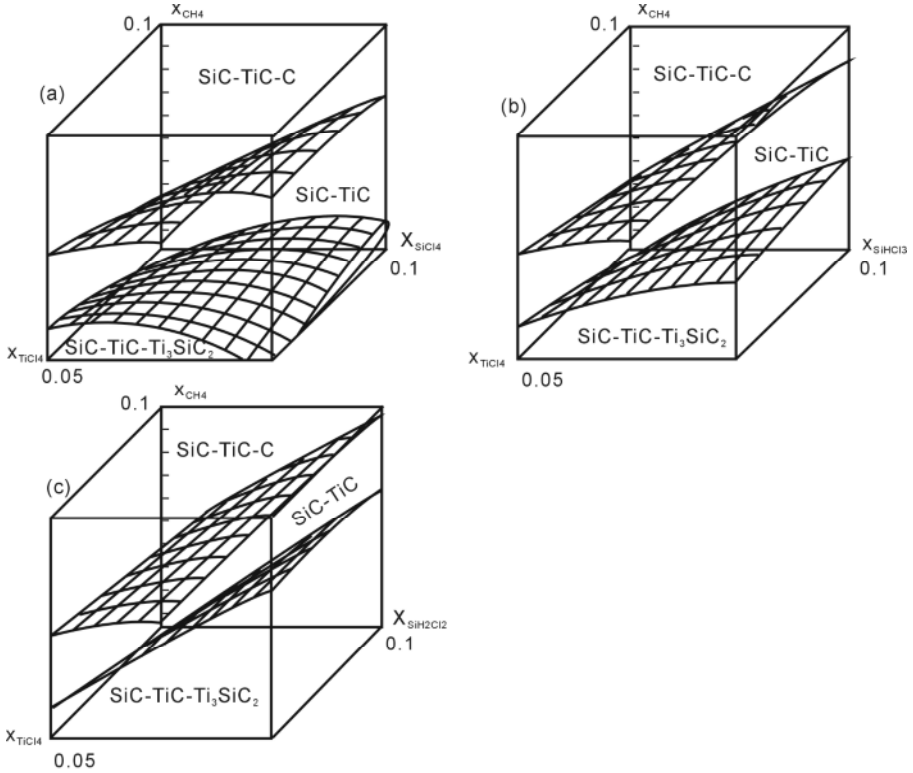


Figure D.19. CVD phase diagram of Si-Ti-Cl-C-H in H_2 at 1 atm [31]

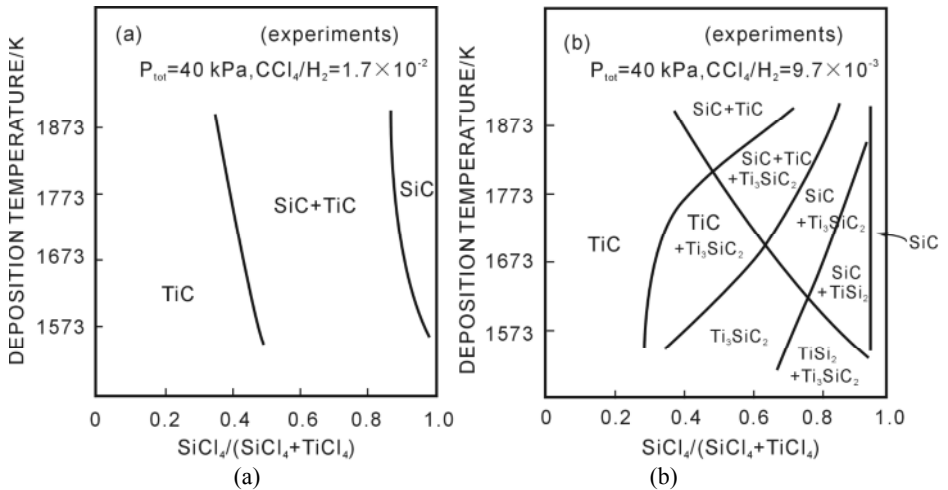


Figure D.20. CVD phase diagram of $TiCl_4-SiCl_4-H_2$ system at 40 kPa [32]: (a) $CCl_4/H_2 = 1.7 \times 10^{-2}$ and (b) $CCl_4/H_2 = 9.7 \times 10^{-3}$

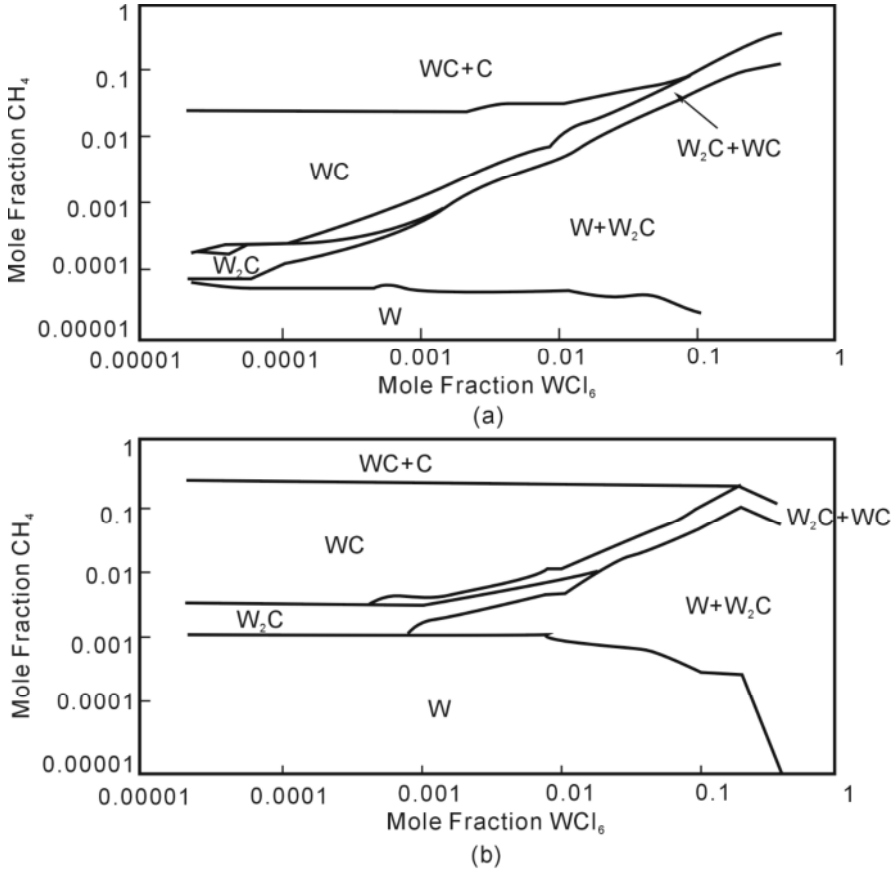


Figure D.21. CVD phase diagram of $\text{WCl}_6\text{-CH}_4\text{-H}_2\text{-Ar}$ system at 500°C at (a) 20 Torr and (b) 200 Torr [33]

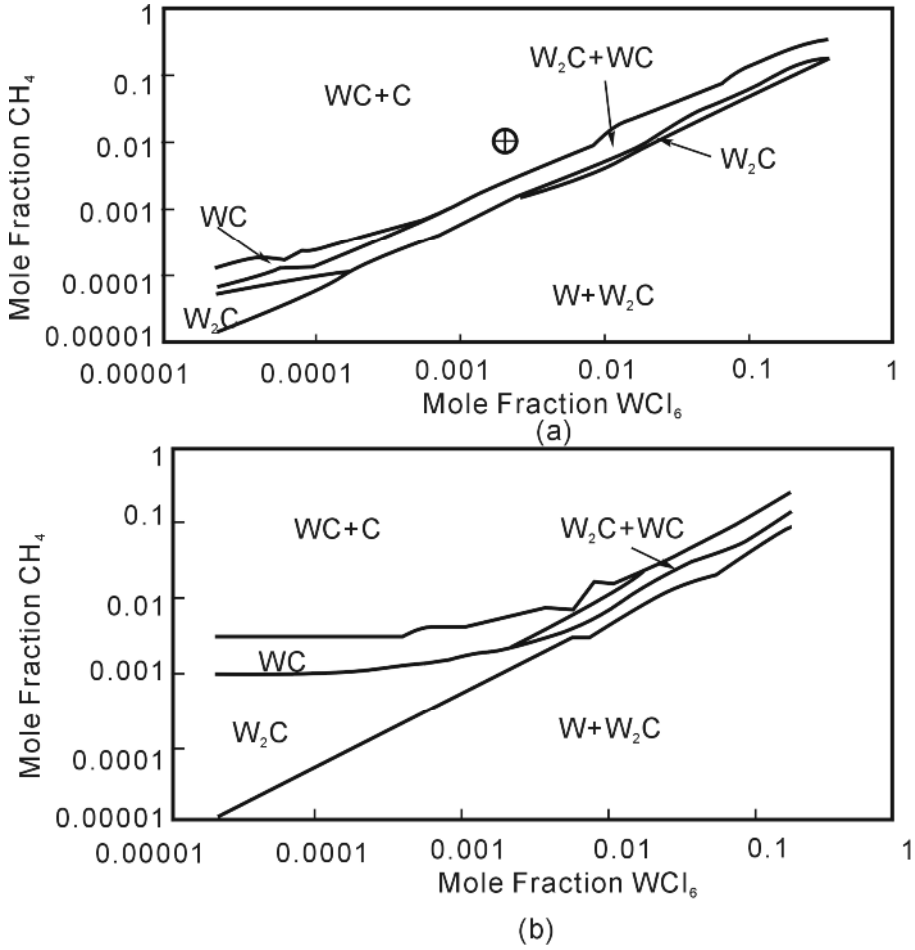


Figure D.22. CVD phase diagram of $\text{WCl}_6\text{-CH}_4\text{-H}_2\text{-Ar}$ system at (a) 20 Torr and (b) 200 Torr at 1000°C [33]

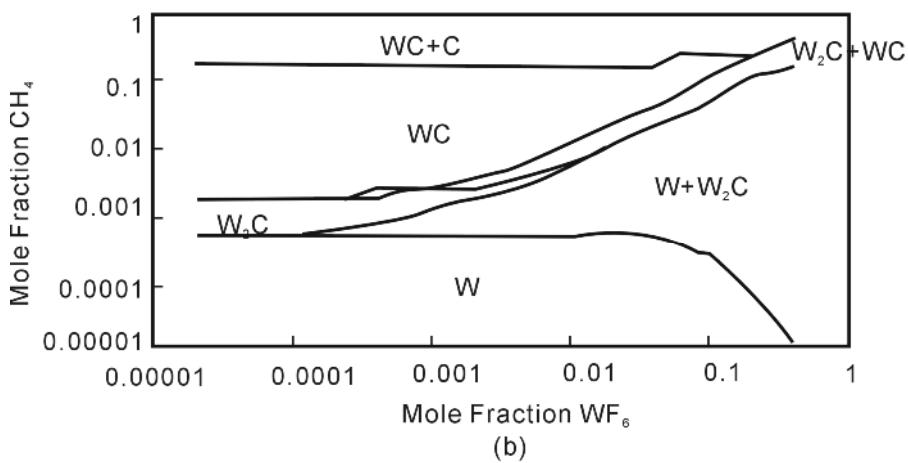
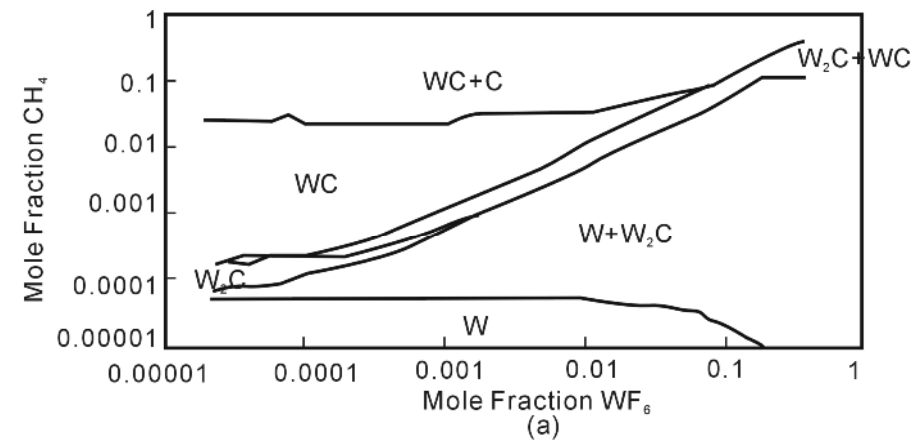


Figure D.23. CVD phase diagram of $\text{WF}_6\text{-CH}_4\text{-H}_2\text{-Ar}$ system at a pressure of (a) 20 Torr and (b) 200 Torr at 500 °C [33]

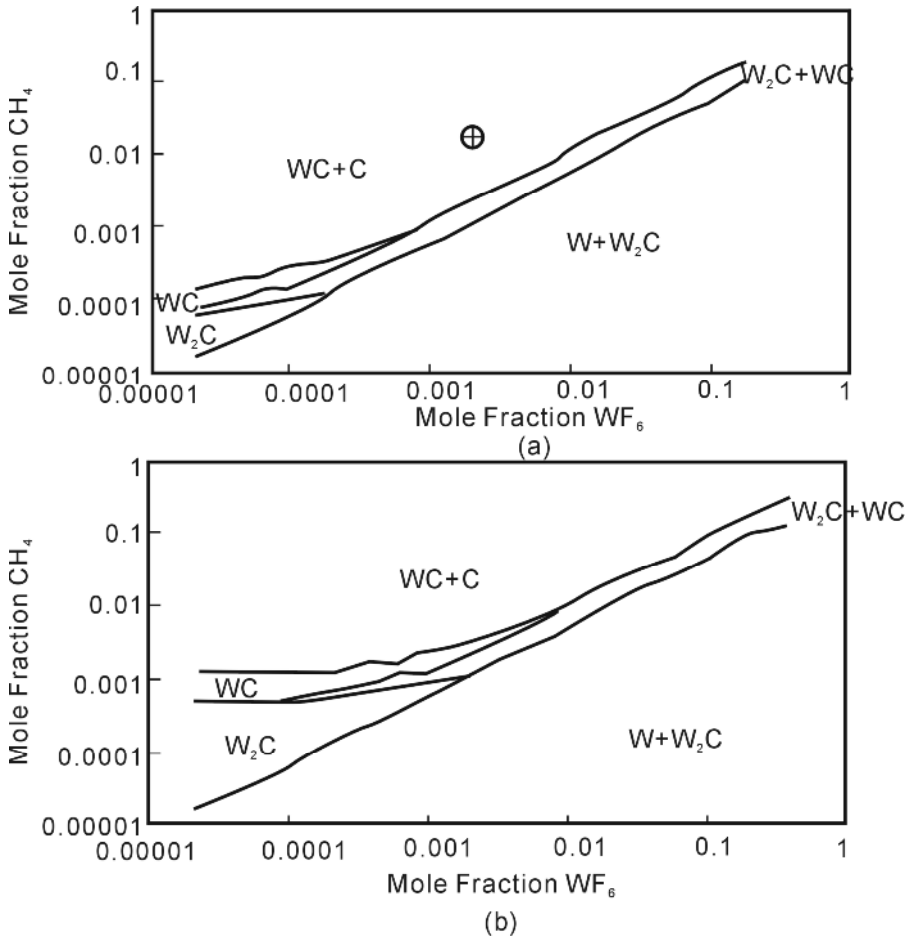
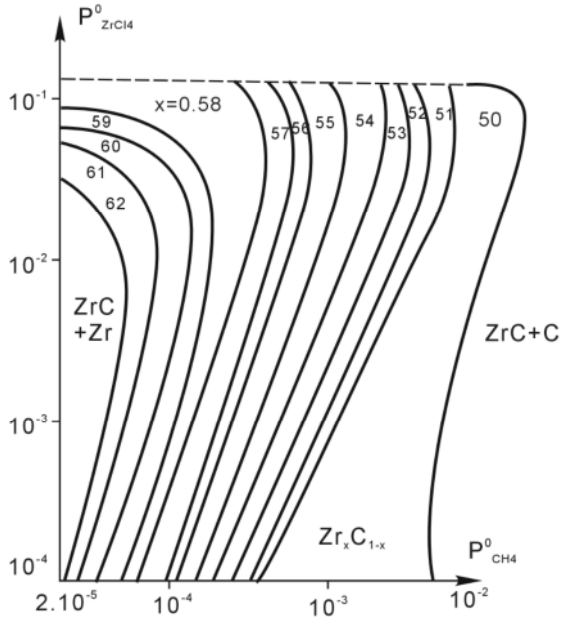
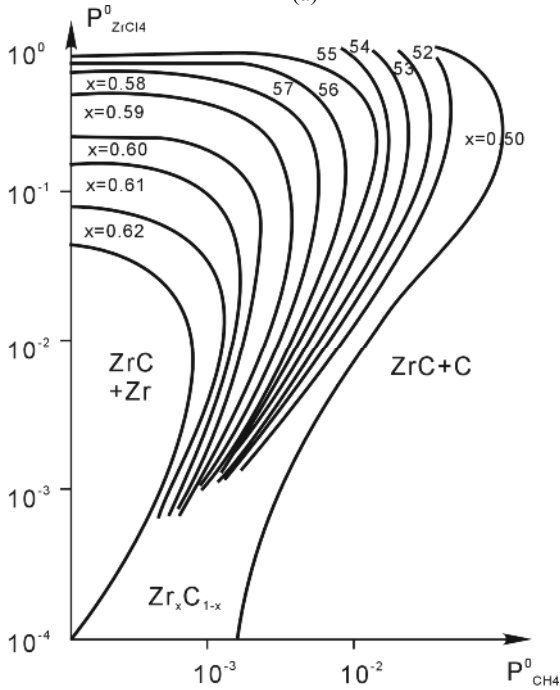


Figure D.24. CVD phase diagram of WF_6 - CH_4 - H_2 -Ar at 1000 °C at (a) 20 Torr and (b) 200 Torr [33]



(a)



(b)

Figure D.25. CVD phase diagram of $\text{ZrCl}_4\text{-CH}_4\text{-H}_2$ system at 1 atm at (a) 1400 K and (b) 1900 K [34]

D.3 Chemical Vapour Deposition Phase Diagrams for Nitrides

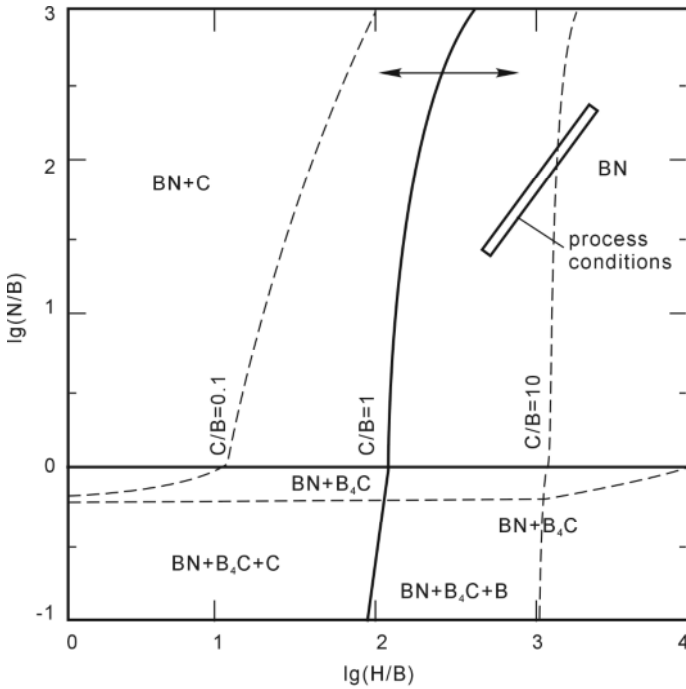


Figure D.26. CVD BN diagram of $H_3B_3N_3(CH_3)_3-NH_3-H_2$ system at 1200 K [35]

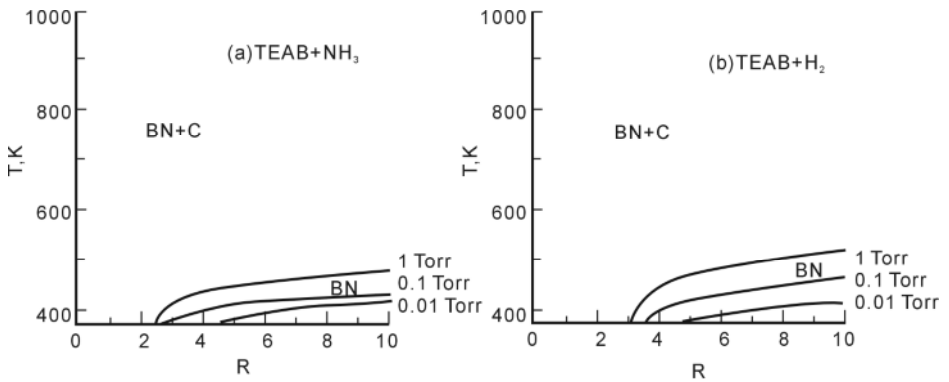


Figure D.27. CVD phase diagram of (a) TEAB-NH₃ system and (b) TEAB-H₂ system, $R = X/TEAB, X = NH_3$ or H_2 [36] TEAB: $H_3B:N(C_2H_5)_3$

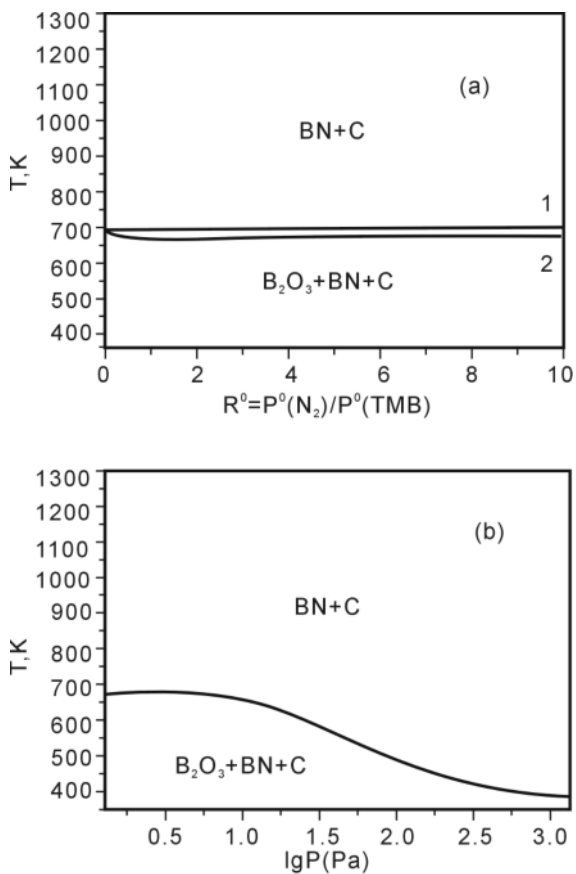


Figure D.28. CVD BC_xN_y from $B_3N_3H_3(CH_3)_3-N_2$ system, TMB: methylborazine, $B_3N_3H_3(CH_3)_3$, 1: $P_{total} = 1.33$ Pa, 2: $P_{total} = 13.3$ Pa [37]

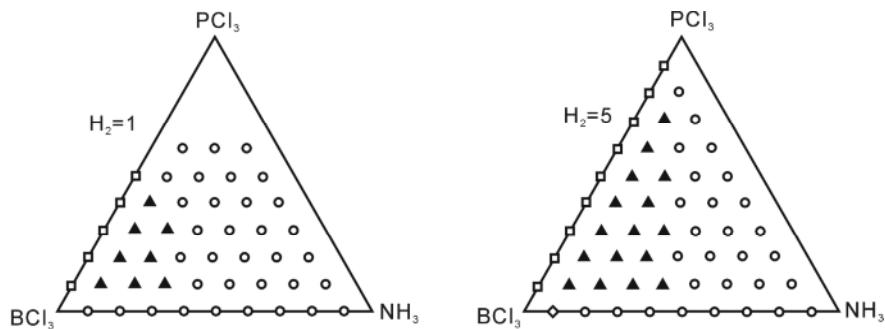


Figure D.29. Condensed species in B-N-Cl-H-P system (973 K, 10 Torr, $H_2 = 1$ mol and 5 mol, no O_2 , \circ : BN, \diamond : B+BN, \square : BP, \blacktriangle : BN+BP) [38]

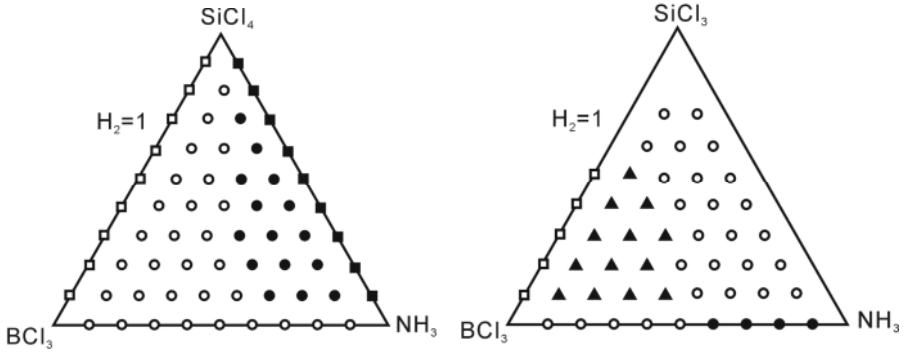


Figure D.30. Condensed species in the B-N-Cl-H-Si system (973 K, 10 Torr, $H_2 = 1$ mole, no O_2 , \circ : BN, \square : SiB_{14} , \bullet : $BN+Si_3N_4$, \blacksquare : Si_3N_4) [38]

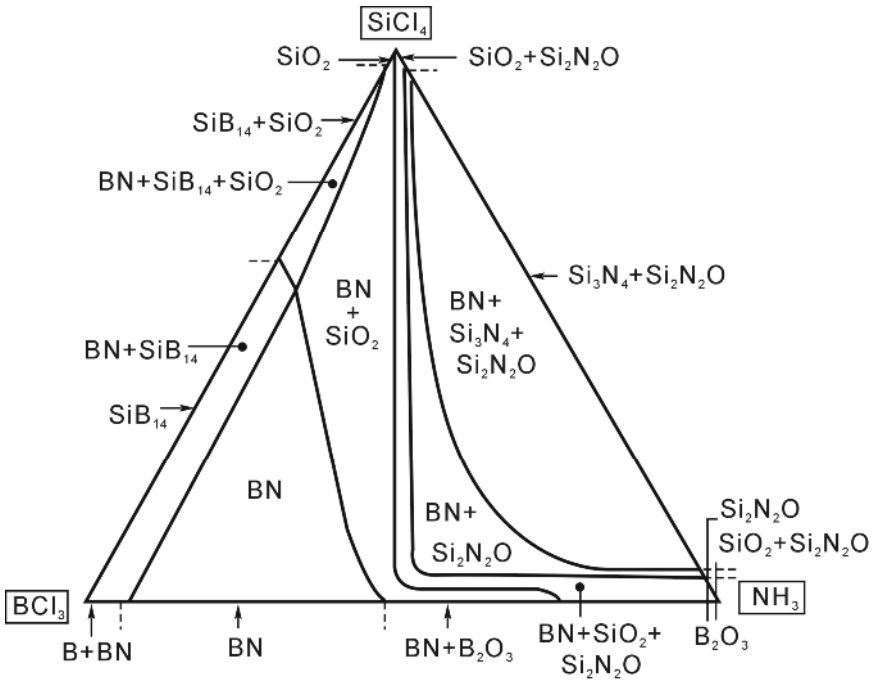


Figure D.31. CVD phase diagram of B-N-Cl-H-Si-O system ($T=973$ K, $P=10$ Torr, $H_2=1$ mol, $O_2 = 0.01$ mol) [38]

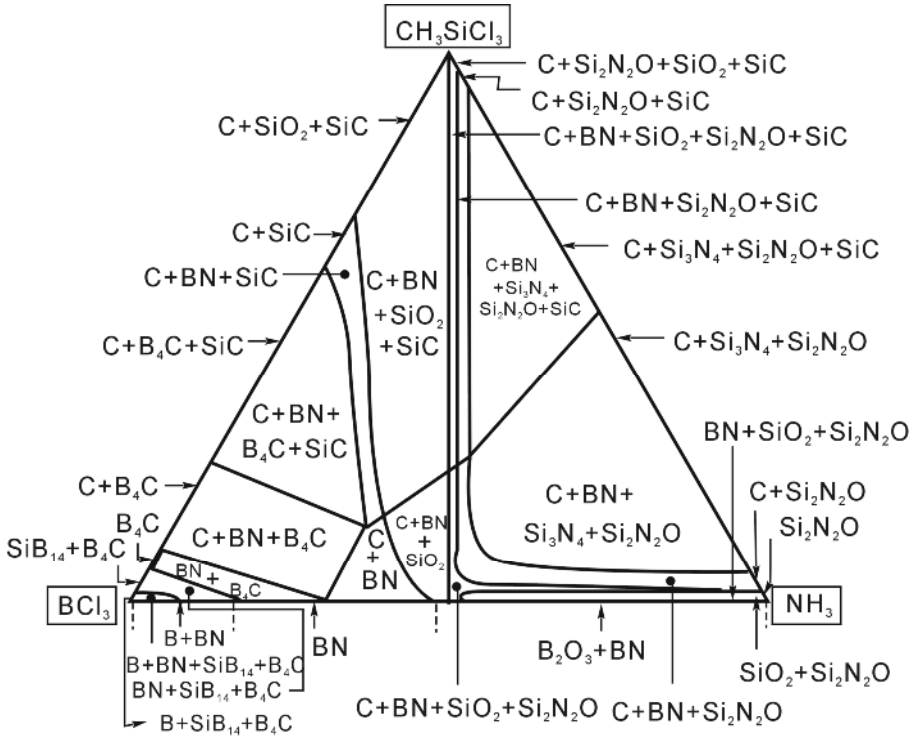


Figure D.32. CVD phase diagram of B-N-Cl-H-Si-O-C system ($T = 973$ K, $P = 10$ Torr, $H_2 = 5$ mol, $O_2 = 0.01$ mol) [38]

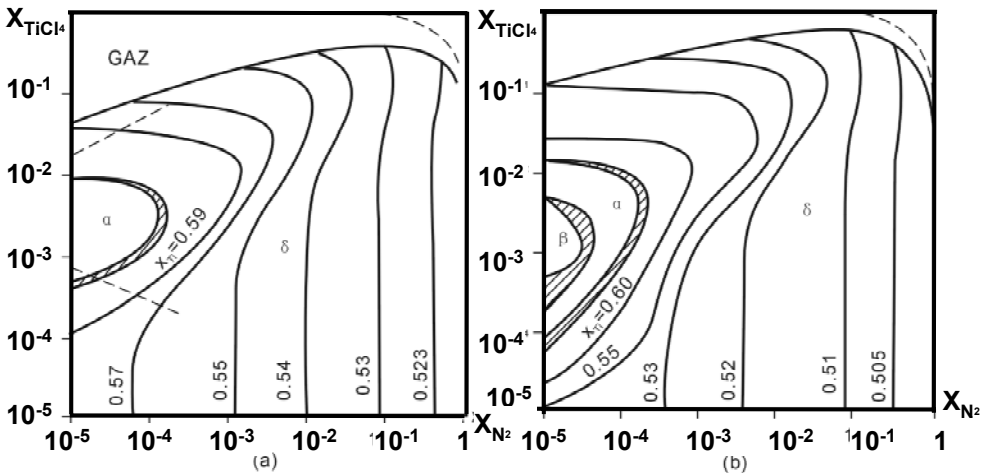


Figure D.33. CVD TiN diagram of $TiCl_4$ - N_2 system at 1900 K: (a) 5×10^{-3} atm, (b) 1 atm [39]

D.4 Chemical Vapour Deposition Phase Diagrams for Oxides

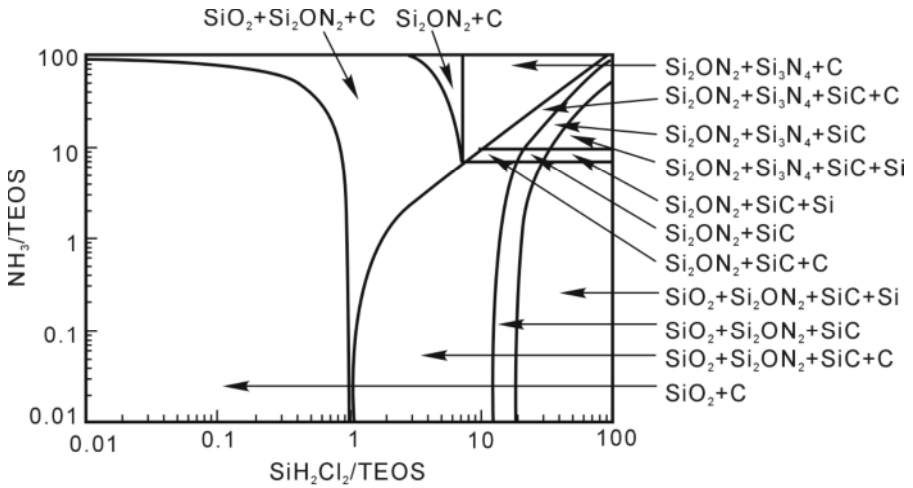


Figure D.34. CVD phase diagram of TEOS-SiH₂Cl₂-NH₃ system at 710°C, 300 Torr [40] TEOS: Si(OC₂H₅)₄

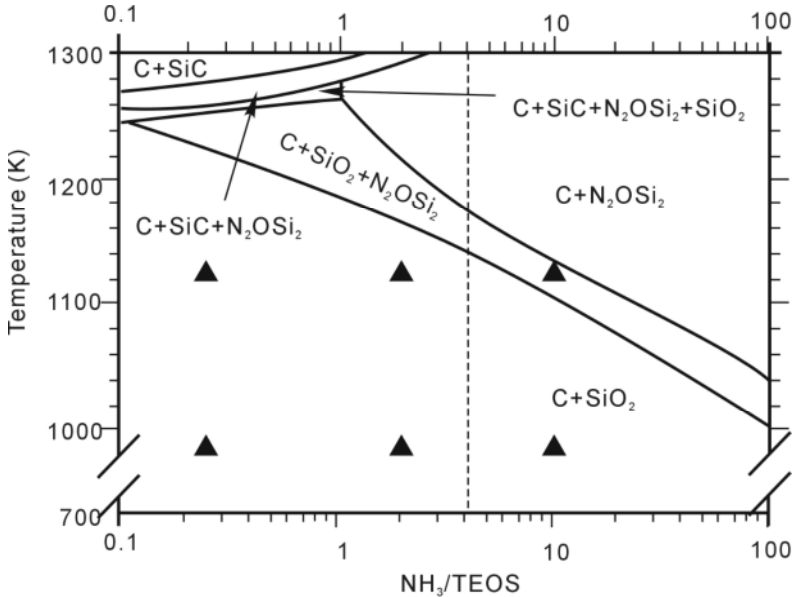


Figure D.35. CVD phase diagram of TEOS-NH₃ [41], TEOS: Si(OC₂H₅)₄

D.5 Chemical Vapour Deposition Phase Diagrams for Silicides

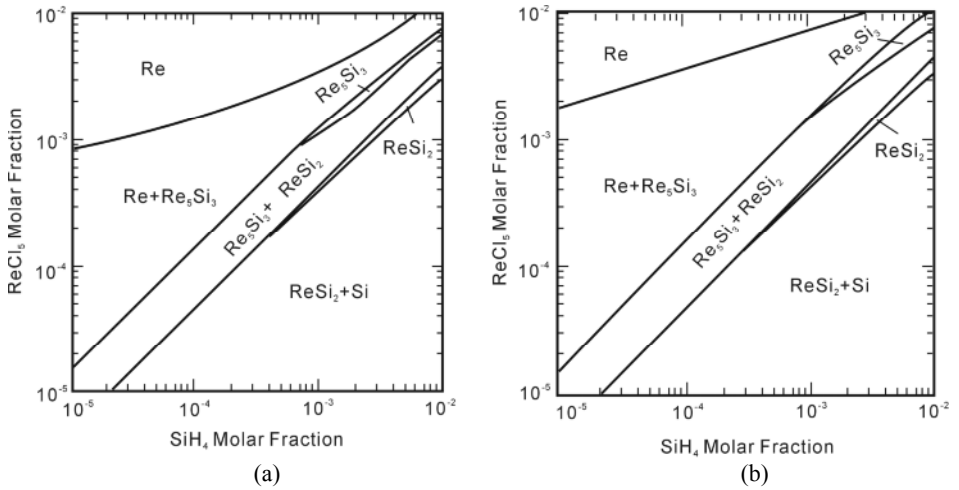


Figure D.36. CVD phase diagram of ReCl_5 - SiH_4 -Ar system at 9 Torr, $X_{\text{Ar}} = 0.9$ versus SiH_4 and ReCl_5 mol fraction at (a) 923 K and (b) 1073 K [42]

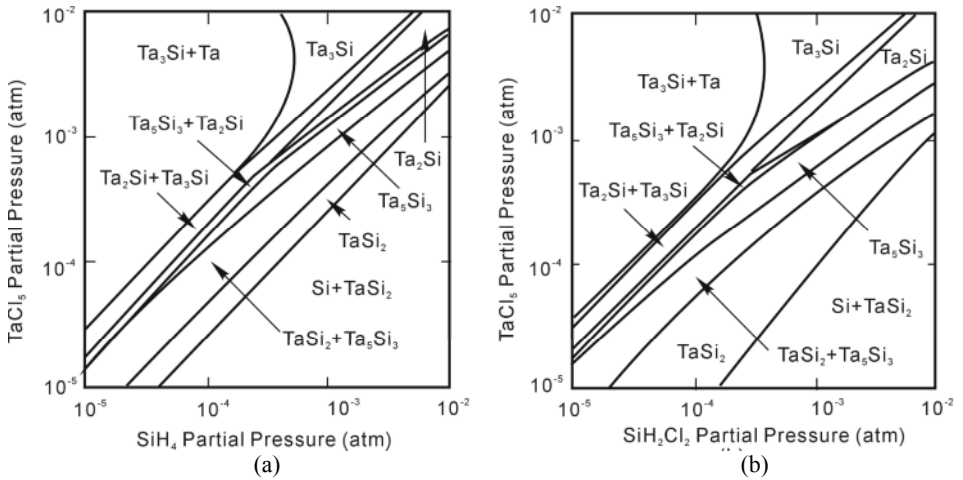


Figure D.37. CVD phase diagram of (a) TaCl_5 - SiH_4 -Ar- H_2 system and (b) TaCl_5 - SiH_2Cl_2 -Ar- H_2 system at 1000 K, $P_{\text{total}} = 1$ atm, $P_{\text{Ar}} = 0.9$ atm, $P_{\text{H}_2} = 0.1 - P_{\text{TaCl}_5} - P_{\text{SiH}_4}$ [43]

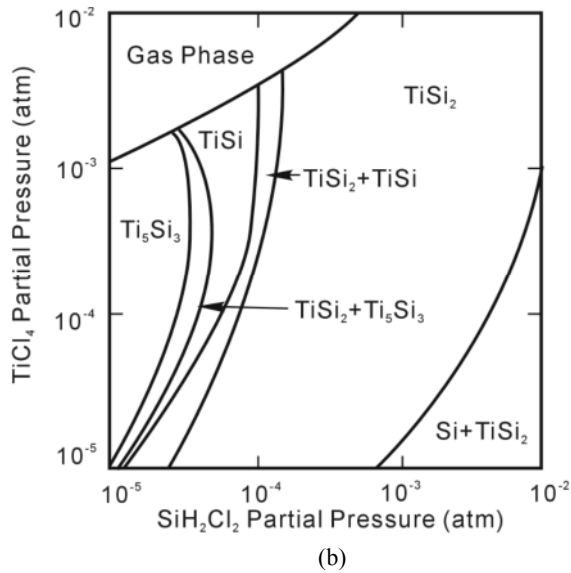
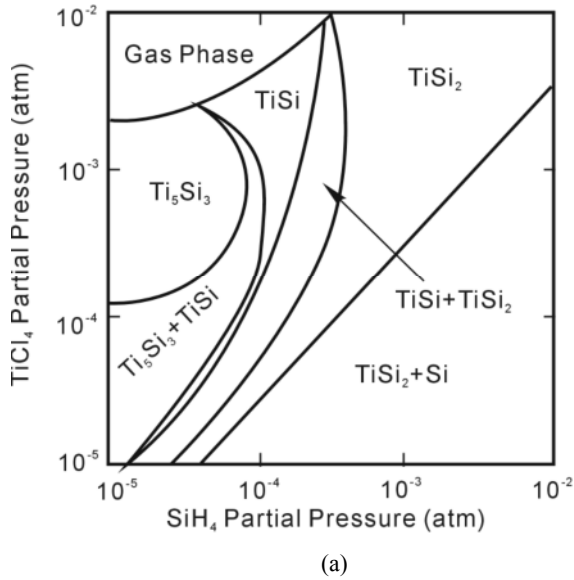
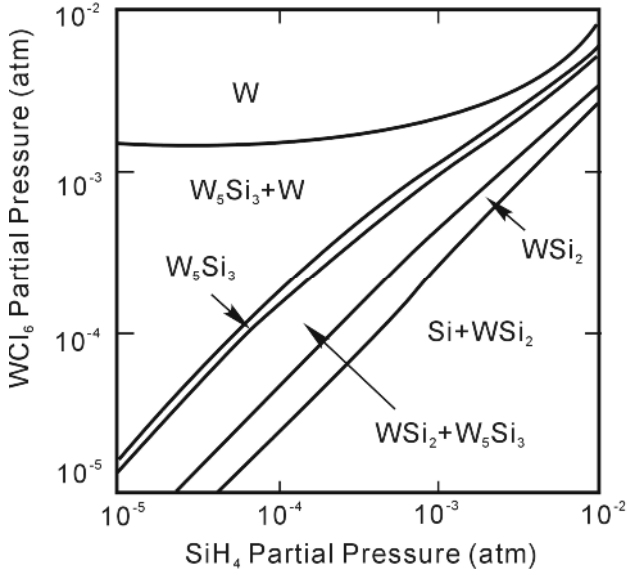
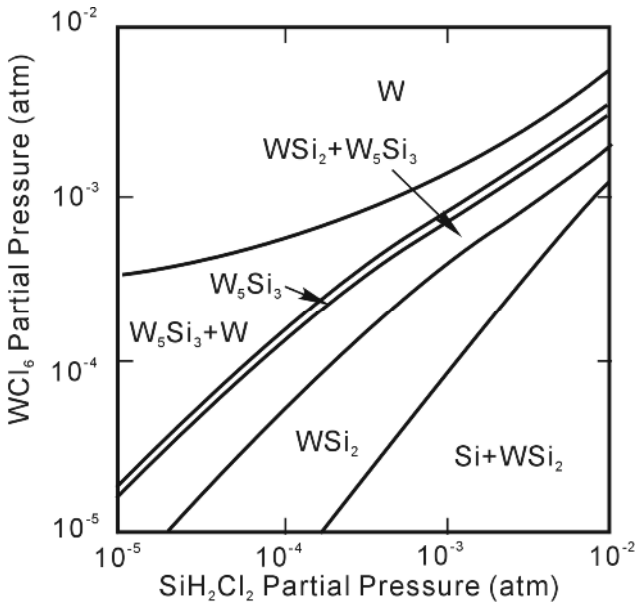


Figure D.38. CVD phase diagram of (a) $\text{TiCl}_4\text{-SiH}_4\text{-Ar-H}_2$ system and (b) $\text{TiCl}_4\text{-SiH}_2\text{Cl}_2\text{-Ar-H}_2$ system at 1000 K, $P_{total} = 1 \text{ atm}$, $P_{Ar} = 0.9 \text{ atm}$, $P_{H_2} = 0.1 - P_{TiCl_4} - P_{SiH_4}$ [43]



(a)



(b)

Figure D.39. CVD phase diagram of (a) WCl_6 - SiH_4 -Ar- H_2 system and (b) WCl_6 - SiH_2Cl_2 -Ar- H_2 system at 1000 K, $P_{\text{total}} = 1$ atm, $P_{\text{Ar}} = 0.9$ atm, $P_{\text{H}_2} = 0.1 - P_{\text{WCl}_6} - P_{\text{SiH}_4}$ [43]

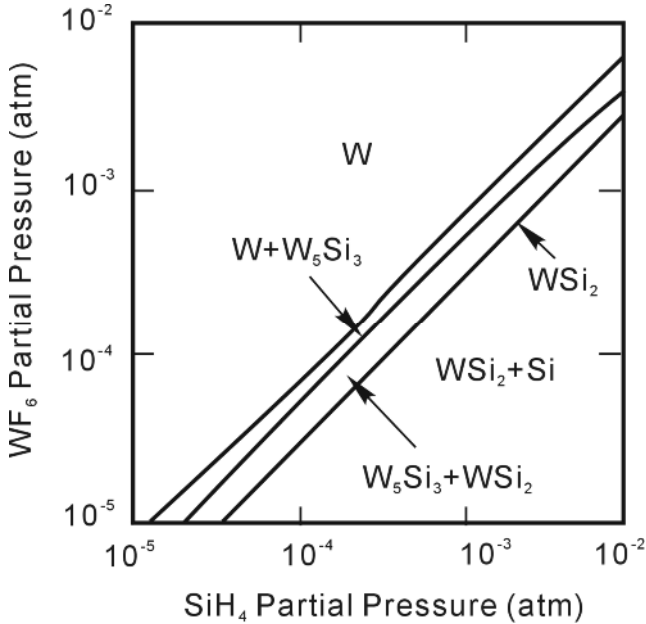


Figure D.40. CVD phase diagram of WF_6 - SiH_4 -Ar- H_2 system at 1000 K, $P_{\text{total}} = 1 \text{ atm}$, $P_{\text{Ar}} = 0.9 \text{ atm}$, $P_{\text{H}_2} = 0.1 - P_{\text{WF}_6} - P_{\text{SiH}_4}$ [43]

References

- [1] Ziko JK (1988) Metal-organic chemical vapour deposition: technology and equipment, In Schuergraf KK (ed) Handbook of thin film deposition processes and techniques, Noyes, Park Ridge, NJ, pp234–269
- [2] Kuech TF, Jensen KF (1991) OMVPE of compound semiconductors. In: Vossen JL and Kern W (eds) Thin film processes II, Academic, New York, pp369–442
- [3] Bessonov AA, Morozova NB, Gelfond NV, Semyannikov PP, Trubin SV, Shevtsov YV, Shubin YV, Igumenov IK (2007) Dimethylgold(III) carboxylates as new precursors for gold CVD, Surf Coat Technol, vol 201, pp9099–9103
- [4] Drozov AA, Troyanov SI, Kuzmina NP, Martyneko LI, Alikhanyan AS, Malkerova IP (1993) Synthesis and properties of barium diketonates as precursors for MOCVD. J Phys IV, 2, C-379–384
- [5] Fulyigin VN, Kaul AR, Pozigun SA (1993) Effect of CVD process parameters on phase and chemical composition of BSCCO thin film. J Phys IV, 2, C3-361–366
- [6] Shapiro ZM (1995) Iodide-decomposition process for production of zirconium. In: Lustman B and Kerze F Jr (eds) The metallurgy of zirconium. McGraw-Hill, New York, pp135–215
- [7] Shelton SM (1995) Zirconium production method. In: Lustman B and Kerze F Jr (eds) The metallurgy of zirconium. McGraw-Hill, New York, pp59–101

- [8] Morozova NB, Zharkova GJ, Semyannikov PP, Sysoev SV, Igumenov IK, Fedotova NE, Gelfond NV (2001) Vapor pressure of precursors for CVD on the base of platinum group metals. *J de Physique IV*, 11, Pr3-609–616
- [9] Morozova NB, Gelfond NV, Semyannikov PP, Trubin SV, Igumenov IK, Fabra LG (2003) Thermal properties of Ir(I) precursors: acetylacetonato (1,5-cyclooctadiene) iridium (I) and (methylcyclopentadienyl)(1,5-cyclooctadiene) iridium (I). In: Allendorf MD, Maury F, Teyssandier F (eds) Proceedings of 16th international symposium on chemical vapor deposition/ Jointly held with the Euro CVD-14, Electrochemical Society, Pennington, NJ, pp120–127
- [10] Gmehling B, Diesne G, Hohenman K, Emig G (1997) MOCVD of Noble Metal on Micro Fibers. In: Allendorf MD, Bernard C (eds) Proceeding of 14th international and Euro CVD-11 conference on chemical vapor deposition, Electrochemical Society, Pennington, NJ, pp600–607
- [11] Feurer R, Reynier A, Serp P, Kalck P, Morancho R (1995) OMCVD on fluidized divided substrates: a potential method for the preparation of catalysts. *J de Physique IV*, 5, C-1037–1043
- [12] Van Der Vis MGM, Cordfuke EHP, Konings RJM (1995) The thermodynamic properties of tetraethoxysilane (TEOS) and an infrared study of its thermal decomposition, vapor pressure of TEOS. *J de Physique IV*, 5, C5-75–82
- [13] Sone H, Kaneko T, Miyakawa N (2000) In situ measurements and growth kinetics of silicon carbide chemical vapor deposition from methyltrichlorosilane. *J Cryst Growth* 219:245–252
- [14] van Mol AMB, de Croon MHJM, Spee CIMA, Schouten JC (1999) Kinetic mechanism of the decomposition of dimethyltin dichloride. *J de Physique IV*, 9, Pr8-165–172
- [15] Huchet G, Teyssandier F (1990) Crystalline TiC obtained at 700 °C by OMCVD. In: Spear KE, Cullen GW (eds) Proceedings of the 11th international conference on chemical vapour deposition. Electrochemical Society, Pennington, NJ, pp703–709
- [16] Pulver M, Wahl G, Scheytt H, Sommer M (1993) Deposition of ZrO₂ and Y₂O₃-stabilized ZrO₂ from-diketonates. *J de Physique IV*, 2, C3-305–312
- [17] Silicone Research Group in Chengguang Institute of Chemical Engineering (1986) Silicone monomer and polymer. Chemical Industry Press, Beijing
- [18] Vandembulke L and Leparoux M (1995) Silicon and boron containing components by CVD and CVI for high temperature ceramic composites, *J de Physique*, 5, C5-735–751
- [19] Golda E M, Gallios B (1992) Chemical vapor deposition of multiphase boron-carbon-silicon ceramics. In: Besmann TM, Gallois BM, Warren JW (eds) Chemical vapor deposition of refractory metals and ceramics II. Materials Research Society, Pittsburgh, PA, pp167–172
- [20] Spear KE, Dirckx RR (1990) Predicting the chemistry in CVD system, In: Besmann TM, Gallois BM (eds) Chemical vapor deposition of refractory metals and ceramics. Materials Research Society, Pittsburgh, PA, pp19–30
- [21] Pierson JF, Belmonte T, Michel H (2001) Thermodynamic and experimental study of low temperature ZrB₂ chemical vapor deposition. *J de Physique IV*, 11, Pr3-85–91
- [22] Maury F, Gueroudji L, Vahlas C, Abisset S, Pelletier L (1997) Carbon free Cr metal thin film deposition at low temperature by MOCVD. In: Allendorf MD, Bernard C (eds) Proceedings of the 14th International Conference on Chemical Vapor Deposition/Jointly held with the Euro CVD-11. Electrochemical Society, Pennington, NJ, pp944–951
- [23] Schuster F, Schouler MC, Bernard C, Maury F, Morancho R, Nowak JF (1990) Thermodynamic and experimental study of Cr-N-C MOCVD coatings. In Spear KE,

- Cullen GW (eds) Proceedings of the 11th international conference on chemical vapour deposition. Electrochemical Society, Pennington, NJ, pp113–119
- [24] Stinton DP, Lackey WJ, Lauf RJ, Besmann TM (1984) Fabrication of ceramic-ceramic composites by chemical vapour deposition, *Ceram Eng Sci Proc* 5:668–676
- [25] Lowden RA, More KL, Besmann TM, James RD (1990) Microstructural characterization of multiphase coatings produced by chemical vapour deposition. In: Besmann TM, Gallois BM (eds) Chemical vapor deposition of refractory metals and ceramics. Materials Research Society, Pittsburgh, PA, pp159–165
- [26] Sourdiaucourt P, Derre A, David P, Delhaes P (1997) Thermodynamic study of the hafnium-carbon system for hafnium carbide chemical vapour deposition. In: Allendorf MD, Bernard C (eds) Proceedings of the 14th international conference on chemical vapor deposition/Jointly held with the Euro CVD-11. Electrochemical Society, Pennington, NJ, pp31–39
- [27] Naslain R, Langlais F, Fedou R (1989) The CVI-processing of ceramic matrix composites. *J de Physique II*, C5, 191–207
- [28] Kingon AI, Lutz LJ, Liaw P, Davis RF (1983) Thermodynamic calculations for the chemical vapour deposition of silicon carbide. *J Am Ceram Soc* 66:558–566
- [29] Fainer NI, Kosinova ML, Rumyantsev YM, Kuznetsov FA (1999) RPECVD thin silicon carbonitride films using hexamethyldisilazane. *J de Physique IV*, 9, Pr8-769–775
- [30] Roels N, Platon F, Aubreton J, Desmaison J (1990) Chemical vapour deposition of silicon nitride: study of the interrelationships of experimental parameters, carbon content, oxidation and wear properties. In Spear KE, Cullen GW (eds) Proceedings of the 11th international conference on chemical vapor deposition. Electrochemical Society, Pennington, NJ, pp717–723
- [31] Touanen M, Teyssandier F, Ducarrior M (1989) Theoretical approach to chemical vapour deposition in the atomic system Ti-Si-C-Cl-H. *J Mater Sci Lett* 8:98–101
- [32] Goto T, Hirai T (1987) Preparation of SiC-TiC in-situ composites by chemical vapour deposition. In: Cullen GW (ed) Proceedings of the 10th international conference on chemical vapour deposition. Electrochemical Society, Pennington, NJ, pp1070–1079
- [33] Fitzsimmons M, Sarin V K (1995) Comparison of WCl₆-CH₄-H₂ and WF₆-CH₄-H₂ systems for growth of WC coatings. *Surf Coat Technol* 76-77:250–255
- [34] Ducarrior M, Salles P, Bernard C (1985) Thermodynamics of ZrC equilibrium condition calculated for deposition from a CH₄-ZrCl₄-H₂ gaseous mixture. *J Electrochem Soc* 132:704–706
- [35] Jorg A, Zimmermann E, Schierling M, Cremer R, Neuschütz D (1997) Constitution and deposition mechanism of hexagonal boron nitride formed by CVD from trimethylborazine. In: Allendorf MD, Bernard C (eds) Proceedings of the 14th international conference on chemical vapor deposition/Jointly held with the Euro CVD-11. Electrochemical Society, Pennington, NJ, pp504–511
- [36] Kosinova ML, Fainer NI, Rumyantsev YM, Golubenko AN, Kuznetsov FA (1999) LPCVD boron carbonitride films from triethylamine borane. *J de Physique IV*, 9, Pr8-915–921
- [37] Sulyaeva VS, Rumyantsev YM, Kosinova ML, Golubenko AN, Fainer NI, Kuznetsov FA (2007) Plasma enhanced chemical vapour deposition of BC_xN_y films prepared from N-trimethylborazine: modelling, synthesis and characterization, *Surf Coat Technol* 201:9009–9014
- [38] Leparoux M, Boussant Y, Vandenbulcke L (1997) Thermodynamic analyses of the chemical vapour infiltration in the B-N-Si and B-N-P systems. In: Allendorf MD, Bernard C (eds) Proceedings of the 14th international conference on chemical vapor

- deposition/Jointly held with the Euro CVD-11. Electrochemical Society, Pennington, NJ, pp496–503
- [39] Teyssandier F, Bernard C, Ducarrior M (1988) Thermodynamic and experimental study of CVD of non-stoichiometric titanium nitride from $TiCl_4$ - N_2 - H_2 mixtures. *J Mater Sci* 23:135–140
- [40] Vamvakas VE, Berjoan R, Schamm S, Davazoglou D, Vahlas C (2001) Low pressure chemical vapor deposition of silicon oxynitride films using tetraethylorthosilicate, dechlorosilane and ammonia mixtures. *J de Physique IV*, 11, Pr3-231–238
- [41] Vahlas C, Davazoglou D, Vamvacas VE, de Parseval P (1997) Thermochemistry and composition of LPCVD silicon oxides films grown from NH_3 /TEOS mixtures. In: Allendorf MD, Bernard C (eds) Proceedings of the 14th international conference on chemical vapor deposition/Jointly held with the Euro CVD-11. Electrochemical Society, Pennington, NJ, pp1175–1182
- [42] Dutron AM, Blanquet, Bourhila EN, Madar R, Bernard C (1995) A thermodynamic and experimental approach to $ReSi_2$ LPCVD. *Thin Solid Films* 259:25–31
- [43] Bernard C, Madar R, Paulear Y (1989) Chemical vapour deposition of refractory metal silicides for VLSI metallization. *Solid State Technol* 32:79–84

Appendix E Acknowledgment of Figures and Tables Adopted from Other Sources

- Figure 1.3b is reprinted from Materials Research Society, M J Buiting and A H Reader, Influence of impurities and microstructure on the resistivity of LPCVD titanium nitride films, in T M Besmann and B M Gallois editors Chemical vapour deposition of refractory metals and ceramic, pp. 199–204, 1990, with permission from Materials Research Society.
- Figure 1.3c is reprinted from Chemical Engineering Science, Vol. 54, H Komiyama, Y Shimogaki and Y Egashira, Chemical reaction engineering in the design of CVD reactors, pp. 1941–1957, 1999, with permission from Elsevier.
- Figure 1.4a is reprinted from Ultramet, SEM image of polished cross-section of Ultramet HfC/SiC coating showing layered structure, Picture of thin-wall rhenium chambers manufactured by chemical vapour deposition at Ultramet for tactical propulsion applications, with permission from Ultramet.
- Figure 1.4b is reprinted from Solid State Ionics, Vol. 141–142, R Naslain, R Pailler, X Bourrat, S Bertrand, F Heurtevent, P Dupel and F Lamouroux, Synthesis of highly tailored ceramic matrix composites by pressure-pulsed CVI, pp. 541–548, 2001, with permission from Elsevier.
- Figure 1.5 is reprinted from McGraw–Hill, Z M Shapiro, Iodide-deposition process for production of zirconium in B Lustman and F Kerze eds, The metallurgy of zirconium, pp. 135–215, 1995, with permission from McGraw–Hill
- Figure 1.6 is reprinted from Academic Press, M Ohring, The materials science of thin films, p. 148, 1992, with permission from Academic Press.
- Figure 1.7 is reprinted with kind permission from Springer London: The blue laser diode, 1997, pp. 13–169, S Nakamura and G Fasol.
- Figure 1.8a is reprinted from Ultramet, SEM image of polished cross-section of Ultramet HfC/SiC coating showing layered structure, Picture of thin-wall rhenium chambers manufactured by chemical vapour deposition at Ultramet for tactical propulsion applications, with permission from Ultramet.
- Figure 1.8b is reprinted from American Ceramic Society Bulletin, Vol. 72, B Haigis and M Pickering, CVD scaled up for commercial production of bulk SiC, pp. 74–78, 1993, with permission from Blackwell.
- Figure 1.9 is reprinted from Advanced Engineering Materials, Vol. 4, F Christin, Design, fabrication, and application of thermostructural composites (TSC) like C/C, C/SiC, and SiC/SiC composites, pp. 903–912, 2002, with permission from Wiley - VCH.
- Figure 1.10 is reprinted from Journal of American Ceramic Society, Vol. 73, A G Evans, Perspective on the development of high-toughness ceramics, pp. 187–206, 1990, with permission from Blackwell.
- Figure 1.11 is reprinted from American Ceramic Society Bulletin, Vol. 65, P J Laicq, G A Bernhart, M M Dauchier and J G Mace, SiC/SiC composite ceramics, pp. 336–338, 1986, with permission from Blackwell.
- Figure 1.12a is reprinted from Rare Metal Materials and Engineering, Vol. 34, J Z Li, L T Zhang, L F Cheng, Y D Xu and D X Li, investigation on interfacial zone in continuous fiber-reinforced ceramic composites, pp. 170–175, 2005, with permission from Xibei Youse Jinshu Yanjiuyuan.

- Figure 1.12b is reprinted from *Materials Science and Engineering: A*, Vol. 300, Y D Xu, L F Cheng, L T Zhang, H F Yin and X W Yin, Mechanical properties of 3D fiber reinforced C/SiC composites, pp. 196–202, 2001, with permission from Elsevier.
- Table 1.2 is reprinted from *Journal of American Ceramic Society*, Vol. 73, A G Evans, Perspective on the development of high-toughness ceramics, pp. 187–206, 1990, with permission from Blackwell.
- Figure 2.6 is reprinted from McGraw–Hill, N S Harris, *Modern vacuum practice*, pp. 72–85, 1989, with permission from McGraw–Hill.
- Figure 2.7 is reprinted from McGraw–Hill, N S Harris, *Modern vacuum practice*, pp. 72–85, 1989, with permission from McGraw–Hill.
- Figure 2.8 is reprinted from Chapman Hall, N T M Dennis and T A Heppell, *Vacuum system design*, 1968, with permission from Chapman Hall.
- Figure 2.9 is reprinted from Butterworth Heinemann, D Hucknall, *Vacuum technology and application*, 1991, with permission from Butterworth Heinemann
- Figure 2.10 is reprinted from Elsevier Science Publishers, 3rd edition, A Roth, *Vacuum technology*, 1990, with permission from Elsevier.
- Figure 2.11 is reprinted from Elsevier Science Publishers, 3rd edition, A Roth, *Vacuum technology*, 1990, with permission from Elsevier.
- Figure 2.12 is reprinted from McGraw–Hill, N S Harris, *Modern vacuum practice*, pp. 72–85, 1989, with permission from McGraw–Hill.
- Figure 2.19 is printed with kind permission from Springer London: The blue laser diode, 1997, pp. 36–37, S Nakamura and G Fasol, Figures 4.1 and 4.2.
- Table 2.3 is reprinted from: Butterworth Heinemann, D Hucknall, *Vacuum technology and application*, 1991, with permission from Butterworth Heinemann
- Table 2.6 is reprinted from Butterworth Heinemann, D Hucknall, *Vacuum technology and application*, 1991, with permission from Butterworth Heinemann
- Table 2.6 is reprinted from Chapman Hall, N T M Dennis and T A Heppell, *Vacuum system design*, 1968, with permission from Chapman Hall.
- Figure 3.5 is reprinted from *Journal de Physique IV*, Vol. 5, H J Boer, Mass flow controlled evaporation system, C5-961–966, 1995, with permission from EDP Science.
- Figure 3.6 is reprinted from *Journal de Physique IV*, Vol. 5, H J Boer, Mass flow controlled evaporation system, C5-961–966, 1995, with permission from EDP Science.
- Figure 3.7 is reprinted from The Electrochemical Society, K Kawahara, K Fukase, Y Inoue, E Taguchi and K Yoneda, CVD spinel on Si, in G W Cullen, ed, *Proceedings of the 10th International Conference on Chemical Vapor Deposition*, pp. 588–602, 1987, with permission from The Electrochemical Society.
- Figure 3.8 is reprinted from *American Ceramic Society Bulletin*, Vol. 70, A J Sherman, R H Tuffias and R B Kaplan, Refractory ceramic foams: a novel, new high-temperature structure, pp. 1025–1029, 1991, with permission from Blackwell.
- Figure 3.9 is reprinted from *The Trade & Technical Press*, 1st edition, I C J Benard, *Handbook of fluid metering*, p. 101, 1988, with permission from The Trade & Technical Press.
- Figure 3.10 is reprinted from *Journal de Physique IV*, Vol. 9, I H J Boer, Precision mass flow metering for CVD applications, Pr8-869–876, 1999, with permission from EDP Science.
- Figure 3.11a is reprinted from Chapman Hall, 4th revised edition, J Yarwood, *High vacuum technique: theory, practice and properties of materials*, p. 231, 1975, with permission from Chapman Hall.
- Figure 3.11b Reprinted from Van Nostrand Reinhold, R C Merrick, *Valve selection and specification guide*, 1991, with permission from Van Nostrand Reinhold.

- Figure 3.12 is reprinted from *Journal de Physique IV*, Vol. 2, K Brennfleck and H Reich, CVD of SiC in large coating vessels, C2-467–474, 1991, with permission from EDP Science.
- Figure 3.13 is reprinted from *Journal of Crystal Growth*, Vol. 102, D I Fotiadis and S Kieda, Transport phenomena in vertical reactors for metalorganic vapour phase epitaxy, pp. 411–470, 1990, with permission from Elsevier.
- Figure 3.14a is printed with kind permission from Springer Science+ Business Media: *Journal of Materials Science*, Chemical vapor-deposited silicon nitride Part 1 Preparation and some properties, Vol. 11, 1976, pp. 593–603, K Niihara and Toshio Hirai, Figure 2.
- Figure 3.14b is reprinted from Oxford University Press, 2nd edition, S A Campbell, *The science and engineering of microelectronic fabrication*, p. 340, 2001, with permission from Oxford University Press.
- Figure 3.18 is reprinted from Wiley, 5th edition, B R Munson, D F Young and T H Okiishi, *Fundamentals of fluid mechanics*, 2006, with permission from Wiley.
- Figure 3.20 is reprinted from Wiley, 5th edition, B R Munson, D F Young and T H Okiishi, *Fundamentals of fluid mechanics*, 2006, with permission from Wiley.
- Figure 3.21 is reprinted from Oxford University Press, 2nd edition, S A Campbell, *The science and engineering of microelectronic fabrication*, p. 340, 2001, with permission from Oxford University Press.
- Figure 3.22 is reprinted from Wiley, 5th edition, B R Munson, D F Young and T H Okiishi, *Fundamentals of fluid mechanics*, 2006, with permission from Wiley.
- Figure 3.23 is reprinted from Wiley, 5th edition, B R Munson, D F Young and T H Okiishi, *Fundamentals of fluid mechanics*, 2006, with permission from Wiley.
- Figure 3.24 is reprinted from *Vacuum*, Vol. 37, W G Baechler, Cryopumps for research and industry, p. 21–29, 1987, with permission from Elsevier.
- Figure 3.28 is reprinted from *Journal of Materials Research*, Vol. 13, Z W Pan, H L Li and L T Zhang, Laser synthesis and crystallization of nanocomposite Si₃N₄ Powder, pp. 1996–2002, 1998, with permission from Materials Research Society.
- Figure 3.29 is reprinted from *Journal of Materials Research*, Vol. 13, Z W Pan, H L Li and L T Zhang, Laser synthesis and crystallization of nanocomposite Si₃N₄ Powder, pp. 1996–2002, 1998, with permission from Materials Research Society.
- Figure 3.30 is reprinted from Specialty Material, www.specmaterials.com, with permission from Specialty Material.
- Figure 3.31 is reprinted from *Journal of American Ceramic Society*, Vol. 81, R T Bhatt and D R Hull, Strength-degrading mechanisms for chemically-vapor-deposited SCS-6 silicon carbide fibers in an argon environment, pp. 957–964, 1998, with permission from Blackwell.
- Figure 3.32 is printed with kind permission from Springer Science+ Business Media: *Journal of Materials Science*, A functionally gradient coating on carbon fiber for C/Al composites, Vol. 29, 1994, pp. 2641–2647, J K Yu, H L Li and B L Shang.
- Figure 3.33 is printed with kind permission from Springer Science+ Business Media: *Journal of Materials Science*, A functionally gradient coating on carbon fiber for C/Al composites, Vol. 29, 1994, pp. 2641–2647, J K Yu, H L Li and B L Shang.
- Figure 3.34 is reprinted from Materials Research Society, A W Moore, Facility for continuous CVD coating of ceramic fibers, in T M Besmann, B M Gallois and J W Warren eds, *Chemical vapour deposition of refractory metals and ceramics II*, pp. 269–274, 1992, with permission from Materials Research Society.
- Figure 3.35 is reprinted from *Materials Science and Engineering: R: Reports*, Vol. 53, C Vahlas, B G Caussat, P Serp and G N Angelopoulos, Principles and applications of CVD powder technology, pp. 1–72, 2006, with permission from Elsevier.

- Figure 3.36 is reprinted from *Materials Science and Engineering: R: Reports*, Vol. 53, C Vahlas, B G Caussat, P Serp and G N Angelopoulos, Principles and applications of CVD powder technology, pp. 1–72, 2006, with permission from Elsevier.
- Figure 3.37 is reprinted from *Journal of Nuclear Materials*, Vol. 376, S Ueta, J Aihara, A Yasuda, H Ishibashi, T Takayama and K Sawa, Fabrication of uniform ZrC coating layer for the coated fuel particle of the very high temperature reactor, pp. 146–151, 2008, with permission from Elsevier.
- Figure 3.38 is reprinted with kind permission from Springer Science+Business Media: *Journal of Materials Science*, Growth of beta-silicon carbide whiskers by the VLS process, Vol. 20, 1985, pp. 1160–1166, J V Milewski, F D Gac, J J Petrovic and S R Skaggs, Figures 1 and 6.
- Figure 3.39a is reprinted from *Carbon*, Vol. 29, S Motojima M Kawaguchi and K Nozaki, Preparation of coiled carbon fibers by catalytic pyrolysis of acetylene, and its morphology and extension characteristics, pp. 379–385, 1991, with permission from Elsevier.
- Figure 3.39b is reprinted from the Electrochemical Society, S Motojima, T Hamamoto, N Ueshima, Y Kojima and H Iwanaga, Preparation and properties of ceramic micro-coils by CVD process, in M D Allendorf and C Bernard eds, *Proceedings of the 14th international conference on chemical vapour deposition/jointly held with the EUROCV D-11*, pp. 433–430, 1997, with permission from the Electrochemical Society.
- Figure 3.40 is reprinted from *IEEE Publications*, Vol. 9, S S Shoup, S Shanmugham, D Cousins and A T Hunt, Low-cost combustion chemical vapour deposition of epitaxial buffer layers and superconductor, *IEEE Transactions on Applied Superconductivity*, pp. 2426–2429, 1999, with permission from IEEE.
- Figure 3.41a is printed with permission from Springer Science+Business Media: *Journal of Materials Science*, Monolithic material fabrication by chemical vapour deposition, Vol. 23, 1988, pp. 4331–4339, J S Goela and R L Taylor, Figure 2.
- Figure 3.41b is reprinted from *American Ceramic Society Bulletin*, Vol. 76, L Burn and R Haas, Silicon carbide, p. 52, 2000, with permission from Blackwell Publishing-Journals.
- Table 3.2 is reprinted from *Hemisphere*, N B Vargaftik, 1983, 2nd ed, *Handbook of physical properties of liquids and gases, pure substances and mixtures*.
- Table 3.3 is reprinted from *China Machine Press*, Beijing, S J Li, 1980, *Engineering fluid mechanics*.
- Table 3.4 is reprinted from Y Z Jiang, *Industrial electric furnaces*, Tsinghua University Press, Beijing, 1993.
- Table 3.4 is reprinted from V Paschkis and J Persson, *Industrial electric furnaces and appliances*, New York: Interscience Publishers, 1960.
- Table 3.5 is reprinted from R W Worrall and B G Liptak, *Thermocouples*, in G Liptak ed, *Temperature measurement*, Pennsylvania, Chilton, 1993.
- Table 3.6 is reprinted from *Wiley*, 5th edition, B R Munson, D F Young and T H Okiishi, *Fundamentals of fluid mechanics*, 2006, with permission from Wiley.
- Table 3.8 is reprinted from *Silicone research group in Chengguang Institute of Chemical Engineering*, *Silicone monomer and polymer*, Chemical Industry Press, Beijing, 1986.
- Table 3.9 is reprinted from *Journal de Physique IV*, Vol. 5, S Motojima, I Hasegawa and H Iwanaga, Vapour growth of micro-coiled ceramic fibres and their properties, C5-1061–1068, 1995, with permission from EDP Science.
- Table 3.10 is printed with permission from Springer Science+Business Media: *Journal of Materials Science*, Monolithic material fabrication by chemical vapour deposition, Vol. 23, 1988, pp. 4331–4339, J S Goela and R L Taylor, Figure 2.

- Table 3.11 is reprinted from American Ceramic Society Bulletin, Vol. 76, L Burn and R Haas, Silicon carbide, p. 52, 2000, with permission from Blackwell.
- Figure 4.1 is reprinted from Journal de Physique IV, Vol. 5, A G Davis, J H van Breda, P Moretto and J Ordelman, Development of TiN nano-composite coatings for wear resistance, C5-831–840, 1995, with permission from EDP Science.
- Figure 4.2 is reprinted from Journal of Crystal Growth, Vol. 116, H P Tang, L Vescan and H Luth, Equilibrium thermodynamic analysis of the Si-Ge-Cl-H system for atmospheric and low pressure CVD of $\text{Si}_{1-x}\text{Ge}_x$, pp. 1–14, 1992, with permission from Elsevier.
- Figure 4.3 is reprinted from Journal of American Ceramic Society, Vol. 68, G S Fischman and W T Petuskey, Thermodynamic analysis and kinetic implications of chemical vapour deposition of SiC from Si-C-Cl-H gas systems, pp. 185–190, 1985, with permission from Blackwell.
- Figure 4.4 is reprinted from Journal of American Ceramic Society, Vol. 68, G S Fischman and W T Petuskey, Thermodynamic analysis and kinetic implications of chemical vapour deposition of SiC from Si-C-Cl-H gas systems, pp. 185–190, 1985, with permission from Blackwell.
- Figure 4.5 is reprinted from Journal of American Ceramic Society, Vol. 66, A J Kuta and R F Davis, Thermodynamic calculations for the chemical vapor deposition of silicon nitride, pp. 551–558, 1983, with permission from Blackwell.
- Figure 4.6 is reprinted from Journal of American Ceramic Society, Vol. 66, A J Kuta and R F Davis, Thermodynamic calculations for the chemical vapor deposition of silicon nitride, pp. 551–558, 1983, with permission from Blackwell.
- Figure 4.7 is reprinted from Journal de Physique IV, Vol. 2, M Nadal, T Grenet and F Teyssandier, Titanium borides deposited by chemical vapor deposition thermodynamic calculation and experiments, C3-511–518, 1993, with permission from EDP Science.
- Figure 4.8 is reprinted from Journal of Electrochemical Society, Vol. 142, N Thomas, A M Dutron, C Vahlas, C Bernard and R Madar, Influence of hydrogen pressure on the properties of CVD tungsten silicide films, pp. 1608–1614, 1995, with permission from the Electrochemical Society.
- Figure 4.9 is reprinted from the Electrochemical Society, W J Lackey, A W Smith, D M Dillard and D J Twait, Co-deposition of dispersed phase ceramic composites, in G W Cullen, ed, Proceedings of the 10th international conference on chemical vapor deposition, pp. 1008–1027, 1987, with permission from the Electrochemical Society.
- Figure 4.10 is reprinted from Journal of Materials Research, Vol. 11, P D Mulpuri and V K Sarin, Synthesis of mullite coatings by chemical vapor deposition, pp. 1315–1324, 1996, with permission from Materials Research Society.
- Figure 4.11 is reprinted from Journal of Materials Research, Vol. 11, P D Mulpuri and V K Sarin, Synthesis of mullite coatings by chemical vapor deposition, pp. 1315–1324, 1996, with permission from Materials Research Society.
- Figure 4.12 is reprinted from Journal of Electrochemical Society, Vol. 141, G D Papanoulitis and S V Sotirchos, On the homogeneous chemistry of the thermal decomposition of methyltrichlorosilane: thermodynamic analysis and kinetic modeling, pp. 1599–1611, 1994, with permission from the Electrochemical Society.
- Figure 4.13 is reprinted from Journal of Electrochemical Society, Vol. 141, G D Papanoulitis and S V Sotirchos, On the homogeneous chemistry of the thermal decomposition of methyltrichlorosilane: thermodynamic analysis and kinetic modeling, pp. 1599–1611, 1994, with permission from the Electrochemical Society.
- Figure 4.14 is reprinted from Journal of Electrochemical Society, Vol. 141, G D Papanoulitis and S V Sotirchos, On the homogeneous chemistry of the thermal

- decomposition of methyltrichlorosilane: thermodynamic analysis and kinetic modeling, pp. 1599–1611, 1994, with permission from the Electrochemical Society.
- Figure 4.15 is reprinted from Materials Research Society, T H Osterheld and M D Allendorf, The decomposition of methyltrichlorosilane in hydrogen and helium, in B M Gallois, W Y Lee and M A Pickering eds, Chemical vapour deposition of refractory metals and ceramics III, pp. 27–32, 1995, with permission from Materials Research Society.
 - Figure 4.17 is reprinted from Journal of Crystal Growth, Vol. 155, F Loumagne, F Langlais and R Naslain, Experimental kinetic study of the chemical vapour deposition of SiC-based ceramics from CH₃SiCl₃/H₂ gas precursor, pp. 198–204, 1995, with permission from Elsevier.
 - Figure 4.18 is reprinted from Journal of Crystal Growth, Vol. 219, H Sone, T Kaneko and N Miyakawa, In situ measurements and growth kinetics of silicon carbide chemical vapor deposition from methyltrichlorosilane, pp. 245–252, 2000, with permission from Elsevier.
 - Figure 4.19 is reprinted from Institute of Physics Publishing, Bristol UK, Handbook of thin film process technology, L Vescan, Introduction and general discussion, in D A Glocker and S I Shah eds, 1995, B1.0:1-12, with permission from Institute of Physics Publishing, Bristol UK.
 - Figure 4.20 is reprinted from Wiley, A S Grove, Physics and technology of semiconductor devices, 1967, with permission from Wiley.
 - Table 4.1 is reprinted from Noyes Publications, L P Hunt, Silicon precursors: their manufacture and properties, in W C O'Mara, R B Herring and L P Hunt eds, Handbook of semiconductor silicon technology, pp. 1–33, 1990, with permission from Noyes.
 - Table 4.2 is reprinted from Materials Research Society, C Bernard and R Madar, Thermochemistry in CVD-on the choice of halide gas species, In: T M Besmann, B M Gallois and J W Warren eds, Chemical vapor deposition of refractory metals and ceramics II, pp. 3–15, 1992, with permission from Materials Research Society.
 - Table 4.3 is reprinted from Journal of Electrochemical Society, Vol. 141, G D Papasouliotis and S V Sotirchos, On the homogeneous chemistry of the thermal decomposition of methyltrichlorosilane: thermodynamic analysis and kinetic modeling, pp. 1599–1611, 1994, with permission from The Electrochemical Society, Inc.
 - Table 4.4 is reprinted from Journal of American Ceramic Society, Vol. 68, G S Fischman and W T Petuskey, Thermodynamic analysis and kinetic implications of chemical vapour deposition of SiC from Si-C-Cl-H gas systems, pp. 185–190, 1985, with permission from Blackwell.
 - Table 4.5 is reprinted from Journal of Electrochemical Society, Vol. 141, G D Papasouliotis and S V Sotirchos, On the homogeneous chemistry of the thermal decomposition of methyltrichlorosilane: thermodynamic analysis and kinetic modeling, pp. 1599–1611, 1994, with permission from the Electrochemical Society.
 - Table 4.6 is reprinted from Materials Research Society, S V Sotirchol and G D Papasouliotis, Kinetic modeling of the deposition of SiC from methyltrichlorosilane, in T M Besmann, B M Gallois and J W Warren eds, Chemical vapor deposition refractory metals and ceramics II, pp. 35–40, 1992, with permission from Materials Research Society.
 - Figure 5.1 is reprinted from Journal de Physique IV, Vol. 2, E Fitzer, W Fritz and G Schoch, The chemical vapor impregnation of porous solids, modeling of the CVI-process, C-2-143–150, 1991, with permission from EDP Science.
 - Figure 5.2 is reprinted from Advanced Engineering Materials, Vol. 4, F Christin, Design, fabrication and application of thermostructural composites TSC like C/C, C/SiC, and SiC/SiC composites, pp. 903–912, 2002, with permission from Wiley-VCH, Weinheim.

- Figure 5.6 is reprinted from the Electrochemical Society, R Fedou, F Langlais and R Naslain, On the modeling of the chemical vapor infiltration of SiC-based ceramics in a straight cylindrical pore, in K E Spear and G W Cullen, eds, Proceedings of the 11th international conference on chemical vapour deposition, pp. 513–524, 1990, with permission from the Electrochemical Society.
- Figure 5.9 is reprinted from Carbon, Vol. 23, S Marinkovic and S Dimitrijevic, Carbon/carbon composites prepared by chemical vapour deposition, pp. 691–699, 1985, with permission from Elsevier.
- Figure 5.10 is reprinted from Materials Sciences and Engineering: A, Vol. 300, Y D Xu, L F Cheng, L T Zhang, H F Yin and X W Yin, Mechanical properties of 3D fiber reinforced C/SiC composites, pp. 196–202, 2001, with permission from Elsevier.
- Figure 5.11 is reprinted from Materials Sciences and Engineering: A, Vol. 300, Y D Xu, L F Cheng, L T Zhang, H F Yin and X W Yin, Mechanical properties of 3D fiber reinforced C/SiC composites, pp. 196–202, 2001, with permission from Elsevier.
- Figure 5.12 is reprinted from Materials Sciences and Engineering: A, Vol. 300, Y D Xu, L F Cheng, L T Zhang, H F Yin and X W Yin, Mechanical properties of 3D fiber reinforced C/SiC composites, pp. 196–202, 2001, with permission from Elsevier.
- Figure 5.13 is reprinted from Materials Sciences and Engineering: A, Vol. 300, Y D Xu, L F Cheng, L T Zhang, H F Yin and X W Yin, Mechanical properties of 3D fiber reinforced C/SiC composites, pp. 196–202, 2001, with permission from Elsevier.
- Figure 5.14 is reprinted from Materials Sciences and Engineering: A, Vol. 300, Y D Xu, L F Cheng, L T Zhang, H F Yin and X W Yin, Mechanical properties of 3D fiber reinforced C/SiC composites, pp. 196–202, 2001, with permission from Elsevier.
- Figure 5.17 is reprinted from International Journal of Applied Ceramic Technology, Vol. 2, F A Christin, A global approach to fiber nD architectures and self-sealing matrices: from research to production, pp. 97–104, 2005, with permission from International Journal of Applied Ceramic Technology.
- Figure 5.18 is reprinted from Ceramic Engineering and Science Proceedings, Vol. 5, A J Caputo and W J Lackey, Fabrication of fiber-reinforced ceramic composites by chemical vapor infiltration, pp. 654–667, 1984, with permission from Wiley.
- Figure 5.19 is reprinted from Materials Research Society, D P Stinton, R A Lowden and T M Besmann, Fibre-reinforced tubular composites by chemical vapour infiltration, In T M Besmann, B M Gallois and J W Warren eds, Chemical vapour deposition of refractory metals and ceramics II, pp. 233–238, 1992, with permission from Materials Research Society.
- Figure 5.20 is reprinted from Journal of Nuclear Materials, Vol. 219, T M Besmann, J C McLaughlin and H T Lin, Fabrication of ceramic composites: forced CVI, pp. 31–35, 1995, with permission from Elsevier.
- Figure 5.21 is reprinted from Journal of Materials Research, S Vaidyaraman, W J Lackey, G B Freeman, P K Agrawal and M D Langman, Fabrication of carbon-carbon composites by forced flow-thermal gradient chemical vapour infiltration, pp. 1469–1477, 1995, with permission from Materials Research Society.
- Figure 5.24 is reprinted from Materials Research Society, C Y Tsai and S B Desu, Contribution of gas-phase reactions to the deposition of SiC by a forced-flow chemical vapor infiltration process, in T M Besmann, B M Gallois and J W Warren eds, Chemical vapour deposition of refractory metals and ceramics II, pp. 227–232, 1992, with permission from Materials Research Society.
- Figure 5.25 is reprinted from Journal of Nuclear Materials, Vol. 233–237, L L Snead, R H Jones, A Kohyama and P Fenici, Statue of silicon carbide composites for fusion, pp. 26–36, 1996, with permission from Elsevier.

- Figure 5.26 is reprinted from *Journal of Nuclear Materials*, Vol. 219, T M Besmann, J C McLaughlin and H T Lin, *Fabrication of ceramic composites: forced CVI*, pp. 31–35, 1995, with permission from Elsevier.
- Figure 5.28 is reprinted from *American Ceramic Society Bulletin*, Vol. 67, J D Buckley, *Carbon-carbon: a overview*, pp. 364–368, 1988, with permission from Blackwell.
- Figure 5.29 is reprinted from *Materials Sciences and Engineering: R: Reports*, Vol. 20, I Golecki, *Rapid vapor-phase densification of refractory composites*, pp. 37–124, 1997, with permission from Elsevier.
- Figure 5.30 is reprinted from *Carbon*, Vol. 44, J G Zhao, K Z Li, H J Li and C Wang, *The influence of thermal gradient on pyrocarbon deposition in carbon/carbon composites during the CVI process*, pp. 786–791, 2006, with permission from Elsevier.
- Figure 5.31 is reprinted from *Carbon*, Vol. 41, Z H Tang, D N Qu, J Xiong and Z Q Zou, *Effect of infiltration conditions on the densification behavior of carbon/carbon composites prepared by a directional-flow thermal gradient CVI process*, pp. 2703–2710, 2003, with permission from Elsevier.
- Figure 5.32 is reprinted from *Carbon*, Vol. 44, J G Zhao, K Z Li, H J Li and C Wang, *The influence of thermal gradient on pyrocarbon deposition in carbon/carbon composites during the CVI process*, pp. 786–791, 2006, with permission from Elsevier.
- Figure 5.33 is reprinted from *Carbon*, Vol. 44, J G Zhao, K Z Li, H J Li and C Wang, *The influence of thermal gradient on pyrocarbon deposition in carbon/carbon composites during the CVI process*, pp. 786–791, 2006, with permission from Elsevier.
- Figure 5.34 is reprinted from *Journal of American Ceramic Society*, Vol. 88, S F Tang, J J Deng, H F Du, W C Liu and K Yang, *Fabrication and microstructure of C/SiC composites using a novel heaterless chemical vapor infiltration technique*, pp. 3253–3255, 2005, with permission from Blackwell.
- Figure 5.35 is reprinted from *Journal of American Ceramic Society*, Vol. 88, S F Tang, J J Deng, H F Du, W C Liu and K Yang, *Fabrication and microstructure of C/SiC composites using a novel heaterless chemical vapor infiltration technique*, pp. 3253–3255, 2005, with permission from Blackwell.
- Figure 5.36 is reprinted from John Wiley & Sons, R B Bird, W E Stewart and E N Lightfoot, *Transport Phenomena*, p. 269, 1960, with permission from Wiley.
- Figure 5.37 is reprinted from US Patent, M Houdayer, J Spitz and D Tran-Van, *Process for the densification of a porous structure*, 1984, with permission from US Patent.
- Figure 5.38 is reprinted from *Carbon*, Vol. 39, D Rovillain, M Trinquescoste, E Bruneton, A Derre, P David and P Delhaes, *Film boiling chemical vapor infiltration: An experimental study on carbon/carbon composites materials*, pp. 1355–1365, 2001, with permission from Elsevier.
- Figure 5.39 is reprinted from *Carbon*, Vol. 39, D Rovillain, M Trinquescoste, E Bruneton, A Derre, P David and P Delhaes, *Film boiling chemical vapor infiltration: An experimental study on carbon/carbon composites materials*, pp. 1355–1365, 2001, with permission from Elsevier.
- Figure 5.40 is reprinted from *Carbon*, Vol. 39, D Rovillain, M Trinquescoste, E Bruneton, A Derre, P David and P Delhaes, *Film boiling chemical vapor infiltration: An experimental study on carbon/carbon composites materials*, pp. 1355–1365, 2001, with permission from Elsevier.
- Figure 5.41 is printed with kind permission from Springer Science+Business Media: *Journal of Materials Science*, *Reinforcement and antioxidizing of porous carbon by pulse CVI of SiC*, Vol. 24, 1989, pp. 3756–3762, K Sugiyama and E Yamamoto, Figure 1.
- Figure 5.44a is reprinted from *Solid State Ionics*, Vol. 141–142, R Naslain, R Pailler, X Bourrat, S Bertrand, F Heurtevent, P Dupel and F Lamouroux, *Synthesis of highly*

tailored ceramic matrix composites by pressure-pulsed CVI, pp. 541–548, 2001, with permission from Elsevier.

- Figure 5.44b is reprinted from *Composites Science and Technology*, Vol. 59, F Lamouroux, S Bertrand, R Pailler, R Naslain and M Cataldi, Oxidation-resistant carbon-fiber-reinforced ceramic-matrix composites, pp. 1073–1085, 1999, with permission from Elsevier.
- Figure 5.44c is reprinted from *Composites Science and Technology*, Vol. 59, F Lamouroux, S Bertrand, R Pailler, R Naslain and M Cataldi, Oxidation-resistant carbon-fiber-reinforced ceramic-matrix composites, pp. 1073–1085, 1999, with permission from Elsevier.
- Figure 5.45 is reprinted from *International Journal of Applied Ceramic Technology*, Vol. 2, F A Christin, A global approach to fiber nD architectures and self-sealing matrices: from research to production, pp. 97–104, 2005, with permission from *International Journal of Applied Ceramic Technology*.
- Figure 5.46 is reprinted from *Journal de Physique IV*, Vol. 2, P Reagan, Chemical vapor composites CVC, C3-541–548, 1993, with permission from EDP Science.
- Figure 5.47 is reprinted from *Journal de Physique IV*, Vol. 2, P Reagan, Chemical vapor composites CVC, C3-541–548, 1993, with permission from EDP Science.
- Table 5.1 is reprinted from *Materials Sciences and Engineering: R: Reports*, Vol. 20, I Golecki, Rapid vapor-phase densification of refractory composites, pp. 37–124, 1997, with permission from Elsevier.
- Table 5.2 is reprinted from *Carbon*, Vol. 35, E Bruneton, B Narcy and A Oberlin, Carbon-carbon composites prepared by a rapid densification process I: Synthesis and physico-chemical data, pp. 1593–1598, 1997, with permission from Elsevier.
- Table 5.3 is reprinted from *Carbon*, Vol. 35, E Bruneton, B Narcy and A Oberlin, Carbon-carbon composites prepared by a rapid densification process I: Synthesis and physico-chemical data, pp. 1593–1598, 1997, with permission from Elsevier.
- Figure 6.1 is reprinted from *Materials Research Society*, K E Spear and R R Dirks, Predicting the chemistry in CVD system in T M Besmann and B M Gallois eds, Chemical vapour deposition of refractory metals and ceramics, pp. 19–30, 1990, with permission from *Materials Research Society*.
- Figure 6.3a is reprinted from *Phys Met Metallogr (USSR)*, Vol. 28, B A Movchan and A V Demchishin, Investigations of the structure and properties of thick Ni, Ti, W, Al₂O₃ and ZrO₂ vacuum condensates, 1969, pp. 83–90
- Figure 6.3b is reprinted from *Journal of Vacuum Science & Technology*, Vol. 11, J A Thornton, Influence of apparatus geometry and deposition conditions on the structure and topography of thick sputtered coatings, pp. 666–669, 1974, with permission from *American Institute of Physics*.
- Figure 6.4 is reprinted from *Journal of Vacuum Science & Technology*, Vol. 11, J M Blocher, Structure/property/process relationships in chemical vapour deposition CVD, pp. 680–686, 1974, with permission from *American Institute of Physics*.
- Figure 6.5 is reprinted from *Chemical Physics Letters*, Vol. 299, Pan Z W Pan, S S Xie, B H Chang, L F Sun, W Y Zhou and G Wang, Direct growth of aligned open carbon nanotubes by chemical vapour deposition, pp. 97–102, 1999, with permission from Elsevier.
- Figure 6.7 is reprinted from *Materials Science and Engineering: R: Reports*, Vol. 53, C Vahlas, B G Caussat and P Serp, Principles and applications of CVD powder technology, pp. 1–72, 2006, with permission from Elsevier.
- Figure 6.8 is reprinted with kind permission from Springer Science+Business Media: *Journal of Materials Science*, Morphology and growth mechanism of silicon carbide

chemical vapor deposited at low temperature and normal atmosphere, Vol. 34, 1999, pp. 551–555, Y D Xu, L F Cheng, L T Zhang and W C Zhou.

- Figure 6.9 is reprinted with kind permission from Springer Science+Business Media: Journal of Materials Science, Morphology and growth mechanism of silicon carbide chemical vapor deposited at low temperature and normal atmosphere, Vol. 34, 1999, pp. 551–555, Y D Xu, L F Cheng, L T Zhang and W C Zhou.
- Figure 6.10 is reprinted with kind permission from Springer Science+Business Media: Journal of Materials Science, Chemical vapour-deposited silicon nitride Part 1 Preparation and some properties, Vol. 11, 1976, pp. 593–603, K Niihara and T Hirai.
- Figure 6.11 is reprinted with kind permission from Springer Science+Business Media: Journal of Materials Science, Chemical vapour-deposited silicon nitride Part 1 Preparation and some properties, Vol. 11, 1976, pp. 593–603, K Niihara and T Hirai.
- Figure 6.12 is reprinted with kind permission from Springer Science+Business Media: Journal of Materials Science, Chemical vapour-deposited silicon nitride Part 1 Preparation and some properties, Vol. 11, 1976, pp. 593–603, K Niihara and T Hirai.
- Figure 6.13b is reprinted from Journal of American Ceramic Society, Vol. 47, L F Coffin, Structure-property relations for pyrolytic graphite, pp. 473–478, 1964, with permission from Blackwell.
- Figure 6.14 is reprinted from Chemical Engineering Science, Vol. 54, H Komiyama, Y Shimogaki and Y Egashira, Chemical reaction engineering in the design of CVD reactors, pp. 1941–1957, 1999, with permission from Elsevier.
- Figure 6.15 is reprinted from Chemical Engineering Science, Vol. 54, H Komiyama, Y Shimogaki and Y Egashira, Chemical reaction engineering in the design of CVD reactors, pp. 1941–1957, 1999, with permission from Elsevier.
- Figure 6.16 is reprinted from Journal of American Ceramic Society, Vol. 74, L S Hong and H Komiyama, Chemical vapor deposition of CuO_x films by CuI and O_2 : Role of cluster formation on film morphology, pp. 1597–1604, 1991, with permission from Blackwell.
- Figure 6.17 is reprinted from Taylor & Francis Group, K J Huttinger, Fundamentals of chemical vapour deposition in hot wall reactors, in P Delhaes ed, Fibres and Composites, pp. 75–86, 2003, with permission from Taylor & Francis.
- Figure 6.18 is reprinted from Carbon, Vol. 41, Z J Hu, W G Zhang, K J Huttinger, B Reznik and D Gerthsen, Influence of pressure, temperature and surface area/volume ratio on the texture of pyrolytic carbon deposited from methane, pp. 749–758, 2003, with permission from Elsevier.
- Figure 6.19 is reprinted from Carbon, Vol. 41, Z J Hu, W G Zhang, K J Huttinger, B Reznik and D Gerthsen, Influence of pressure, temperature and surface area/volume ratio on the texture of pyrolytic carbon deposited from methane, pp. 749–758, 2003, with permission from Elsevier.
- Figure 6.20 is reprinted from Chemical Engineering Science, Vol. 54, H Komiyama, Y Shimogaki and Y Egashira, Chemical reaction engineering in the design of CVD reactors, pp. 1941–1957, 1999, with permission from Elsevier.
- Figure 6.21 is reprinted with kind permission from Springer Science+Business Media: Journal of Materials Science, Characterization and properties of controlled nucleation thermochemical deposition CNTD-silicon carbide, Vol. 15, 1980, pp. 2183–2191, S Dutta, R W Rice, H C Graham and M C Mendiratta.
- Figure 6.22 is reprinted with kind permission from Springer Science+Business Media: Journal of Materials Science, Characterization and properties of controlled nucleation thermochemical deposition CNTD-silicon carbide, Vol. 15, 1980, pp. 2183–2191, S Dutta, R W Rice, H C Graham and M C Mendiratta.

- Figure 6.23 is reprinted from *Journal of Crystal Growth*, Vol. 35, W A Bryant, Producing extended area deposits of uniform thickness by a new chemical vapour deposition technique, pp. 257–261, 1976, with permission from Elsevier.
- Figure 6.24 is reprinted from *Journal of Crystal Growth*, Vol. 35, W A Bryant, Producing extended area deposits of uniform thickness by a new chemical vapour deposition technique, pp. 257–261, 1976, with permission from Elsevier.
- Figure 6.25 is reprinted from *Carbon*, Vol. 40, P Delhaes, Review: Chemical vapor deposition and infiltration processes of carbon materials, pp. 641–657, 2002, with permission from Elsevier.
- Figure 6.27 is reprinted from McGraw–Hill, A Mironer, *Engineering fluid mechanics*, pp. 287–288, 1979, with permission from McGraw–Hill.
- Figure 6.28 is reprinted from Wiley, 4th edition, B R Munson, D F Young and T H Okiishi, *Fundamentals of fluid mechanics*, 2002, with permission from Wiley.
- Table 6.1 is reprinted from Materials Research Society, K E Spear and R R Dirks, Predicting the chemistry in CVD system in T M Besmann and B M Gallois eds, *Chemical vapour deposition of refractory metals and ceramics*, pp. 19–30, 1990, with permission from Materials Research Society.
- Table 6.2 is reprinted from *Journal of the Electrochemical Society*, Vol. 137, K Watanabe and H Komiyama, Micro/macro cavity method applied to the study of the step coverage formation mechanism of SiO₂ films by LPCVD, pp. 1222–1227, 1990, with permission from *Journal of the Electrochemical Society*.
- Table 6.3 is reprinted from *Journal of Crystal Growth*, Vol. 35, W A Bryant, Producing extended area deposits of uniform thickness by a new chemical vapour deposition technique, pp. 257–261, 1976, with permission from Elsevier.
- Table 6.4 is reprinted from *Carbon*, Vol. 40, P Delhaes, Review: Chemical vapor deposition and infiltration processes of carbon materials, pp. 641–657, 2002, with permission from Elsevier.
- Figure D.1 is reprinted from *Journal de Physique IV*, Vol. 5, L Vandenbulke and M Leparoux, Silicon and boron containing components by CVD and CVI for high temperature ceramic composites, C5-735–751, 1995, with permission from EDP Science.
- Figure D.2 is reprinted from Materials Research Society, E M Golda and B Gallios, Chemical vapor deposition of multiphase boron-carbon-silicon ceramics, in T M Besmann, B M Gallois and J W Warren eds, *Chemical vapor deposition of refractory metals and ceramics II*, pp. 167–172, 1992, with permission from Materials Research Society.
- Figure D.3 is reprinted from Materials Research Society, K E Spear and R R Dirks, Predicting the chemistry in CVD system, in T M Besmann and B M Gallois eds, *Chemical vapor deposition of refractory metals and ceramics*, pp. 19–30, 1990, with permission from Materials Research Society.
- Figure D.4 is reprinted from *Journal de Physique IV*, Vol. 11, J F Pierson, T Belmonte and H Michel, Thermodynamic and experimental study of low temperature ZrB₂ chemical vapor deposition, Pr3-85–91, 2001, with permission from EDP Science.
- Figure D.5 is reprinted from *Journal de Physique IV*, Vol. 11, J F Pierson, T Belmonte and H Michel, Thermodynamic and experimental study of low temperature ZrB₂ chemical vapor deposition, Pr3-85–91, 2001, with permission from EDP Science.
- Figure D.6 is reprinted from the Electrochemical Society, F Maury, L Gueroudji, C Vahlas, S Abisset and L Pelletier, Carbon free Cr metal thin film deposition at low temperature by MOCVD, in M D Allendorf and C Bernard eds, *Proceedings of the 14th international conference on chemical vapor deposition/jointly held with the EUROCV D-11*, pp. 944–951, 1997, with permission from The Electrochemical Society.

- Figure D.7 is reprinted from the Electrochemical Society, F Schuster, M C Schouler, C Bernard, F Maury, R Morancho and J F Nowak, Thermodynamic and experimental study of Cr-N-C MOCVD coating, in K E Spear and G W Cullen eds, Proceedings of the 11th international conference on chemical vapour deposition, pp. 113–119, 1990, with permission from the Electrochemical Society.
- Figure D.8 is reprinted from Ceramic Engineering and Science Proceedings, Vol. 5, D P Stinton, W J Lackey, R J Lauf and T M Besmann, Fabrication of ceramic-ceramic composites by chemical vapor deposition, pp. 668–676, 1984, with permission from Wiley.
- Figure D.9 is reprinted from Materials Research Society, R A Lowden, K L More, T M Besmann and R D James, Microstructural characterization of multiphase coatings produced by chemical vapor deposition, In: T M Besmann and B M Gallois eds, Chemical vapor deposition of refractory metals and ceramics, pp. 159–165, 1990, with permission from Materials Research Society
- Figure D.10 is reprinted from the Electrochemical Society, P Sourdiaucourt, A Derre, P David and P Delhaes, Thermodynamics study of the hafnium-carbon system for hafnium carbide chemical vapor deposition, in M D Allendorf and C Bernard eds, Proceedings of the 14th international conference on chemical vapor deposition/jointly held with the EUROCV D-11, pp. 31–39, 1997, with permission from the Electrochemical Society.
- Figure D.11 is reprinted from the Electrochemical Society, P Sourdiaucourt, A Derre, P David and P Delhaes, Thermodynamics study of the hafnium-carbon system for hafnium carbide chemical vapor deposition, in M D Allendorf and C Bernard eds, Proceedings of the 14th international conference on chemical vapor deposition/jointly held with the EUROCV D-11, pp. 31–39, 1997, with permission from the Electrochemical Society.
- Figure D.12 is reprinted from the Electrochemical Society, P Sourdiaucourt, A Derre, P David and P Delhaes, Thermodynamics study of the hafnium-carbon system for hafnium carbide chemical vapor deposition, in M D Allendorf and C Bernard eds, Proceedings of the 14th international conference on chemical vapor deposition/jointly held with the EUROCV D-11, pp. 31–39, 1997, with permission from the Electrochemical Society.
- Figure D.13 is reprinted from Materials Research Society, R A Lowden, K L More, T M Besmann and R D James, Microstructural characterization of multiphase coatings produced by chemical vapor deposition, In: T M Besmann and B M Gallois eds, Chemical vapor deposition of refractory metals and ceramics, pp. 159–165, 1990, with permission from Materials Research Society
- Figure D.14 is reprinted from Ceramic Engineering and Science Proceedings, Vol. 5, D P Stinton, W J Lackey, R J Lauf and T M Besmann, Fabrication of ceramic-ceramic composites by chemical vapor deposition, pp. 668–676, 1984, with permission from Wiley.
- Figure D.15 is reprinted from Journal de Physique II, Vol. C5, R Naslain, F Langlais and R Fedou, The CVI-processing of ceramic matrix composites, pp. 191–207, 1989, with permission from EDP Science.
- Figure D.16 is reprinted from Journal of American Ceramic Society, Vol. 66, A I Kingon, L J Lutz, P Liaw and R F Davis, Thermodynamic calculations for the chemical vapor deposition of silicon carbide, pp. 558–566, 1983, with permission from Blackwell.
- Figure D.17 is reprinted from Journal de Physique IV, Vol. 9, N I Fainer, M L Kosinova, Y M Romyantsev and F A Kuznetsov, RPECVD thin silicon carbonitride films using hexamethyldisilazane, Pr8-769–775, 1999, with permission from EDP Science.
- Figure D.18 is reprinted from the Electrochemical Society, N Roels, F Platon, J Aubretton and J Desmaison, Chemical vapor deposition of silicon nitride: study of the interrelationships of experimental parameters, carbon content, oxidation and wear properties, in K E Spear and G W Cullen eds, Proceedings of the 11th International

Conference on Chemical Vapor Deposition, pp. 717–723, 1990, with permission from the Electrochemical Society.

- Figure D.19 is reprinted from *Journal of Materials Science Letters*, Vol. 8, M Touanen, F Teyssandier, and M Ducarrior, Theoretical approach to chemical vapour deposition in the atomic system Ti-Si-C-Cl-H, pp. 98–101, 1989, with permission from Chapman and Hall.
- Figure D.20 is reprinted from the Electrochemical Society, T Goto and T Hirai, Preparation of SiC-TiC in-situ composites by chemical vapour deposition, in G W Cullen ed, *Proceedings of the 10th international conference on chemical vapour deposition*, 1987, pp. 1070–1079, with permission from the Electrochemical Society.
- Figure D.21 is reprinted from *Surface and Coatings Technology*, Vol. 76–77, M Fitzsimmons and V K Sarin, Comparison of WC16-CH4-H2 and WF6-CH4-H2 systems for growth of WC coatings, pp. 250–255, 1995, with permission from Elsevier.
- Figure D.22 is reprinted from *Surface and Coatings Technology*, Vol. 76–77, M Fitzsimmons and V K Sarin, Comparison of WC16-CH4-H2 and WF6-CH4-H2 systems for growth of WC coatings, pp. 250–255, 1995, with permission from Elsevier.
- Figure D.23 is reprinted from *Surface and Coatings Technology*, Vol. 76–77, M Fitzsimmons and V K Sarin, Comparison of WC16-CH4-H2 and WF6-CH4-H2 systems for growth of WC coatings, pp. 250–255, 1995, with permission from Elsevier.
- Figure D.24 is reprinted from *Surface and Coatings Technology*, Vol. 76–77, M Fitzsimmons and V K Sarin, Comparison of WC16-CH4-H2 and WF6-CH4-H2 systems for growth of WC coatings, pp. 250–255, 1995, with permission from Elsevier.
- Figure D.25 is reprinted from *Journal of the Electrochemical Society*, Vol. 132, M Ducarroir, P Salles and C Bernard, Thermodynamics of ZrC equilibrium condition calculated for deposition from a CH4-ZrCl4-H2 gaseous mixture, pp. 704–706, 1985, with permission from the Electrochemical Society.
- Figure D.26 is reprinted from the Electrochemical Society, A Jorg, E Zimmermann, M Schierling, R Cremer and D Neuschutz, Constitution and deposition mechanism of hexagonal boron nitride formed by CVD from trimethylborazine, in M D Allendorf and C Bernard eds, *Proceedings of the 14th international conference on chemical vapor deposition/jointly held with the EUROCV D-11*, pp. 504–511, 1997, with permission from the Electrochemical Society.
- Figure D.27 is reprinted from *Journal de Physique IV*, Vol. 9, M L Kosinova, N I Fainer, Y M Romyantsev, A N Golubenko and F A Kuznetsov, LPCVD boron carbonitride films from triethylamine borane, Pr8-915–921, 1999, with permission from EDP Science.
- Figure D.28 is reprinted from *Surface & Coatings Technology*, Vol. 201, V S Sulyaeva, Y M Romyantsev, M L Kosinova, A N Golubenko, N I Fainer and F A Kuznetsov, Plasma enhanced chemical vapour deposition of BC_xN_y films prepared from N-trimethylborazine: modelling, synthesis and characterization, pp. 9009–9014, 2007, with permission from Elsevier.
- Figure D.29 is reprinted from the Electrochemical Society, M Leparoux, Y Boussant and L Vandenbulcke, Thermodynamic analyses of the chemical vapor infiltration in the B-N-Si and B-N-P system, in M D Allendorf and C Bernard eds, *Proceedings of the 14th international conference on chemical vapor deposition/jointly held with the EUROCV D-11*, pp. 496–503, 1997, with permission from the Electrochemical Society.
- Figure D.30 is reprinted from the Electrochemical Society, M Leparoux, Y Boussant and L Vandenbulcke, Thermodynamic analyses of the chemical vapor infiltration in the B-N-Si and B-N-P system, in M D Allendorf and C Bernard eds, *Proceedings of the 14th international conference on chemical vapor deposition/jointly held with the EUROCV D-11*, pp. 496–503, 1997, with permission from the Electrochemical Society.

- Figure D.31 is reprinted from the Electrochemical Society, M Leparoux, Y Boussant and L Vandenbulcke, Thermodynamic analyses of the chemical vapor infiltration in the B-N-Si and B-N-P system, in M D Allendorf and C Bernard eds, Proceedings of the 14th international conference on chemical vapor deposition/jointly held with the EUROCVD-11, pp. 496–503, 1997, with permission from the Electrochemical Society.
- Figure D.32 is reprinted from the Electrochemical Society, M Leparoux, Y Boussant and L Vandenbulcke, Thermodynamic analyses of the chemical vapor infiltration in the B-N-Si and B-N-P system, in M D Allendorf and C Bernard eds, Proceedings of the 14th international conference on chemical vapor deposition/jointly held with the EUROCVD-11, pp. 496–503, 1997, with permission from the Electrochemical Society.
- Figure D.33 is reprinted with kind permission from Springer Science+Business Media: Journal of Materials Science, Thermodynamic and experimental study of CVD of non-stoichiometric titanium nitride from $TiCl_4$ - N_2 - H_2 mixtures, Vol. 23, 1988, pp. 135–140, F Teyssandier, C Bernard and M Ducarrior.
- Figure D.34 is reprinted from Journal de Physique IV, Vol. 11, V E Vamvakas, R Berjoan, S Schamm, D Davazoglou and C Vahlas, Low pressure chemical vapor deposition of silicon oxynitride films using tetraethylorthosilicate, dechlorosilane and ammonia mixtures, Pr3-231–238, 2001, with permission from EDP Science.
- Figure D.35 is reprinted from the Electrochemical Society, C Vahlas, D Davazoglou, V E Vamvacas and P de Parseval, Thermochemistry and composition of LPCVD silicon oxides films grown from NH_3 /TEOS mixtures, in M D Allendorf and C Bernard eds, Proceedings of the 14th international conference on chemical vapor deposition/jointly held with the EUROCVD-11, pp. 1175–1182, 1997, with permission from the Electrochemical Society.
- Figure D.36 is reprinted from Thin Solid Films, Vol. 259, A M Dutron, E Blanquet, N Bourhila, R Madar and C Bernard, A thermodynamic and experimental approach to $ReSi_2$ LPCVD, pp. 25–31, 1995, with permission from Elsevier.
- Figure D.37 is reprinted from Solid State Technology, Vol. 32, C Bernard, R Madar and Y Paulear, Chemical vapour deposition of refractory metal silicides for VLSI metallization, pp. 79–84, 1989, with permission from Pennwell.
- Figure D.38 is reprinted from Solid State Technology, Vol. 32, C Bernard, R Madar and Y Paulear, Chemical vapour deposition of refractory metal silicides for VLSI metallization, pp. 79–84, 1989, with permission from Pennwell.
- Figure D.39 is reprinted from Solid State Technology, Vol. 32, C Bernard, R Madar and Y Paulear, Chemical vapour deposition of refractory metal silicides for VLSI metallization, pp. 79–84, 1989, with permission from Pennwell.
- Figure D.40 is reprinted from Solid State Technology, Vol. 32, C Bernard, R Madar and Y Paulear, Chemical vapour deposition of refractory metal silicides for VLSI metallization, pp. 79–84, 1989, with permission from Pennwell.
- Table B.2 is reprinted from Chemical Industry Press, Silicone Research Group, Edited by Chengguang institute of chemical engineering, Silicone monomer and polymer, page 93, 1986, with permission from Chemical Industry Press.

Index

A

A/V ratio, 216, 234, 235, 236, 237, 238
activation energy, 153, 156, 158, 237
additive method, 2, 3
adsorption, 2, 36, 104, 154, 155, 156, 157, 215, 236, 237
aero-engine, 10, 12, 76, 111, 174, 179, 180
amorphous deposit, 222, 226, 227
atmospheric pressure CVD, 76
Avogadro's law, 30
Avogadro's number, 30

B

Boltzmann's constant, 32, 33
bond energy, 151
boundary condition, 170, 184, 197, 251, 252, 253, 255, 258, 260
boundary layer, 2, 62, 63, 64, 66, 67, 68, 69, 83, 147, 159, 160, 161, 162, 165, 215, 221, 240, 244, 245, 246
Boyle's law, 29
bubbling, 82, 106, 168
buffer, 11, 117, 118

bulk diffusion, 219, 221
buoyancy, 65, 66, 91
butterfly valve, 88, 100

C

carbonyl, 7, 81
carrier gas, 77, 80, 82, 83, 106, 209
ceramic matrix composite, viii, 10, 13, 14, 17, 20, 21, 137, 161, 165, 166, 167, 174, 175, 179, 215
Chapman–Enskog theory, 56, 57
Charpy impact test, 177
chemical reaction controlled regime, 171
chemical trap, 79, 103, 105
chemical vapour composite, 208
chemical vapour deposition, 1, 16, 17, 20, 21, 31, 36, 77, 89, 120, 221, 222, 223, 224, 226, 227, 228, 229, 234, 241
chemical vapour infiltration, 21, 59, 76, 201
Clausius–Clapeyron equation, 69, 70
coating, 2, 3, 4, 11, 15, 38, 61, 76, 79, 88, 112, 113, 114, 115, 116, 117, 118, 119, 120, 121, 122, 129, 132, 134, 141, 142, 145,

159, 160, 161, 162, 165, 173,
184, 195, 218, 219, 238, 239, 261
co-deposition, 6, 132, 138, 140, 141,
142, 143, 145
coefficient of contraction, 96, 97
coefficient of discharge, 97
coefficient of velocity, 97
coiled fibre, 119, 120, 121, 122, 132,
134, 221, 222
cold trap, 79, 103, 104
cold wall CVD, 76
collision diameter, 56, 57
columnar structure, 219, 239, 240
combustion liner, 179
composite, vii, viii, ix, 11, 12, 20,
21, 115, 137, 142, 165, 167, 169,
172, 174, 175, 177, 179, 180,
187, 195, 207, 208, 209
compression ratio, 44, 45, 51, 100
concentration boundary layer, 68,
160, 161
concentration gradient, 8, 54, 55, 60,
159, 160, 161, 168, 170, 173,
185, 188, 221
conductance, 39, 40, 41, 100
cone structure, 226, 227
conformal coverage, 3
conical diffuser, 94, 96
continuous CVD, viii, 76, 110, 112,
114
continuum, 38, 63, 64

conversion efficiency, 102, 167, 173,
187, 190, 193, 200
coolant, 103, 104
cosine law, 35
criteria, 79
critical residence time, 229, 234
cryo-condensation, 103
cryo-sorption, 103
cryo-trapping, 103
CVD phase diagram, viii, 129, 134,
135, 136, 137, 138, 139, 140,
141, 143, 144, 145, 146, 148,
149, 150, 151, 152, 153, 154, 156
CVD system, viii, 1, 10, 38, 51, 52,
53, 62, 72, 75, 76, 77, 79, 89, 94,
95, 97, 98, 108, 121, 129, 132,
134, 135, 147, 238, 246, 248,
250, 251, 252, 254, 256, 258,
261, 262
cylinder model, 195, 196

D

Dalton's law of partial pressures, 30
Damkijhler number, 170, 185
delivery, 77, 79, 82, 83, 84, 85, 86,
89
depositing time, 76
desorption, 2, 154, 155, 159, 215
diffusion collision integral, 56
diffusivity, 55, 56, 57, 58, 60, 66, 67,
68, 161, 168, 169, 171, 250

dimensionless parameter, 63, 64, 66,
170, 184
direct measurement, 51
directional-flow TG-CVI, 192
distributor, 62, 77, 89, 93, 94, 95, 96,
181
drag coefficient, 244, 246
drag force, 61, 62, 63, 85, 243, 245,
246
droplet, 119
dry ice, 104, 105
dynamic fracture toughness, 177
dynamic viscosity, 55, 61, 64, 67,
161

E

elementary kinetic theory, 55, 57
elementary reaction, 231, 232, 235
energy system, 78
engineering design, 72
enthalpy, 69, 70, 130, 131, 147, 155
enthalpy of sublimation, 70
entropy, 130, 147
epitaxial growth, 76, 162, 221
equilibrium constant, 130, 134, 135,
155, 156
equilibrium constant approach, 135
exhaust cone, 179
exhaust pressure, 41, 42, 45, 100
exit, 62, 77, 89, 95, 96, 97, 99, 101,
103, 106

explosion limit, 107

F

Fick diffusion, 59, 60, 63, 64, 66, 67,
69, 171
Fick law, 55
flame stabilizer, 179
flaps, 179
flash method, 83
flow field, 247, 261
fluidized-bed CVD, 115
forced convection, 65, 91, 206
forced CVI, 16, 162, 165, 181
forced-flow CVI, 167
Fourier law, 55, 195, 197
fracture toughness, 14, 137, 174, 176
Frank–van der Merwe mode, 217
free convection, 65, 66, 91, 263
free molecular flow, 38, 64
free radical, 152

G

gas ballast, 46
gas constant, 30, 40, 69, 83, 135, 237
gas law, 29
gaseous precursor, 82, 109, 129,
165, 173
Gibbs free energy, 129, 130, 131,
132, 133, 134, 135, 136, 143,
145, 151, 162

Gibbs free energy minimisation,
135, 136
Gibbs phase rule, 134
grain boundary diffusion, 219
guidance tool, 265, 266

H

head loss coefficient, 95, 101, 102
heat capacity, 87, 130
heating element, 7, 89, 98, 99, 101,
103, 106, 168, 180, 181, 191,
194, 199, 200, 215
Hertz–Knudsen Law, 36
heterogeneous chemical reaction, 15,
147, 153, 154, 159, 215, 235, 236
high vacuum, 38, 42, 43, 45
high-temperature ceramic matrix, 20
high-temperature CVD, 76
homogeneous chemical reaction, 2,
15, 147, 151
Hot-wall continuous CVD, 114, 115
hydraulics, 61, 62
hydrodynamics, 61, 62

I

ideal gas, 29, 30, 94, 135
indirect measurement, 51, 52
inertial forces, 62, 65
initial condition, 259
injector, 77, 89, 92, 93, 114, 122,
181

intermediate, 39, 60, 113, 155, 156,
200, 217, 229, 230
intermediate flow, 39
intermolecular potential, 56
isothermal/isobaric CVI (I-CVI),
167
isotropic structure, 194
iterative, 259, 260

K

kinematic viscosity, 64, 66, 67, 68
kinetic theory, 29, 31, 55, 60
kinetics, viii, 61, 129, 147, 153, 154,
157, 158, 159, 162, 171, 172,
234, 235
Knudsen diffusion, 59, 60
Knudsen diffusivity, 60
Knudsen Law, 35
Knudsen number, 63
Kroll process, 8

L

Langmuir isotherm adsorption, 155
Langmuir–Hinshelwood isotherm,
157, 236
laser induced CVD, 10, 77
leak detection, 51
leakage, 38, 41, 44, 45, 51, 52, 53,
54, 106, 181
light emitting diodes (LEDs), 10
line-of-sight process, 3

liquid air, 104
 liquid immersion CVI (LI-CVI), 167
 liquid metal, 6, 67, 69, 111
 liquid nitrogen, 104
 liquid precursor, 69, 82, 83, 84, 85,
 86, 198, 199, 201, 202, 204
 loss coefficient, 93, 95, 96, 100, 102
 low pressure CVD, 76
 low vacuum, 45
 lowest pressure, 41, 44, 45, 47

M

mass conservation equation, 169
 mass flow controller, 78, 82, 85, 86,
 87, 194
 mass spectrometer, 53, 54, 57, 59,
 60, 63, 64, 65, 88, 152
 mass transfer rate constant, 160
 mass-to-charge ratio, 152
 Maxwell–Boltzmann distribution, 31
 mean free path, 31, 33, 34, 35, 38,
 55, 56, 60, 63
 mean velocity, 31, 32, 55, 65
 mechanical pump, 45, 46, 47, 49, 50,
 51
 medium vacuum, 38, 43
 mesh generation, 252, 254
 metal organic compound, 81
 metal-organic CVD (MOCVD), 10
 microstructure evolution, viii, 216
 micro-trench, 4, 238

mineral oil, 47
 minimum gas flow velocity, 116
 mixer, 82
 molecular flow, 39, 40
 morphology, 5, 119, 217, 220, 221,
 222, 223, 224, 226, 227, 228, 239
 most probable velocity, 32
 mullite, 144, 145
 multilayered coatings, 5

N

natural convection, 91, 92
 Navier–Stokes equation, 64, 257
 needle valve, 88, 109
 neutralisation reaction, 106
 Newton’s viscous law, 55

O

one-dimensional model, 169, 172,
 202
 overall model, 200, 206

P

pebble structure, 226
 perfect gas, 29, 30, 52, 69, 92, 130,
 203
 permeability, 61
 photo CVD, 10, 77
 physical vapour deposition, 1, 3, 216
 plasma-enhanced CVD, 10, 77
 polishability, 123

polycrystal growth, 221, 222
 porosity, 60, 61, 167, 173, 203
 porous media, 59, 61
 post-processing, 251, 261
 powder, 3, 21, 85, 108, 109, 110,
 112, 119, 123, 162, 223
 Prandtl number, 66, 67, 68
 pressure range, 38, 41, 42, 45, 51,
 158, 206, 236
 processing parameter, viii, 10, 29,
 76, 113, 123, 129, 147, 183, 185,
 190, 206, 207, 215, 216, 217,
 218, 234, 243
 processing variable, 216
 pulsed CVD · 76, 203, 241, 242, 243
 pulsed CVI (P-CVI), 167
 pump oil, 46, 47, 48, 100, 103, 105
 pumping speed, 41, 42, 45, 51, 106
 purification, 7, 76, 204
 pyrometer, 98

R

radical, viii, 148, 149, 150, 151, 152,
 153, 231, 232, 233
 reaction chamber, 1, 29, 30, 39, 43,
 46, 52, 53, 54, 62, 77, 78, 79, 80,
 82, 83, 85, 88, 89, 91, 92, 93, 97,
 98, 100, 103, 114, 115, 119, 121,
 129, 166, 173, 178, 181, 205,
 206, 226, 234, 241, 243, 244,
 250, 251, 258, 261, 262, 263, 265

reaction mechanism, 151, 229, 230,
 231, 232, 235
 reactive melt infiltration (RMI), 166
 reactor, 1, 12, 43, 66, 76, 77, 80, 82,
 83, 88, 89, 90, 91, 93, 98, 99,
 101, 103, 106, 108, 109, 110,
 111, 112, 113, 114, 115, 119,
 120, 121, 122, 132, 134, 178,
 188, 198, 199, 200, 206, 208, 209
 re-circulation, 83, 91, 92, 262, 264,
 265
 refractory metals and ceramics, 19
 residence time, 36, 100, 106, 153,
 173, 206, 216, 229, 230, 231,
 233, 234, 243, 244, 262, 263, 265
 retort, 77, 89, 90, 91, 92, 93, 98, 115,
 123, 258
 Reynolds number, 62, 64, 65, 246,
 247
 root mean square velocity, 32
 roots pump, 42, 100
 rotator flow meter, 85, 86, 87

S

Schmidt number, 68, 161
 scramjet engine, 179
 scrubber, 79, 103, 106, 107
 self-ignition point, 107
 silicon carbide, viii, 12, 20, 113,
 137, 165, 174, 204, 207, 208,
 222, 223, 224, 226, 227, 228

silicon nitride, 13, 20, 138, 140
 smooth laminar structure, 194, 243
 solid precursor, 70, 83, 85, 86, 87
 soot, 7, 105, 106, 168, 189, 190, 233,
 234
 space discretisation, 252, 255, 259
 space shuttle, 12, 174, 179
 Stanski–Krastanov mode, 217
 sticking coefficient, 154, 216, 232,
 236
 streamline injector, 94, 96
 structure zone model, 217
 subtractive method, 2, 3
 supersaturation, 216, 220, 221, 222,
 223, 224, 226, 227, 228
 surface coverage, 155, 156, 157
 surface diffusion, 218, 219, 221, 222
 synthetic oil, 47

T

temperature boundary layer, 62, 67
 temperature gradient, 54, 55, 83,
 180, 182, 183, 184, 188, 191,
 193, 194, 195, 198, 201, 203, 240
 thermal conductivity, 55, 56, 59, 67,
 83, 104, 123, 191, 195, 197
 thermal gradient CVI (TG-CVI), 188
 thermal protection system, 12, 174,
 179
 thermocouple gauge, 52
 thermocouples, 52, 98, 100, 182, 190

thermodynamics, viii, 159, 162
 Thiele number, 170
 titanium boride, 141
 transition diffusion, 60
 transport coefficient, 55, 58
 tungsten silicide, 142
 turbine, 179

U

ultra-high vacuum, 5, 41, 64, 76
 ultra-high vacuum CVD, 76
 UO₂ kernel, 117, 118

V

vacuum system, 38, 39, 41, 99, 168
 vacuum technology, viii, 29
 vapour pressure, 29, 37, 41, 46, 47,
 48, 51, 68, 69, 70, 79, 83
 vapour-liquid-solid, 119, 221
 vapour-solid, 119, 221
 velocity boundary layer, 62, 67, 68,
 246
 velocity gradient, 55, 250
 Vena contracta effect, 95, 96, 99,
 101, 103, 106
 venting, 103, 106
 viscosity collision integral, 56
 viscous flow, 39
 viscous forces, 65, 66
 visualisation, 251, 261
 Volmer–Weber mode, 217

W

Weibull distribution, 175

Weibull modulus, 175

Whisker growth, 119